

# **New transition metal complexes with N, O-donor ligands and their properties**

**THESIS SUBMITTED FOR THE DEGREE OF  
DOCTOR OF PHILOSOPHY (SCIENCE)**

**OF**

**JADAVPUR UNIVERSITY**

**2023**



**BY**

**ARPITA BARMA**

**DEPARTMENT OF CHEMISTRY**

**JADAVPUR UNIVERSITY**

**KOLKATA – 700032**

**WEST BENGAL, INDIA**





## CERTIFICATE FROM THE SUPERVISOR

This is to certify that the thesis entitled “**New transition metal complexes with N,O-donor ligands and their properties**” submitted by Arpita Barma, who got her name registered on 01.10.2018 for the award of Ph.D. (Science) degree of Jadavpur University, is absolutely based upon her work under my supervision and guidance. This thesis or any part of it has not been submitted to any other Institute/ University for the award of any degree or diploma.

Date: 13.01.2023

*Partha Roy*

(Dr. Partha Roy)

Professor

Department of Chemistry

Jadavpur University

Kolkata - 700032

*Professor Partha Roy*  
Department of Chemistry  
Jadavpur University  
Kolkata - 700032

*Dedicated to  
my papa and maa...*

## Acknowledgements

This thesis is the account of five years of work in the field of coordination chemistry at Department of Chemistry, Jadavpur University, Kolkata, India, which would not have been possible without the help of many. First and foremost, I would like to express my gratitude to my supervisor, **Dr. Partha Roy**, for his guidance, constant encouragement and constructive criticisms. Without his restless support and guidance, I would not be able to complete this strenuous journey. His guidance, suggestion, support enable me to develop an understanding of the research subject and to cheerfully engage in new scientific discovery endeavour. I would sincerely acknowledge him for patiently scrutinizing my thesis and making this work a success.

I would like to thank my labmates Ankita Roy, Aradhita Bhattacharjee, Dinesh Maity, Ananta Hazra, Sibshankar Bari, Sneha Ghosh, Suparna Roy for their cooperation and suggestions during my research.

I owe a deep sense of gratitude to my collaborators Professor Corrado Rizzoli, University degli studi di parma, Parma, Italy, Dr. Pritam Ghosh, Vellore Institute of Technology, Professor Parimal Karmakar, Department of Life science & Bio-technology, Jadavpur University, Professor Swapan Kumar Bhattacharya, Department of Chemistry, Jadavpur University for their kind cooperation.

I thank profusely Council of Scientific & Industrial Research (CSIR), New Delhi for financial support to carry out my research work.

I would like to acknowledge Professor Subratanath Koner, the Head, Department of Chemistry, Jadavpur University and Professor Sourav Das, Section in-Charge, Inorganic Chemistry Section, Department of Chemistry, Jadavpur University for providing the departmental facilities and a special thank goes to all the non-teaching staffs of this department. I would also express my sincere gratitude to the authorities of Jadavpur University for allowing me to use necessary infrastructure.

Last but not the least, it would not have been possible to complete this dissertation without the love and support of my parents, Diya, Dadavai, Joy and Aahana whose unflinching faith in my abilities helped me to overcome many obstacles and march ahead in spite of failures. Without them this dissertation is simply impossible.

Date:

(Arpita Barma)  
Department of Chemistry  
Jadavpur University  
Kolkata-700032

	Page
Preface	xii-xiii
List of abbreviations	xiv-xv
<b>Chapter 1: Introduction</b>	<b>1-113</b>
1.1 General introduction	2-3
1.2 Schiff Base Ligands	3-14
1.2.1 2-Hydroxy-1-naphthaldehyde-derived Schiff bases	4-6
1.2.2 Salicylaldehyde-derived Schiff bases	6-8
1.2.3 4-Methyl-2,6-diformylphenol (DFP)-derived Schiff bases	8-9
1.2.4 Types of Schiff bases based on chelating property	9-14
1.3 Schiff Base Transition Metal Complexes	14-22
1.3.1 Schiff Base Transition Metal Complexes of various nuclearity	15-22
1.4 Choice of Metallo-Elements under Investigation	22-23
1.5 Applications of Schiff Base Metal Complexes	24-78
1.5.1 Metal Organic Framework in detection of Pesticides	24-31
1.5.2 Schiff base metal complexes as Catalyst in Biological Activity	32-41
1.5.3 Schiff Base Metal Complexes as Catalyst	41-62
1.5.3.1 Oxidation Reaction	41-47
1.5.3.2 Brief literature survey on catalytic oxidation with Schiff Base Copper Complexes	47-62
1.5.4 Schiff Base Metal Complexes as Electro-Catalysts in Hydrogen Evolution	62-78
1.5.4.1 Reaction Mechanism of HER	64-65
1.5.4.2 Brief literature survey on HER catalyzed by Schiff Base Metal Complexes	65-78
1.6 Aim of the present work	78
1.7 Instrumentation	79-89
1.7.1 Ultraviolet Spectroscopy	79-81
1.7.2 Fluorescence Spectroscopy	81-83
1.7.3 Cyclic Voltammetry	83-86
1.7.4 Gas Chromatography	86-88
1.7.5 Other standard tools used for the characterization of the sample	88-89
1.8 References	89-113
<b>Chapter 2: Density Functional Theory Analysis of Host-Guest Interactions in Cu(II)-Based Metal-Organic Frameworks for Pesticide Detection</b>	<b>114-160</b>
2.1 Introduction	115
2.2 Experimental Section	116-117
2.2.1 Materials and Physical Methods	116
2.2.2 Synthesis of [Cu(4,4'-bipy)(sa)] <sub>n</sub> (2.1)	116
2.2.3 Crystallographic Data Collection and Refinement	117
2.3 Results and Discussion	118-157
2.4 Conclusions	157-158
2.5 References	158-160

<b>Chapter 3:</b>	<b>Synthesis and characterization of a mononuclear nickel(II) complex with N,O-donor ligand: Its DNA/HSA protein binding properties and tumor suppressive function</b>	<b>161-195</b>
3.1	Introduction	162-163
3.2	Experimental Section	163-166
3.2.1	Materials and methods	163-164
3.2.2	Synthesis	164
3.2.2.1	Synthesis of 1-((2-piperidin-1-yl)ethylimino)methyl)naphthalene-2-ol (HL)	164
3.2.2.2	Synthesis of Complex 3.1	164
3.2.3	X-ray data collection and structure determination	164-165
3.2.4	DNA binding and cleavage studies	165
3.2.5	HSA binding studies	165
3.2.6	MTT assay	165
3.2.7	Apoptotic nuclear morphology study by DAPI staining	165
3.2.8	Roles of caspase-3 in complex-induced apoptosis in A549 cells	165-166
3.3	Results and discussion	167-190
3.3.1	Synthesis and characterization	167-171
3.3.1.1	Synthesis and characterization of HL	167-168
3.3.1.2	Synthesis and characterization of complex 3.1	169-171
3.3.2	Crystal structure of complex 3.1	171-172
3.3.3	DNA binding studies	173-178
3.3.3.1	UV-visible spectral studies	173-174
3.3.3.2	Fluorescence quenching studies	174-175
3.3.3.3	Circular Dichroism spectral studies	175-176
3.3.3.4	DNA cleavage studies	176-177
3.3.3.5	DNA cleavage in the presence of reactive oxygen species	177-178
3.3.3.6	DNA interaction in the presence of groove binders	179
3.3.4	HSA binding studies	179-188
3.3.4.1	Absorption spectra studies	179-181
3.3.4.2	Fluorescence quenching studies	181-184
3.3.4.3	Energy transfer mechanism and binding distance between complex 3.1 and HSA	184-185
3.3.4.4	IR spectral studies	185-186
3.3.4.5	3D fluorescence spectral studies	186-187
3.3.4.6	CD spectral studies on changes of the HSA conformation with complex 3.1	187-188
3.3.4.7	Oxidative damage of HSA by complex 3.1	188
3.3.5	Cytotoxicity evaluation	188-189
3.3.5.1	MTT assay	188-189
3.3.6	Apoptosis evaluation	189-190
3.3.6.1	Apoptotic nuclear morphology study by DAPI staining	189-190
3.3.6.2	Treatment of complex 3.1 in A549 promotes apoptosis	190
3.4	Conclusions	191
3.5	References	191-195



<b>Chapter 4:</b>	<b>Dinuclear Copper(II) Complexes with N,O Donor Ligands: Partial Ligand Hydrolysis and Alcohol Oxidation Catalysis</b>	<b>196-226</b>
4.1	Introduction	197-199
4.2	Experimental Section	199-201
4.2.1	Materials and physical methods	199-200
4.2.2	Synthesis	200-201
4.2.2.1	Synthesis of 3,3'-(2-hydroxy-5-methyl-1,3-phenylene)bis(methan-1-yl-1-ylidene)bis(azan-1-yl-1-ylidene)bis(2,2-Dimethylpropane-1-ol) (H <sub>3</sub> L')	200
4.2.2.2	Synthesis of 2,2'-(((2-hydroxy-5-methyl-1,3-phenylene)bis(methanylylidene))bis(azanylylidene))bis(propane-1-ol) (H <sub>3</sub> L'')	200
4.2.2.3	Synthesis of [Cu <sub>2</sub> (L <sup>1</sup> ) <sub>2</sub> ] (4.1)	200
4.2.2.4	Synthesis of [Cu <sub>2</sub> (L <sup>2</sup> ) <sub>2</sub> ] (4.2)	201
4.2.3	X-ray data collection and structure determination	201
4.2.4	Alcohol oxidation procedure	201
4.3	Results and discussion	202-220
4.3.1	Synthesis of H <sub>3</sub> L', H <sub>3</sub> L'', complex 4.1 and complex 4.2	202-204
4.3.2	Crystal structures of complex 4.1 and 4.2	205-207
4.3.3	Room temperature magnetic moment determination	207-208
4.3.4	UV-vis spectral studies	208-209
4.3.5	FT-IR spectral studies	209-210
4.3.6	Mass spectral studies	210-211
4.3.7	Electrochemical studies	211-213
4.3.8	Alcohol oxidation studies	213-220
4.4	Conclusions	220
4.5	References	220-226
<b>Chapter 5:</b>	<b>Mononuclear nickel(II) complexes as electrocatalyst in hydrogen evolution reactions: Effect of alkyl side chain length</b>	<b>227-289</b>
5.1	Introduction	228-230
5.2	Experimental Section	230-233
5.2.1	Materials and physical methods	230
5.2.2	Synthesis of Complexes 5.1, 5.2 and 5.3 as the catalyst	230-232
5.2.2.1	Synthesis of 1-((4-hydroxybutylimino)methyl)naphthalen-2-ol (HL <sup>1</sup> ), 1-((5-hydroxypentylimino)methyl)naphthalen-2-ol (HL <sup>2</sup> ) and 1-((6-hydroxyhexylimino)methyl)naphthalen-2-ol (HL <sup>3</sup> )	230-231
5.2.2.2	Synthesis of [Ni(L <sup>1</sup> )] (5.1)	231-232
5.2.2.3	Synthesis of [Ni(L <sup>2</sup> )] (5.2) and [Ni(L <sup>3</sup> )] (5.3)	232
5.2.3	X-ray data collection and structure determination	232-233
5.3	Results and Discussion	233-284
5.3.1	Synthesis of ligands and their characterization by ESI mass and <sup>1</sup> H spectral analysis	233-236
5.3.2	Characterization of complexes 5.1, 5.2 and 5.3	236-284
5.3.2.1	Crystal structures of complexes 5.1, 5.2 and 5.3	236-240
5.3.2.2	ESI-mass, FT-IR, UV-vis and <sup>1</sup> H NMR spectral characterization of the complexes	240-247
5.3.2.3	Electrochemistry	248-265
5.3.2.3.1	Cyclic voltammetric studies	248-251

	5.3.2.3.2	Electrocatalytic Hydrogen Evolution in DMF: CV Studies	251-256
	5.3.2.3.3	Electrocatalytic Hydrogen Evolution: CPE Studies	256-262
	5.3.2.3.4	Determination of the reaction mechanism of HER using Tafel analysis	262-263
	5.3.2.3.5	Electrocatalytic Hydrogen Evolution: Control Experiments	263-264
	5.3.2.4	Computational analysis of catalysts and intermediates by DFT-D4	265-284
5.4	Conclusions		284-285
5.5	References		285-289
<b>Chapter 6: Mononuclear nickel and copper complexes as electrocatalyst for generation of hydrogen from acetic acid</b>			<b>290-318</b>
6.1	Introduction		291-292
6.2	Experimental Section		292-294
	6.2.1	Materials and physical methods	292-293
	6.2.2	Syntheses of ligand and complexes	293-294
	6.2.2.1	Synthesis of 1,1'-(1E,1'E)-(propane-1,2-diylbis(azan-1-yl-1-ylidene))bis(methan-1-yl-1-ylidene)dinaphthalen-2-ol (H <sub>2</sub> L)	293
	6.2.2.2	Synthesis of [Ni(L)] (6.1)	293
	6.2.2.3	Synthesis of [Cu(L)] (6.2)	293-294
	6.2.3	X-ray data collection and structure determination	294
6.3	Results and discussion		294-314
	6.3.1	Synthesis and characterization of the ligand	294-296
	6.3.2	Characterization of the complexes	296-314
	6.3.2.1	Crystal structure of complex 6.1	296-298
	6.3.2.2	UV-vis spectral studies	298-299
	6.3.2.3	FTIR spectral studies	299-300
	6.3.2.4	ESI-mass spectral studies	300-301
	6.3.2.5	Electrochemistry	301-314
	6.3.2.5.1	Cyclic voltammetric studies	301-303
	6.3.2.5.2	Electrocatalytic Hydrogen Evolution in DMF: CV Studies	303-307
	6.3.2.5.3	Stability analysis of the catalyst	307-308
	6.3.2.5.4	Electrocatalytic Hydrogen Evolution: CPE Studies	308-312
	6.3.2.5.5	Electrocatalytic Hydrogen Evolution: Control Experiments	312-313
	6.3.2.5.6	Comparative discussion	313-314
6.4	Conclusions		314
6.5	References		314-318
<b>List of Publications</b>			<b>320</b>



## **Preface**

The work presented in this thesis entitled “**New transition metal complexes with N, O-donor ligands and their properties**” has been carried out in the Department of Chemistry, Jadavpur University during the period of 2017-2022.

Different techniques like UV-Vis, FTIR, <sup>1</sup>H NMR, Mass spectrometry, Cyclic Voltammetry, and single crystal X-ray diffraction analysis have been utilized to characterize the synthesized products. In some cases, computational studies using density functional theory (DFT) have been performed for a better understanding of the experimental observations.

The Thesis consists of six chapters which are summarized as follows:

**Chapter 1** gives a concise introduction on coordination chemistry followed by brief and recent literature survey on (a) Schiff bases derived from 2-Hydroxy-1-naphthaldehyde, Salicylaldehyde, 4-Methyl-2,6-diformylphenol, (b) Schiff base transition metal complexes, (c) Applications of Schiff base metal complexes in various fields of research. A brief overview of the present work is also highlighted.

**Chapter 2** describes a Cu(II)-Based Metal-Organic Framework whose response towards toxic pesticides has been investigated by density functional theory (DFT) analysis.

**Chapter 3** represents synthesis and characterization of a mononuclear nickel(II) complex with N, O-donor ligand, which plays a significant role in DNA/HSA protein binding and exhibits selective cytotoxicity towards cancer cell.

**Chapter 4** deals with synthesis and characterization of two dinuclear copper(II) complexes with partially hydrolyzed DFP based ligands. Both of these complexes have been used as effective catalysts for the oxidation of some benzyl alcohols in the presence of tert-butyl hydroperoxide (TBHP) as the oxidant.

**Chapter 5** presents synthesis and characterization of three mononuclear nickel(II) complexes which act as the electrocatalyst for hydrogen evolution reaction (HER) using acetic acid (AA) and trifluoroacetic acid (TFA) as the proton source in DMF. Some theoretical calculations have also been performed with insight in hydrogen evolution mechanism and effect of chain lengths of the ligands on the catalytic activity.

**Chapter 6** deals with electrocatalytic proton reduction reaction (or HER) by two neutral, monomeric transition metal complexes, where Ni(II) and Cu(II) have been chosen as the metal

centres. Both of them have been synthesized by conventional method and characterized by several standard methods. The effect of change of metal centre on the generation of hydrogen evolution reaction has been examined.

Date:

(Arpita Barma)  
Department of Chemistry  
Jadavpur University  
Kolkata-700032

## **List of Abbreviations**

DFP	4-Methyl-2,6-diformylphenol
DTBC	di-tert-Butylcatechol
TEMPO	(2,2,6,6-Tetramethylpiperidin-1-yl)oxyl
Py	Pyridine
TBHP	tert-Butyl hydroperoxide
NaOH	Sodium hydroxide
TFA	Trifluoroacetic acid
AcOH	Acetic acid
H <sub>2</sub> O <sub>2</sub>	Hydrogen peroxide
SOD	Superoxide dismutase
PBS	Phosphate buffered saline
SRB	Sulforhodamine B
MOF	Metal–organic framework
PCP	Porous coordination polymer
BDC	1,4-Benzene dicarboxylic acid
BTC	1,3,5-Benzene tricarboxylic acid
H <sub>3</sub> Imdc	4,5-Imidazole dicarboxylic acid
BPDC	Biphenyldicarboxylic acid
BPy	Bipyridine
BPEE	1,2-bis(4-pyridyl)ethylene
PANI	Polyaniline
CPF	Chlorpyrifos
TMB	3,3',5,5'-tetramethylbenzidine
MOF	Metal–organic framework
PCP	Porous coordination polymer
BDC	1,4-Benzene dicarboxylic acid
BTC	1,3,5-Benzene tricarboxylic acid
H <sub>3</sub> Imdc	4,5-Imidazole dicarboxylic acid
BPDC	Biphenyldicarboxylic acid
BPEE	1,2-bis(4-pyridyl)ethylene
NT	Nanotube
DFT	Density functional theory
DSPME	Dispersive solid phase microextraction
SBSE	Stir-bar sorptive extraction
BET	Brunauer–Emmett–Teller
NMR	Nuclear magnetic resonance Spectroscopy
SEM	Scanning electron microscope
EDS	Energy-dispersive X-ray spectroscopy
XRD	X-ray diffraction
FTIR	Fourier Transform Infrared Spectroscopy
UV	Ultraviolet
vis	Visible
CD	Circular dichroism
CV	Cyclic voltammetry
LSV	Linear sweep voltammetry
$\lambda$	Wavelength
%T	Percentage of transmittance
h	Hours

MS	Mass spectrometry
GC	Gas chromatography
HPLC	High-performance liquid chromatography
CD-IMS	Corona discharge ion mobility spectrometry
DNA	Deoxyribonucleic acid
BSA	Bovine serum albumin
HSA	Human serum albumin
MMT	Montmorillonite
OMMT	Organically modified montmorillonite
PEG	Polyethylene glycol
MTT	3-(4,5-dimethylthiazol-2-yl)-2,5-diphenyltriazolium bromide
MEDPT	N,N-bis[3-aminopropyl]methylamine
HER	Hydrogen evolution reaction
CPE	Controlled potential electrolysis
TOF	Turnover frequency
TON	Turnover number
DMF	N,N-dimethylformamide
THF	Tetrahydrofuran
H <sub>2</sub> O	Water
ACN	Acetonitrile
EtOH	Ethanol
A	Crystallographic distance along 'x' axis of a unit cell (in angstrom)
B	Crystallographic distance along 'y' axis of a unit cell (in angstrom)
C	Crystallographic distance along 'z' axis of a unit cell (in angstrom)
A	Crystallographic angle in a unit cell between b and c (in degree)
B	Crystallographic angle in a unit cell between c and a (in degree)
Γ	Crystallographic angle in a unit cell between a and b (in degree)
P	Density (in g cm <sup>-3</sup> )
Mo-Kα	Molybdenum Kα radiation
F(000)	Crystallographic (000) plane
ORTEP	Oak Ridge thermal ellipsoid plot





# Chapter 1

## Introduction

### **Abstract**

Discussion on Schiff base ligands and Schiff base transition metal complexes are incorporated in this chapter. A brief literature survey is also presented here which contains four parts. The first one deals with some recently reported 2-Hydroxy-1-naphthaldehyde-derived, Salicylaldehyde-derived, 4-Methyl-2,6-diformylphenol (DFP)-derived Schiff bases along with types of Schiff bases based on chelating property. It is followed by a brief literature survey on Schiff base transition metal complexes of varying nuclearity. The next one consists of discussion on application of Schiff base metal complexes. Lastly it contains a concise discussion on the aim of the present thesis work which is elaborately discussed in the following chapters.

## 1.1 General introduction

Coordination chemistry is a branch of inorganic chemistry which deals with the study of coordination compounds where a metal ion is attached to ligands by coordinate bonds. A coordination compound is represented as follows:

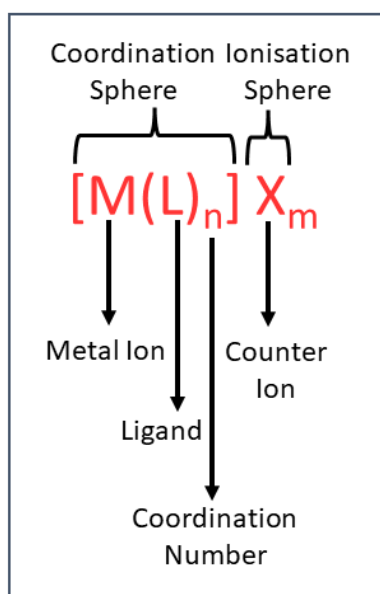


**Figure 1.1:** Representation of a coordination compound.

The coordination number defines the geometry of the complexes (**Table 1.1**). Werner's theory, valence bond theory, crystal field theory, ligand field theory or adjusted crystal field theory have been proposed to describe the bonding of such complexes. The characteristic properties such as colour, magnetism, variable oxidation states make these coordination complexes more attractive towards the researchers.

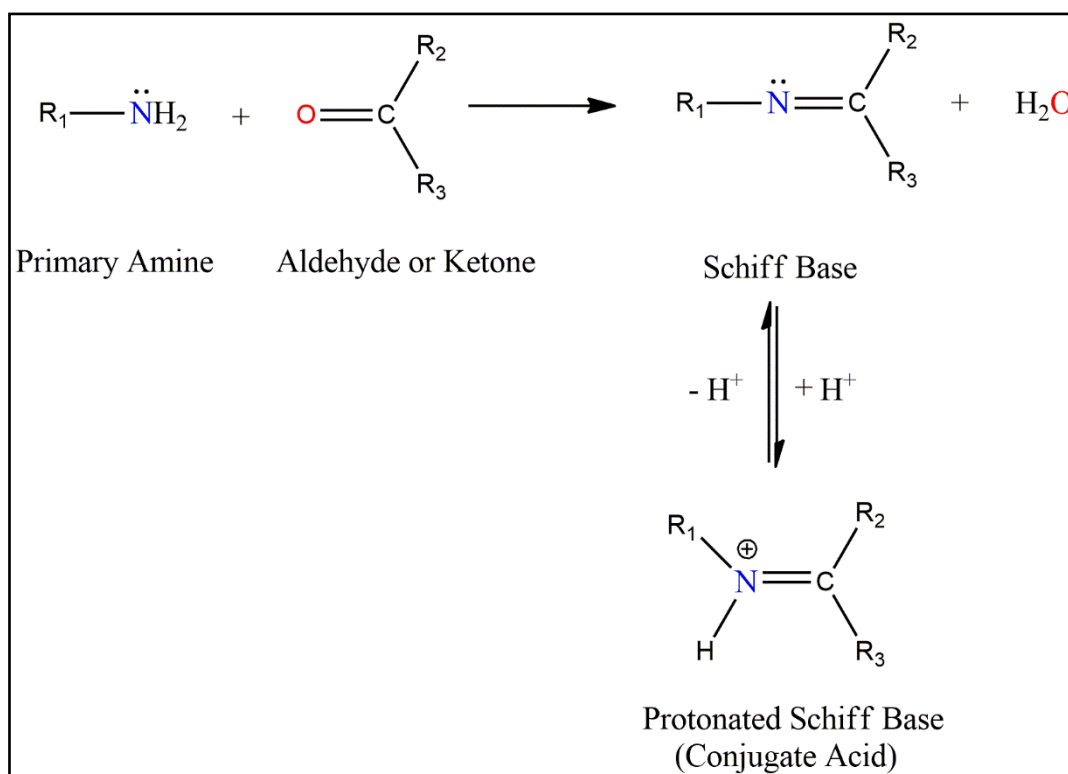
**Table 1.1:** Coordination Numbers and the corresponding geometries.

Coordination No.	Geometry
2	Linear
3	Trigonal planar, Trigonal pyramidal
4	Square planar, Tetrahedral
5	Trigonal bipyramidal
6	Octahedral, Trigonal prismatic
7	Pentagonal bipyramidal, Monocapped octahedral Monocapped trigonal prismatic
8	Dodecahedral, Hexagonal bipyramidal Cube, Square antiprismatic, Bicapped trigonal prismatic
9	Tricapped trigonal prismatic

In the recent years, coordination chemistry of transition metal complexes is gaining much attention due to their versatile applications in the various fields of chemical and medical sciences. It has inspired the researchers to design and fabricate novel metal complexes, far and wide.

### 1.2 Schiff Base Ligands

The term “Schiff base” is named after Hugo Schiff (1834–1915),<sup>1.1a,b</sup> who is an Italian naturalized chemist and German by nationality. He was renowned for the synthesis of the first so-called Schiff base in 1864<sup>1.2a,b</sup> and paved the path of the chemistry of Schiff base. Schiff bases are prepared by one step condensation between any primary amine (NH<sub>2</sub>) and a ketone (CO) or an aldehyde (CHO) under specific conditions of temperature and pH with a very high yield (Scheme 1.1).<sup>1.3a-h</sup>



**Scheme 1.1:** General scheme for formation of Schiff bases.

From the structural view point, a Schiff base (also known as azomethine or imine) is a nitrogen analogue of a ketone or aldehyde in which the carbonyl group (CO) has been replaced by an azomethine or imine group. The structural unit of Schiff bases also possesses many other hetero-elements like oxygen (O) and sulphur (S) as main component for chelate formation with metals. The bonding ability of Schiff base ligands depends largely on the nature of donor atoms acting as coordination site, steric factors and their electronegativity. Electron donating character of the imine double bond due to the presence of lone pair electrons on nitrogen atom

(N) and low electronegativity of nitrogen, N-atom of the azomethine group ( $>C=N$ ) make Schiff base an active ligand. Presently, active and well-designed Schiff base ligands are considered as “privileged ligands”<sup>1.4a,b</sup> because of the easy tunability of their stereo-electronic structures and they make an important area of research with increasing interest due to the simple method of synthesis, variation in properties, versatile nature and diverse ranges of applications such as biological activities,<sup>1.5a-c</sup> catalytic activities,<sup>1.6a-f</sup> electroluminescent properties,<sup>1.7a-c</sup> fluorescence properties,<sup>1.8a-c</sup> non-linear optical (NLO) properties,<sup>1.9</sup> applications in sensors<sup>1.10</sup> and organic photovoltaic materials.<sup>1.11</sup>

Among all Schiff bases ‘Salen type’ Schiff bases are perhaps the most popular one. Schiff base formed by the condensation of salicylaldehyde and ethylenediamine is almost universally denoted by ‘H<sub>2</sub>salen’ [**sal** (from salicylaldehyde) and **en** (from ethylene diamine) = **salen**].<sup>1.12a,b</sup> Such N<sub>2</sub>O<sub>2</sub> donor Schiff base ligands have been reported in the chemical literature.<sup>1.13a-d</sup>

Here, the discussion is focussed on (a) 2-hydroxy-1-naphthaldehyde-derived Schiff bases, (b) salicylaldehyde-derived Schiff bases and (c) 4-methyl-2,6-diformylphenol-derived Schiff bases resulting in different ratios of N- and O-donor atoms that leads to NO<sub>2</sub>, NO<sub>3</sub>, NO<sub>4</sub>, and N<sub>2</sub>O type of core structure.

### 1.2.1 2-Hydroxy-1-naphthaldehyde-derived Schiff bases

2-Hydroxy-1-naphthaldehyde is usually used as an excellent functionalised backbone for the preparation of different transition metal–salen complexes.<sup>1.14a-e</sup> Reimer-Tiemann formylation of 2-naphthol is the best method to prepare it.<sup>1.15</sup> The salicylic functional group present in 2-hydroxy-1-naphthaldehyde is a popular reaction counterpart for nucleophilic addition reactions due to the presence of carbonyl group which is activated by a phenolic hydrogen through an intramolecular hydrogen bond formation. 2-Hydroxy-1-naphthaldehyde is one of the most extensively used aldehyde for the development of different Schiff base metal complexes due to its donor as well as acceptor sites. By the chemical manipulation of the amine group, we can develop a variety of transition metal complexes which is one of main objectives of this thesis.



Qi *et al*<sup>1.16</sup> synthesized Cu(II) and Ni(II) complexes based on Schiff base ligand **1** and investigated the cancer cytotoxicity, cell migration, and apoptosis properties of both complexes.

Kurt *et al*<sup>1.17</sup> developed the Schiff base ligand **2** which is further reacted with 2,6-diamino pyridine to form another ligand. It was then utilized to form Cu(II), Fe(II) and Pd(II)

complexes. DNA binding properties of the ligand as well as the metal complexes were investigated.

Sarkar *et al*<sup>1,18</sup> reported two 2-hydroxy-1-naphthaldehyde based Schiff base ligands, **3** and **4**. Three new mononuclear manganese(III) complexes were derived from these ligands among them one possesses catalase activity.

Narang *et al*<sup>1,19</sup> reported ligands formed by condensation of 2-hydroxy-1-naphthaldehyde with *o*-phenylenediamine (**4**) and of 2-hydroxy-1-naphthaldehyde with 1,8-diaminonaphthalene (**5**) in 2:1 molar ratio and the ligands were characterized using FTIR and NMR techniques. These ligands were used to form complex with various metallic salts like  $\text{CoCl}_2 \cdot 6\text{H}_2\text{O}$ ,  $\text{CoNO}_3 \cdot 7\text{H}_2\text{O}$ ,  $\text{CoSO}_4$ ,  $\text{FeCl}_3$  and have been successfully anchored onto montmorillonite (MMT), organically modified montmorillonite (OMMT, Closite30B), and polyethylene glycol (PEG). They exhibited good catalytic activity and some of them (salen– $\text{CoSO}_4$  and naphthen– $\text{CoSO}_4$ ) were used as catalysts along with tetradecyltrimethyl ammonium bromide as cocatalyst for the chemical fixation of carbon dioxide through its reaction with propylene oxide to give propylene carbonate.

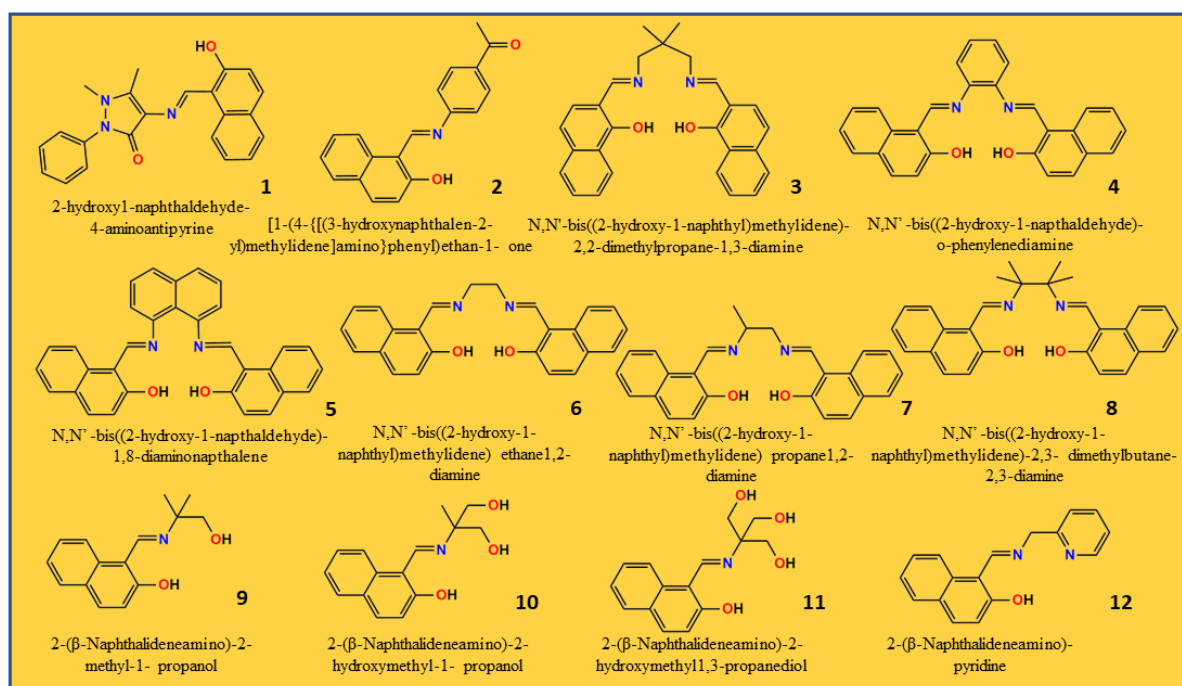


**Figure 1.2:** 2-hydroxy-1-naphthaldehyde-derived Schiff bases

Sato *et al* and Li *et al*<sup>1,20a,b</sup> synthesized a very simple 2-hydroxy-1-naphthaldehyde based Schiff base ligand **6** by mixing 2-hydroxy-1-naphthaldehyde and ethylene diamine in 2:1 mole ratio. The former also reported the ligand **8**. Here, manganese(III) acetate dihydrate and sodium isocyanate complexed with the ligands and the resulting complexes were utilized for magnetic susceptibility measurements in the range of 4.4-300 K. Whereas for the latter, an exceptional

six-connected 3D nanowater framework constructed from turbine-type  $(\text{H}_2\text{O})_{18}$  clusters has been observed in the ligand derived Mn(III) Schiff base complex  $[\text{Mn}(\text{vanen})(\text{Cl})(\text{H}_2\text{O})] \cdot 2\text{H}_2\text{O}$  (where,  $\text{H}_2\text{vanen} = \text{N},\text{N}'\text{-bis}(3\text{-methoxysalicylidene})\text{-}1,2\text{-diaminoethane}$ ).

Kara and co-workers<sup>1,21</sup> reported Schiff base ligand **7** synthesized by the reaction of 1,2-diaminopropane with 3-methoxysalicylaldehyde. It formed a mononuclear manganese complex, Diaqua $[\text{N},\text{N}'\text{-bis}(3\text{-methoxysalicylidene})\text{propane-}1,2\text{-diaminato}]$ manganese(III) nitrate monohydrate.

Rao *et al*<sup>1,22</sup> reported four Schiff base ligands, **9-12**, where 2-hydroxy-1-naphthaldehyde was condensed with a variety of amines having additional ligating centres, and the resulting products were characterized by single crystal XRD study, and also by analytical and spectral methods.

### 1.2.2 Salicylaldehyde-derived Schiff bases

Salicylaldehyde is another key precursor to a variety of transition metal–salen complexes due to the presence of salicylic functional group. By introducing different substituents (Cl or Br) on the benzene ring of the salicylaldehyde unit and by varying the amines a series of Schiff bases were developed.

Shi *et al*<sup>1,23</sup> reported a series of Schiff base ligands (compounds **1-26**) (**Figure 1.3**) which were prepared by condensation between 5-chloro-salicylaldehyde and primary amines. The chemical structures of all these 26 compounds were established by means of elemental and ESI-MS, <sup>13</sup>C



NMR, <sup>1</sup>H NMR spectral analyses. These compounds were assayed for antibacterial (*Staphylococcus aureus*, *Pseudomonas fluorescens*, *Escherichia coli* and *Bacillus subtilis*) and antifungal (*Trichophyton rubrum*, *Candida albicans* and *Aspergillus niger*) activities by MTT (3-(4,5-dimethylthiazol-2-yl)-2,5-diphenyl tetrazolium bromide) method.

Satapathi *et al*<sup>1,24</sup> synthesized Cu(II) and Ni(II) complexes developed by using the Schiff base ligand **27**. Both these complexes were employed to inspect their DNA and HSA binding efficacy.

Deilami *et al*<sup>1,25</sup> prepared a Schiff base ligand **28** from the reaction of 5-bromo salicylaldehyde and allylamine. It was then complexed with  $\text{Zn}(\text{NO}_3)_2 \cdot 6\text{H}_2\text{O}$ ,  $\text{Ni}(\text{OAc})_2 \cdot 4\text{H}_2\text{O}$ , and  $\text{CoCl}_2 \cdot 6\text{H}_2\text{O}$ . The ligand and its complexes were characterized by elemental analysis, UV-Vis, FT-IR spectroscopy and <sup>1</sup>H-NMR technique and the electrochemical properties of the three complexes were investigated.

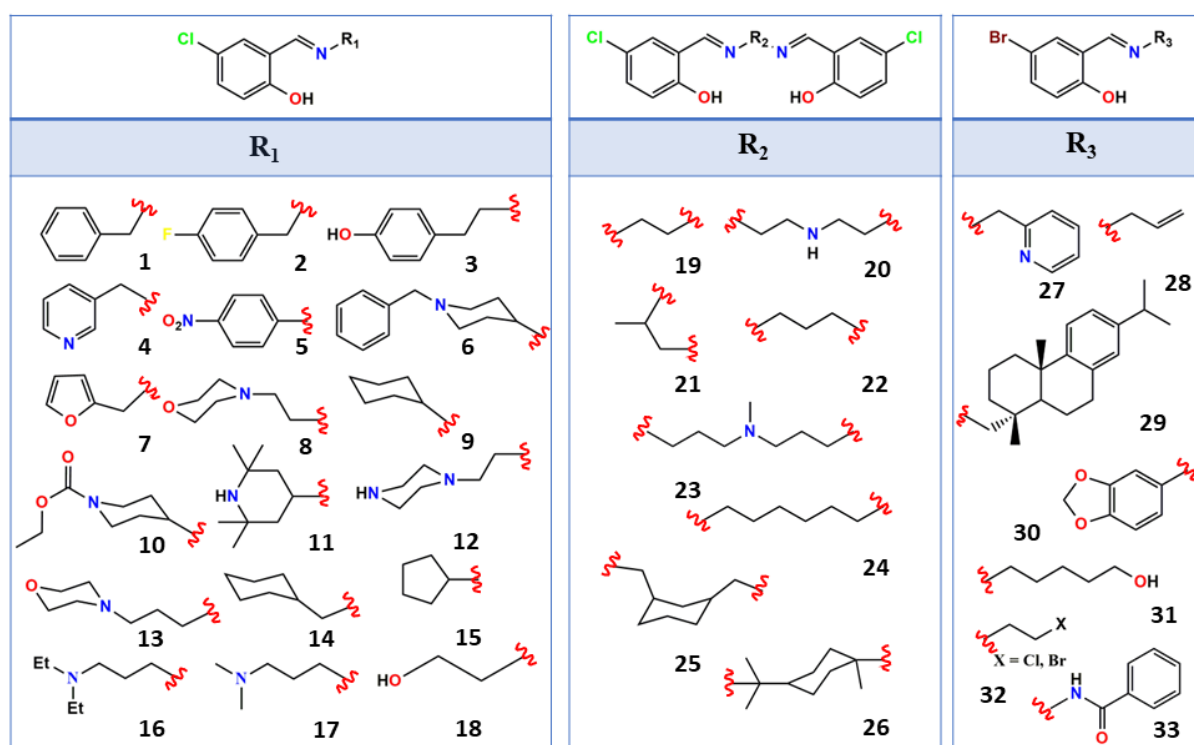


**Figure 1.3:** 5-Chloro and 5-Bromo salicylaldehyde-derived Schiff bases

Fei *et al.*<sup>1.26</sup> reported synthesis and characterization of a chiral Schiff base (**29**) and its chiral dinuclear copper complex. The interactions of the Schiff base as well as the complex with salmon sperm DNA were investigated by UV, fluorescence, CD spectroscopic techniques and viscosity measurements,

Metal complexes of Cd(II), Co(II), Cu(II), Fe(III), Hg(II), Mn(II) Ni(II), Zn(II) and Ag(I) were synthesized by Sundararajan *et al.*<sup>1.27</sup> from Schiff base ligand, **30**, synthesized by the condensation of 5-bromo salicylaldehyde and 3,4-(methylenedioxy)aniline. They were characterized by different standard techniques. The ligand and its metal complexes were tested for their antifungal and antibacterial inhibition potential against some pathogens revealed that metal complexes were more biologically active than the free ligand. The percentage antioxidant activities were also observed more for the complexes than that of the ligand.

Another 5-bromo-salicylaldehyde based Schiff base ligand (**31**) was reported by Modak *et al.*<sup>1.28</sup> which was used to synthesize an aqua bridged dinuclear nickel(II) complex. They investigated catecholase activity and magnetic properties of the complex.

Kursunlu *et al.*<sup>1.29</sup> investigated the synthesis and spectroscopic characterization of some Schiff bases derived from 5-bromo-salicylaldehyde (**32**) and their corresponding metal complexes.

This study led to the conception that the Schiff bases derived from 5-bromo-salicylaldehyde would possess potential antimicrobial properties.

Patel *et al*<sup>1,30</sup> reported mixed ligand copper(II) and nickel(II) complexes which involved the ligand **33**. They were well characterized. Antibacterial and DNA cleavage activity of these complexes were investigated.

### 1.2.3 4-Methyl-2,6-diformylphenol (DFP)-derived Schiff bases

4-Methyl-2,6-diformylphenol (DFP), also called 2-hydroxy-5-methylbenzene-1, 3-dialdehyde and 2-hydroxy-5-methylisophthalaldehyde, is another excellent functionalised backbone for the synthesis of different transition metal complexes. In 1970, Robson, for the first time, reported a dinucleating N,O donor Schiff-base ligand involving 2-aminophenol as the amine and 4-methyl-2,6-diformylphenol as the aldehyde.<sup>1,31a,b</sup> As DFP possesses two formyl groups, there is plenty of scope to design a series of macrocyclic as well as acyclic ligands<sup>1,32a-d</sup> (**Figure 1.4**) suitable for synthesis of effective multinuclear transition metal complexes.<sup>1,33a-d</sup> Thus, in the emerging area of cluster-based coordination systems, a notable progress has been observed in recent times on the formation and growth of 3d metal ion clusters involving the ligands derived from nucleating ligand, DFP.

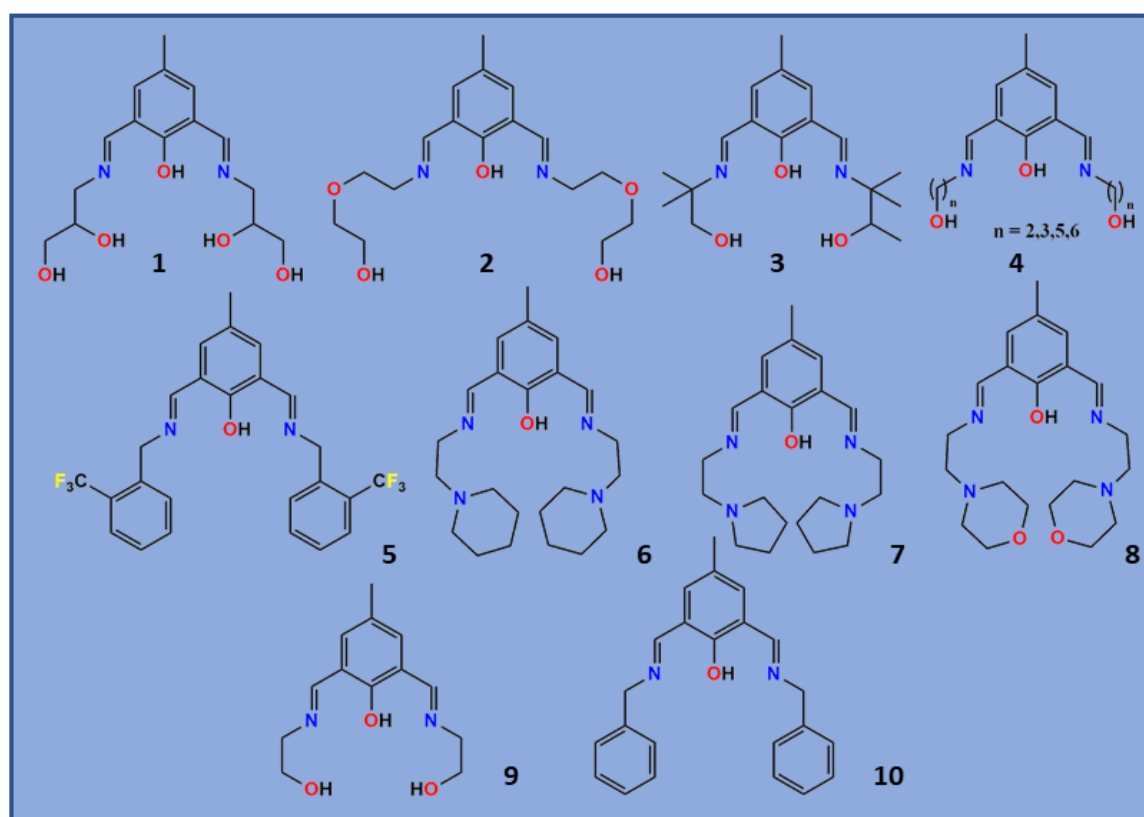


**Figure 1.4:** 4-Methyl-2,6-diformylphenol-derived Schiff bases



Naskar *et al*<sup>1.34</sup> reported DFP based ligand (**1**) for fluorescent and colorimetric detection of  $\text{Cu}^{2+}$  in Tris-buffer (pH 7.4) solution.

Mahapatra *et al*<sup>1.35</sup> reported ether-alcohol arm bearing DFP based ligand (**2**) and then they examined its role to establish the function of carboxylate ancillary ligands in the growth of  $[\text{Cu}_4]$  aggregates around oxido and hydroxido nuclei.

Pait *et al*<sup>1.36</sup> reported the ligand (**3**), synthesized from the one step condensation of 2,6-diformyl-4-methylphenol and 2-amino-2-methyl-1-propanol in methanol. It was utilized for the formation of carboxylato and carbonato bridged nickel(II)-based aggregates. The temperature dependence of the magnetic properties of these samples were investigated.

Halder *et al*<sup>1.37</sup> reported five DFP based ligands, (**4**), where the amine chain length was varied. Four tetranuclear and one pentanuclear complexes of Cu(II) were synthesized from these ligands. These multinuclear complexes were utilized as the catalyst for the epoxidation of olefins in the presence of TBHP as the oxidant under mild conditions.

Jana *et al*<sup>1.38</sup> reported the ligand (**5**) synthesized from 2-trifluoromethyl-1-phenylmethanamine and 4-methyl-2,6-diformylphenol in acetonitrile. It then formed a tetranuclear copper(II) complex for which the temperature dependent magnetic property was investigated.

Roy *et al*<sup>1.39</sup> reported three DFP base ligands (**6-8**) synthesized by 1:2 Schiff-base condensation in acetonitrile between DFP and 1-(2-aminoethyl)-piperidine, 1-(2-aminoethyl)-pyrrolidine and 4-(2-aminoethyl)-morpholine, respectively. Here the  $\text{N}_4\text{O}$  donors were used for the detection of  $\text{Zn}^{2+}$  ion.

Mandal *et al*<sup>1.40</sup> reported DFP based ligand (**9**) used in self-assembly of an azido-bridged  $[\text{Ni}^{\text{II}}_6]$  cluster featuring four fused defective cubanes. The ability of the ligand **9** to aggregate, together with the bridging properties of azide, was explored here with the preparation of the hexanuclear complex. The magnetic properties of the complex were investigated through variable-temperature susceptibility measurements.

Roy *et al*<sup>1.41</sup> Roy *et* synthesized the ligand (**10**) by refluxing the mixture of 4-methyl-2,6-diformylphenol and phenylmethanamine in acetonitrile. The ligand was used as zinc ion-selective luminescent probe for biological application under physiological conditions.

#### **1.2.4 Types of Schiff bases based on chelating property**

Based on number of donor atoms available for coordination with metal ion, ligands may be of several types. They are shown schematically and in **Table 1.2** with examples:

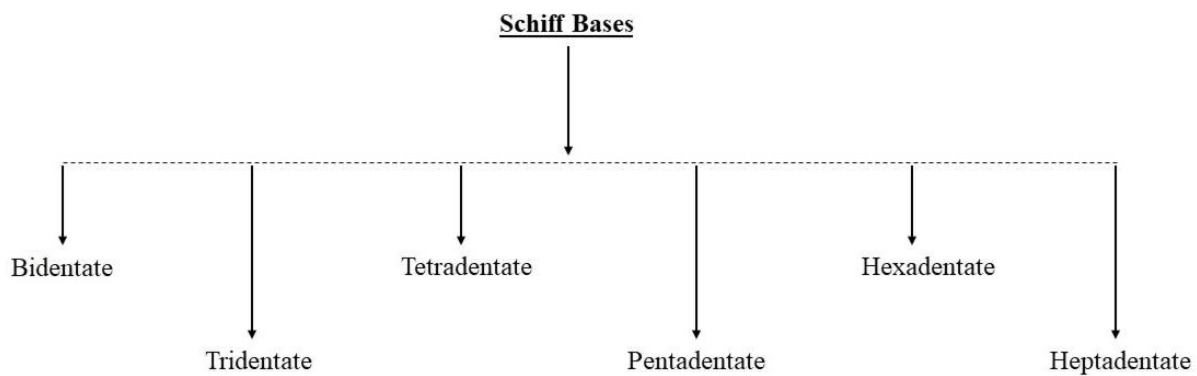
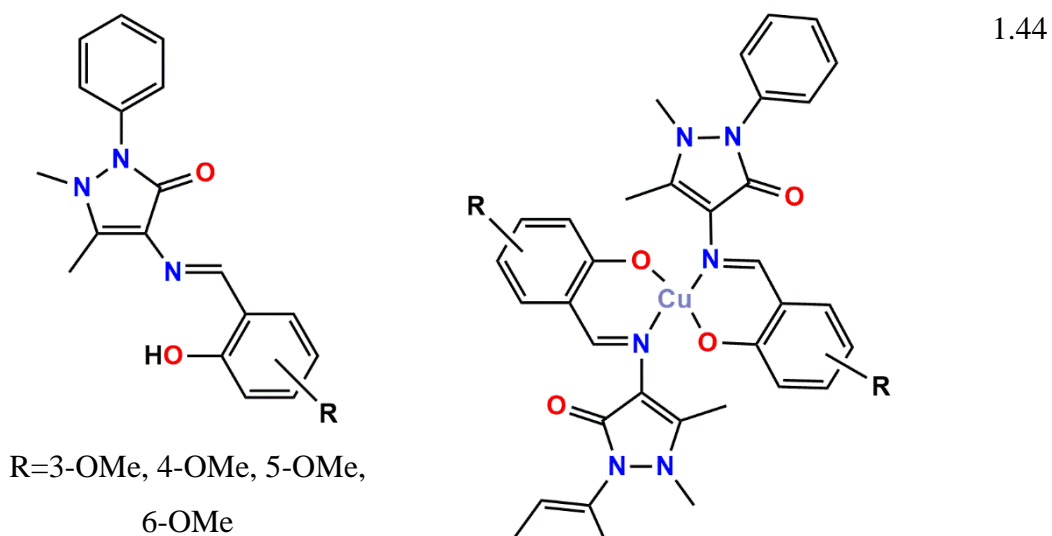
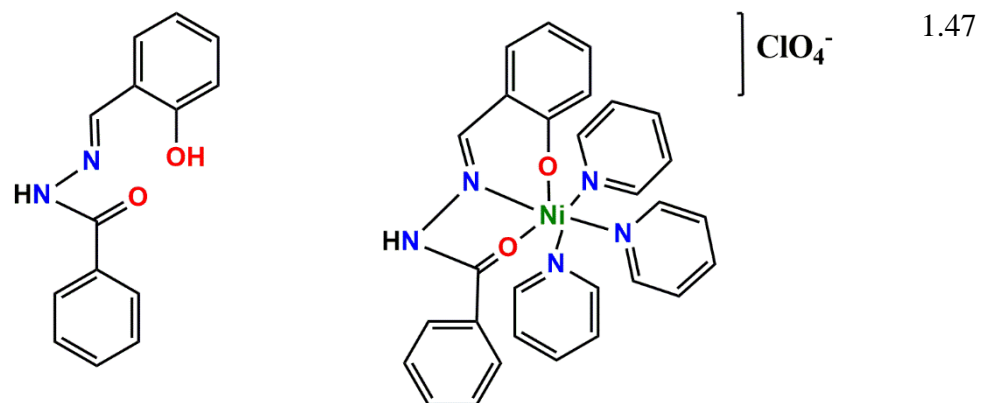
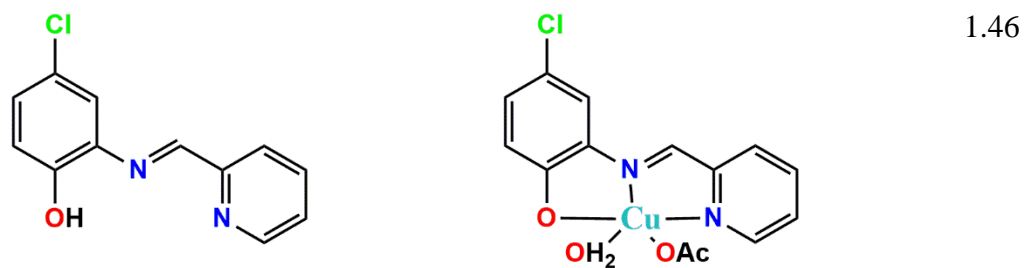
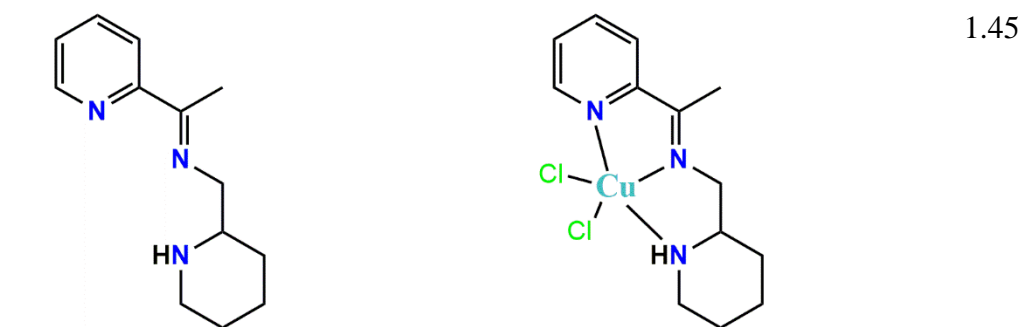


**Table 1.2:** Types of Schiff bases based on chelating property.

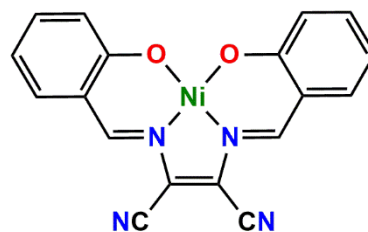
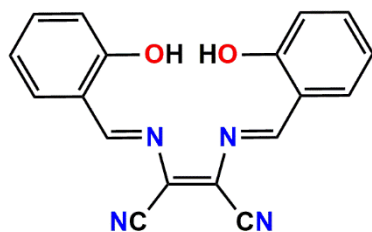
Denticity of Ligand	Ligand	Complex	Ref.
Bidentate			1.42
			1.43



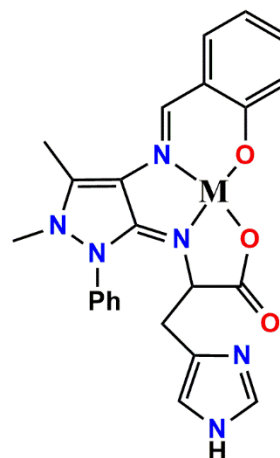
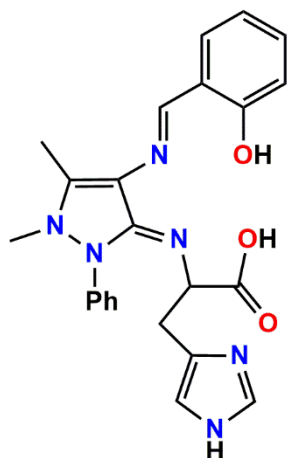
Tridentate



Tetradentate

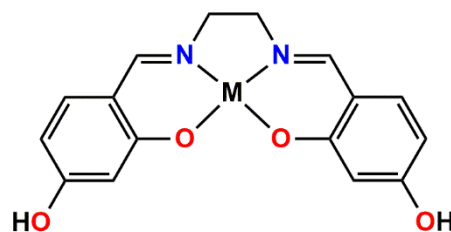
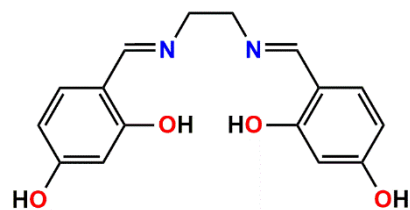


1.48



1.49

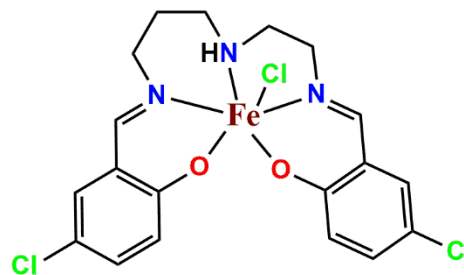
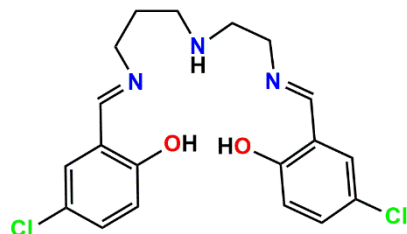
M = Cu(II), Ni(II), Co(II), VO(IV) and Zn(II)



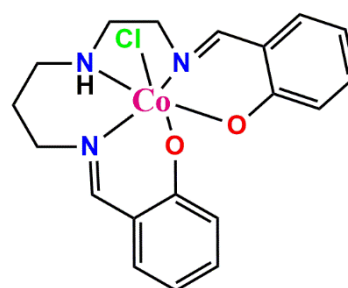
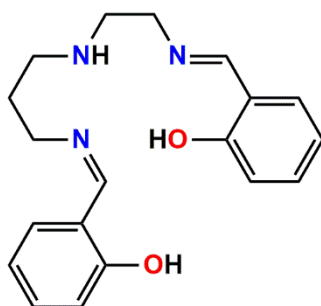
1.50

M= Cu or Ni

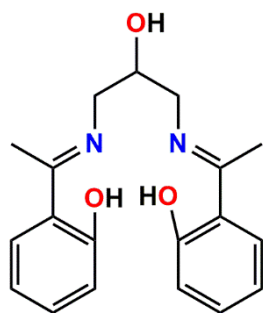
Pentadentate



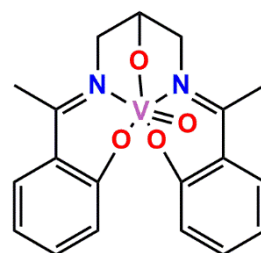
1.51



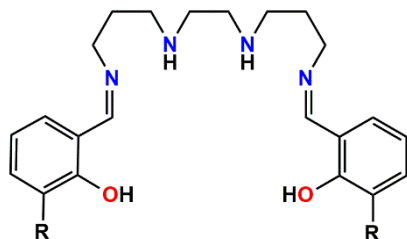
1.52



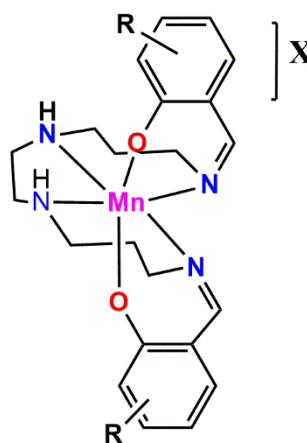
1.53



Hexadentate



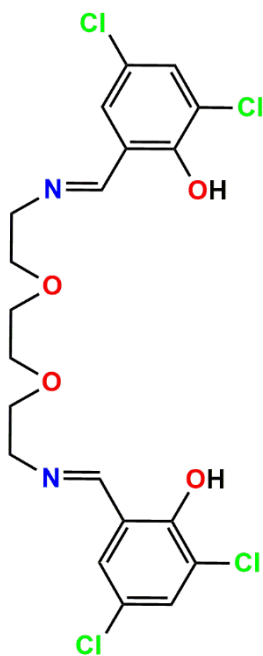
1.54



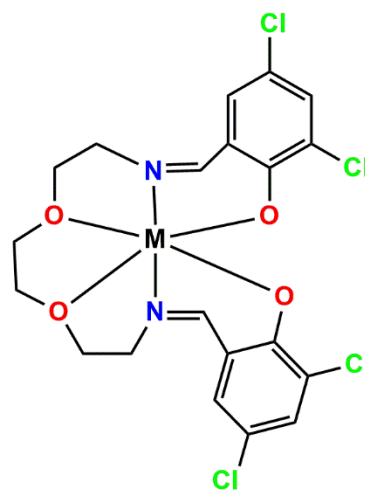
R=3-OMe OR 3-OEt

X= BPh<sub>4</sub>/ PF<sub>6</sub>.H<sub>2</sub>O/ ClO<sub>4</sub>.H<sub>2</sub>O/ BF<sub>4</sub>.H<sub>2</sub>O/

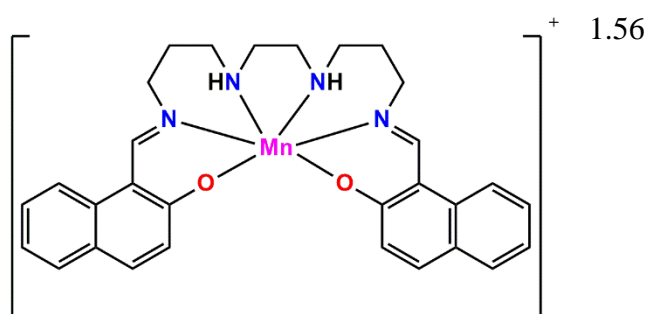
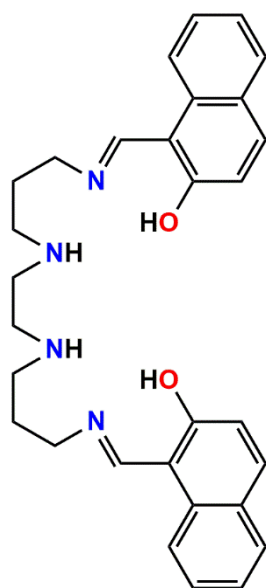
NO<sub>3</sub>



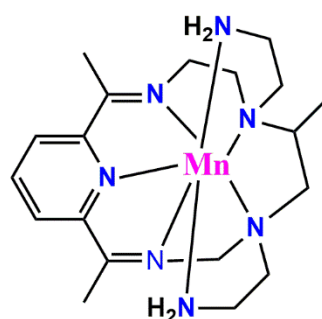
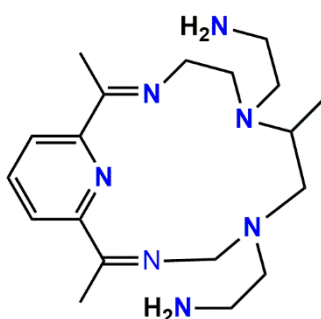
1.55



M= Cu, Co, Ni, Zn



Heptadentate



### 1.3 Schiff Base Transition Metal Complexes

These fascinating Schiff base ligands have played an important role in the development of coordination chemistry as they readily form stable complexes with most of the transition metals<sup>1.58a,b</sup> by diversified synthetic procedures (**Figure 1.5**). Transition metal Schiff base complexes are generally formed by the chelation of Schiff base ligands with metal ions at variable oxidation states. The chelation occurring thus makes the complex compounds more stable and changes the physiological profile of the complexes.<sup>1.59</sup> In the ligation process, vacant metal d-orbitals make available space for the easy coordination of nonbonding electrons of donor atoms of the ligand and sometimes this ligation takes place by deprotonation process. On the other hand, Schiff base ligands coordinate metals through imine nitrogen and another donor, usually linked to the aldehyde. The structure of the Schiff base metal complex can be tuned by judicious choice of the reactants and on the ground of requirement for the coordination of the metal centre. Moreover, these ligands can control the performance of metal ions which offers opportunity to utilize such complexes in the diverse application fields such as

magnetism,<sup>1.60a-i</sup> catalysis,<sup>1.61a-l</sup> biological sciences,<sup>1.62a-g</sup> optoelectronics,<sup>1.63a-c</sup> sensing<sup>1.64a-e</sup> etc.

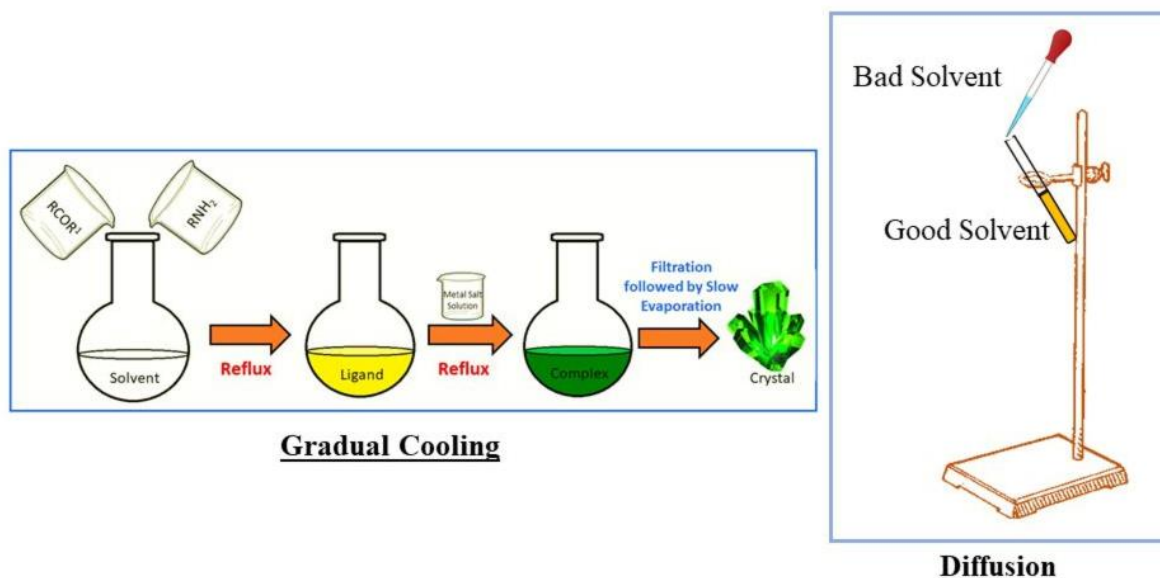


**Figure 1.5:** Different synthetic procedures.

### 1.3.1 Schiff Base Transition Metal Complexes of various nuclearity

Some mono-, di-, tri-, tetra-, penta- and hexanuclear Schiff base complexes of copper(II) and nickel(II) are shown in **Figure 1.6**, **Figure 1.7**, **Figure 1.8**, **Figure 1.9**, **Figure 1.10** and **Figure 1.11**, respectively.

Ghosh *et al*<sup>1.65</sup> reported four new Ni(II) complexes **1**, **2**, **23**, **30**. N,N'-bis(3-methoxysalicylidene)diethylenetriamine ( $H_2L^2$ ), the flexidentate ligand, having seven potential donor atoms reacted with nickel nitrate in different ligand : metal ratios and thus one mononuclear (**2**), one tetranuclear (**23**) and one hexanuclear (**30**) Ni(II) complexes were obtained. Complex **1** was formed by template synthesis. Single-crystal XRD study revealed that both the complexes **1** and **2** are mononuclear with a square planar geometry around the metal centre, whereas other two complexes, **23** and **30**, possess tetranuclear and hexanuclear structures respectively, with octahedral metal centres. Variable temperature molar magnetic susceptibility measurements show that the tetranuclear complex is ferromagnetically coupled having two exchange couplings,  $J_1 = 0.64 \text{ cm}^{-1}$  and  $J_2 = 8.41 \text{ cm}^{-1}$ , whereas the hexanuclear complex is antiferromagnetically coupled having four exchange couplings,  $J_1 = -5.60 \text{ cm}^{-1}$ ,  $J_2 = -9.39 \text{ cm}^{-1}$ ,  $J_3 = -5.18 \text{ cm}^{-1}$  and  $J_4 = 3.72 \text{ cm}^{-1}$ . As the bridging angles in these complexes are close to the crossover angle, these changes are good enough for this reversal of magnetic coupling.

Fekri *et al.*<sup>66</sup> synthesized one mononuclear Ni(II) **3** and two dinuclear Cu(II) complexes **8,9** from a tridentate Schiff base ligand, H<sub>2</sub>L (where, H<sub>2</sub>L = (N-(2-hydroxybenzylideneamino) benzamide)) in the presence of 3-methylpyridine, pyridine and the corresponding metal salts. The structures of these complexes were determined through X-ray crystallography which indicated the coordination geometry is square-pyramidal in **3**, while the dinuclear complexes show an octahedral geometry. They are further characterized by FT-IR, UV-Vis, Raman spectroscopies and cyclic voltammetry (CV). These complexes act as DNA-binding components and antibacterial agents and hence can be considered as potential pharmaceutical bioactive compounds. Finally, molecular docking simulation studies were conducted and the results indicated that the dinuclear complex **8** is a suitable potential candidate drug for the binding the InhA target in *M. tuberculosis*.

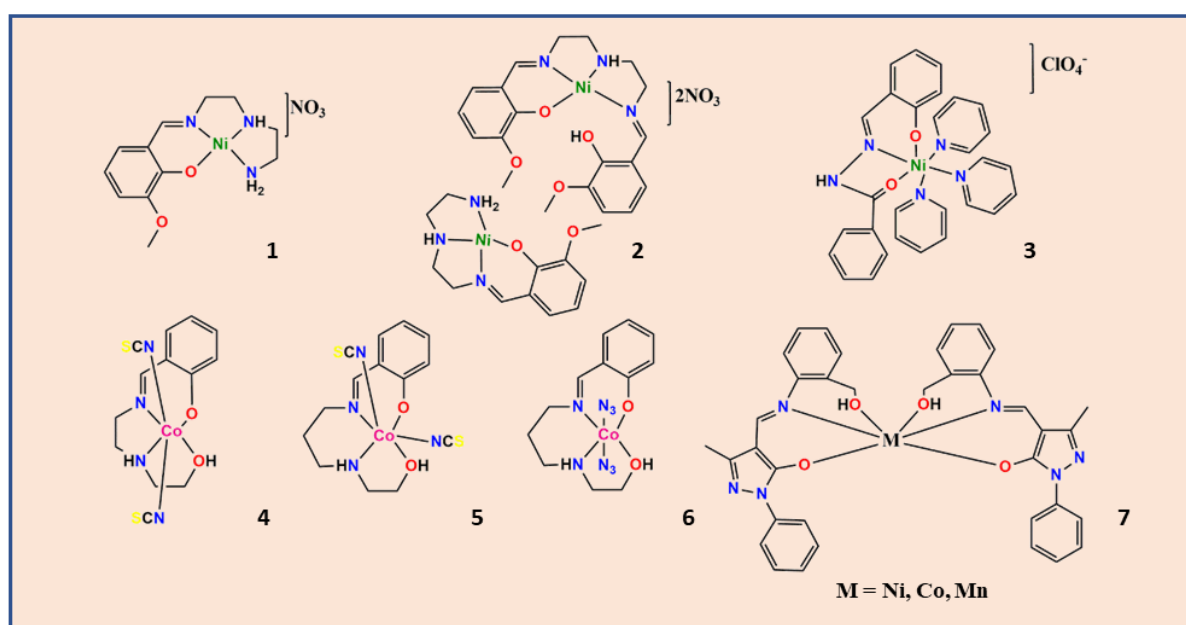


**Figure 1.6:** Mononuclear transition metal Schiff base complexes.

Mandal *et al.*<sup>67</sup> reported three mononuclear **4, 5, 6** and one dinuclear **10** cobalt(III) complexes from two Schiff-base ligands, H<sub>2</sub>L<sup>1</sup> and H<sub>2</sub>L<sup>2</sup> respectively with ONNO donor atoms (where, H<sub>2</sub>L<sup>1</sup> = (E)-2-((2-(2-hydroxyethylamino)ethylimino)methyl)phenol and H<sub>2</sub>L<sup>2</sup> = (E)-2-((3-(2-hydroxyethylamino)propylimino)methyl)phenol) in the presence of two pseudohalides, like SCN<sup>-</sup> and N<sub>3</sub><sup>-</sup>. These complexes were thoroughly characterized by using various physicochemical studies such as UV-Vis, FT-IR, EPR, ESI-MS and single crystal XRD study. In complex **4**, the two thiocyanate ligands (SCN<sup>-</sup>) are trans to each other, whereas, in complex **5** both of them are cis to each other with addition of one additional methylene group to the ligand system. Complex **6** is mononuclear while complex **10** is dinuclear in the presence of the azide co-anionic ligand. All these experimentally observed facts were rationalized by DFT



calculations which established the fact that the different nuclearity and cis–trans stereochemistry are the results of cooperative outcome of the ligand backbone and pseudohalide co-ligand effects. Catecholase like activity of all these four complexes were investigated in DMF using 3,5-DTBC as a model substrate.

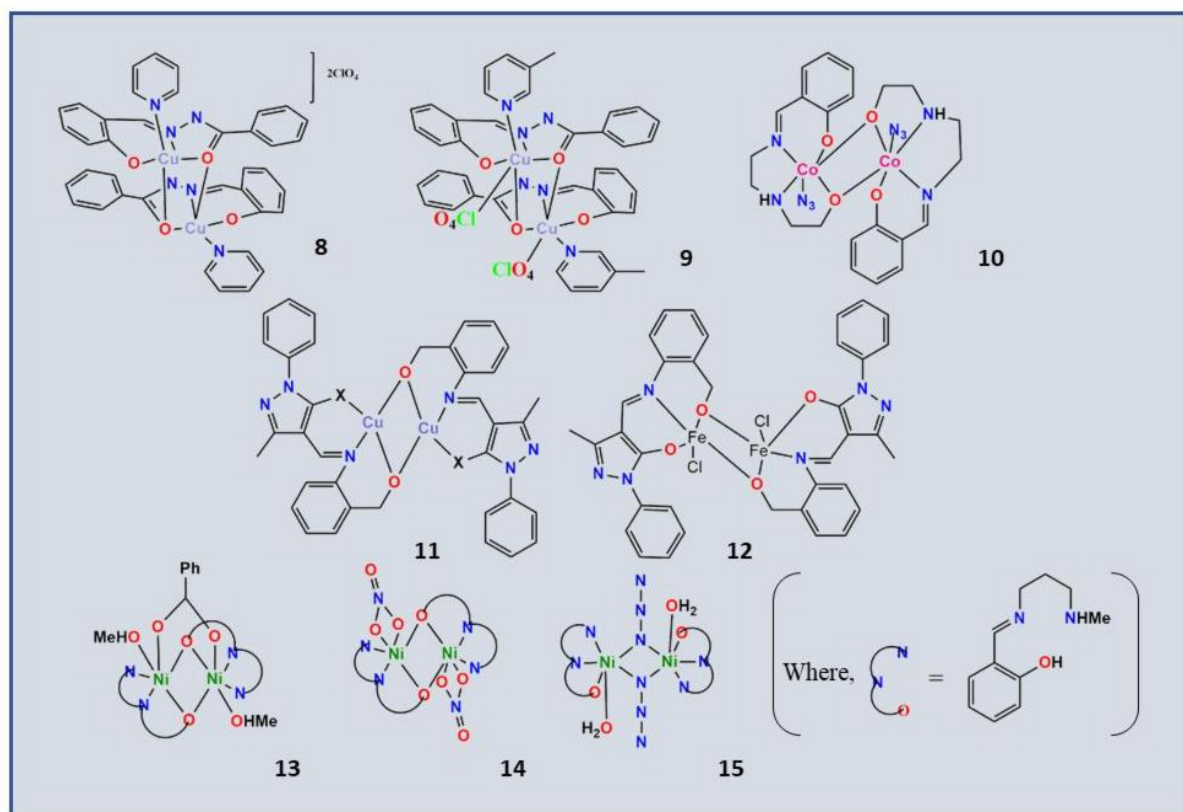


**Figure 1.7:** Dinuclear transition metal Schiff base complexes.

Burlov *et al*<sup>1.68</sup> synthesized a series of mononuclear complexes **7** and binuclear complexes **11**, **12** with different transition metal ions from potentially tridentate NO<sub>2</sub> ligand incorporating phenolic oxygen, alcoholic oxygen and azomethine N donor atoms. Their structures were established by single crystal XRD study which indicated Mn(II), Co(II) and Ni(II) complexes are mononuclear, whereas the Cu(II) and Fe(III) ions form  $\mu_2$ -oxo-bridged binuclear species. Mukherjee *et al*<sup>1.69</sup> reported structural and magnetic versatility of five Ni(II) complexes **13-15**, **19**, **34** derived from a tridentate Schiff base ligand, HL, (where, HL = (2-[(3-Methylamino-propylimino)-methyl]-phenol)), and the polyatomic monoanions N<sub>3</sub><sup>-</sup>, NO<sub>3</sub><sup>-</sup>, NO<sub>2</sub><sup>-</sup> or PhCOO<sup>-</sup>. The structural analysis revealed that for all these five complexes, the Ni(II) ions occupy a distorted octahedral geometry. Complexes **13** and **14** are dinuclear having di- $\mu$ -1,1-azido and di- $\mu_2$ -phenoxo bridges, respectively. Complex **15** is also a dinuclear Ni(II) complex with di- $\mu_2$ -phenoxo-bridged but it has an additional syn-syn benzoate bridge. Compound **19** possesses a linear trinuclear structure with the tridentate Schiff base ligand coordinated to the terminal

nickel atoms which are linked to the central Ni(II) by carboxylate and phenoxo bridges. Complex **34** consists of a dinuclear moiety, bridged by di- $\mu_2$ -phenoxo together with a cis-( $\mu$ -nitrito $_{1\kappa}O:2\kappa N$ ) nitrite ion. Variable-temperature magnetic susceptibility measurements were done with these complexes which indicated that complex **13** shows ferromagnetic exchange interactions within the dimer (where,  $J = 23.5(3) \text{ cm}^{-1}$ ) together with antiferromagnetic interdimer interactions (where,  $J = -0.513(3) \text{ cm}^{-1}$ ), whereas compounds **14** and **15** show intradimer antiferromagnetic interactions (where,  $J = -24.27(6)$  and  $-16.48(4) \text{ cm}^{-1}$ , respectively). Ferromagnetic coupling (where,  $J = 6.14(2) \text{ cm}^{-1}$ ) is also observed in complex **19** for the linear centro-symmetric Ni(II) trimer, whereas complex **34** shows an alternating intra-chain antiferromagnetic coupling ( where,  $J_1 = -32.1(1) \text{ cm}^{-1}$  and  $J_2 = -3.2(1) \text{ cm}^{-1}$ ).

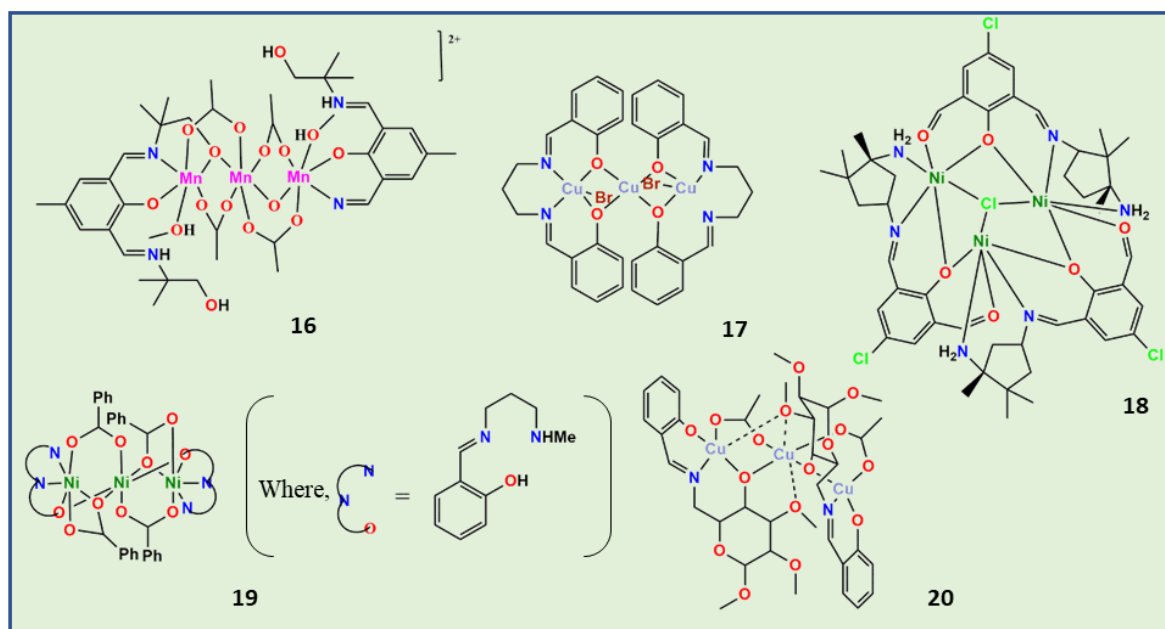


**Figure 1.8:** Trinuclear transition metal Schiff base complexes.

Chattopadhyay *et al*<sup>1.70</sup> utilized two branched, flexible and sterically constrained di- and tripodal side arms around a phenol backbone in ligands  $H_3L^1$  (2,6-Bis{(1-hydroxy-2-methylpropan-2-ylimino)methyl}-4-methylphenol) and  $H_5L^2$  (2,6-bis[{1-hydroxy-2-(hydroxymethyl)butan-2-ylimino}methyl]-4-methylphenol) to isolate  $[Mn_3]$  **16** and  $[Mn_6]$  **31** coordination aggregates. The magnetic characterization of these complexes established that the properties were dominated by intramolecular anti-ferromagnetic exchange interactions and this was further confirmed using DFT calculations. Both the complexes **16** and **31** showed effective solvent-dependent catechol oxidation toward 3,5-di-tert-butylcatechol in air.

Saha *et al*<sup>1.71</sup> reported a linear double phenoxide-bridged trinuclear Cu(II) Schiff base complex **17** derived from a tetradentate (ONNO) donor Schiff base ligand and  $CuBr_2$ . Single crystal

XRD study of this trinuclear complex revealed that the two terminal copper atoms are in square pyramidal geometry, while the central copper atom surrounded by four phenoxide oxygen atoms is in a square planar geometry. Variable temperature magnetic susceptibility measurement study was done for this complex showing strong antiferromagnetic intra-trimer interactions between the copper centres with a  $J$  value of  $-302 \text{ cm}^{-1}$ .

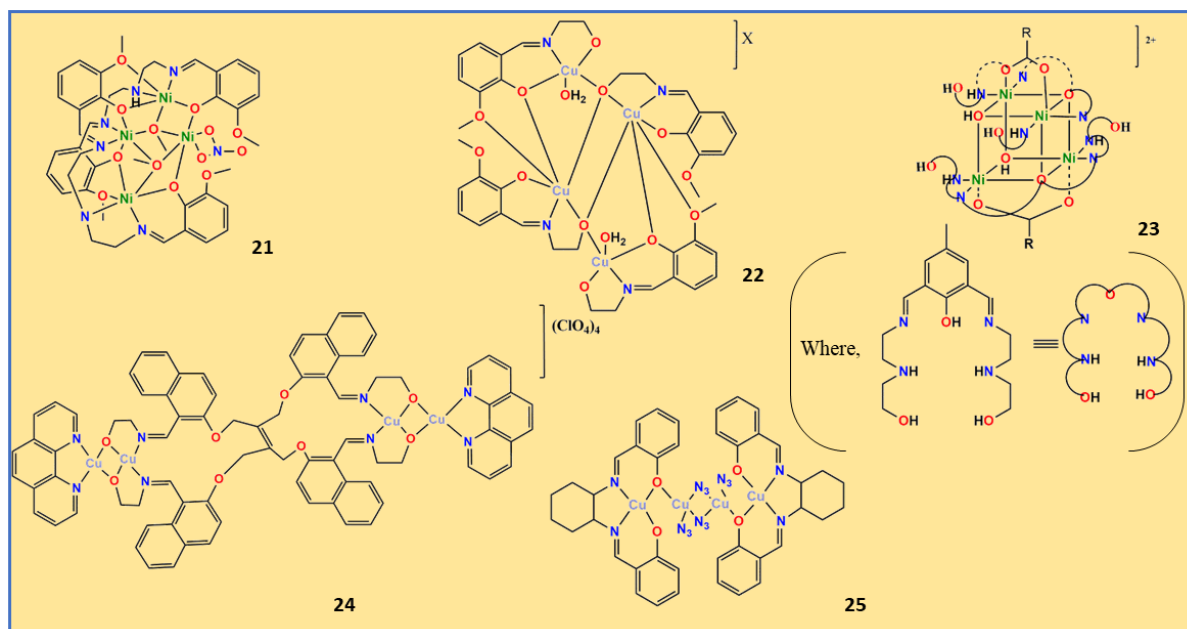


**Figure 1.9:** Tetranuclear transition metal Schiff base complexes.

Jiang *et al.*<sup>1.72</sup> reported the trinuclear **18** and the pentanuclear **29** complexes bearing enantiopure or racemic ligands. Single-crystal XRD studies on **18** reveal that the asymmetric unit of the complex contains one trinuclear [1 + 1] acyclic nickel(II) divalent cation, two  $\text{NO}_3^-$  anions, and four water molecules. Here three six-coordinate nickel(II) centres exhibit an elongated octahedral geometry, where each metal ion is coordinated by one oxygen atom belonging to the aldehyde group, one  $\mu_3\text{-Cl}$  atom, two nitrogen atoms belonging to one camphoric diamine unit and two  $\mu_2$ -phenol oxygen atoms belonging to different phenylic rings. On the other, **29** contains four five-coordinate and one six-coordinate copper(II) centres countered by four  $\mu_2\text{-Cl}$ , two  $\mu_2$ -bridging phenol oxygen atoms and two  $\mu_3\text{-OH}$  bridges. Moreover, in both the cases degradation of macrocyclic ligands occurs at the chiral carbon atoms belonging to camphoric diamine units bearing the methyl group because of their stronger spatial crowding effects than the ones bearing the hydrogen atom. For the trinuclear complex, **18**, variable-temperature magnetic susceptibility measurements were done.

Roth *et al.*<sup>1.73</sup> reported the trinuclear copper(II) complex **20** synthesized from the tridentate aminosaccharide-derived Schiff-base ligand  $\text{H}_2\text{L} = 6\text{-N}(\text{salicylidene})\text{amino-6-deoxy-1,2,3-tri-O-methyl}\beta\text{-D-glucopyranoside}$ . Structure of the complex was characterized. The trinuclear

complex unit was described as two terminal copper–ligand entities bridged by a central copper acetate moiety, with the copper centres arranged in a triangular manner. The existence of the trinuclear structure was confirmed by IR and UV/vis spectroscopic studies. The temperature dependence of the magnetic susceptibility of the complex showed a moderate antiferromagnetic coupling with a coupling constant  $J$  of  $-34 \text{ cm}^{-1}$ .

Ghosh *et al.*<sup>1.74</sup> synthesized a tetranuclear complex **21** and confirmed the structure by Single-crystal X-ray diffraction study. Variable temperature molar magnetic susceptibility measurements showed that complex **21** is ferromagnetically coupled having two exchange couplings,  $J_1 = 0.64 \text{ cm}^{-1}$  and  $J_2 = 8.41 \text{ cm}^{-1}$ .

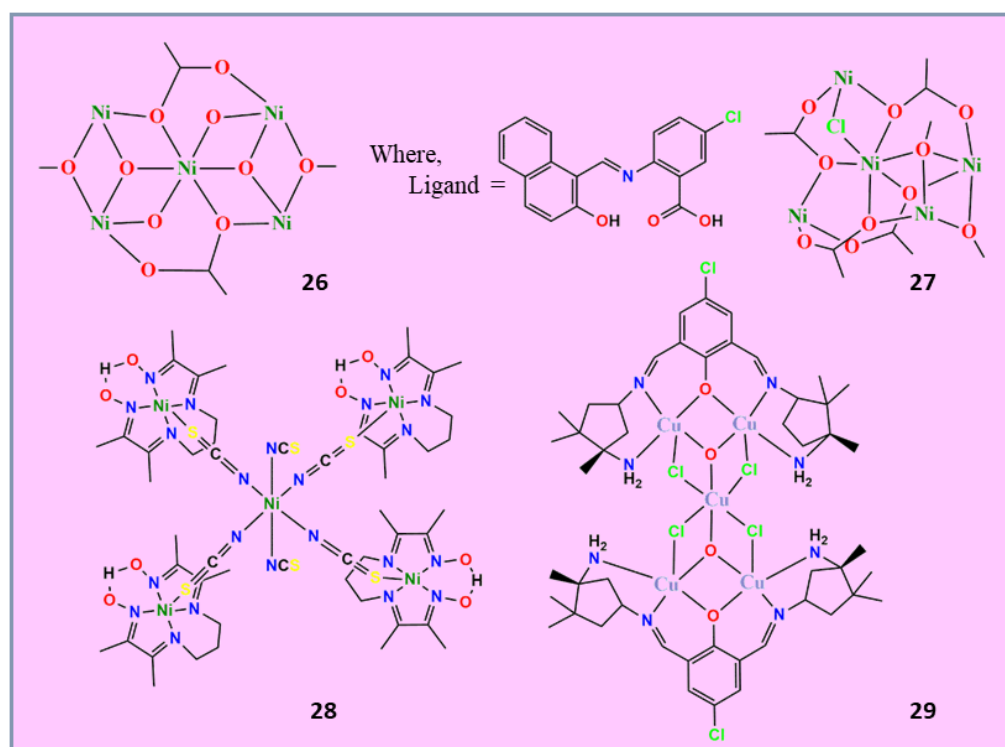


**Figure 1.10:** Pentanuclear transition metal Schiff base complexes.

Manna *et al.*<sup>1.75</sup> synthesized two tetranuclear Schiff base copper(II) complexes, **22**, namely  $[\text{Cu}_4(\text{L})_2(\text{LH})_2(\text{H}_2\text{O})_2](\text{ClO}_4)_2 \cdot 3\text{H}_2\text{O}$  and  $[\text{Cu}_4(\text{L})_2(\text{LH})_2(\text{H}_2\text{O})_2](\text{ClO}_4) \cdot (\text{tp})_{0.5} \cdot 3\text{H}_2\text{O}$  (where  $\text{H}_2\text{L} = 2-[(2\text{-hydroxy-ethylimino)-methyl}]-6\text{-methoxy-phenol}$  and  $\text{tp} = \text{terephthalate}$ ). Single crystal XRD study showed that both of these complexes contain double open cubane core, in which two metal centres are in a square pyramidal environment and the other two metal centres exhibit a slightly distorted octahedral coordination geometry. The interaction of these complexes with calf thymus DNA, BSA and HSA were investigated. Using 3,5-DTBC as a model substrate, both the complexes also showed catecholase-like activity.

Chattopadhyay *et al.*<sup>1.76</sup> reported three tetranuclear nickel(II) complexes, **23**,  $[\text{Ni}_4(\mu_3\text{-H}_2\text{L})_2(\mu_3\text{-OH})_2(\mu_{1,3}\text{-CH}_3\text{CO}_2)_2](\text{ClO}_4)_2$ ,  $[\text{Ni}_4(\mu_3\text{-H}_2\text{L})_2(\mu_3\text{-OH})_2(\mu_{1,3}\text{-C}_2\text{H}_5\text{CO}_2)_2](\text{ClO}_4)_2 \cdot 0.5 \text{ H}_2\text{O}$  and  $[\text{Ni}_4(\mu_3\text{-H}_2\text{L})_2(\mu_3\text{-OH})_2(\mu_{1,3}\text{-O}_2\text{C-C}_6\text{H}_4\text{-pNO}_2)_2](\text{ClO}_4)(\text{p-NO}_2\text{-C}_6\text{H}_4\text{-CO}_2) \cdot \text{DMF} \cdot 5\text{H}_2\text{O}$ . These tetranuclear complexes were obtained by the reaction of  $\text{Ni}(\text{ClO}_4)_2 \cdot 6\text{H}_2\text{O}$  with  $\text{H}_3\text{L}$  (where,  $\text{H}_3\text{L} = 2,6\text{-bis}((2\text{-}(2\text{-hydroxyethylamino)ethylimino)methyl)\text{-4-methylphenol})$  and  $\text{RCO}_2\text{Na}$  (where,  $\text{R} = \text{CH}_3, \text{C}_2\text{H}_5, \text{p-NO}_2\text{C}_6\text{H}_4$ ). They were characterized by X-ray crystallography and magnetic measurements. Studies on their magnetic behaviour revealed that the exchange coupling within these complexes is predominantly antiferromagnetic in nature.

Karaoğlu *et al.*<sup>1.77</sup> reported homo-tetranuclear Cu(II) complex **24** of a potentially bis-hexadentate  $\text{N}_2\text{O}_4$  Schiff base. The structures of the Schiff base and the complex were determined by spectroscopic data (IR,  $^1\text{H}$  and  $^{13}\text{C}$  NMR, UV-vis, electrospray ionisation mass spectra), elemental analyses, molar conductivities and magnetic susceptibility measurement.

Khalaji *et al.*<sup>1.78</sup> reported a tetranuclear copper(II) complex **25** synthesized from an  $\text{N}_2\text{O}_2$ -chelating Schiff-base ligand  $\text{sal}_2\text{hn}$  [where,  $\text{sal}_2\text{hn} = \text{N,N}'\text{-bis}(\text{salicylidene})\text{-1,2-diaminocyclohexane}$ ] and  $\text{Cu}(\text{NO}_3)_2 \cdot 3\text{H}_2\text{O}$  in the presence of a large excess of  $\text{NaN}_3$  (reagent ratios (metal:L: $\text{N}_3$ ) = 2:1:8). Its crystal structure was thoroughly investigated with the help of single crystal XRD study which revealed that in this complex the copper(II) ions are bridged alternately by end-on azido and phenoxo- $\text{sal}_2\text{hn}$  ligands.

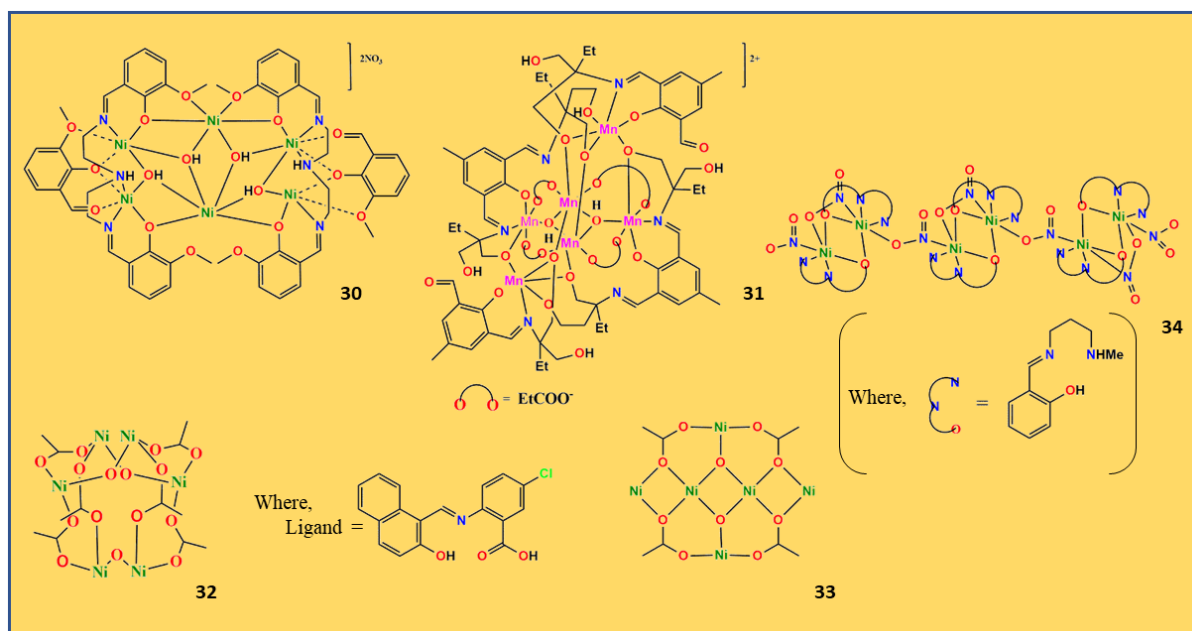


**Figure 1.11:** Hexanuclear transition metal Schiff base complexes.

Perlepe *et al.*<sup>1.79</sup> employed the chelating and fluorescent bridging ligand  $\text{N-naphthalidene-2-amino-5-chlorobenzoic acid}$  ( $\text{nacbH}_2$ ) in Ni(II) cluster chemistry that led to a series of

pentanuclear **26**, **27** and hexanuclear **32**, **33** compounds with different structural motifs, optical and magnetic properties, as well as an interesting 1-D coordination polymer. Their structures were established by single crystal XRD study. The nature of the organic base used for the deprotonation of the free  $\text{nacBH}_2$  and the reaction solvent were found to affect dramatically the structural and chemical identities of the resulting compounds.

Maity *et al*<sup>1.80</sup> reported the first thiocyanato bridged penta-nuclear complex **28**  $[\{(\text{NiL}_2)(\mu\text{-SCN})\}_4\text{Ni}(\text{NCS})_2] \cdot 2\text{CH}_3\text{CN}$ , (where, the ligand,  $\text{HL}_2 = 3\text{-(hydroxyimino)butan-2-ylidene)amino)propylimino)butan-2-one oxime}$ ). Its structure was established by single crystal X-ray diffraction study which revealed the central nickel(II) metal ion is coordinated by six nitrogen atoms of six thiocyanate groups, four of which utilize their sulphur atoms to connect four  $\text{NiL}_2$  moieties to form a penta-nuclear complex.

#### 1.4 Choice of Metallo-Elements under Investigation

In the present research work, two of the 3d-metals, viz. Ni(II) and Cu(II) have been considered for the formation of stable mononuclear and dinuclear complexes. The partly filled d-orbitals of these metals offer a significant role in the coordination behaviour with Schiff base ligands with N, O donor atoms.

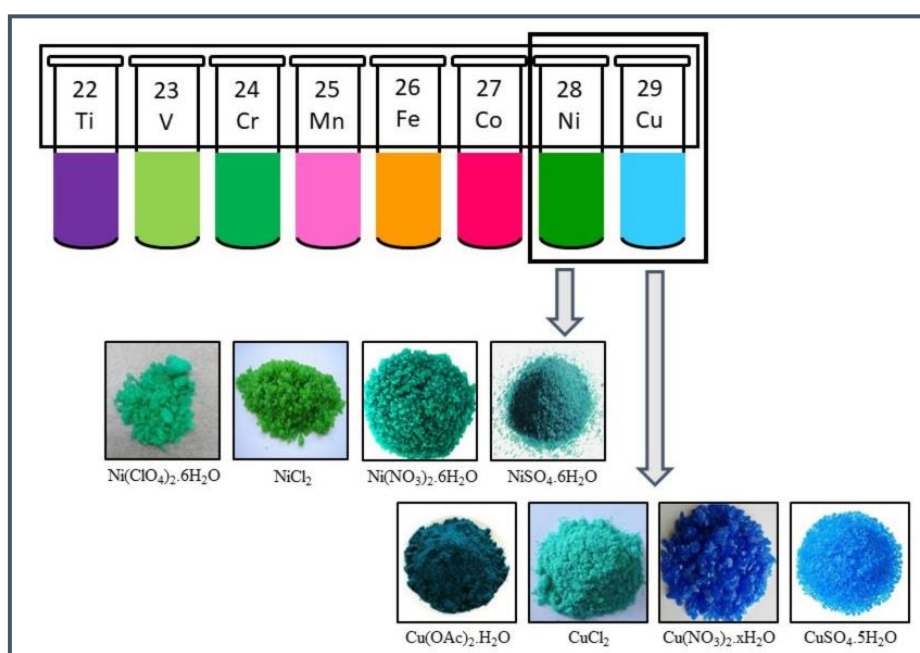


Figure 1.12: 3d-Transition Metals

##### 1.4.1 Nickel

In 1751, Cronstedt discovered the element nickel and it was first purified as a metal by Berthier in the early 1800s. Nickel is the earth's 7th most abundant transition metal with a very rich coordination chemistry.<sup>1.81</sup> It exists mostly in +2 oxidation state in its complexes. Nickel in this

oxidation state may have a variety of coordination numbers and geometries. But octahedral, tetrahedral and square planar geometries are the most common. The enzyme chemistry in the bio-medical science highlights nickel as an essential component in many of enzymes present in the human body, without which the normal metabolic functions are inconceivable.<sup>1,82</sup> Moreover, among various transition-metal ions (for example, Fe, Co, Mo, Ni, V, Cu, etc.) nickel has gained much attention as a promising hydrogen evolution reaction (HER) catalyst due to its pH stability, low cost, fascinating electronic properties and anticipated synergistic effect that dramatically alter surface properties of materials to favour electrocatalysis. Literatures report the multifunctional biological activities as well as the electrocatalytic properties of nickel Schiff bases complexes and hence nickel has considered for the research.

### **1.4.2 Copper**

Another 3d transition metal, copper, is a natural element which is essential to all forms of life and after iron and zinc, it is the third most abundant trace element found in the human body. It was first to be an essential biological element in 1920s when anemia was found to result from copper deficiency in animals and the addition of copper salts improved this adversity. Copper also serves as a catalytic component in many enzymes like galactose oxidase (GO), laccases, hemocyanin, cytochrome c oxidase, superoxide dismutase, etc. Its coordination chemistry is limited to its two accessible oxidation states, +1 and +2. The +1 oxidation state has a diamagnetic  $d^{10}$  electronic configuration and forms complexes without any crystal field stabilization energy. These complexes are biologically relevant due to its reductive activation towards molecular oxygen. The +2 oxidation state exists as a  $d^9$  electronic configuration which favours coordination with various ligands and the resulting complexes assume square planar to distorted octahedral geometries. Crystal field stabilization energy of the complexes makes them less labile towards ligand exchange phenomenon and is regarded as the best candidate for catalytic activities due to their facility of preparation, flexibility, capability of stabilizing unusual oxidation states and successful performance in mimicking particular geometries around metal centres. A large number of Cu(II) Schiff base complexes acting as homogeneous catalyst in versatile catalytic reactions exist in the literature and hence in this research, copper has drawn particular attention for catalyst design.

## 1.5 Applications of Schiff Base Metal Complexes

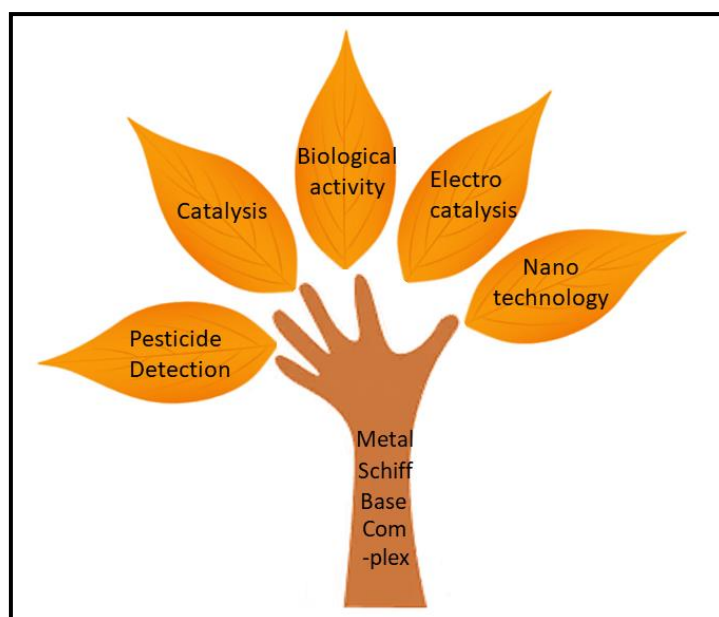


**Figure 1.13:** Various applications of transition metal Schiff base complexes.

### 1.5.1 Metal Organic Framework in detection of Pesticides:

In recent years, a noticeable demand for agricultural productivity has been realized due to the rapid population growth and economic development. To fulfil this demand, development of genetically superior, hybrid seeds, advancement in cultivation science and efficient utilization of potent pesticides become a significant challenge for humankind.<sup>1.83a,b</sup> Pesticides are synthetic compounds which are essential and indispensable in agriculture to meet the requirement of feeding. Generally chemical pesticides are highly used to protect crops for the purpose of increasing agricultural productivity.<sup>1.84a,b</sup> But it has been noticed that nearly 1% of the total applied pesticides are literally used by the targeted species and rest of the 99% applied pesticides are bioaccumulated through the food chain.<sup>1.85a,b</sup> In general, pesticides are classified according to their chemical structures, for example, organophosphorus, organochlorines, carbamates, chlorophenols, and synthetic pyrethroids (**Scheme 1.2**).<sup>1.86</sup> Among them, organophosphate pesticides have emerged as one of the most widely utilized pesticides in the whole world due to its high toxicity, strong selectivity, short residual period, high efficiency and rapid degradation.<sup>1.87a,b</sup> Owing to high toxicity, the pesticide residues produced in agricultural products, water and soil lead to safety hazards.<sup>1.88a-f</sup> Inhalation through the respiratory system, skin penetration upon dermal exposure, eye and oral exposures are the well-defined paths of pesticide toxicity (**Figure 1.14**). All these lead to short-term health issues like nausea, eye and skin irritation, headache, dizziness and chronic diseases like asthma, cancer, diabetes, neurological disorders.<sup>1.89a,b</sup>



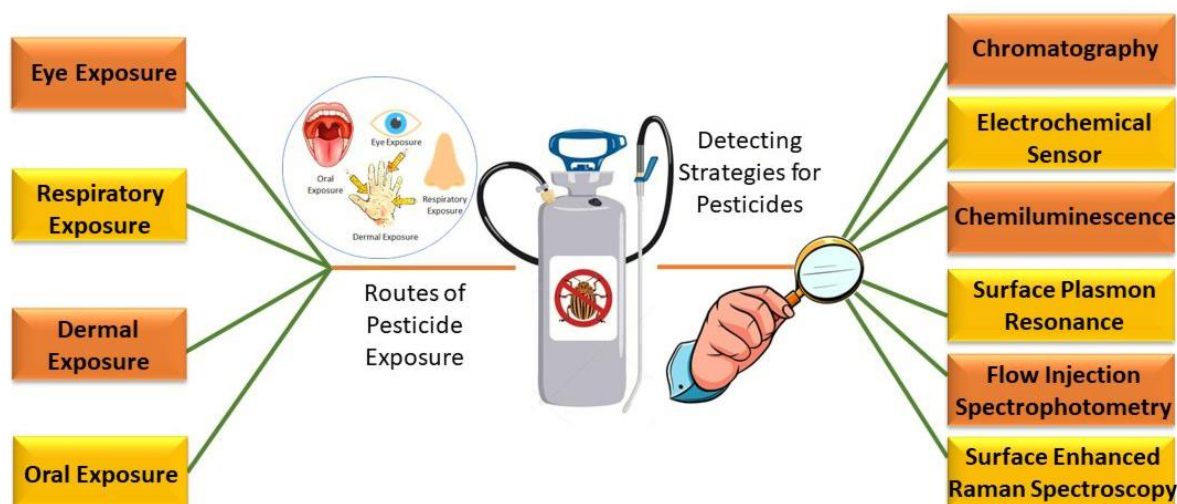
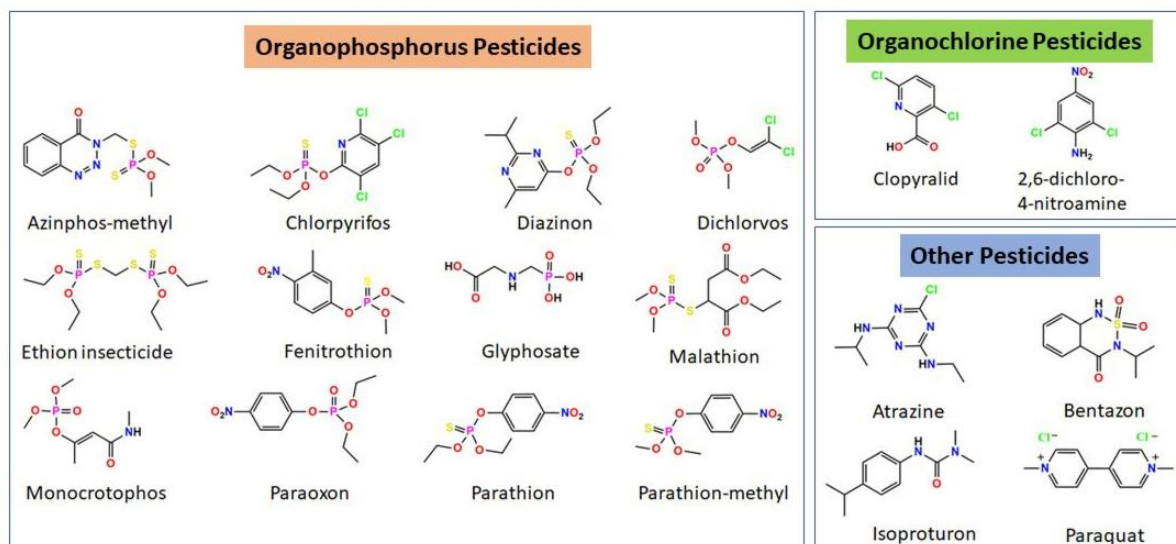


**Figure 1.14:** Exposure routes and various detecting strategies for pesticides.

Therefore, development of novel and effective techniques for swift and dependable quantification as well as detection of pesticides in different environmental matrices (e.g., surface waters and wastewater) is critical to ensure public safety and security. The conventional detecting methods include gas chromatography (GC),<sup>1.90</sup> high-performance liquid chromatography (HPLC),<sup>1.90</sup> capillary electrophoresis,<sup>1.91a,b</sup> Potentiometry,<sup>1.92a,b</sup> and flow injection spectrophotometry.<sup>1.93</sup> However, these conventional methods have some limitations including high analytical costs, time-consuming procedures (in sample preparation and pre-treatment), and sophisticated instrumentation.<sup>1.94</sup> Thus, growing demand has been observed for reliable and quick methods for detecting various pesticides in environmental samples and this has been partially achieved by using various sensing methodologies.

In recent years, immense attention has been received by the wide application range of porous materials owing to prominent surface properties.<sup>1.95</sup> Metal–organic frameworks (MOFs), also called porous coordination polymers (PCPs), form a fascinating class of highly ordered crystalline coordination polymers that are self-assembled by the combination of metal ions/clusters and organic bridging linkers/ligands connected via coordination bonds. **(Figure 1.15).**<sup>1.96a,b</sup> This coordination of metal clusters/ions with ligands results in the formation of extended infinite networks. In 1995, the concept of MOF was first introduced by the Yaghi group.<sup>1.97</sup> Till date different varieties of MOFs were reported in the literature with designed structural, electrical, optical, magnetic and catalytic properties by choosing appropriate metal ions and organic ligands **(Scheme 1.3).**<sup>1.98</sup>



**Scheme 1.2:** The categories and names of various pesticides.

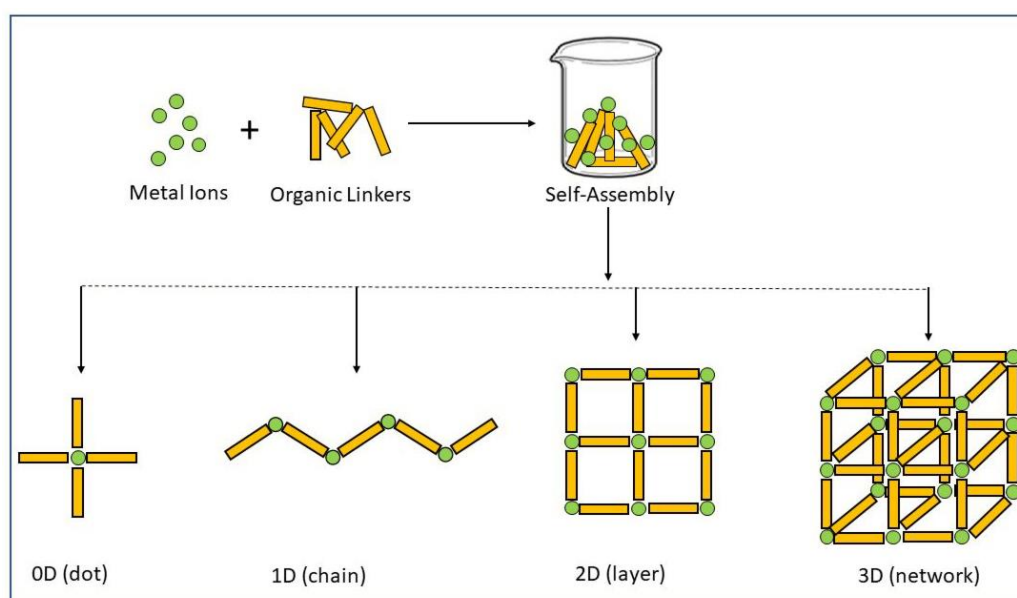
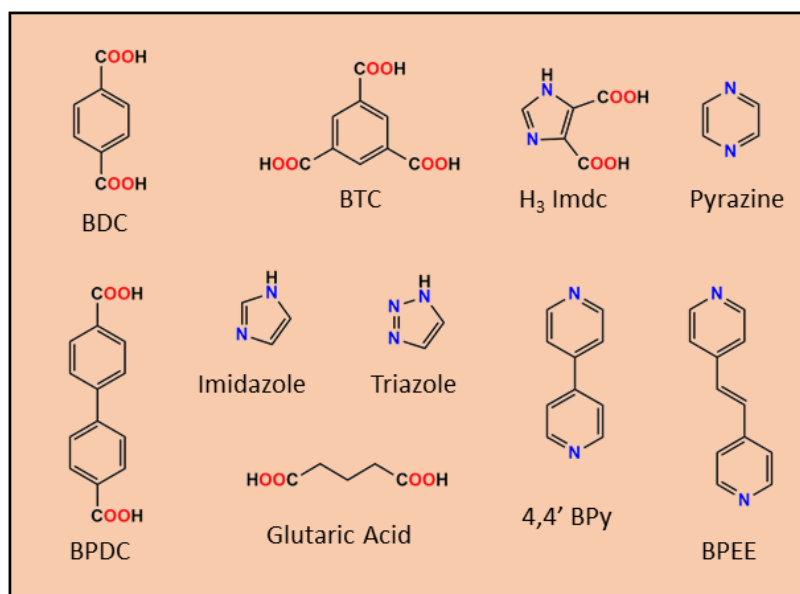


**Figure 1.15:** Schematic representation of formation of MOF.

Owing to their robust 3D architecture, tight packing and unique properties i.e. mesoporous nature, high specific surface area, permanent porosity, tailorable pore size, high density of active sites, outstanding thermal stability and facile conjugation with the guest species. Considering this structural property-functional capability relationship, the design of MOF can result into the construction of new MOFs that are highly efficient for a diverse range of applications.<sup>1.99a-x</sup>



**Scheme 1.3:** Structure of common organic ligands used in the synthesis of MOFs. BDC: 1,4-benzene dicarboxylic acid, BTC: 1,3,5-benzene tricarboxylic acid, H<sub>3</sub> Imdc: 4,5-imidazole dicarboxylic acid, BPDC: biphenyldicarboxylic acid, 4,4'BPY: 4,4'-bipyridine, BPEE: 1,2-bis(4-pyridyl)ethylene.

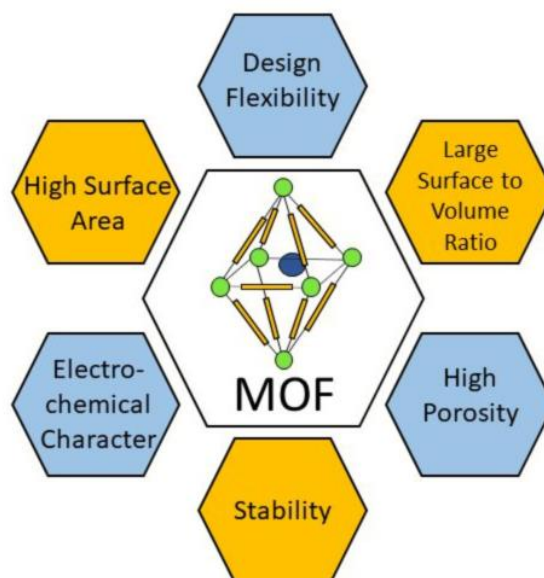


**Figure 1.16:** Various characteristics of MOF.

Moreover, diverse structure, high surface area, reversible adsorption and tunable chemical functionalization of MOFs make them potential sensing candidates in chemical sensors.<sup>1.100</sup> The physical, chemical and structural changes in MOF upon adsorption of guest molecules have been utilized for detection of different types of analytes, including anions, metal ions, small-molecules, nitroaromatics, bio-chemicals, volatile organic compounds and specially pesticides.<sup>1.101a-d</sup> The methods working individually or simultaneously for selective adsorption

of pesticides by MOFs include hydrogen bonding interactions,  $\pi$ - $\pi$  interactions, electrostatic interactions, breathing effects, adsorption onto coordinatively unsaturated sites, size-sieving effects (**Figure 1.17**).<sup>1.102a,b</sup> In recent years, combination of various properties of MOFs including luminescence and porosity also makes them potential candidates for detecting pesticides. In 2014, the first MOF-based probe was introduced by Li and co-workers to detect pesticides with high sensitivity and selectivity.<sup>1.103</sup> Thereafter, MOFs have been utilized as one of the most promising and excellent probe materials to detect various pesticides.

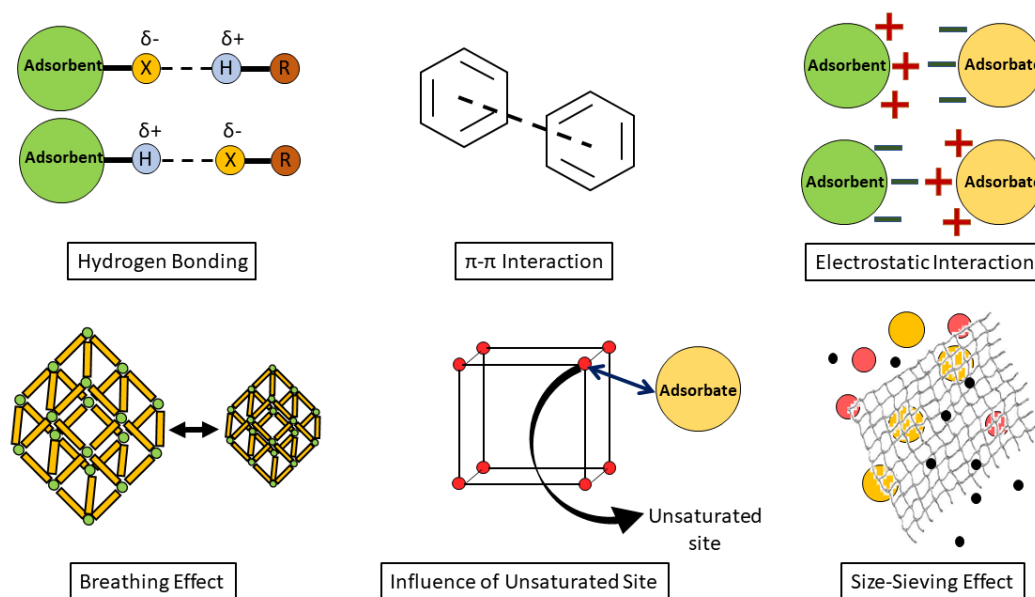


**Figure 1.17:** Schematic diagram of possible mechanisms for removal of hazardous materials via MOFs.

To understand the interactions between analytes and MOF-based materials more thoroughly, theoretical calculations such as density functional theory (DFT)<sup>1.104a,b</sup> and molecular simulation<sup>1.105</sup> are used. Both of these tools provide the information regarding to the force, structural and total energy information along with the charge density of the system for the adsorption reactions that cannot be given by the current spectroscopic and experimental methods.<sup>1.106a,b</sup> These results are helpful for designing the structure of MOFs and optimizing their adsorption performance.

Between these two tools mentioned above, DFT, a most important theoretical tool to explain the experimental results and spectroscopic analysis at the atomic level.<sup>1.107a-f</sup> Another advantage of DFT calculations is that it can provide information about the most stable adsorption structure, system charge density as well as total adsorption energy,<sup>1.108a,b</sup> which are essential for the identification of underlying mechanisms.<sup>1.107c</sup> Several studies have been reported in the literature where DFT calculations have been used to explain experimental

adsorption phenomena.<sup>1.109a-f</sup> The limitation of the use of DFT is its long processing time and the energy comparison between the optimized structures remains less accurate.

Molecular simulations is another technique which can provide information regarding to the positions and potential energies of all the adsorbates during the adsorption process, which is not accessible easily by experimental techniques. Moreover, it can also predict macroscopic phenomena, such as adsorption heats and adsorption isotherms. To date, this technique has been widely used to predict gas adsorption onto MOFs.<sup>1.110a-e</sup> Nalaparaju *et al.* conducted a molecular simulation for the first time for the exchange of  $\text{Pb}^{2+}$  ions with  $\text{Na}^+$  ions in Na-*rho*-ZMOF at 298 K.<sup>1.111</sup> Till date, there have been fewer application of molecular simulations reported in characterizing the metal ion adsorption on MOF-based materials.<sup>1.112a,b</sup> The factor, long computational time, limits its application.

Habila *et al.*<sup>1.113</sup> reported a copper-benzyl tricarboxylic acid based metal organic frameworks (Cu-BTC-MOFs) which was characterized with SEM, EDS, XRD, FTIR and surface area analysis. Cu-BTC-MOFs has shown a high efficiency as an adsorbent for enrichment of malathion by dispersive solid phase microextraction (DSPME) from food and water samples. This can be attributed to the unique structure of the MOFs where the metal centre (copper) and benzene tricarboxylic-ligand are well organized and act as suitable matrix for adsorption/desorption of malathion. After performing the microextraction procedures, malathion was determined by ultra-performance liquid chromatography-tandem mass spectrometry. The microextraction procedures showed a detection limit of  $4.0 \mu\text{g L}^{-1}$  and the quantification limit of  $10.0 \mu\text{g L}^{-1}$ . For malathion, the optimum recoveries from aqueous solution were obtained at pH 6 and with using 2 mL of ethyl acetate as the eluent. The absolute recovery% was found to be  $\geq 92\%$  when the feasibility of the proposed method was determined by evaluating the addition/recovery studies of malathion from the real samples. Furthermore, the recovery% was obtained in the range of 93%-100% when some ions were tested as co-interfering ions. Thus they confirm that the developed microextraction procedure based on Cu-BTC-MOFs as extractor for dispersive solid phase microextraction is independent of matrix and it can be applied for various real samples including different matrix or various malathion content.

Bhardwaj *et al.*<sup>1.114</sup> reported for the first time the thin film assembly of silica-coated water-stable copper-MOF,  $\text{Cu}_3(\text{BTC})_2$  [ $\text{Cu}_3(\text{BTC})_2@ \text{SiO}_2$ , BTC] on a conducting substrate of  $\text{NH}_2\text{-BDC}$  [ $\text{NH}_2\text{-BDC}$ ] doped polyaniline. These thin films were further bioconjugated with antiatrazine antibodies to create a novel immunosensing platform. They found its application

in the sensitive conductometric sensing of atrazine (2-chloro-4-ethylamino-6-isopropylamino-s-triazine), an extensively used pesticide for agricultural purpose. They have investigated various structural and spectral characteristics of the synthesized material and its bioconjugate. Atrazine was detected by these MOF thin films with a high sensor sensitivity (i.e. with a very low limit of detection at 0.01 nM) along with a high specificity in the presence of diverse pesticides such as endosulfan, parathion, paraoxon, malathion, and monocrotophos.

Abdelhameed *et al.*<sup>115</sup> reported the effectiveness of copper-based metal-organic framework, Cu-BTC, also called HKUST-1 (chemical formula  $\text{Cu}_3(\text{BTC})_2$ ) as an adsorbent for removal of organophosphorus insecticide  $^{14}\text{C}$ -ethion from wastewater. The synthesized product was characterized by SEM, EDS, XRD, FTIR. They have performed equilibrium and kinetic experiments under different operating conditions (sorbent dose, temperature and pH), followed by their rigorous modeling and analysis. At pH = 7, temperature = 25 °C, time = 150 min, ethion concentration = 75 mg L<sup>-1</sup>, and Cu-BTC dose = 0.425 g L<sup>-1</sup>, they found the sorbent capacity of ca. 122 mg g<sup>-1</sup> and removal of 94% of  $^{14}\text{C}$ -ethion from aqueous solution. They have also observed that  $^{14}\text{C}$ -ethion/Cu-BTC isotherms show two plateaus (BET type IV) and are reliably represented by Brunauer-Deming-Deming-Teller and Zhu-Gu models with deviations of only 1.99 and 3.95%, respectively. Finally, FTIR and simple pore size considerations reveal the fundamental understanding of the adsorption mechanism which states that the ethion molecule coordinates to two copper(II) atoms across the MOF channel via the phosphoryl (P-O) group. They have also performed the reusability tests showing that Cu-BTC was stable and maintained good adsorption performance over six cycles. Thus they claim Cu-BTC MOFs as a promising material for removing pesticides from wastewater.

Liu *et al.*<sup>116</sup> reported fabrication of an attractive magnetically controlled Cu-MOF-based aptasensor for rapid determination of chlorpyrifos (CPF). This aptasensor has been prepared by the attachment of the colorimetric labels onto the magnetic carrier by the hybridization reaction between aptamer and the complementary DNA. They have achieved chlorpyrifos detection by monitoring the changes in the color of the TMB/H<sub>2</sub>O<sub>2</sub> solution before and after incubation of this aptasensor with chlorpyrifos via exposure to external magnetic force. The most important characteristics of this aptasensor are its high sensitivity and selectivity towards CPF over other interfering pesticides. It showed a detection limit of 4.4 ng/mL with a linear range of 0–1250 ng/mL under the optimal conditions. They have applied this aptasensor successfully for the spiked test of chlorpyrifos in vegetable and fruits samples with good recovery, which were in good agreement with GC-MS analysis data. They have also observed

that combination of Cu based MOFs with Fe<sub>3</sub>O<sub>4</sub> nanoparticles not only leads to the development of facile and efficient phase separation, but also expands the MOF's target scope from glucose or H<sub>2</sub>O<sub>2</sub> to pesticides.

Liu and coworkers<sup>1.117</sup> prepared a magnetic Cu–benzene-1,3,5-tricarboxylate (BTC) MOF (M-MOF) using a Fe<sub>4</sub>O<sub>3</sub>–graphene oxide–β-cyclodextrin nanocomposite as the magnetic core and support. The obtained M-MOF has been characterized, and its adsorption capacity was investigated based on isotherm experiments, adsorption kinetics and adsorption model analysis. They have found that the M-MOF has a large Brunauer–Emmett–Teller surface area of 250.33 m<sup>2</sup> g<sup>-1</sup> and high super-paramagnetism with saturation magnetization of 10.47 emu g<sup>-1</sup>. This is used for rapid adsorption and removal of neonicotinoid insecticide pollutants in tap water samples. The insecticides have hydrophobic groups, nitrogen-containing groups and delocalized large π bonds from their benzene rings or five-membered heterocycles. M-MOF can therefore adsorb neonicotinoid via interactions between functional groups and the MO. Moreover, supramolecular recognition of Fe<sub>4</sub>O<sub>3</sub>–GO–β-CD and the hydrophobic inner cavities significantly enhance the adsorption capacity and rate of M-MOFs for neonicotinoid insecticides.

Heidarbeigi *et al*<sup>1.118</sup> reported copper-benzene-1,4-dicarboxylic acid metal-organic framework (Cu-BDC) which was directly synthesized for the first time on a helical copper wire and used as a sorbent for stir-bar sorptive extraction (SBSE) of fenthion from water and fruit samples. The sorbent (Cu-BDC) was fabricated on a helical shape copper wire by a fast and simple in-situ growth method, first step of which involves the chemical conversion of copper substrate to copper hydroxide NTs performed in an alkaline solution followed by formation of Cu-BDC through a neutralization reaction. CD-IMS in positive mode was applied for the detection of the analyte (fenthion). They have investigated some synthesis and extraction parameters affecting the extraction efficiency such as concentration of benzene-1,4-dicarboxylic acid, ionic strength, sample pH, extraction temperature, stirring rate and extraction time to attain high extraction efficiency. Under optimal conditions, it showed a detection limit of 0.1 μg L<sup>-1</sup> with the linear dynamic range of 0.5–80 μg L<sup>-1</sup> for analyte determination. The applicability of the method was investigated for the analysis of different samples such as well water, agricultural wastewater and orange and it showed good efficiency with recovery > 88% for the extraction of fenthion from the real samples.

### 1.5.2 Schiff Base Metal Complexes as Catalyst in Biological Activity:

Another important area of Co-ordination chemistry is “Bio-inorganic chemistry” which involves the biological processes and development of new drugs. Over the past decades, the interactions between bio-macromolecules and drugs get special interests of biology and chemistry researchers.<sup>1.119</sup> Particularly considerable interest had been developed in the preparation and characterization of Schiff Base-transition metal complexes to check the role of metal active sites in several catalytic biological processes. Transition metal complexes with Schiff Base ligands are most suitable choice in this field as they can regulate the metal uptake, trafficking and excretion in biological systems, which may limit the side effects and provide better activities in drug resistance cells.<sup>1.120</sup> These biologically active derivatives possess various bio-medicinal properties, including antibacterial, antifungal, antioxidant, anti-inflammatory, antitumor, anticancer and herbicidal activities.<sup>1.121a-h</sup>

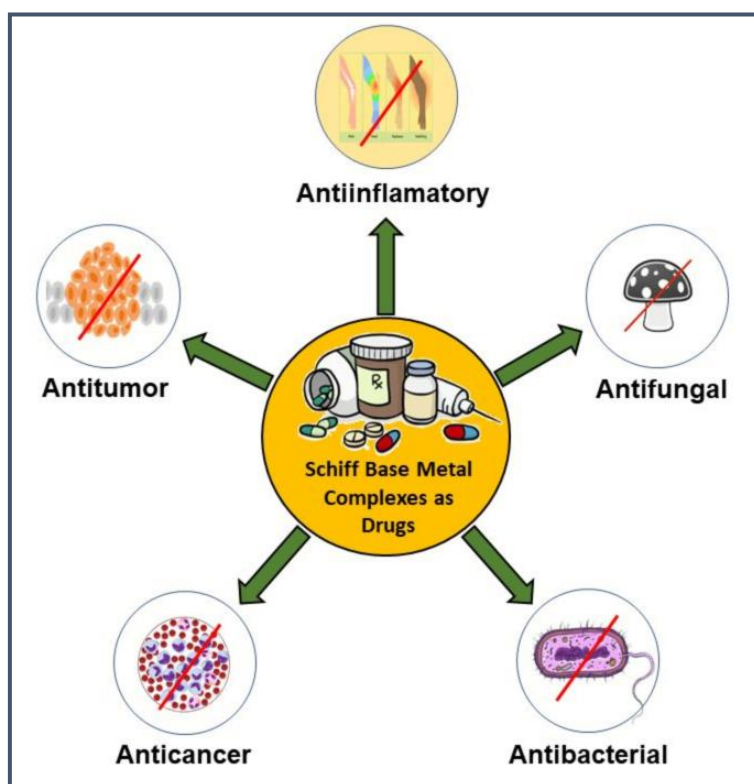


**Figure 1.18:** Biological applications of Schiff base metal complexes.

For the past few decades, people have been suffering from cancer, the most fatal diseases in the world. It refers to a class of multigenic disease characterized by a variety of genetic and epigenetic alterations and it can be treatable by preventing the rapid proliferation of cancer cells for which the replication of DNA is to be arrested.<sup>1.122</sup> Cisplatin was the first metal based drug that emerged in the late 19th century and the efficiency of this complex as a potent anticancer drug opened the gate of unexplored world of metal-based chemotherapeutic



agents.<sup>1.123</sup> Despite the clinical success of cisplatin, the challenges for utility of this metal-based drug still remain due to severe systemic toxicity, intrinsic drug resistance and high cost issues.<sup>1.124a-c</sup> Therefore, for the clinical therapy, more effective, target specific, less toxic, and preferably non-covalently binding cisplatin derivatives have been developed.<sup>1.125a-e</sup>

Nickel is one of the most essential elements for biological systems as it lies at the active site of various enzymes like urease, carbon monoxide dehydrogenase, hydrogenase and methyl-S-coenzyme M reductase.<sup>1.126a-d</sup> Ni(II) complexes with various geometries such as tetrahedral, square planer, trigonal bipyramidal, square pyramidal, octahedral, etc have been developed over a long period of time.<sup>1.127</sup> It has been reported in literature that nickel complexes with these various geometries exhibit a variety of biological activities, such as antiepileptic, anticonvulsant agents, antibacterial, antifungal, antimicrobial, vitamins and anticancer/antiproliferative activities.<sup>1.128a-m</sup>

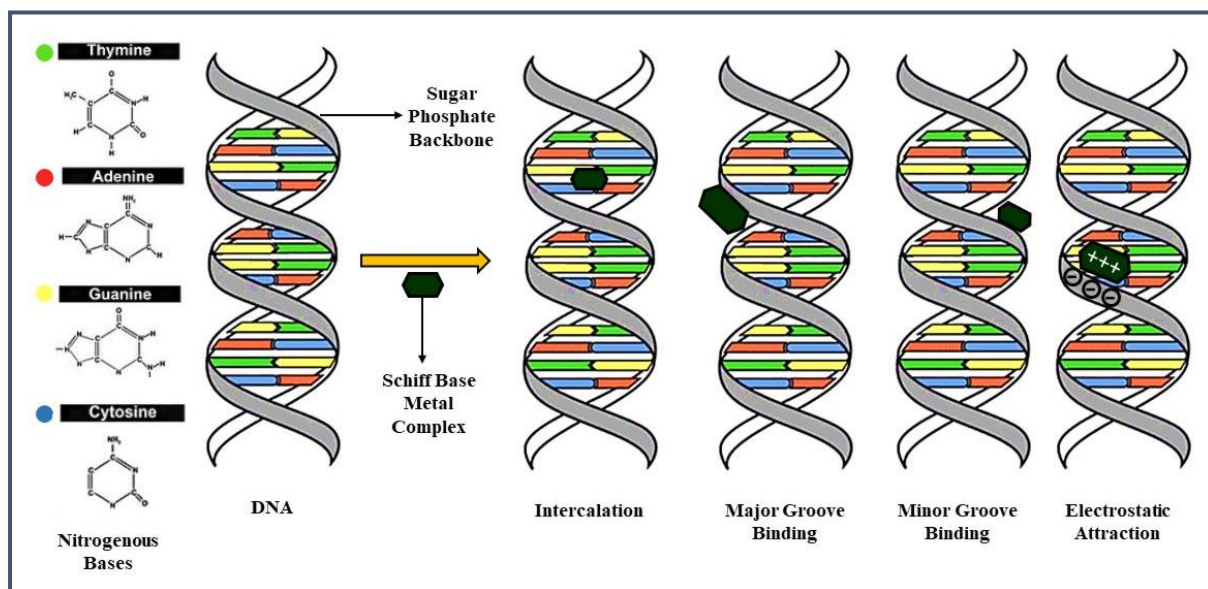


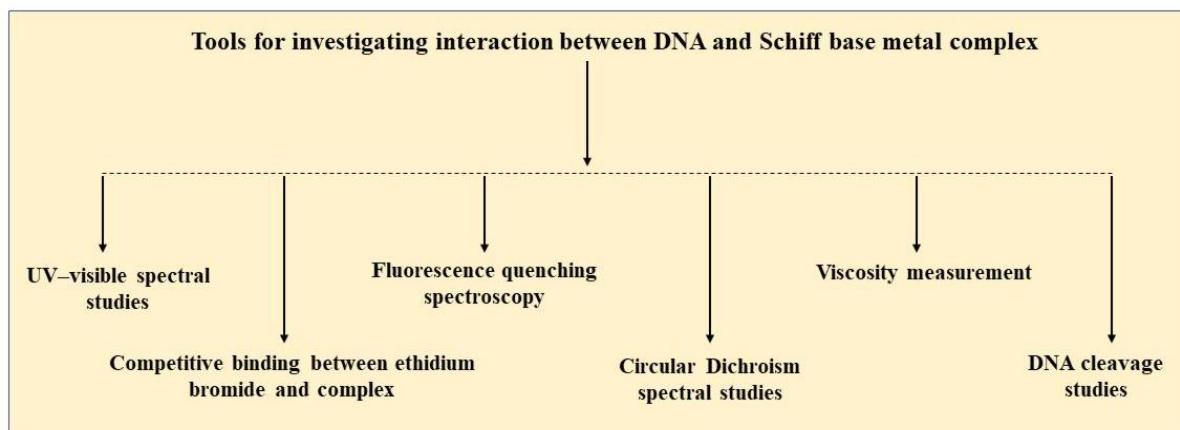
**Figure 1.19:** Schematic representation of various binding modes of DNA.

Recently, Ni(II) complexes are utilized as potential anticancer drugs and sometimes these complexes are more useful than the well-known cisplatin.<sup>1.129</sup> The literature revealed that Ni(II) complexes enter into a cell by phagocytosis, travel to the nucleus, and cause oxidative breakage in DNA strand, DNA-DNA cross-links and DNA-protein cross-link. The metal ion is known to bind well to guanine via the N7 nitrogen atom of the purine's imidazole ring. Such binding is thought to be responsible for the fact that sub millimolar concentrations of Ni(II) will cause conformational change in DNA, i.e from the right-handed B helical form to a left-handed Z helical form.<sup>1.130</sup> All of these observations collectively suggest that Ni(II) coordination compounds would display interesting binding and cleavage reactivity with nucleic acids. Thus

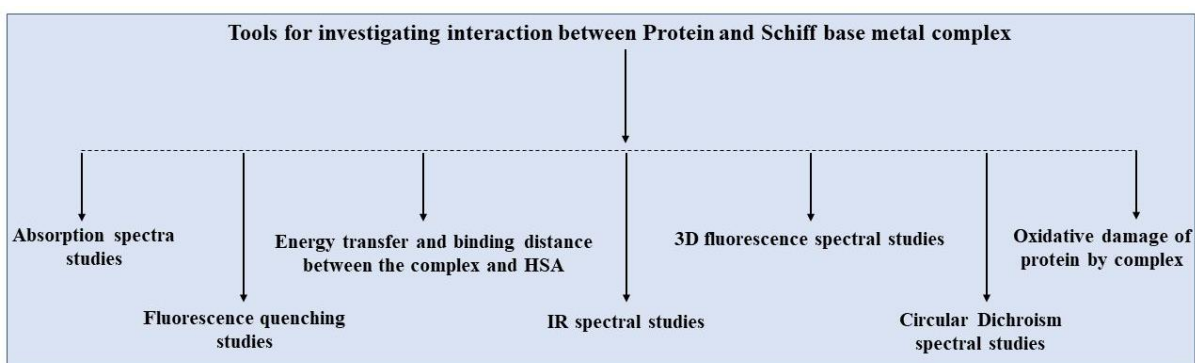
investigation of the interaction between Ni(II) complexes and DNA plays an important role in molecular biology as well as in cancer healing.<sup>1.131a-e</sup>

DNA, related to the replication, transcription, mutation of genes, has been identified as a primary intracellular target for anticancer drug design. It has been considered as the most promising biological receptors for the development of chemotherapeutic agents as many small molecules show anticancer activities by binding with DNA. This alters DNA replication, blocks the division of cancer cells and causes the cell death.<sup>1.132</sup> Molecules can bind to DNA through various non-covalent interactions such as groove binding, intercalation and non-specific electrostatic surface binding (**Figure 1.19**). An understanding on the binding modes of the complexes to DNA would give the understanding of the biochemical mechanism of action of the metal complexes.<sup>1.133</sup> It has been observed that by changing both the ligands and metal ions, it is possible to modify the interaction mode of the complex with nucleic acids.<sup>1.134a-c</sup> Thus, to design transition metal complexes as effective chemotherapeutic agents, it is essential to investigate the interactions of the transition metal complexes with DNA.<sup>1.135a,b</sup> The potential binding ability and the nature of binding of the metal complexes with DNA are investigated by the tools mentioned in **Scheme 1.4**.

On the other hand, investigation of the interactions of metal-based drug with serum proteins have attracted much attention in the transport and metabolism of drug in blood under physiological conditions.<sup>1.136</sup> In particular, HSA is the most explored one. It is the most abundant and most versatile protein present in the human plasma acting as the most versatile transporter and disposer of various endogenous and exogenous molecules.<sup>1.137a-e</sup> Interaction of a drug with a protein forms a stable protein–drug complex, which plays an important effect on the distribution, metabolism and the efficacy of the drug.<sup>1.138</sup> It has been observed that binding of a metallodrug to albumin brings about an increased drug solubility in plasma, decreased toxicity and protection against oxidation of the bound drug.<sup>1.139</sup> Thus, the decrease in toxicity and immunogenicity makes HSA an ideal choice for drug delivery agent. Another important role of HSA is to scavenge free radicals as an antioxidant and to maintain the osmotic blood pressure. Furthermore, this serum protein is known to accumulate in tumors and serves as carrier conjugate of various organic anticancer drugs viz., chlorambucil, doxorubicin and paclitaxel.<sup>1.140</sup> Therefore, investigation on the protein binding of drugs has imperative and fundamental importance for assessment of the therapeutic efficacy of the drug and its delivery towards the target cells at molecular level.



**Scheme 1.4:** Tools used for the investigation of the potential binding ability and the nature of binding of the transition metal complexes with DNA.



**Scheme 1.5:** Tools used for the investigation of the potential binding ability of the transition metal complexes with HSA.

Patra *et al.*<sup>1,141</sup> synthesized two almost identical square planer neutral complexes  $[\text{Ni}(\text{L}^1)_2]$  (**Ni-1**) and  $[\text{Ni}(\text{L}^2)_2]$  (**Ni-2**) [where,  $\text{HL}^1 = 2\text{-}[(2\text{-Methoxy-ethylimino)-methyl}]\text{-phenol}$  and  $\text{HL}^2 = 2\text{-Methoxy-6-}[(2\text{-methoxy-ethylimino)-methyl}]\text{-phenol}$ ]. Their structures were confirmed by single-crystal XRD study (**Figure: 1.20**). Geometry optimization of these two complexes using functional B3LYP were also in good agreement with the structural results obtained from the XRD study. The interesting structural feature of the complexes is the presence of C-H... $\pi$  interactions which results 2D and 1D supramolecular network in complexes **Ni-1** and **Ni-2**, respectively.

Interaction of complexes with calf thymus DNA (CT-DNA) was investigated indicating the intercalative binding mode of the complexes with CT-DNA. The calculated intrinsic binding constant values with CT-DNA are  $(1.43 \pm 0.56) \times 10^6 \text{ M}^{-1}$  (for **Ni-1**) and  $(1.25 \pm 0.79) \times 10^6 \text{ M}^{-1}$  (for **Ni-2**). Furthermore, interaction of the complexes with BSA and HSA were studied by various spectroscopic techniques. The results revealed that the complexes interact with albumin proteins through ground state association mechanism.

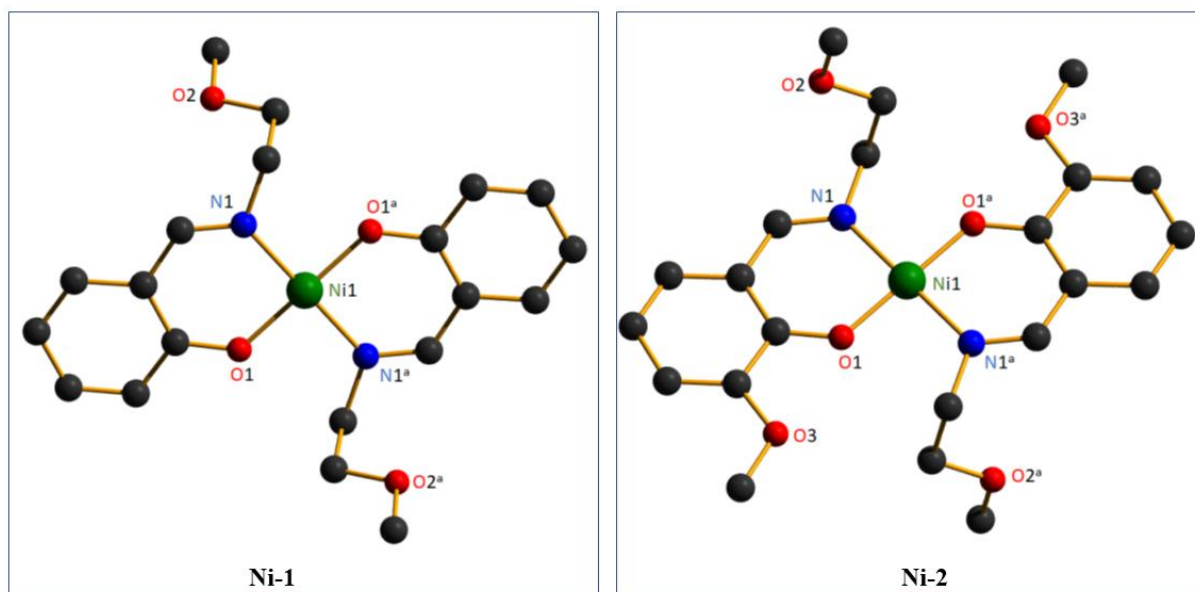


**Figure 1.20:** Crystal structures of complex **Ni-1** and **Ni-2**. Hydrogen atoms are omitted for clarity.

Jana *et al.*<sup>142</sup> discussed synthesis of one mononuclear Ni(II) complex  $[\text{Ni}(\text{L}')_2](\text{ClO}_4)_2$ , where  $\text{L}' = \text{Piperidine-2-yl-N-(pyridine-2-ylmethylene)methanamine}$ , complex **Ni-3**, along with its DNA binding, cell viability,  $\text{H}_2\text{O}_2$  sensing, antibacterial properties and photo catalytic activity. The single crystal XRD study showed that the Ni(II) ion in this complex possesses an octahedral geometry (**Figure 1.21**).

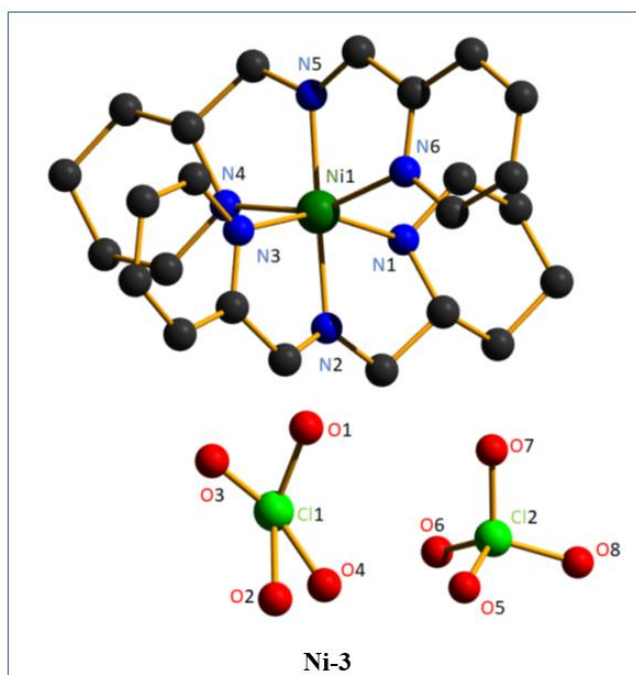


**Figure 1.21:** Crystal structure of complex **Ni-3**. Hydrogen atoms are omitted for clarity.

The antibacterial study for metal salt, ligand and complex was performed using *Staphylococcus aureus*. The results indicated that complex **Ni-3** possesses very good antibacterial property. The complex is also efficient in binding DNA through partial intercalation as well as minor-groove binding. It has been confirmed by molecular docking study performed with B-DNA model sequence. Moreover, the cell viable activity of the ligand along with the nickel complex was measured in vitro against the Hela cell and it showed that the complex is biocompatible in nature.

Kim *et al.*<sup>143</sup> synthesized a novel nickel(II) complex **Ni-4** having a pyrrolyl-iminophosphine (PNN) pincer. The molecular structures of complex **Ni-4** were established by single-crystal XRD study, demonstrating a distorted square planar geometry around the nickel centre comprising two 5-membered metallacyclic rings (**Figure 1.22**). Cytotoxicity study of the complex was carried out with (a) A549 (lung), (b) SK-OV-3 (ovarian), (c) SM-MEL-2 (skin), and (d) HCT15 (colon) human cancer cell lines by using SRB assay. They used cisplatin as a positive control. IC<sub>50</sub> values observed were greater than 30 for each case.

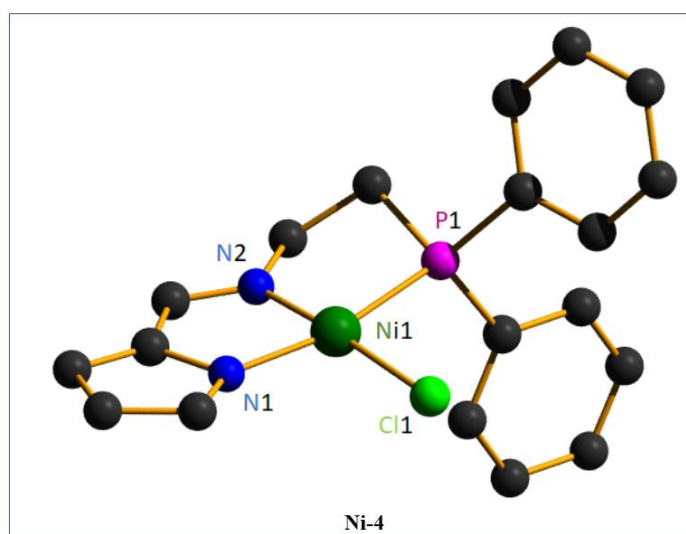


**Figure 1.22:** Crystal structure of complex **Ni-4**. Hydrogen atoms are omitted for clarity.

Venkateswarlu *et al.*<sup>144</sup> synthesized a mononuclear nickel(II) complex **Ni-5** with a bidentate O,N donor Schiff base ligand. The structure of complex **Ni-5** has been confirmed by single crystal XRD study which demonstrated that the metal centre is in square planar geometry.

The ethidium bromide displacement assay and absorption spectral titrations confirmed that the complex can bind DNA prominently through the intercalative mode with the intrinsic binding constant ( $K_b$ )  $7.79 \times 10^3 \text{ M}^{-1}$ . Gel electrophoresis also showed that the complex can induce

double strand breaks of supercoiled pBR322 plasmid DNA through both photolytic and oxidative pathways.

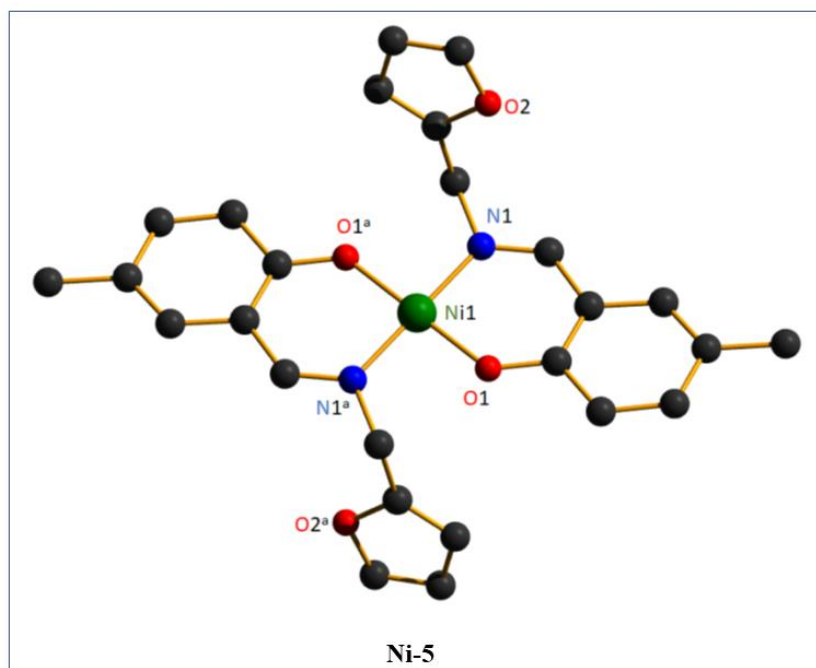


**Figure 1.23:** Crystal structure of complex **Ni-5**. Hydrogen atoms are omitted for clarity.

It exhibited significant cytotoxic effects towards the human breast adenocarcinoma cell line (MCF-7) ( $IC_{50} = 64.54 \pm 0.25$ ) and the oral carcinoma cell line (KB3) ( $IC_{50} = 75.07 \pm 0.83$ ). Moreover, the complex is capable of inhibiting the growth of bacteria to a fairly good extent. Thus, they suggested that the complex can possibly be useful for the design and synthesis of new metal-based drugs by tuning various different factors.

Keypour *et al*<sup>1.145</sup> reported two mononuclear nickel(II) complexes, **Ni-6** and **Ni-7**, which differ in the geometry around the metal centre and also in arm lengths of the ligands. The single crystal X-ray diffraction study revealed that the Ni(II) ion in complex **Ni-6** has a distorted square-planar environment whilst this ion has distorted octahedral environment in complex **Ni-7** (**Figure 1.24**).

They observed that the variation of the arm lengths of the ligands has an important impact on the formation and structure of the complexes. The DNA cleavage study has been carried out with these complexes. But both the complexes failed to show any cleavage activity on the pBR322 DNA without  $H_2O_2$ . However, these complexes showed antibacterial effects against three Gram-positive bacteria, three Gram-negative bacteria and three yeast, *Candida krusei* ATCC 1424, *Candida albicans* ATCC 10231 and *Candida tropicalis* ATCC 13803.

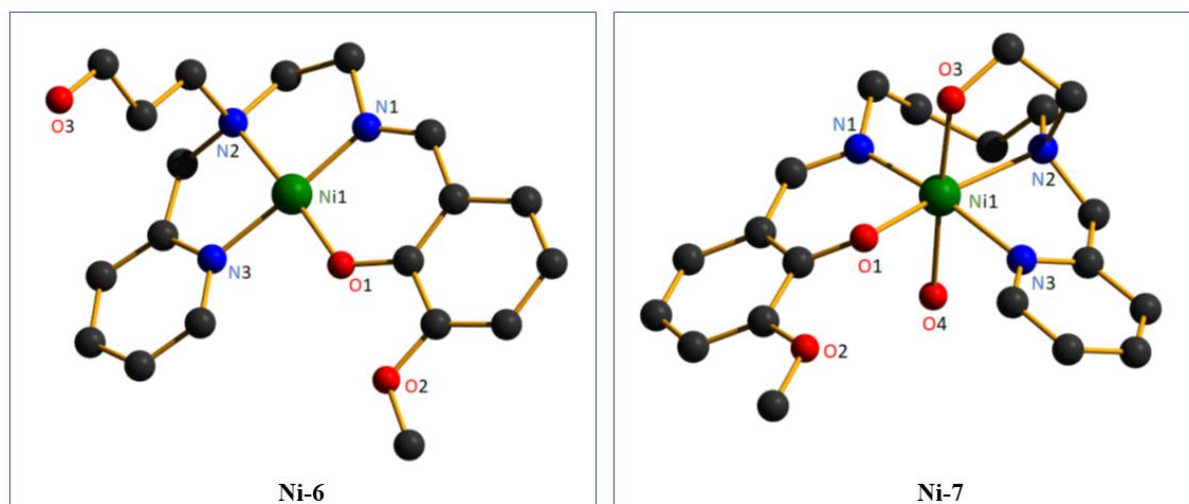


**Figure 1.24:** Crystal structure of complex **Ni-6** and complex **Ni-7**. Hydrogen atoms are omitted for clarity.

Wei *et al.*<sup>1.146</sup> synthesized two hexacoordinated octahedral nickel(II) complexes, [Ni(o-van-gln)(phen)(H<sub>2</sub>O)](**Ni-8**) and [Ni(sal-gln)(phen)(H<sub>2</sub>O)](**Ni-9**) [where, o-van-gln = a Schiff base derived from o-vanillin and glutamine, sal-gln = a Schiff base derived from salicylaldehyde and glutamine, phen = 1,10-phenanthroline]. The crystal structures of the two complexes confirmed the distorted octahedral coordination geometry (**Figure 1.25**). An interesting feature observed for each crystal is formation of a two-dimensional network structure by intermolecular hydrogen bonds.

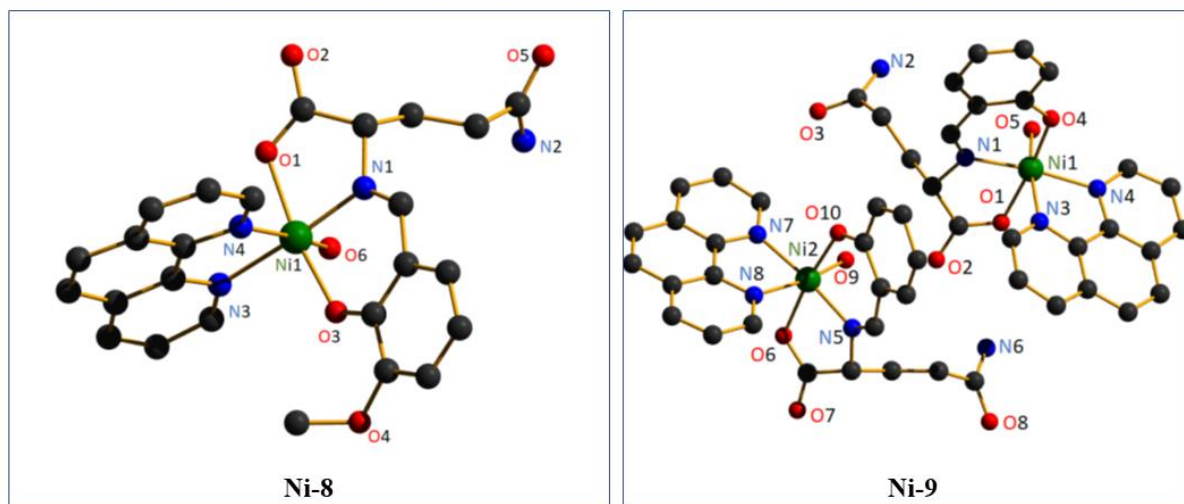


**Figure 1.25:** Crystal structure of complex **Ni-8** and complex **Ni-9**. Hydrogen atoms are omitted for clarity.

The DNA binding study revealed that both of these complexes are capable of binding calf thymus DNA via an intercalative mode. The obtained intrinsic binding constants ( $K_b$ ) and the numbers of binding sites ( $n$ ),  $1.01 \times 10^5$  and 1.05 for complex **Ni-8** and  $7.85 \times 10^4 \text{ M}^{-1}$  and 0.997

for complex **Ni-9** indicated that the former exhibits higher interaction with CT-DNA than the latter. Furthermore, the interactions between the Ni(II) complexes with BSA have also been investigated by spectroscopic studies. The results showed that both the complexes can quench the intrinsic fluorescence of BSA in a static quenching process. Site-selective competitive binding investigation revealed that the binding sites of the two complexes located in site I in sub-domains IIA of BSA. Assay of SOD activity of the Ni(II) complexes showed that they exhibit significant superoxide scavenging activity with  $IC_{50}$  values of  $3.4 \times 10^{-5}$  M for complex **Ni-8** and  $4.3 \times 10^{-5}$  M for complex **Ni-9**. From the observations they concluded that these two nickel(II) glutamine Schiff base complexes, which can affect the structural changes on DNA and bind to BSA, can act as the potential anticancer drugs.

Mukherjee *et al*<sup>1,147</sup> investigated DNA and HSA binding study of a mononuclear nickel complex, **Ni-10**,  $[Ni^{II}(H_2pydmedpt)]^{2+} \cdot 2Cl^{-}$ , which was prepared by the in situ reaction of pyridoxal (pyd), a vitamers of vitamin B<sub>6</sub>, medpt and nickel(II) acetate. The structure of complex **Ni-10** was established by single crystal XRD study which indicated that the binding of the Schiff base ligand to the metal centre involved two imine nitrogens, two phenolato oxygens and one amine nitrogen (**Figure 1.26**). It also revealed that the coordination geometry around the nickel atom is intermediate between square-pyramidal and trigonal-bipyramidal. The interesting feature observed in the crystal is the formation of supramolecular one dimensional chain structures that are stabilized by  $\pi$ - $\pi$  stacking and hydrogen bonding interactions.

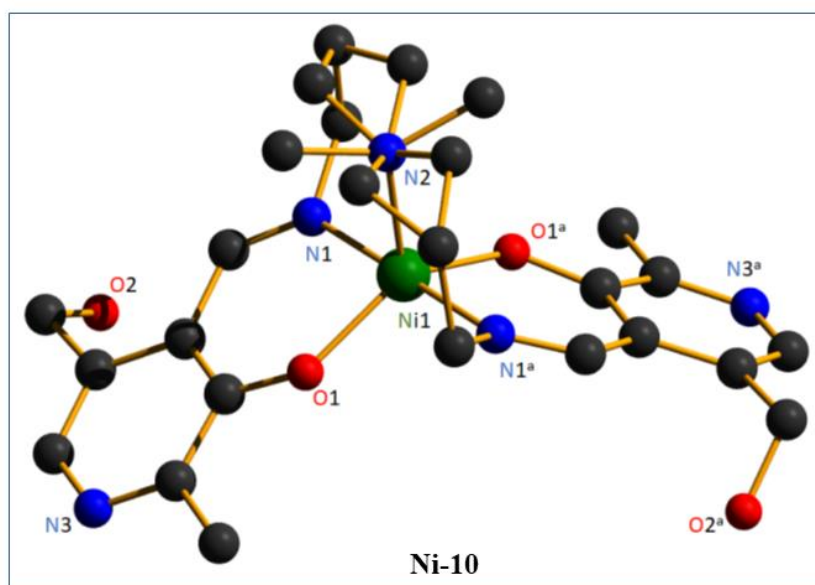


**Figure 1.26:** Crystal structure of complex **Ni-10**. Hydrogen atoms and one molecule of symmetry equivalent water of crystallization are omitted for clarity.



The competitive binding of complex **Ni-10** with DNA was studied in the concentration range of 40 to 400  $\mu\text{M}$  and apparent binding constant was determined as  $6.7 \times 10^3 \text{ M}^{-1}$ . On the other, HSA binding study was carried out at concentrations of 800–1000  $\mu\text{M}$  and 400–500  $\mu\text{M}$  for the complex and HSA, respectively, in PBS buffer at pH 7.4. But in this case, no binding was observed, instead, hydrolysis of the complex took place under the experimental conditions used and the resulting  $\text{Ni}^{2+}$  ions bound with HSA.

### 1.5.3 Schiff Base Metal Complexes as Catalyst

Schiff base complexes of transition metal ions show high catalytic activity both in homogeneous and heterogeneous media resulting the enhancement of the yield and product selectivity. The convenient synthesis route and thermal stability of Schiff base ligands have significant contribution in their possible applications in catalysis as metal complexes.<sup>1.148</sup> The activity of these Schiff base metal complexes varies with the various type of ligands coordinated, number of coordination sites and nature of the metal ions. In chemical literature, the catalytic activity of such metal complexes has been reported in various different reactions as given in the **Figure 1.27**.

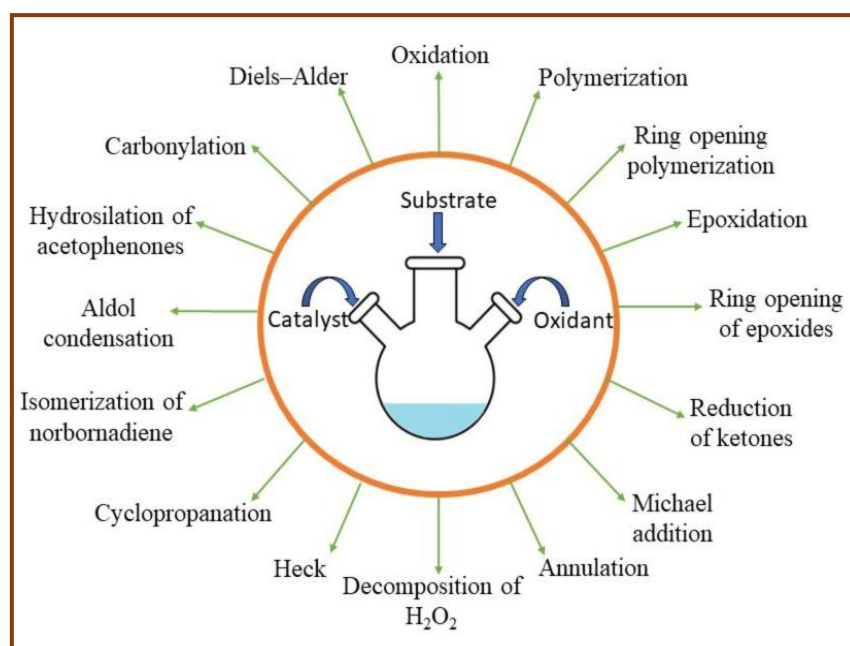


**Figure 1.27:** Various reactions catalyzed by metal Schiff base complexes.

#### 1.5.3.1 Oxidation reaction

From scientific and practical view point, oxidation process is very important without which life would not exist. In modern organic chemistry, selective catalytic oxidations have been the focus of extensive investigation and their importance has been highlighted in terms of Nobel

Prizes. Schiff base metal complexes have the ability to bind oxygen and hence they are chosen as the potential catalysts for the oxidation of various organic compounds.

Among various transition metals, copper is cheap and widespread in nature. Detailed investigation, supported by chemical literature, revealed that copper Schiff base complexes possess excellent catalytic activity in various oxidation reactions<sup>1.149a-c</sup> such as oxidation of alkane,<sup>1.150a-f</sup> alkene,<sup>1.151a,b</sup> sulfide,<sup>1.152</sup> catechol,<sup>1.153a,b</sup> alcohol<sup>1.154a,b</sup> etc. and deserve themselves as an efficient catalyst in this field.

#### **1.5.3.1.1 Oxidation of Alkanes**

In numerous areas including homogeneous catalysis, bioinorganic, and green chemistry, the search for efficient, mild and direct routes for oxidative functionalization of alkanes to industrially valuable products constitutes a subject of high relevance. A promising approach is made on the design and development of new copper (II) complexes which, with an appropriate oxidizing agent, are capable to convert alkanes into different oxidation products (alkyl hydroperoxides, alcohols, aldehydes, ketones or carboxylic acids) under mild conditions. In this regard, Pombeiro et al. reported a landmark work on oxidation of cyclohexane catalyzed by copper.<sup>1.150a</sup> After that a number of copper complexes were employed as the catalyst for such oxidation reactions.<sup>1.155</sup>

#### **1.5.3.1.2 Oxidation of Alkenes**

Alkenes, a primary petrochemical source, are another privileged building blocks in organic synthesis. They are converted into corresponding epoxides as the main product by copper complexes as the catalyst using various oxidants such as molecular oxygen, hydrogen peroxide, tert.-butyl hydroperoxide etc.<sup>1.156a-d</sup> Catalytic epoxidation of the alkene is one of the important industrial reactions for the production of a wide variety of fine chemicals.<sup>1.157a,b</sup> Thus catalytic olefin epoxidations become an important topic of research in both organic synthesis and bioinorganic modelling of oxidase.

#### **1.5.3.1.3 Oxidation of Sulfides**

Recently, considerable interest in sulfoxide compounds has been increased as sulfoxide derivatives have a wide range of important potential applications as convenient precursors or intermediates in the preparation of natural products and valuable physiologically and pharmacologically active molecules. They also act as an important integral and supplementary parts in many pharmaceutical and biological active molecules such as omeprazole and fipronil.<sup>1.158a-j</sup> Therefore, it is of current interest to develop economically and environmentally more sustainable procedures for the preparation of this sulfoxide functionality. Sulfides are

important substrate source for the synthesis of sulfoxides. Schiff base metal complex catalyzed synthesis of sulfoxide from sulfide has been widely developed using “green oxidants” like hydrogen peroxide.<sup>1.159a-c</sup> Chemical literature reported that copper Schiff base complexes as the catalyst can give a good yield and selectivity for common sulfides.<sup>1.160a-e</sup>

#### **1.5.3.1.4 Oxidation of Catechol**

Catechol oxidase, also known as catecholase, is a plant-based enzyme having an antiferromagnetically coupled dicopper(II) center. It catalyzes the oxidation of catechols to the corresponding quinones in the presence of aerial oxygen to protect the plant from damage caused by insects and pathogens.<sup>1.161</sup> The catechol oxidation reaction is commonly used in the determination of hormonally active compounds like adrenaline, catecholamines, dopamine and noradrenaline.<sup>1.162</sup> Researchers have developed metal complexes of Schiff bases which imitate the function of catecholase.<sup>1.163a-c</sup> It is well documented that copper Schiff base complexes serve as efficient catechol oxidase models.<sup>1.164a-c</sup>

#### **1.5.3.1.5 Oxidation of Alcohol**

The aerobic alcohol oxidation catalyzed by metal Schiff base complexes provides one of the most promising green chemical pathways to a class of valuable chemicals including lactones, aldehydes or ketones, which therefore, represent one of the most critical organic transformations in current synthetic chemistry.<sup>1.165a,b</sup> This can be achieved by following several methods and using different reagents.<sup>1.166</sup> The classical methodology involves the stoichiometric use of heavy metals, notably Cr and Mn,<sup>1.167</sup> containing toxic and/or hazardous oxidizing agents.<sup>1.168</sup> Alternatively metal-free oxidation, such as the Swern and Pfitzner-Moffat protocols, involves moisture-sensitive oxidants and environmentally undesirable reaction media, such as chlorinated solvents.<sup>1.169</sup> The atom economy of these methods is also extremely disadvantageous. Therefore, use of appropriate catalyst for such transformation is an alternative option in terms of environmental pollution and economy. In the search for new catalysts, Cu-based systems constitute an attractive alternative<sup>1.170a,b</sup> as copper is an inexpensive, non-toxic metal and presents in many enzymes which are involved in the alcohol oxidation.

#### **Galactose Oxidase: Biomimetic Systems for Alcohol Oxidation**

Development of ‘bioinspired’ or ‘biomimetic’ metal based redox-catalysts is one of the popular topics of research nowadays. Undoubtedly galactose oxidase (GO) forms the most appealing example for this biocatalytic alcohol oxidation.<sup>1.171a,b</sup> Galactose oxidase (GO) is a fungal enzyme (68 kDa) which acts as a broad-spectrum catalyst for the two-electron oxidation of various different primary alcohols to the corresponding aldehyde solely with the reduction of

dioxygen to  $\text{H}_2\text{O}_2$ .<sup>1.172a,b</sup> This enzyme was first isolated in 1959<sup>1.173</sup> and its crystal structure was reported in 1991.<sup>1.174</sup>

### Structure of the Active Site of GO:

The crystal structure revealed that the active site of this biocatalyst involves a mononuclear copper(II) species with a distorted square pyramidal geometry with Tyr495 occupying the axial position. Whereas, His496, His581, Tyr272 and an exogenous ligand  $\text{H}_2\text{O}$  coordinate the copper in equatorial positions. The most striking feature of the complex is the presence of cross-linkage of Tyr272 to Cys228 via a thioether bond at the ortho position of the OH group, which presumably lowers the tyrosyl/tyrosine redox potential. This enzyme is believed to exist in three well-defined oxidation levels: (a) the CuII-tyrosyl radical oxidized form, (b) an intermediate CuII-tyrosinate form, and (c) the reduced CuI -tyrosine form. But the former and latter forms are only catalytically active. Both the forms (a) and (c) undergo a rapid bimolecular comproportionation that affords the catalytically inactive CuII-tyrosinate form.<sup>1.175</sup>

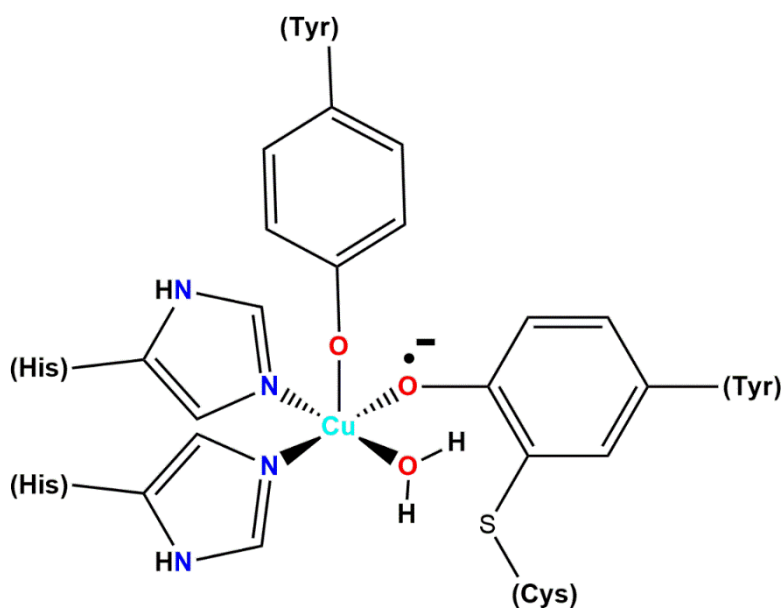


**Figure 1.28:** Active site of galactose oxidase (GO)

### Catalytic mechanism of GO

The catalytic mechanism of galactose oxidase has been extensively studied (**Figure 1.29**).<sup>1.176</sup> At first, the active species A coordinates to the primary alcohol leading to the formation of the metal-phenoxy radical complex B. Then it abstracts proton from the substrate by the axial tyrosinate (Tyr495) followed by a rapid intramolecular electron transfer from the intermediate ketyl radical anion with reduction of Cu(II) to Cu(I) (complex C). Complex C then reacts with dioxygen to form the hydroperoxo copper(II) (complex D) and the aldehyde is liberated. Finally, the active form of the enzyme GO is obtained by releasing dihydrogen peroxide.

Thus, galactose oxidase has been the major source of inspiration for scientists over the last two decades in designing an efficient copper catalyst for the oxidation of alcohols and excellent ample examples have been reported in the literature.<sup>1.177a-f</sup>

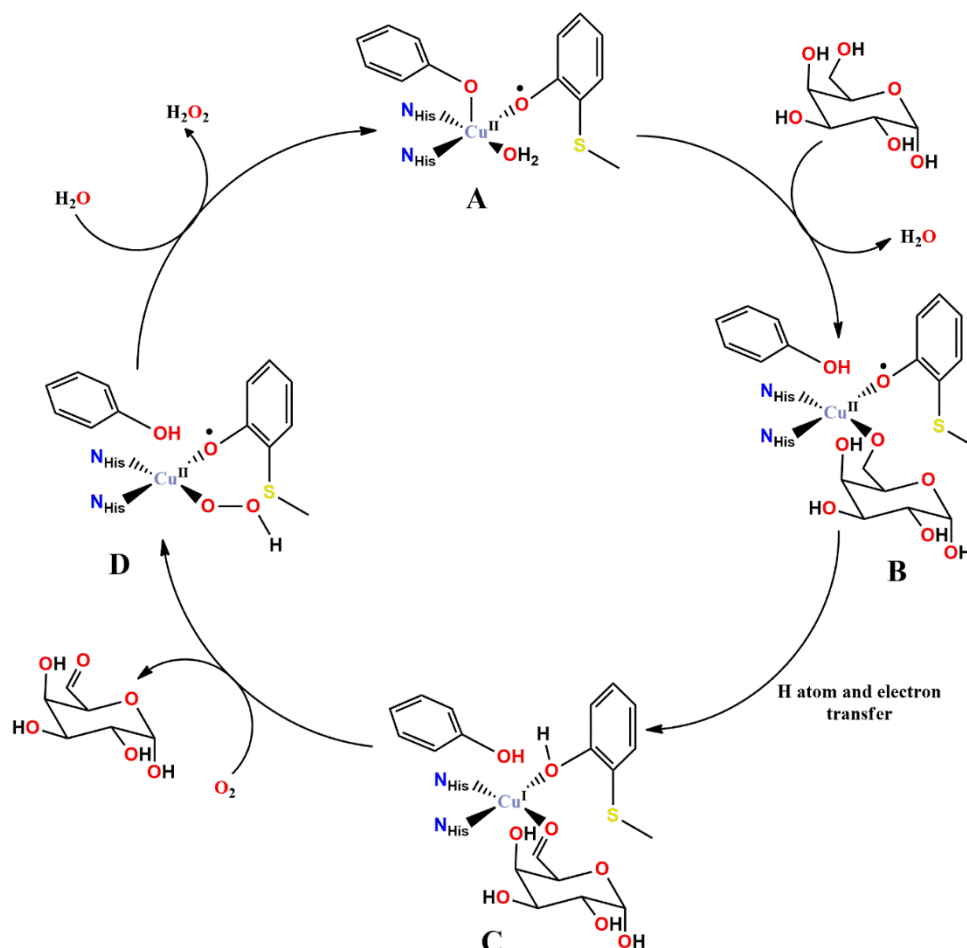


**Figure 1.29:** Proposed catalytic cycle of galactose oxidase.<sup>1.176a,b</sup>

### Bio-inspired Copper(II)-Schiff base catalysts

Stack and co-workers<sup>1.178</sup> reported the first efficient synthetic biomimetic copper catalyst, **Cu-1**, in 1998. The biomimetic copper complex showed many of the properties of galactose oxidase, including the catalytic conversion of an alcohol to an aldehyde.

The synthetic complexes reported here (**Figure 1.30**) were synthesized from two  $N_2O_2$  donors having a binaphthyl backbone and thioether functions, namely BSI ( $R_1 = SPr^i$  and  $R_2 = {}^tBu$ ) and BSP ( $R_1 = SPh$  and  $R_2 = {}^tBu$ ). The X-ray crystal structure of one cupric complex, **Cu-1**, i.e.  $[Cu(II)BSI]$ , confirms the formation of a monomeric, four-coordinate, distorted square planar Cu(II) complex (**Figure 1.30**).

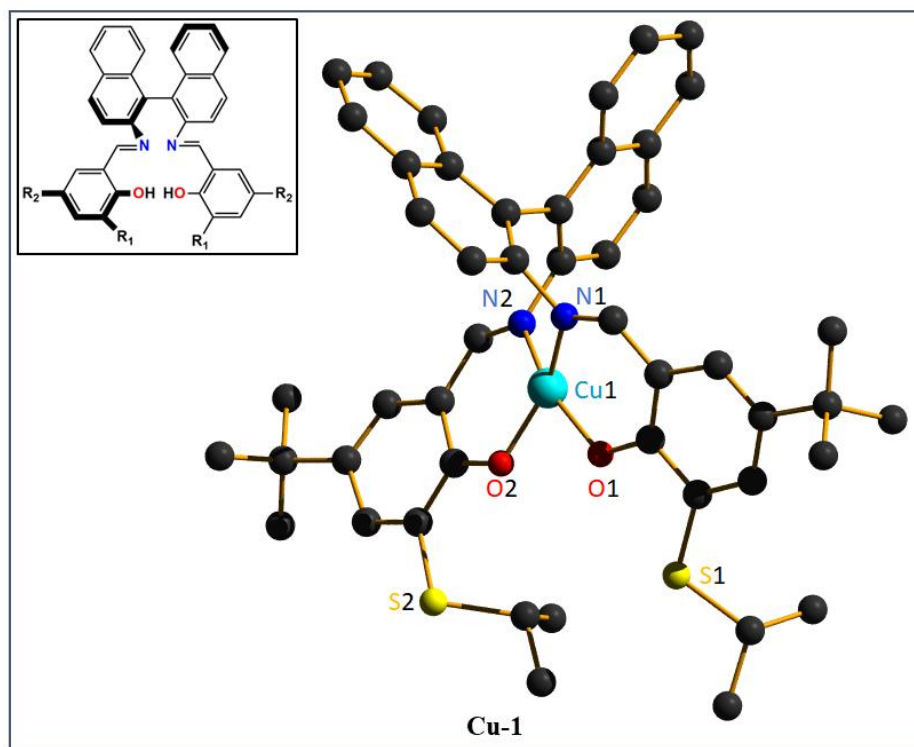


**Figure 1.30:** ORTEP representation (50% thermal ellipsoids) of the X-ray crystal structure of **Cu-1**. Inset: Structure of the  $N_2O_2$  ligand designed to mimic the active site of galactose oxidase upon coordination with copper(II) ion.

**Table 1.3:** Turnovers achieved in the  $[Cu^{II}(BSP)]^-$  and  $[Cu^{II}(BDB)]^-$ -catalyzed oxidation of alcohols at room temperature.<sup>1,178</sup>

Catalyst <sup>a</sup>	TON/ Solvent-free		TON/ 1.5 M solution in Acetonitrile		
	Benzyl alcohol <sup>b</sup>	1-Phenylethanol	Benzyl alcohol <sup>c</sup>	1-Phenylethanol	Cinnamyl alcohol
$[Cu^{II}BSP(BF_4)]^-$	1300	-	-	-	-
$[Cu^{II}BSP]$	1300	60	400	30	40
$[Cu^IBSP]^-$	900	-	-	-	-
$[Cu^{II}BDP]$	200	30	40	30	30

<sup>a</sup>Typical conditions: 0.05 mol% Cu-complex, 0.2-0.5 mol% base, 1atm  $O_2$ , RT, 20 h.

<sup>b</sup>0.01 % catalyst and 2 % base.

<sup>c</sup>0.005 mol% catalyst and 0.2 mol% base.

These complexes were used as efficient catalysts to convert allylic and benzylic alcohols to their respective aldehydes or ketones in the presence of a basic co-catalyst, i.e., lithium or sodium methoxide (**Table 1.3**).<sup>1,178</sup> It reveals that a TON of 1300 was achieved by using 0.01 to 0.06 % of the  $[Cu^{II}BSP]$  coordination compound as catalyst and here the corresponding aldehydes were the final products. The oxidation reactions were also performed in acetonitrile,

although the catalyst is much less efficient in this solvent. The explanations of the lower activity of  $[\text{Cu}^{\text{II}}\text{BDB}]$  (BDB ( $\text{R}_1 = \text{tBu}$  and  $\text{R}_2 = \text{tBu}$ ), may be the followings: (1) the steric hindrance produced by the four bulky tert-butyl groups which hinder an easy coordination of the alcoholic substrate to the copper ion; (2) absence of a thioether bond which may play a role during the catalytic cycle of the enzyme.

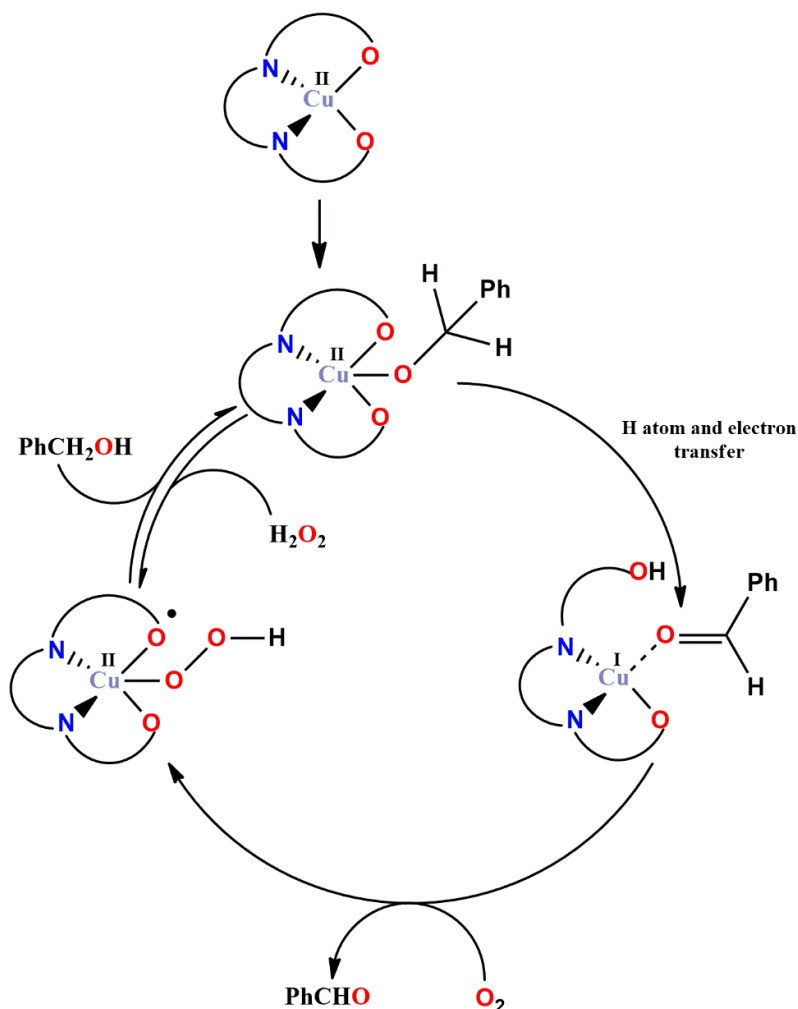


**Figure 1.31:** Proposed catalytic cycle for the biomimetic complex  $[\text{Cu}^{\text{II}}\text{BSP}]$ .<sup>1.178</sup>

A mechanism for this reaction has also been proposed with the most effective catalyst and substrate,  $[\text{Cu}^{\text{II}}\text{BSP}]$ , and benzyl alcohol, respectively. The alcohol first coordinates to the catalyst precursor  $[\text{Cu}^{\text{II}}\text{BSP}]$ , which results in the formation of a metal-phenoxyl radical complex. This so formed species then undergoes the substrate  $\text{C}^\alpha\text{-H}$  proton abstraction by the radical, followed by a rapid intramolecular electron transfer with reduction of  $\text{Cu}^{\text{II}}$  to  $\text{Cu}^{\text{I}}$ . This is the rate-determining step. After that, the copper(I) species reacts with dioxygen and as a result, a hydroperoxo copper(II) is formed with the release of the carbonyl product. Finally, the active species is reformed (**Figure 1.31**).

### 1.5.3.2 Brief literature survey on catalytic oxidation with Schiff Base Copper Complexes:

In literature, many mononuclear copper Schiff base complexes (**Cu-2 to Cu-11**) have been reported over the last two decades (**Figure 1.32**) which not only resemble the active-site of galactose oxidase structurally, but also functionally mimic the enzyme activity in carrying out two-electron oxidation of a wide variety of primary alcohols to the corresponding aldehydes under ambient conditions. The results of the catalysis are given in **Table 1.4**.

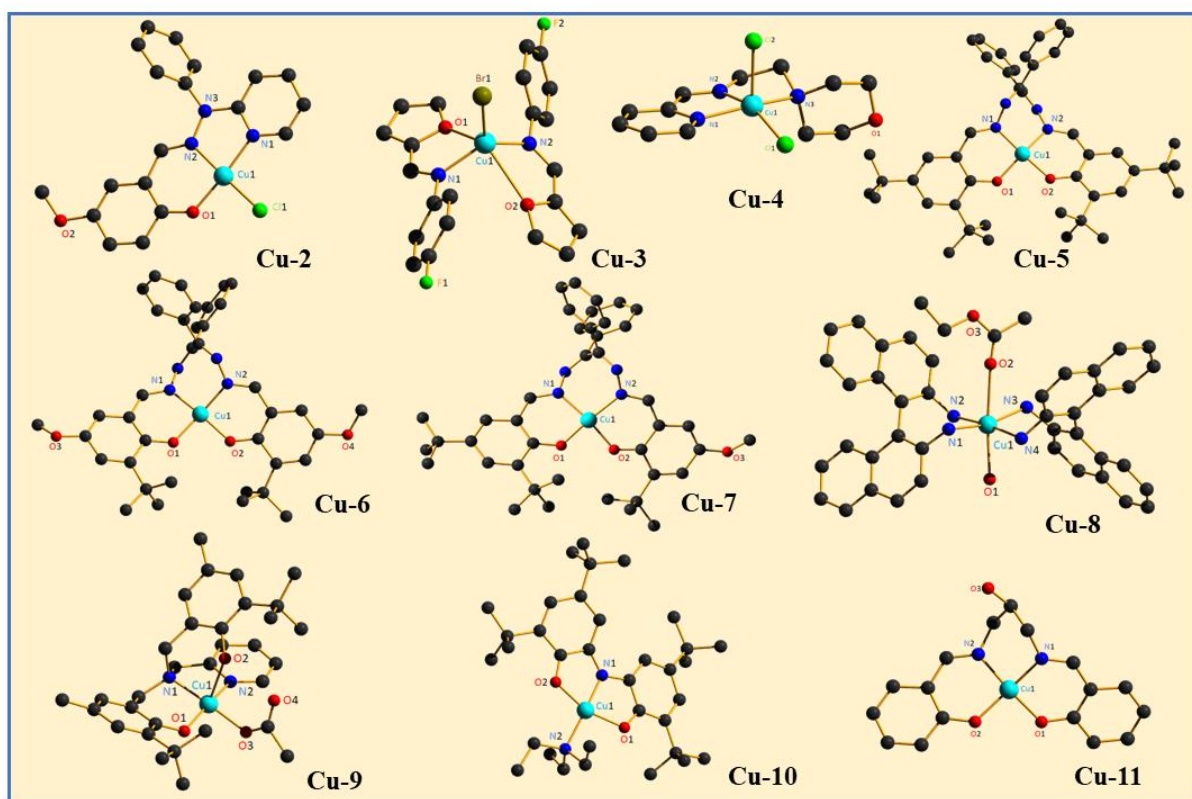


**Figure 1.32:** Crystal structures of some reported mononuclear copper complexes relevant to metal site galactose oxidase.

**Table 1.4:** Benzyl alcohol oxidation catalyzed by mononuclear copper complexes (**2-11**).

Entry	Catalyst	Solvent	Additive	Temp (°C)	Time (h)	Yield	TON	Ref.
1	<b>Cu-2</b>	CH <sub>3</sub> CN/ H <sub>2</sub> O	Base	70	24	55%	275	1.179
2	<b>Cu-3</b>	CH <sub>3</sub> CN	NMI	RT	24	> 99% (100%)	-----	1.180
3	<b>Cu-4</b>	CH <sub>3</sub> CN	-----	RT	14	90%	18	1.181



4	<b>Cu-5</b>	Solvent free	NaOH	RT	20	-----	823	1.182
5	<b>Cu-6</b>	Solvent free	NaOH	RT	20	-----	1036	Do
6	<b>Cu-7</b>	Solvent free	NaOH	RT	20	-----	979	Do
7	<b>Cu-8</b>	CH <sub>3</sub> NO <sub>2</sub>	-----	RT	22	71%	-----	1.183
8	<b>Cu-9</b>	CH <sub>3</sub> CN	NaOH and 1,2- dichloro benzene( internal standard)	RT	24	-----	272	1.184
9	<b>Cu-10</b>	THF	-----	20	20	55%	-----	1.185
10	<b>Cu-11<sup>b</sup></b>	-----	KOH	40	-----	-----	5.83 (for EtOH substra te)	1.186

<sup>b</sup>Substrate used were ethanol, n-propanol, or hydroxyacetone

In literature, dinuclear copper complexes based on simple Schiff base-type N,O-ligands have also been reported to catalyse the aerobic oxidation of primary alcohols, suggesting the great potential of multimetallic copper complexes in this premises.

Jehdaramarn *et al*<sup>1.187</sup> described how appended hydroxyl groups and ligand chain length affect the coordination and oxidation activity of dinuclear copper complexes (**Cu-12**, **Cu-13**) namely [2-((Pyridin-2-ylmethylene)amino)ethanol]copper(II) chloride (**Cu-12**) and [3-((Pyridin-2-ylmethylene)amino)propanol]copper(II) chloride (**Cu-13**) synthesized by the treatment of a series of (imino)pyridine ligands bearing appended hydroxyl groups, 2-((pyridin-2-

ylmethylene)amino)ethanol (Hpyet) for (**Cu-12**), and 3-((pyridin-2-ylmethylene)amino)propanol (Hpypr) for (**Cu-13**) with one equiv. of  $\text{CuCl}_2 \cdot 2\text{H}_2\text{O}$ .

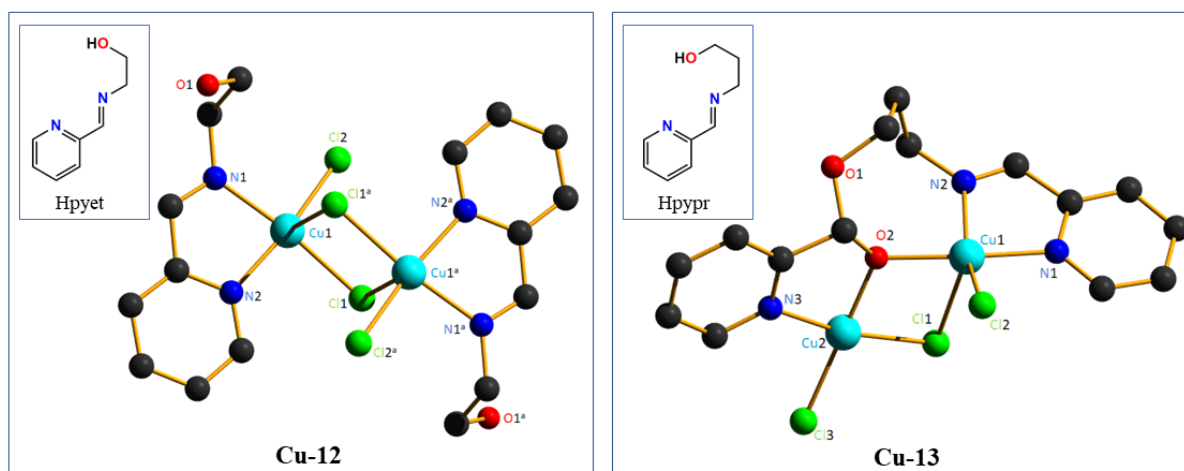
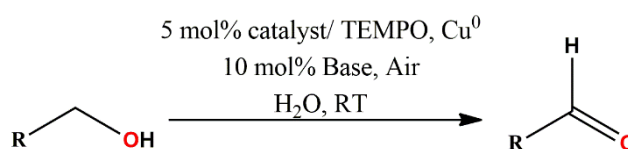


**Figure 1.33:** The ORTEP representation of **Cu-12** and **Cu-13** with thermal ellipsoids at the 50% probability level. Inset: The corresponding ligands.

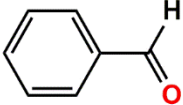
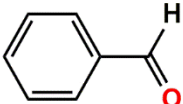
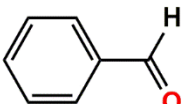
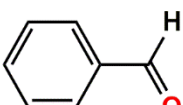
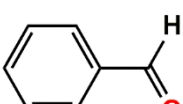
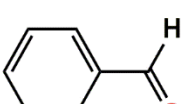
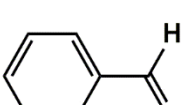
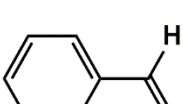
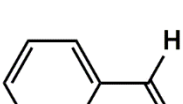
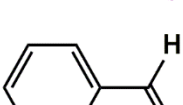
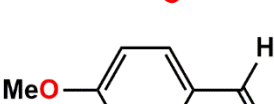
The crystal structure obtained for **Cu-12** shows a bidentate N,N binding with no Cu–OH interactions, whereas, surprisingly, a slightly longer propyl analogue gave a considerably different crystal structure for the dinuclear Cu(II) complex **Cu-13** (**Figure 1.33**), as a result of a nucleophilic addition of the appended propyl alcohol to the aldehyde group of 2-pyridinecarboxaldehyde. In the chloride-bridged asymmetric complex **Cu-12**, the copper centre resides in a square pyramidal geometry ( $\tau = 0.06$ ) whereas in alkoxy O-bridged complex **Cu-13** the copper centre resides in a distorted square pyramidal geometry ( $\tau = 0.26$ ).

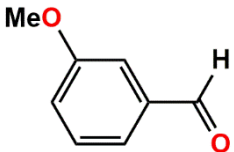
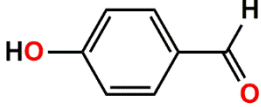
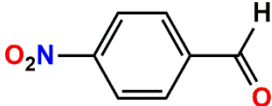
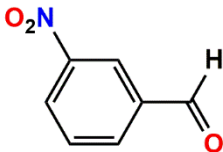
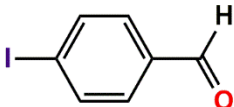
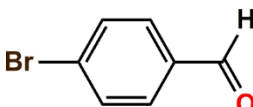
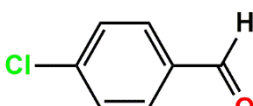
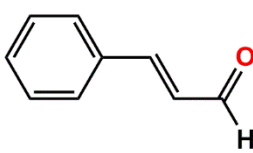
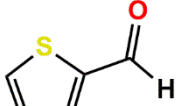
The Cu complex/ $\text{Cu}^0$ /TEMPO/ $\text{Na}_2\text{CO}_3$  catalyst system generally exhibited good activity for aerobic oxidation of various benzyl alcohol derivatives, cinnamyl alcohol, and 2-thiophenemethanol to benzaldehyde in  $\text{H}_2\text{O}$  at room temperature. The results of the catalytic reactions are tabulated below: (**Table 1.5**)



**Scheme 1.6:** Schematic representation of model reaction used for optimization.

**Table 1.5:** Result of catalytic aerobic oxidation by **Cu-12** and complex **Cu-13<sup>a</sup>**

Entry	Catalyst	Aldehyde	Base	Time (h)	Conversion (%)
1	<b>Cu-12</b>		Na <sub>2</sub> CO <sub>3</sub>	16	93
2	<b>Cu-13</b>		Na <sub>2</sub> CO <sub>3</sub>	16	94
3	<b>Cu-12</b>		Cs <sub>2</sub> CO <sub>3</sub>	16	84
4	<b>Cu-12</b>		K <sub>3</sub> PO <sub>4</sub>	16	58
5	<b>Cu-12</b>		NMI	16	87
6	<b>Cu-12</b>		Na <sub>2</sub> CO <sub>3</sub>	16	86
7	CuCl <sub>2</sub>		Na <sub>2</sub> CO <sub>3</sub>	16	37
8	CuCl <sub>2</sub> /Hpyet		Na <sub>2</sub> CO <sub>3</sub>	16	62
9	<b>Cu-12</b>		Na <sub>2</sub> CO <sub>3</sub>	16	75
10	-----		Na <sub>2</sub> CO <sub>3</sub>	16	18
11	<b>Cu-12</b>		Na <sub>2</sub> CO <sub>3</sub>	16	>99

12	Cu-12		Na <sub>2</sub> CO <sub>3</sub>	16	69
13	Cu-12		Na <sub>2</sub> CO <sub>3</sub>	16	>99
14	Cu-12		Na <sub>2</sub> CO <sub>3</sub>	48	42
15	Cu-12		Na <sub>2</sub> CO <sub>3</sub>	48	51
16	Cu-12		Na <sub>2</sub> CO <sub>3</sub>	16	>99
17	Cu-12		Na <sub>2</sub> CO <sub>3</sub>	16	59 (87)
18	Cu-12		Na <sub>2</sub> CO <sub>3</sub>	16	58 (93)
19	Cu-12		Na <sub>2</sub> CO <sub>3</sub>	8	>99
20	Cu-12		Na <sub>2</sub> CO <sub>3</sub>	16	76 (>99)

<sup>a</sup>Reaction conditions: alcohol substrate (1.0 mmol), catalyst (0.025 mmol), base (0.10 mmol), TEMPO (0.050 mmol), four Cu<sup>0</sup> sheets with a total area of 1 cm<sup>2</sup> in H<sub>2</sub>O (5 mL) at room temperature under aerobic conditions with 0.010 mmol of anisole as an internal standard.

Czepa *et al*<sup>1,188</sup> reported a dinuclear copper complex **Cu-14** synthesized by the treatment of Cu(ClO<sub>4</sub>)<sub>2</sub>·6H<sub>2</sub>O with the ligand HL having N<sub>2</sub>O-donor moiety based on benzothiazole unit. The crystal structure of this complex interestingly contains two different +1 charged complexes (**Figure 1.34**), one more-or-less typical monomeric CuL(CH<sub>3</sub>OH)<sub>2</sub> and one dimeric of quite unique composition Cu<sub>2</sub>L<sub>2</sub>(CH<sub>3</sub>OH)<sub>2</sub>(ClO<sub>4</sub>), with one of perchlorate oxygen atoms in bridging

position. All three copper atoms are penta coordinated having more or less regular tetragonal pyramid environment around them. It is worth mentioning that the dimeric structure of complex **Cu-14** is additionally strengthened by a pair of intramolecular OH(methanol)⋯O(ligand) hydrogen bonds.

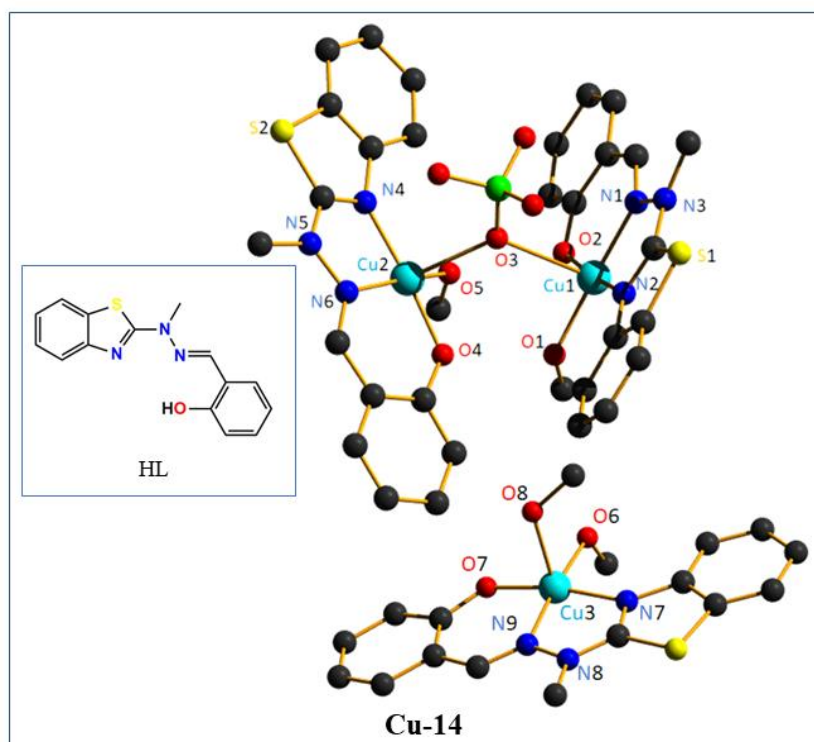
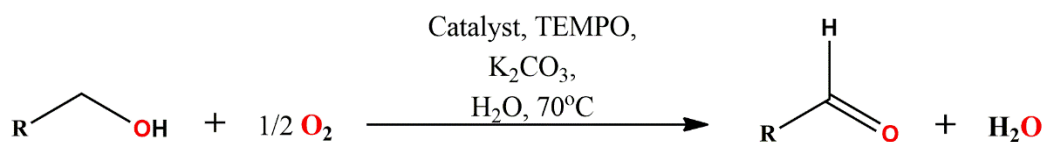


**Figure 1.34:** The ORTEP representation of **Cu-14** [dimeric ( $\mu$ -O, top) and monomeric (bottom)] with thermal ellipsoids at the 33% probability level. Inset: The corresponding ligand HL.

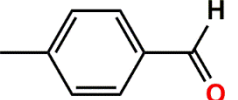
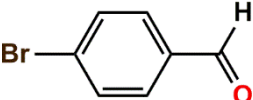
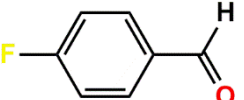
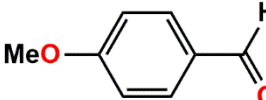
The complex appeared to be highly effective catalyst in oxidation of benzyl alcohol and its derivatives mediated by TEMPO in aqueous media. The observed catalytic activity towards the benzyl alcohol and its derivatives is enlisted in the **Table 1.6**.



**Scheme 1.7:** Schematic representation of model reaction used for optimization.

**Table 1.6:** Result of catalytic oxidation by complex **Cu-14**<sup>a</sup>

Entry	Aldehyde	Yield(%) <sup>b</sup>	Selectivity <sup>b</sup>
1		> 99	> 99

2		> 99	> 99
3		> 99	> 99
4		> 99	> 99
5		> 99	> 99

<sup>a</sup>Reaction condition: 0.01 mmol (1 mol% based on substrate) of catalyst, 0.05 mmol (5 mol%) of TEMPO, 1 mmol of substrate and K<sub>2</sub>CO<sub>3</sub> aqueous solution (3.33 ml, 1 M), 70 °C, 1 atm, air; 24 h.

<sup>b</sup>Calculated based on <sup>1</sup>H NMR spectroscopy.

Hazra *et al*<sup>1,189</sup> applied the advantage of the ability of coordination of the sulfonate group of the acyclic Schiff base 2-[(2-hydroxy-3-methoxyphenyl)methylideneamino]benzenesulfonic acid (H<sub>2</sub>L) to form two diphenoxo-bridged dicopper complexes [CuL(py)]<sub>2</sub> (**Cu-15**) and CuL(EtOH)<sub>2</sub>·2H<sub>2</sub>O (**Cu-16**). The structures of these dinuclear complexes are well established by single crystal X-ray diffraction study (**Figure 1.35**).

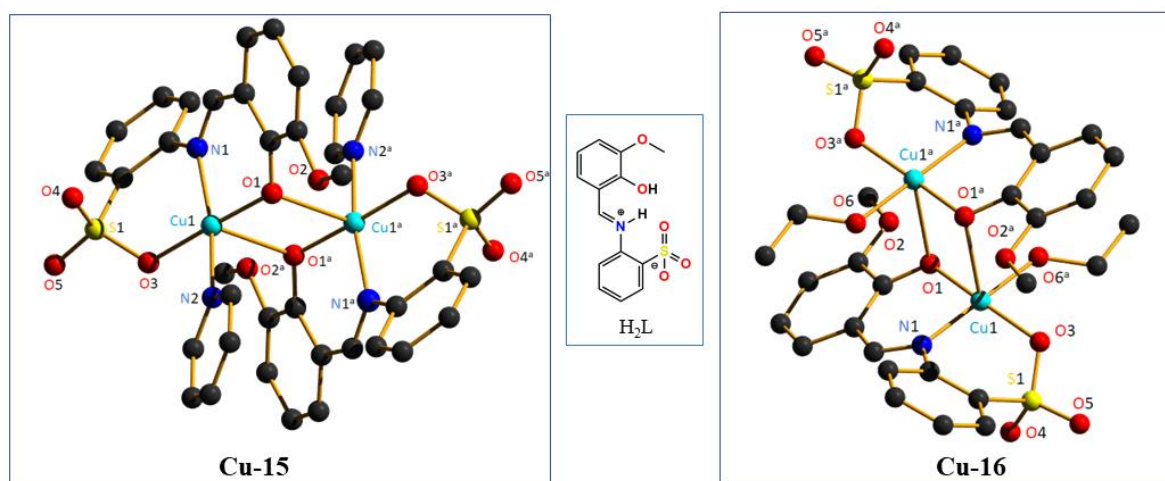
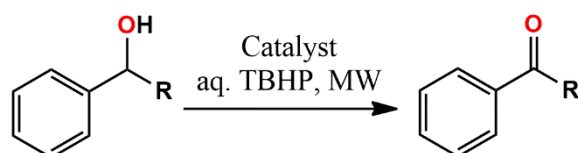


**Figure 1.35:** The ORTEP representation of **Cu-15** and **Cu-16**. In between: The corresponding ligands. Symmetry codes to generate equivalent atoms: 1-x, 1-y, 1-z for **Cu-15** and -x, 2-y, 2-z for complex **Cu-16**.

These complexes along with their salt precursor Cu(OAc)<sub>2</sub>·H<sub>2</sub>O were applied as efficient and selective catalysts for the homogeneous oxidation of benzyl alcohol and 1-phenylethanol to

benzaldehyde or acetophenone, respectively, using TBHP as oxidizing agent, under optimized conditions of low power (10 W) microwave irradiation, 100 °C, 20 min reaction time (or 150 for benzaldehyde) and additive- and solvent free medium. The catalytic data is enlisted in **Table 1.7**.



**Scheme 1.8:** Schematic representation of model reaction used for optimization.

**Table 1.7:** Selected data for the optimized MW-assisted additive- and solvent free homogenous oxidation of 1-phenylethanol (entries 1-4) and benzyl alcohol (entries 5-8) using **Cu-15** and complex **Cu-16**<sup>a</sup>.

Entry	Catalyst	Yield (%) <sup>b</sup>	TOF (h <sup>-1</sup> ) <sup>c</sup>	Selectivity (%) <sup>d</sup>
1	<b>Cu-15</b>	99.6	7.6 x 10 <sup>3</sup>	> 99
2	<b>Cu-16</b>	94.3	7.1 x 10 <sup>3</sup>	98
3	Cu(OAc) <sub>2</sub> .2H <sub>2</sub> O	18.7	1.4 x 10 <sup>3</sup>	51
4	-----	4.9	-----	83
5	<b>Cu-15</b>	99.2	922	98
6	<b>Cu-16</b>	91.7	917	> 99
7	Cu(OAc) <sub>2</sub> .2H <sub>2</sub> O	16.3	163	63
8	-----	2.3	-----	76

<sup>a</sup>Reaction conditions: 2.5 mmol of alcohol, 1 μmol (0.04 mol% vs. substrate) of catalyst, 100 °C, 5 mmol of TBHP (2 eq. 70% in H<sub>2</sub>O), 20 min (1-phenylethanol) or 150 min (benzyl alcohol) of MW irradiation (10 W).

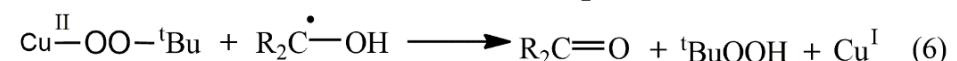
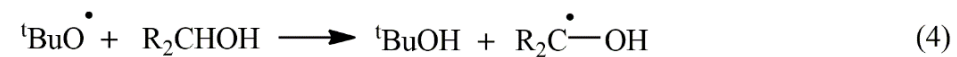
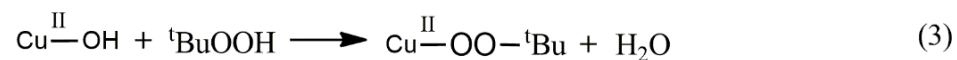
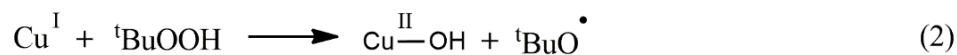
<sup>b</sup>Moles of ketone or aldehyde per 100 moles of alcohol.

<sup>c</sup>TOF = number of moles of ketone or aldehyde per mole of catalyst (TON) per hour.

<sup>d</sup>Moles of ketone or aldehyde per mole of converted alcohol.

They have also proposed the possible mechanistic pathway for the alcohol peroxidative oxidation as presented by the following equations (1) - (6). It was reported that the oxidation proceeds mainly via a radical mechanism involving both carbon- and oxygen-centred radicals.

They have also observed a strong inhibition effect when the reaction occurred in presence of the carbon-radical trap  $\text{CBrCl}_3$  or the oxygen-radical trap  $\text{Ph}_2\text{NH}$ .



Naeimi *et al.*<sup>1.190</sup> reported a bis-chloro-bridged binuclear Cu(II) complex, **Cu-17**,  $[(\text{HL})\text{Cu}(\mu_2\text{-Cl})_2\text{Cu}(\text{HL})] \cdot 1.5\text{CH}_3\text{OH}$  which was prepared *in situ* by refluxing the ligand (E)-1-(((2-hydroxypropyl)imino)methyl)naphthalen-2-ol ( $\text{H}_2\text{L}$ ) with dihydrate copper (II) chloride in methanol. The structure of the metal complex was determined by X-ray crystal structure analysis which reveals that the ligand is coordinated to the central metal ion via its alkoxy oxygen, imine nitrogen, and deprotonated phenolic oxygen atoms and the coordination sphere of Cu(II) is completed by the two bridging chloride anions (**Figure 1.36**). It also indicated that there are two complexes with three lattice methanol molecules.

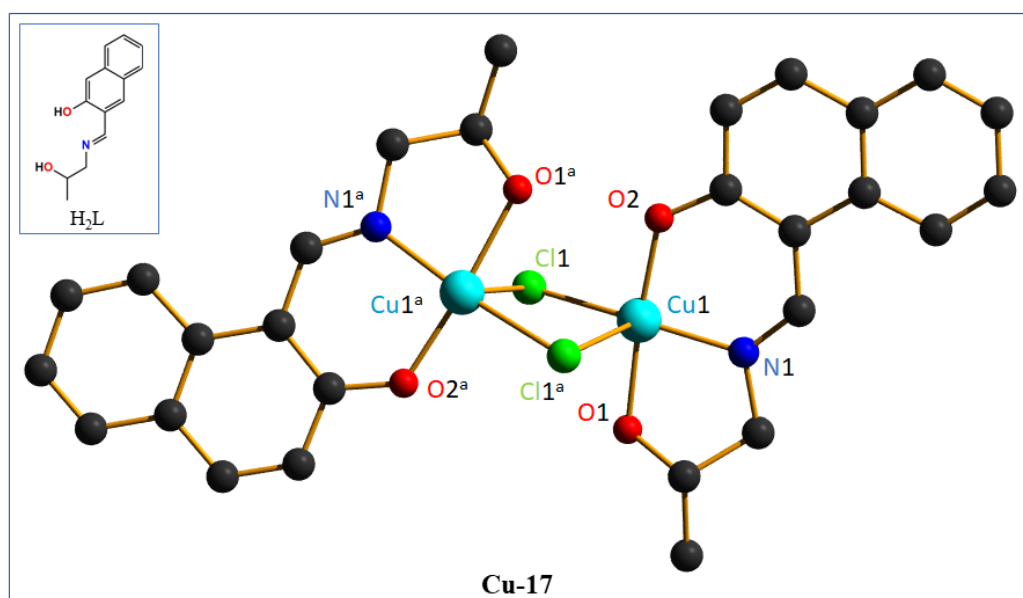
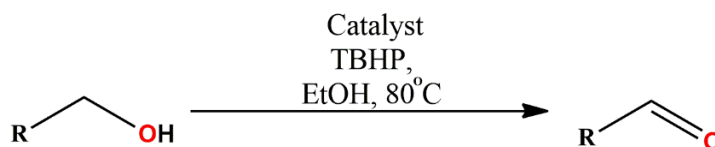


**Figure 1.36:** The ORTEP representation of **Cu-17** with thermal ellipsoids at the 50% probability level. Inset: The corresponding ligand  $\text{H}_2\text{L}$ .



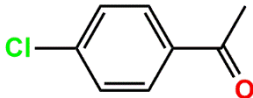
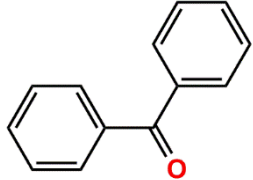
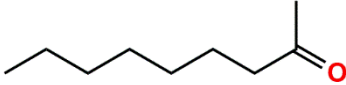
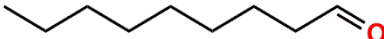
The complex was found as an efficient and selective catalyst towards the oxidation of alcohols in ethanol using TBHP as oxidizing agent. The detailed report of catalysis with this complex **Cu-17** is given in **Table 1.8**.



**Scheme 1.9:** Schematic representation of model reaction used for optimization.

**Table 1.8:** Result of catalytic oxidation by complex **Cu-17**<sup>a</sup>

Entry	Aldehyde/ Ketone	Time (h) <sup>b</sup>	Yield (%) <sup>c</sup>
1		1	90
2		1	85
3		2	85
4		2	85
5		1	90
6		2	85
7		2	75
8		1	95
9		1	95

10		2	90
11		2	85
12		2	75
13		2	83

<sup>a</sup>Reaction Condition: 0.5 mmol of alcohol, 0.01 mmol of catalyst, 0.5 mmol of TBHP, 80 °C; (alcohol: TBAP:catalyst = 100:100:2).

<sup>b</sup>All the products were identified by comparison with authentic and commercial samples.

<sup>c</sup>Yields of the isolated products. No over oxidation products were observed for all substrates.

Zhang *et al*<sup>1,191</sup> synthesized the chiral copper(II)-based Schiff base complex **Cu-18** through one-pot self-assembly reaction. Upon reacting 3,5-di-tert-butyl-2-hydroxybenzaldehyde, the bulky amino alcohol (1*S*,2*R*)-2-amino-1,2-diphenylethanol, with copper(II) acetate in the presence of triethylamine, **Cu-18** has been isolated as single crystals. X-ray structural analysis shows the complex contain a [Cu<sub>2</sub>(μ-O)<sub>2</sub>N<sub>2</sub>O<sub>2</sub>] core (**Figure 1.37**).

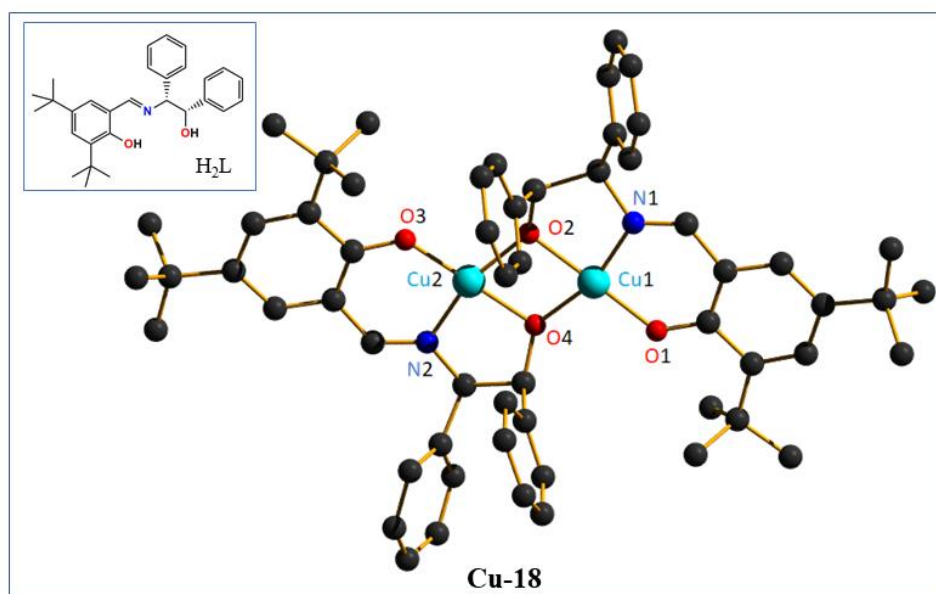
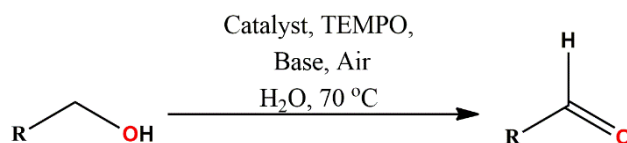


**Figure 1.37:** The ORTEP representation of **Cu-18** with thermal ellipsoids at the 50% probability level. Inset: The corresponding ligand H<sub>2</sub>L.

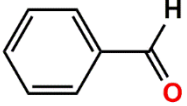
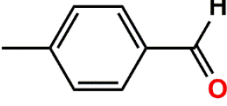
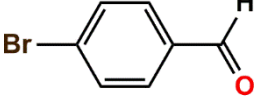
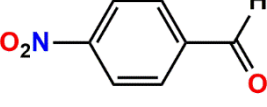
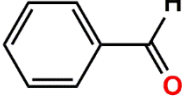
This complex has been applied to the catalytic aerobic oxidation of various benzyl alcohol derivatives into corresponding aldehydes mediated by TEMPO. The fact that aldehydes were

selectively formed as sole products and no corresponding carboxylic acids detected is likely due to the known ability of TEMPO to scavenge free radicals, preventing the aldehydes from further auto-oxidation. The results of the catalytic reactions are given in (Table 1.9).



**Scheme 1.10:** Schematic representation of model reaction used for optimization.

**Table 1.9:** Result of catalytic oxidation by complex **Cu-18**<sup>a</sup>

Entry	Complex	Substrate/complex	Base	Aldehyde	Yield (%) <sup>b</sup>	TON
1	<b>Cu-18</b>	200/1	K <sub>2</sub> CO <sub>3</sub>		78	156
2	<b>Cu-18</b>	200/1	K <sub>2</sub> CO <sub>3</sub>		95	190
3	<b>Cu-18</b>	200/1	K <sub>2</sub> CO <sub>3</sub>		98	196
4	<b>Cu-18</b>	200/1	K <sub>2</sub> CO <sub>3</sub>		14	28
5	Cu(OAc) <sub>2</sub>	100/1	K <sub>2</sub> CO <sub>3</sub>		12	12

<sup>a</sup>Reaction Condition: 1 mmol of the substrate, 0.05 mmol (5 mol%) of TEMPO and 0.0025 mmol (0.25 mol%) of catalyst precursor in 5 mL of 0.2 M aqueous K<sub>2</sub>CO<sub>3</sub> solution, 1 atm. air, 70°C, 22 h.

<sup>b</sup> Yields based on GC-MS analysis, selectivity >99% in all cases.

Pattanayak *et al.*<sup>1,192</sup> synthesized binuclear Cu(II) complex [Cu<sub>2</sub>(L)(μ-OH)](ClO<sub>4</sub>)<sub>2</sub> (**Cu-19**) by reacting a multidentate ligand with Cu(II) perchlorate in methanol. The structure of **Cu-19** was authenticated by single crystal X-ray diffraction, which showed that the ligand binds each of the two Cu(II) centers in an (N, O, S) fashion in a distorted square pyramidal geometry where the two copper centers are bridged by l-phenoxo and l-hydroxo oxygen atoms (**Figure 1.38**). The apical position of one copper center is occupied by one perchlorate ion and the other center

is occupied by a water molecule. The hydrogen bonds, mediated through solvent water and perchlorate anions stabilize the packing of the molecule.

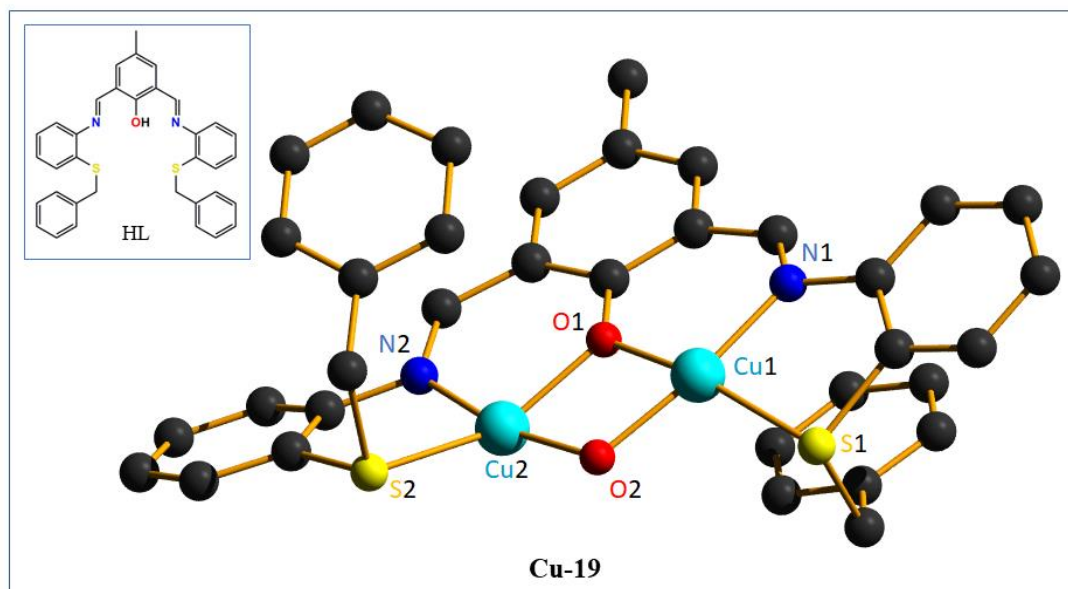
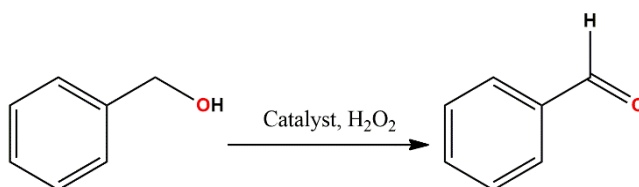


**Figure 1.38:** The ORTEP representation of **Cu-19**. Inset: The corresponding ligand HL.

The activity of this binuclear complex as a catalyst towards the liquid biphasic peroxidative oxidation of benzyl alcohol to benzaldehyde was tested in the presence of  $\text{H}_2\text{O}_2$  as an oxidant under atmospheric conditions.



**Scheme 1.11:** Schematic representation of model reaction used for optimization.

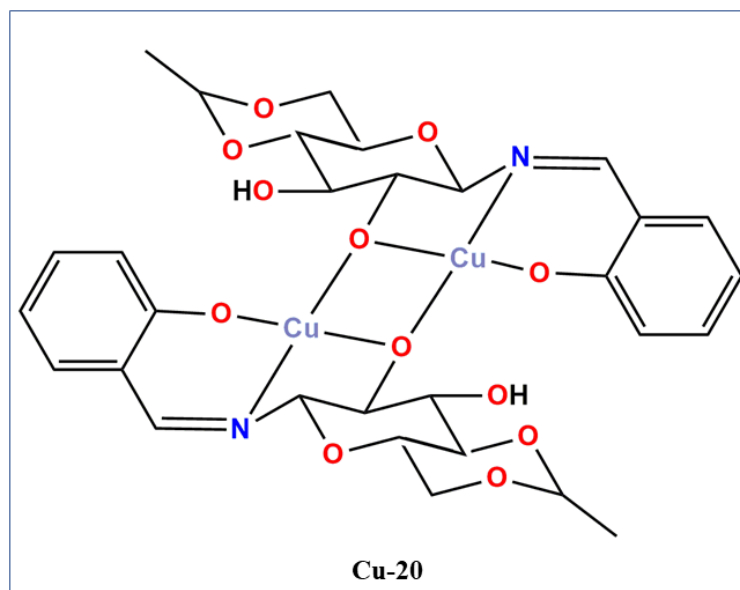
**Table 1.10:** Result of catalytic oxidation by complex **Cu-19**<sup>a</sup>

Entry	Catalyst	Time (h)	Temp (°C)	Yield(%) <sup>b</sup>
1	<b>Cu-19</b>	1	70	90

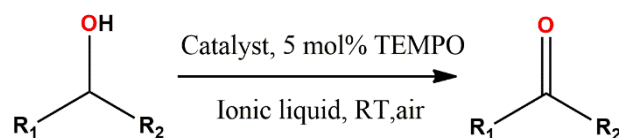
<sup>a</sup>Reaction Condition: 5 mmol Benzyl alcohol, catalyst 4 mol%, 5 mL 30%  $\text{H}_2\text{O}_2$  at 70 °C for 1 h.

<sup>b</sup>The conversion was calculated on the basis of the isolated yield.

Soni *et al.*<sup>1.193</sup> reported a 4,6-*O*-ethylidene- $\beta$ -D-glucopyranosylamine saccharide derived dinuclear Cu(II) complex, **Cu-20** (**Scheme 1.12**). The complex oxidizes primary and secondary alcohols selectively to corresponding carbonyl compounds in the presence of TEMPO in ionic liquid. They observed that the rate of oxidation of primary alcohols was in general faster than that of secondary ones. The result of the catalytic conversion in details is given in **Table 1.11**.



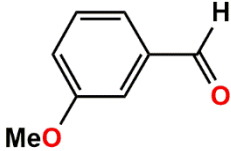
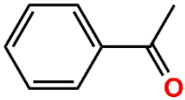
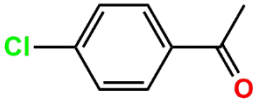
Scheme 1.12: Structure of Cu-20



Scheme 1.13: Schematic representation of model reaction used for optimization.

Table 1.11: Result of catalytic oxidation by complex Cu-20<sup>a</sup>

Entry	R <sub>1</sub>	R <sub>2</sub>	Aldehyde/Ketone	Time (h)	Yield (%) <sup>b</sup>
1	C <sub>6</sub> H <sub>5</sub>	H		4	82 <sup>c</sup>
2	<i>p</i> -ClC <sub>6</sub> H <sub>5</sub>	H		6	78
3	<i>p</i> -OHC <sub>6</sub> H <sub>5</sub>	H		10	70
4	<i>p</i> -OMeC <sub>6</sub> H <sub>5</sub>	H		12	78
5	<i>p</i> -NO <sub>2</sub> C <sub>6</sub> H <sub>5</sub>	H		12	65

6	<i>m</i> -OMeC <sub>6</sub> H <sub>4</sub>	H		10	75
7	C <sub>6</sub> H <sub>5</sub>	CH <sub>3</sub>		6	69
8	<i>p</i> -ClC <sub>6</sub> H <sub>4</sub>	CH <sub>3</sub>		6	71

<sup>a</sup>Reaction Condition: Primary or secondary alcohol (1.0 mmol), TEMPO (0.05 mmol), catalyst (0.05 mmol) in 1-butyl-3-methyl-3H-imidazol-1-ium tetrafluoroborate [bmim][BF<sub>4</sub>] (1.5 mL), RT, 4–12 h. The progress of the reaction was monitored by TLC, final product was isolated by extraction with diethyl ether and purified by column chromatography using 5% ethyl acetate in hexane.

<sup>b</sup>Isolated yield.

<sup>c</sup>Yield of four consecutive cycles was 82, 75, 70 and 65% respectively.

#### 1.5.4 Schiff Base Metal Complexes as Electro-Catalysts in Hydrogen Evolution

Over the past century, constantly increasing energy demands worldwide due to global development and growth in population as well as climate changes brought about by emission of greenhouse gases from burning of fuels have accelerated our need to develop technologies for clean and renewable energy that can resolve the current problems and sustain long-term development.<sup>1.194a-g</sup> Current renewable energy resources viz. wind, solar and geothermal energies lead to low energy delivery efficiencies and thus limit their daily applications.<sup>1.194b, d</sup> However, converting these energy resources into chemical fuels which can be stored and transported is a prospective solution.

Molecular hydrogen gas (H<sub>2</sub>) is considered as one of the most promising fuel candidates owing to its high gravimetric energy density, relatively high abundance, and zero emission during consumption.<sup>1.195a,b</sup> It has been prepared mainly from an industrial steam reforming process that converts natural gas with water into hydrogen and carbon monoxide. However the low energy efficiency of the conversion process and the presence of carbon-containing residues result in the low purity of hydrogen products and high cost, respectively.<sup>1.196</sup> To this end, a renewable, clean and efficient technique for hydrogen production without the addition of further problems is the key element for the successful realization of hydrogen economy. In this prospect, development of apposite catalytic materials to design a cost-effective and energy-

efficient and system for hydrogen generation from water or proton source remains as a challenge.

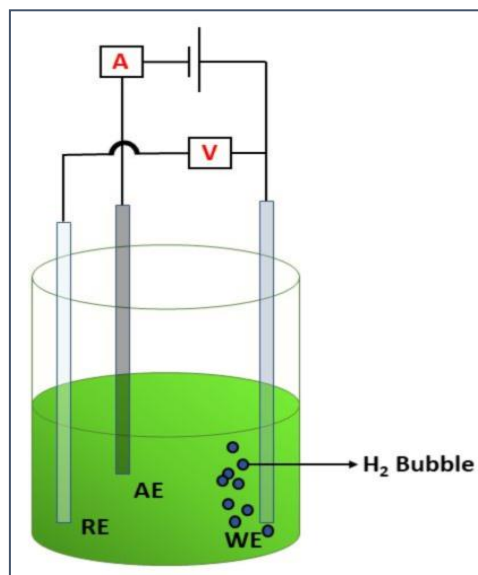


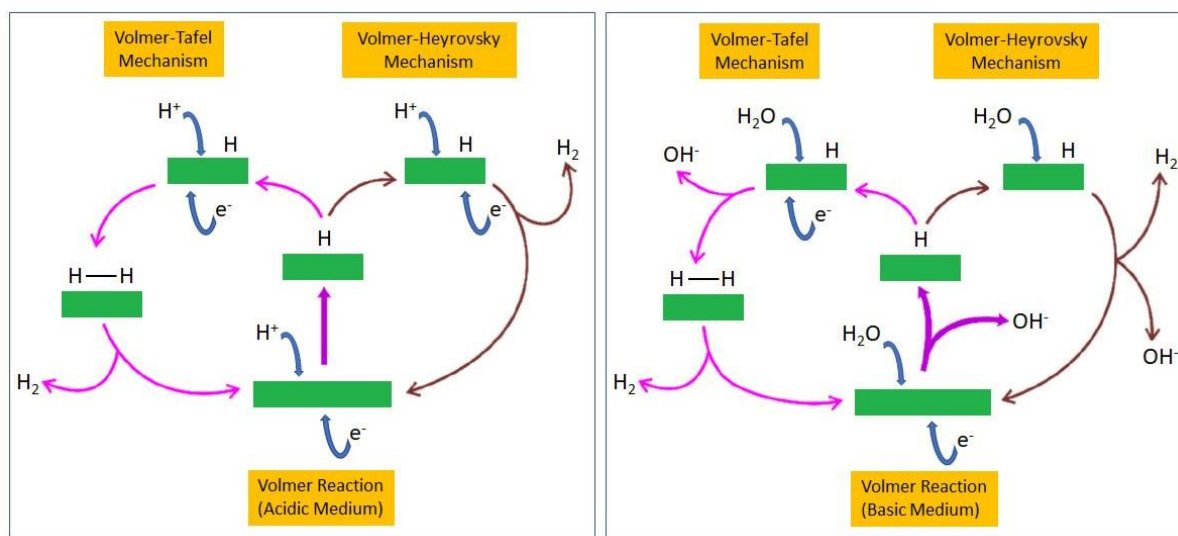
**Figure 1.39:** Schematic representation of energy related applications, hydrogen evolution reaction (HER) with three electrode system.

Hydrogen evolution reaction (HER) is a half reaction of water (or other proton source) splitting that converts protons into hydrogen.<sup>1.197a,b</sup> But it involves slow kinetics as the multiple elemental reactions induce an accumulation of energy barriers.<sup>1.197a,b</sup> Here, a variety of HER catalysts have come to play significant roles in expediting the reaction rates. Among all HER catalysts, platinum-based catalysts stand out with almost no overpotential at onset and rapid current increase over voltage increment.<sup>1.198a-c</sup> However, they are non-affordable for large-scale applications due to limited reserves on earth and high cost, thereby promoting the development of cheap alternatives with high activity and durability. Many non-precious metal-based compounds have been reported in literature exhibiting excellent HER catalytic activity in acidic medium<sup>1.199a-r</sup> as well as in alkaline medium.<sup>1.200a-j</sup> Recently, as an efficient and economical replacement to these expensive metal precursors, nickel-based electrocatalysts show very promising electrocatalytic activity and stability toward hydrogen evolution reaction (HER). The high synergistic effect acting between neighboring heteroatoms and nickel results in much better surface adsorption properties which promotes the electrocatalytic properties of resulting materials. Although nickel exists in +2 oxidation state in most of the commonly known nickel compounds, it is capable of acquiring other valences (-1 to +4) also, which makes it highly susceptible toward undergoing various electronic transitions. Along with these properties, low price, strong strength, high elemental abundance, high corrosion resistance, better ductility,

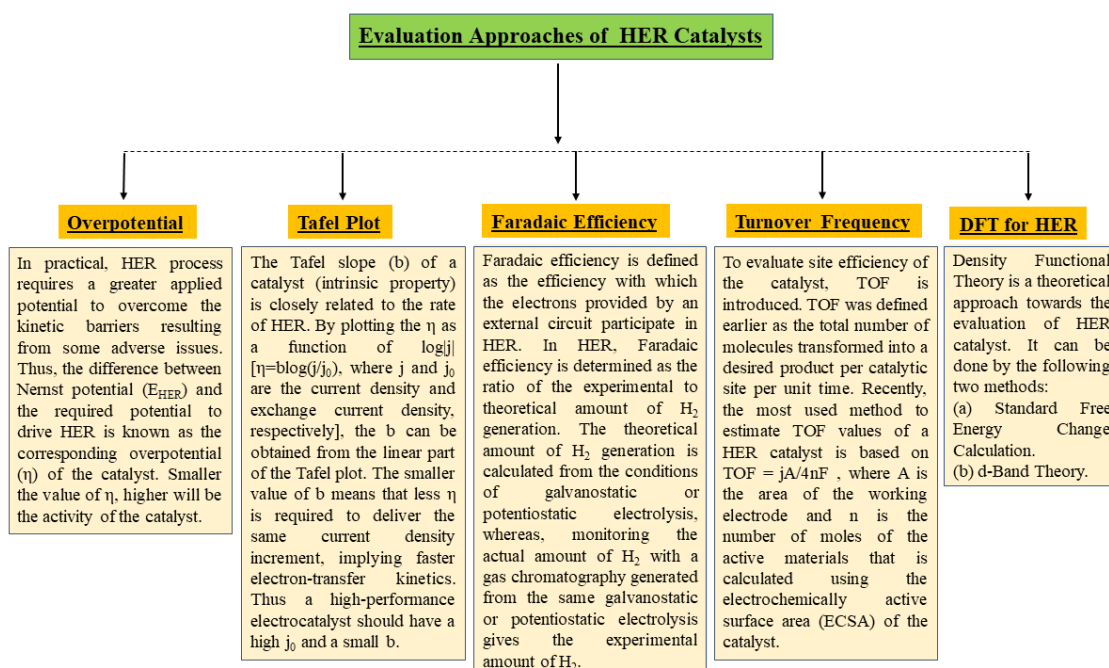
good heat conduction, and high electrical conductivity makes nickel-based materials a very frequent choice for designing electrocatalytic materials.

### 1.5.4.1 Reaction Mechanism of HER

Mechanistically, there are three possible principal steps involved in the electrochemical hydrogen evolution process for the reduction of protons in alkaline media or in acidic media to hydrogen molecules on the surface of an electrode with a minimum external potential applied (Scheme 1.14).<sup>1,201</sup>



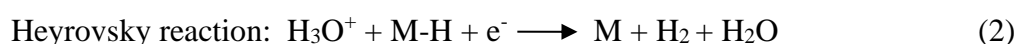
**Scheme 1.14:** Mechanism of hydrogen evolution on the surface of an electrode in acidic (left) and alkaline (right) solutions, proton source: water.



**Scheme 1.15:** Schematic representation of some evolution approaches of HER catalysts.



The first step is the proton discharge electrosorption step (Volmer reaction), where a proton reacts with an electron to form an adsorbed hydrogen atom (H) on the electrode material surface (M). Second one is the electronic-desorption step (Heyrovsky reaction) and/or catalytic-recombination step (Tafel reaction). The Heyrovsky step involves diffusion of another proton to the H followed by the reaction with a second electron that produces H<sub>2</sub>. In the case of Tafel step, two Hs in the vicinity combine on the electrode surface to evolve H<sub>2</sub>. Thus, the overall hydrogen evolution reaction can be written as:<sup>1,202a-c</sup>



M. Abudayyeh *et al*.<sup>203</sup> reported one literature (**Cu-21**) and two new complexes (**Cu-22** and **Cu-23**) as electrocatalysts for HER in ACN with acetic acid as the proton source. All of them were prepared by 1:1:1 reaction of the appropriate ligand with TEA and Cu(BF<sub>4</sub>)<sub>2</sub>·H<sub>2</sub>O. When their structures were determined by single crystal X-ray crystallography, it reveals that **Cu-21** has square planar, **Cu-22** has square pyramidal and **Cu-23** has trigonal bipyramidal copper(II) geometries (**Figure 1.40**).

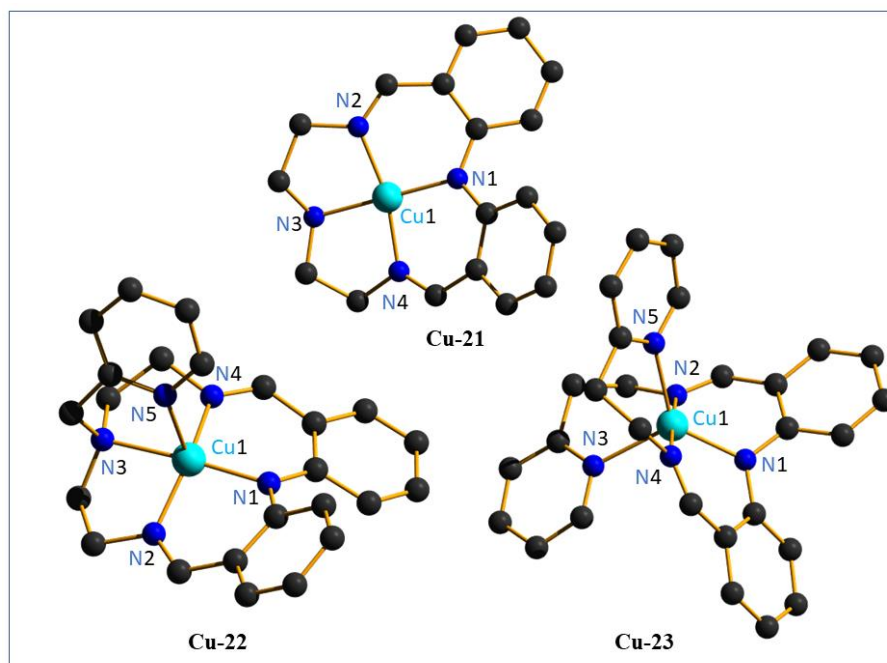
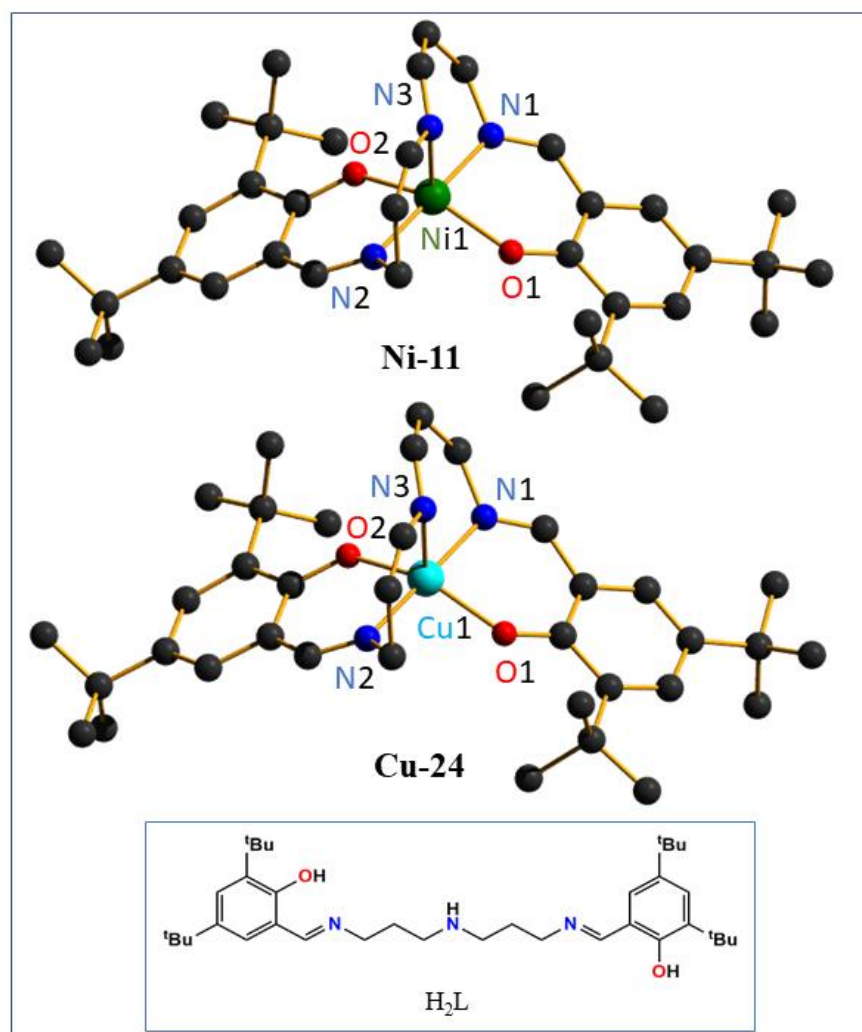


**Figure 1.40:** The ORTEP representation of **Cu-21** to **Cu-23**.

To evaluate the electrocatalytic activity of these complexes for hydrogen evolution, controlled potential coulometry has been carried out at an applied potential of  $-1.60$  V vs AgNO<sub>3</sub>/Ag for 2 hours. For **Cu-21**, they obtained the TON value of 4.7, whereas for the rest two complexes

the obtained TON value is  $< 1.1$ . The results also showed that the electrocatalytic HER activity of **Cu-21** is retained for more than 6 hours. Thus, the promising electrocatalytic HER activity has been observed in the case of the square planar macrocyclic **Cu-21** over the other two complexes having the metal centre penta-coordinated.

Hong *et al.*<sup>1,204</sup> investigated the efficiency of **Ni-11** and **Cu-24** in catalytic HER activity and helped in better understanding about the supporting role of Schiff-base ligands in the HER reaction process (**Figure 1.41**). The complexes were synthesized by the reaction of equimolar amounts of the pentadentate ligand  $H_2L$ ,  $Et_3N$  and  $M(NO_3)_2 \cdot 6H_2O$  [ $M = Ni, Cu$ ] in a mixed solvent of dichloromethane and methanol at room temperature. The single crystal X-ray crystallography confirmed the structures of both the complexes. Electrocatalytic proton reduction activity of these complexes was investigated in acetonitrile under  $N_2$  atmosphere using acetic acid as the proton source. The electrocatalytic data are enlisted in the **Table 1.12**.

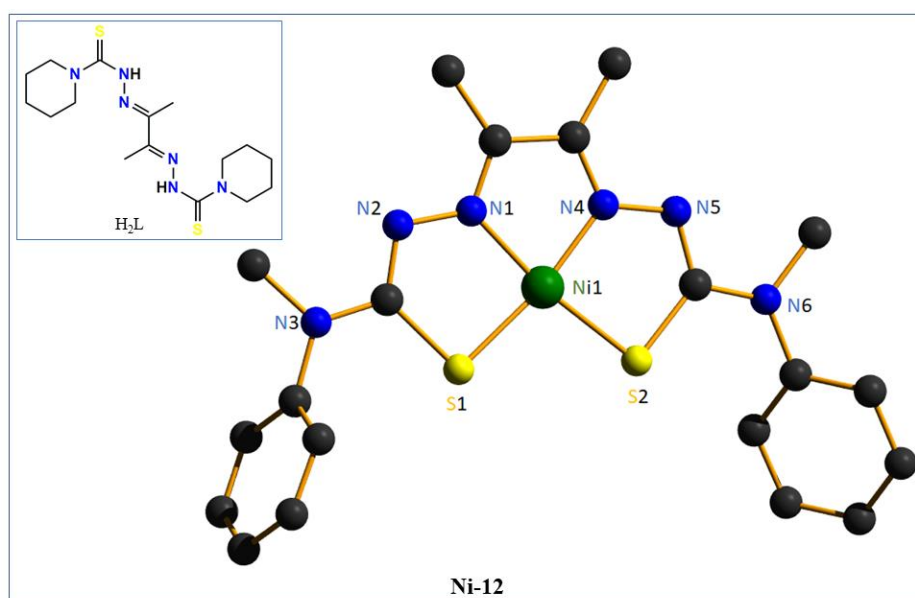


**Figure 1.41:** The ORTEP representation of **Ni-11** and **Cu-24**. Inset: The corresponding ligand ( $H_2L$ ).

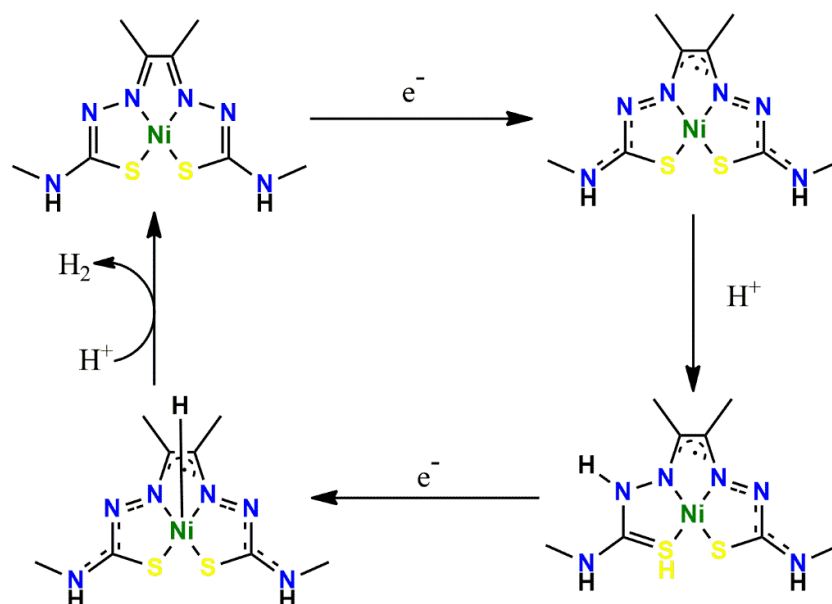
**Table 1.12:** Result of the electrocatalytic H<sub>2</sub> evolution reaction.

Entry	Complex	Proton source	Solvent	TOF (s <sup>-1</sup> )	Faradaic efficiency (%)
1	Ni-11	Acetic acid	MeCN	63827.5	67.3
2	Cu-24			70139.5	74

Jain *et al*<sup>1.205a</sup> reported the electrocatalytic behaviour of the neutral, monomeric Ni(II) complex, Ni-12, for ligand-assisted metal-centred hydrogen evolution in ACN and DMF. The structure of Ni-12 was previously confirmed by single crystal X-ray crystallography by West (Figure 1.42).<sup>1.205b</sup> The results of the electrochemical studies are enlisted in the Table 1.13. They also proposed a ligand-assisted metal-centred mechanism for HER supported by computational investigations (Scheme 1.16).

**Figure 1.42:** The ORTEP representation of Ni-12.**Table 1.13:** Result of the electrocatalytic H<sub>2</sub> evolution reaction catalyzed by Ni-12

Entry	Solvent	Proton Source	TON	TOF (S <sup>-1</sup> )	Faradaic efficiency (%)
1	ACN	CH <sub>3</sub> COOH	48	4161	87.4
2	ACN	CF <sub>3</sub> COOH	24	1324	75.3
3	DMF	CH <sub>3</sub> COOH	13	1196	58.7
4	DMF	CF <sub>3</sub> COOH	3	115	51.3



**Scheme 1.16:** Proposed HER Mechanism with Ni-12.

Zhang *et al*<sup>1,206</sup> reported mononuclear nickel complex, **Ni-13** supported by phenylenediamine ligand. The complex was synthesized by the reaction of N,N'-bis(2-amino-3,5-di-tert-butylphenyl)-o phenylenediamine, H<sub>2</sub>L, with Ni(ClO<sub>4</sub>)<sub>2</sub>·6H<sub>2</sub>O. The single crystal X-ray crystallography confirmed the mononuclear structure (**Figure 1.43**). Electrochemical investigations showed that **Ni-13** can catalyse hydrogen generation effectively both from acetic acid and aqueous buffer. The results of the electrocatalytic reaction are given in (**Table 1.14**).

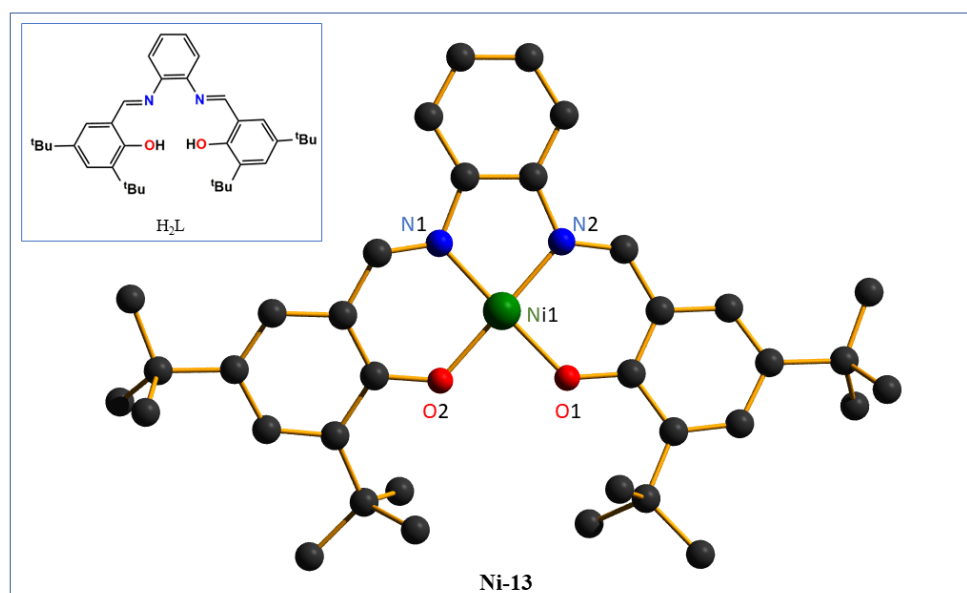


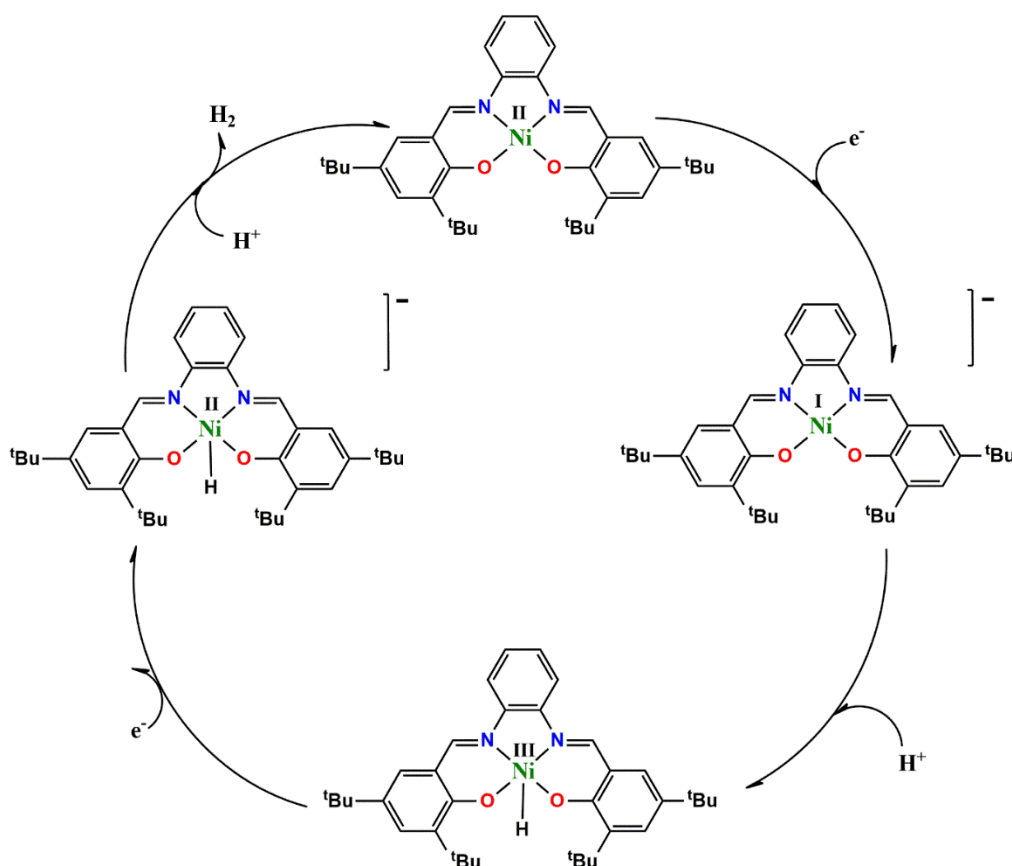
**Figure 1.43:** The ORTEP representation of **Ni-13** with thermal ellipsoids at the 50% probability level. Inset: The corresponding ligand H<sub>2</sub>L.

**Table 1.14:** Result of the electrocatalytic H<sub>2</sub> evolution reaction catalyzed by Ni-13.

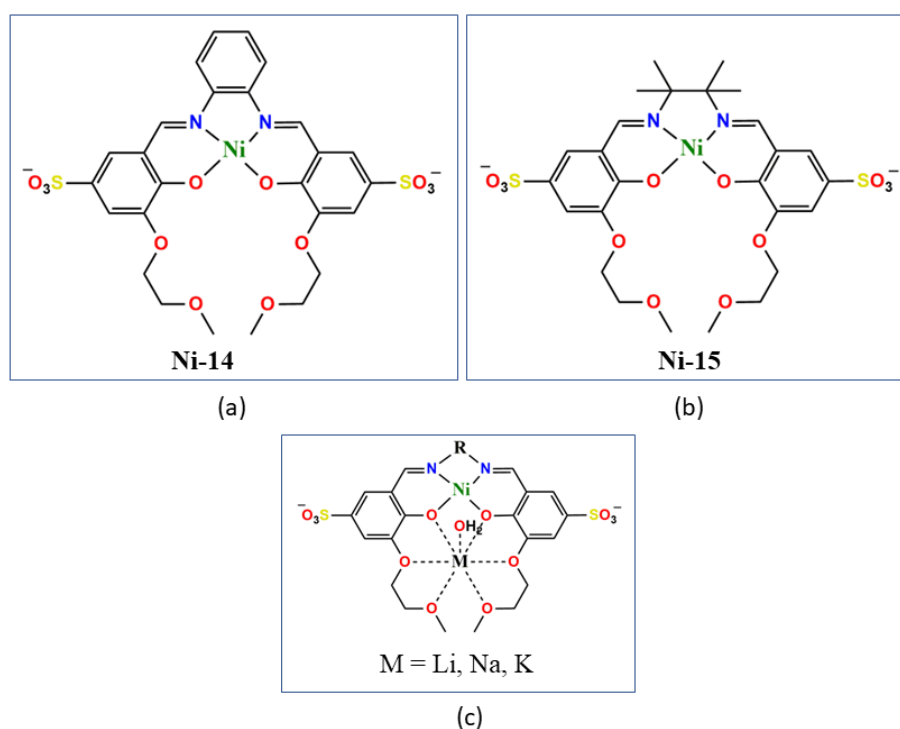
Entry	Complex	Proton Source	Solvent	Charge (mC) <sup>a</sup>	TOF <sup>b</sup>	Overpotential (V)	The amount of H <sub>2</sub> (L) <sup>c</sup>	Faradaic efficiency <sup>d</sup>
1	Ni-13	Acetic acid	ACN	100	89.56	0.942	6.5 X 10 <sup>-5</sup>	-----
2	Ni-13	Water	H <sub>2</sub> O	1473	1331.23	0.838	7.12 X 10 <sup>-3</sup>	90.59%

<sup>a</sup>2 min of electrolysis<sup>b</sup>Moles of hydrogen per mole of catalyst per hour.<sup>c</sup>Electrolysis for 2 h for the former case and 1 h for the later under -1.45 V versus Ag/AgCl<sup>d</sup>Over an electrolysis period of 1 h.

They also proposed a possible catalytic cycle for the generation of hydrogen from acetic acid mediated by Ni-13 (Scheme 1.17).

**Scheme 1.17:** The possible catalytic mechanism for proton reduction by Ni-13.

Shao *et al.*<sup>1,207</sup> developed two water-soluble mononuclear Ni complexes (**Ni-14**, **Ni-15**) supported by chelating ether groups, salicylaldimine ligands with pendant that can bind Lewis acids such as alkali metal cations. These complexes were tested as electrocatalysts for the production of H<sub>2</sub> in both acidic and neutral aqueous solutions. The most interesting features of these complexes are (i) the presence of the sulfonate groups that improves water solubility and (ii) the presence of the chelating methoxyethoxy group that binds to hydrated alkali metal cations to provide hydrogen-bonding stabilisation and enhance electrocatalytic proton reduction reactivity.

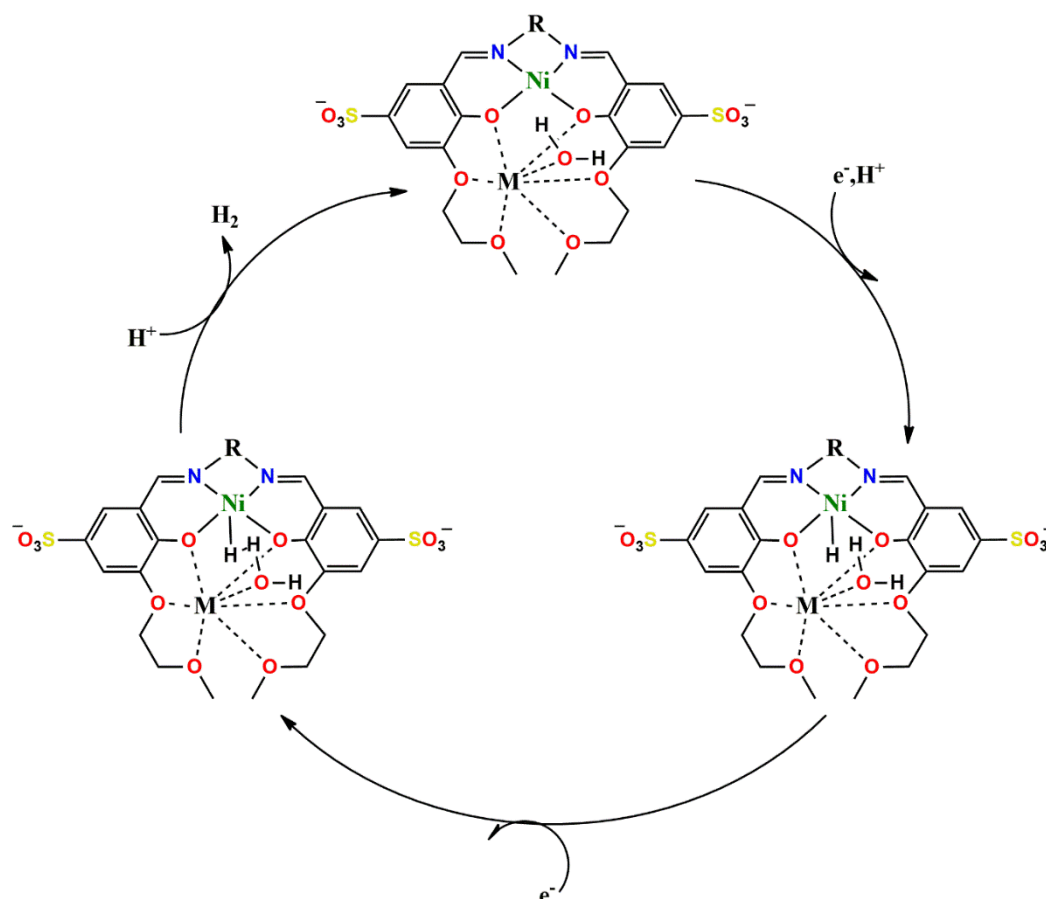


**Scheme 1.18:** Structure of (a) **Ni-14**, (b) **Ni-15**, (c) mode of binding of alkali metal in the complexes.

They found that **Ni-15** functioned similarly to **Ni-14** but with lower electrocatalytic activity. Thus, they performed all subsequent studies with **Ni-14**. At first, **Ni-14** was tested as electrocatalyst for H<sub>2</sub> production in DMF with weak acid (acetic acid) as well as with a strong one (TFA). In the presence of weak proton donor i.e. acetic acid (AcOH), there is a moderate current increase with little change to the onset current whereas when the stronger acid, TFA, was used as the proton source, a dramatic increase in the catalytic current is observed over the background with an anodic shift of the onset current. They also recorded cyclic voltammogram of **Ni-14** in neutral water with sodium sulphate (Na<sub>2</sub>SO<sub>4</sub>) as the electrolyte which exhibited a

remarkable enhancement in the catalytic current at an onset of -1.05 V vs. NHE, corresponding to an overpotential of 0.59 V.

Next, they explored the effects of the pendant ether on **Ni-14** by conducting CVs in the presence of  $n\text{-Bu}_4\text{NCl}$ ,  $\text{KPF}_6$ ,  $\text{Li}_2\text{SO}_4$  and  $\text{Na}_2\text{SO}_4$  as the electrolytes in 0.10 M acetic acid. Highest electrocatalytic current was obtained with  $\text{Li}^+$  electrolyte indicating the most Lewis acidic  $\text{Li}^+$  corresponds to the fastest catalytic behaviour. Thus, the results emphasised on the necessity for prudent management of second sphere effects around the catalytic centre (**Scheme 1.19**).



**Scheme 1.19:** Proposed catalytic cycle illustrating how the alkali metal and other Lewis acid cations can direct protons potentially in close proximity to the catalytic Ni centre.

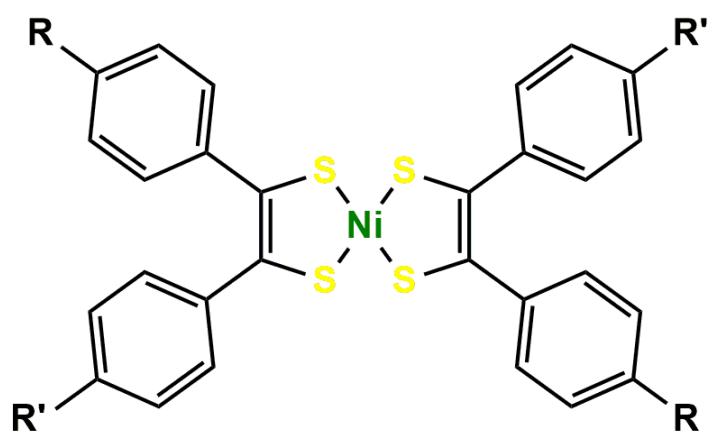
Finally, they explored the performance of **Ni-14** as electrocatalyst in the economical and sustainable seawater reaction medium. The electrocatalytic data is enlisted in the **Table 1.15**.

**Table 1.15:** TON and TOF calculations from CPE measurements.

Working Electrode	Experimental Quantity	Seawater Charge (C)	$\text{Li}_2\text{SO}_4$	$\text{Na}_2\text{SO}_4$	$\text{KPF}_6$	$\text{MgSO}_4$	$n\text{-Bu}_4\text{NCl}$	$\text{NiCl}_2$
		10.8	0.575	3.55	6.57	1.67	1.27	1.53

Mercury pool	Faradaic efficiency %	79.5	52.2	80.7	56.1	52.7	3.33	42.5
	TON (mol H <sub>2</sub> mol <sup>-1</sup> <b>10</b> cm <sup>-2</sup> )	7.14	0.249	2.34	3.06	0.733	0.0354	0.542
	TOF (mol H <sub>2</sub> mol <sup>-1</sup> <b>10</b> cm <sup>-2</sup> h <sup>-1</sup> )	3.57	0.125	1.19	1.53	0.366	0.0177	0.271
Carbon paper	Charge (C)	22.7	37.9	21.5	19.3	-----	13.4	-----
	Faradaic efficiency %	56.9	53.2	52.0	57.1	-----	48.9	-----
	TON (mol H <sub>2</sub> mol <sup>-1</sup> <b>10</b> cm <sup>-2</sup> )	5.99	9.33	5.17	5.09	-----	3.01	-----
	TOF (mol H <sub>2</sub> mol <sup>-1</sup> <b>10</b> cm <sup>-2</sup> h <sup>-1</sup> )	2.99	4.67	2.59	2.55	-----	1.52	-----

Zarkadoulas *et al.*<sup>208</sup> synthesized and characterized a series of neutral and monoanionic nickel diphenyl-1,2-dithiolene complexes (**Ni-16 to Ni-18**) with varying numbers of methoxy groups on the benzene rings present in the ligand framework (**Scheme 1.20**). Among them the structures of **Ni-17**, neutral asymmetric [Ni{S<sub>2</sub>C<sub>2</sub>(Ph)(Ph-*p*-OCH<sub>3</sub>)<sub>2</sub>}<sub>2</sub>], and **Ni-18**, monoanion of the symmetric [Ni{S<sub>2</sub>C<sub>2</sub>(Ph-*p*-OCH<sub>3</sub>)<sub>2</sub>}<sub>2</sub>] with NBu<sub>4</sub><sup>+</sup> as a counterion, were structurally characterized by single-crystal X-ray crystallography (**Figure 1.49**).



Complex 7: R=R'=H

Complex 8: R=H, R'=OMe

Complex 9: R=R'=OMe

**Scheme 1.20:** Structure of **Ni-16 to Ni-18** under Study.



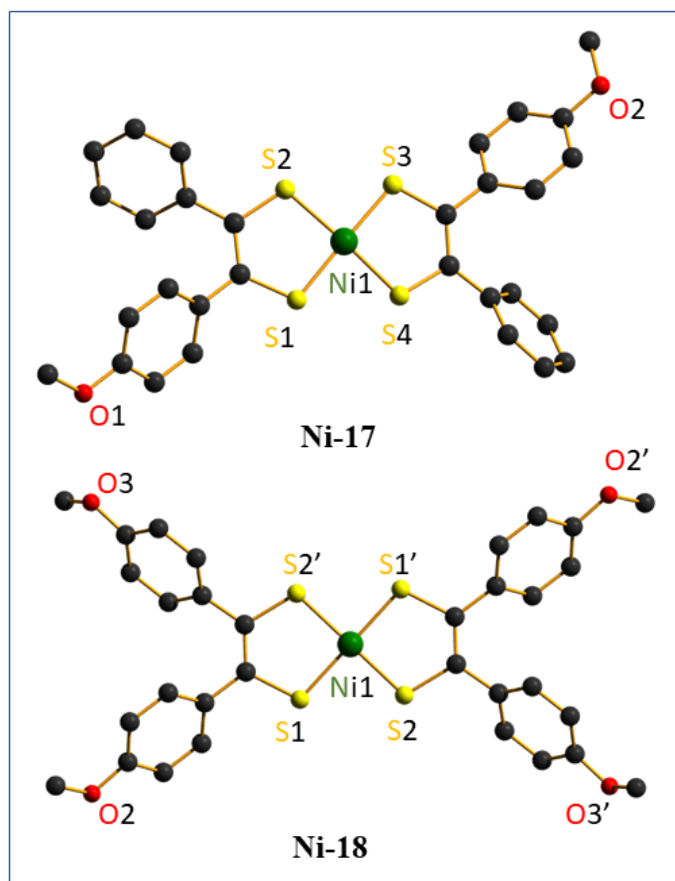


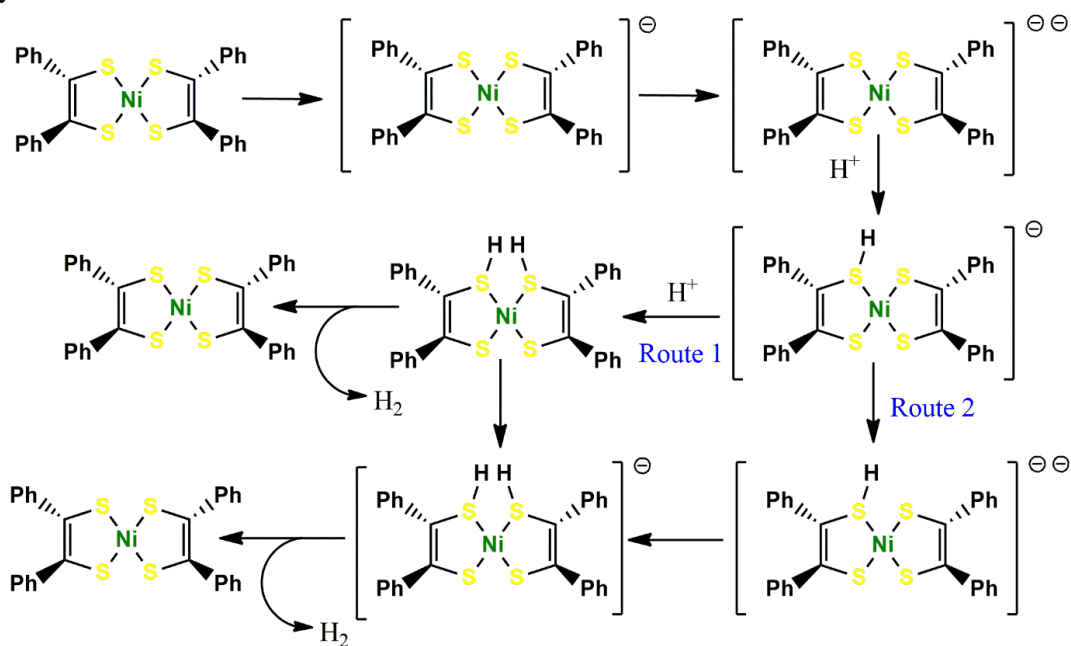
**Figure 1.44:** The ORTEP representation of Ni-17 and Ni-18. In Ni-18, the  $\text{NBu}_4^+$  counterion is omitted for clarity.

All the three complexes were employed as electrocatalysts for proton reduction in DMF with trifluoroacetic acid (TFA) as the proton source. The results of bulk electrolysis in the presence of 50 mM TFA are enlisted in the **Table 1.16**. The similarity obtained in the experimental data regardless of whether the neutral or anionic form of the complexes utilized indicates that the neutral form actually acts as a precatalyst. They also carried out theoretical investigations by using density functional theory (DFT) as a tool for interpretation of the reactive centres of the complexes and the structural conformations of the intermediates, from which putative reaction mechanisms have been proposed (**Scheme 1.21**). The proposed mechanism shows two different main routes after protonation of the dianion of the catalyst in accordance with the experimental data which indicates the role of the influence of the methoxy groups and the concentration of the acid.

**Table 1.16:** Result of the electrocatalytic H<sub>2</sub> evolution reaction catalyzed by Ni-16 to Ni-18.

Entry	Complex	Proton source	Solvent	TON	Faradaic yield <sup>a</sup>
1	Ni-16	TFA	DMF	15	0.66
2	Ni-17			25	0.83
3	Ni-18			12	0.74

<sup>a</sup>Bulk electrolysis was performed at potential  $-1.67$  V vs Fc+/0 for a 3 h time period with a catalyst concentration of 1 mM



**Scheme 1.21:** Proposed Mechanism of proton reduction by Ni-16 in the presence of CF<sub>3</sub>COOH.

Cao *et al.*<sup>1,209</sup> reported a mononuclear copper(II) complex (**Cu-25**) as a molecular electrocatalyst synthesized by the reaction between 2,3-bis(2-hydroxybenzylideneimino)-2,3-butenedinitrile (H<sub>2</sub>L) and CuCl<sub>2</sub>·2H<sub>2</sub>O (**Figure 1.45**). The structure of the complex was confirmed by X-ray crystallography. Electrochemical studies performed on a glassy carbon (GC) electrode indicate that the catalyst can not only produce hydrogen from acetic acid but also from water without use of additional acids. The results also indicate that **Cu-25** is highly active and robust in both organic and aqueous media. The results of the electrochemical studies are enlisted in the **Table 1.17**.

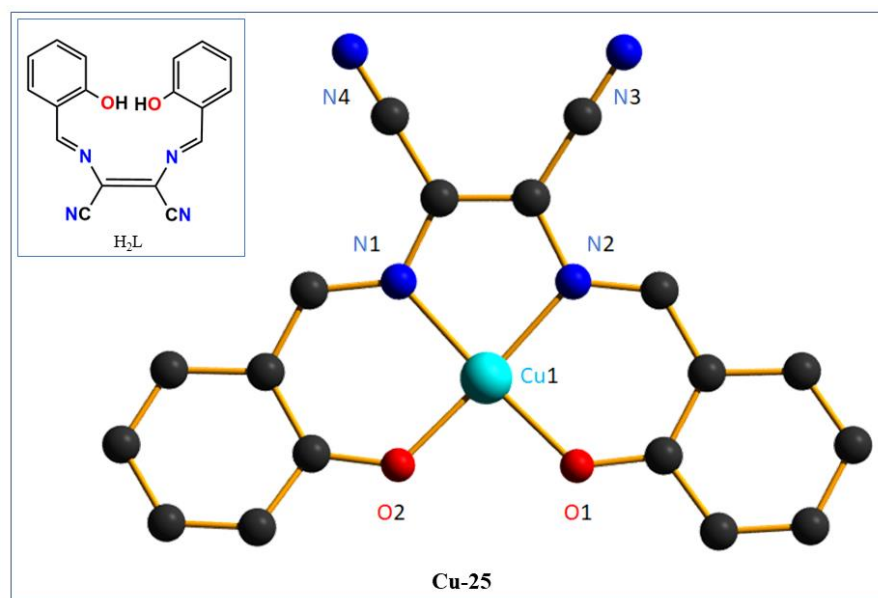


**Figure 1.45:** The ORTEP representation of **Cu-25**. Inset: The corresponding ligand **H<sub>2</sub>L**.

**Table 1.17:** Result of the electrocatalytic H<sub>2</sub> evolution reaction catalyzed by **Cu-25**.

Entry	Complex	Proton source	Solvent	Overpotential	TOF	Faradaic efficiency
1	<b>Cu-25</b>	Acetic acid	DMF	-----	255 h <sup>-1</sup>	-----
2	<b>Cu-25</b>	Water	H <sub>2</sub> O	817 mV	457 h <sup>-1</sup> (in buffer, pH 7)	91.5%

Cao *et al*<sup>1,210</sup> reported a new nickel based molecular electrocatalyst, **Ni-19**, synthesized from the reaction of 2,3-bis(2-hydroxybenzylideneimino)-2,3-butenedinitrile (**H<sub>2</sub>L**) (**Figure 1.46**, inset) and Ni(CH<sub>3</sub>CO<sub>2</sub>)<sub>2</sub>·2H<sub>2</sub>O. The structure of **Ni-19** was established by XRD study. Electrochemical studies showed that this complex can catalyse hydrogen evolution not only from AcOH but also from H<sub>2</sub>O without using additional acids. Moreover, this highly active catalyst is robust in both organic and aqueous media. The results of the electrochemical studies are enlisted in the **Table 1.18**. They observed sustained proton reduction catalysis at glassy carbon electrode to give hydrogen over a 42 h electrolysis time period and no decomposition of the electrocatalyst was observed.

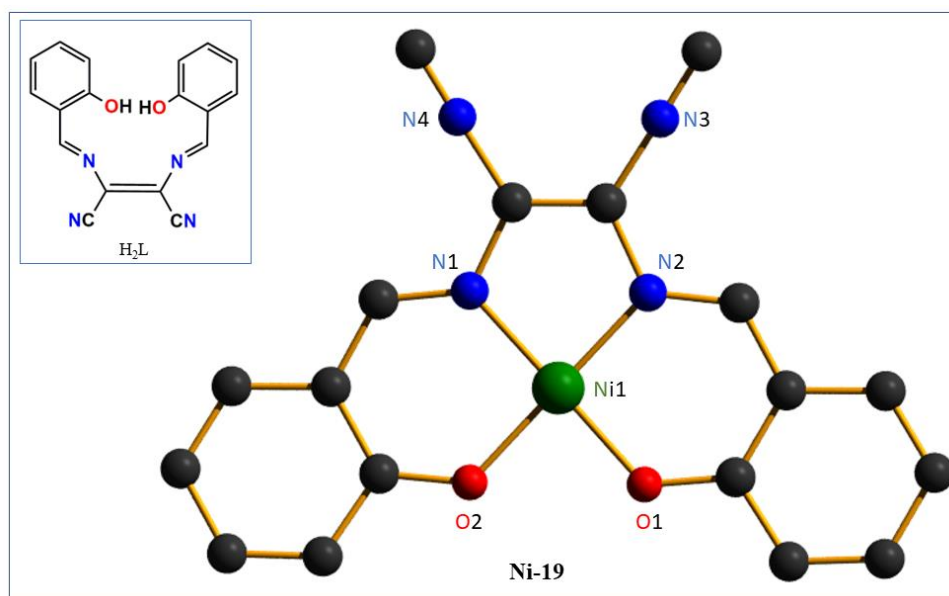


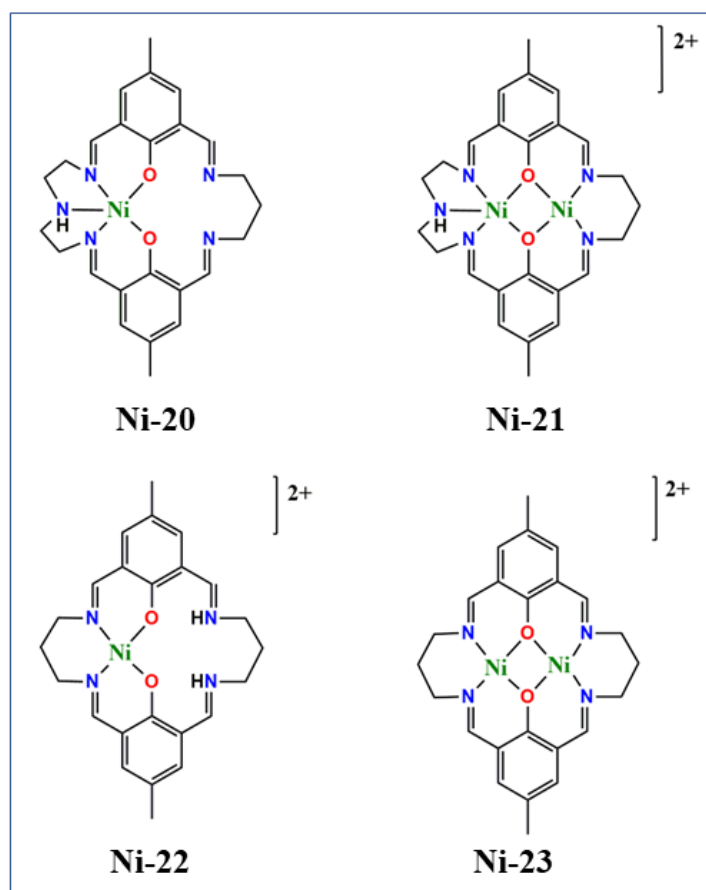
**Figure 1.46:** The ORTEP representation of **Ni-19**. Inset: The corresponding ligand **H<sub>2</sub>L**.

**Table 1.18:** Result of the electrocatalytic H<sub>2</sub> evolution reaction catalyzed by **Ni-19**.

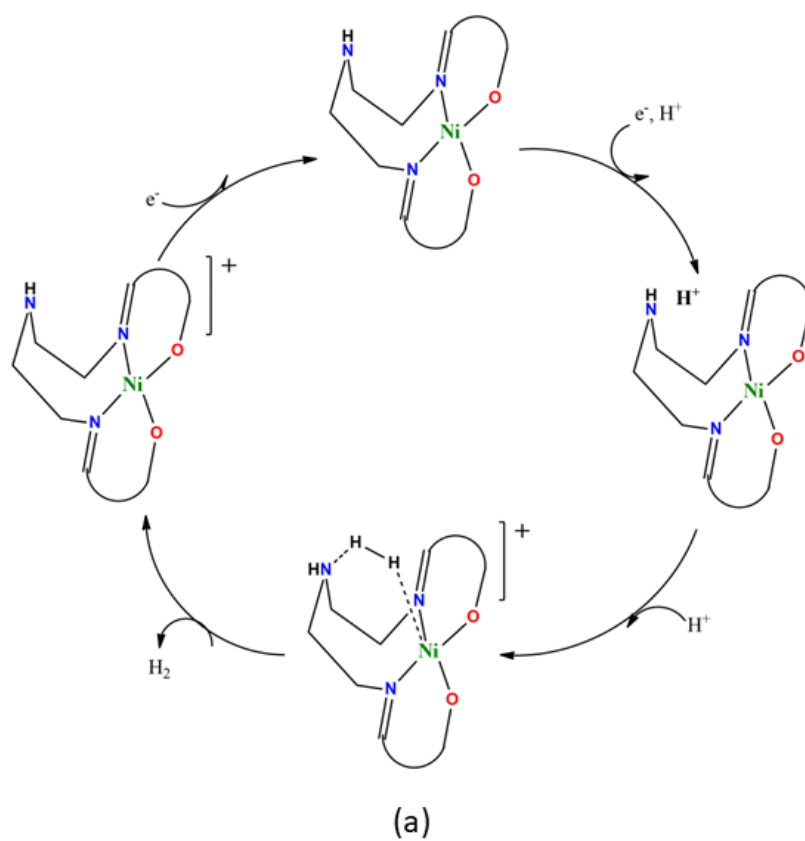
Entry	Complex	Proton source	Solvent	Overpotential	TOF
1	<b>Ni-19</b>	Acetic acid	DMF	320 mV	193 h <sup>-1</sup>
2	<b>Ni-19</b>	Water	H <sub>2</sub> O	-----	574 h <sup>-1</sup>

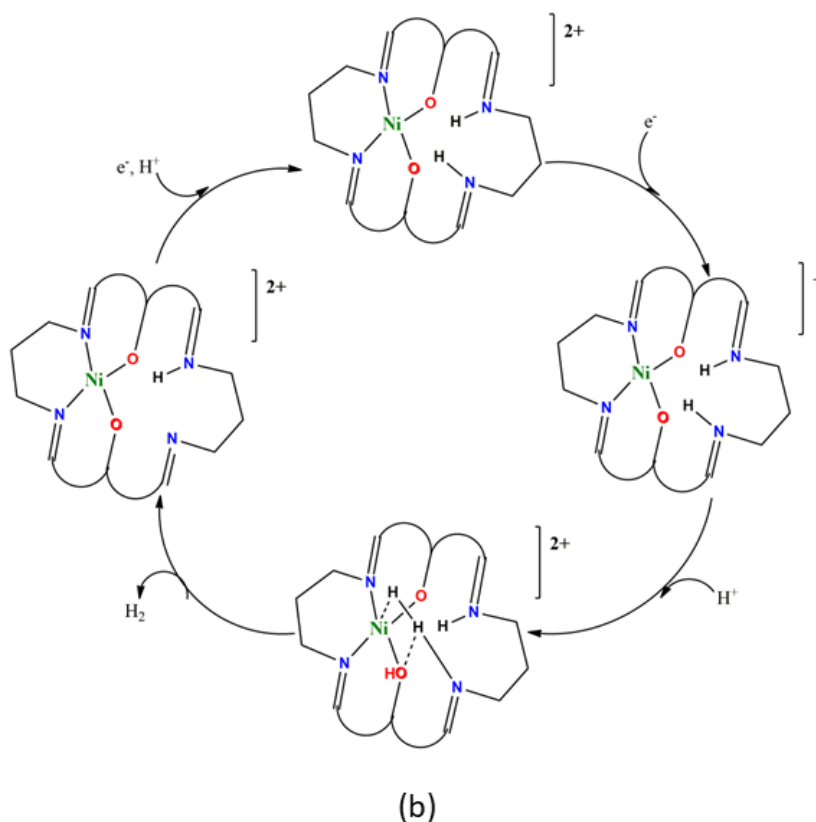
(in buffer, pH 6)

Martin *et al.*<sup>1,211</sup> investigated a series of mononuclear and dinuclear tetraiminodiphenolate nickel(II) macrocyclic complexes, **Ni-20** to **Ni-23**, as functional models of the active site of [Ni-Fe]-hydrogenase (**Scheme 1.22**). Their electrocatalytic activity towards the evolution of dihydrogen were tested in DMF or DMSO (0.1 mol L<sup>-1</sup> TBAPF<sub>6</sub>) solutions with increasing concentrations of TFA. The mononuclear complexes, i.e **Ni-20** and **Ni-22** presented the best ratio of the catalytic current, *i<sub>c</sub>*, in relation to the concentration of the acid (6.31 and 5.64 μA/mM, respectively), which suggested strongly the importance of ligands containing N or O atoms serving as proton acceptors close to the metal center. They have also proposed a reductive pathway to electrocatalysis toward dihydrogen production by **Ni-20** and **Ni-22** in the presence of CF<sub>3</sub>CO<sub>2</sub>H as proton source (**Scheme 1.23**).



Scheme 1.22: Structures of Ni-20 to Ni-23.





**Scheme 1.23:** The possible catalytic cycles for proton reduction by (a) Ni-20, (b) Ni-22 in the presence of  $\text{CF}_3\text{COOH}$ .

### 1.6 Aim of the present work

From the overall discussion so far, it is quite evident that why the study of transition metal complexes attracts an immense interest to the researchers now-a-days. In this regard, the present research work has been attempted with a view to synthesize novel Schiff base transition metal complexes associated with nickel(II) and copper(II). Among them, one is copper based coordination polymer containing uncoordinated oxygen of  $\text{C}=\text{O}$  groups. The uncoordinated oxygen has been explored for its interaction with toxic pesticides by theoretical density functional theory analysis. Another one is mononuclear nickel complex which has been synthesized, characterized and employed to bind DNA/HSA. Two dinuclear copper complexes have also been synthesized, characterized and applied as efficient catalysts towards alcohol oxidation. The rest nickel and copper complexes have been utilized as electrocatalysts towards hydrogen evolution reaction.

## 1.7 Instrumentation

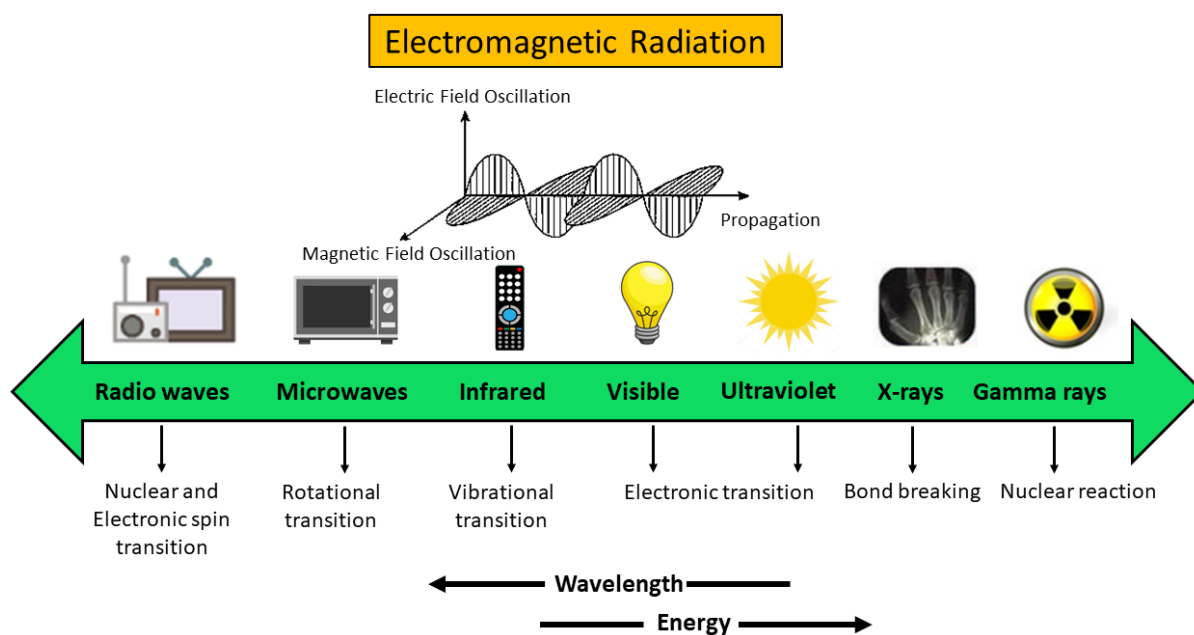


Figure 1.47: Types of Electromagnetic Radiation.

Table 1.19: Impacts of Electromagnetic radiation in a molecule.

Serial Number	Electromagnetic Radiation	Corresponding Wavelength	Energy of Photon	Event occurs after absorption
1.	Radio waves	1 mm - 1 m	1.2 $\mu$ eV - 1.2 MeV	Oscillation of mobile electrons
2.	Microwaves	15 $\mu$ m - 1 mm	1.2 - 80 MeV	Molecular rotations
3.	Infra-Red	750 - 15 $\mu$ m	80 - 1.7 eV	Molecular vibrations
4.	Visible	400 - 750 nm	1.7 - 3.1 eV	Transition of outer atomic electrons
5.	UV	10 - 400 nm	3.1 - 124 eV	Transition of outer atomic electrons
6.	X-rays	0.01 nm - 10 nm	124 eV - 120 keV	Transition of inner atomic electrons
7.	Gamma rays	1 < 0.01 nm	> 1 MeV	Nuclear Reaction

## 1.7.1 Ultraviolet Spectroscopy

Ultraviolet and visible spectroscopy is mainly used to detect the presence and the nature of the conjugated multiple bonds or aromatic rings that can lead to valuable structural proposals. It deals with the recording of the absorption of radiations in the ultraviolet (UV) and visible (VIS) regions of the electromagnetic spectrum ranging from 200 to 800 nm. Absorption of this

electromagnetic radiation induces the excitation of an electron from a lower to higher molecular orbital. Generally, the most probable transition observed here is from the highest occupied molecular orbital (HOMO) to the lowest unoccupied molecular orbital (LUMO). **Figure 1.48** describes the electronic transitions involved in the UV-visible region.

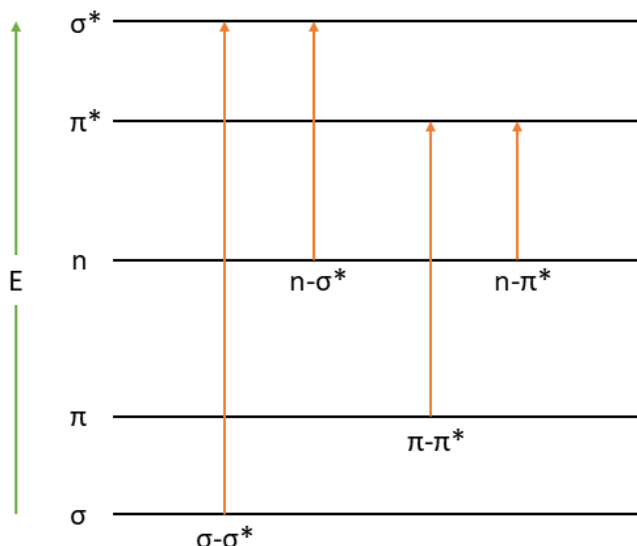


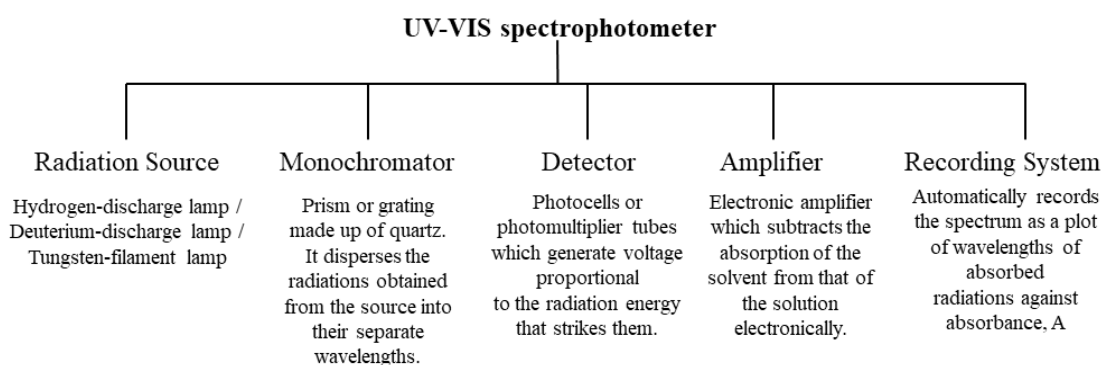
**Figure 1.48:** Electronic energy levels and transitions.

### 1.7.1.1 Principles of Ultraviolet Spectroscopy

A UV-visible spectrophotometer records a UV-VIS spectrum as a plot of wavelength of absorbed radiation (nm) versus the intensity of absorption in terms of absorbance (A) as defined by the Beer-Lambert law. According to Beer-Lambert law,

$$A = \log \frac{I_0}{I} = \epsilon cl$$

where, A = absorbance,  $I_0$  = intensity of light incident upon sample cell, I = intensity of light leaving sample cell,  $\epsilon$  = molar absorptivity, c = molar concentration of solute, l = length of sample cell (cm).



**Scheme 1.24:** Schematic diagram of a double-beam UV-VIS spectrophotometer.



### 1.7.1.2 Instrumentation

Most UV-VIS spectrophotometers are double-beam instruments and consist of a radiation source, monochromator, detectors, amplifier and recording system as shown in **Figure 1.49**.

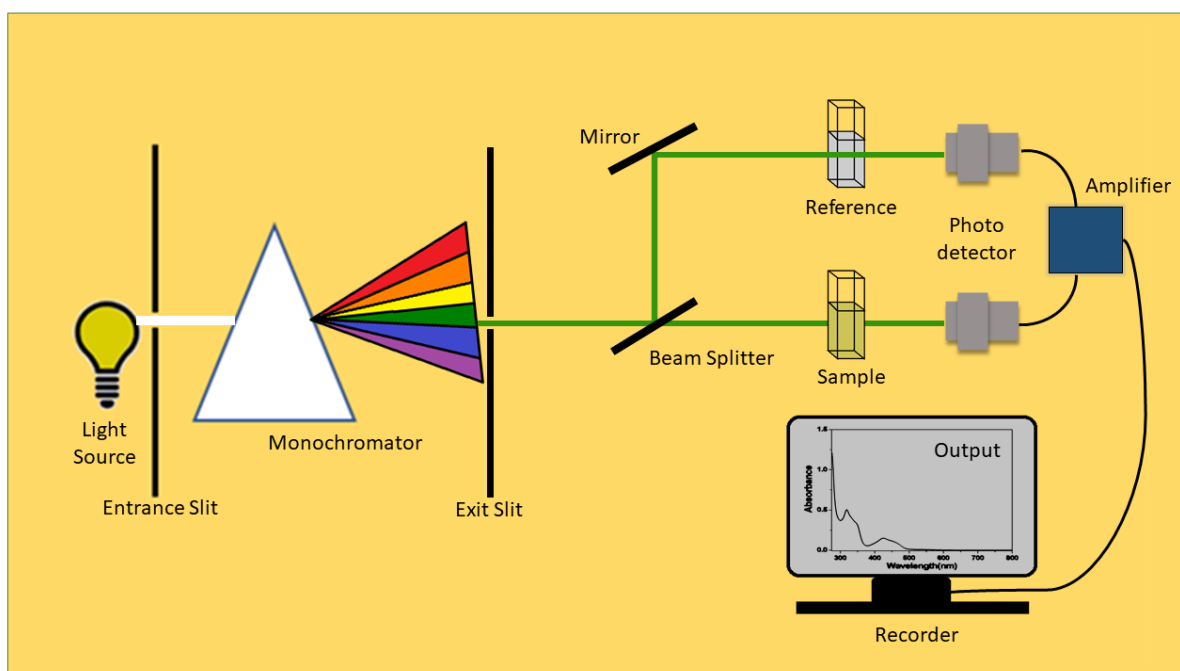


**Figure 1.49:** Schematic diagram of a UV-VIS Spectrophotometer.

### 1.7.2 Fluorescence Spectroscopy

Fluorescence spectroscopy is an analytical tool used for analysing the spectral distribution of the emitted light from the sample. For the last few decades, fluorescence technique is getting more popular because of having the following advantages:

(a) The ultra-high sensitivity, (b) super-fast response time, as fast as  $10^{-8}$ - $10^{-10}$  second, (c) The non-destructive and non-interfering nature, (d) Applicability in solid, liquid and even in gaseous media.

#### 1.7.2.1 Principles of Fluorescence Spectroscopy

In general, most of the molecules remain in ground state at room temperature. But when the molecule is irradiated with electromagnetic radiation (generally lies in the ranges of UV and visible region), it leads to excitation of an electron of the molecule from its HOMOs to its LUMO. The absorption spectrum of the molecule is measured via UV-visible spectroscopy. The excited molecule, being unstable, returns to its ground state via dissipating the excess energy, mainly in two ways: firstly, in non-radiative decay process (includes collisions with some other molecules or vibrational decays via internal conversion, conformational changes, intramolecular charge transfer, energy transfer, formation of exciplex etc.) and secondly, via radiative decay which includes luminesces (fluorescence and phosphorescence or delayed

fluorescence). The Perrin-Jablonski diagram (proposed by Dr. Alexander Jablonski in 1935) illustrates these incidents occurring after the absorbance of a photon in a simplified way (**Figure 1.50**).

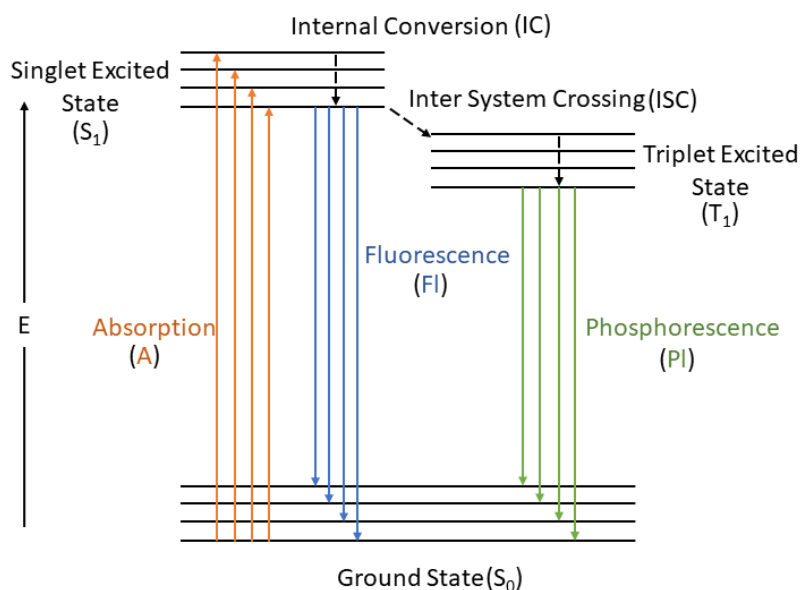


**Figure 1.50:** Perrin-Jablonski diagram explaining different photophysical events

The diagram shows that after light absorption, the electron from the lowest vibrational energy level of ground electronic state (which is a singlet state, denoted by  $S_0$ ) jumps to any of the upper vibrational energy level of higher electronic energy level (which is also a singlet state, denoted by  $S_1$ ). Hence the upper vibrational energy levels of  $S_1$  state are populated with electron density which immediately relaxes to the lowest vibrational level of the same state within  $< 10^{-12}$  second via vibrational relaxation process, known as Internal Conversion (IC). Now, depending on the nature of molecule, either the electron in lowest vibrational level of  $S_1$  state returns back to the ground vibration level of  $S_0$  state by emitting the excess energy as “Fluorescence” or may jump to the nearest triplet state ( $T_1$ ) via Intersystem Crossing (ISC) and then after internal conversion (IC) returns back to  $S_0$  state via emitting excess energy as “Phosphorescence”. Since phosphorescence is a spin forbidden process, it is a delayed radiative process, whereas, being a spin allowed transition, fluorescence process is very fast, occurs less than a pico to micro second.

### 1.7.2.2 Instrumentation

Spectrofluorometer consists of a radiation source, monochromator, polarizer, detector, recording system as shown in **Figure 1.51**.

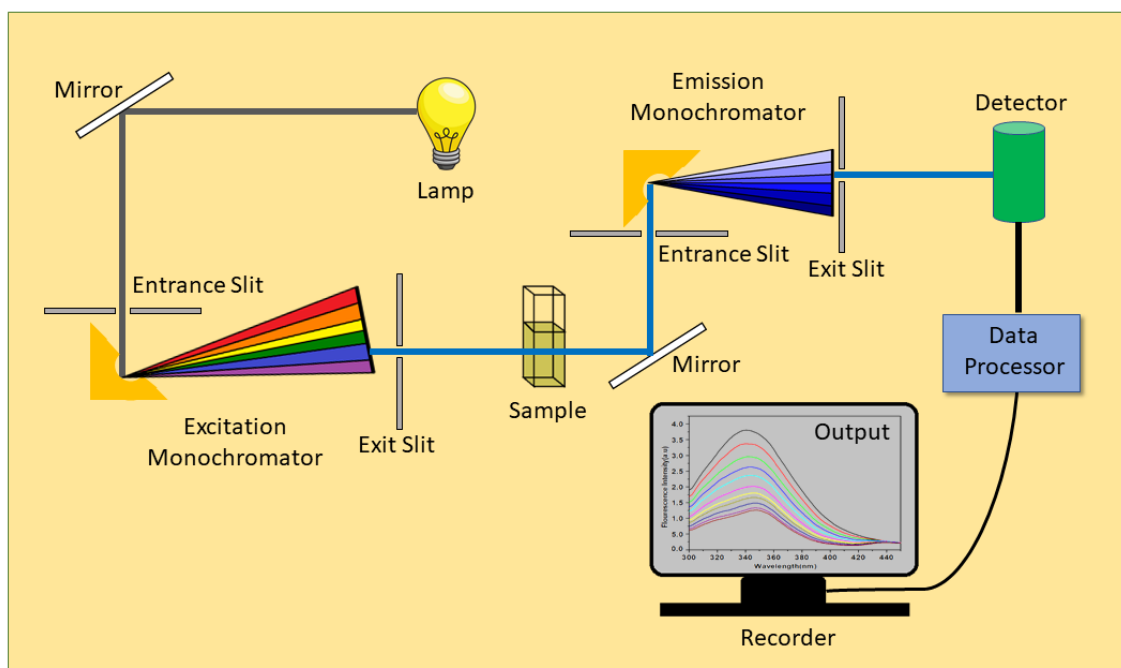
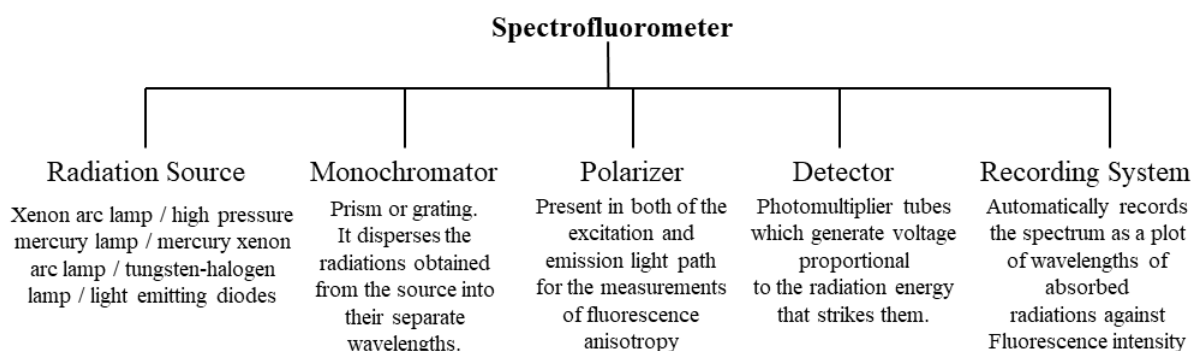


**Figure 1.51:** Schematic diagram of a spectrofluorometer.



**Scheme 1.25:** Schematic diagram of a spectrofluorometer.

### 1.7.3 Cyclic Voltammetry

Cyclic voltammetry (CV) is a popular electrochemical technique commonly used to investigate the redox processes (reduction and oxidation) of molecular species. Cyclic voltammetry also provides valuable information regarding electron transfer-initiated chemical reactions, which include catalysis. In a cyclic voltammogram, the X-axis represents a parameter, applied potential (E), that is imposed on the system, whereas the Y-axis represents the response, that is the resulting current (i) passed (**Figure 1.52**).

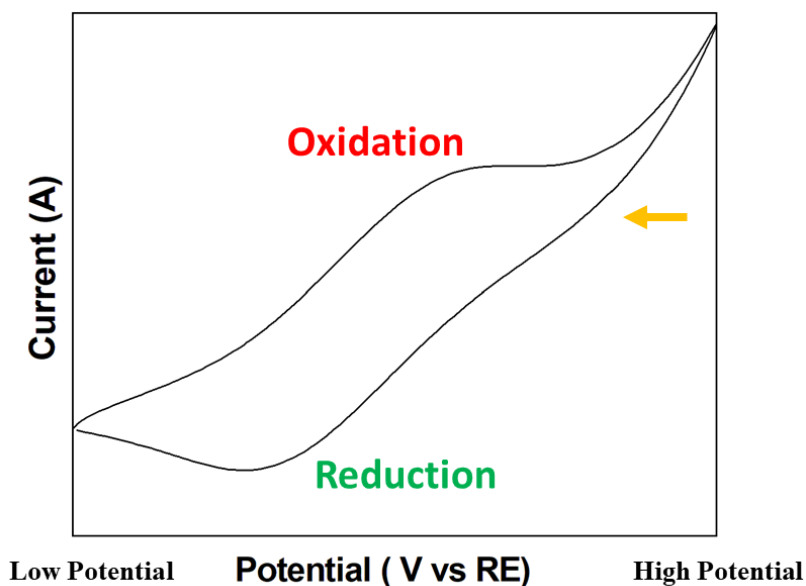


**Figure 1.52:** Representation of a cyclic voltammogram according to IUPAC convention.

**1.7.3.1 Principles of Cyclic Voltammetry**

Voltammetry is a technique where the current is measured by varying the potential between two electrodes. Voltammetric methods include LSV and CV. CV is the logical extension of LSV where the potential is applied to the working electrode in a triangular wave form (both forward and reverse directions) (**Figure 1.53**). Thus, a complete current-potential profile of a redox system is obtained.

**Some important equations associated with cyclic voltammetry**

(a) Nernst equation (**equation 1.1**) provides how the applied potential controls the concentration of the redox species at the electrode surface.

$$E = E^0 - \frac{RT}{nF} \ln \frac{C_R}{C_O} \dots\dots\dots(1.1)$$

where, **E** = Cell potential at the interest of temperature, **E<sup>0</sup>** = Standard cell potential, **R** = Universal gas constant (8.314 J.K<sup>-1</sup>.mol<sup>-1</sup>), **T** = Absolute temperature, **n** = Number of electrons transferred, **F** = Faraday’s constant (96485 C/mol), **C<sub>R</sub>** and **C<sub>O</sub>** = Concentrations of the reduced and oxidized species respectively.

(b) Randles–Sevcik equation is worth mentioning here (**equation 1.2**) which states how the peak current **i<sub>p</sub>** (A) increases linearly with the square root of the scan rate **v** (Vs<sup>-1</sup>) for electrochemically reversible electron transfer processes involving freely diffusing redox species.

$$i_p = 0.4463 \left( \frac{n^3 F^3}{RT} \right)^{1/2} A[cat](Dv)^{1/2} \dots\dots\dots(1.2)$$

where,  $i_p$  = Peak current (amperes),  $n$  = Number of electrons transferred in a redox cycle,  $F$  = Faraday's constant (96485 C/mol),  $R$  = Universal gas constant (8.314 J.K<sup>-1</sup>.mol<sup>-1</sup>),  $T$  = Absolute temperature (298 K),  $A$  = The electrode surface area in working (cm<sup>2</sup>),  $C$  = Molar concentration of redox-active species (mol/cm<sup>3</sup>),  $D$  = The diffusion coefficient (cm<sup>2</sup>/s),  $v$  = Scan rate in V/s.

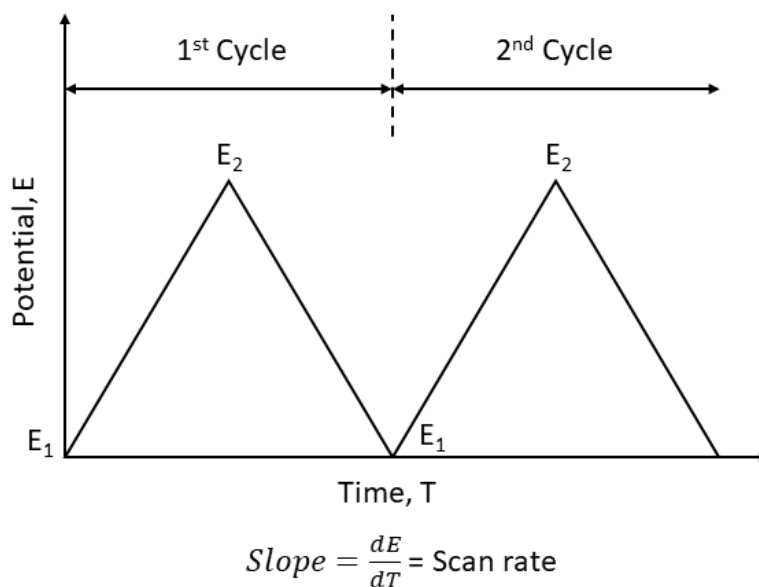
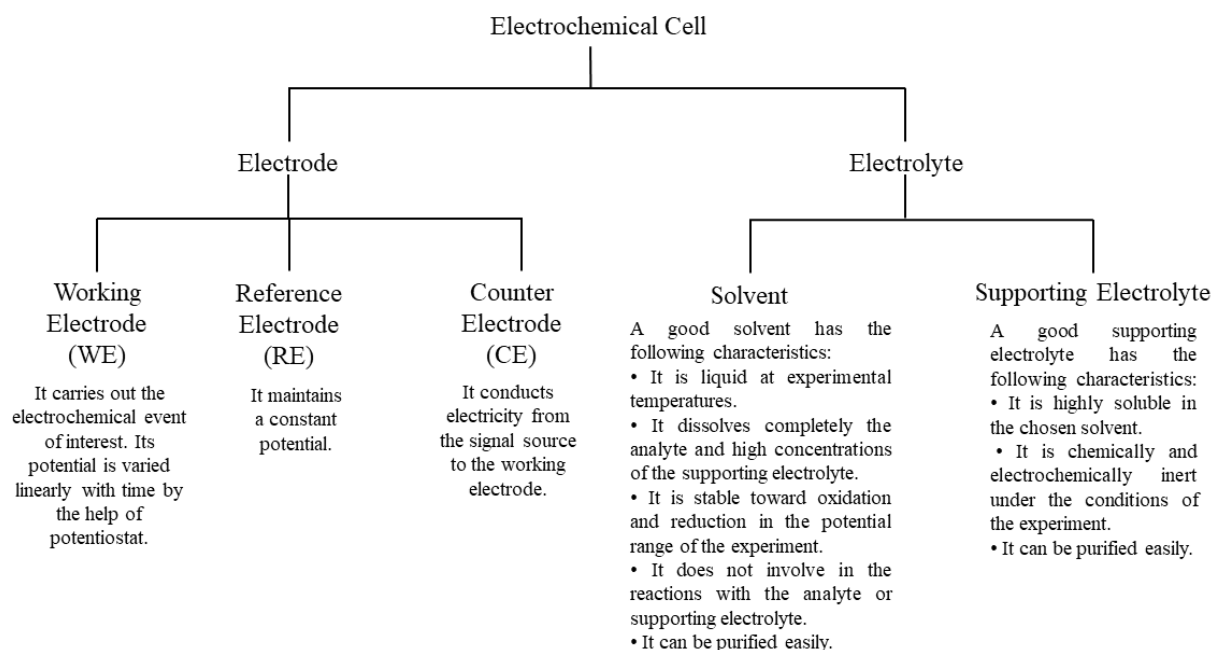


**Figure 1.53:** A triangular excitation signal applied in cyclic voltammetry.

### 1.7.3.2 Instrumentation

An electrochemical cell (**Scheme 1.26**) used in cyclic voltammetry experiment contains the following parts:



**Scheme 1.26:** Parts of an electrochemical cell.

A cyclic voltammetry consists of an electrochemical cell, a potentiostat, a current to voltage converter and a recording system as shown in **Figure 1.54**.

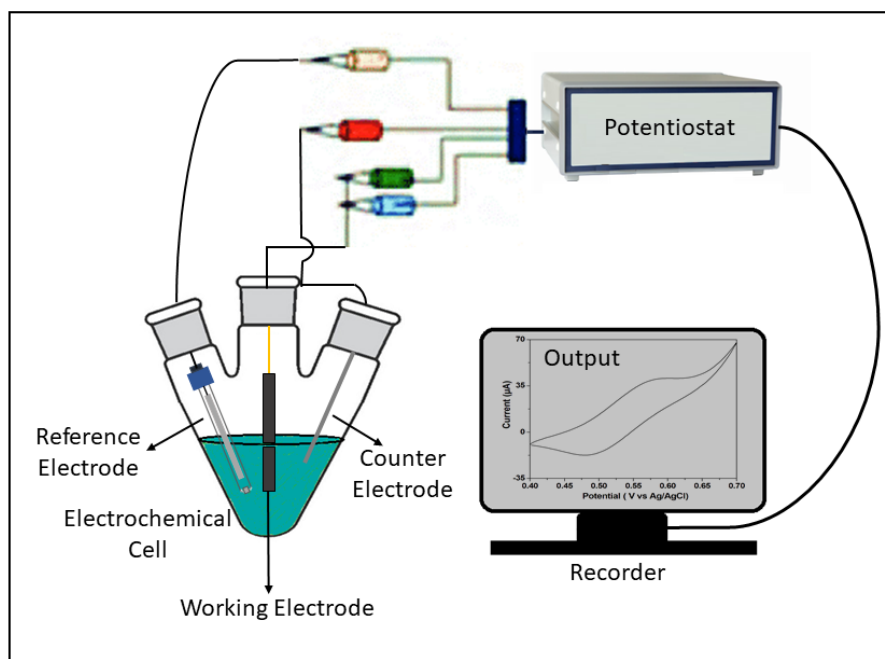


**Figure 1.54:** Schematic diagram of a cyclic voltammetry.

#### 1.7.4 Gas Chromatography

Gas chromatography is a common type of chromatographic technique used for analysing a compound that can be vapourised without decomposition.

##### 1.7.4.1 Principles of Gas Chromatography

Gas chromatography is based on the principle of “partition”. Here, at first the mixture of components to be separated is converted into vapour and then it is allowed to mix with the gaseous mobile phase. Among the components, the one which has more affinity towards the stationary phase, travels slower and thus it is eluted later. Whereas the component having less affinity towards the stationary phase travels faster and it is eluted out first. Thus, the components are separated according to their partition coefficient. After separation, they reach to the flame, get ionised and electrons are released. The electrodes present across the flame detect the electrons and as a result current flows. The current is then amplified and sent to the integrator. A gas chromatogram represents detector’s response against retention time (**Figure 1.55**). Measuring the retention time and comparing this with that of a standard of a pure substance make it possible to identify the peak qualitatively. The amount of substance can also be determined quantitatively as the area under the peak is proportional to the concentration.

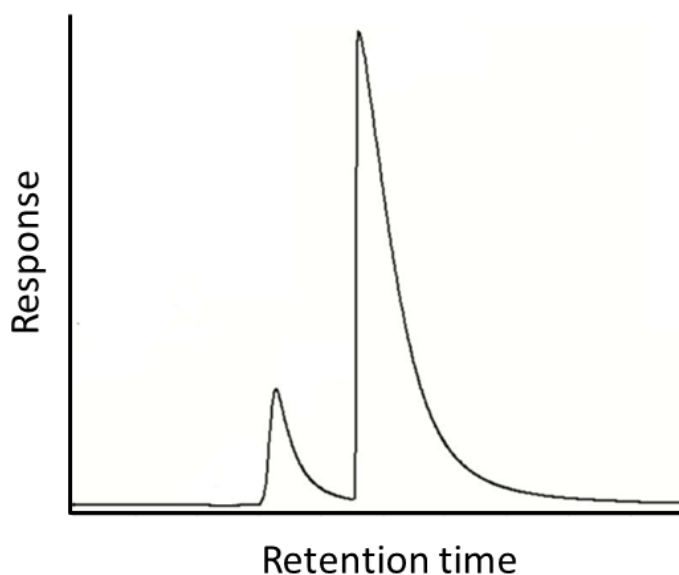
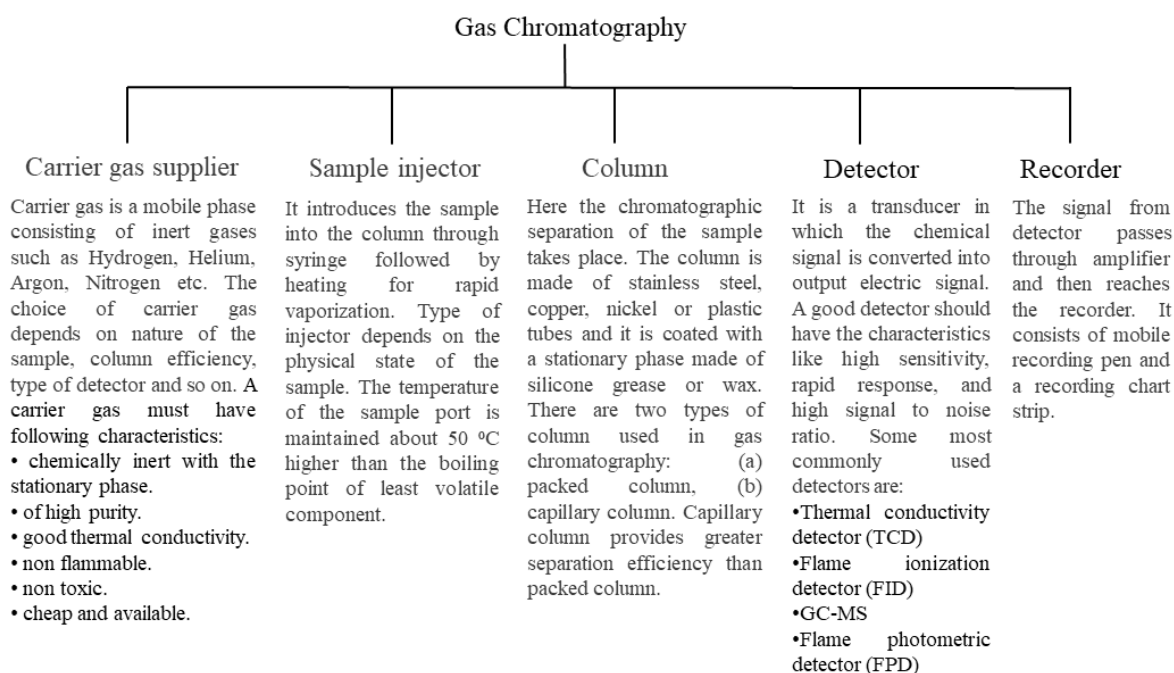


**Figure 1.55:** Representation of a gas chromatogram

**1.7.4.2 Instrumentation**

A typical gas chromatograph consists of the following parts as shown in **Scheme 1.27**.



**Scheme 1.27:** Parts of a gas chromatograph.

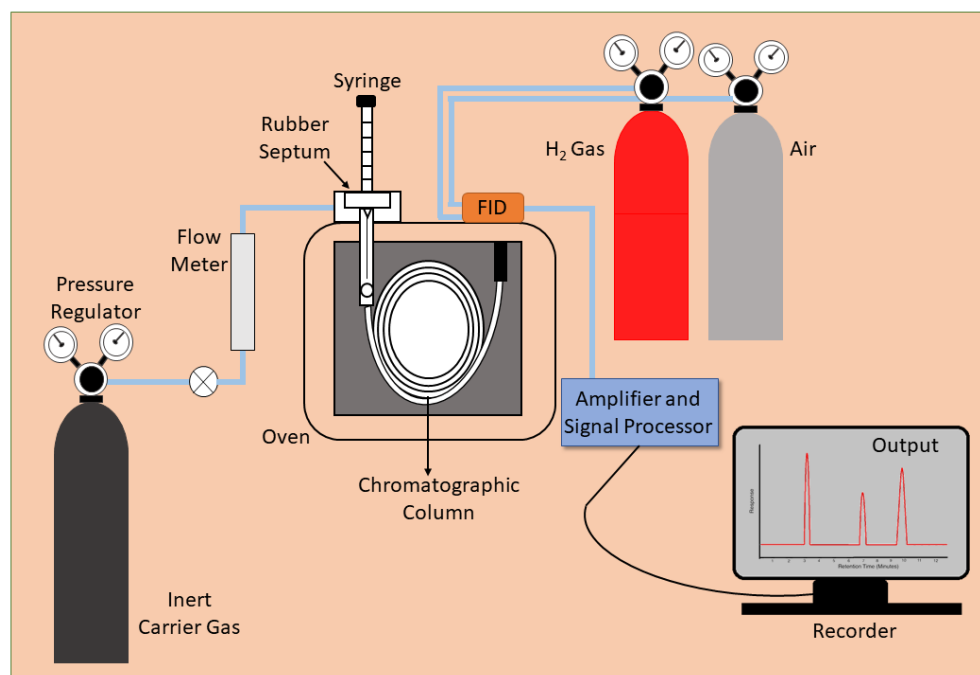


**Figure 1.56:** Schematic diagram of a gas chromatography.

### **1.7.5 Other standard tools used for the characterization of the sample**

<b>Serial No.</b>	<b>Standard Tool</b>	<b>Instrument</b>
1	Elemental Analyses	Perkin Elmer 2400C elemental analyser.
2	Fourier Transform Infrared Spectroscopy (FTIR)	Perkin Elmer spectrometer (Spectrum Two) with the samples by using ATR method.
3	$^1\text{H}$ Nuclear Magnetic Resonance Spectroscopy (NMR)	Bruker 300 or 400 MHz spectrometer using DMSO- $d_6$ as solvent and tetramethylsilane as internal standard.
4	Mass Spectrometry	Waters' HRMS spectrometer (Model: XEVO G2QTOF) and QTOF Micro YA263 mass spectrometer in ESI positive mode.
5	Single crystal X-ray diffraction studies	An automated Bruker D8 VENTURE diffractometer using graphite monochromatized Mo $K\alpha$ ( $\lambda = 0.71073 \text{ \AA}$ ) radiation. Data were processed using the Bruker SAINT package. <sup>1,212</sup> Absorption corrections based on multi scans using the SADABS software were applied to all intensity data. The structures were solved by



---

direct methods using SHELXT<sup>1.213</sup> and refined by full-matrix least-squares techniques on F<sup>2</sup> using the SHELXS-2014/7 program.<sup>1.214</sup>

---

## 1.8 References

- 1.1 (a) U. Schiff, *Introduzione allo studio della chimica secondo le lezioni fatte nel Museo di scienze naturali in Firenze, Roma*, **1876**;  
(b) T.T. Tidwell, *Angew. Chem. Int. Ed.* **2008**, *47*, 1016–1020.
- 1.2 (a) H. Schiff, *Ann. Chem. Suppl.* **1864**, *3*, 343–349;  
(b) H. Schiff, *Justus Liebigs Ann. Chem.* **1864**, *131*, 118–119.
- 1.3 (a) L. Mandal, S. Mandal, S. Mohanta, *New J. Chem.* **2017**, *41*, 4689–4701;  
(b) A. Panja, N. C. Jana, S. Adak, P. Brandão, L. Dlháň, J. Titiš and R. Boča, *New J. Chem.* **2017**, *41*, 3143–3153;  
(c) K. Hu, F. Li, Z. Zhang, F. Liang, *New J. Chem.* **2017**, *41*, 2062–2072;  
(d) S. Dey, A. Roy, G. P. Maiti, S. K. Mandal, P. Banerjee, P. Roy, *New J. Chem.* **2016**, *40*, 1365–1376;  
(e) F. A. Mautner, R. C. Fischer, M. Spell, A. R. Acevedo, D. H. Tran, S. S. Massoud, *Crystals* **2016**, *6*, 91;  
(f) S. Adhikari, S. Lohar, B. Kumari, A. Banerjee, R. Bandopadhyay, J. S. Matalobos, D. Das, *New J. Chem.* **2016**, *40*, 10094–10099;  
(g) J. L. Segura, M. J. Mancheño, F. Zamora, *Chem. Soc. Rev.* **2016**, *45*, 5635–5671;  
(h) T. T. Tidwell, *Angew. Chem., Int. Ed.* **2008**, *47*, 1016–1020.
- 1.4 (a) T.P. Yoon, E.N. Jacobsen, *Science* **2003**, *299*, 1691–1693;  
(b) P.G. Cozzi, *Chem. Soc. Rev.* **2004**, *33*, 410–421.
- 1.5 (a) H. Naeimi, Z.S. Nazifi, S.M. Amininezhad, M. Amouheidari, *J. Antibiot.* **2013**, *66*, 687–689;  
(b) M. Hajrezaie, M. Paydar, C.Y. Looi, S.Z. Moghadamtousi, P. Hassandarvish, M.S. Salga, H. Karimian, K. Shams, M. Zahedifard, N.A. Majid, H.M. Ali, M.A. Abdulla, *Sci. Rep.* **2015**, *5*, 9097;  
(c) T. Mukherjee, J.C. Pessoa, A. Kumar, A.R. Sarkar, *Dalton Trans.* **2013**, *42*, 2594–2607.
- 1.6 (a) A. Lehwess-Litzmann, P. Neumann, C. Parthier, S. Lüdtkke, R. Golbik, R. Ficner, K. Tittmann, *Nat. Chem. Biol.* **2011**, *7*, 678–684;

- (b) P. Aadao, M.L. Kuznetsov, S. Barroso, A.M. Martins, F. Avecilla, J.C. Pessoa, *Inorg. Chem.* **2012**, *51*, 11430–11449;
- (c) D. Gong, B. Wang, X. Jia, X. Zhang, *Dalton Trans.* **2014**, *43*, 4169–4178.
- (d) P. Das, W. Linert, *Coord. Chem. Rev.* **2016**, *311*, 1–23;
- (e) W. Al Zoubi, Y.G. Ko, *J. Organomet. Chem.* **2016**, *822*, 173–188;
- (f) A.M. Abu-Dief, I.M.A. Mohamed, *J. Basic Appl. Sci.* **2015**, *4*, 119–133.
- 1.7 (a) C.M. Che, S.C. Chan, H.F. Xiang, M.C. Chan, Y. Liu, Y. Wang, *Chem. Commun.* **2004**, 1484–1485;
- (b) L. Zhou, C.C. Kwok, G. Cheng, H. Zhang, C.M. Che, *Opt. Lett.* **2013**, *38*, 2373–2375;
- (c) T. Sano, Y. Nishio, Y. Hamada, H. Takahashi, T. Usuki, K. Shibata, *J. Mater. Chem.* **2000**, *10*, 157–161.
- 1.8 (a) S.H. Li, F.R. Chen, Y.F. Zhou, J.N. Wang, H. Zhang, J.G. Xu, *Chem. Commun.* **2009**, 4179–4181;
- (b) S.A. Lee, G.R. You, Y.W. Choi, H.Y. Jo, A.R. Kim, I. Noh, S.J. Kim, Y. Kim, C. Kim, *Dalton Trans.* **2014**, *43*, 6650–6659;
- (c) A. Ganguly, B.K. Paul, S. Ghosh, S. Kar, N. Guchhait, *Analyst* **2013**, *138*, 6532–6541.
- 1.9 C.R. Nayar, R. Ravikumar, *J. Coord. Chem* **2014**, *67*, 1–16.
- 1.10 W. Al Zoubi, N. Al Mohanna, *Spectrochim. Acta Part A: Mol. Biomol. Spectrosc.* **2014**, *132*, 854–870.
- 1.11 A.W. Jeevadason, K.K. Murugavel, M.A. Neelakantan, *Renew. Sustain. Energy Rev.* **2014**, *36*, 220–227.
- 1.12 (a) A. Panja, N. Shaikh, M. Ali, P. Vojtíšek, P. Banerjee, *Polyhedron* **2003**, *22*, 1191–1198;
- (b) J.D. Miller, F.D. Olevor, *J. Inorg. Nucl. Chem.* **1972**, *34*, 1873–1877.
- 1.13 (a) S. Majumder, S. Pasayat, A.K. Panda, S.P. Dash, S. Roy, A. Biswas, M.E. Varma, B.N. Joshi, E. Garribba, C. Kausar, S.K. Patra, W. Kaminsky, A. Crochet, R. Dinda, *Inorg. Chem.* **2017**, *56*, 11190–11210;
- (b) S. Saha, C.R. Choudhury, G. Pilet, A. Frontera, S. Mitra, *J. Coord. Chem.* **2017**, *70*, 1389–1405;
- (c) Z. Lu, M. Yuan, F. Pan, S. Gao, D. Zhang, D. Zhu, *Inorg. Chem.* **2006**, *45*, 3538–3548;

- (d) C.A. McAuliffe, R.V. Parish, *Inorg. Chim. Acta* **1986**, *115*, 91–94.
- 1.14 (a) X. Ran, L. Wang, Y. Lin, J. Hao, D. Cao, *Appl. Organometal. Chem.* **2010**, *24*, 741–747;  
(b) S. Ganguly, M.G.B. Drew, R.M. Gomila, A. Frontera, A. Ghosh, *Inorganica Chim. Acta* **2021**, *521*, 120351;  
(c) A. Singh, A. Maji, A. Mohanty, K. Ghosh, *J. Organomet. Chem.* **2021**, *934*, 121631;  
(d) A.K. Patel, R.N. Jadeja, R.J. Butcher, M.K. Kesharwani, J. Kästner, M. Muddassir, *Polyhedron* **2021**, *195*, 114969;  
(e) M. Ismael, A.-M.M.A.-Mawgoud, M.K. Rabia, A. Abdou, *J. Mol. Struct.* **2021**, *1227*, 129695.
- 1.15 Fosse, *Bull. Soc. Chim. France* **1901**, *25*, 373.
- 1.16 J. Qi, Y. Luo, Q. Zhou, G. Su, X. Zhang, X. Nie, M. Lv, W. Li, *J. Mol. Struct.* **2022**, *1255*, 132458.
- 1.17 B. Kurt, H. Temel, M. Atlan, S. Kaya, *J. Mol. Struct.* **2020**, *1209*, 127928.
- 1.18 N. Sarkar, P.K. Bhaumik, S. Chattopadhyay, *Polyhedron* **2016**, *115*, 37–46.
- 1.19 S. Narang, R. Mehta, S.N. Upadhyay, *Ind. Eng. Chem. Res.* **2013**, *52*, 3967–3973.
- 1.20 (a) Y. Sato, H. Miyasaka, N. Matsumoto, H. Okawa, *Inorg. Chim. Acta* **1996**, *247*, 57–63;  
(b) C.-H. Li, K.-L. Huang, J.-M. Dou, Y.-N. Chi, Y.-Q. Xu, L. Shen, D.-Q. Wang, C.-W. Hu, *Cryst. Growth Des.* **2008**, *8*, 3141–3143.
- 1.21 H. Kara, *Anal. Sci.* **2008**, *24*, x263–x264.
- 1.22 D.J. Williams, W.T. Pennington, D.V. Derveer, J.T. Anderton, K.M. White, *J. Chem. Crystallogr.* **2003**, *33*, 465–472.
- 1.23 L. Shi, H.-M. Ge, S.-H. Tan, H.-Q. Li, Y.-C. Song, H.-L. Zhu, R.-X. Tan, *Eur. J. Med. Chem.* **2007**, *42*, 558–564.
- 1.24 D. Satapathi, M. Das, K. Rajak, S. Laha, M.M. Islam, I. Choudhuri, N. Bhattacharyya, S. Das, B.C. Samanta, T. Maity, *Appl. Organomet. Chem.* **2022**, *36*, e6473.
- 1.25 A.B. Deilami, M. Salehi, A. Arab, A. Amiri, *Inorg. Chim. Acta* **2018**, *476*, 93–100.
- 1.26 B.-L. Fei, W.-S. Xu, H.-W. Tao, W. Li, Y. Zhang, J.-Y. Long, Q.-B. Liu, B. Xia, W.-Y. Sun, *J. Photochem. Photobiol. B, Biol.* **2014**, *132*, 36–44.
- 1.27 M.L. Sundararajan, T. Jeyakumar, J. Anandakumaran, B.K. Selvan, *Spectrochim. Acta A Mol. Biomol. Spectrosc.* **2014**, *131*, 82–93.

- 1.28 R. Modak, Y. Sikdar, S. Mandal, S. Chatterjee, A. Bieńko, J. Mroziński, S. Goswami, *Inorg. Chim. Acta* **2014**, *416*, 122–134.
- 1.29 A.N. Kursunlu, E. Guler, F. Sevgi, B. Ozkalp, *J. Mol. Struct.* **2013**, *1048*, 476–481.
- 1.30 R.N. Patel, S.P. Rawat, M. Choudhary, V.P. Sondhiya, D.K. Patel, K.K. Shukla, D. K. Patel, Y. Singh, R. Pandey, *Inorg. Chim. Acta* **2012**, *392*, 283–291.
- 1.31 (a) R. Robson, *Aust. J. Chem.* **1970**, *23*, 2217–2224;  
(b) R. Robson, *Inorg. Nucl. Chem. Lett.* **1970**, *6*, 125.
- 1.32 (a) P. Roy, M. Manassero, K. Dhara, P. Banerjee, *Polyhedron* **2009**, *28*, 1133–1137;  
(b) P. Roy, *J. Coord. Chem.* **2009**, *62*, 2003–2011;  
(c) P.A. Vigato, V. Peruzzo, S. Tamburini, *Coord. Chem. Rev.* **2012**, *256*, 953–1114;  
(d) A.K. Ghosh, M. Pait, M. Shatruk, V. Bertolasi, D. Ray, *Dalton Trans.* **2014**, *43*, 1970.
- 1.33 (a) S. Petit, P. Neugebauer, G. Pilet, G. Chastanet, A.-L. Barra, A.B. Antunes, W. Wernsdorfer, D. Luneau, *Inorg. Chem.* **2012**, *51*, 6645–6654;  
(b) S.S. Tandon, S.D. Bunge, J. Sanchiz, L.K. Thompson, *Inorg. Chem.* **2012**, *51*, 3270–3282;  
(c) S.T. Meally, C. McDonald, G. Karotsis, G.S. Papaefstathiou, E.K. Brechin, P.W. Dunne, P. McArdle, N.P. Powera, L.F. Jones, *Dalton Trans.* **2010**, *39*, 4809;  
(d) D. Mandal, V. Bertolasi, J. Ribas-Ariño, G. Aromí, D. Ray, *Inorg. Chem.* **2008**, *47*, 3465–3467.
- 1.34 B. Naskar, R. Modak, D.K. Maiti, A. Bauzá, A. Frontera, P.K. Maiti, S. Mandal, S. Goswami, *RSC Adv.* **2017**, *7*, 11312–11321.
- 1.35 T. Singha Mahapatra, A. Bauzá, D. Dutta, S. Mishra, A. Frontera, D. Ray, *ChemistrySelect* **2016**, *1*, 64 – 74.
- 1.36 M. Pait, A. Bauzá, A. Frontera, E. Colacio, D. Ray, *Inorg. Chem.* **2015**, *54*, 4709–4723.
- 1.37 S. Halder, S. Dey, C. Rizzoli, P. Roy, *Polyhedron* **2014**, *78*, 85–93.
- 1.38 M.S. Jana, S. Dey, J.L. Priego, R.J. Aparicio, T.K. Mondal, P. Roy, *Polyhedron* **2013**, *59*, 101–106.
- 1.39 P. Roy, K. Dhara, M. Manassero, P. Banerjee, *Inorg. Chim. Acta* **2009**, *362*, 2927–2932.
- 1.40 D. Mandal, V. Bertolasi, J. Ribas-Ariño, G. Aromí, D. Ray, *Inorg. Chem.* **2008**, *47*, 3465–3467.

- 1.41 P. Roy, K. Dhara, M. Manassero, J. Ratha, P. Banerjee, *Inorg. Chem.* **2007**, *46*, 6405–6412.
- 1.42 A.B. Deilami, M. Salehi, A. Amiri, A. Arab, *J. Mol. Struct.* **2019**, *1181*, 190–196.
- 1.43 L.-Z. Li, C. Zhao, T. Xu, H.-W. Ji, Y.-H. Yu, G.-Q. Guo, H. Chao, *J. Inorg. Biochem.* **2005**, *99*, 1076–1082.
- 1.44 H. Kargar, F.A. Meybodi, R.B. Ardakani, M.R. Elahifard, V. Torabi, M.F. Mehrjardi, M.N. Tahir, M. Ashfaq, K.S. Munawar, *J. Mol. Struct.* **2021**, *1230*, 129908.
- 1.45 K. Jana, S. Das, H. Puschmann, S.C. Debnath, A. Shukla, A.K. Mahanta, M. Hossain, T. Maity, B.C. Samanta, *Inorg. Chim. Acta* **2019**, *487*, 128–137.
- 1.46 X. Qiao, Z.-Y. Ma, C.-Z. Xie, F. Xue, Y.-W. Zhang, J.-Y. Xu, Z.-Y. Qiang, J.-S. Lou, G.-J. Chen, S.-P. Yan, *J. Inorg. Biochem.* **2011**, *105*, 728–737.
- 1.47 R. Fekri, M. Salehi, A. Asadi, M. Kubicki, *Polyhedron* **2017**, *128*, 175–187.
- 1.48 J.-P. Cao, T. Fang, L.-Z. Fu, L.-L. Zhou, S. Zhan, *Int. J. Hydrog. Energy* **2014**, *39*, 10980 – 10986.
- 1.49 A. Palanimurugan, A. Dhanalakshmi, P. Selvapandian, A. Kulandaisamy, *Heliyon* **2019**, *5*, e02039.
- 1.50 T.H. Sanatkar, A. Khorshidi, E. Sohoul, J. Janczak, *Inorg. Chim. Acta* **2020**, *506*, 119537.
- 1.51 C. Krüger, P. Augustín, I. Nemeč, Z. Trávníček, H. Oshio, R. Boca, F. Renz, *Eur. J. Inorg. Chem.* **2012**, *2013*, 902–915.
- 1.52 L. Pogány, J. Moncol, M. Gál, I. Šalitroš, R. Boca, *Inorg. Chim. Acta* **2017**, *462*, 23–29.
- 1.53 M.R. Maurya, M. Bisht, N. Chaudhary, F. Avecilla, U. Kumar, H.-F. Hsu, *Polyhedron* **2013**, *54*, 180–188.
- 1.54 B. Gildea, M.M. Harris, L.C. Gavin, C.A. Murray, Y. Ortin, H.M. Bunz, C.J. Harding, Y. Lan, A.K. Powell, G.G. Morgan, *Inorg. Chem.* **2014**, *53*, 6022–6033.
- 1.55 A.A. Alothman, E.S. Al-Farraj, W.A. Al-Onazi, Z.M. Almarhoon, A.M. Al-Mohaimed, *Arab. J. Chem.* **2020**, *13*, 3889–3902.
- 1.56 S.-Z. Zhao, C.-Y. Qin, S. Wang, M. Yamashita, Y.-H. Li, W. Huang, *Dalton Trans.* **2020**, *49*, 4293–4305.
- 1.57 H. Khanmohammadi, S. Amani, M.H. Abnosi, H.R. Khavasi, *Spectrochim. Acta Part A Mol. Biomol. Spectrosc.* **2010**, *77*, 342–347.
- 1.58 (a) P.A. Vigato, S. Tamburini, *Coord. Chem. Rev.* **2004**, *248*, 1717–2128;

- (b) R.M. Clarke, T. Storr, *Dalton Trans.* **2014**, *43*, 9380–9391.
- 1.59 G. Ceyhan, C. Çelik, S. Uruş, İ. Demirtaş, M. Elmastaş, M. Tümer, *Spectrochim. Acta A Mol. Biomol. Spectrosc.* **2011**, *81*, 184–198.
- 1.60 (a) S. Karasawa, K. Nakano, D. Yoshihara, N. Yamamoto, J.-i. Tanokashira, T. Yoshizaki, Y. Inagaki, N. Koga, *Inorg. Chem.* **2014**, *53*, 5447–5457;
- (b) A. M. Abu-Dief, I. M. A. Mohamed, Beni-Suef, *Univ. J. Basic Appl. Sci.* **2015**, *4*, 119–133;
- (c) R. E. P. Winpenny, *Chem. Soc. Rev.*, **1998**, *27*, 447–452;
- (d) P. Roy, M. Nandi, M. Manassero, M. Ricco', M. Mazzani, A. Bhaumik, P. Banerjee, *Dalton Trans.*, **2009**, 9543–9554;
- (e) M. Ando, Y. Sasaki, K. Akiyoshi, *RSC Adv.* **2020**, *10*, 12833–12840;
- (f) T. Basak, C.J. Gómez-García, R.M. Gomila, A. Frontera, S. Chattopadhyay, *RSC Adv.* **2021**, *11*, 3315–3323;
- (g) A. Banerjee, S. Herrero, Á Gutiérrez, S. Chattopadhyay, *Polyhedron* **2020**, *190*, 114756;
- (h) P. Bhunia, S. Maity, J. Mayans, A. Ghosh, *New J. Chem.* **2022**, *46*, 4363–4372;
- (i) X.-S. Gao, C.-C Ni, X.-M Ren, *Polyhedron* **2017**, *138*, 225–231.
- 1.61 (a) S. Halder, A. Mukherjee, K. Ghosh, S. Dey, M. Nandi, P. Roy, *J. Mol. Struct.* **2015**, *1101*, 1–7;
- (b) S. Halder, S. Dey, C. Rizzoli, P. Roy, *Polyhedron* **2014**, *60*, 85–93;
- (c) M. Nandi, P. Roy, *Indian J. Chem.* **2013**, *52A*, 1263–1268;
- (d) P. Roy, M. Manassero, *Dalton Trans.* **2010**, *39*, 1539–1545;
- (e) P. Roy, K. Dhara, M. Manassero, P. Banerjee, *Inorg. Chem. Commun.* **2008**, *11*, 265–269;
- (f) T. Punniyamurthy, L. Rout, *Coord. Chem. Rev.* **2008**, *252*, 134–154;
- (g) K. C. Gupta, A. K. Sutar, *Coord. Chem. Rev.* **2008**, *252*, 1420–1450;
- (h) K. C. Gupta, A. K. Sutar, C.-C. Lin, *Coord. Chem. Rev.* **2009**, *253*, 1926–1946;
- (i) L. Canali, D. C. Sherrington, *Chem. Soc. Rev.* **1999**, *28*, 85–93;
- (j) W.A. Zoubi, Y.G. Ko, *Appl. Organomet. Chem.* **2017**, *31*, e3574;
- (k) J.S. Kirar, S. Khare, *RSC Adv.* **2018**, *8*, 18814-18827;
- (l) A. Al-Hunaiti, B. Abu-Radaha, D. Wraith, T. Repo, *RSC Adv.* **2022**, *12*, 7864-7871.
- 1.62 (a) W.-J. Lian, X.-T. Wang, C.-Z. Xie, H. Tian, X.-Q. Song, H.-T. Pan, X. Qiao, J.-Y. Xu, *Dalton Trans.* **2016**, *45*, 9073–9087;

- (b) R. Vafazadeh, F. Jafari, M.M. Heidari, A.C. Willis, *J. Coord. Chem.* **2016**, *69*, 1313–1325;
- (c) B. K. Seth, A. Saha, S. Haldar, P. P. Chakraborty, P. Saha, S. Basu, *J. Photochem. Photobiol. B, Biol.* **2016**, *162*, 463–472;
- (d) M. Zaki, S. Hairat, S. Kamaal, N.H. Aljarba, N.S. AL-Johani, S. Alkahtani, *J. Mol. Struct* **2022**, *1265*, 133351;
- (e) K. Paliwal, P. Haldar, P.K.S. Antharjanam, M. Kumar, *ACS Omega* **2022**, *7*, 2881–2896;
- (f) M. Ariyaeifar, H.A. Rudbari, M. Sahihi, Z. Kazemi, A.A. Kajani, H. Zali-Boeini, N. Kordestani, G. Bruno, S. Gharaghani, *J. Mol. Struct* **2018**, *1161*, 497–511;
- (g) L. Zarei, Z. Asadi, E. Samolova, M. Dusek, Z. Amirghofran, *Inorg. Chim. Acta* **2020**, *509*, 119674.
- 1.63 (a) S. Halder, A. Layek, K. Ghosh, C. Rizzoli, P. P. Ray, P. Roy, *Dalton Trans.* **2015**, *44*, 16149–16155;
- (b) S. Roy, A. Dey, P. P. Ray, J. Ortega-Castro, A. Frontera, S. Chattopadhyay, *Chem. Commun.* **2015**, *51*, 12974–12976;
- (c) V. Stavila, A. A. Talin, M. D. Allendorf, *Chem. Soc. Rev.* **2014**, *43*, 5994–6010.
- 1.64 (a) S. Halder, J. Mondal, J. Ortega-Castro, A. Frontera, P. Roy, *Dalton Trans.* **2017**, *46*, 1943–1950;
- (b) M.Y. Fan, P. Fu, J. Li, Z.M. Su, X. Li, Q.Q. Pan, X.L. Hu, *CrystEngComm* **2021**, *23*, 929–934;
- (c) W. Wang, Y. Zhang, J. Zhang, G. Li, D. Leng, Y. Gao, J. Gao, H. Lu, *Sens. Actuators B Chem.* **2021**, *328*, 129045;
- (d) M. Pamei, A. Puzari, *Nano-Struct. Nano-Objects* **2019**, *19*, 100364;
- (e) S. Chand, M. Mondal, S.C. Pal, A. Pal, S. Maji, D. Mandal, M.C. Das, *New J. Chem.* **2018**, *42*, 12865–12871.
- 1.65 T.K. Ghosh, P. Mahapatra, S. Jana, A. Ghosh, *CrystEngComm* **2019**, *21*, 4620–4631.
- 1.66 R. Fekri, M. Salehi, A. Asadi, M. Kubicki, *Polyhedron* **2017**, *128*, 175–187.
- 1.67 A. Mandal, S. Dasgupta, S. Ganguly, A. Bauzá, A. Frontera, D. Das, *Dalton Trans.* **2017**, *46*, 15257–15268.
- 1.68 A.S. Burlov, A.I. Uraev, D.A. Garnovskii, K.A. Lyssenko, V.G. Vlasenko, Y.V. Zubavichus, V.Y. Murzin, E.V. Korshunova, G.S. Borodkin, S.I. Levchenkov, I.S. Vasilchenko, V.I. Minkin, *J. Mol. Struct* **2014**, *1064*, 111–121.

- 1.69 P. Mukherjee, M.G.B. Drew, C.J. Gómez-García, A. Ghosh, *Inorg. Chem.* **2009**, *48*, 5848–5860.
- 1.70 K. Chattopadhyay, G.A. Craig, M.J.H. Ojea, M. Pait, A. Kundu, J. Lee, M. Murrie, A. Frontera, D. Ray, *Inorg. Chem.* **2017**, *56*, 2639–2652.
- 1.71 S. Saha, A. Sasmal, C. Roy Choudhury, C.J. Gómez-García, E. Garrriba, S. Mitra, *Polyhedron* **2014**, *69*, 262–269.
- 1.72 J.-C. Jiang, Z.-L. Chu, W. Huang, G. Wang, X.-Z. You, *Inorg. Chem.* **2010**, *49*, 5897–5911.
- 1.73 A. Roth, J. Becher, C. Herrmann, H. Görls, G. Vaughan, M. Reiher, D. Klemm, W. Plass, *Inorg. Chem.* **2006**, *45*, 10066–10076.
- 1.74 T.K. Ghosh, P. Mahapatra, S. Jana, A. Ghosh, *CrystEngComm* **2019**, *21*, 4620–4631.
- 1.75 S. Manna, E. Zangrando, H. Puschmann, S.C. Manna, *Polyhedron* **2019**, *162*, 285–292.
- 1.76 K. Chattopadhyay, G.A. Craig, A. Kundu, V. Bertolasi, M. Murrie, D. Ray, *Inorg. Chem.* **2016**, *55*, 10783–10792.
- 1.77 K. Karaoğlu, T. Baran, İ. Değirmencioglu, K. Serbest, *Spectrochim. Acta A Mol. Biomol. Spectrosc.* **2011**, *79*, 867–872.
- 1.78 A.D. Khalaji, H. Hadadzadeh, K. Fejfarova, M. Dusek, *Polyhedron*, **2010**, *29*, 807–812.
- 1.79 P.S. Perlepe, L. Cunha-Silva, V. Bekiari, K.J. Gagnon, S.J. Teat, A. Escuer, T.C. Stamatatos, *Dalton Trans.* **2016**, *45*, 10256–10270.
- 1.80 D. Maity, S. Chattopadhyay, A. Ghosh, M.G.B. Drew, G. Mukhopadhyay, *Inorg. Chim. Acta* **2011**, *365*, 25–31.
- 1.81 N.N. Greenwood, A. Earnshaw, *Chemistry of the Elements*, 2<sup>nd</sup> edition, **1997**.
- 1.82 J.L. Boer, S.B. Mulrooney, R.P. Hausinger, *Arch. Biochem. Biophys.* **2014**, *544*, 142–152.
- 1.83 (a) J. Chen, Y. Huang, P. Kannan, L. Zhang, Z. Lin, J. Zhang, T. Chen, L. Guo, *Anal. Chem.* **2016**, *88*, 2149–2155;  
(b) M. Kesik, F. E. Kanik, J. Turan, M. Kolb, S. Timur, M. Bahadir, L. Toppare, *Sens. Actuators, B* **2014**, *205*, 39–49.
- 1.84 (a) K. He, Z. Li, L. Wang, Y. Fu, H. Quan, Y. Li, X. Wang, S. Gunasekaran, X. Xu, *ACS Appl. Mater. Interfaces* **2019**, *11*, 26250–26260;  
(b) J. Feng, G. Yang, Y. Mei, X. Cao, Y. Wang, H. Li, Q. Lu, *Sens. Actuators B Chem.* **2018**, *271*, 264–270.



- 1.85 (a) K.-H. Kim, E. Kabir, S.A. Jahan, *Sci. Total Environ.* **2017**, 575, 525–535;  
(b) X. Zhu, H. Zheng, X. Wei, Z. Lin, L. Guo, B. Qiu, G. Chen, *Chem. Commun.* **2013**, 49, 1276–1278.
- 1.86 J. George, Y. Shukla, *J. Proteom.* **2011**, 74, 2713–2722.
- 1.87 (a) Y. Cao, L. Wang, C. Shen, C. Wang, X. Hu, G. Wang, *Sens. Actuators B Chem.* **2019**, 283, 487–494;  
(b) Y. Zhao, X. Xu, L. Qiu, X. Kang, L. Wen, B. Zhang, *ACS Appl. Mater. Interfaces* **2017**, 9, 15164–15175.
- 1.88 (a) A. G. Smith, S. D. Gangolli, *Food Chem. Toxicol.* **2002**, 40, 767–779;  
(b) K. H. Kim, E. Kabir, S. A. Jahan, *Sci. Total Environ.* **2017**, 575, 525–535;  
(c) X. Zhu, H. Zheng, X. Wei, Z. Lin, L. Guo, B. Qiu, G. Chen, *Chem. Commun.* **2013**, 49, 1276–1278;  
(d) A. Wang, S. Costello, M. Cockburn, X. Zhang, J. Bronstein, B. Ritz, *Eur. J. Epidemiol.* **2011**, 26, 547–555;  
(e) H. F. Cui, W. W. Wu, M. M. Li, X. Song, Y. Lv, T. T. Zhang, *Biosens. Bioelectron.* **2018**, 99, 223–229;  
(f) S. O. Obare, C. De, W. Guo, T. L. Haywood, T. A. Samuels, C. P. Adams, N. O. Masika, D. H. Murray, G. A. Anderson, K. Campbell, K. Fletcher, *Sensors*, **2010**, 10, 7018–7043.
- 1.89 (a) B. Dinabandhu, *Econ. Polit. Wkly.* **2000**, 35, 16–22;  
(b) A. Evenset, I.G. Hallanger, M. Tessmann, N. Warner, A. Ruus, K. Borgå, G. W. Gabrielsen, G. Christensen, P.E. Renaud, *Sci. Total Environ.* **2016**, 542, 108–120.
- 1.90 P. Kumar, K.-H. Kim, A. Deep, *Biosens. Bioelectron.* **2015**, 70, 469–481.
- 1.91 (a) P.-L. Chang, M.-M. Hsieh, T.-C. Chiu, *Int. J. Environ. Res. Public Health* **2016**, 13, 409;  
(b) Z.E. Rassi, *Electrophoresis* **1997**, 18, 2465–2481.
- 1.92 (a) J.C. Fernando, K.R. Rogers, N.A. Anis, J.J. Valdes, R.G. Thompson, A.T. Eldefrawi, M.E. Eldefrawi, *J. Agric. Food Chem.* **1993**, 41, 511–516;  
(b) C. Ristori, C.D Carlo, M. Martini, A. Barbaro, A. Ancarani, *Anal. Chim. Acta* **1996**, 325, 151–160.
- 1.93 Y.-H. Zheng, T.-C. Hua, D.-W. Sun, J.-J. Xiao, F. Xu, F.-F. Wang, *J. Food Eng.* **2006**, 74, 24–29.
- 1.94 D. K. Singha, P. Majee, S. K. Mondal, P. Mahata, *ChemistrySelect* **2017**, 2, 5760–5768.

- 1.95 K.S. Lakhi, D.-H. Park, K. Al-Bahily, W. Cha, B. Viswanathan, J.-H Choy, A. Vinu, *Chem. Soc. Rev.* **2017**, *46*, 72–101.
- 1.96 (a) C. Janiak, J.K. Vieth, *New J. Chem.* **2010**, *34*, 2366–2388;  
(b) H. Li, M. Eddaoudi, M. O’Keeffe, O. M. Yaghi, *Nature*, **1999**, *402*, 276–279.
- 1.97 O.M. Yaghi, G.M. Li, H.L. Li, *Nature* **1995**, *378*, 703–706.
- 1.98 S.Z. Li, F.W. Huo, *Nanoscale* **2015**, *7*, 7482–7501.
- 1.99 (a) K. Sumida, D. L. Rogow, J. A. Mason, T. M. McDonald, E. D. Bloch, Z. R. Herm, T.-H. Bae, J.R. Long, *Chem. Rev.* **2012**, *112*, 724–781;  
(b) R. Banerjee, A. Phan, B. Wang, C. Knobler, H. Furukawa, M. O’Keeffe, O.M. Yaghi, *Science* **2008**, *319*, 939–943;  
(c) J. Yang, C.A. Trickett, S.B. Alahmadi, A.S. Alshammari, O.M. Yaghi, *J. Am. Chem. Soc.* **2017**, *139*, 8118–8121;  
(d) J.-R. Li, R.J. Kuppler, H.-C. Zhou, *Chem. Soc. Rev.* **2009**, *38*, 1477–1504;  
(e) P. Nugent, Y. Belmabkhout, S D. Burd, A.J. Cairns, R. Luebke, K. Forrest, T. Pham, S. Ma, B. Space, L. Wojtas, M. Eddaoudi, M.J. Zaworotko, *Nature* **2013**, *495*, 80–84;  
(f) M. Kurmoo, *Chem. Soc. Rev.* **2009**, *38*, 1353–1379;  
(g) P. Mahata, S. Natarajan, P. Panissod, M. Drillon, *J. Am. Chem. Soc.* **2009**, *131*, 10140–10150;  
(h) C. He, D. Liu, W. Lin, *Chem. Rev.* **2015**, *115*, 11079–11108;  
(i) P. Horcajada, R. Gref, T. Baati, P.K. Allan, G. Maurin, P. Couvreur, G. Ferey, R. E. Morris, C. Serre, *Chem. Rev.* **2012**, *112*, 1232–1268;  
(j) A.H. Chughtai, N. Ahmad, H.A. Younus, A. Laypkov, F. Verpoort, *Chem. Soc. Rev.* **2015**, *44*, 6804–6849;  
(k) Y.-B. Huang, J. Liang, X.-S. Wang, R. Cao, *Chem. Soc. Rev.* **2017**, *46*, 126–157;  
(l) P. Ji, K. Manna, Z. Lin, A. Urban, F. X. Greene, G. Lan, W. Lin, *J. Am. Chem. Soc.* **2016**, *138*, 12234–12242;  
(m) M.S. Deenadayalan, N. Sharma, P.K. Verma, C.M. Nagaraja, *Inorg. Chem.* **2016**, *55*, 5320–5327;  
(n) Z.-L. Wu, C.-H. Wang, B. Zhao, J. Dong, F. Lu, W.- H. Wang, W.-C. Wang, G.-J. Wu, J.-Z. Cui, Cheng, *Angew. Chem., Int. Ed.* **2016**, *55*, 4938–4942;  
(o) Y. Hasegawa, T. Nakanishi, *RSC Adv.* **2015**, *5*, 338–353;  
(p) M.-S. Wang, S.-P. Guo, Y. Li, L.-Z. Cai, J.-P. Zou, G. Xu, W.-W. Zhou, F.-K. Zheng, G.-C. Guo, *J. Am. Chem. Soc.* **2009**, *131*, 13572–13573;

- (q) Q. Gong, Z. Hu, B.J. Deibert, T.J. Emge, S.J. Teat, D. Banerjee, B. Mussman, N. D. Rudd J. Li, *J. Am. Chem. Soc.* **2014**, *136*, 16724–16727;
- (r) T.-W. Duan, B. Yan, *J. Mater. Chem. C* **2014**, *2*, 5098–5104;
- (s) P. Ramaswamy, N.E. Wong, G.K.H. Shimizu, *Chem. Soc. Rev.* **2014**, *43*, 5913–5932;
- (t) M. Yoon, K. Suh, S. Natarajan, K. Kim, *Angew. Chem., Int. Ed.* **2013**, *52*, 2688–2700;
- (u) M. Sadakiyo, T. Yamada, H. Kitagawa, *J. Am. Chem. Soc.* **2014**, *136*, 13166–13169;
- (v) P. Ramaswamy, N.E. Wong, B.S. Gelfand, G.K.H. Shimizu, *J. Am. Chem. Soc.* **2015**, *137*, 7640–7643;
- (w) S. Horike, D. Umeyama, S. Kitagawa, *Acc. Chem. Res.* **2013**, *46*, 2376–2384;
- (x) R.-W. Huang, Y.-S. Wei, X.-Y. Dong, X.-H. Wu, C.-X. Du, S.-Q. Zang, T.C.W. Mak, *Nat. Chem.* **2017**, *9*, 689.
- 1.100 A. Chidambaram, K.C. Stylianou, *Inorg. Chem. Front.* **2018**, *5*, 979–998.
- 1.101 (a) X. Wang, L. L. Zhang, J. Yang, F. L. Liu, F. N. Dai, R. M. Wang, D. F. Sun, J. *Mater. Chem. A* **2015**, *3*, 12777–12785;
- (b) P. Mahata, S. K. Mondal, D. K. Singha, P. Majee, *Dalton Trans.* **2017**, *46*, 301–328;
- (c) J. Rocha, L. D. Carlos, F. A. A. Paz, D. Ananias, *Chem. Soc. Rev.* **2011**, *40*, 926–940;
- (d) C. H. Chen, X. S. Wang, R. Cao, *Dalton Trans.* **2018**, *47*, 3452–3458.
- 1.102 (a) Y. Gao, G. Liu, M. Gao, X. Huang, D. Xu, *Crit Rev Anal Chem* **2020**, *50*, 472–484;
- (b) Z. Hasan, S.H. Jhung, *J. Hazard. Mater.* **2015**, *283*, 329–339.
- 1.103 X. F. Zheng, L. Zhou, Y. M. Huang, C. G. Wang, J. G. Duan, L. L. Wen, Z. F. Tian, D. F. Li, *J. Mater. Chem. A* **2014**, *2*, 12413–12422.
- 1.104 (a) J. Li, Y. Liu, X. Wang, G. Zhao, Y. Ai, B. Han, T. Wen, T. Hayat, A. Alsaedi, X. Wang, *Chem. Eng. J.* **2017**, *330*, 1012–1021;
- (b) D. Banerjee, W. Xu, Z. Nie, L.E. Johnson, C. Coghlan, M.L. Sushko, D. Kim, M. J. Schweiger, A.A. Kruger, C.J. Doonan, *Inorg. Chem.* **2016**, *55*, 8241–8243.
- 1.105 L. Li, W. Ma, S. Shen, H. Huang, Y. Bai, H. Liu, *ACS Appl. Mater. Interfaces* **2016**, *8*, 31032–31041.

- 1.106 (a) K. Liu, S. Zhang, X. Hu, K. Zhang, A. Roy, G. Yu, *Environ. Sci. Technol.* **2015**, *49*, 8657–8665;  
(b) S. Yang, A.J. Ramirez-Cuesta, R. Newby, V. Garcia-Sakai, P. Manuel, S.K. Callear, S.I. Campbell, C.C. Tang, M. Schröder, *Nat. Chem.* **2015**, *7*, 121–129.
- 1.107 (a) Y. Sun, Z. Wu, X. Wang, C. Ding, W. Cheng, S. Yu, X. Wang, *Environ. Sci. Technol.* **2016**, *50*, 4459–4467;  
(b) X. Wang, S. Yang, W. Shi, J. Li, T. Hayat, X. Wang, *Environ. Sci. Technol.* **2015**, *49*, 11721–11728;  
(c) Y. Sun, S. Yang, Y. Chen, C. Ding, W. Cheng, X. Wang, *Environ. Sci. Technol.* **2015**, *49*, 4255–4262;  
(d) Z. Jin, X. Wang, Y. Sun, Y. Ai, X. Wang, *Environ. Sci. Technol.* **2015**, *49*, 9168–9175;  
(e) A. Ladeira, V. Ciminelli, H. Duarte, M. Alves, A. Ramos, *Geochim. Cosmochim. Acta* **2001**, *65*, 1211–1217;  
(f) J. Li, Q. Wu, X. Wang, Z. Chai, W. Shi, J. Hou, T. Hayat, A. Alsaedi, X. Wang, *J. Mater. Chem. A* **2017**, *5*, 20398–20406.
- 1.108 (a) Y. Peng, H. Huang, D. Liu, C. Zhong, *ACS Appl. Mater. Interfaces* **2016**, *8*, 8527–8535;  
(b) M. Carboni, C. W. Abney, S. Liu, W. Lin, *Chem. Sci.* **2013**, *4*, 2396–2402.
- 1.109 (a) S. Rapti, A. Pournara, D. Sarma, I.T. Papadas, G.S. Armatas, A.C. Tsipis, T. Lazarides, M.G. Kanatzidis, M.J. Manos, *Chem. Sci.* **2016**, *7*, 2427–2436;  
(b) R. Ricco, K. Konstas, M.J. Styles, J.J. Richardson, R. Babarao, K. Suzuki, P. Scopece, P. Falcaro, *J. Mater. Chem. A* **2015**, *3*, 19822–19831;  
(c) J. W. Jun, M. Tong, B. K. Jung, Z. Hasan, C. Zhong, S. H. Jhung, *Chem. Eur. J.* **2015**, *21*, 347–354;  
(d) G. Yuan, Y. Tian, J. Liu, H. Tu, J. Liao, J. Yang, Y. Yang, D. Wang, N. Liu, *Chem. Eng. J.* **2017**, *326*, 691–699;  
(e) L. Zhu, C. Xiao, X. Dai, J. Li, D. Gui, D. Sheng, L. Chen, R. Zhou, Z. Chai, T. E. Albrecht-Schmitt, S. Wang, *Environ. Sci. Technol. Lett.* **2017**, *4*, 316–322;  
(f) X. Zhang, D. Sarma, Y. Wu, L. Wang, Z. Ning, F. Zhang, M.G. Kanatzidis, *J. Am. Chem. Soc.* **2016**, *138*, 5543–5546.
- 1.110 (a) T. Düren, Y.-S. Bae, R. Q. Snurr, *Chem. Soc. Rev.* **2009**, *38*, 1237–1247;  
(b) R.B. Getman, Y. Bae, C.E. Wilmer, R.Q. Snurr, *Chem. Rev.* **2011**, *112*, 703–723;

- (c) W. Zhuang, D. Yuan, D. Liu, C. Zhong, J. Li, H. Zhou, *Chem. Mater.* **2011**, *24*, 18–25;
- (d) J. Jiang, R. Babarao, Z. Hu, *Chem. Soc. Rev.* **2011**, *40*, 3599–3612;
- (e) J. Jiang, *Mol. Simul.* **2014**, *40*, 516–536.
- 1.111 A. Nalaparaju, J. Jiang, *J. Phys. Chem. C* **2012**, *116*, 6925–6931.
- 1.112 (a) L. Li, W. Ma, S. Shen, H. Huang, Y. Bai, H. Liu, *ACS Appl. Mater. Interfaces* **2016**, *8*, 31032–31041;
- (b) T. Zheng, Z. Yang, D. Gui, Z. Liu, X. Wang, X. Dai, S. Liu, L. Zhang, Y. Gao, L. Chen, D. Sheng, Y. Wang, J. Diwu, J. Wang, R. Zhou, Z. Chai, T. E. Albrecht-Schmitt, S. Wang, *Nat. Commun.* **2017**, *8*, 15369.
- 1.113 M. Habila, B. Alhenaki, A. El-Marghany, M. Sheikh, A. Ghfar, Z. ALOthman, M. Soylak, *J. Sep. Sci.* **2020**, *43*, 3103–3109.
- 1.114 S.K. Bhardwaj, N. Bhardwaj, G.C. Mohanta, P. Kumar, A.L. Sharma, K.-H. Kim, A. Deep, *ACS Appl. Mater. Interfaces* **2015**, *7*, 26124–26130.
- 1.115 R.M. Abdelhameed, H. Abdel-Gawad, C.M. Silva, J. Rocha, B. Hegazi, A.M.S. Silva, *Int. J. Environ. Sci. Technol.* **2018**, *15*, 2283–2294.
- 1.116 Q. Liu, Z. He, H. Wang, X. Feng, P. Han, *Microchim Acta* **2020**, *187*, 524.
- 1.117 G. Liu, L. Li, D. Xu, X. Huang, X. Xu, S. Zheng, Y. Zhang, H. Lin, *Carbohydr. Polym.* **2017**, *175*, 584–591.
- 1.118 M. Heidarbeigi, M. Saraji, M.T. Jafari, *J. Chromatogr. A* **2021**, *1651*, 462279.
- 1.119 P.B. Kandagal, S. Ashoka, J. Seetharamappa, S.M.T. Shaikh, Y. Jadegoud, O.B. Ijare, *J. Pharm. Biomed. Anal.* **2006**, *41*, 393–399.
- 1.120 C. Santini, M. Pellei, V. Gandin, M. Porchia, F. Tisato, C. Marzano, *Chem. Rev.* **2014**, *114*, 815.
- 1.121 (a) A. Bartyzel, *J. Coord. Chem.* **2013**, *66*, 4292–4303;
- (b) Z.C. Liu, B.D. Wang, Z.Y. Yang, Y. Li, D.D. Qin, T.R. Li, *Eur. J. Med. Chem.* **2009**, *44*, 4477–4484;
- (c) M. Wang, L.F. Wang, Y.Z. Li, Q.X. Li, Z.D. Xu, D.M. Qu, *Transit. Metal. Chem.* **2001**, *26*, 307–310;
- (d) J.D. Rajput, S.D. Bagul, S.K. Tadavi, R.S. Bendre, *Med. Aromat. Plants (Los Angel)* **2016**, *5*, 2167;
- (e) A.A. Bekhit, H.M. Ashour, Y.S. Ghany, A.E. Bekhit, A. Baraka, *Eur. J. Med. Chem.* **2008**, *43*, 456–463;

- (f) N. Raman, A. Selvan, S. Sudharsan, *Spectrochim Acta A* **2011**, *79*, 873–883;
- (g) K.E. Erkkila, D.T. Odom, J.K. Barton, *Chem. Rev* **1999**, *99*, 2777–2796;
- (h) B.L. Fei, W.S. Xu, H.W. Tao, W. Li, Y. Zhang, J.Y. Long, Q.B. Liu, B. Xia, W.Y. Sun, *J. Photochem. Photobiol. B: Biology* **2014**, *132*, 36–44.
- 1.122 T. Helleday, E. Petermann, C. Lundin, B. Hodgson, R.A. Sharma, *Nat. Rev. Cancer* **2008**, *8*, 193–204.
- 1.123 B. Rosenberg, L. van Camp, J.E. Trosko, V.H. Mansour, *Nature* **1969**, *222*, 385–386.
- 1.124 (a) B. Rosenberg, L. Vancamp, T. Krigas, *Nature* **1965**, *205*, 698–699;
- (b) B. Rosenberg, E. Renshaw, L. Vancamp, J. Hartwick, J. Drobnik, *J. Bacteriol.* **1967**, *93*, 716–721;
- (c) L. Kelland, *Nat. Rev. Cancer* **2007**, *7*, 573–584.
- 1.125 (a) A.H. Calvert, S.J. Harland, D.R. Newell, Z.H. Siddik, A.C. Jones, T.J. McElwain, S. Raju, E. Wiltshaw, I.E. Smith, J.M. Baker, M.J. Peckham, K.R. Harrap, *Cancer Chemother. Pharmacol.* **1982**, *9*, 140–147;
- (b) C.R. Culy, D. Clemett, L.R. Wiseman, *Drugs* **2000**, *60*, 895–924;
- (c) J.R. Eckardt, D.L. Bentsion, O.N. Lipatov, I.S. Polyakov, F.R. MacKintosh, D.A. Karlin, G.S. Baker, H.B. Breitz, *J. Clin. Oncol.* **2009**, *27*, 2046–2051;
- (d) R. Duncan, *Adv. Drug Deliv. Rev.* **2009**, *61*, 1131–1148;
- (e) J.Q. Zhang, K. Li, K.M. Jiang, Y.W. Cong, S.P. Pu, X.G. Xie, Y. Jin, J. Lin, *RSC Adv.* **2016**, *6*, 17074–17082.
- 1.126 (a) N. Raman, S. Sobha, *Inorg. Chem. Commun.* **2012**, *17*, 120–123;
- (b) S. Betanzos-Lara, C. Gomez-Ruiz, L.R. Barron-Sosa, I. Gracia-Mora, M. FloresAlamo, N. Barba-Behrens, *J. Inorg. Biochem.* **2012**, *114*, 82–93;
- (c) V. Oliveri, G. Vecchio, *Eur. J. Med. Chem.* **2016**, *120*, 252–274;
- (d) X. Totta, A.A. Papadopoulou, A.G. Hatzidimitriou, A. Papadopoulos, G. Psomas, *J. Inorg. Biochem.* **2015**, *145*, 79–93.
- 1.127 J. Ma, F.L. Jiang, L. Chen, M.Y. Wu, S.Q. Zhang, D. Han, R. Feng, M.C. Hong, *Cryst. Growth Des.* **2011**, *11*, 3273–3281.
- 1.128 (a) N.C. Kasuga, K. Sekino, C. Koumo, N. Shimada, M. Ishikawa, K. Nomiya, *J. Inorg. Biochem.* **2001**, *84*, 55–65;
- (b) M. Alexiou, I. Tsivikas, C.D. Samara, A.A. Pantazaki, P. Trikalitis, N. Lalioti, D.A. Kyriakidis, D.P. Kessissoglou, *J. Inorg. Biochem.* **2003**, *93*, 256–264;

- (c) R. Kurtaran, L.T. Yildirim, A.D. Azaz, H. Namli, O. Atakol, *J. Inorg. Biochem.* **2005**, *99*, 1937–1944;
- (d) W. Luo, X.G. Meng, X.Z. Sun, F.P. Xiao, J.F. Shen, Y. Zhou, G.Z. Cheng, Z.P. Ji, *Inorg. Chem. Commun.* **2007**, *10*, 1351–1354;
- (e) Z. Afrasiabi, E. Sinn, W.S. Lin, Y.F. Ma, C. Campana, S. Padhye, *J. Inorg. Biochem.* **2005**, *99*, 1526–1531;
- (f) S.M. Pradeepa, H.S.B. Naik, B.V. Kumar, K.I. Priyadarsini, *Spectrochim. Acta A Mol. Biomol. Spectrosc.* **2013**, *101*, 132–139;
- (g) M.P. Sathisha, U.N. Shetti, V.K. Revankar, K.S.R. Pai, *Eur. J. Med. Chem.* **2008**, *43*, 2338–2346;
- (h) L.J.K. Boerner, J.M. Zaleski, *Curr. Opin. Chem. Biol.* **2005**, *9*, 135–144;
- (i) V.C. Silveira, M.P. Abbott, M. Cavicchioli, M.B. Goncalves, H.M. Petrilli, L. de Rezende, A.T. Amaral, D.E.P. Fonseca, G.F. Caramori, A.M. da Costa Ferreira, *Dalton Trans.* **2013**, *42*, 6386–6396;
- (j) A. Patra, T.K. Sen, A. Ghorai, G.T. Musie, S.K. Mandal, U. Ghosh, M. Bera, *Inorg. Chem.* **2013**, *52*, 2880–2890;
- (k) X.-W. Li, L. Tao, Y.-T. Li, Z.-Y. Wu, C.-W. Yan, *Eur. J. Med. Chem.* **2012**, *54*, 697–708;
- (l) J. Costa Pessoa, I. Tomaz, *Curr. Med. Chem.* **2010**, *17*, 3701–3778;
- (m) S. Mukhopadhyay, R.K. Gupta, R.P. Paitandi, N. Rana, G. Sharma, B. Koch, L. K. Rana, M.S. Hundal, D.S. Pandey, *Organometallics* **2015**, *34*, 4491.
- 1.129 S.Y. Lee, A. Hille, C. Frias, B. Kater, B. Bonitzki, S. Wolfl, H. Scheffler, A. Prokop, R. Gust, *J. Med. Chem.* **2010**, *53*, 6064–6070.
- 1.130 C.N. Sudhamani, H.S. Bhojya Naik, T.R. Ravikumar Naik, M.C. Prabhakara, *Spectrochim. Acta A Mol. Biomol. Spectrosc.* **2009**, *72*, 643–647.
- 1.131 (a) B. Duff, V.R. Thangella, B.S. Creaven, M. Walsh, D.A. Egan, *Eur. J. Pharmacol.* **2012**, *689*, 45–55;
- (b) A.T. Chaviara, P.C. Christidis, A. Papageorgiou, E. Chrysogelou, D.J. Hadjipavlou-Litina, C.A. Bolos, *J. Inorg. Biochem.* **2005**, *99*, 2102–2109;
- (c) A. Bhunia, S. Manna, S. Mistri, A. Paul, R.K. Manne, M.K. Santra, V. Bertolasi, S.C. Manna, *RSC Adv.* **2015**, *5*, 67727–67737;
- (d) S. Mistri, A. Paul, A. Bhunia, R.K. Manne, M.K. Santra, H. Puschmann, S.C. Manna, *Polyhedron* **2016**, *104*, 63–72;

- (e) M. Chen, X.Y. Tang, S.P. Yang, H.H. Li, H.Q. Zhao, Z.H. Jiang, J.X. Chen, W.H. Chen, *Dalton Trans.* **2015**, *44*, 13369–13377.
- 1.132 S. Tabassum, M. Ahmad, M. Afzal, M. Zaki, P.K. Bharadwaj, *J. Photochem. Photobiol. B* **2014**, *140*, 321–331.
- 1.133 S. Tabassum, M. Zaki, M. Ahmad, M. Afzal, S. Srivastav, S. Srikrishna, F. Arjmand, *Eur. J. Med. Chem.* **2014**, *83*, 141–154.
- 1.134 (a) A.E. Friedman, J.C. Chambron, J.P. Sauvage, N.J. Turro, J.K. Barton, *J. Am. Chem. Soc.* **1990**, *112*, 4960–4962;  
(b) T.P. Shields, J.K. Barton, *Biochemistry* **1995**, *34*, 15037–15048;  
(c) A.S. Sitlani, E.C. Long, A.M. Pyle, J.K. Barton, *J. Am. Chem. Soc.* **1992**, *114*, 2303–2312.
- 1.135 (a) N. Farrell, *Coord. Chem. Rev.* **2002**, *232*, 1–4;  
(b) M.X. Li, L.Z. Zhang, C.L. Chen, J.Y. Niu, B.S. Ji, *J. Inorg. Biochem.* **2012**, *106*, 117–125.
- 1.136 S. Roy, S. Roy, S. Saha, R. Majumdar, R.R. Dighe, E.D. Jemmis, A.R. Chakravarty, *Dalton Trans.* **2011**, *40*, 1233–1242.
- 1.137 (a) W.H. Ang, E. Daldini, L. Juillerat-Jeanneret, P.J. Dyson, *Inorg. Chem.* **2007**, *46*, 9048–9050;  
(b) T. Kosta, T. Maryama, M. Otagiri, *Pharm. Res.* **1997**, *14*, 1607–1612;  
(c) V.T.G. Chuang, U. Kragh-Hansen, M. Otagiri, *Pharm. Res.* **2002**, *19*, 569–577;  
(d) R.K. Jain, *Cancer Res.* **1990**, *50*, 814s–819s;  
(e) Y.F. Sun, H. Wu, G.Q. Zhao, Y. Shi, *Luminescence* **2015**, *30*, 79–85.
- 1.138 P. Krishnamoorthy, P. Sathyadevi, R.R. Butorac, A.H. Cowley, N.S.P. Bhuvanesh, N. Dharmaraj, *Dalton Trans.* **2012**, *41*, 4423–4436.
- 1.139 F. Faridbod, M.R. Ganjali, B. Larijani, S. Riahi, A.A. Saboury, M. Hosseini, P. Norouzi, C. Pillip, *Spectrochim. Acta A* **2011**, *78*, 96–101.
- 1.140 V.T.G. Chuang, U. Kragh-Hansen, M. Otagiri, *Pharm. Res.* **2002**, *19*, 569–577.
- 1.141 A. Patra, H. Puschmann, S.C. Manna, *Polyhedron* **2021**, *201*, 115146.
- 1.142 K. Jana, R. Maity, H. Puschmann, A. Mitra, R. Ghosh, S.C. Debnath, A. Shukla, A. K. Mahanta, T. Maity, B.C. Samanta, *Inorg. Chim. Acta* **2021**, *515*, 120067.
- 1.143 Y. Kim, J. Lee, Y.-H. Son, S.-U. Choi, M. Alam, S. Park, *J. Inorg. Biochem.* **2020**, *205*, 111015.



- 1.144 K. Venkateswarlu, N. Ganji, S. Daravath, K. Kanneboina, K. Rangan, Shivaraj, *Polyhedron* **2019**, *171*, 86–97.
- 1.145 H. Keypour, M. Shayesteh, M. Rezaeivala, S. Dhers, F.Ö. Küp, M. Güllü, S. Ng, *J. Mol. Struct.* **2017**, *1148*, 568–576.
- 1.146 Q. Wei, J. Dong, P. Zhao, M. Li, F. Cheng, J. Kong, L. Li, *J. Photochem. Photobiol. B, Biol.* **2016**, *161*, 355–367.
- 1.147 T. Mukherjee, J.C. Pessoa, A. Kumar, A.R. Sarkar, *Dalton Trans.* **2013**, *42*, 2594–2607.
- 1.148 K. C. Gupta, A. K. Sutar, *Coord. Chem. Rev.* **2008**, *252*, 1420–1450.
- 1.149 (a) T. Punniyamurthy, L. Rout, *Coord. Chem. Rev.* **2008**, *252*, 134–154;  
(b) K.C. Gupta, A.K. Sutar, *Coord. Chem. Rev.* **2008**, *252*, 1420–1450;  
(c) K.C. Gupta, A.K. Sutar, C.-C. Lin, *Coord. Chem. Rev.* **2009**, *253*, 1926–1946.
- 1.150 (a) A. M. Kirillov, M. N. Kopylovich, M. V. Kirillova, M. Haukka, M. F. C. G. da Silva, A. J. L. Pombeiro, *Angew. Chem.* **2005**, *117*, 4419–4423;  
(b) P. Roy, K. Dhara, M. Manassero, P. Banerjee, *Eur. J. Inorg. Chem.* **2008**, 4404–4412;  
(c) G. B. Shul’pin, *J. Mol. Catal. A* **2002**, *189*, 39–66;  
(d) G. B. Shul’pin, Y. N. Kozlov, L. S. Shul’pina, A. R. Kudinov, D. Mandell, *Inorg. Chem.* **2009**, *48*, 10480–10482;  
(e) M. Nandi, P. Roy, *Indian J. Chem.* **2013**, *52A*, 1263–1268;  
(f) D.D. Mal, S. Khilari, D. Pradhan, *Green Chem.* **2018**, *20*, 2279–2289.
- 1.151 (a) Z.-L. Li, G.-C. Fang, Q.-S. Gu, X.-Y. Liu, *Chem. Soc. Rev.* **2020**, *49*, 32–48;  
(b) R. Sadasivan, A. Patel, *Inorg. Chim. Acta* **2020**, *510*, 119757.
- 1.152 T. Tamoradi, M. Ghadermazi, A. Ghorbani-Choghamarani, *Catal. Lett.* **2018**, *148*, 857–872.
- 1.153 (a) K. Moschovitis, C.N. Banti, N. Kourkoumelis, E.E. Moushi, T. Lazarides, S. K. Hadjikakou, *Inorg. Chim. Acta* **2020**, *500*, 119209;  
(b) N. Beyazit, D. Çakmak, C. Demetgül, *Tetrahedron* **2017**, *73*, 2774–2779.
- 1.154 (a) S. Hazra, L.M.D.R.S. Martins, M.F.C.G. da Silva, A.J.L. Pombeiro, *RSC Adv.* **2015**, *5*, 90079–90088;  
(b) A. Jehdaramarn, S. Pornsuwan, P. Chumsaeng, K. Phomphrai, P. Sangtrirutnugul, *New J. Chem.* **2018**, *42*, 654–661.

- 1.155 A.M. Kirillov, M.V. Kirillova, A.J.L. Pombeiro, *Coord. Chem. Rev.* **2012**, *256*, 2741–2759.
- 1.156 (a) G. Das, R. Shukla, S. Mandal, R. Singh, P.K. Bharadwaj, *Inorg. Chem.* **1997**, *36* 323–329;  
(b) S. Bunce, R.J. Cross, L.J. Farrugia, S. Kunchandy, L.L. Meason, K.W. Muir, M. O'Donnell, R.D. Peacock, D. Stirling, S.J. Teat, *Polyhedron* **1998**, *17*, 4179–4187;  
(c) S. Zolezzi, E. Spodine, A. Decinti, *Polyhedron* **2003**, *22*, 1653–1658;  
(d) X.-H. Lu, Q.-H. Xia, H.-J. Zhan, H.-X. Yuan, C.-P. Ye, K.-X. Su, G. Xu, *J. Mol. Catal. A: Chem.* **2006**, *250*, 62–69.
- 1.157 (a) S. Ulmann, *Encyclopedia of Industrial Chemistry*, 6th edition, New York, **1998**;  
(b) K.A. Jørgenson, *Chem. Rev.* **1989**, *89*, 431.
- 1.158 (a) J. Gao, L. Lu, W. Zhou, G. Gao, M. He, *J Porous Mater* **2008**, *15*, 127–132;  
(b) I. Fernandez, N. Khair, *Chem Rev* **2003**, *103*, 3651–3706;  
(c) M. Darabi, T. Tamoradi, M. Ghadermazi, A. Ghorbani-Choghamarani, *Transit Met Chem* **2017**, *42*, 703–710;  
(d) A. Rezaeifard, M. Jafarpour, H. Raissi, E. Ghiamati, A. Tootoonchi, *Polyhedron* **2011**, *30*, 592–598;  
(e) M. Kazemi, L. Shiri, *J Sulfur Chem* **2015**, *36*, 613–623;  
(f) H.B. Jeon, K.T. Kim, S.H. Kim, *Tetrahedron Lett* **2014**, *55*, 3905–3908;  
(g) M. Khanmoradi, M. Nikoorazm, A. Ghorbani-Choghamarani, *Appl Organomet Chem.* **2017**, *31*, e3693;  
(h) L. Shiri, A. Ghorbani-Choghamarani, M. Kazemi, *Res Chem Intermed* **2017**, *43*, 2707–2724;  
(i) S.J. Behroozi, W. Kim, K.S. Gates, *J Org Chem* **1995**, *60*, 3964–3966;  
(j) A. Ghorbani-Choghamarani, P. Zamani, *J Iran Chem Soc* **2011**, *8*, 142–148.
- 1.159 (a) M.D. Rosa, M. Lamberti, C. Pellicchia, A. Scettri, R. Villano, A. Soriente, *Tetrahedron Lett.* **2006**, *47*, 7233–7235;  
(b) F. Hosseinpour, H. Golchoubian, *Tetrahedron Lett.* **2006**, *47*, 5195–5197;  
(c) G. Romanowski, J. Kira, *Polyhedron* **2013**, *53*, 172–178.
- 1.160 (a) S.M. Islam, A.S. Roy, P. Mondal, K. Tuhina, M. Mobarak, J. Mondal, *Tetrahedron Lett.* **2012**, *53*, 127–131;  
(b) A.N. Kharat, A. Bakhoda, T. Hajiashrafi, *J. Mol. Catal. A: Chem.* **2010**, *333*, 94–99;

- (c) S.M. Islam, A.S. Roy, P. Mondal, N. Salam, S. Paul, *Catal. Lett.* **2013**, *143*, 225–233;
- (d) P. Gogoi, M. Kalita, T. Bhattacharjee, P. Barman, *Tetrahedron Lett.* **2014**, *55*, 1028–1030;
- (e) M. Khorshidifard, H.A. Rudbari, B. Askari, M. Sahihi, M.R. Farsani, F. Jalilian, G. Bruno, *Polyhedron* **2015**, *95*, 1–13.
- 1.161 S.K. Mal, M. Mitra, H. Yadav, C.S. Purohit, A.R. Choudhury, R. Ghosh, *Polyhedron* **2016**, *111*, 118–122.
- 1.162 A.L. Abuhijleh, J. Khalaf, *Eur. J. Med. Chem.* **2010**, *45*, 3811–3817.
- 1.163 (a) K.C. Gupta, A.K. Sutar, *Coord Chem Rev* **2008**, *252*, 1420–1450;
- (b) D.M. Boghaei, S. Mohebi, *Tetrahedron* **2002**, *58*, 5357–5366;
- (c) T. Punniyamurthy, B. Bhatia, M.M. Reddy, G.C. Maikap, J. Iqbal, *Tetrahedron* **1997**, *53*, 7649–7670.
- 1.164 (a) M. Louloudi, K. Mitopoulou, E. Evaggelou, Y. Deligiannakis, N. Hadjiliadis, *J Mol Catal A Chem.* **2003**, *198*, 231–240;
- (b) D. Sadhukhan, A. Ray, R.J. Butcher, C.J. Gómez García, B. Dede, S. Mitra, *Inorg. Chim. Acta* **2011**, *376*, 245–254;
- (c) B. Sreenivasulu, M. Vetrichelvan, F. Zhao, S. Gao, J.J. Vittal, *Eur. J. Inorg. Chem.* **2005**, 4635–4645.
- 1.165 (a) M. Hudlick, *Oxidations in Organic Chemistry*, American Chemical Society, Washington, DC, **1990**;
- (b) I.W.C.A. Arends, R.A. Sheldon, *Modern Oxidation Methods*, **2004**.
- 1.166 T. Mallat, A. Baiker, *Chem. Rev.* **2004**, *104*, 3037–3058.
- 1.167 G. Cainelli, G. Cardillo, *Chromium Oxidants in Organic Chemistry*, Berlin, **1984**.
- 1.168 J. March, *Advance Organic Chemistry; Reaction, Mechanisms and Structure*, 4<sup>th</sup> edition, New York, **1992**.
- 1.169 T. T. Tidwell, *Organic Reactions*, New York, **1990**.
- 1.170 (a) I.E. Marko, A. Gautier, R.L. Dumeunier, K. Doda, F. Philippart, S.M. Brown, C.J. Urch, *Angew. Chem. Int. Ed.* **2004**, *43*, 1588–1591;
- (b) P. Gamez, I.W.C.E. Arends, J. Reedijk, R.A. Sheldon, *Chem. Commun.* **2003**, 2414–2415.
- 1.171 (a) S. Itoh, M. Taki, S. Takayama, S. Nagatomo, T. Kitagawa, N. Sakurada, R. Arakawa, S. Fukuzumi, *Angew. Chem. Int. Ed.* **1999**, *38*, 2774–2776;

- (b) H. Oshita, Y. Shimazaki, *Chem. Eur. J.* **2020**, *26*, 8324–8340.
- 1.172 (a) J. P. Klinman, *Chem. Rev.* **1996**, *96*, 2541–2562;  
(b) J. Stubbe, W.A. van der Donk, *Chem. Rev.* **1998**, *98*, 705–762.
- 1.173 J.A.D. Cooper, W. Smith, M. Bacila, H. Medina, *J. Biol. Chem.* **1959**, *234*, 445–448.
- 1.174 N. Ito, S.E.V. Phillips, C. Stevens, Z.B. Ogel, M.J. Mcpherson, J.N. Keen, K.D.S. Yadav, P.F. Knowles, *Nature* **1991**, *350*, 87–90.
- 1.175 C. Wright, A.G. Sykes, *J. Inorg. Biochem.* **2001**, *85*, 237–243.
- 1.176 (a) P.F. Knowles, N. Ito, *Perspectives in Bioinorganic Chemistry*, London, **1993**;  
(b) A.J. Baron, C. Stevens, C. Wilmot, K.D. Seneviratne, V. Blakeley, D. M. Dooley, S.E.V. Phillips, P.F. Knowles, M.J. Mcpherson, *J. Biol. Chem.* **1994**, *269*, 25095–25105;  
(c) C. Parmeggiani, F. Cardona, *Green Chem* **2012**, *14*, 547–564 ;  
(d) D. Yin, S. Urresti, M. Lafond, E.M. Johnston, F. Derikvand, L. Ciano, J.G. Berrin, B. Henrissat, P.H. Walton, G.J. Davies, H. Brumer, *Nat Commun* **2015**, *6*, 10197;  
(e) L. Que, W.B. Tolman, *Nature* **2008**, *455*, 333–340;  
(f) A.K. Nairn, S.J. Archibald, R. Bhalla, B.C. Gilbert, E.J. MacLean, S.J. Teat, P.H. Walton, *Dalton Trans* **2006**, *1*, 172–176;  
(g) P. Chaudhuri, M. Hess, T. Weyhermuller, K. Wieghardt, *Angew Chem* **1999**, *38*, 1095–1098;  
(h) K. Asami, A. Takashina, M. Kobayashi, S. Iwatsuki, T. Yajima, A. Kochem, M.V. Gastel, F. Tani, T. Kohzuma, F. Thomas, Y. Shimazaki, *Dalton Trans* **2014**, *43*, 2283–2293;  
(i) S. Itoh, M. Taki, S.E.Takayama, S. Nagatomo, T. Kitagawa, N. Sakurada, R. Arakawa, S. Fukuzumi, *Angew Chem* **1999**, *38*, 2774–2776;  
(j) S. Itoh, M. Taki, S. Fukuzumi, *Coord Chem Rev* **2000**, *198*, 3–20;  
(k) V.B. Arion, S. Platzner, P. Rapta, P. Machata, M. Breza, D. Vegh, L. Dunsch, J. Telser, S. Shova, T.C.O.M. Leod, A.J.L. Pombeiro, *Inorg Chem* **2013**, *52*, 524–7540.
- 1.177 (a) P. Chaudhuri, M. Hess, T. Weyhermüller, K. Wieghardt, *Angew. Chem. Int. Ed.* **1999**, *38*, 1095–1098;  
(b) S. Itoh, M. Taki, S. Takayama, S. Nagatomo, T. Kitagawa, N. Sakurada, R. Arakawa, S. Fukuzumi, *Angew. Chem. Int. Ed.* **1999**, *38*, 2774–2776;  
(c) F. Michel, F. Thomas, S. Hamman, E. Saint-Aman, C. Bucher, J.L. Pierre, *Chem. Eur. J.* **2004**, *10*, 4115–4125;

- (d) B.A. Jazdzewski, W.B. Tolman, *Coord. Chem. Rev.* **2000**, *200*, 633–685;
- (e) J.L. Pierre, *Chem. Soc. Rev.* **2000**, *29*, 251–257;
- (f) D. Zurita, I. GautierLuneau, S. Menage, J.L. Pierre, E. Saint-Aman, *J. Biol. Inorg. Chem.* **1997**, *2*, 46–55.
- 1.178 Y.D. Wang, J.L. DuBois, B. Hedman, K.O. Hodgson, T.D.P. Stack, *Science* **1998**, *279*, 537–540.
- 1.179 A.K. Dhara, K. Kumar, S. Kumari, U.P. Singh, K. Ghosh, *Transit. Met. Chem.* **2020**, *45*, 159–172.
- 1.180 E. Lagerspets, K. Lagerblom, E. Heliövaara, O.-M. Hiltunen, K. Moslova, M. Nieger, T. Repo, *Mol. Catal.* **2019**, *468*, 75–79.
- 1.181 A. Bhattacharjee, S. Halder, K. Ghosh, C. Rizzoli, P. Roy, *New J. Chem.* **2017**, *41*, 5696–5706.
- 1.182 H. Shi, Y. Yin, *Inorg. Chim. Acta* **2014**, *421*, 446–450.
- 1.183 S.K. Alamsetti, S. Mannam, P. Mutupandi, G. Sekar, *Chem. Eur. J.* **2009**, *15*, 1086–1090.
- 1.184 A. John, M.M. Shaikh, P. Ghosh, *Dalton Trans.* **2008**, 2815–2824.
- 1.185 P. Chaudhuri, M. Hess, T. Weyhermüller, K. Wieghardt, *Angew. Chem. Int. Ed.* **1999**, *38*, 1095–1098.
- 1.186 M. Sato, S. Tanaka, K. Kaeriyama, *J. Chem. Soc., Chem. Commun.* **1986**, 873–874.
- 1.187 A. Jehdaramarn, S. Pornsuwan, P. Chumsaeng, K. Phomphrai, P. Sangtrirutnugul, *New J. Chem.* **2018**, *42*, 654–661.
- 1.188 W. Czepa, M.A. Fik, S. Witomska, M. Kubicki, G. Consiglio, P. Pawluć, V. Patroniak, *ChemistrySelect* **2018**, *3*, 9504–9509.
- 1.189 S. Hazra, L.M.D.R.S. Martins, M.F.C. Guedes da Silva, A.J.L. Pombeiro, *RSC Adv.* **2015**, *5*, 90079–90088.
- 1.190 A. Naeimi, S. Saeednia, M. Yoosefian, H.A. Rudbari, V.M. Nardo, *J. Chem. Sci.* **2015**, *127*, 1321–1328.
- 1.191 G. Zhang, G. Proni, S. Zhao, E.C. Constable, C.E. Housecroft, M. Neuburger, J.A. Zampese, *Dalton Trans.* **2014**, *43*, 12313–12320.
- 1.192 P. Pattanayak, J.L. Pratihari, D. Patra, P. Brandão, D. Mal, V. Felix, *Polyhedron* **2013**, *59*, 23–28.
- 1.193 K. Soni, A. Kumar, A.K. Sah, *Catal. Commun.* **2012**, *17*, 95–98.

- 1.194 (a) T.R. Cook, D.K. Dogutan, S.Y. Reece, Y. Surendranath, T.S. Teets, D.G. Nocera, *Chem. Rev.* **2010**, *110*, 6474–6502;  
(b) H.B. Gray, *Nat. Chem.* **2009**, *1*, 7;  
(c) A. Kudo, Y. Miseki, *Chem. Soc. Rev.* **2009**, *38*, 253–278;  
(d) N.S. Lewis, D.G. Nocera, *Proc. Natl. Acad. Sci. USA* **2006**, *103*, 15729–15735;  
(e) Y.Y. Liang, Y.G. Li, H.L. Wang, H.J. Dai, *J. Am. Chem. Soc.* **2013**, *135*, 2013–2036;  
(f) M.G. Walter, E.L. Warren, J.R. McKone, S.W. Boettcher, Q.X. Mi, E.A. Santori, N.S. Lewis, *Chem. Rev.* **2010**, *110*, 6446–6473;  
(g) H.L. Wang, H.J. Dai, *Chem. Soc. Rev.* **2013**, *42*, 3088–3113.
- 1.195 (a) G.W. Crabtree, M.S. Dresselhaus, M.V. Buchanan, *Physics Today* **2004**, *57*, 39–44;  
(b) M.S. Dresselhaus, I.L. Thomas, *Nature* **2001**, *414*, 332–337.
- 1.196 P. Häussinger, R. Lohmüller, A.M. Watson, Hydrogen. In *Ullmann's Encyclopedia of Industrial Chemistry*, Germany, **2000**.
- 1.197 (a) A. Lasia, Hydrogen evolution reaction. In *Handbook of Fuel Cells*, New York, **2010**;  
(b) N. Danilovic, R. Subbaraman, D. Strmcnik, V.R. Stamenkovic, N.M. Markovic, *J. Serb. Chem. Soc.* **2013**, *78*, 2007–2015.
- 1.198 (a) K. Zeng, D.K. Zhang, *Prog. Energy Combust. Sci.* **2010**, *36*, 307–326;  
(b) J.K. Nørskov, T. Bligaard, A. Logadottir, J.R. Kitchin, J.G. Chen, S. Pandelov, U. Stimming, *J. Electrochem. Soc.* **2005**, *152*, J23–J26;  
(c) J. Greeley, T.F. Jaramillo, J. Bonde, I. Chorkendorff, J.K. Nørskov, *Nat. Mater.* **2006**, *5*, 909–913.
- 1.199 (a) B. Hinnemann, P.G. Moses, J. Bonde, K.P. Jørgensen, J.H. Nielsen, S. Horch, I. Chorkendorff, J.K. Nørskov, *J. Am. Chem. Soc.* **2005**, *127*, 5308–5309;  
(b) T.F. Jaramillo, K.P. Jørgensen, J. Bonde, J.H. Nielsen, S. Horch, I. Chorkendorff, *Science* **2007**, *317*, 100–102;  
(c) J. Bonde, P.G. Moses, T.F. Jaramillo, J.K. Nørskov, I. Chorkendorff, *Faraday Discuss.* **2009**, *140*, 219–231;  
(d) Y.G. Li, H.L. Wang, L.M. Xie, Y.Y. Liang, G.S. Hong, H.J. Dai, *J. Am. Chem. Soc.* **2011**, *133*, 7296–7299;

- (e) C.L. Choi, J. Feng, Y.G. Li, J. Wu, A. Zak, R. Tenne, H.J. Dai, *Nano Res.* **2013**, *6*, 921–928;
- (f) D.S. Kong, J.J. Cha, H.T. Wang, H.R. Lee, Y. Cui, *Energy Environ. Sci.* **2013**, *6*, 3553–3558;
- (g) E.J. Popczun, J.R. McKone, C.G. Read, A.J. Biacchi, A.M. Wiltrout, N.S. Lewis, R.E. Schaak, *J. Am. Chem. Soc.* **2013**, *135*, 9267–9270;
- (h) D. Voiry, H. Yamaguchi, J.W. Li, R. Silva, D.C.B. Alves, T. Fujita, M.W. Chen, T. Asefa, V.B. Shenoy, G. Eda, *Nat. Mater.* **2013**, *12*, 850–855;
- (i) L. Cheng, W.J. Huang, Q.F. Gong, C.H. Liu, Z. Liu, Y.G. Li, H.J. Dai, *Angew. Chem., Int. Ed.* **2014**, *53*, 7860–7863;
- (j) M.S. Faber, R. Dziejczak, M.A. Lukowski, N.S. Kaiser, Q. Ding, S. Jin, *J. Am. Chem. Soc.* **2014**, *136*, 10053–10061;
- (k) M.S. Faber, M.A. Lukowski, Q. Ding, N.S. Kaiser, S. Jin, *J. Phys. Chem. C* **2014**, *118*, 21347–21356;
- (l) M.-R. Gao, X. Cao, Q. Gao, Y.-F. Xu, Y.-R. Zheng, J. Jiang, S.-H. Yu, *ACS Nano* **2014**, *8*, 3970–3978;
- (m) P. Jiang, Q. Liu, Y.H. Liang, J.Q. Tian, A.M. Asiri, X.P. Sun, *Angew. Chem., Int. Ed.* **2014**, *53*, 12855–12859;
- (n) D.S. Kong, H.T. Wang, Z.Y. Lu, Y. Cui, *J. Am. Chem. Soc.* **2014**, *136*, 4897–4900;
- (o) E.J. Popczun, C.G. Read, C.W. Roske, N.S. Lewis, R.E. Schaak, *Angew. Chem.* **2014**, *126*, 5531–5534;
- (p) H.T. Wang, C. Tsai, D.S. Kong, K.R. Chan, F. AbildPedersen, J.K. Nørskov, Y. Cui, *Nano Res.* **2015**, *8*, 566–575;
- (q) Y.J. Zhang, Q.F. Gong, L. Li, H.C. Yang, Y.G. Li, Q.B. Wang, *Nano Res.* **2015**, *8*, 1108–1115;
- (r) D.-Y. Wang, M. Gong, H.-L. Chou, C.-J. Pan, H.-A. Chen, Y.P. Wu, M.-C. Lin, M.Y. Guan, J. Yang, C.-W. Chen, *J. Am. Chem. Soc.* **2015**, *137*, 1587–1592.
- 1.200 (a) M.D. Merrill, R.C. Dougherty, *J. Phys. Chem. C* **2008**, *112*, 3655–3666;
- (b) F. Jiao, H. Frei, *Energy Environ. Sci.* **2010**, *3*, 1018–1027;
- (c) D.K. Bediako, B. Lassalle-Kaiser, Y. Surendranath, J. Yano, V.K. Yachandra, D.G. Nocera, *J. Am. Chem. Soc.* **2012**, *134*, 6801–6809;
- (d) L. Trotochaud, J.K. Ranney, K.N. Williams, S.W. Boettcher, *J. Am. Chem. Soc.* **2012**, *134*, 17253–17261;

- (e) M. Gong, Y.G. Li, H.L. Wang, Y.Y. Liang, J.Z. Wu, J. G. Zhou, J. Wang, T. Regier, F. Wei, H.J. Dai, *J. Am. Chem. Soc.* **2013**, *135*, 8452–8455;
- (f) M.W. Louie, A.T. Bell, *J. Am. Chem. Soc.* **2013**, *135*, 12329–12337;
- (g) C.C.L. McCrory, S. Jung, J.C. Peters, T.F. Jaramillo, *J. Am. Chem. Soc.* **2013**, *135*, 16977–16987;
- (h) H. Tüysüz, Y.J. Hwang, S.B. Khan, A.M. Asiri, P.D. Yang, *Nano Res.* **2013**, *6*, 47–54;
- (i) Z.Y. Lu, H.T. Wang, D. Kong, K. Yan, P.-C. Hsu, G.Y. Zheng, H.B. Yao, Z. Liang, X.M. Sun, Y. Cui, *Nat. Commun.* **2014**, *5*, 4345;
- (j) F. Song, X.L. Hu, *Nat. Commun.* **2014**, *5*, 4477.
- 1.201 C.G. Morales-Guio, L.-A. Stern, X. Hu, *Chem. Soc. Rev.* **2014**, *43*, 6555–6569.
- 1.202 (a) V.M. Nikolic, S.L. Maslovara, G.S. Tasic, T.P. Brdaric, P.Z. Lausevic, B.B. Radak, M.P. Marceta Kaninski, *Appl. Catal. B* **2015**, *179*, 88–94;
- (b) Y. Liu, H. Yu, X. Quan, S. Chen, H. Zhao, Y. Zhang, *Sci Rep* **2014**, *4*, 6843;
- (c) E. Gileadi, *Physical Electrochemistry: Fundamentals, Techniques and Applications*, 2<sup>nd</sup> edition, **2011**.
- 1.203 A.M. Abudayyeh, O. Schott, H.L.C. Feltham, G.S. Hanan, S. Brooker, *Inorg. Chem. Front.* **2021**, *8*, 1015–1029.
- 1.204 X.-S. Hong, D. Huo, W.-J. Jiang, W.-J. Long, J.-D. Leng, L. Tong, Z.-Q. Liu, *ChemElectroChem* **2020**, *7*, 4956–4962.
- 1.205 (a) R. Jain, A. Al Mamun, R.M. Buchanan, P.M. Kozlowski, C.A. Grapperhaus, *Inorg. Chem.* **2018**, *57*, 13486–13493;
- (b) D.X. West, J.S. Ives, G.A. Bain, A.E. Liberta, J. Valdes-Martínez, K.H. Ebert, S. Hernandez-Ortega, *Polyhedron* **1997**, *16*, 1895–1905.
- 1.206 Y.-X. Zhang, L.-Z. Tang, Y.-F. Deng, S.-Z. Zhan, *Inorg. Chem. Commun.* **2016**, *72*, 100–104.
- 1.207 H. Shao, S.K. Muduli, P.D. Tran, H.S. Soo, *Chem. Commun.* **2016**, *52*, 2948–2951.
- 1.208 A. Zarkadoulas, M.J. Field, C. Papatriantafyllopoulou, J. Fize, V. Artero, C.A. Mitsopoulou, *Inorg. Chem.* **2016**, *55*, 432–444.
- 1.209 J.-P. Cao, T. Fang, L.-Z. Fu, L.-L. Zhou, S.-Z. Zhan, *Int. J. Hydrog. Energy* **2014**, *39*, 13972–13978.
- 1.210 J.-P. Cao, T. Fang, L.-Z. Fu, L.-L. Zhou, S.-Z. Zhan, *Int. J. Hydrog. Energy* **2014**, *39*, 10980–10986.



- 1.211 M. Graça, M.B. Martin, M. Vidotti, F.S. Nunes, *Int. J. Hydrog. Energy* **2012**, *37*, 14094–14102.
- 1.212 *APEX-II*, *SAINT* and *SADABS*, Bruker AXS Inc., Madison, WI, **2008**.
- 1.213 G.M. Sheldrick, *Acta Cryst.* **2015**, *A71*, 3–8.
- 1.214 G.M. Sheldrick, *Acta Cryst.* **2015**, *C71*, 3–8.

## Chapter 2

### **Density Functional Theory Analysis of Host - Guest Interactions in Cu(II)-Based Metal-Organic Frameworks for Pesticide Detection**

#### **Abstract**

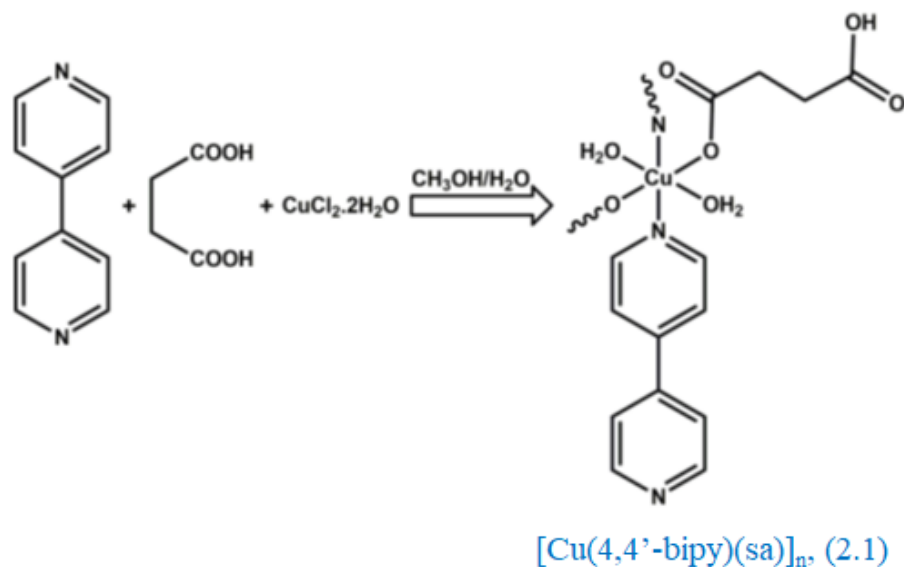
A metal organic framework (MOF) (**2.1**), having the formula  $[\text{Cu}(4,4'\text{-bipy})(\text{sa})]_n$  (where 4,4'-bipy is 4,4'-bipyridine and sa is succinate dianion), has been synthesized under ambient conditions and characterized by single-crystal X-ray diffraction analysis. The surface of the MOF mimics a 2D honeycomb structure. The uncoordinated oxygen of succinate dianion has been explored for its interaction with toxic pesticides by theoretical density functional theory analysis, and it reveals the selective identification of atrazine- and dicofol-like pesticides. The rational design of  $\text{Cu}^{2+}$  MOFs with aliphatic acid is the key factor toward the identification of pesticides, as the same MOF background with  $\text{Cd}^{2+}$  does not show any significant interaction.

## 2.1 Introduction

Metal–organic frameworks (MOFs) have been extensively explored during the last couple of decades in several fields,<sup>2.1,2.2</sup> especially for gas adsorption,<sup>2.3–2.7</sup> sensing,<sup>2.8,2.9</sup> catalysis,<sup>2.10–2.14</sup> molecular magnets,<sup>2.15–2.18</sup> optoelectronic devices,<sup>2.19–2.23</sup> and so on. The application of the MOF materials in wastewater treatment<sup>2.24,2.25</sup> as well as in fluorescence<sup>2.26,2.27</sup> is one of the hot topics nowadays. In recent years, MOFs have been used as chemosensors for several toxic materials owing to their robust 3D architecture and tight packing.<sup>2.28–2.34</sup> The tight skeleton of MOFs provides a rigid framework, which is, in general, stable in the presence of guest molecules. Host–guest interactions, in general, follow noncovalent  $\pi$ – $\pi$  or hydrogen-bonding interactions; as a consequence, the appropriate design of MOFs' skeletons is very important. Target-specific groups can be introduced for specific interactions toward guest moieties. Depending on the nature of the guest, the MOF's skeleton can be tuned; for example, for ionic substances, polar groups like –OH or –NH can be used, whereas for neutral substances, an aromatic  $\pi$ – $\pi$  interaction can be explored. In this respect, MOFs as sensors for ionic substances or picric acid have been extensively studied by the scientific community, and there are plenty of reports in the literature.<sup>2.28,2.29,2.31–2.34</sup> On the contrary, pesticides are another class of biologically toxic substances, where several organochlorine-, organofluorine-, or benzamide based pesticides are known to be biohazardous owing to their toxic effect on living organisms. As of now, there are very few reports that deal with studies on the detection of pesticides.<sup>2.35–2.41</sup>

It would be advantageous to use a MOF as a host owing to its robust structure and insolubility in common solvents, and, as a consequence, it could be used for heterogeneous sensing. Such a heterogeneous phase interaction makes it possible to use the host in a reversible manner, as it has been observed that after the process of sensing, the MOF's surface could be washed with solvents and eventually could be reused.<sup>2.42</sup> Therefore, designing the MOF's surface has become a fundamental target for researchers.

As a first time report, a copper-based MOF with succinic acid and 4,4'-bipyridine has been developed (**Scheme 2.1**), whose X-ray structure shows that it mimics the morphological features of a 2D honeycomb-like structure. An interesting feature observed in the structure is the presence of uncoordinated C=O groups of succinate dianion, which exist as dangling entities and instigated us to explore the MOF's response to toxic pesticides by density functional theory (DFT) analysis.



**Scheme 2.1:** Synthetic Route of the  $[\text{Cu}(4,4'\text{-bipy})(\text{sa})]_n$  (2.1)

## 2.2 Experimental section

### 2.2.1 Materials and Physical Methods

4,4'-Bipyridine, copper(II) chloride dihydrate, and succinic acid were purchased from Sigma-Aldrich and used as received. All other chemicals including solvents were of reagent grade and were used as received without further purification. Elemental analyses (carbon, hydrogen, and nitrogen) were performed using a Perkin-Elmer 2400C elemental analyzer. The theoretical calculation was performed using the Turbomole software package [a development of University of Karlsruhe and Forschungs-zentrum Karlsruhe GmbH, TURBOMOLE GmbH (V 7.3), since 2007; available from <http://www.turbomole.com>] in macOS Mojave (version 10.14.4) work station.

### 2.2.2 Synthesis of $[\text{Cu}(4,4'\text{-bipy})(\text{sa})]_n$ (2.1)

A methanolic solution (4.0 mL) of 4,4'-bipyridine (4-bpd) (1.0 mmol, 0.156 g) was added to an aqueous solution (4.0 mL) of succinic acid (1.0 mmol, 0.118 g) taken in a beaker and stirred for 30 min to mix well.  $\text{CuCl}_2 \cdot 2\text{H}_2\text{O}$  (1.0 mmol, 0.170 g) was dissolved in 4.0 mL of water in a separate test tube. The previously prepared mixed ligand solution was then slowly and carefully layered with the aqueous  $\text{CuCl}_2$  solution using 5.0 mL of a 1:1 v/v methanol and water mixture as buffer. Blue needle-shaped crystals suitable for single-crystal X-ray diffraction analyses were obtained after a few days. The crystals were collected and washed with the methanol–water mixture and dried in vacuum (yield = 72%). Anal. calcd (%) for  $\text{C}_{14}\text{H}_{20}\text{N}_2\text{O}_8\text{Cu}$ : C, 41.19; H, 4.90; N, 6.87. Found: C, 41.12; H, 4.85; N, 6.89.

### 2.2.3 Crystallographic Data Collection and Refinement

A suitable blue single crystal of **2.1** was mounted on the tip of a glass fiber coated with commercially available super glue. X-ray single crystal data were collected at room temperature using a Bruker APEX-II diffractometer equipped with a fine-focus, sealed tube X-ray source with graphite monochromated Mo K $\alpha$  radiation ( $\lambda = 0.71073$  Å). The data were integrated using a SAINT program,<sup>2,43</sup> and absorption correction was made with SADABS. The structure was solved with the help of SHELXT,<sup>2,44</sup> following direct methods, and refined by full-matrix least-squares on  $F^2$  using SHELXL-2018/3<sup>2,45</sup> with anisotropic displacement parameters for all non-hydrogen atoms. The water H atoms could be located in a difference Fourier map and were refined by constraining the O–H bond lengths and considering the H $\cdots$ H separations to be 0.86(1) and 1.36(2) Å, respectively, with  $U_{\text{iso}}(\text{H}) = 1.5U_{\text{eq}}(\text{O})$ . The H32 and H42 hydrogen atoms were disordered over two orientations with site occupancies of 0.5. All other H atoms were placed geometrically and refined as riding, with C–H = 0.93 to 0.97 Å and with  $U_{\text{iso}}(\text{H}) = 1.2U_{\text{eq}}(\text{C})$ . Crystallographic data for the crystal structure of **2.1** in CIF format have been deposited in the Cambridge Crystallographic Data Centre (CCDC) under deposition number CCDC-1918966. The data can be obtained free of charge via [www.ccdc.cam.ac.uk/data\\_request/cif](http://www.ccdc.cam.ac.uk/data_request/cif) (or from the Cambridge Crystallographic Data Centre, 12 Union Road, Cambridge CB21EZ, U.K.).

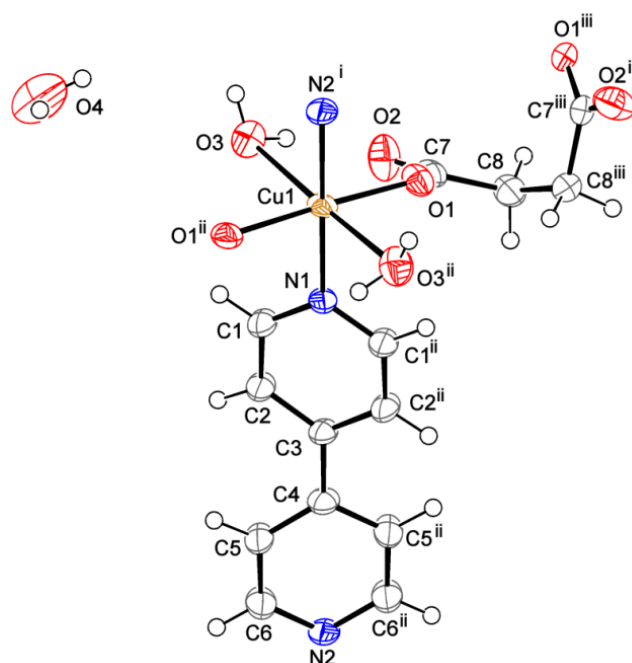


**Figure 2.1:** Asymmetric unit of **2.1** with displacement ellipsoids drawn at the 50% probability level. Only one component of the disordered water H atoms is shown. Symmetry codes: (i)  $1+x, 1+y, z$ ; (ii)  $y, x, 2/3 - z$ ; and (iii)  $x, 1+x - y, 5/6 - z$ .

## 2.3 Results and Discussion

The MOF [Cu(4,4'-bipy)(sa)]<sub>n</sub> (**2.1**) was synthesized by the reaction of copper(II) chloride, 4,4'-bipyridine, and succinic acid in methanol/water medium through a slow diffusion process. Needle shaped blue crystals thus obtained were suitable for X-ray diffraction analysis. The structure of **2.1** was already reported in the literature,<sup>2,46</sup> but no discussion of the molecular and supramolecular features was included in the paper. As evident from the structure resolution, **2.1** is a 3D coordination polymer whose asymmetric unit consists of two water molecules and half each of a copper atom, a 4,4'-bipyridine molecule, and a succinate dianion. The copper atom and the nitrogen atoms of the bipyridine molecule lie on a two-fold axis, and the carboxylate groups of the anion act as monodentate ligands through the O1 oxygen atom. The metal adopts an elongated octahedral coordination geometry (**Figure 2.1** and **Table 2.1** for crystallographic data), where the axial positions are occupied by the oxygen atoms (O3) of two water molecules with distances of 2.532(3) Å and an O–Cu–O angle of 177.26(9)° (**Tables 2.2** and **2.3** for selected bond distances and bond angles). The equatorial plane is provided by two carbonyl oxygen atoms (O1) of succinate dianions and two nitrogen atoms (N1, N2) of 4,4'-bipyridine molecules. The Cu–O1, Cu–N1, and Cu–N2 bond distances are 1.958(2), 2.020(3), and 1.999(3) Å, respectively. The equatorial N–Cu–N bond angle is 180° for symmetry requirements, whereas the O–Cu–O angle is 177.08(12)°.

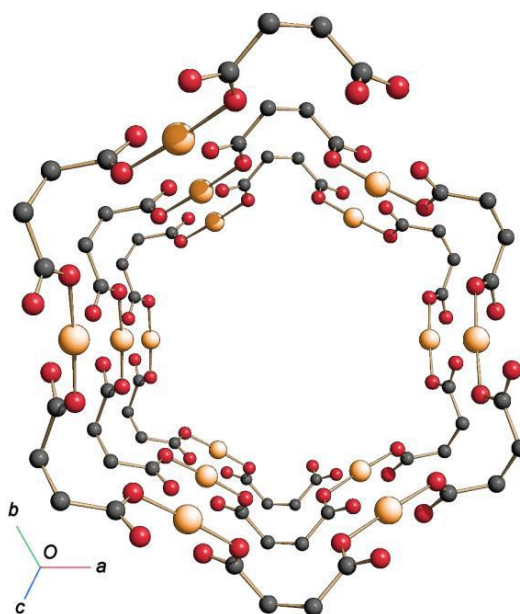


**Figure 2.2:** Perspective view down the *c* axis showing the left-handed helix of **2.1**.

In the crystal, the copper atoms and the succinate dianions are linked into chains along the *c* axis to form left-handed helices (**Figure 2.2**), which are connected by the 4,4'-bipyridine ligands, producing a polymeric 3D network. Pairs of water molecules of crystallization are

hosted inside cavities of  $\sim 82 \text{ \AA}^3$  (**Figure 2.3(a)**), the surface of which is delimited by the coordinated water molecules, the O2 uncoordinated carboxylate oxygen atoms, and the ethyl fragment of the succinate dianions. The topology of the framework can be described as a **qzd** (quartz-dual) “dense” net with point (Schläfli) symbol  $\{7^5 \cdot 9\}$  (**Figure 2.3(b)**). The 3D polymeric network is stabilized by O–H $\cdots$ O hydrogen-bonding interactions involving the coordinated and uncoordinated water molecules as hydrogen donors (**Table 2.4** and **Figure 2.4**). The crystal structure, when extended in the crystallographic axis *c*, forms an extremely symmetrical structure with hexagons, which, upon further expansion, shows a honeycomb-like morphology (**Figure 2.5**).

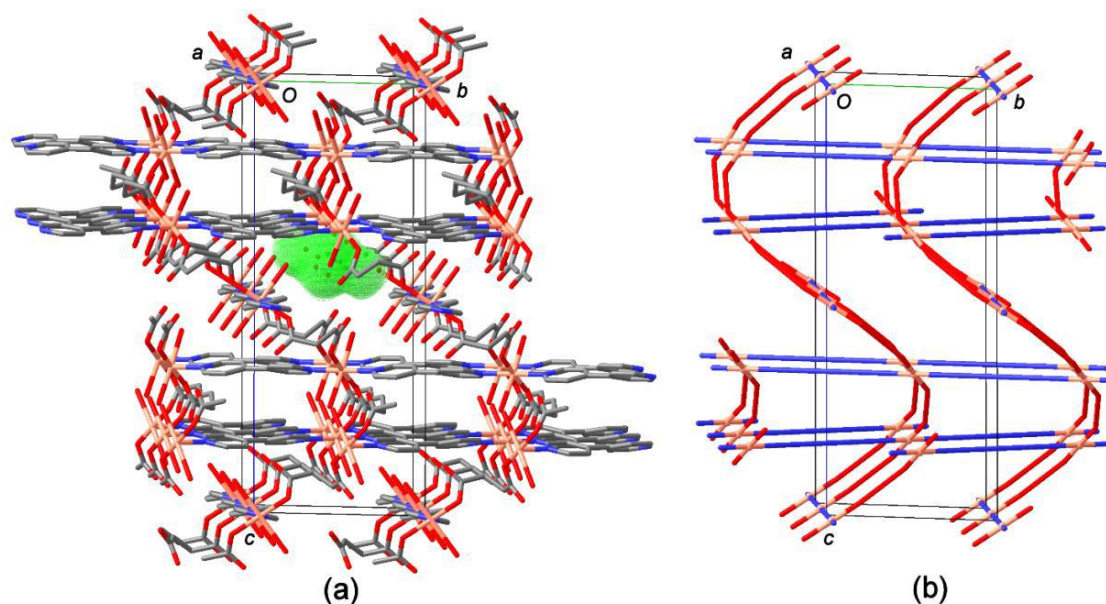


**Figure 2.3(a):** The three-dimensional framework of **2.1** approximately viewed along the *a* axis showing a cavity in the structure (green dots). Hydrogen atoms and water molecules hosted in the cavities are omitted for clarity. (b) Topological representation of the **qzd** net of **2.1**; the blue and red sticks represent the 4,4'-bipyridine ligand and the succinate dianion, respectively.

**Table 2.1:** Crystal data for **2.1**

Formula	$\text{C}_{14}\text{H}_{20}\text{CuN}_2\text{O}_8$
Formula weight	407.86
Crystal system	Hexagonal
Space group	P 65 2 2
<i>a</i> /Å	11.0643(16)
<i>b</i> /Å	11.0643(16)
<i>c</i> /Å	24.997(4)
$\alpha$ /°	90.00

$\beta/^\circ$	90.00
$\gamma/^\circ$	120.00
$V/\text{\AA}^3$	2650.1(10)
Z	6
$D_s/\text{g cm}^{-3}$	1.533
$\mu/\text{mm}^{-1}$	1.280
F(000)	1266
$\theta$ range/ $^\circ$	2.13-25.51
Reflections collected	15225
Unique reflections	1663
Reflections $I > 2\sigma(I)$	1506
$R_{\text{int}}$	0.0523
Goodness-of-fit ( $F^2$ )	1.068
Absolute structure	Flack x determined using 533 quotients [(I+)-(I-)]/[(I+)+(I-)] (Parsons, Flack & Wagner, Acta Cryst. B69 (2013) 249-259)
Absolute structure parameter	0.030(11)
$R_1$ ( $I > 2\sigma(I)$ ) <sup>a</sup>	0.029
$wR_2$ <sup>b</sup>	0.0758
$\Delta\rho_{\text{max/min}}/e \text{\AA}^3$	-0.50, 0.19

<sup>a</sup> $R_1 = \sum ||F_o| - |F_c|| / \sum |F_o|$ , <sup>b</sup> $wR_2 = [\sum (w(F_o^2 - F_c^2)^2) / \sum w(F_o^2)^2]^{1/2}$ .

**Table 2.2:** Bond distances ( $\text{\AA}$ ) of **2.1**

Cu1–O1	1.958(2)	N2–C6	1.335(4)
Cu1–O1	1.958(2)	C1–C2	1.364(4)
Cu1–N2	1.999(3)	C1–H1	0.9300
Cu1–N1	2.020(3)	C2–C3	1.390(4)
O1–C7	1.265(4)	C2–H2	0.9300
O2–C7	1.244(4)	C3–C4	1.474(5)
O3–H31	0.847(12)	C4–C5	1.375(4)



O3–H32A	0.855(13)	C4–C5	1.375(4)
O3–H32B	0.853(13)	C5–C6	1.371(4)
O4–H41	0.855(13)	C5–H5	0.9300
O4–H42A	0.855(13)	C6–H6	0.9300
O4–H42B	0.860(13)	C7–C8	1.511(4)
N1–C1	1.336(3)	C8–C8	1.503(6)
N1–C1	1.336(3)	C8–H8A	0.9700
N2–C6	1.335(4)	C8–H8B	0.9700

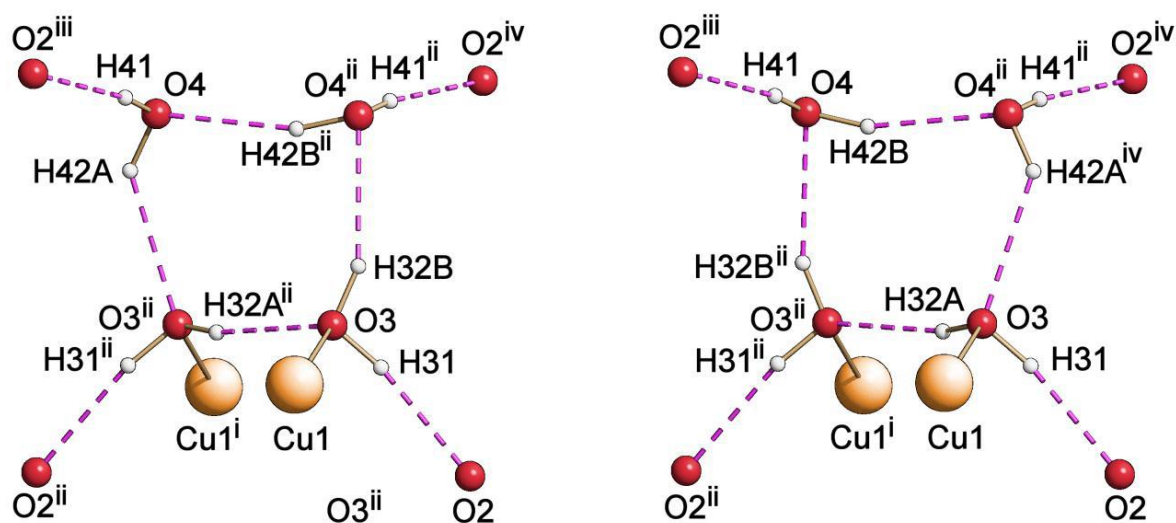


**Figure 2.4:** Detail of the hydrogen bonds in **2.1** involving the disordered water H atoms. Symmetry codes: (i)  $y, -x+y, 1/6+z$ ; (ii)  $x, x-y, 5/6-z$ ; (iii)  $1+x-y, x, -1/6+z$ ; (iv)  $1+x-y, 1-y, 1-z$ .

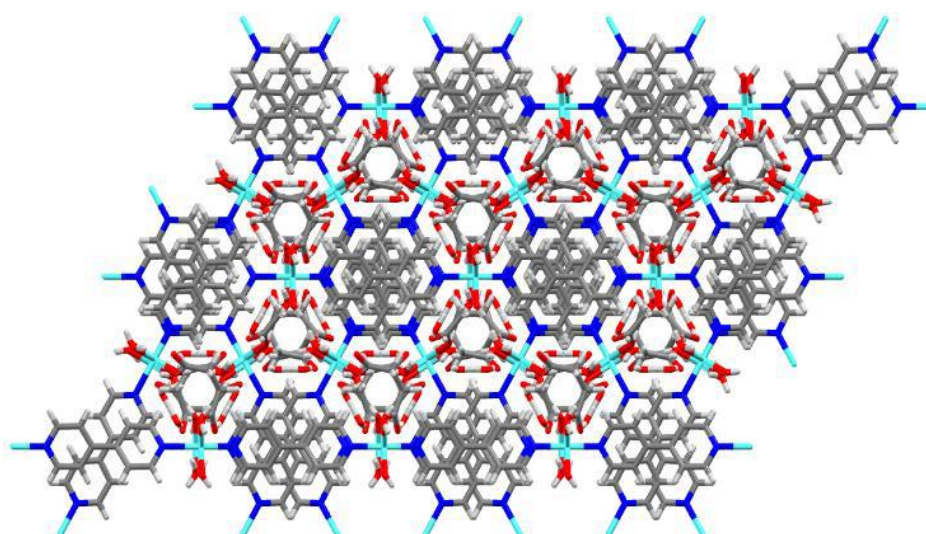


**Figure 2.5:** Packing diagram of **2.1** viewed along the  $c$  axis.

**Table 2.3:** Bond angles (°) of **2.1**.

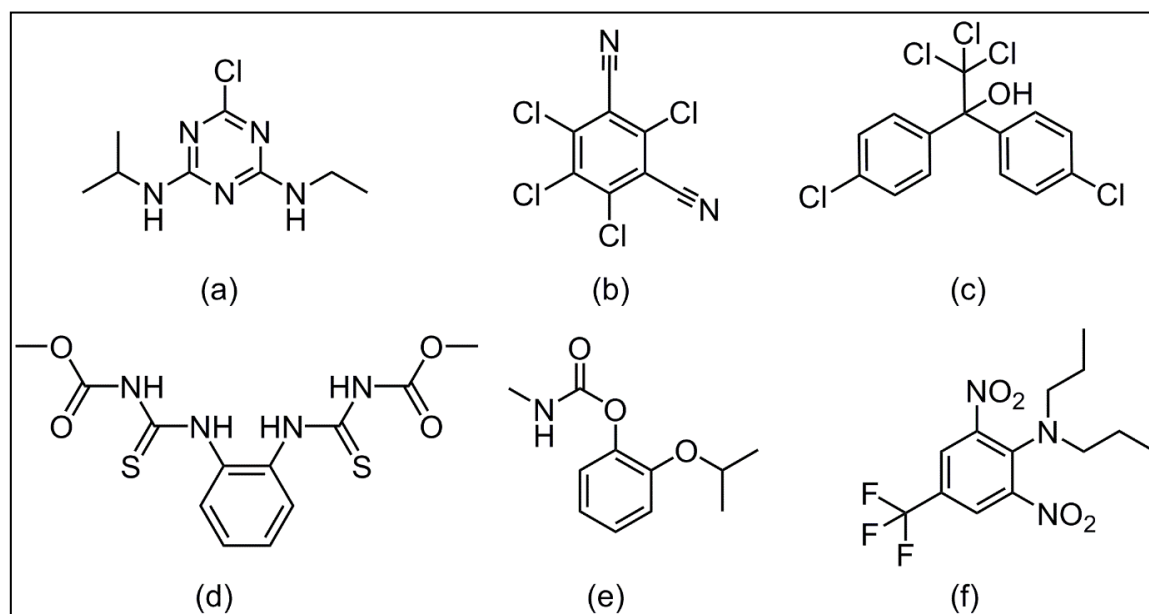
O1–Cu1–O1	177.08(12)	C3–C2–H2	119.8
O1–Cu1–N2	91.46(6)	C2–C3–C2	116.2(4)
O1–Cu1–N2	91.46(6)	C2–C3–C4	121.92(19)
O1–Cu1–N1	88.54(6)	C2–C3–C4	121.92(19)
O1–Cu1–N1	88.54(6)	C5–C4–C5	116.7(4)
N2–Cu1–N1	180.00(4)	C5–C4–C3	121.6(2)
C7–O1–Cu1	126.6(2)	C6–C5–C4	120.4(3)
H31–O3–H32A	108(3)	C6–C5–H5	119.8
H31–O3–H32B	107(3)	C4–C5–H5	119.8
H41–O4–H42A	105(3)	N2–C6–C5	122.4(3) S5
H41–O4–H42B	105(3)	N2–C6–H6	118.8
C1–N1–C1	117.8(4)	C5–C6–H6	118.8
C1–N1–Cu1	121.12(19)	O2–C7–O1	124.4(3)
C1–N1–Cu1	121.12(19)	O2–C7–C8	119.2(3)
C6–N2–C6	117.6(4)	O1–C7–C8	116.3(3)
C6–N2–Cu1	121.19(18)	C8–C8–C7	114.9(3)
C6–N2–Cu1	121.19(18)	C8–C8–H8A	108.6
N1–C1–C2	122.7(3)	C7–C8–H8A	108.6
N1–C1–H1	118.7	C8–C8–H8B	108.6
C2–C1–H1	118.7	C7–C8–H8B	108.6
C1–C2–C3	120.4(3)	H8A–C8–H8B	107.5
C1–C2–H2	119.8		

**Table 2.4:** Hydrogen-bond geometry (Å, °) in **2.1**.

D–H...A	D–H	H...A	D...A	D–H...A
O3–H31...O2	0.85(4)	1.91(4)	2.710(5)	158(4)
O3–H32A...O3 <sup>i</sup>	0.85(6)	2.03(6)	2.851(5)	162(4)
O3–H32B...O4 <sup>i</sup>	0.85(3)	2.00(3)	2.814(5)	158(5)
O4–H41...O2 <sup>ii</sup>	0.86(3)	1.93(2)	2.775(4)	167(2)
O4–H42A...O3 <sup>i</sup>	0.86(5)	2.20(8)	2.814(5)	128(5)
O4–H42B...O4 <sup>i</sup>	0.86(11)	1.99(9)	2.829(8)	164(7)

Symmetry codes: (i) x, x-y, 0.8333-z; (ii) 1+x-y, x, -0.1667+z.

The presence of uncoordinated carbonyl groups in the structure of **2.1** prompted us to explore its ability as a chemosensor. The effect of coordinated water molecules could also be accounted for; however, as a structural property, the effect of the dangling oxygen of the acid groups is very interesting. With previous experience in the field of supramolecular chemistry, in this work, we have targeted rarely explored neutral analytes, that is, pesticides. Indeed, pesticides are chemicals that are used to control/kill pests, rodents, insects, fungi, or other weeds for agricultural and domestic purposes.<sup>2,47</sup> Therefore, pesticides are potentially toxic to living organisms, including human beings. Thus the use of these substances must be carried out following careful and thorough scientific procedures. Several pesticides are banned worldwide owing to their high toxic effect on living beings, and it is certainly severely toxic and unsafe to use and work with them. However, still, such pesticides are sometimes used by people. In this respect, we have selected a series of pesticides for our studies, for example, atrazine, chlorothalonil, dicofol, thiophanate-methyl, propoxur, and trifluralin, which are either banned or potentially toxic to mankind (**Scheme 2.2**). Because of the acute toxicity of these pesticides, DFT calculations have been used as a tool to investigate their host–guest interactions.



**Scheme 2.2:** Molecular Structure of Pesticides: (a) Atrazine, (b) Chlorothalonil, (c) Dicofol, (d) Thiophanate-Methyl, (e) Propoxur, and (f) Trifluralin

DFT considering the dispersion correction, that is, DFT- (D3), has been utilized for the proper monitoring of the possible interactions between the host and the guest. Owing to the possibility of a noncovalent host–guest interaction, a dispersion correction has been considered. The def2-SVP and TZVP basis set levels have been used for nonmetallic atoms

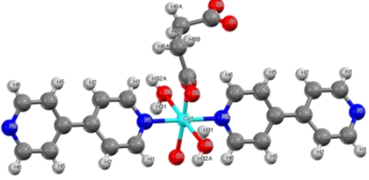
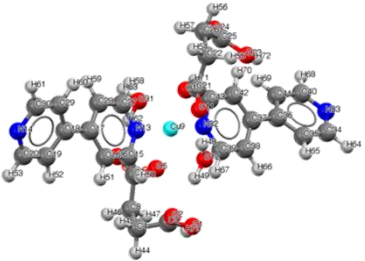
and metal ions, respectively, with the B3LYP hybrid function. Initially, the primary unit of the MOF, that is, the immediate coordination of one Cu center, was considered for the calculation, keeping in mind the computational time (**Figure 2.6** and **Tables 2.5** and **2.6**). The selected bond distances of the structures obtained from single-crystal X-ray diffraction analysis and DFT are of comparable values (**Table 2.6**). All guest pesticides were optimized at the same level of DFT (**Tables 2.7–2.12**). Furthermore, the pesticide molecules were again optimized with the host MOF to visualize the host–guest interaction using the solvent model for water.

**Table 2.5:** Geometry optimized coordinates of **2.1**.

O	0.83405	5.30517	12.0561	O	-1.137	5.67245	12.9689
C	-0.4881	5.50177	11.9539	C	-1.0966	5.40585	10.5697
O	-0.2497	7.94397	11.1962	O	-0.594	8.68552	9.10318
C	-0.4439	7.78395	9.94696	C	-0.4499	6.3169	9.51785
Cu	-0.2616	9.5712	12.3448	O	-0.268	11.1532	13.557
O	-1.1819	10.1399	15.3445	O	-0.029	8.0503	14.1629
N	-2.3178	9.54676	12.3775	N	-9.4248	9.60388	12.5176
C	-3.0056	8.39941	12.4768	C	-4.3965	8.37066	12.5081
C	-5.1209	9.57156	12.4319	C	-6.6029	9.5833	12.4604
C	-7.3531	8.51664	11.9396	C	-8.7472	8.577	11.9903
C	-0.7098	11.1309	14.756	C	-0.6367	12.458	15.511
O	2.1017	12.4902	15.076	O	1.9359	13.8134	13.2798
C	1.42647	13.3178	14.2639	C	0.01816	13.5941	14.733
C	-2.9915	10.7046	12.3143	C	-4.3804	10.7617	12.3334
C	-7.3158	10.6607	13.0107	C	-8.7116	10.6207	13.0165
O	-0.2568	10.9871	10.4055	N	1.76883	9.65597	12.267
N	8.85028	10.1618	12.5007	C	8.1995	9.19417	13.158
C	6.81102	9.04853	13.1414	C	6.03531	9.95796	12.4041
C	4.55715	9.85256	12.3529	C	3.90608	8.61308	12.4806
C	2.51631	8.55649	12.4352	C	8.11342	11.0292	11.7959
C	6.72061	10.9734	11.7172	C	3.74948	10.9884	12.1724
C	2.36639	10.846	12.1285	H	-1.0185	4.35345	10.2464
H	-2.1654	5.63621	10.6732	H	-0.9702	6.21621	8.55528
H	0.60012	6.0261	9.32965	H	-0.6051	8.66444	14.6826
H	-0.5402	7.24864	13.9572	H	-2.4232	7.4792	12.5476
H	-4.9036	7.41094	12.6152	H	-6.8673	7.65486	11.4787
H	-9.3403	7.752	11.5796	H	-1.665	12.7373	15.793
H	-0.1036	12.2648	16.4549	H	0.07011	14.4972	15.3667
H	-0.5623	13.8633	13.84	H	-2.3899	11.6137	12.2586
H	-4.8729	11.7317	12.2554	H	-6.7994	11.5151	13.4517
H	-9.2755	11.4542	13.4507	H	-0.4226	10.1899	9.83091
H	-1.0567	11.5234	10.3187	H	8.81084	8.49212	13.7363
H	6.34749	8.24527	13.7167	H	4.47139	7.68797	12.5999
H	1.97454	7.61472	12.5349	H	8.65534	11.8149	11.2573

H	6.18605	11.7047	11.1088	H	4.17865	11.9873	12.086
H	1.71013	11.7041	11.9926	H	2.99657	12.3711	14.7095
H	1.24405	5.18479	11.184				

**Table 2.6:** Comparison of X-ray and DFT data.

Bonds (Å)	X-Ray Data	DFT Data
X-Ray (DFT)		
Cu1-N1 (Cu9-N13)	2.02	2.05
Cu1-N2 (Cu9-N32)	1.99	2.03
Cu1-O3 (Cu1-O31)	2.53	2.40
Cu1-O1 (Cu1-O10)	1.96	1.99
C7-O1 (C21-O10)	1.26	1.27
C7-O2 (C21-O11)	1.24	1.24
C7-C8 (C21-C22)	1.51	1.52
N1-C1 (N13-C27)	1.34	1.34
C1-C2 (C27-C28)	1.36	1.39
C2-C3 (C28-C17)	1.39	1.40
C3-C4 (C17-C18)	1.47	1.48
C4-C5 (C18-C29)	1.38	1.40
C5-C6 (C29-C30)	1.37	1.39
C6-N2 (C30-N14)	1.33	1.33

**Table 2.7:** Geometry optimized coordinates of atrazine

Cl	3.80068	6.55176	17.625	C	4.32934	4.92988	17.173
C	4.82206	2.8288	17.7658	C	4.99123	3.48787	15.5952
N	4.58568	4.75406	15.8965	N	4.41156	4.06716	18.1604

N	5.12009	2.50337	16.4981	N	4.94496	1.87856	18.7076
C	4.56049	2.02912	20.1117	C	3.05044	1.84847	20.2966
C	5.37339	1.04947	20.9549	H	5.1861	0.95241	18.3676
H	4.82374	3.05817	20.3979	H	5.12378	1.16573	22.0203
H	6.4538	1.22077	20.8289	H	5.1509	0.00708	20.6686
H	2.49824	2.58026	19.6875	H	2.77083	1.99659	21.3519
H	2.73982	0.8344	19.9946	N	5.26659	3.20888	14.31
C	5.25784	4.18615	13.2307	C	6.53312	5.02524	13.1643
H	5.62009	2.27555	14.1273	H	5.11213	3.62987	12.2925
H	4.38409	4.83975	13.3667	H	6.48297	5.73094	12.3194
H	7.42063	4.38633	13.0285	H	6.65957	5.60551	14.0917

**Table 2.8:** Geometry optimized coordinates of chlorothalonil.

Cl	1.98871	5.94727	17.3999	C	3.19375	4.7595	17.1058
C	4.46483	2.79726	17.8359	C	4.90382	3.78406	15.6489
C	3.91086	4.75762	15.8968	C	3.47523	3.77731	18.0712
C	5.17582	2.80636	16.6225	C	4.74119	1.80156	18.8246
N	4.96767	0.9921	19.624	C	5.62911	3.79299	14.4163
N	6.22103	3.79691	13.4187	Cl	3.59287	5.94093	14.6964
Cl	2.61942	3.74983	19.5575	Cl	6.38163	1.6187	16.3287

**Table 2.9:** Geometry optimized coordinates of dicofol

C	1.95933	9.40716	11.5481	C	8.63796	9.29642	13.6327
C	7.35382	9.18143	14.17	C	6.33973	10.0079	13.6851
C	6.59808	10.952	12.6814	C	4.18031	11.0583	12.0033
C	4.16143	10.1491	10.9309	C	3.06348	9.3247	10.6958
C	8.91601	10.2175	12.6211	C	7.89198	11.0425	12.1513
C	3.06045	11.1194	12.8417	C	1.94933	10.3	12.6182
H	7.14473	8.44921	14.9512	H	5.33441	9.89892	14.0927
H	5.02491	10.0854	10.2674	H	3.06664	8.62326	9.86
H	9.92089	10.2905	12.2023	H	8.10168	11.7579	11.3577
H	3.02014	11.8021	13.6867	H	1.08284	10.3619	13.2783
C	5.48566	11.8639	12.1508	O	5.89186	12.319	10.8823
C	5.36946	13.1632	13.0663	Cl	6.89413	14.0973	12.9813
Cl	4.05412	14.216	12.4357	Cl	5.06526	12.8102	14.7906
Cl	0.57466	8.37773	11.2676	Cl	9.91462	8.25987	14.228
H	5.14986	12.7878	10.4686				

**Table 2.10:** Geometry optimized coordinates of thiophanate-methyl.

N	3.20204	5.48655	17.7715	C	4.4295	4.81081	17.5719
C	6.42776	3.72637	18.4009	C	6.15696	4.08935	16.0212
C	4.91351	4.69127	16.2556	C	5.19304	4.32494	18.6422

C	6.91058	3.60932	17.09	H	4.81491	4.43262	19.6585
H	7.87676	3.13612	16.9007	H	3.1127	6.37152	17.2757
H	7.02092	3.35479	19.2396	H	6.51723	3.99449	14.9969
N	4.08675	5.13713	15.196	H	3.1219	4.81354	15.233
C	4.42497	5.98162	14.1831	S	5.86784	6.8148	14.112
N	3.41782	6.05096	13.239	C	3.27359	6.92739	12.1682
O	3.99419	7.84688	11.8714	O	2.16157	6.57612	11.5038
C	1.82462	7.37781	10.3645	H	2.6531	5.38409	13.3237
H	0.90079	6.9494	9.95935	H	2.62634	7.33591	9.61266
H	1.66112	8.42364	10.6632	C	2.13049	5.0682	18.5
S	1.99344	3.54288	19.1608	N	1.18434	6.07014	18.6053
C	-0.1062	6.01535	19.1219	O	-0.679	5.05194	19.5651
O	-0.6271	7.24978	19.0388	C	-1.9686	7.40508	19.5191
H	1.44118	6.99152	18.2565	H	-2.2189	8.46199	19.372
H	-2.029	7.14364	20.5857	H	-2.6592	6.76675	18.9487

**Table 2.11:** Geometry optimized coordinates of propoxur

O	2.5367	4.14377	18.0201	C	3.84106	3.80071	17.7107
C	5.83947	2.53224	18.1902	C	5.72785	3.93267	16.2034
C	4.41868	4.31396	16.527	C	4.53752	2.91891	18.5313
C	6.42657	3.04458	17.031	H	4.0474	2.54596	19.4331
H	7.44403	2.75444	16.7579	H	6.3889	1.84014	18.8318
H	6.20343	4.31793	15.3013	O	3.62925	5.13281	15.7988
C	4.1981	6.05411	14.8437	C	4.95277	7.16424	15.5647
C	3.02651	6.56689	14.0243	H	5.76368	6.76256	16.1908
H	4.26528	7.73449	16.2083	H	5.39987	7.8527	14.8313
H	2.31072	7.0972	14.6727	H	2.50284	5.73304	13.5328
H	3.38108	7.26419	13.2503	H	4.88348	5.49744	14.1822
C	2.19933	5.45278	18.2822	O	1.03558	5.78745	18.1866
N	3.20905	6.25424	18.6719	C	2.98353	7.65794	18.9575
H	2.49701	8.15692	18.1046	H	3.95243	8.13864	19.1428
H	2.34321	7.7953	19.8445	H	4.14114	5.87101	18.7807

**Table 2.12:** Geometry optimized coordinates of trifluralin.

O	2.17299	6.92719	16.4865	O	1.56624	4.86989	16.7673
N	7.314	6.12518	15.5963	N	2.41716	5.73902	16.6386
O	8.18276	6.7484	16.1846	O	7.35999	5.80241	14.4217
C	3.82441	5.34341	16.7429	C	5.4223	4.2298	18.1628
C	6.14947	5.67497	16.3787	C	4.82222	5.96179	15.9395
C	4.10463	4.4569	17.7837	C	6.45263	4.87715	17.4688
H	3.2742	4.00456	18.3243	H	7.49839	4.72037	17.7365
N	4.5667	6.72982	14.8341	C	5.20788	8.04736	14.6991
H	4.43155	8.81287	14.8906	H	5.93246	8.16321	15.5173

C	5.88579	8.33642	13.3587	H	6.61195	7.54079	13.1379
H	5.14027	8.3214	12.5472	C	6.58174	9.69766	13.3815
H	7.04792	9.91913	12.4091	H	7.37435	9.72714	14.1483
H	5.86944	10.5092	13.6058	C	3.43307	6.47193	13.9387
H	2.49994	6.909	14.3326	H	3.65749	7.01881	13.0128
C	3.24058	4.99658	13.5797	H	2.36271	4.9489	12.9142
H	2.96345	4.40249	14.4657	C	4.4567	4.37299	12.8952
H	4.26814	3.31782	12.6429	H	5.35029	4.41867	13.5356
H	4.69742	4.90804	11.9612	C	5.76048	3.29028	19.2864
F	4.68096	2.96306	20.0259	F	6.68108	3.81926	20.1284
F	6.2914	2.12543	18.8292				

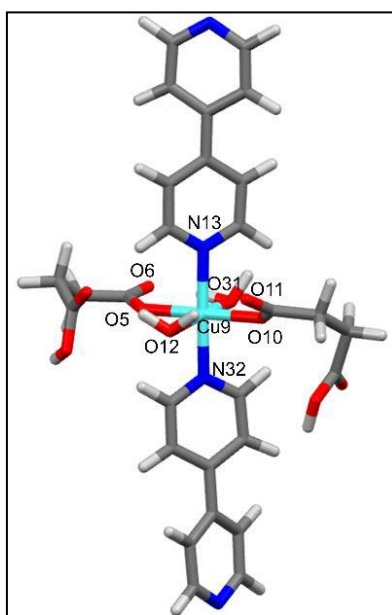


**Figure 2.6:** Geometry-optimized structure of the single unit of the MOF, where the immediate coordination of  $\text{Cu}^{2+}$  has been considered.

The geometry-optimized structures of **2.1** with the pesticides was carefully investigated. The uncoordinated atom of succinate dianion in **2.1** interacts via hydrogen-bonding interactions with  $\text{-NH}$  protons from the atrazine molecule with  $\text{O}\cdots\text{H}$  distances of 1.85 to 1.93 Å (**Figure 2.7(a)** and **Table 2.13** for coordinates). Interestingly, water molecules are not involved in the interaction with the guest molecule, rather they stabilize the cluster by hydrogen bonding with the uncoordinated oxygen atom via the formation of a six membered ring ( $\text{O}\cdots\text{H}$  distance: 1.69 Å). The specific interaction of the uncoordinated oxygen atom with the guest  $\text{-NH}$  group is the key factor for the formation of the stabilized host–guest adduct. It is advantageous for future work that the coordinated solvent molecule does not take any leading role in the host–guest interaction because the solvent molecules are not a part of the designed architecture. Hence, the superiority of using an aliphatic ligand like succinic acid in designing the MOF is justified.



In the case of chlorothalonil, an organochlorine pesticide, we expected that ring-to-ring ( $\pi$ - $\pi$ ) interactions might be possible because the presence of multiple chloride groups makes the ring electron-deficient and could promote a  $\pi$ - $\pi$  interaction with bipyridine moiety. The bipyridine moiety has indeed been incorporated into the framework with this purpose. The optimized structure of **2.1** with chlorothalonil shows no ring-to-ring interaction as well as no hydrogen-bonding interaction between water and chlorothalonil Cl atoms. The optimized structure (**Figure 2.7(b)** and **Table 2.14** for coordinates) also reveals that the guest is situated far away from the host, which suggests the nonaffinity of the host toward this particular guest. Dicofol (**Figure 2.7(c)** and **Table 2.15** for coordinates), another example of an organochlorine miticide derived from dichlorodiphenyltrichloroethane (DDT), has been chosen for host-guest interaction studies at the level of DFT-D3. It is found that this compound can also, in principle, interact with **2.1** via hydrogen bonds through the -Cl and -OH groups or via  $\pi$ - $\pi$  interactions through the aromatic rings. The optimized structure reveals that **2.1** participates in a very weak  $\pi$ - $\pi$  interaction with the aromatic ring of dicofol, with a centroid-to-centroid distance of 4.37 Å. Although the interaction takes place, the presence of a bulky trichloromethane group creates a steric hindrance, preventing further closeness of the rings.

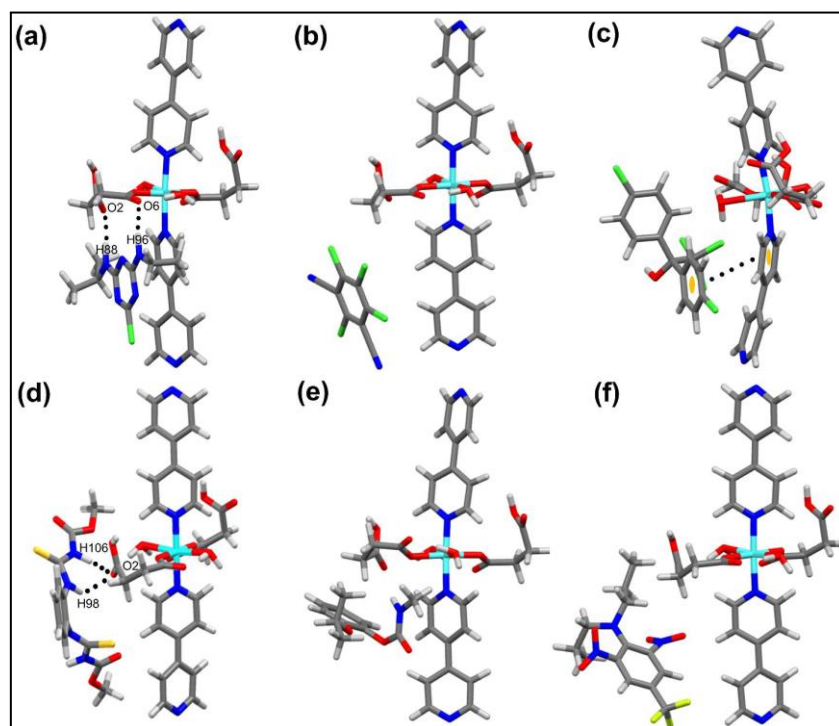


**Figure 2.7:** Geometry optimized structure of (a) atrazine $\subset$ **2.1**; (b) chlorothalonil $\subset$ **2.1**; (c) dicofol $\subset$ **2.1**; (d) thiophanate-methyl $\subset$ **2.1**; (e) propoxur $\subset$ **2.1**; (f) trifluralin $\subset$ **2.1**.

**Table 2.13:** Geometry optimized coordinates of atrazine $\subset$ **2.1**.

O	0.89437	4.77689	12.0568	O	-1.2184	4.99089	12.6276
---	---------	---------	---------	---	---------	---------	---------

---

C	-0.4003	4.85673	11.7321	C	-0.7637	4.68672	10.2739
O	-0.2667	7.32291	11.0201	O	-0.5574	8.02154	8.90582
C	-0.3373	7.13986	9.77057	C	-0.0925	5.69804	9.33509
Cu	-0.5092	8.87669	12.2471	O	-0.6823	10.4058	13.5086
O	-1.3054	9.24709	15.3336	O	-0.1278	7.29972	13.9811
N	-2.5628	8.72892	12.2644	N	-9.6685	8.79186	12.5296
C	-3.216	7.98447	13.1665	C	-4.6018	7.98795	13.2754
C	-5.3663	8.78272	12.4087	C	-6.8467	8.79414	12.4651
C	-7.5678	7.68524	12.9327	C	-8.9616	7.73382	12.944
C	-1.0505	10.3066	14.7266	C	-1.182	11.6263	15.4856
O	1.53037	11.9663	15.1169	O	1.27801	13.3321	13.3632
C	0.79459	12.7468	14.3102	C	-0.6525	12.841	14.7311
C	-3.2761	9.50348	11.4334	C	-4.6636	9.55535	11.4693
C	-7.5897	9.90261	12.0298	C	-8.9838	9.85045	12.0811
O	-0.4721	10.3263	10.2465	N	1.50744	9.17398	12.2271
N	8.49766	10.3739	12.616	C	7.93471	9.32986	13.2366
C	6.56817	9.04765	13.1878	C	5.71956	9.89497	12.4568
C	4.2606	9.64462	12.373	C	3.7361	8.34217	12.4401
C	2.35969	8.14925	12.3661	C	7.6911	11.1822	11.9174
C	6.31225	10.9912	11.8091	C	3.34555	10.7006	12.2225
C	1.98463	10.4227	12.149	H	-0.4849	3.66114	9.97832
H	-1.8515	4.78716	10.1896	H	-0.4545	5.55512	8.30791
H	1.00274	5.55133	9.30213	H	-0.659	7.85999	14.6032
H	-0.6132	6.47992	13.7828	H	-2.6091	7.3674	13.8242
H	-5.0731	7.37147	14.0405	H	-7.0584	6.77129	13.2345
H	-9.5305	6.86608	13.2965	H	-2.2503	11.7669	15.7195
H	-0.6701	11.5012	16.4516	H	-0.7374	13.7413	15.3653
H	-1.2315	13.035	13.8184	H	-2.6964	10.0791	10.7142
H	-5.1892	10.1785	10.747	H	-7.0994	10.8079	11.6682
H	-9.5707	10.7128	11.7447	H	-0.5217	9.56282	9.61317
H	-0.8733	11.0884	9.80865	H	8.60236	8.67726	13.8106
H	6.17585	8.18816	13.734	H	4.39011	7.47458	4.39011
H	1.91216	7.15627	12.424	H	8.16195	12.0312	11.409
H	5.71822	11.6816	11.2079	H	3.67355	11.74	12.1834
H	1.24813	11.2161	12.0354	H	2.44661	11.9659	14.7853
H	1.45096	4.66028	11.2695	Cl	-8.0373	6.89358	9.54187
C	-6.293	6.74212	9.75776	C	-4.5498	5.86361	10.8623
C	-4.2158	7.30694	9.12955	N	-5.5581	7.46141	8.93891
N	-5.9054	5.93828	10.7232	N	-3.6804	6.51249	10.0716
N	-4.0624	5.10667	11.8582	C	-4.8826	4.34087	12.7955
C	-5.3017	2.99663	12.193	C	-4.1186	4.17613	14.108
N	-3.378	7.98479	8.32996	C	-3.7778	8.93568	7.30719
C	-3.8033	10.3802	7.80673	H	-3.0499	5.12281	12.0103

---

H	-5.7959	4.92669	12.9827	H	-4.7295	3.62037	14.8348
H	-3.8638	5.15357	14.5464	H	-3.1788	3.6237	13.9495
H	-5.8615	3.15507	11.2589	H	-5.9463	2.44165	12.8934
H	-4.4157	2.37879	11.9715	H	-2.3827	7.93477	8.56783
H	-3.0652	8.84265	6.47161	H	-4.7683	8.64389	6.93281
H	-4.0493	11.0696	6.98351	H	-2.8208	10.6727	8.21184
H	-4.5575	10.5091	8.59768				

**Table 2.14:** Geometry optimized coordinates of chlorothalonil **2.1**.

O	0.90597	5.15605	11.9985	O	-1.0782	5.43561	12.9172
C	-0.4229	5.30135	11.9012	C	-1.0342	5.19588	10.5198
O	-0.3018	7.74665	11.163	O	-0.5968	8.50228	9.06702
C	-0.4585	7.59644	9.9073	C	-0.4325	6.13274	9.46631
Cu	-0.3454	9.35465	12.3389	O	-0.3842	10.9215	13.5724
O	-1.2431	9.86453	15.3616	O	-0.0509	7.82982	14.1261
N	-2.4032	9.27151	12.3778	N	-9.5049	9.22418	12.3011
C	-3.0691	8.1068	12.3899	C	-4.4601	8.05071	12.3776
C	-5.2042	9.24176	12.3601	C	-6.6855	9.23228	12.3455
C	-7.4027	8.25558	11.6383	C	-8.7982	8.2984	11.6416
C	-0.8102	10.8751	14.7767	C	-0.7732	12.1981	15.5411
O	1.95846	12.3212	15.0812	O	1.73459	13.6558	13.2998
C	1.25016	13.1348	14.2834	C	-0.162	13.3611	14.767
C	-3.0976	10.4187	12.3708	C	-4.4873	10.4492	12.3616
C	-7.4287	10.2066	13.0299	C	-8.8233	10.1543	12.9804
O	-0.4108	10.7979	10.4177	N	1.6791	9.50859	12.2328
N	8.74183	10.2421	12.3854	C	8.12947	9.2549	13.0505
C	6.74619	9.06528	13.0497	C	5.93412	9.9495	12.3209
C	4.4598	9.79636	12.2859	C	3.85199	8.53424	12.405
C	2.46446	8.43223	12.3759	C	7.97006	11.0855	11.689
C	6.57879	10.9862	11.6265	C	3.61318	10.9072	12.1307
C	2.23498	10.7198	12.1035	H	-0.9287	4.14973	10.187
H	-2.1067	5.38863	10.6406	H	-0.9663	6.02467	8.51149
H	0.62075	5.87202	9.25451	H	-0.6348	8.41655	14.6686
H	-0.5394	7.01411	13.9201	H	-2.4669	7.19727	12.4282
H	-4.955	7.07885	12.412	H	-6.8833	7.49103	11.061
H	-9.37	7.55186	11.081	H	-1.8078	12.4417	15.833
H	-0.2267	12.015	16.4791	H	-0.1337	14.26	15.4083
H	-0.7586	13.6184	13.8814	H	-2.5113	11.3393	12.3828
H	-5.0001	11.4114	12.3357	H	-6.9355	10.9861	13.6133
H	-9.4133	10.9038	13.52	H	-0.5154	10.004	9.82545
H	-1.2461	11.2776	10.3324	H	8.76927	8.57295	13.6222
H	6.31412	8.2486	13.6304	H	4.44972	7.62743	12.5049
H	1.95591	7.47163	12.4694	H	8.48086	11.8874	11.1438

H	6.01411	11.7001	11.0246	H	4.00851	11.9206	12.0522
H	1.54869	11.5571	11.9889	H	2.85326	12.2334	14.7059
H	1.31809	5.05362	11.1251	Cl	-4.4584	5.114	8.53922
C	-5.5966	4.35178	9.58832	C	-7.8637	4.20047	10.5023
C	-6.1373	2.6615	11.276	C	-5.211	3.27437	10.4039
C	-6.9256	4.80402	9.63676	C	-7.4615	3.13144	11.3229
C	-9.2111	4.67606	10.5459	N	-10.299	5.07823	10.5827
C	-5.7311	1.56912	12.1054	N	-5.4054	0.68268	12.7786
Cl	-3.5996	2.67308	10.3493	Cl	-7.4334	6.1116	8.63559
Cl	-8.5978	2.39381	12.386				

**Table 2.15:** Geometry optimized coordinates of dicofol $\square$ 2.1.

O	0.2587	5.14098	13.5977	O	-1.7177	5.53215	14.4884
C	-1.0827	5.05427	13.5694	C	-1.6834	4.30947	12.3955
O	-1.5847	6.92772	11.8672	O	-1.0643	6.76048	9.69119
C	-1.269	6.2754	10.8182	C	-1.1469	4.76679	11.0337
Cu	-1.4573	8.86266	12.307	O	-1.3684	10.8084	12.6622
O	-1.4832	10.6953	14.9048	O	-0.6179	8.23768	14.3685
N	-3.4333	8.84452	12.8474	N	-10.482	8.26765	12.8086
C	-4.0034	7.7659	13.4079	C	-5.3835	7.65047	13.5417
C	-6.2153	8.68247	13.0803	C	-7.6884	8.54045	13.0507
C	-8.2782	7.2981	12.7709	C	-9.6662	7.21679	12.6567
C	-1.3924	11.3226	13.8336	C	-1.2902	12.8457	13.8808
O	1.06189	12.706	12.4034	O	0.00417	13.0383	10.4601
C	-0.0092	13.0556	11.6732	C	-1.1765	13.5138	12.5142
C	-4.2094	9.87353	12.469	C	-5.5937	9.83596	12.5752
C	-8.544	9.63759	13.2241	C	-9.921	9.44898	13.0942
O	-2.335	9.13284	9.84012	N	0.40734	8.9699	11.5247
N	6.96005	9.63184	8.87096	C	6.75545	9.18208	10.1149
C	5.48883	9.0293	10.6822	C	4.35471	9.36368	9.92454
C	2.98602	9.22446	10.4771	C	2.68221	8.25037	11.4443
C	1.38689	8.15638	11.9431	C	5.88051	9.94966	8.14634
C	4.57212	9.83752	8.62055	C	1.93986	10.063	10.0555
C	0.66943	9.89976	10.5972	H	-1.4743	3.23475	12.5352
H	-2.771	4.44496	12.4472	H	-1.6845	4.2511	10.2238
H	-0.085	4.49582	10.8919	H	-1.0323	9.0428	14.7699
H	-1.0927	7.45029	14.6858	H	-3.3337	6.96335	13.7244
H	-5.8015	6.74477	13.9823	H	-7.6657	6.4141	12.5926
H	-10.136	6.25635	12.417	H	-2.1763	13.2241	14.4154
H	-0.4236	13.0903	14.5146	H	-1.0614	14.6044	12.6446
H	-2.0794	13.3574	11.9086	H	-3.6916	10.7348	12.0436
H	-6.179	10.6799	12.212	H	-8.1523	10.6288	13.4553
H	-10.599	10.3005	13.2207	H	-1.7865	8.32254	9.66745

H	-3.1729	8.75281	10.1371	H	7.64574	8.92979	10.7022
H	5.39882	8.67428	11.7102	H	3.44157	7.55485	11.803
H	1.1133	7.42317	12.7039	H	6.058	10.3124	7.12747
H	3.73848	10.0993	7.96674	H	2.1038	10.8561	9.32519
H	-0.1623	10.5371	10.2987	H	1.76977	12.437	11.7904
H	0.65996	4.67294	12.8474	C	-2.8187	7.1123	5.29797
C	-7.5117	10.0057	9.6929	C	-6.1711	9.93794	9.30833
C	-5.6637	8.73247	8.82569	C	-6.4784	7.59565	8.72439
C	-4.7634	6.50659	7.22575	C	-5.1288	6.79714	5.90133
C	-4.168	7.09739	4.93516	C	-8.347	8.89292	9.59026
C	-7.826	7.69443	9.09799	C	-3.4043	6.53181	7.56098
C	-2.4301	6.83141	6.60769	C	-5.9185	6.26229	8.2145
O	-6.9686	5.59344	7.56042	C	-5.5072	5.34531	9.45383
Cl	-6.9706	4.80729	10.3477	Cl	-4.6709	3.86182	8.86279
Cl	-4.4547	6.19103	10.6374	Cl	-1.6027	7.48996	4.09384
Cl	-8.1458	11.5134	10.3224	H	-5.5291	10.8164	9.38459
H	-4.6181	8.69496	8.51991	H	-6.1824	6.79204	5.62079
H	-4.4651	7.32158	3.90946	H	-9.3922	8.95799	9.89538
H	-8.4776	6.8275	9.00574	H	-3.0534	6.33243	8.56767
H	-1.3801	6.84476	6.90235	H	-6.6162	4.78094	7.16229

**Table 2.16:** Geometry optimized coordinates of thiophanate-methylc2.1.

O	-0.312	5.22618	10.4177	O	-2.1786	5.5504	11.529
C	-1.5608	5.68791	10.4796	C	-2.1883	6.20926	9.21068
O	-0.8664	8.10916	10.6427	O	-0.9723	9.61927	8.9802
C	-1.0531	8.46349	9.43199	C	-1.3771	7.2959	8.4996
Cu	-0.5823	9.19568	12.2988	O	-0.3269	10.2491	13.9696
O	-1.3912	8.85934	15.3825	O	-0.5765	7.13414	13.5252
N	-2.6052	9.48727	12.4244	N	-9.6491	10.3274	12.8988
C	-3.4453	8.46061	12.2225	C	-4.8255	8.59847	12.3105
C	-5.3787	9.85448	12.6076	C	-6.8481	10.0287	12.7011
C	-7.7251	9.19264	11.9895	C	-9.1009	9.38446	12.1214
C	-0.7721	9.90681	15.117	C	-0.4956	10.8964	16.2495
O	2.20991	10.5911	15.7397	O	2.31473	12.4243	14.4618
C	1.70718	11.7385	15.258	C	0.362	12.0913	15.8462
C	-3.1146	10.6905	12.728	C	-4.4842	10.9187	12.8188
C	-7.424	11.0206	13.5114	C	-8.8149	11.1252	13.5766
O	-0.2364	11.1828	11.0013	N	1.42925	8.90941	12.1742
N	8.45458	7.90225	12.4593	C	7.59672	6.93283	12.8002
C	6.20892	7.07914	12.7554	C	5.66209	8.30313	12.3367
C	4.19599	8.5148	12.2733	C	3.31358	7.45231	12.0103
C	1.94257	7.6878	11.9722	C	7.93594	9.06943	12.0584
C	6.56441	9.31939	11.9823	C	3.63174	9.78596	12.474

C	2.25035	9.94014	12.4106	H	-2.326	5.33879	8.54462
H	-3.1929	6.56262	9.47459	H	-1.9195	7.66546	7.61853
H	-0.4168	6.89918	8.12143	H	-1.0387	7.61045	14.2594
H	-1.1892	6.48033	13.1557	H	-3.0008	7.49368	11.9887
H	-5.454	7.71784	12.1819	H	-7.3504	8.39752	11.3435
H	-9.7929	8.73843	11.5687	H	-1.4687	11.2436	16.6341
H	-0.0275	10.3296	17.069	H	0.56095	12.7229	16.7303
H	-0.146	12.7247	15.1067	H	-2.3955	11.4909	12.913
H	-4.8386	11.9256	13.0426	H	-6.8061	11.6937	14.1084
H	-9.2717	11.891	14.214	H	-0.5305	10.6952	10.1836
H	-0.9213	11.8482	11.1524	H	8.03075	5.9829	13.1325
H	5.57023	6.25066	13.0662	H	3.68593	6.44515	11.8189
H	1.22698	6.8863	11.7856	H	8.64614	9.85522	11.7768
H	6.21231	10.2904	11.63	H	4.24945	10.6557	12.7012
H	1.77731	10.9086	12.5653	H	3.07467	10.4397	15.3172
H	0.08813	5.38833	9.5472	N	-2.9602	2.8182	10.7782
C	-3.5785	2.60799	9.53425	C	-3.532	2.16916	7.15199
C	-5.5916	2.88845	8.19086	C	-4.9471	2.92944	9.43146
C	-2.8767	2.2206	8.38133	C	-4.8872	2.5101	7.04908
N	-5.6668	3.2531	10.6151	C	-6.2297	4.45408	10.9078
S	-5.9148	5.86035	10.0679	N	-7.1268	4.3517	11.962
C	-7.4933	5.34631	12.857	O	-6.9088	6.38375	13.0543
O	-8.5957	4.95696	13.5102	C	-9.0695	5.85051	14.5281
C	-1.8786	2.20338	11.3492	S	-1.2751	0.72057	10.8883
N	-1.3705	3.00685	12.3483	C	-0.3364	2.79084	13.2442
O	0.25402	1.76393	13.4755	O	-0.1007	3.97372	13.8372
C	0.95537	4.04815	14.7932	H	-1.8189	1.97412	8.45718
H	-5.3942	2.47294	6.08237	H	-3.3448	3.60798	11.2939
H	-2.9734	1.87237	6.26101	H	-6.6499	3.14947	8.13727
H	-5.7776	2.504	11.2972	H	-7.579	3.45091	12.1063
H	-9.9578	5.37271	14.9569	H	-9.3318	6.82512	14.0911
H	-8.3015	5.99663	15.3016	H	-1.6771	3.98949	12.3267
H	0.97839	5.0971	15.1107	H	1.91574	3.76771	14.3345
H	0.75713	3.38662	15.6501				

**Table 2.17:** Geometry optimized coordinates of propoxur<sub>c</sub>2.1

O	0.73311	5.10695	12.4493	O	-1.3964	5.4004	12.9322
C	-0.5618	5.17035	12.0828	C	-0.8511	4.89232	10.6233
O	-0.6666	7.54658	10.9915	O	0.36162	8.02147	9.05237
C	-0.102	7.23107	9.89234	C	-0.0073	5.72299	9.64905
Cu	-0.5678	9.23746	12.0587	O	-0.5591	10.9131	13.1302
O	-1.4589	10.0535	15.0036	O	-0.3348	7.87315	13.9861

---

N	-2.6048	9.27643	12.1139	N	-9.6939	9.54554	12.2819
C	-3.3131	8.23432	12.57	C	-4.7008	8.26553	12.6517
C	-5.3969	9.40412	12.218	C	-6.8766	9.45507	12.2411
C	-7.6457	8.31179	11.971	C	-9.0378	8.41212	12.0024
C	-1.0077	10.995	14.3239	C	-0.9682	12.3905	14.9456
O	1.77532	12.3903	14.5635	O	1.6485	13.5443	12.6511
C	1.11755	13.1385	13.6644	C	-0.3022	13.4498	14.0739
C	-3.2484	10.3867	11.7249	C	-4.6345	10.4874	11.7505
C	-7.5638	10.6451	12.5262	C	-8.9603	10.6355	12.5376
O	-0.3501	10.4606	9.93819	N	1.46644	9.31026	11.9999
N	8.53862	9.89532	12.3578	C	7.87622	8.99981	13.1002
C	6.4894	8.84191	13.0647	C	5.72871	9.65981	12.2133
C	4.25313	9.53782	12.1369	C	3.60542	8.31329	12.376
C	2.21785	8.24273	12.3036	C	7.81594	10.6751	11.5444
C	6.42588	10.6002	11.4372	C	3.44328	10.6427	11.8248
C	2.06267	10.486	11.7602	H	-0.6767	3.81869	10.4431
H	-1.9215	5.065	10.4695	H	-0.3036	5.50996	8.611
H	1.06299	5.45251	9.69708	H	-0.8875	8.53431	14.4753
H	-0.8409	7.04812	13.8955	H	-2.7515	7.34505	12.8607
H	-5.2318	7.40361	13.0543	H	-7.1715	7.36703	11.7034
H	-9.6494	7.52888	11.7852	H	-2.0069	12.6847	15.1686
H	-0.4608	12.2985	15.9182	H	-0.2692	14.4115	14.6162
H	-0.8641	13.6235	13.1464	H	-2.6238	11.2117	11.3778
H	-5.1108	11.3978	11.3849	H	-7.026	11.566	12.7595
H	-9.5073	11.5568	12.7688	H	-0.0665	9.6168	9.49388
H	-1.0399	10.8309	9.37123	H	8.47608	8.37005	13.7671
H	6.01492	8.10267	13.7122	H	4.17173	7.41027	12.6067
H	1.68171	7.3154	12.5076	H	8.36765	11.4018	10.9373
H	5.90317	11.2566	10.7395	H	3.86805	11.6321	11.6517
H	1.40652	11.321	11.5228	H	2.67869	12.2417	14.2302
H	1.29951	4.84382	11.7055	O	-5.4456	6.2849	10.3215
C	-4.7452	5.09706	10.433	C	-3.8209	3.34459	11.8136
C	-3.8013	3.12754	9.39175	C	-4.4383	4.36796	9.26013
C	-4.4463	4.59103	11.6931	C	-3.502	2.62194	10.6638
O	-4.8204	4.94341	8.10018	C	-4.2379	4.54175	6.8423
C	-2.7736	4.95743	6.77625	C	-5.0917	5.20082	5.77272
C	-4.9781	7.33151	9.55269	O	-5.7827	8.09495	9.06372
N	-3.6344	7.42933	9.4743	C	-2.9747	8.45023	8.68702
H	-4.7088	5.1787	12.5733	H	-3.0054	1.65217	10.7455
H	-3.5729	2.95576	12.8026	H	-3.5464	2.54562	8.50594
H	-2.1855	4.49456	7.5821	H	-2.6848	6.0514	6.86061
H	-2.3355	4.64398	5.81664	H	-5.0485	6.29718	5.87317
H	-6.141	4.88249	5.86537	H	-4.7272	4.92424	4.77208
H	-4.3237	3.44551	6.74968	H	-3.737	9.00741	8.12985

H	-2.2607	8.00044	7.98029	H	-2.4158	9.14134	9.33007
H	-3.0613	6.84288	10.0712				

**Table 2.18:** Geometry optimized coordinates of trifluralin $\square$ 2.1.

O	0.0475	5.45224	10.2296	O	-1.9544	5.80408	11.082
C	-1.2036	5.9276	10.133	C	-1.6124	6.52099	8.7978
O	-0.5918	8.4806	10.46	O	-0.3192	9.9454	8.77542
C	-0.5258	8.80451	9.22809	C	-0.6879	7.62513	8.26297
Cu	-0.5058	9.53429	12.1668	O	-0.4815	10.4853	13.9272
O	-1.627	8.97395	15.1391	O	-0.6462	7.38721	13.2268
N	-2.572	9.82724	12.07	N	-9.605	10.9208	11.764
C	-3.4111	8.82597	11.7618	C	-4.7911	9.00265	11.7001
C	-5.3474	10.267	11.9575	C	-6.8136	10.4967	11.8907
C	-7.6232	9.79433	10.9815	C	-8.9979	10.0417	10.9578
C	-1.0586	10.0726	14.9924	C	-1.0481	11.0426	16.1782
O	1.73201	10.9308	16.424	O	2.03099	12.7219	15.1163
C	1.29175	12.0203	15.7755	C	-0.1793	12.2864	15.9993
C	-3.0869	11.0386	12.3331	C	-4.4532	11.3014	12.2843
C	-7.4536	11.4225	12.7317	C	-8.8369	11.5926	12.6303
O	-0.0888	11.56	10.8971	N	1.55038	9.35234	12.2335
N	8.63228	8.7581	12.6811	C	7.83239	7.69865	12.8543
C	6.43905	7.76043	12.7749	C	5.82032	8.99316	12.5038
C	4.3422	9.11767	12.4099	C	3.54204	8.05227	11.9592
C	2.16013	8.20892	11.8864	C	8.04657	9.93347	12.4209
C	6.66335	10.1038	12.3253	C	3.68097	10.3055	12.7681
C	2.29437	10.3816	12.6644	H	-1.6499	5.6937	8.06694
H	-2.6372	6.89866	8.91427	H	-1.0647	7.99818	7.29961
H	0.32506	7.23297	8.0539	H	-1.1702	7.81346	13.9513
H	-1.239	6.80791	12.7191	H	-2.9679	7.84816	11.5611
H	-5.416	8.1362	11.4817	H	-7.1952	9.08014	10.2762
H	-9.6326	9.50069	10.2468	H	-2.0939	11.3465	16.3549
H	-0.7456	10.4703	17.0685	H	-0.2457	12.911	16.9085
H	-0.5218	12.9051	15.1591	H	-2.3759	11.823	12.6009
H	-4.8047	12.3147	12.4853	H	-6.8945	11.993	13.476
H	-9.3439	12.3076	13.2888	H	-0.1677	11.0485	10.0455
H	-0.8164	12.1968	10.8622	H	8.32027	6.74137	13.0725
H	5.85141	6.85621	12.9454	H	3.98446	7.1053	11.6459
H	1.51243	7.40175	11.5393	H	8.70938	10.7946	12.2755
H	6.25886	11.091	12.0933	H	4.22665	11.1692	13.1513
H	1.75596	11.2872	12.9452	H	2.68882	10.8441	16.2585
H	0.54442	5.58465	9.40553	O	-4.9768	2.43406	7.25664
O	-7.0043	2.09608	6.58163	N	-6.1114	4.63675	11.9521
N	-6.1867	2.57808	7.35281	O	-5.6952	5.71817	12.3397



O	-6.2731	3.66094	12.6641	C	-6.6846	3.44838	8.42705
C	-7.9958	5.42771	8.85456	C	-6.5117	4.53147	10.5359
C	-6.0984	3.42721	9.7261	C	-7.6444	4.37644	8.0163
C	-7.3953	5.51459	10.1159	N	-5.2494	2.44885	10.189
C	-3.9359	2.82958	10.7523	C	-3.5557	2.20896	12.1021
C	-2.0943	2.50168	12.454	C	-5.3743	1.03933	9.78207
C	-6.7961	0.46827	9.84712	C	-7.4074	0.46238	11.25
C	-8.99	6.4765	8.43328	F	-9.4439	6.2762	7.18971
F	-8.4435	7.71423	8.46921	F	-10.056	6.51376	9.25616
H	-8.0593	4.29414	7.01193	H	-7.655	6.31593	10.8094
H	-3.1738	2.54916	9.99852	H	-3.8833	3.92668	10.8211
H	-4.2221	2.59777	12.887	H	-3.7112	1.11777	12.0756
H	-1.8429	2.10338	13.4497	H	-1.8912	3.58452	12.4518
H	-1.4077	2.03807	11.7249	H	-4.9291	0.86613	8.78676
H	-4.7503	0.47311	10.4878	H	-6.7318	-0.5636	9.46154
H	-7.467	0.99517	9.14775	H	-8.4239	0.03801	11.2327
H	-7.4678	1.47745	11.672	H	-6.8005	-0.1465	11.9413

After the series of organochlorine-based pesticides, a systemically active benzimidazole fungicide, for example, thiophanate-methyl, has been chosen (**Figure 2.7(d)** and **Table 2.16** for coordinates). Its interaction with **2.1** consists of a hydrogen-bonding interaction between the nonligating oxygen of succinate dianion and a secondary amine of thiophanatemethyl ( $\text{H}\cdots\text{O}$  distance: 1.82 Å). Then, we chose a carbamate insecticide, propoxur (commercially known as Baygon), because it is sometimes toxic to many bird species, honeybees, or aquatic life like fish. The optimized structure showed no interaction between the host and the guest (**Figure 2.7(e)** and **Table 2.17** for coordinates). The steric hindrance of the  $-\text{CH}_3$  group adjacent to  $-\text{NH}$  perhaps does not facilitate the sensing property. Moreover, the results of the calculation suggest that the presence of the  $-\text{NH}$  moiety does not ascertain sensing, rather it strictly depends on other parameters, such as adjacent groups, steric crowding, and so on. We further moved on toward a representative of herbicides, for example, trifluralin, which contains nitro groups as well as fluorine. It was expected that nitro groups could make the ring electron-deficient, and thus  $\pi$ - $\pi$  stacking, as it happens with dicofol, might play a vital role. However, after optimization, no trace of interaction between the host and the guest was observed (**Figure 2.7(f)** and **Table 2.18** for coordinates). Natural bond orbital (NBO) analysis of **1** and its host-guest adduct with the pesticides were executed and is tabulated (**Tables 2.19–2.25**, **Figure 2.8(a)–2.8(g)**). For example, the O2 and O6 populations from spin density are 0.00026 and  $-0.00047$  for **2.1**, which, after interaction with atrazine, altered to 0.00039 and  $-0.00009$ . For further verification regarding the geometry, the vibrational stretching of **2.1** and an adduct

of **2.1** with atrazine were studied, and no negative vibration was found. The zero-point energy (ZPE) of the MOF and the MOF–atrazine adduct was then calculated and was found to be 1472.93 and 2083.19 kJ/mol.

**Table 2.19:** NBO analysis of **2.1**. atomic population from spin density

atom	sum	n(s)	n(p)	n(d)	n(f)	n(g)
1 o	0.00015	-0.00001	0.00017	0	0	0
2 o	0.00026	-0.00002	0.00027	0	0	0
3 c	0.00027	0.00001	0.00026	0	0	0
4 c	-0.0004	-0.0002	-0.0002	0	0	0
5 o	0.04937	0.00446	0.04463	0.00029	0	0
6 o	-0.0005	0.00051	-0.001	0	0	0
7 c	-0.0027	-0.001	-0.0024	0.00058	0	0
8 c	0.00714	0.00182	0.0053	0.00001	0	0
9 cu	0.79111	-0.0066	-0.0072	0.80485	0.00001	0
10 o	0.05865	0.0046	0.05379	0.00025	0	0
11 o	-0.00008	0.00044	-0.0005	0	0	0
12 o	-0.0007	-0.0001	-0.0005	0	0	0
13 n	0.05022	0.00853	0.04131	0.00037	0	0
14 n	-0.0006	0	-0.0006	0	0	0
15 c	-0.007	-0.0011	-0.0059	0.00009	0	0
16 c	0.0056	0.00085	0.00476	0	0	0
17 c	-0.004	-0.00008	-0.004	0	0	0
18 c	0.00064	0	0.00065	- 0.00001	0	0
19 c	-0.0008	-0.00005	-0.0007	0	0	0
20 c	0.00032	0.00001	0.00032	0	0	0
21 c	-0.0043	-0.0011	-0.0034	0.00031	0	0
22 c	0.00868	0.00212	0.00655	0.00002	0	0
23 o	0.00011	0.00001	0.0001	0	0	0
24 o	0.00002	-0.00001	0.00003	0	0	0
25 c	0.00009	0.00002	0.00007	0	0	0
26 c	-0.0003	0	-0.0003	0	0	0
27 c	-0.0073	-0.0011	-0.0063	0.00009	0	0
28 c	0.00539	0.0008	0.00459	0	0	0
29 c	-0.0008	-0.00004	-0.0007	0	0	0
30 c	0.00031	0	0.00031	0	0	0
31 o	-0.0005	-0.0002	-0.0003	0	0	0
32 n	0.05281	0.0077	0.04472	0.00039	0	0
33 n	-0.0006	0	-0.0006	0	0	0
34 c	0.00032	0	0.00032	0	0	0
35 c	-0.0008	-0.00004	-0.0007	0	0	0
36 c	0.00068	0	0.00069	- 0.00001	0	0

37 c	-0.0041	-0.00005	-0.0041	0	0	0
38 c	0.00589	0.0009	0.005	0	0	0
39 c	-0.0071	-0.0012	-0.0061	0.0001	0	0
40 c	0.00034	0.00001	0.00034	0	0	0
41 c	-0.0008	-0.00005	-0.0008	0	0	0
42 c	0.00589	0.00091	0.00499	0	0	0
43 c	-0.0075	-0.0012	-0.0064	0.00009	0	0
44 h	-0.00005	-0.00005	0	0	0	0
45 h	0	0	0	0	0	0
46 h	0.00064	0.00062	0.00002	0	0	0
47 h	-0.0002	-0.0002	0	0	0	0
48 h	-0.00007	-0.00006	-0.00001	0	0	0
49 h	-0.0002	-0.0002	0	0	0	0
50 h	0.0014	0.00141	-0.00001	0	0	0
51 h	0.00018	0.00017	0	0	0	0
52 h	0	0	0	0	0	0
53 h	0	0	0	0	0	0
54 h	-0.0002	-0.0002	0.00002	0	0	0
55 h	-0.00009	-0.0001	0.00002	0	0	0
56 h	-0.00004	-0.00004	0	0	0	0
57 h	0.00007	0.00007	0	0	0	0
58 h	0.00136	0.00137	-0.00001	0	0	0
59 h	0.00017	0.00016	0	0	0	0
60 h	0	0	0	0	0	0
61 h	0	0	0	0	0	0
62 h	-0.0001	-0.0001	0	0	0	0
63 h	-0.0002	-0.0002	0	0	0	0
64 h	0	0	0	0	0	0
65 h	0	0	0	0	0	0
66 h	0.00017	0.00016	0.00001	0	0	0
67 h	0.00169	0.0017	-0.00001	0	0	0
68 h	0	0	0	0	0	0
69 h	-0.00001	-0.00001	0	0	0	0
70 h	0.00015	0.00014	0	0	0	0
71 h	0.00181	0.00181	-0.00001	0	0	0
72 h	-0.00002	-0.00002	0	0	0	0
73 h	0	0	0	0	0	0

**Table 2.20:** NBO analysis of atrazine $\subset$ 2.1

atomic populations from spin density:

atom	sum	n(s)	n(p)	n(d)	n(f)	n(g)
1 o	0.00009	0.00002	0.00011	0	0	0
2 o	0.00039	0	0.00039	0	0	0

3 c	0.00003	0.00001	0.00002	0	0	0
4 c	-0.0004	-0.0002	-0.0003	0	0	0
5 o	0.04604	0.00506	0.04065	0.00033	0	0
6 o	0.00009	0.0006	-0.0007	0	0	0
7 c	-0.0031	-0.001	-0.0027	0.00059	0	0
8 c	0.00677	0.00167	0.0051	0	0	0
9 cu	0.78813	-0.0067	-0.0072	0.802	0.00001	0
10 o	0.06278	0.00535	0.05715	0.00028	0	0
11 o	-0.0002	0.00061	-0.0009	0	0	0
12 o	-0.0004	-0.0001	-0.0003	0	0	0
13 n	0.05019	0.00832	0.0415	0.00037	0	0
14 n	-0.0006	0	-0.0006	0	0	0
15 c	-0.0066	-0.0012	-0.0054	0.00009	0	0
16 c	0.0054	0.00078	0.00462	0	0	0
17 c	-0.0037	0.00007	-0.0036	0	0	0
18 c	0.00062	0.00001	0.00062	0.00001	0	0
19 c	-0.0007	0.00004	-0.0007	0	0	0
20 c	0.00031	0.00001	0.00031	0	0	0
21 c	-0.0049	-0.0013	-0.0043	0.00073	0	0
22 c	0.00907	0.0022	0.00687	0	0	0
23 o	0.00011	0.00001	0.0001	0	0	0
24 o	0.00003	0.00001	0.00002	0	0	0
25 c	0.00007	0	0.00006	0	0	0
26 c	-0.0002	0.00006	-0.0003	0	0	0
27 c	-0.0068	-0.0012	-0.0057	0.00008	0	0
28 c	0.00535	0.00078	0.00457	0	0	0
29 c	-0.0007	0.00003	-0.0007	0	0	0
30 c	0.00029	0	0.00029	0	0	0
31 o	-0.0002	-0.0002	0.00005	0	0	0
32 n	0.05433	0.008	0.04597	0.00036	0	0
33 n	-0.0006	0	-0.0006	0	0	0
34 c	0.00033	0	0.00032	0	0	0
35 c	-0.0008	0.00004	-0.0007	0	0	0
36 c	0.00068	0	0.00069	0.00001	0	0
37 c	-0.0042	0.00005	-0.0042	0	0	0
38 c	0.00601	0.00089	0.00513	0.00001	0	0
39 c	-0.0072	-0.0012	-0.0061	0.00009	0	0
40 c	0.00034	0.00001	0.00034	0	0	0
41 c	-0.0008	0.00005	-0.0008	0	0	0
42 c	0.00605	0.00092	0.00513	0.00001	0	0
43 c	-0.0075	-0.0012	-0.0064	0.00009	0	0
44 h	0.00006	0.00006	0	0	0	0
45 h	0.00003	0.00003	0	0	0	0
46 h	0.00069	0.00067	0.00002	0	0	0

47 h	-0.0003	-0.0003	0	0	0	0
48 h	0	0	0	0	0	0
49 h	-0.0001	-0.0001	0	0	0	0
50 h	0.00131	0.00132	0.00001	0	0	0
51 h	0.0002	0.0002	0	0	0	0
52 h	0	0	0	0	0	0
53 h	0	0	0	0	0	0
54 h	-0.0001	-0.0002	0.00002	0	0	0
55 h	0.00004	0.00006	0.00002	0	0	0
56 h	0.00003	0.00003	0	0	0	0
57 h	-0.0001	-0.0001	0	0	0	0
58 h	0.00139	0.0014	0.00001	0	0	0
59 h	0.00017	0.00016	0	0	0	0
60 h	0	0	0	0	0	0
61 h	0	0	0	0	0	0
62 h	-0.0001	-0.0001	0	0	0	0
63 h	-0.0001	-0.0001	0	0	0	0
64 h	0	0	0	0	0	0
65 h	0	0	0	0	0	0
66 h	0.00017	0.00017	0	0	0	0
67 h	0.00166	0.00167	0.00001	0	0	0
68 h	0	0	0	0	0	0
69 h	0.00001	0.00001	0	0	0	0
70 h	0.00015	0.00015	0	0	0	0
71 h	0.00181	0.00182	0.00001	0	0	0
72 h	0.00003	0.00003	0	0	0	0
73 h	0.00001	0.00001	0	0	0	0
74 cl	0.00001	0	0.00001	0	0	0
75 c	0.00003	0	0.00003	0	0	0
76 c	-0.0001	0	-0.0001	0	0	0
77 c	0.00005	0.00002	0.00002	0	0	0
78 n	0.00002	0	0.00002	0	0	0
79 n	0.00002	0	0.00002	0	0	0
80 n	0.00002	0.00001	0.00001	0	0	0
81 n	0.00001	0.00001	0.00001	0	0	0
82 c	0	0	0	0	0	0
83 c	0	0	0	0	0	0
84 c	0.00001	0	0.00002	0	0	0
85 n	0.00004	0	0.00003	0	0	0
86 c	0	0	0	0	0	0
87 c	0.00002	0.00001	0.00001	0	0	0
88 h	0	0	0	0	0	0
89 h	0	0	0	0	0	0
90 h	0	0	0	0	0	0

91 h	0.00002	0.00002	0	0	0	0
92 h	0	0	0	0	0	0
93 h	0	0	0	0	0	0
94 h	0	0	0	0	0	0
95 h	0	0	0	0	0	0
96 h	0.00001	0.00001	0	0	0	0
97 h	0	0	0	0	0	0
98 h	0	0	0	0	0	0
99 h	0	0	0	0	0	0
100 h	0.00002	0.00002	0	0	0	0
101 h	0.00001	0.00001	0	0	0	0

**Table 2.21:** NBO analysis of chlorothalonil-2.1.

atomic populations from spin density

atom	sum	n(s)	n(p)	n(d)	n(f)	n(g)
1 o	0.00014	-0.00001	0.00015	0	0	0
2 o	0.00028	-0.00001	0.00029	0	0	0
3 c	0.00025	0.00001	0.00024	0	0	0
4 c	-0.0003	-0.0002	-0.0001	0	0	0
5 o	0.04896	0.00444	0.04422	0.0003	0	0
6 o	-0.0005	0.0005	-0.001	0	0	0
7 c	-0.0028	-0.001	-0.0024	0.00056	0	0
8 c	0.00715	0.00183	0.00532	0.00001	0	0
9 cu	0.79185	-0.0065	-0.0071	0.80544	0.00001	0
10 o	0.0584	0.00454	0.05362	0.00024	0	0
11 o	-0.0002	0.00043	-0.0006	0	0	0
12 o	-0.0007	-0.0002	-0.0005	0	0	0
13 n	0.04937	0.00833	0.04067	0.00037	0	0
14 n	-0.0005	0	-0.0005	0	0	0
15 c	-0.0068	-0.0011	-0.0058	0.00009	0	0
16 c	0.0055	0.00086	0.00464	0	0	0
17 c	-0.004	-0.00008	-0.0039	0	0	0
18 c	0.00058	-0.00001	0.0006	-0.00001	0	0
19 c	-0.0007	-0.00005	-0.0007	0	0	0
20 c	0.00029	0	0.00029	0	0	0
21 c	-0.004	-0.0012	-0.0031	0.00029	0	0
22 c	0.00866	0.00213	0.00651	0.00001	0	0
23 o	0.00012	0.00001	0.0001	0	0	0
24 o	0.00002	-0.00001	0.00002	0	0	0
25 c	0.0001	0.00002	0.00008	0	0	0
26 c	-0.0003	-0.00001	-0.0003	0	0	0
27 c	-0.0072	-0.001	-0.0063	0.00009	0	0
28 c	0.00528	0.00079	0.0045	0	0	0

29 c	-0.0007	-0.00005	-0.0007	0	0	0
30 c	0.00029	0	0.00029	0	0	0
31 o	-0.0005	-0.0002	-0.0003	0	0	0
32 n	0.05332	0.00774	0.0452	0.00037	0	0
33 n	-0.0006	0	-0.0006	0	0	0
34 c	0.00032	0	0.00032	0	0	0
35 c	-0.0008	-0.00004	-0.0007	0	0	0
36 c	0.00067	0	0.00068	-0.00001	0	0
37 c	-0.0041	-0.00005	-0.0041	0	0	0
38 c	0.00591	0.0009	0.00502	0	0	0
39 c	-0.0071	-0.0012	-0.0061	0.00009	0	0
40 c	0.00034	0.00001	0.00034	0	0	0
41 c	-0.0008	-0.00005	-0.0007	0	0	0
42 c	0.00594	0.00093	0.00502	0	0	0
43 c	-0.0075	-0.0012	-0.0064	0.00009	0	0
44 h	-0.00005	-0.00005	0	0	0	0
45 h	0	0	0	0	0	0
46 h	0.00057	0.00055	0.00002	0	0	0
47 h	-0.0002	-0.0002	0	0	0	0
48 h	-0.00006	-0.00005	-0.00001	0	0	0
49 h	-0.0002	-0.0002	0	0	0	0
50 h	0.00138	0.00139	-0.00001	0	0	0
51 h	0.00018	0.00017	0	0	0	0
52 h	-0.00001	-0.00001	0	0	0	0
53 h	0	0	0	0	0	0
54 h	-0.0002	-0.0002	0.00002	0	0	0
55 h	-0.00009	-0.0001	0.00002	0	0	0
56 h	-0.00005	-0.00005	0	0	0	0
57 h	0.00007	0.00007	0	0	0	0
58 h	0.00133	0.00134	-0.00001	0	0	0
59 h	0.00016	0.00016	0	0	0	0
60 h	-0.00001	-0.00001	0	0	0	0
61 h	0	0	0	0	0	0
62 h	-0.0001	-0.0001	0	0	0	0
63 h	-0.0002	-0.0002	0	0	0	0
64 h	0	0	0	0	0	0
65 h	0	0	0	0	0	0
66 h	0.00018	0.00017	0.00001	0	0	0
67 h	0.00169	0.0017	-0.00001	0	0	0
68 h	0	0	0	0	0	0
69 h	-0.00001	-0.00001	0	0	0	0
70 h	0.00015	0.00015	0	0	0	0
71 h	0.00183	0.00184	-0.00001	0	0	0
72 h	-0.00002	-0.00002	0	0	0	0

73 h	0	0	0	0	0	0
74 cl	0	0	0	0	0	0
75 c	0	0	0	0	0	0
76 c	0	0	0	0	0	0
77 c	0	0	0	0	0	0
78 c	0	0	0	0	0	0
79 c	0	0	0	0	0	0
80 c	0	0	0	0	0	0
81 c	0	0	0	0	0	0
82 n	0	0	0	0	0	0
83 c	0	0	0	0	0	0
84 n	0	0	0	0	0	0
85 cl	0	0	0	0	0	0
86 cl	0	0	0	0	0	0
87 cl	0	0	0	0	0	0

**Table 2.22:** NBO analysis of dicofolc2.1.

atomic populations from spin density

atom	sum	n(s)	n(p)	n(d)	n(f)	n(g)
1 o	0.00004	-0.00001	0.00005	0	0	0
2 o	0.00023	-0.00001	0.00024	0	0	0
3 c	0.0002	0.00001	0.0002	0	0	0
4 c	-0.0002	-0.00001	-0.0002	0	0	0
5 o	0.04889	0.00459	0.04394	0.00036	0	0
6 o	0.00053	0.00042	0.00011	0	0	0
7 c	-0.0024	-0.0008	-0.002	0.00033	0	0
8 c	0.00759	0.00185	0.00574	0	0	0
9 cu	0.7847	-0.0075	-0.008	0.8002	0.00001	0
10 o	0.0629	0.00464	0.05802	0.00024	0	0
11 o	0.00001	0.00048	-0.0005	0	0	0
12 o	-0.0007	-0.0001	-0.0006	0	0	0
13 n	0.04975	0.0079	0.04149	0.00036	0	0
14 n	-0.0006	0	-0.0006	0	0	0
15 c	-0.007	-0.0011	-0.006	0.00008	0	0
16 c	0.00566	0.00086	0.00481	0	0	0
17 c	-0.004	-0.00008	-0.004	0	0	0
18 c	0.0006	-0.00001	0.00061	-0.00001	0	0
19 c	-0.0007	-0.00005	-0.0007	0	0	0
20 c	0.00028	0	0.00028	0	0	0
21 c	-0.0044	-0.0012	-0.0035	0.00033	0	0
22 c	0.00916	0.00214	0.007	0.00001	0	0
23 o	0.00012	0	0.00012	0	0	0



24 o	0.00008	0	0.00008	0	0	0
25 c	0.00007	0.00003	0.00004	0	0	0
26 c	-0.0004	-0.00001	-0.0003	0	0	0
27 c	-0.0068	-0.0008	-0.0061	0.00008	0	0
28 c	0.00534	0.00077	0.00457	0	0	0
29 c	-0.0007	-0.00005	-0.0007	0	0	0
30 c	0.0003	0.00001	0.0003	0	0	0
31 o	-0.0005	-0.00008	-0.0004	0	0	0
32 n	0.0543	0.0081	0.04581	0.00039	0	0
33 n	-0.0007	0	-0.0007	0	0	0
34 c	0.00034	0.00001	0.00034	0	0	0
35 c	-0.0008	-0.00004	-0.0008	0	0	0
36 c	0.0007	0	0.00071	-0.00001	0	0
37 c	-0.0043	-0.00005	-0.0043	0	0	0
38 c	0.00599	0.00087	0.00512	0	0	0
39 c	-0.0074	-0.0013	-0.0062	0.0001	0	0
40 c	0.00035	0.00001	0.00035	0	0	0
41 c	-0.0008	-0.00005	-0.0008	0	0	0
42 c	0.00614	0.00094	0.0052	0	0	0
43 c	-0.0077	-0.0012	-0.0066	0.00009	0	0
44 h	-0.00003	-0.00003	0	0	0	0
45 h	0.00005	0.00005	0	0	0	0
46 h	-0.00009	-0.0001	0.00003	0	0	0
47 h	0.00001	-0.00002	0.00003	0	0	0
48 h	-0.00007	-0.00006	-0.00001	0	0	0
49 h	-0.0002	-0.0002	0	0	0	0
50 h	0.00148	0.00149	-0.00001	0	0	0
51 h	0.00017	0.00017	0	0	0	0
52 h	-0.00001	-0.00001	0	0	0	0
53 h	0	0	0	0	0	0
54 h	-0.0002	-0.0002	0.00002	0	0	0
55 h	-0.0001	-0.0001	0.00002	0	0	0
56 h	-0.00005	-0.00005	0	0	0	0
57 h	0.00008	0.00007	0	0	0	0
58 h	0.00132	0.00132	0	0	0	0
59 h	0.00018	0.00017	0	0	0	0
60 h	0	0	0	0	0	0
61 h	0	0	0	0	0	0
62 h	-0.00008	-0.00008	0	0	0	0
63 h	-0.0002	-0.0002	0	0	0	0
64 h	0	0	0	0	0	0
65 h	0	0	0	0	0	0
66 h	0.0002	0.0002	0	0	0	0
67 h	0.00158	0.00159	-0.00001	0	0	0

68 h	0	0	0	0	0	0
69 h	-0.00001	0	0	0	0	0
70 h	0.00016	0.00015	0	0	0	0
71 h	0.0018	0.00181	-0.00001	0	0	0
72 h	-0.00002	-0.00002	0	0	0	0
73 h	0	0	0	0	0	0
74 c	0	0	0	0	0	0
75 c	0.00002	0	0.00002	0	0	0
76 c	0.00001	0.00001	0	0	0	0
77 c	0.00001	0	0.00001	0	0	0
78 c	-0.00001	0	-0.00001	0	0	0
79 c	0	0	0	0	0	0
80 c	0	0	0	0	0	0
81 c	0	0	0	0	0	0
82 c	-0.00001	0	-0.00001	0	0	0
83 c	0.00001	0	0.00001	0	0	0
84 c	-0.00001	0	-0.00001	0	0	0
85 c	0	0	0	0	0	0
86 c	0	0	0	0	0	0
87 o	0	0	0	0	0	0
88 c	-0.00007	-0.00001	-0.00005	0	0	0
89 cl	-0.00001	0	-0.00001	0	0	0
90 cl	0	0	0	0	0	0
91 cl	-0.00002	-0.00003	0.00002	-0.00001	0	0
92 cl	0	0	0	0	0	0
93 cl	0.00002	0	0.00002	0	0	0
94 h	-0.00002	-0.00002	0	0	0	0
95 h	-0.00001	-0.00001	0	0	0	0
96 h	0	0	0	0	0	0
97 h	0	0	0	0	0	0
98 h	0	0	0	0	0	0
99 h	0	0	0	0	0	0
100 h	-0.00001	-0.00001	0	0	0	0
101 h	-0.00001	-0.00001	0	0	0	0
102 h	0	0	0	0	0	0

**Table 2.23:** NBO analysis of thiophanate-methylc2.1.

atomic populations from spin density

atom	sum	n(s)	n(p)	n(d)	n(f)	n(g)
1 o	0.00025	-0.00001	0.00026	0	0	0
2 o	0.00025	-0.00002	0.00027	0	0	0
3 c	0.00047	0.00002	0.00044	0	0	0
4 c	-0.0003	-0.0002	-0.0002	0	0	0

5 o	0.04831	0.00491	0.0431	0.00029	0	0
6 o	-0.0004	0.00049	-0.0009	0	0	0
7 c	-0.0028	-0.001	-0.0024	0.00056	0	0
8 c	0.00694	0.00181	0.00513	0.00001	0	0
9 cu	0.7906	-0.0063	-0.0071	0.80406	0.00001	0
10 o	0.05957	0.00475	0.05455	0.00026	0	0
11 o	-0.0002	0.00043	-0.0006	0	0	0
12 o	-0.0006	-0.0001	-0.0004	0	0	0
13 n	0.05219	0.00841	0.0434	0.00038	0	0
14 n	-0.0007	0	-0.0007	0	0	0
15 c	-0.0074	-0.0012	-0.0062	0.00008	0	0
16 c	0.00583	0.00078	0.00506	0	0	0
17 c	-0.0042	-0.00007	-0.0041	0	0	0
18 c	0.0007	0.00002	0.0007	-0.00001	0	0
19 c	-0.0008	-0.00005	-0.0008	0	0	0
20 c	0.00033	0.00001	0.00033	0	0	0
21 c	-0.0049	-0.0012	-0.0045	0.00085	0	0
22 c	0.0089	0.00222	0.00667	0.00001	0	0
23 o	0.00011	0.00001	0.00011	0	0	0
24 o	0.00003	-0.00001	0.00004	0	0	0
25 c	0.0001	0.00003	0.00007	0	0	0
26 c	-0.0003	-0.00001	-0.0003	0	0	0
27 c	-0.0073	-0.0013	-0.0062	0.00009	0	0
28 c	0.00563	0.00083	0.0048	0	0	0
29 c	-0.0008	-0.00004	-0.0008	0	0	0
30 c	0.00034	0.00001	0.00034	0	0	0
31 o	-0.0005	-0.0002	-0.0003	0	0	0
32 n	0.05133	0.00744	0.04348	0.00041	0	0
33 n	-0.0006	0	-0.0006	0	0	0
34 c	0.00031	0	0.00031	0	0	0
35 c	-0.0007	-0.00004	-0.0007	0	0	0
36 c	0.00064	0	0.00066	-0.00001	0	0
37 c	-0.004	-0.00005	-0.004	0	0	0
38 c	0.00576	0.00089	0.00488	0	0	0
39 c	-0.0068	-0.0011	-0.0058	0.00009	0	0
40 c	0.00033	0.00001	0.00033	0	0	0
41 c	-0.0008	-0.00005	-0.0007	0	0	0
42 c	0.00572	0.00088	0.00485	-0.00001	0	0
43 c	-0.0073	-0.0012	-0.0062	0.00009	0	0
44 h	-0.00007	-0.00007	0	0	0	0
45 h	0	0	0	0	0	0
46 h	0.00056	0.00054	0.00002	0	0	0
47 h	-0.0002	-0.0002	0	0	0	0
48 h	-0.0001	-0.0001	0	0	0	0

49 h	-0.0002	-0.0002	0	0	0	0
50 h	0.0015	0.00151	-0.00001	0	0	0
51 h	0.00021	0.00021	0	0	0	0
52 h	0.00001	0.00001	0	0	0	0
53 h	0	0	0	0	0	0
54 h	-0.0002	-0.0002	0.00001	0	0	0
55 h	-0.00009	-0.0001	0.00001	0	0	0
56 h	-0.00005	-0.00005	0	0	0	0
57 h	0.00007	0.00007	0	0	0	0
58 h	0.00143	0.00144	-0.00001	0	0	0
59 h	0.00018	0.00018	0	0	0	0
60 h	0	0	0	0	0	0
61 h	0	0	0	0	0	0
62 h	-0.0001	-0.0001	0	0	0	0
63 h	-0.0002	-0.0002	0	0	0	0
64 h	0	0	0	0	0	0
65 h	0	0	0	0	0	0
66 h	0.00017	0.00016	0.00001	0	0	0
67 h	0.00167	0.00168	-0.00001	0	0	0
68 h	0	0	0	0	0	0
69 h	-0.00001	-0.00001	0	0	0	0
70 h	0.00015	0.00015	0	0	0	0
71 h	0.00175	0.00176	-0.00001	0	0	0
72 h	-0.00002	-0.00002	0	0	0	0
73 h	0	0	0	0	0	0
74 n	0	0	0	0	0	0
75 c	0	0	0	0	0	0
76 c	0	0	0	0	0	0
77 c	0	0	0	0	0	0
78 c	0	0	0	0	0	0
79 c	0	0	0	0	0	0
80 c	0	0	0	0	0	0
81 n	0.00001	0	0.00001	0	0	0
82 c	0.00001	0	0.00001	0	0	0
83 s	0.00002	0	0.00002	0	0	0
84 n	0	0	0	0	0	0
85 c	0	0	0	0	0	0
86 o	0.00003	0.00001	0.00002	0	0	0
87 o	0	0	0	0	0	0
88 c	0	0	0	0	0	0
89 c	0	0	0	0	0	0
90 s	0	0	0	0	0	0
91 n	0	0	0	0	0	0
92 c	0	0	0	0	0	0

93 o	0	0	0	0	0	0
94 o	0	0	0	0	0	0
95 c	-0.00001	0	-0.00001	0	0	0
96 h	0	0	0	0	0	0
97 h	0	0	0	0	0	0
98 h	0	0	0	0	0	0
99 h	0	0	0	0	0	0
100 h	0	0	0	0	0	0
101 h	0	0	0	0	0	0
102 h	0	0	0	0	0	0
103 h	0	0	0	0	0	0
104 h	0	0	0	0	0	0
105 h	0	0	0	0	0	0
106 h	0	0	0	0	0	0
107 h	-0.00001	-0.00001	0	0	0	0
108 h	0	0	0	0	0	0
109 h	0	0	0	0	0	0

**Table 2.24:** NBO analysis of propoxur<sub>c</sub>2.1.

atomic populations from spin density

atom	sum	n(s)	n(p)	n(d)	n(f)	n(g)
1 o	-0.00001	-0.00002	0	0	0	0
2 o	0.00023	-0.00002	0.00025	0	0	0
3 c	0.00016	0	0.00016	0	0	0
4 c	-0.0001	0.00001	-0.0002	0	0	0
5 o	0.04681	0.00476	0.04173	0.00033	0	0
6 o	0.00043	0.00034	0.00008	0	0	0
7 c	-0.0021	-0.0008	-0.0016	0.00031	0	0
8 c	0.00715	0.0018	0.00535	0	0	0
9 cu	0.7874	-0.0071	-0.0075	0.802	0.00001	0
10 o	0.06375	0.00493	0.05857	0.00026	0	0
11 o	0.00014	0.00059	-0.0005	0	0	0
12 o	-0.0005	-0.0001	-0.0004	0	0	0
13 n	0.05246	0.0084	0.04367	0.00039	0	0
14 n	-0.0006	0	-0.0006	0	0	0
15 c	-0.007	-0.0011	-0.006	0.00009	0	0
16 c	0.00583	0.00088	0.00495	0	0	0
17 c	-0.0041	-0.00009	-0.004	0	0	0
18 c	0.0006	-0.00001	0.00062	-0.00001	0	0
19 c	-0.0008	-0.00006	-0.0007	0	0	0
20 c	0.00031	0	0.00031	0	0	0
21 c	-0.0054	-0.0011	-0.005	0.0007	0	0
22 c	0.00935	0.00224	0.00711	0	0	0

23 o	0.0001	0	0.00011	0	0	0
24 o	0.00004	-0.00001	0.00004	0	0	0
25 c	0.00009	0.00003	0.00006	0	0	0
26 c	-0.0004	-0.00002	-0.0004	0	0	0
27 c	-0.0077	-0.0013	-0.0065	0.00009	0	0
28 c	0.00566	0.00083	0.00484	0	0	0
29 c	-0.0007	-0.00005	-0.0007	0	0	0
30 c	0.00029	0	0.00029	0	0	0
31 o	-0.0004	-0.0002	-0.0002	0	0	0
32 n	0.05027	0.00738	0.04247	0.00042	0	0
33 n	-0.0006	0	-0.0006	0	0	0
34 c	0.0003	0	0.0003	0	0	0
35 c	-0.0007	-0.00004	-0.0007	0	0	0
36 c	0.00063	0	0.00064	-0.00001	0	0
37 c	-0.0039	-0.00004	-0.0039	0	0	0
38 c	0.00562	0.00083	0.0048	0	0	0
39 c	-0.0065	-0.0011	-0.0055	0.0001	0	0
40 c	0.00032	0.00001	0.00032	0	0	0
41 c	-0.0008	-0.00005	-0.0007	0	0	0
42 c	0.00565	0.00087	0.00479	-0.00001	0	0
43 c	-0.0072	-0.0012	-0.0061	0.00009	0	0
44 h	-0.00002	-0.00002	0	0	0	0
45 h	0	0	0	0	0	0
46 h	-0.00009	-0.0001	0.00002	0	0	0
47 h	0.00001	-0.00001	0.00003	0	0	0
48 h	-0.00008	-0.00008	0	0	0	0
49 h	-0.0002	-0.0002	0	0	0	0
50 h	0.00155	0.00156	-0.00001	0	0	0
51 h	0.0002	0.0002	0	0	0	0
52 h	0	0	0	0	0	0
53 h	0	0	0	0	0	0
54 h	-0.0002	-0.0002	0.00001	0	0	0
55 h	-0.0001	-0.0001	0.00001	0	0	0
56 h	-0.00005	-0.00005	0	0	0	0
57 h	0.00011	0.0001	0	0	0	0
58 h	0.00155	0.00157	-0.00001	0	0	0
59 h	0.00018	0.00018	0	0	0	0
60 h	-0.00001	-0.00001	0	0	0	0
61 h	0	0	0	0	0	0
62 h	-0.00006	-0.00005	0	0	0	0
63 h	-0.0002	-0.0002	0	0	0	0
64 h	0	0	0	0	0	0
65 h	0	0	0	0	0	0
66 h	0.00018	0.00018	0	0	0	0

67 h	0.00146	0.00147	-0.00001	0	0	0
68 h	0	0	0	0	0	0
69 h	-0.00001	-0.00001	0	0	0	0
70 h	0.00014	0.00013	0	0	0	0
71 h	0.00174	0.00175	-0.00001	0	0	0
72 h	-0.00001	-0.00001	0	0	0	0
73 h	-0.00001	-0.00001	0	0	0	0
74 o	0.00003	0	0.00003	0	0	0
75 c	-0.00001	0	-0.00001	0	0	0
76 c	-0.00001	0	-0.00001	0	0	0
77 c	0	0	0	0	0	0
78 c	0	0	0	0	0	0
79 c	0	0	0	0	0	0
80 c	0	0	0	0	0	0
81 o	0	0	0	0	0	0
82 c	0	0	0	0	0	0
83 c	0	0	0	0	0	0
84 c	0	0	0	0	0	0
85 c	0	0.00001	0	0	0	0
86 o	-0.00003	0	-0.00003	0	0	0
87 n	-0.00003	0	-0.00003	0	0	0
88 c	-0.00009	-0.00002	-0.00007	0	0	0
89 h	-0.00001	-0.00001	0	0	0	0
90 h	0	0	0	0	0	0
91 h	0	0	0	0	0	0
92 h	0	0	0	0	0	0
93 h	0	0	0	0	0	0
94 h	0	0	0	0	0	0
95 h	0	0	0	0	0	0
96 h	0	0	0	0	0	0
97 h	0	0	0	0	0	0
98 h	0	0	0	0	0	0
99 h	0	0	0	0	0	0
100 h	-0.00002	-0.00002	0	0	0	0
101 h	-0.00003	-0.00003	0	0	0	0
102 h	-0.00006	-0.00006	0	0	0	0
103 h	-0.00007	-0.00007	0	0	0	0

**Table 2.25:** NBO analysis of trifluralin $\subset$ 2.1.

atomic populations from spin density

atom	sum	n(s)	n(p)	n(d)	n(f)	n(g)
1 o	0.00013	-0.00001	0.00013	0	0	0
2 o	0.00026	-0.00001	0.00027	0	0	0

3 c	0.00017	0.00001	0.00016	0	0	0
4 c	-0.0003	-0.0001	-0.0002	0	0	0
5 o	0.05	0.00434	0.04541	0.00025	0	0
6 o	-0.0005	0.00051	-0.001	0	0	0
7 c	-0.0029	-0.001	-0.0025	0.00054	0	0
8 c	0.00754	0.00188	0.00565	0.00001	0	0
9 cu	0.7869	-0.0072	-0.0072	0.80124	0.00001	0
10 o	0.06006	0.00459	0.05523	0.00024	0	0
11 o	-0.0003	0.00045	-0.0008	0	0	0
12 o	-0.0006	-0.0001	-0.0005	0	0	0
13 n	0.05161	0.00897	0.04237	0.00028	0	0
14 n	-0.0006	0	-0.0006	0	0	0
15 c	-0.0069	-0.0011	-0.0058	0.00008	0	0
16 c	0.00552	0.00083	0.00469	0	0	0
17 c	-0.0039	-0.00007	-0.0038	0	0	0
18 c	0.0006	-0.00001	0.00062	-0.00001	0	0
19 c	-0.0007	-0.00005	-0.0007	0	0	0
20 c	0.0003	0	0.0003	0	0	0
21 c	-0.0043	-0.0012	-0.0039	0.00074	0	0
22 c	0.00915	0.00225	0.00689	0.00001	0	0
23 o	0.00008	0	0.00009	0	0	0
24 o	0.00004	0	0.00004	0	0	0
25 c	0.00007	0.00003	0.00004	0	0	0
26 c	-0.0003	-0.00004	-0.0003	0	0	0
27 c	-0.0071	-0.0011	-0.0062	0.00009	0	0
28 c	0.00536	0.0008	0.00457	0	0	0
29 c	-0.0007	-0.00004	-0.0007	0	0	0
30 c	0.00029	0	0.00029	0	0	0
31 o	-0.0005	-0.0002	-0.0003	0	0	0
32 n	0.05294	0.00807	0.04458	0.00028	0	0
33 n	-0.0006	0	-0.0006	0	0	0
34 c	0.00031	0	0.00031	0	0	0
35 c	-0.0007	-0.00004	-0.0007	0	0	0
36 c	0.00065	0	0.00066	-0.00001	0	0
37 c	-0.004	-0.00005	-0.004	0	0	0
38 c	0.0057	0.00086	0.00485	-0.00001	0	0
39 c	-0.0069	-0.0011	-0.0059	0.00009	0	0
40 c	0.00032	0.00001	0.00032	0	0	0
41 c	-0.0008	-0.00004	-0.0007	0	0	0
42 c	0.0058	0.00091	0.0049	-0.00001	0	0
43 c	-0.0073	-0.0011	-0.0062	0.00008	0	0
44 h	-0.00007	-0.00007	0	0	0	0
45 h	0.00001	0.00001	0	0	0	0



46 h	0.00049	0.00047	0.00002	0	0	0
47 h	-0.0002	-0.0002	0	0	0	0
48 h	-0.00002	-0.00001	0	0	0	0
49 h	-0.0002	-0.0002	0	0	0	0
50 h	0.00139	0.0014	-0.00001	0	0	0
51 h	0.00016	0.00016	0	0	0	0
52 h	-0.00001	-0.00001	0	0	0	0
53 h	0	0	0	0	0	0
54 h	-0.0002	-0.0002	0.00001	0	0	0
55 h	-0.00009	-0.0001	0.00001	0	0	0
56 h	-0.00006	-0.00006	0	0	0	0
57 h	0.0001	0.0001	0	0	0	0
58 h	0.00135	0.00136	-0.00001	0	0	0
59 h	0.00015	0.00015	0	0	0	0
60 h	-0.00001	-0.00001	0	0	0	0
61 h	0	0	0	0	0	0
62 h	-0.0001	-0.00009	0	0	0	0
63 h	-0.0002	-0.0002	0	0	0	0
64 h	0	0	0	0	0	0
65 h	0	0	0	0	0	0
66 h	0.00017	0.00016	0	0	0	0
67 h	0.00155	0.00156	-0.00001	0	0	0
68 h	0	0	0	0	0	0
69 h	-0.00001	-0.00001	0	0	0	0
70 h	0.00013	0.00013	0	0	0	0
71 h	0.00171	0.00172	-0.00001	0	0	0
72 h	0	0	0	0	0	0
73 h	-0.00001	-0.00001	0	0	0	0
74 o	0	0	0	0	0	0
75 o	0	0	0	0	0	0
76 n	0	0	0	0	0	0
77 n	0	0	0	0	0	0
78 o	0.00001	0	0.00001	0	0	0
79 o	0	0	0	0	0	0
80 c	0	0	0	0	0	0
81 c	0	0	0	0	0	0
82 c	0	0	0	0	0	0
83 c	0	0	0	0	0	0
84 c	0	0	0	0	0	0
85 c	0	0	0	0	0	0
86 n	0	0	0	0	0	0
87 c	0	0	0	0	0	0
88 c	0	0	0	0	0	0
89 c	0	0	0	0	0	0

---

90 c	0	0	0	0	0	0
91 c	0	0	0	0	0	0
92 c	0	0	0	0	0	0
93 c	0	0	0	0	0	0
94 f	0	0	0	0	0	0
95 f	0	0	0	0	0	0
96 f	0	0	0	0	0	0
97 h	0	0	0	0	0	0
98 h	0	0	0	0	0	0
99 h	0	0	0	0	0	0
100 h	0	0	0	0	0	0
101 h	0	0	0	0	0	0
102 h	0	0	0	0	0	0
103 h	0	0	0	0	0	0
104 h	0	0	0	0	0	0
105 h	0	0	0	0	0	0
106 h	0	0	0	0	0	0
107 h	0	0	0	0	0	0
108 h	0	0	0	0	0	0
109 h	0	0	0	0	0	0
110 h	0	0	0	0	0	0
111 h	0	0	0	0	0	0
112 h	0	0	0	0	0	0

---

The crystal structure of the Cd–MOF with the same ligands is reported in the literature and has been obtained from the Cambridge Structural Database (CSD).<sup>2,48</sup> The immediate coordination of the Cd–MOF was optimized (**Table 2.26** for coordinates) and further examined with dicofol, which primarily showed weak/no  $\pi$ – $\pi$  interaction with Cd–MOF (**Table 2.27** for coordinates). This shows the role of the central metal ion in making the skeleton of MOF **2.1** an effective chemosensor.

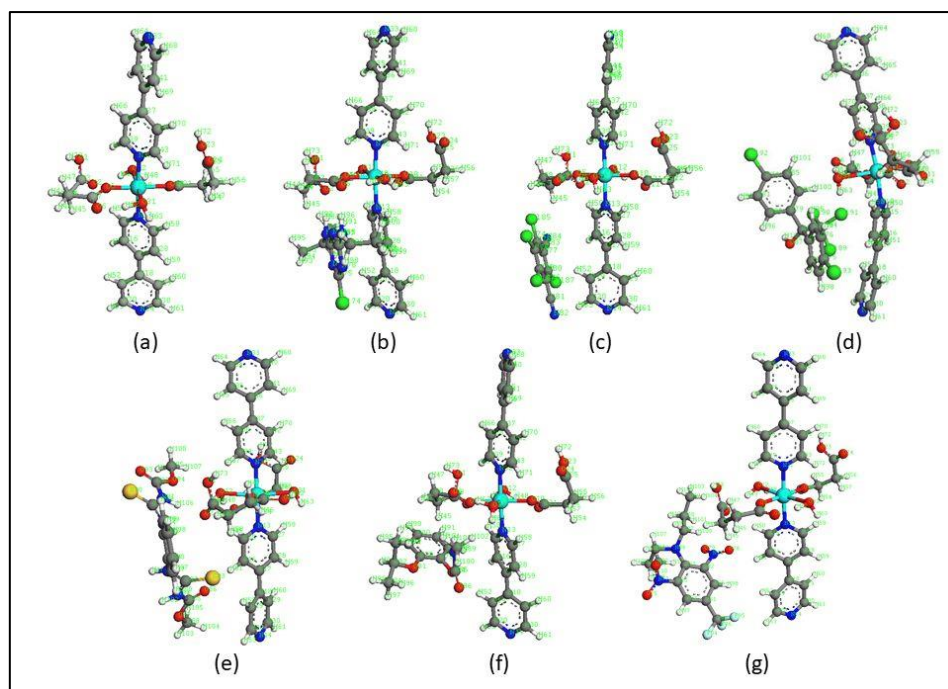


**Figure 2.8:** Atom numbering scheme of (a) **2.1**; (b) atrazine  $\subset$  **2.1**; (c) chlorothalonil  $\subset$  **2.1**; (d) dicofol  $\subset$  **2.1**; (e) thiophanate-methyl  $\subset$  **2.1**; (f) propoxur  $\subset$  **2.1**; (g) trifluralin  $\subset$  **2.1**.

**Table 2.26:** Geometry optimized coordinates of Cd-MOF.

Cd	11.7058	-6.8302	9.19586	O	11.6784	-4.6553	8.35086
O	11.7283	-4.7314	10.5647	O	12.7294	-0.0022	10.0688
O	11.06	0.33174	11.5227	N	9.36235	-6.7919	9.28463
C	8.62818	-6.1803	8.34536	C	7.24029	-6.1054	8.41115
C	6.56803	-6.6888	9.49845	C	7.35317	-7.3265	10.4738
C	8.73721	-7.3541	10.3304	C	11.6999	-4.0865	9.49129
C	11.7172	-2.5667	9.4867	C	11.6008	-1.9328	10.87
C	11.7388	-0.4299	10.8676	N	2.27912	-6.5248	9.83387
C	2.96759	-5.547	9.2327	C	4.35707	-5.5535	9.09473
C	5.09078	-6.6329	9.61286	C	4.36668	-7.6565	10.2451
C	2.97636	-7.5561	10.3258	O	11.7313	-8.3864	11.093
O	11.6823	-7.017	6.56244	O	11.6894	-9.1741	9.02477
N	14.0458	-6.7883	9.23226	N	21.1455	-6.5595	9.54066
C	20.4977	-6.5229	8.36997	C	19.1066	-6.5598	8.25619
C	18.327	-6.6445	9.42114	C	19.0088	-6.6846	10.6481
C	20.4042	-6.6375	10.6525	C	14.7488	-6.1234	8.30558
C	16.1379	-6.052	8.32615	C	16.8465	-6.6916	9.35746
C	16.0938	-7.3767	10.3261	C	14.7058	-7.4013	10.2268
O	12.6481	-12.542	13.9579	O	11.2246	-13.108	12.3701
C	11.9895	-12.284	12.8149	C	12.2628	-10.935	12.1893
C	11.6514	-10.777	10.8049	C	11.7044	-9.3529	10.2769
O	13.1516	-1.8294	6.36879	O	10.9597	-2.1183	5.98843
O	12.1185	-6.952	4.52773	C	12.0889	-2.5529	5.98852

C	12.491	-3.9479	5.5757	C	11.2743	-4.8743	5.456
C	11.6869	-6.305	5.52346	H	9.17093	-5.7387	7.50806
H	6.6951	-5.6118	7.60587	H	6.90091	-7.782	11.3555
H	9.37697	-7.8348	11.0749	H	12.6566	-2.2626	8.99975
H	12.3974	-2.3326	11.5208	H	10.9121	-2.2253	8.81665
H	10.6442	-2.1782	11.3507	H	2.38811	-4.7046	8.83816
H	4.85429	-4.713	8.60764	H	4.86811	-8.5357	10.6534
H	2.40287	-8.3541	10.8111	H	21.1138	-6.4642	7.46555
H	18.6463	-6.545	7.2667	H	18.4687	-6.7302	11.5955
H	20.944	-6.6613	11.606	H	14.1741	-5.6236	7.52421
H	16.6544	-5.4829	7.55235	H	16.5776	-7.9062	11.1478
H	14.091	-7.9234	10.9641	H	11.8602	-10.162	12.8665
H	10.5873	-11.067	10.8377	H	13.3539	-10.771	12.1653
H	12.1272	-11.445	10.0726	H	13.0506	-3.8828	4.62841
H	10.7402	-4.704	4.50894	H	13.191	-4.3106	6.3389
H	10.6019	-4.6731	6.299	H	12.8476	-0.9334	6.60456
H	13.2281	-11.803	14.205	H	12.7734	0.96992	10.1317

**Table 2.27:** coordinates of dicofol-Cd-MOF.

Cd	11.1357	-6.6077	8.945981	O	10.8546	-4.5047	9.69684
O	12.2577	-5.1953	11.29057	O	13.8027	-0.6472	10.5897
O	13.2991	-0.3376	12.75136	N	8.70771	-6.989	8.6645
C	8.273	-7.4875	7.498619	C	7.09142	-8.2222	7.39776
C	6.32988	-8.4666	8.551394	C	6.7874	-7.9182	9.76085
C	7.97099	-7.1851	9.766966	C	11.6198	-4.3065	10.702
C	11.7428	-2.8544	11.16947	C	13.1204	-2.5639	11.7941
C	13.4113	-1.0873	11.80984	N	2.8542	-10.992	8.39586
C	3.12161	-10.122	7.413915	C	4.23132	-9.2739	7.41693
C	5.11472	-9.3127	8.505165	C	4.83676	-10.222	9.53754
C	3.70517	-11.033	9.43023	O	10.6493	-8.2032	10.6513
O	11.0949	-6.3468	6.696478	O	11.0282	-9.1237	8.66794
N	13.4784	-6.8808	8.674689	N	20.2738	-8.6921	7.62303
C	19.2731	-9.3595	7.035463	C	17.9253	-9.0363	7.20472
C	17.5772	-7.9606	8.037969	C	18.6289	-7.2651	8.65661
C	19.9447	-7.6667	8.418408	C	13.8705	-7.4059	7.5041
C	15.1907	-7.771	7.256851	C	16.1607	-7.5791	8.25557
C	15.7336	-7.0108	9.467205	C	14.3914	-6.6759	9.63491
O	8.33142	-12.159	13.13315	O	7.24383	-11.003	11.604
C	8.30366	-11.273	12.12193	C	9.62641	-10.643	11.7363
C	9.75959	-10.399	10.23849	C	10.5718	-9.1716	9.8366
O	13.751	-2.5999	8.520954	O	11.8622	-1.5964	7.86313
O	9.81953	-5.4939	5.07963	C	12.6135	-2.55	7.81385
C	12.3953	-3.7877	6.984622	C	10.9539	-3.9506	6.51486

C	10.5949	-5.3661	6.039033	H	8.90889	-7.3053	6.6277
H	6.80778	-8.6572	6.439145	H	6.23568	-8.0667	10.6896
H	8.36346	-6.7677	10.69661	H	11.5401	-2.1947	10.3147
H	13.8966	-3.0681	11.20095	H	10.9441	-2.6597	11.9053
H	13.1715	-2.9441	12.82196	H	2.42112	-10.097	6.57128
H	4.39763	-8.5903	6.582113	H	5.52342	-10.346	10.3762
H	3.48175	-11.759	10.22066	H	19.551	-10.206	6.39771
H	17.161	-9.6347	6.705754	H	18.4361	-6.4047	9.29969
H	20.7704	-7.1294	8.89883	H	13.0926	-7.5072	6.74372
H	15.4568	-8.1841	6.28285	H	16.4302	-6.8468	10.2906
H	14.0164	-6.2141	10.55132	H	9.65718	-9.6682	12.2534
H	8.74979	-10.211	9.83523	H	10.4676	-11.239	12.1241
H	10.1458	-11.278	9.710796	H	13.0954	-3.7413	6.13073
H	10.7019	-3.2328	5.72157	H	12.715	-4.6497	7.58225
H	10.2903	-3.7346	7.368835	H	13.8211	-1.782	9.06222
H	9.24254	-12.328	13.42329	H	13.9331	0.31896	10.6176
C	9.80637	-14.207	10.49494	C	4.61609	-15.09	5.67654
C	5.91814	-15.585	5.791145	C	6.92984	-14.737	6.24497
C	6.65303	-13.403	6.573826	C	8.55729	-13.185	8.20599
C	7.81663	-13.483	9.362798	C	8.42537	-13.996	10.5035
C	4.31625	-13.767	6.009132	C	5.34095	-12.93	6.45236
C	9.92769	-13.47	8.202233	C	10.5588	-13.974	9.34552
C	7.74736	-12.475	7.102914	O	7.09117	-11.378	7.694
C	8.60452	-11.873	5.913846	Cl	7.51624	-11.007	4.77091
Cl	9.76254	-10.673	6.598079	Cl	9.48747	-13.119	4.97214
Cl	10.6007	-14.723	11.9723	Cl	3.33561	-16.153	5.12521
H	6.13555	-16.625	5.542699	H	7.94234	-15.13	6.34485
H	6.74673	-13.274	9.384814	H	7.8437	-14.189	11.4045
H	3.29338	-13.395	5.934902	H	5.11622	-11.9	6.72001
H	10.5439	-13.275	7.328536	H	11.6337	-14.16	9.34138
H	7.75979	-10.805	8.099101				

## 2.4 Conclusions

The DFT-D3 analysis established the utility of MOF-based structurally rigid and less flexible architectures toward their applications in supramolecular noncovalent interactions. Geometry-optimized structures of a series of different organochlorine-, benzamide-, carbamate-, or organofluorine based guests with **2.1** have been studied. The advantage of the Cu<sup>2+</sup>-MOF with aliphatic acid and 4,4'-bipyridine over its analogue of Cd<sup>2+</sup> was established. The aromatic rings of bipyridine actually target the guest via a  $\pi$ - $\pi$  interaction, whereas the uncoordinated oxygen from the succinate dianion acts as an antenna toward different guests possessing secondary -NH or -OH moieties. The outcome of DFT studies clearly reveals that the coordinated water plays a role in the structural stability of the host framework by a

hydrogen-bonding interaction with the adjacent uncoordinated oxygen of succinic acid. It acts as a structural cofactor toward the better stabilization of the host framework. On the contrary, the uncoordinated oxygen is the key factor for the noncovalent interaction between the host and the guest. Our group is actively engaged in the field of using MOFs as a receptor for versatile guest entities, and we expect several significant outcomes in the near future.

## 2.5 References

- 2.1 S. Shimomura, S. Kitagawa, *J. Mater. Chem.* **2011**, *21*, 5537–5546.
- 2.2 H-C. Zhou, S. Kitagawa, *Chem. Soc. Rev.* **2014**, *43*, 5415–5418.
- 2.3 J. A. Mason, M. Veenstra, J. R. Long, *Chem. Sci.* **2014**, *5*, 32–51.
- 2.4 S. Chaemchuen, N. A. Kabir, K. Zhou, F. Verpoort, *Chem. Soc. Rev.* **2013**, *42*, 9304–9332.
- 2.5 J. Liu, P. K. Thallapally, B. P. McGrail, D. R. Brown, J. Liu, *Chem. Soc. Rev.* **2012**, *41*, 2308–2322.
- 2.6 K. Sumida, D. L. Rogow, J. A. Mason, T. M. McDonald, E. D. Bloch, Z. R. Herm, T.-H. Bae, J. R. Long, *Chem. Rev.* **2012**, *112*, 724–781.
- 2.7 E. Barea, C. Montoro, J. A. R. Navarro, *Chem. Soc. Rev.* **2014**, *43*, 5419–5430.
- 2.8 L. E. Kreno, K. Leong, O. K. Farha, M. Allendorf, R. P. Van Duyne, J. T. Hupp, *Chem. Rev.* **2012**, *112*, 1105–1125.
- 2.9 S. Halder, J. Mondal, J. Ortega-Castro, A. Frontera, P. Roy, *Dalton Trans.* **2017**, *46*, 1943–1950.
- 2.10 M. Eddaoudi, D. F. Sava, J. F. Eubank, K. Adil, V. Guillerme, *Chem. Soc. Rev.* **2015**, *44*, 228–249.
- 2.11 J. Liu, L. Chen, H. Cui, J. Zhang, L. Zhang, C. Y. Su, *Chem. Soc. Rev.* **2014**, *43*, 6011–6061.
- 2.12 T. Zhang, W. Lin, *Chem. Soc. Rev.* **2014**, *43*, 5982–5993.
- 2.13 A. Dhakshinamoorthy, H. Garcia, *Chem. Soc. Rev.* **2014**, *43*, 5750–5765.
- 2.14 S. H. A. M. Leenders, R. Gramage-Doria, B. De Bruin, J. N. H. Reek, *Chem. Soc. Rev.* **2015**, *44*, 433–448.
- 2.15 D. Aulakh, L. Liu, J. R. Varghese, H. Xie, T. Islamoglu, K. Duell, C.-W. Kung, C.-E. Hsiung, Y. Zhang, R.J. Drout, O.K. Farha, K.R. Dunbar, Y. Yu Han, M. Wriedt, *J. Am. Chem. Soc.* **2019**, *141*, 2997–3005.
- 2.16 J. Castells-Gil, J.J. Baldoví, C. Martí-Gastaldo, G.M. Espallargas, *Dalton Trans.* **2018**, *47*, 14734–14740.

- 2.17 D. Aulakh, H. Xie, Z. Shen, A. Harley, X. Zhang, A.A. Yakovenko, K.R. Dunbar, M. Wriedt, *Inorg. Chem.* **2017**, *56*, 6965–6972.
- 2.18 P. Mahata, C. M. Draznieks, P. Roy, S. Natarajan, *Cryst. Growth Des.* **2013**, *13*, 155–168.
- 2.19 B. Dutta, A. Dey, C. Sinha, P.P. Ray, M.H. Mir, *Dalton Trans.* **2019**, *48*, 11259–11267.
- 2.20 S. Halder, A. Dey, A. Bhattacharjee, J. Ortega-Castro, A. Frontera, P.P. Ray, P. Roy, *Dalton Trans.* **2017**, *46*, 11239–11249.
- 2.21 S. Halder, A. Layek, K. Ghosh, C. Rizzoli, P.P. Ray, P. Roy, *Dalton Trans.* **2015**, *44*, 16149–16155.
- 2.22 A. A. Talin, A. Centrone, A. C. Ford, M. E. Foster, V. Stavila, P. Haney, R. A. Kinney, V. Szalai, F. E. Gabaly, H. P. Yoon, F. Léonard, M. D. Allendorf, *Science* **2014**, *343*, 66–70.
- 2.23 Stavila, V.; Talin, A. A.; Allendorf, M. D. MOF-Based Electronic and Opto-Electronic Devices. *Chem. Soc. Rev.* **2014**, *43*, 5994–6010.
- 2.24 H.R. Fu, N. Wang, J.-H. Qin, M.-L. Han, L.-F. Ma, F. Wang, *Chem. Commun.* **2018**, *54*, 11645–11648.
- 2.25 Y. Zhao, L. Wang, N.-N. Fan, M.-L. Han, G.-P. Yang, L.-F. Ma, *Cryst. Growth Des.* **2018**, *18*, 7114–7121.
- 2.26 Z. Chen, S. Zhang, S. Zhang, Q. Sun, Y. Xiao, K. Wang, *ChemPlusChem* **2019**, *84*, 190–202.
- 2.27 Y. Guo, X. Feng, T. Han, S. Wang, Z. Lin, Y. Dong, B. Wang, *J. Am. Chem. Soc.* **2014**, *136*, 15485–15488.
- 2.28 Z.-W. Zhai, S.-H. Yang, M. Cao, L.-K. Li, C.-X. Du, S.-Q. Zang, *Cryst. Growth Des.* **2018**, *18*, 7173–7182.
- 2.29 S. Senthilkumar, R. Goswami, V.J. Smith, H.C. Bajaj, S. Neogi, *ACS Sustainable Chem. Eng.* **2018**, *6*, 10295–10306.
- 2.30 W. P. Lustig, S. Mukherjee, N. D. Rudd, A. V. Desai, J. Li, S. K. Ghosh, *Chem. Soc. Rev.* **2017**, *46*, 3242–3285.
- 2.31 H. Halder, P. Ghosh, C. Rizzoli, P. Banerjee, P. Roy, *Polyhedron* **2017**, *123*, 217–225.
- 2.32 S. Mukherjee, A. V. Desai, B. Manna, A. I. Inamdar, S. K. Ghosh, *Cryst. Growth Des.* **2015**, *15*, 4627–4634.

- 2.33 L. H. Cao, F. Shi, W. M. Zhang, S. Q. Zang, T. C. W. Mak, *Chem. Eur. J.* **2015**, *21*, 15705–15712.
- 2.34 J. Ye, L. Zhao, R. F. Bogale, Y. Gao, X. Wang, X. Qian, S. Guo, J. Zhao, G. Ning, *Chem. Eur. J.* **2015**, *21*, 2029–2037.
- 2.35 K. He, Z. Li, L. Wang, Y. Fu, H. Quan, Y. Li, X. Wang, S. Gunasekaran, X. Xu, *ACS Appl. Mater. Interfaces* **2019**, DOI: 10.1021/acsami.9b06151.
- 2.36 K. Vikrant, D.C.W. Tsang, N. Raza, B.S. Giri, D. Kukkar, K.-H. Kim, *ACS Appl. Mater. Interfaces* **2018**, *10*, 8797–8817.
- 2.37 Q. Yang, J. Wang, X. Chen, W. Yang, H. Pei, N. Hu, Z. Li, Y. Suo, T. Li, J. Wang, *J. Mater. Chem. A* **2018**, *6*, 2184–2192.
- 2.38 P. Raj, A. Singh, K. Kaur, T. Aree, A. Singh, N. Singh, *Inorg. Chem.* **2016**, *55*, 4874–4883.
- 2.39 B. H. M. Hussein, G. M. Khairy, R. M. Kamel, *Spectrochim. Acta A* **2016**, *158*, 34–42.
- 2.40 L. Wen, X. Xu, K. Lv, Y. Huang, X. Zheng, L. Zhou, R. Sun, D. Li, *ACS Appl. Mater. Interfaces* **2015**, *7*, 4449–4455.
- 2.41 J. Hou, J. Dong, H. Zhu, X. Teng, S. Ai, M. Mang, *Biosens. Bioelectron.* **2015**, *68*, 20–26.
- 2.42 S. S. Nagarkar, A. V. Desai, S. K. Ghosh, *CrystEngComm* **2016**, *18*, 2994–3007.
- 2.43 APEX-II, SAINT and SADABS, Bruker AXS Inc., Madison, WI, **2008**.
- 2.44 G. M. Sheldrick, *Acta Crystallogr., Sect. A: Fundam. Crystallogr.* **2015**, *71*, 3.
- 2.45 G. M. Sheldrick, *Acta Crystallogr., Sect. C: Cryst. Struct. Commun.* **2015**, *71*, 3.
- 2.46 S.-T. Wu, Y.-R. Wu, Q.-Q. Kang, H. Zhang, L.-S. Long, Z. Zheng, R.-B. Huang, L.-S. Zheng, *Angew. Chem. Int. Ed.* **2007**, *46*, 8475–8479.
- 2.47 The WHO Recommended Classification of Pesticides by Hazard and Guidelines to Classification **2009**.
- 2.48 J. Zhang, Z. J. Li, Y. H. Wen, Y. Kang, J. K. Cheng, Y. G. Yao, *Z. Anorg. Allg. Chem.* **2004**, *630*, 2731–2735.



## Chapter 3

### **Synthesis and characterization of a mononuclear nickel(II) complex with N,O-donor ligand: Its DNA/HSA protein binding properties and tumor suppressive function**

#### **Abstract**

A mononuclear Ni(II) complex,  $[\text{Ni}(\text{HL})_2]\text{Cl}_2 \cdot \text{H}_2\text{O}$  (Complex **3.1**), where HL = 1-((2-piperidin-1-yl)ethylimino)methyl)naphthalene-2-ol has been synthesized under mild conditions. It has been characterized by elemental analysis, cyclic voltammetry, FT-IR, UV-vis, fluorescence and mass spectral analyses. Square planar geometry of the mononuclear complex has been confirmed by single crystal X-ray diffraction analysis. Complex **3.1** interacts with CT DNA with a binding constant of  $3.6 \times 10^3 \text{ M}^{-1}$  which suggests electrostatic interaction between the complex and DNA. The metal complex cleaves plasmid DNA efficiently in the presence of  $\text{H}_2\text{O}_2$ . On the other hand, complex **3.1** binds with the carrier protein, HSA, quite efficiently with a binding constant value of  $7.16 \times 10^5 \text{ M}^{-1}$ . Cytotoxicity of the complex has been checked with lung carcinoma (A549) and normal lung fibroblast cell lines (WI-38). From MTT assay, it has seen that the complex could inhibit the cell proliferation. Western blot analysis suggests that nickel complex is a tumor suppressor.

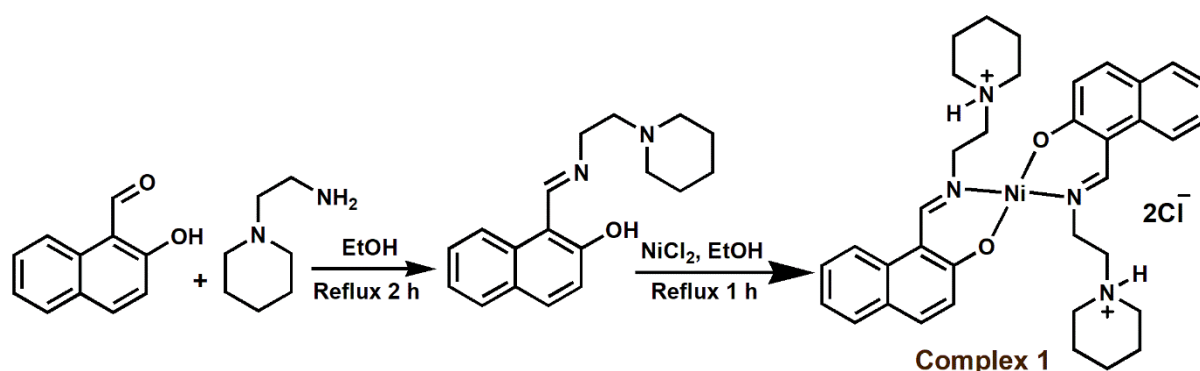
### 3.1. Introduction

Researchers of chemical, biological and medicinal sciences from all over the globe have been engaged to study different transition metal complexes and their interaction with DNA and proteins. DNA is the primary intracellular objective for effective designing of anticancer drugs.<sup>3.1</sup> To design effective metal based chemotherapeutic agents, the interaction of metal complexes with DNA has to be explored as these interactions can lead to damage DNA in cancer cells, which finally results in cell death. The metal complexes can interact with it via covalently or through non-covalent interactions, for example, intercalation, groove binding and electrostatic binding.<sup>3.2</sup> Use of *cis*-platin has been clinically successful to treat most aggressive solid tumors and thereafter, a number of different platinum-based complexes are being reported as antitumor agent. But the challenges for utility of *cis*-platin still remain due to its severe toxicity, intrinsic drug resistance and high cost.<sup>3.3</sup> Therefore, designing and development of effective, target specific, less toxic and preferably non-covalently binding metal based novel anticancer drugs can trigger the apoptosis.

Human serum albumin (HSA), the most abundant proteins, acts as the most versatile transporter and disposer of various endogenous and exogenous molecules to their target organs.<sup>3.4</sup> The lack of toxicity and immunogenicity of HSA makes it ideal for drug delivery. When a drug binds to albumin, drug solubility in plasma is increased. As a result, toxicity as well as protection against oxidation of the bound drug are decreased. However, strong interaction between albumin and small molecules results formation of a stable protein–drug complex affecting the distribution, metabolism and the efficacy of the possible drugs.<sup>3.5</sup> Thus, it is imperative and important to study interaction of albumin protein and drug molecules for evaluating the therapeutic efficacy of the drug and its delivery towards the target organs.

Among the transition metals, a rich and versatile chemistry of nickel with DNA has been supported by the existing literature.<sup>3.6</sup> Its flexible metal coordination behaviour, less toxicity and simple, inexpensive synthesis suggest that nickel(II) complexes are potential candidates for pharmaceutical applications.<sup>3.7</sup> The nickel(II) complexes with thiosemicarbazone,<sup>3.8</sup> thiocarboxamide,<sup>3.9</sup> hydrazone<sup>3.10</sup> and other ligands<sup>3.11-3.13</sup> have been reported for DNA interaction and/or cleavage. On the other hand, some metal complexes of copper and palladium have exhibited tumor suppression properties.<sup>3.14-3.17</sup> However report on antitumor activity of nickel complexes is rare.<sup>3.14</sup> But there is continuous effort to develop more efficient nickel complexes for DNA binding and cleavage.

With these backgrounds, synthesis, characterization, DNA/HSA binding and cytotoxicity properties of a mononuclear nickel(II) complex containing piperidine unit are being reported here (**Scheme 3.1**). Complex **3.1** has been synthesized under ambient conditions. Its interaction with DNA and human serum albumin has been extensively explored. Its cytotoxicity effect on several systems has been evaluated. Recently a mononuclear copper(II) complex with a Schiff-base ligand has been reported and its DNA binding, protein binding and antibacterial activities have been explored.<sup>3,18</sup> It showed effective intercalative binding and HSA could act as effective carrier of it. In continuation of the previous work, here 1-(2-aminoethyl)piperidine instead of 1-cyclohexylmethanamine has been used in anticipation to get one extra donor atom and nickel in place of copper to synthesize the complex aiming to examine the effect of these changes in its DNA and protein binding activities.



**Scheme 3.1:** Synthesis of Complex 3.1

## 3.2. Experimental Section

### 3.2.1. Materials and methods

2-Hydroxy-1-naphthaldehyde, 1-(2-aminoethyl)piperidine, nickel(II) chloride hexahydrate, Human serum albumin (HSA) and Calf thymus (CT)-DNA were obtained from Sigma Aldrich and these were used without any purification. Supercoiled PUC19 plasmid DNA was received from the biotechnology laboratory. Solvents used were purchased from different commercial sources and used as received. Elemental analysis was performed on a 2400 Series-II CHN analyzer, Perkin Elmer, USA. FT-IR spectra were obtained on a Perkin Elmer spectrometer (Spectrum Two) with the solid samples using ATR method. The UV-vis spectral analysis was performed using an Agilent 8453 diode array spectrophotometer. The ESI-MS spectra were recorded on QTOF Waters' HRMS spectrometer (Model XEVO G2QToF). Fluorescence spectra were acquired using a Horiba Fluoromax-4C spectrofluorometer. The cyclic voltammetry instrument used was a personal computer (PC)-controlled PAR model

273A electrochemistry system. A glassy carbon as working electrode, a platinum wire as auxiliary electrode and saturated Ag/AgCl as reference electrode were employed in a standard three-electrode configuration. CD spectrum was obtained utilizing a quartz cuvette of 10 mm path length in a JASCO J-815 CD spectropolarimeter.

### 3.2.2. Synthesis

#### 3.2.2.1. Synthesis of 1-((2-piperidin-1-yl)ethylimino)methylnaphthalene-2-ol (HL)

1-(2-Aminoethyl)piperidine (0.6 mmol, 85.19  $\mu\text{L}$ ) was added to an ethanol solution of 2-hydroxy-1-naphthaldehyde (0.6 mmol, 0.103 g) drop by drop under stirring condition. The stirring was continued for 15 min and the resultant mixture was refluxed for 2 h. The color of the solution turned yellow, indicating the formation of Schiff base ligand. The mixture was then cooled and collected after filtration. Yield = 0.155 g, 92%. Anal. calc. (%) for  $\text{C}_{18}\text{H}_{22}\text{N}_2\text{O}$ : C, 76.58; H, 7.85; N, 9.92. Found: C, 76.77; H, 7.96; N, 9.76.  $^1\text{H}$  NMR (300 MHz  $\text{DMSO}_d$ ;  $\delta$  ppm, TMS): 13.83 (1H, s), 9.07 (1H, s), 8.07 (1H, d,  $J = 8.4$  Hz), 7.71 (1H, d,  $J = 9.2$  Hz), 7.62 (1H, d,  $J = 7.6$  Hz), 7.42 (1H, t,  $J = 7.2$  Hz), 7.19 (1H, t,  $J = 7.2$  Hz), 6.72 (1H, d,  $J = 9.2$  Hz), 3.71 (2H, t,  $J = 3.0$  Hz), 2.76 (2H, t,  $J = 5.2$  Hz), 2.51 (4H, t,  $J = 3.0$  Hz), 1.56 (6H, m). ESI-MS ( $m/z$ ): 283.11 [(HL +  $\text{H}^+$ )].

#### 3.2.2.2. Synthesis of Complex 3.1

A solution of nickel(II) chloride hexahydrate (0.6 mmol, 0.143 g) in 10 mL of ethanol was added to 5 mL ethanol solution of HL (1.2 mmol, 0.339 g) under constant stirring condition. The mixture was stirred for another 15 min. It turned into brownish green in color. The resulting solution was then refluxed for 1 h. It was finally cooled to room temperature and the mixture was filtered to remove any undissolved material(s) and/or precipitate. The filtrate was kept under ambient condition for slow evaporation of solvent. Green single crystals of complex **3.1** suitable for X-ray diffraction study were grown within few days. Yield 0.243 g, 65%. Anal. calc. (%) for  $\text{C}_{36}\text{H}_{46}\text{N}_4\text{NiO}_2\text{Cl}_2$ : C, 60.70; H, 6.51; N, 7.86. Found: C, 60.57; H, 6.64; N, 7.95. ESI-MS ( $m/z$ ): 339.02 [(NiL) $^+$ ].

### 3.2.3. X-ray data collection and structure determination

Data collection and other related parameters for complex **3.1** are given in **Table 3.1**. Single crystal data collections were done using an automated Bruker D8 VENTURE diffractometer with graphite monochromatized Mo  $K\alpha$  radiation. The spots were considered using 10 s counting time. Unit cell parameters were determined from least-squares refinement of setting angles with  $\theta$  in the range  $2.67 \leq \theta \leq 27.091^\circ$ . Data were then processed using Bruker SAINT package.<sup>3,19</sup> Absorption corrections based on multi scans were considered to all intensity data using the SADABS software. The structures were solved by direct methods using

SHELXT<sup>3.20</sup> and refined by full-matrix least-squares techniques on F<sup>2</sup> using the SHELXS-2014/7 program.<sup>3.21</sup> The absorption corrections were carried out by the multi-scan technique. All data were then corrected for Lorentz and polarization effects. Non-hydrogen atoms were refined anisotropically.

#### 3.2.4. DNA binding and cleavage studies

The stock solution of CT-DNA was made in 5 mM Tris–HCl/50 mM NaCl buffer at pH 7.2. It showed a ratio of UV absorbance at 260 nm and 280 nm ( $A_{260}/A_{280}$ ) of about 1.8–1.9 which indicated that the DNA was adequately free of protein.<sup>3.22</sup> Its concentration was measured by using absorbance at 260 nm ( $\epsilon = 6600 \text{ M}^{-1}\text{cm}^{-1}$ ) whereas the plasmid DNA was used as it is in the wet lab for cleavage studies. Absorption titrations were performed in Tris–HCl/NaCl buffer at room temperature to determine the binding affinity of the metal complex towards CT-DNA. The effect of the presence of complex **3.1** to the EB–DNA complex was studied by recording fluorescence emission spectra with excitation at 510 nm and emission maximum at 602 nm. The DNA cleavage experiments were carried out by agarose gel electrophoresis following a published procedure.<sup>3.23</sup>

#### 3.2.5. HSA binding studies

HSA of  $1.0 \times 10^{-4} \text{ M}$  was made by dissolving the protein in Tris–HCl buffer solution (pH 7.2).<sup>3.24</sup> Concentration of the protein was evaluated in a spectrophotometer considering molar extinction coefficient as  $35,219 \text{ M}^{-1}\text{cm}^{-1}$  at 280 nm.

#### 3.2.6. MTT assay

The Lung carcinoma A549 and normal lung fibroblast WI-38 cells at a density ( $1 \times 10^4$ ) were seeded in 24 well tissue culture plate prior to treatment with complex **3.1** at concentrations of (0–200  $\mu\text{M}$ ) for 12 h. After incubation, the cells were washed using  $1 \times \text{PBS}$  twice and then they were incubated with MTT solution (450  $\mu\text{g}/\text{mL}$ ) for 3 to 4 h at 37 °C. The absorbance of the resulting formazon crystals were measured at 570 nm using a spectrophotometer and the values were compared with untreated cells.<sup>3.25</sup>

#### 3.2.7. Apoptotic nuclear morphology study by DAPI staining

To visualize nuclear changes, after exposure of complex **3.1** at LD<sub>50</sub> dose for 12 h and 24 h, cells were washed using  $1 \times \text{PBS}$  thrice and then they were stained with 4',6-diamidino-2-phenylindole (DAPI) in Vectashield ( $0.2 \text{ g mL}^{-1}$ , Vector Laboratories Inc.). Change of nuclear morphology, if any, was noticed under a fluorescence microscope (Leica).<sup>3.26</sup>

#### 3.2.8. Roles of caspase-3 in complex-induced apoptosis in A549 cells

After treatment, the whole cell lysate was extracted with a lysis buffer containing 1% Triton X-100, 50 mM sodium fluoride (NaF), 50 mM sodium chloride (NaCl), 20 mM Tris (pH

7.4), 1 mM EGTA, 1 mM EDTA, 1 mM sodium vanadate ( $\text{Na}_3\text{VO}_4$ ), 0.2 mM phenylmethanesulfonyl fluoride (PMSF), 0.5% NP-40 and protease inhibitors. Equal amounts of cell lysate (50  $\mu\text{g}$ ) were solubilized in loading buffer and then boiled for 5 min, and electrophoresized in 10 % polyacrylamide gel in Tris-glycine buffer (pH 8.3). After that, proteins were transferred to a polyvinylidenedifluoride membrane. Nonspecific binding was restricted using 5% non-fat dry milk and 0.05% Tween-20 in 20 mM Tris-Cl, pH 7.6 (TBS-T). After incubation with the suitable primary antibodies, the membranes were washed with TBS-T and were then incubated again with the respective secondary antibodies.<sup>3,25</sup>

**Table 3.1:** Crystal data of complex **3.1**

Complex	<b>3.1</b>
Formula	$\text{C}_{36}\text{H}_{48}\text{Cl}_2\text{N}_4\text{NiO}_3$
Formula weight	714.39
$T$ (K)	298(2)
Crystal color	Green
Crystal system	Triclinic
Space group	$P - 1$
$a$ (Å)	11.4177(9)
$b$ (Å)	13.2176(10)
$c$ (Å)	13.3395(11)
$\alpha$ (°)	106.450(2)
$\beta$ (°)	106.839(2)
$\gamma$ (°)	103.604(2)
$V$ (Å <sup>3</sup> )	1734.1(2)
$Z$	2
Crystal dimensions (mm)	$0.4 \times 0.2 \times 0.1$
$F(0\ 0\ 0)$	756.0
$D_c$ (g cm <sup>-3</sup> )	1.368
$\lambda$ (Mo K $\alpha$ ) (Å)	0.71073
$\theta$ Range (°)	2.67- 27.091

Complex	<b>3.1</b>
Reflection collected/ unique/observed	58157, 7626, 5962
Absorption correction	multi-scan
$R_{\text{int}}$	0.0542
Final $R_1$ index [ $I > 2\sigma(I)$ ]	0.0737
Final $wR_2$ index (all reflections)	0.1330
Goodness-of-fit	1.087

### 3.3. Results and discussion

#### 3.3.1. Synthesis and characterization

##### 3.3.1.1. Synthesis and characterization of HL

Synthesis of the ligand, 1-((2-piperidin-1-yl)ethylimino)methyl)naphthalene-2-ol (HL) has been carried out by reacting one eqv. of 2-hydroxy-1-naphthaldehyde with one eqv. of 1-(2-aminoethyl)piperidine in ethanol as depicted in **Scheme 3.1**. The ligand has been obtained in good yield and it has been characterized by ESI-mass spectrometric measurement, and FT-IR and  $^1\text{H}$  NMR spectral analysis.

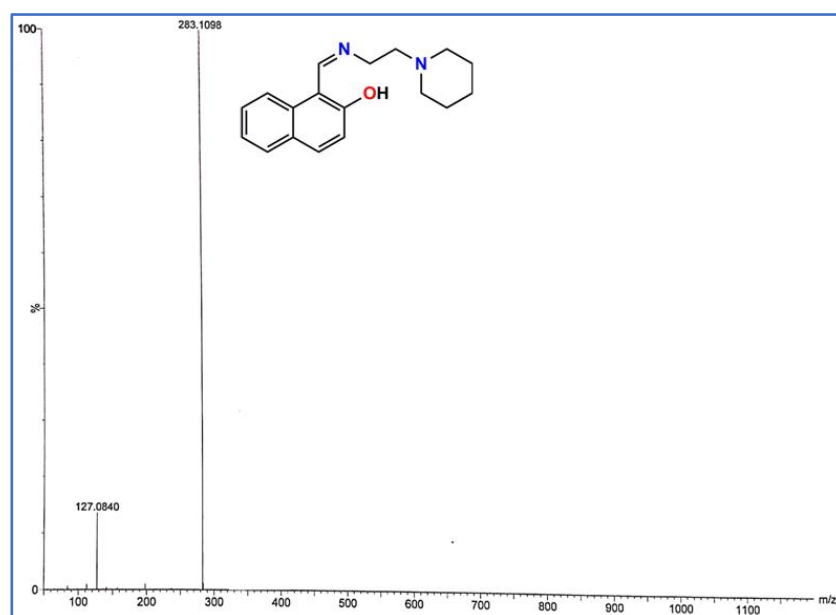


**Figure 3.1:** Mass spectrum of HL in methanol.

ESI-mass spectrometric measurement of the ligand was performed with its methanolic solution (**Figure 3.1**). ESI mass spectrum shows an  $m/z$  peak at 283.11 which may be attributed to the presence of  $[\text{HL} + \text{H}]^+$  species (calculated value: 283.18). It has been further characterized by  $^1\text{H}$  NMR spectral analysis (**Figure 3.2**). It exhibits a peak at 13.83 ppm indicating the presence of phenolic OH proton. Presence of imine proton has been indicated by the appearance of peak at 9.07 ppm. Emergence of this peak confirms the conversion of the aldehyde group into the corresponding azomethine moiety. Peaks for aromatic protons and aliphatic protons appear in their usual positions.

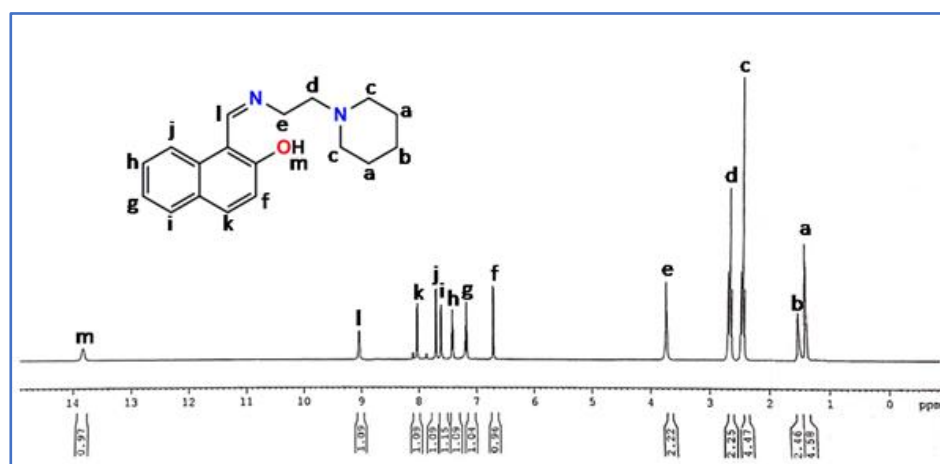


**Figure 3.2:**  $^1\text{H}$  NMR spectrum of HL in DMSO- $d_6$ .

In IR spectrum of the ligand (**Figure 3.3**) a broad absorption band has been obtained around  $3225\text{ cm}^{-1}$  which may be assigned to the O–H stretching arising from the presence of the hydroxyl group. The intense band has appeared at  $1617\text{ cm}^{-1}$  which may be attributed to the presence of the azomethine group (C=N moiety). These bands suggest the formation of the ligand.

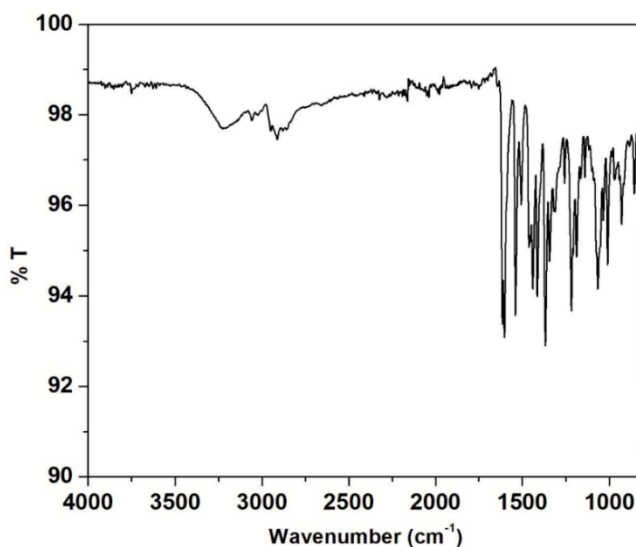


**Figure 3.3:** FT-IR NMR spectrum of HL.



### 3.3.1.2. Synthesis and characterization of complex 3.1

Complex **3.1** has been synthesized by reacting with one eqv. of nickel(II) chloride hexahydrate and two eqv. of HL in ethanol without adding any external base. Complex **3.1** has been obtained in good yield and has been characterized by several standard methods.

ESI mass spectrum of complex **3.1** shows an  $m/z$  peak at 339.02 which may be assigned to the presence of  $[\text{NiL}]^+$  fragment (calculated value: 339.10) (**Figure 3.4**). Another  $m/z$  peak at 283.11 indicates the presence of  $[\text{HL} + \text{H}]^+$  species (calculated value: 283.18) in the solution which may be fragmented from the complex.

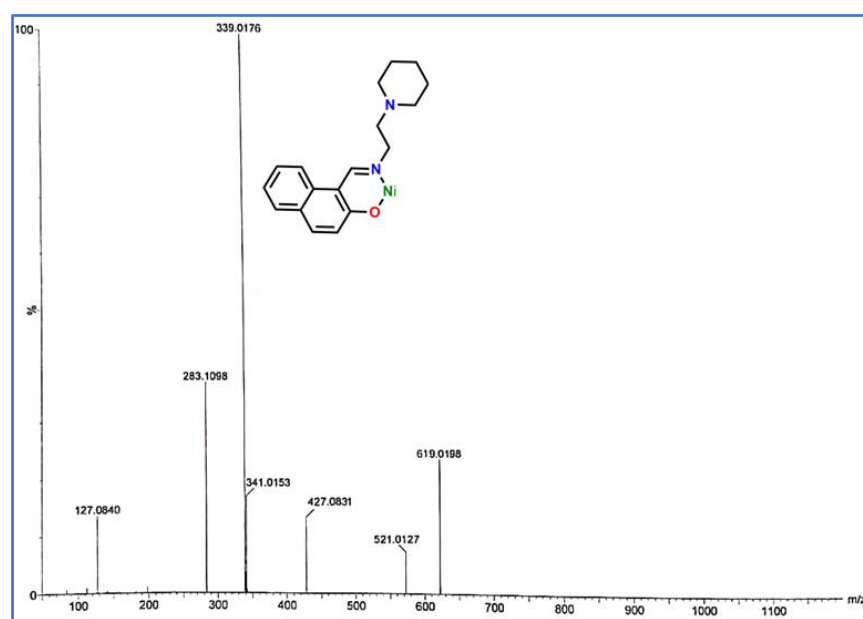


**Figure 3.4:** Mass spectrum of complex **3.1** in methanol.

In IR spectrum of the complex **3.1** (**Figure 3.5**) a broad band around  $3430\text{ cm}^{-1}$  is observed that can be assigned to the O–H stretching arising from the presence of uncoordinated water molecule. The hydrocarbon part of the complex has been evidenced by the presence of unsymmetrical and symmetrical frequencies of  $\nu_{\text{C-H}}$  observed at the region of  $2615\text{--}2958\text{ cm}^{-1}$ . In the spectrum of complex **3.1**, the intense band around  $1658\text{ cm}^{-1}$  is due to the stretching vibration of the azomethine group. The formation of Ni–N and Ni–O bonds in the complex is also shown by the appearance of the bands at  $481$  and  $541\text{ cm}^{-1}$ , respectively. The band at  $481\text{ cm}^{-1}$  may be attributed to  $\nu_{\text{Ni-N}}$  stretching frequency. The band at  $541\text{ cm}^{-1}$  may be assigned to the  $\nu_{\text{Ni-O}}$  stretching frequency.

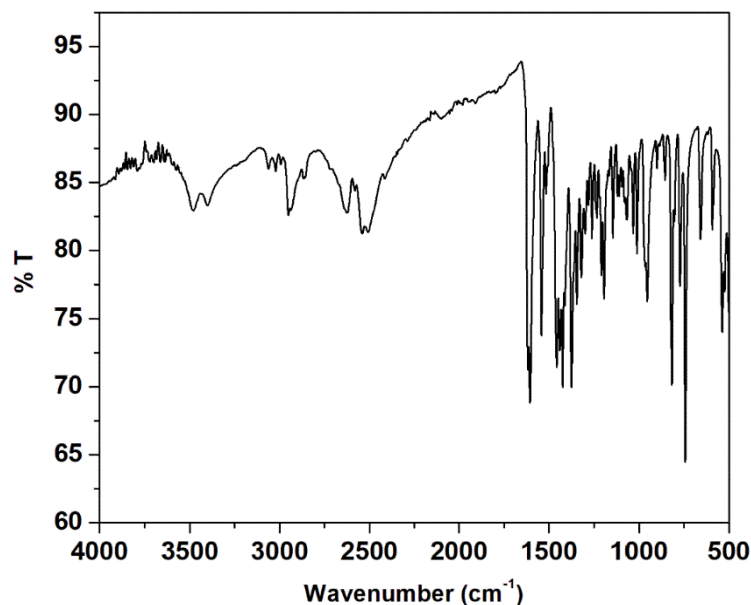


**Figure 3.5:** FT-IR NMR spectrum of complex **3.1**.

The electronic spectrum of complex **3.1** has been recorded in DMF at room temperature (**Figure 3.6**). A broad band at around 600 nm (Inset, **Figure 3.6**) has been observed for the complex which may be assigned to the  $d-d$  transition. This is weaker in intensity as it is Laporte forbidden. Moreover, the complex is almost centro-symmetric which allows very little mixing of  $d$  and  $p$  orbitals. The band at 305 nm may be assigned to  $n-\pi^*$  transitions of  $>C=N$  groups. Whereas higher intensity charge transfer transition is obtained at the wavelength 402 nm for this complex. This is attributed to  $O^-$  (of naphthalen-1-olate)  $\rightarrow Ni(II)$ ,  $N(\text{amino}) \rightarrow Ni(II)$  LMCT (transfer occurs from the MO with ligand-like character to the metal-like one) transitions.

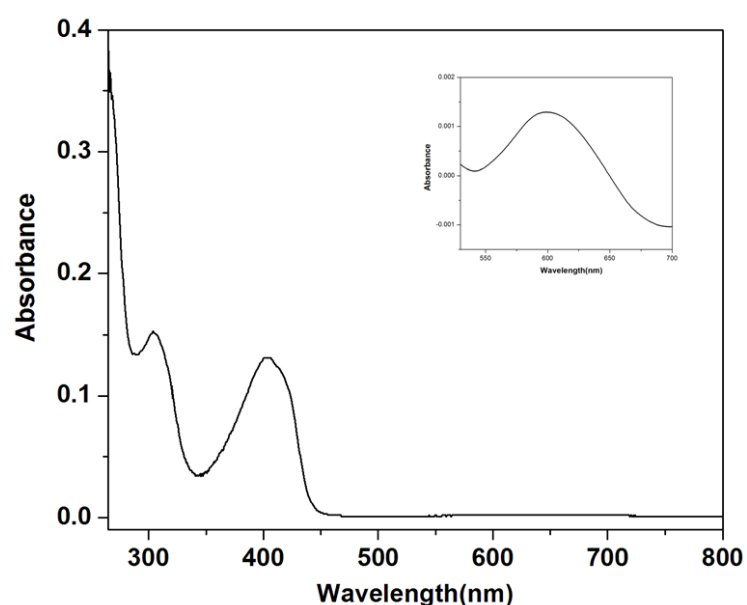


**Figure 3.6:** UV-vis spectrum of complex **3.1** in DMF at room temperature

Electrochemical studies of complex **3.1** have been carried out in DMF using TBAP as supporting electrolyte at room temperature under argon atmosphere. A typical cyclic voltammogram (CV) has been obtained by using a glassy carbon as working electrode and an Ag/AgCl reference electrode (**Figure 3.7**). As shown in the figure, cyclic voltammogram of complex **3.1** in DMF exhibits one quasi-reversible couple and one irreversible couple at  $-1.05$  and  $-1.77$  V, respectively, versus Ag/AgCl, which can be assigned to the metal-centred  $\text{Ni}^{\text{II/I}}$  and  $\text{Ni}^{\text{I/0}}$  processes, respectively.<sup>3,27</sup>

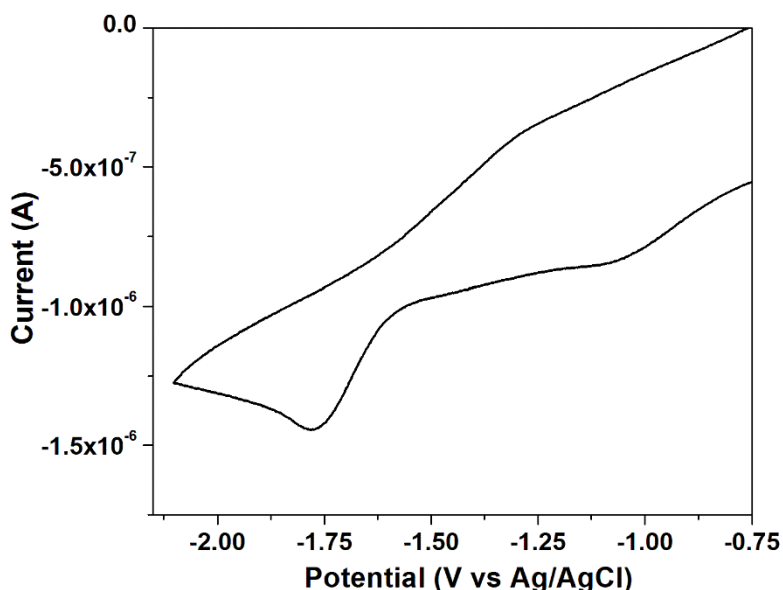


**Figure 3.7:** Cyclic voltammogram of complex **3.1** in DMF with 0.1 M of  $[\text{n-Bu}_4\text{N}](\text{ClO}_4)$  as supporting electrolyte at a scan rate of 25 mV/s. Here ferrocene is the internal standard.

### 3.3.2. Crystal structure of complex 3.1

Complex **3.1** has been obtained from ethanol and it crystallizes in the  $P-1$  space group. An ORTEP diagram of the complex is shown in **Figure 3.8**. Selected bond angles and selected bond lengths are given in **Table 3.2**. Complex **3.1** consists of two deprotonated ligands, one nickel atom, two chloride ions and one water molecule. Nickel atom is in a tetra-coordinated environment. Ni1 is coordinated to two oxygen atoms (O1 and O2) and two nitrogen atoms (N1 and N2). O1 and N1 are from one ligand while O2 and N2 are from another ligand. Both the *trans* angles of O2–Ni1–O1 and N1–Ni1–N2 are  $179.44^\circ$  and  $178.81^\circ$ , respectively and the O–Ni–N bond angles are very close to  $90^\circ$ . Houser et al. used the four-coordinate  $\tau_4$  index for the first time to find out the geometry around a metal center in its four coordination arrangement.<sup>3,28</sup> The value of  $\tau_4$  index is determined using the following formula

$$\tau_4 = \frac{360^\circ - (\alpha + \beta)}{141^\circ}$$

where  $\alpha$  and  $\beta$  are the two largest angles in the complex. For a perfect tetrahedral geometry, its value is 1.00 while  $\tau_4$  index is 0.00 for a perfect square planar geometry. The value of  $\tau_4$  index comes out as 0.004 for complex **3.1** which shows very close square planar geometry around the nickel center. The Ni–O and Ni–N bond lengths are in good agreement with the literature values.<sup>3,29</sup> It is interesting to note that complex cation is formed with two uncoordinated chloride anions. The complex cation is obtained as protonation of two of piperidine N atoms which is quite common for this type complex with other metal ions.<sup>3,30</sup>

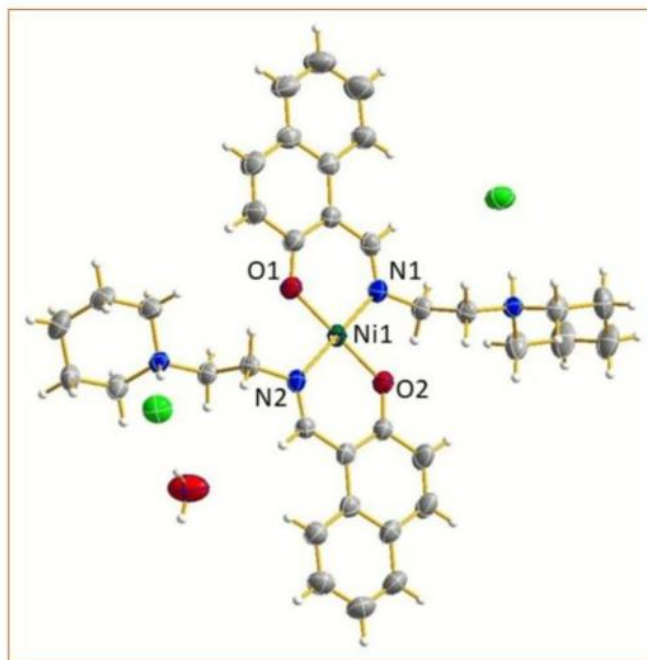


**Figure 3.8:** A perspective view of complex **3.1** with displacement ellipsoids drawn at the 50% probability level.

**Table 3.2:** selected bond length (Å) and bond angles (°)

Ni1–O2	1.830(2)
Ni1–O1	1.834(2)
Ni1–N1	1.906(2)
Ni1–N2	1.908(2)
O2–Ni1–O1	179.44(10)
O2–Ni1–N1	87.35(10)
O1–Ni1–N1	92.16(10)
O2–Ni1–N2	92.13(9)
O1–Ni1–N2	88.37(10)
N1–Ni1–N2	178.81(10)

### 3.3.3. DNA binding studies

#### 3.3.3.1. UV–visible spectral studies

For the development of effective metal based chemotherapeutic drugs, interaction of small molecules or metal complexes with DNA has been studied extensively for last few decades. It has been found that almost all the drugs are able to interact with DNA via a number of ways such as non-covalent interaction (e.g. groove binding), intercalation and non-specific electrostatic surface binding.<sup>3.24, 3.31</sup> Hence, the potential binding ability and the nature of binding of molecules with DNA are observed by using absorption spectroscopy.

The absorption spectra of complex **3.1** have been recorded in absence and in the presence of increasing amount of CT-DNA (at constant concentration of the complex) (**Figure 3.9**). On addition of increasing amounts of CT-DNA to the complex, ratio [DNA]/[Complex **3.1**] is changed as 0.0, 1.8, 3.7, 5.5, 7.3, 9.1, 10.9. The absorption band of free complex at 402 nm undergoes a slight bathochromic shift on addition of DNA and the event indicates that the binding of the metal complex with DNA occurs in a non-covalent mode. The observed hypochromic shift indicated that the complex **3.1** is in groove binding mode with CT DNA.<sup>3.32</sup> However, the nickel complex may bind with the double-helical DNA in different ways which are dependent on the structure, charge and type of ligands. It is well known that DNA has a number of hydrogen bonding sites in its major and minor grooves.<sup>3.33</sup> It is possible that azomethine group of the Schiff-base ligand forms H-bonds with the base pairs of DNA helix which may lead to partial unwinding and destabilization of the DNA double helix structure. In addition to this, the interaction between square planar complex and DNA is stronger than that between octahedral complex and DNA as in the hexacoordinated complex there is no suitable vacant coordination site where the nitrogen atom of DNA base pair can interact with metal ion. To determine the DNA binding ability of the complex, the intrinsic binding constant,  $K_b$ , has been determined using Wolfe–Shimer Equation,<sup>3.34</sup>

$$\frac{[DNA]}{(\epsilon_a - \epsilon_f)} = \frac{[DNA]}{(\epsilon_b - \epsilon_f)} + \frac{1}{K_b(\epsilon_a - \epsilon_f)}$$

where [DNA],  $\epsilon_a$ ,  $\epsilon_f$  and  $\epsilon_b$  represent the concentration of DNA, the apparent extinction coefficient ( $A_{obs}/[M]$ ), the extinction coefficient for free metal complex (M), and the extinction coefficient for the metal complex (M) in the fully bound form, respectively.  $K_b$  is calculated from the ratio of slope to intercept obtained from the plot of  $[DNA]/(\epsilon_a - \epsilon_f)$  vs. [DNA].  $K_b$  has been determined as  $3.6 \times 10^3 \text{ M}^{-1}$ . This value suggests that complex **3.1** binds with CT DNA possibly via electrostatic binding because for intercalative binding, it has been reported that the binding constants are of much higher value.<sup>3.8a,3.10a-b,3.35</sup>

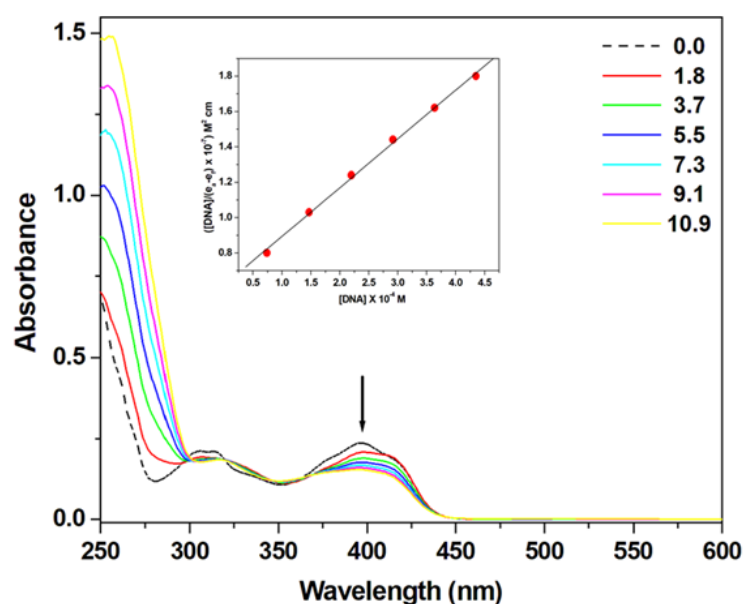


**Figure 3.9:** Absorption spectra of complex **3.1** in absence (dashed line) and in the presence (solid line) of increasing concentration of CT-DNA. [Complex **3.1**] =  $4 \times 10^{-5}$  M. The downside arrow shows the absorbance changes upon increasing the DNA concentration. Inset: linear plot for the calculation of the intrinsic DNA binding constant ( $K_b$ ).

### 3.3.3.2. Fluorescence quenching studies

To investigate binding mode of complex **3.1** with calf thymus DNA, a competitive binding experiment has been performed using ethidium bromide (EB) as a probe. EB is a classical indicator of intercalation. It forms soluble complexes with nucleic acids and exhibit strong fluorescence in the presence of calf thymus DNA because of excellent intercalation of the planar phenanthridinium ring between neighbouring base pairs on the double helix of the DNA. If a molecule is able to replace or exclude the EB from EB-DNA complex or can rupture the secondary structure of CT-DNA, then the increased fluorescence is quenched severely.

The fluorescence of EB-DNA complex has been determined in absence and in the presence of complex **3.1** (Figure 3.10). The mixture containing equimolar ( $1.53 \times 10^{-4}$  M) EB and DNA has been titrated with varying concentration of complex **3.1** ([complex **3.1**]/[DNA]) ratio of 0.29 to 1.50). With the gradual addition of complex **3.1** to CT DNA pretreated with EB solution, the emission intensity at 592 nm quenches in remarkable extent with a red shift. This event clearly demonstrates that EB molecules are replaced from EB bound DNA and complex **3.1** binds with the same DNA with similar affinity. It is clearly evident from the figure that all of the EB molecules are not displaced from the EB-DNA complex, so partial intercalation in addition to the electrostatic interaction cannot be completely ruled out.

Furthermore, the quenching extents have been determined quantitatively by using the following Stern–Volmer equation:<sup>3,36</sup>

$$\frac{I_0}{I} = 1 + K_{sq}r$$

where  $I_0$  and  $I$  represent fluorescence intensity in absence and in the presence of complex **3.1**, respectively, and  $r$  signifies the ratio of concentration of complex **3.1** to concentration of DNA.  $K_{sq}$  is known as the linear Stern–Volmer quenching constant. The quenching plots demonstrate that the fluorescence quenching of EB-DNA complex in the presence of the nickel complex is in excellent agreement with the linear Stern–Volmer equation.  $K_{sq}$  value has been determined as the ratio of the slope to intercept and it has been found to be 0.763. The  $K_{sq}$  value so obtained for complex **3.1** reveals that some of the EB molecules have been displaced from their DNA binding sites, which is in accordance with the results obtained in absorption spectral experiments.

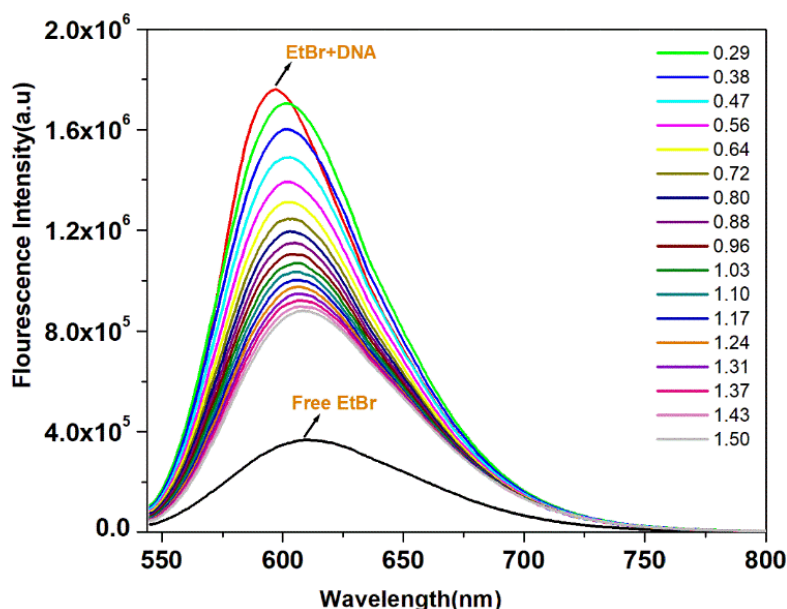


**Figure 3.10:** Emission spectra of EB bound to CT-DNA in absence (red) and in the presence of complex **3.1**.  $[\text{Complex } \mathbf{3.1}]/[\text{DNA}] = 0, 0.29, 0.38, 0.47, 0.56, 0.64, 0.72, 0.80, 0.88, 0.96, 1.03, 1.10, 1.17, 1.24, 1.31, 1.37, 1.43, 150$ ; Inset: Stern–Volmer quenching curve.

### 3.3.3.3. Circular Dichroism spectral studies

Circular Dichroism (CD) spectroscopy is a useful technique to diagnose any changes in the morphology of DNA while studying drug-DNA interactions. The CD spectrum of CT DNA displays a positive band at 274 nm arising from base stacking interactions and a negative band at 243 nm due to the right-handed helicity of B-DNA form, in the UV region. These two bands result from the excitation coupling interactions of the bases and they depend on the tilted orientation on DNA backbone. Thus, they are reasonably sensitive when small molecules

interact with the DNA. Classical intercalative interaction enhances the intensities of both bands. On the other hand, when there is an electrostatic or groove binding interaction between the complex and DNA, small or no perturbation of the base stacking and helicity bands have been observed. It is to mention that hydrophobic base stacking in the oligomers and polymers produces close contacts and Coulombic interaction resulting strong CD bands which correspond to each base transition.<sup>3,37</sup> Therefore, in the presence of small molecules, which restrict interactions between DNA bases and make base stacking weak, should cause a lowering in the intensities of CD bands.

The interaction of complex **3.1** with DNA induces a change in the CD spectrum (**Figure 3.11**). With increasing concentration of the Ni(II) complex, both the positive and negative bands show slight change in the intensity, which implies a non-intercalative groove binding interaction between DNA and complex **3.1** that stabilizes the right-handed B-form of DNA. It is to note that the nickel complex is positively charged ion. So, there is high possibility that the complex **3.1** would exercise strong attraction with the negatively charged phosphate backbone of DNA. Thus, electrostatic binding is highly suggested.

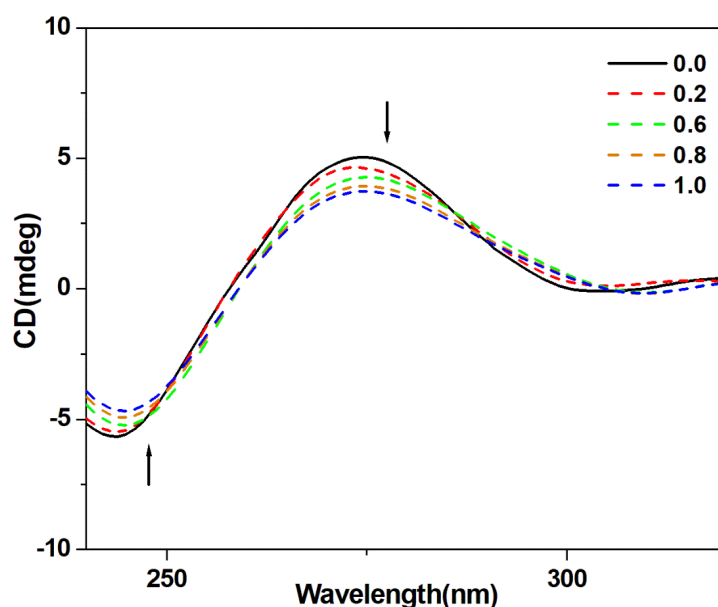


**Figure 3.11:** CD spectra of DNA ( $1.2 \times 10^{-4}$  M) in absence (solid line) and in the presence (dashed line) of complex **3.1** in  $[\text{Complex } 3.1]/[\text{DNA}] = 0.0, 0.2, 0.6, 0.8$  and  $1.0$ .

#### 3.3.3.4. DNA cleavage studies

Transition metal complexes are suitable for application as metallonucleases, because their redox potential can be tuned by the choice of proper metal ion and the ligand. Thus, the DNA cleavage ability of nickel(II) complex has been studied using supercoiled PUC19 plasmid DNA as a substrate in 50 mM Tris-HCl/NaCl buffer (pH=7.2). The original supercoiled form



(i.e. Form I) of plasmid DNA exists in nicked form. When it is cleaved, an open circular relaxed form i.e. Form II is observed.

At first, it has been detected that the DNA cleavage activity of complex **3.1** is dependent on the concentration. Results of gel electrophoretic separations of plasmid PUC19 DNA (0.5  $\mu\text{g}/\mu\text{L}$ ) induced by increasing concentration of complex **3.1** from 20 to 100  $\mu\text{M}$  gradually in 100 mM Tris–HCl/NaCl buffer (pH = 7.2) in the presence  $\text{H}_2\text{O}_2$  (200  $\mu\text{M}$ ) at 37 °C for 30 min have been shown in Fig. 5. With increase in concentration of complex **3.1**, the cleavage becomes more pronounced. Here with increase in complex concentration, Form I gradually diminishes whereas Form II appears, suggesting the single strand DNA cleavage.<sup>3,38</sup> This result indicates that the nickel(II) complex can efficiently cleave plasmid DNA. The control tests have been done also as shown in **Figure 3.12**. The role of  $\text{H}_2\text{O}_2$  is very important in this process because it has been observed from experimental results that in absence of  $\text{H}_2\text{O}_2$ , the DNA cleavage is not very successful. Here,  $\text{H}_2\text{O}_2$  acts as an exogenous activator which enables complex **3.1** to cleave the DNA.

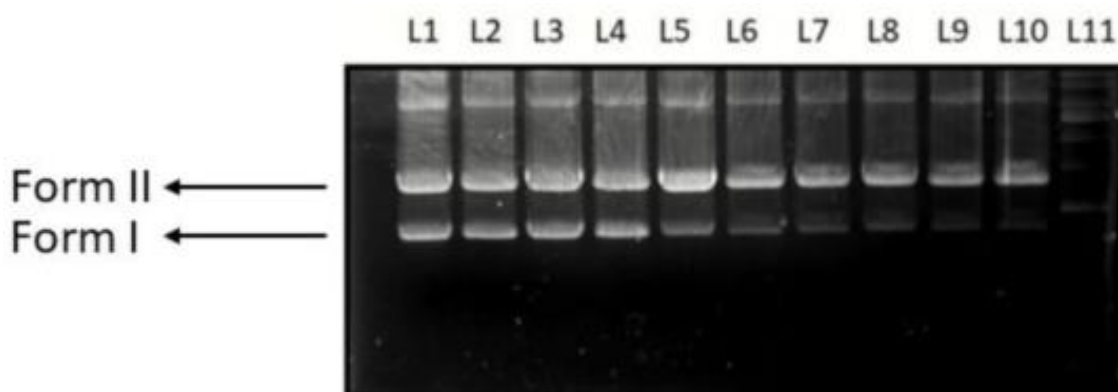


**Figure 3.12:** Agarose gel electrophoresis depicting cleavage of plasmid PUC19 DNA (500 ng) by complex **3.1** at different concentrations for an incubation time of 30 min at 37 °C; Lane 1: DNA+  $\text{H}_2\text{O}$ ; lane 2: DNA+ Complex **3.1** +  $\text{H}_2\text{O}_2$ ; lane 3: DNA + Complex **3.1** + DMSO; lane 4: DNA + DMSO; lane 5: DNA +  $\text{H}_2\text{O}_2$ ; lane 6: DNA +  $\text{H}_2\text{O}_2$  + complex **3.1** (20  $\mu\text{M}$ ); lane 7: DNA +  $\text{H}_2\text{O}_2$ + complex **3.1** (40  $\mu\text{M}$ ); lane 8: DNA +  $\text{H}_2\text{O}_2$  + complex **3.1** (60  $\mu\text{M}$ ); lane 9: DNA +  $\text{H}_2\text{O}_2$  + complex **3.1** (80  $\mu\text{M}$ ); lane 10: DNA +  $\text{H}_2\text{O}_2$  + complex **3.1** (100  $\mu\text{M}$ ); lane 11: Ladder.

### 3.3.3.5. DNA cleavage in the presence of reactive oxygen species

To determine the plausible mechanism for DNA cleavage activity of complex **3.1**, DNA cleavage experiment has been carried out in the presence of various reactive oxygen species (ROS) such as hydroxyl radical scavenger (ethanol), singlet oxygen scavenger,  $^1\text{O}_2$  ( $\text{NaN}_3$ ), hydrogen peroxide scavenger (KI) and chelating agent (EDTA) (**Figure 3.13**). The hydroxy

radical EtOH depicts no inhibitory effect on the cleavage pattern (**Figure 3.13**, lane3) indicative of non-involvement of diffusible hydroxyl radicals in the cleavage process. Additionally, KI and  $\text{NaN}_3$  (**Figure 3.13**, lanes 5 and 6) scarcely quenches the DNA cleavage. However, the chelating agent EDTA completely inhibits DNA cleavage (lane 4), signifying the key role of Ni(II) complex in the DNA breakage. Thus, in the presence of  $\text{H}_2\text{O}_2$ , complex **3.1** cleaves plasmid DNA significantly as mentioned above, which emphasizes the crucial role of  $\text{H}_2\text{O}_2$  in DNA degradation via oxidative cleavage pathway.<sup>3,39</sup>

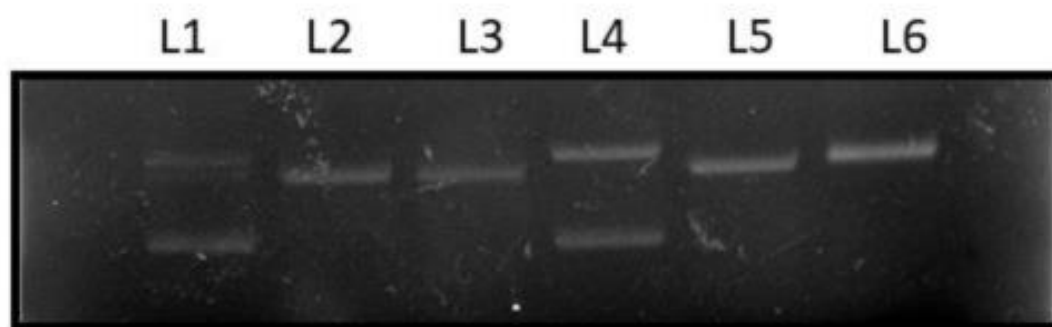


**Figure 3.13:** Agrose gel electrophoresis showing cleavage of plasmid PUC19 DNA (500 ng) incubated with complex **3.1** (40  $\mu\text{M}$ ) in Tris–HCl/NaCl buffer (pH 7.2) at 37 °C for 30 min. lane 1: DNA+ $\text{H}_2\text{O}$ ; lane 2: DNA + complex **3.1** +  $\text{H}_2\text{O}_2$ ; lane 3: DNA +complex **3.1** +  $\text{H}_2\text{O}_2$  + EtOH; lane 4: DNA + complex **3.1** +  $\text{H}_2\text{O}_2$  + EDTA; lane 5: DNA + complex **3.1** +  $\text{H}_2\text{O}_2$  + KI; lane 6: DNA + complex **3.1** +  $\text{H}_2\text{O}_2$  +  $\text{NaN}_3$ .

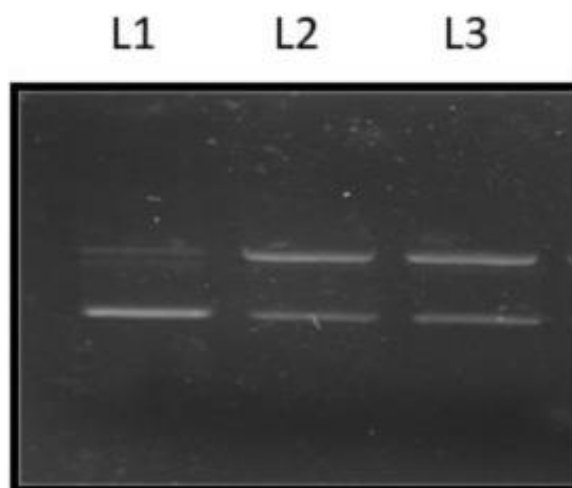


**Figure 3.14:** Cleavage of plasmid PUC19 DNA (0.5  $\mu\text{g}/\mu\text{L}$ ) by complex **3.1** in 100 mM Tris–HCl/NaCl buffer (pH, 7.2) in the presence of DNA minor groove binding agent DAPI and major groove binding agent methyl green (MG); Lane 1: DNA +  $\text{H}_2\text{O}$ ; lane 2: DNA + complex **3.1** + DAPI (8  $\mu\text{M}$ ); lane 3: DNA + complex **3.1** + MG (2.5  $\mu\text{L}$  of a 0.01 mg/mL solution).

### 3.3.3.6. DNA interaction in the presence of groove binders

To ascertain the possible interaction site of complex **3.1** with plasmid PUC19 DNA, the cleavage experiment has been performed with the addition of a minor groove binder, DAPI<sup>3.40</sup> and a major groove binder, methyl green (MG).<sup>3.41</sup> The results show that considerable restriction of the DNA cleavage activity of complex **3.1** has been observed in DAPI bound DNA (**Figure 3.14**, lane 2, 3). This indicates the minor groove binding property of the complex. On the other hand, upon addition of MG to the reaction mixture results in some curbing in the DNA cleavage activity signifying the affinity of the complex **3.1** towards the major groove binding.

### 3.3.4. HSA binding studies

Understanding and characterizing the interaction of a small molecule as drug with blood plasma protein is of immense importance in research because serum albumin makes up of nearly 55% of total blood plasma protein and exhibits its pivotal role in the transportation of exogenous and endogenous molecules in human plasma. Therefore, different spectral techniques are employed to investigate the interaction of complex **3.1** with human serum albumin (HSA).

#### 3.3.4.1. Absorption spectra studies

UV-Vis absorption spectroscopy has been used as a reliable tool to check any alteration in the secondary structure of HSA in the presence of complex **3.1** (**Figure 3.15**). HSA shows a strong absorption peak at 208 nm which may be assigned to  $n \rightarrow \pi^*$  transition for the peptide bond of  $\alpha$  helix. It exhibits another band at 280 nm which is comparatively weak in nature and it may arise due to the presence of the phenyl ring in aromatic acid residues such as Trp, Tyr and Phe.<sup>3.42</sup> Upon addition of complex **3.1** with an increase in concentration ( $3.85\text{-}37.04 \times 10^{-6}$  M) to HSA of constant concentration ( $8.1 \times 10^{-5}$  M), a gradual increase in absorption intensity at 280 nm has been observed. This implies that the aromatic acid residues, which originally reside in a hydrophobic cavity of the protein, are exposed to an aqueous environment to a certain extent. All the observations suggest that complex **3.1** has interacted with the carrier protein via non-covalent interaction most probably via electrostatic interaction. This type of interaction may be influenced by H-bond formation which shows effect in the absorption spectra. The changes in spectra are mainly due to the effect of polar solvent e.g. water and an alteration of the function of micro-environment of the polypeptide chain of HSA protein.

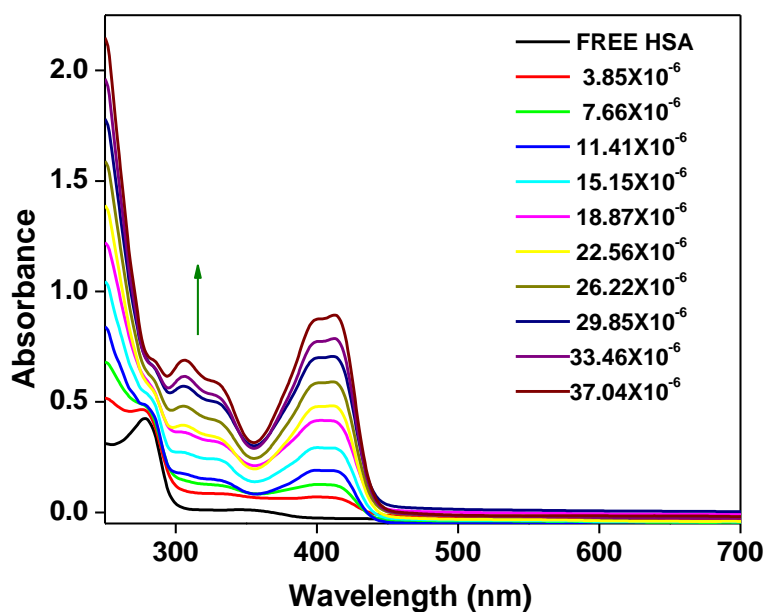
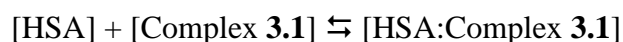


**Figure 3.15:** UV-Vis absorption spectra of complex **3.1** in the presence of HSA obtained in 5 mM Tris–HCl buffer, pH 7.2, at room temperature: [HSA]=  $8.1 \times 10^{-5}$  M; [complex **3.1**] = 0, 3.85, 7.66, 11.41, 15.15, 18.87, 22.56, 26.22, 29.85, 33.46, 37.04  $\mu$ M, respectively. Arrow shows the intensity changes upon increasing concentration of complex **3.1**.

To determine the binding ability of complex **3.1** with HSA quantitatively, the intrinsic binding constant,  $K$ , has been determined by considering that there exists only one type of interaction between the protein and the metal complex in aqueous solution <sup>3,42</sup>,



$$K = [HSA:Complex \mathbf{3.1}] / [HSA][Complex \mathbf{3.1}]$$

where  $K$  is the binding constant and  $[HSA:Complex \mathbf{3.1}] = C_B$

$$\text{Thus, } K = C_B / [C_{HSA} - C_B] [C_{Complex \mathbf{3.1}} - C_B]$$

where,  $C_{HSA}$  and  $C_{Complex \mathbf{3.1}}$  represent analytical concentrations of HSA and the complex, respectively, in the solution, respectively.

From the Beer–Lambert law, we can write

$$C_{HSA} = A_0 / \epsilon_{HSA} \cdot l$$

$$C_B = A - A_0 / \epsilon_B \cdot l$$

where  $A_0$  and  $A$  represent the absorbance of HSA in absence and in the presence of complex **3.1**, respectively at 280 nm <sup>3,7d</sup>.  $\epsilon_{HSA}$  and  $\epsilon_B$  are the molar extinction coefficients of the free protein and the bound complex, respectively, and  $l$  represents the light path of the cuvette as usual (1 cm).

By substituting  $\epsilon_{HSA}$  and  $\epsilon_B$  in Equations

$$A_0 / (A - A_0) = \epsilon_{HSA} / \epsilon_B + \epsilon_{HSA} \cdot l / \epsilon_B K C_{Complex \mathbf{3.1}} \cdot l$$

Thus, the double reciprocal plot of  $1/(A - A_0)$  vs.  $1/[\text{Complex 3.1}]$  is linear (Figure 3.16) and the binding constant can be estimated from the ratio of the intercept and the slope.  $K_B$  has been calculated to be  $1.6 \times 10^4 \text{ M}^{-1}$ . The  $K_B$  value suggests that complex **3.1** binds moderately to HSA followed by conformational changes in its structure.

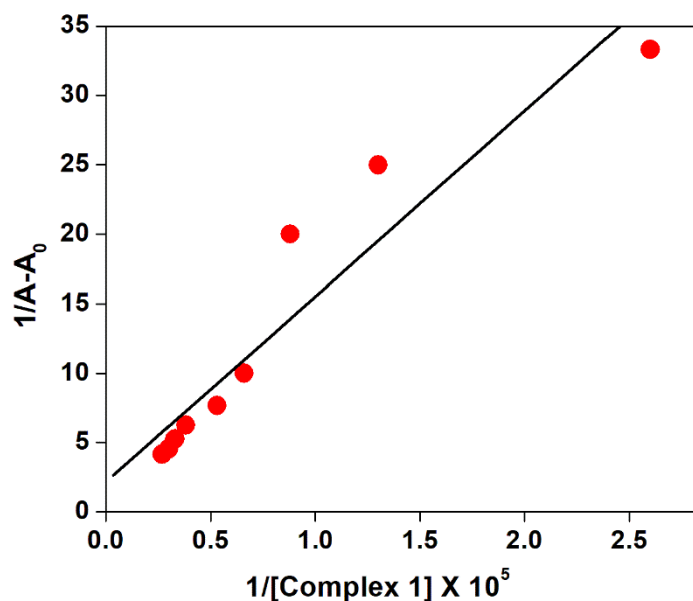


**Figure 3.16:** Plot of  $1/A - A_0$  vs.  $1/[\text{Complex 3.1}]$ . The binding constant estimated from the ratio of the intercept to the slope as  $1.6 \times 10^4 \text{ M}^{-1}$ .

### 3.3.4.2. Fluorescence quenching studies

Fluorescence spectroscopy is another effective method used to monitor progress of the interaction of small molecules with the bio macromolecules. The fluorescence emission spectra of HSA have been measured in the range of 300–450 nm by exciting HSA at 280 nm in the presence of increasing concentration of the Ni(II) complex (**Figure 3.17**). HSA displays fluorescence mainly due to the presence of tryptophan residue ( $\lambda_{\text{ex}}$ : 295 nm). Another residue phenylalanine has a low quantum yield. On the other hand, fluorescence of tyrosine residue is generally quenched if it is in ionized form or resides near to an  $-\text{NH}_2$  group, a  $-\text{COOH}$  group or a tryptophan because Tyr and Phe do not absorb in this region. HSA displays a strong fluorescence peak at 344 nm, while complex **3.1** does not show any fluorescence under the same experimental conditions. The fluorescence intensity of the HSA (fixed concentration,  $6.5 \times 10^{-5} \text{ M}$ ) decreases gradually with increasing concentration of the complex ( $3.85 \times 10^{-6}$  to  $37.04 \times 10^{-6} \text{ M}$ ) and it is accompanied by a hypsochromic or red shift (10 nm) from the initial HSA emission intensity indicating the enhancement in polarity of the microenvironment about Trp residue.<sup>3,43</sup> These results indicate the binding ability of complex **3.1** to HSA. The complex induces conformational changes in HSA. The intramolecular force, that is for maintaining the

secondary structure, may be changed and hydrophobicity is also decreased signifying that the tryptophan residues are more uncovered to the solvent medium.

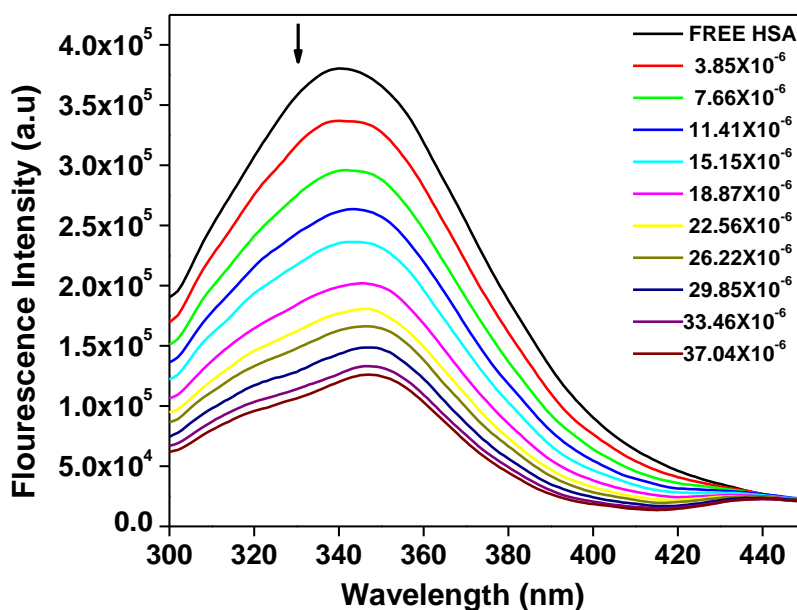


**Figure 3.17:** The fluorescence quenching spectra of HSA by different concentrations of complex **3.1** with the excitation wavelength at 280 nm in 5 mM Tris–HCl buffer, pH 7.2, at room temperature:  $[HSA] = 6.5 \times 10^{-5}$  M; the concentration of complex **3.1** = 0, 0.76, 1.51, 2.25, 2.98, 3.70, 4.41, 5.12, 5.81  $\times 10^{-5}$  M. Arrow shows the intensity changes upon increasing concentration of the quencher.

Commonly, by the following Stern–Volmer equation, fluorescence quenching can be described:<sup>3.44</sup>

$$\frac{F_0}{F} = 1 + K_q \tau_0 [Q] = 1 + K_{sv} [Q]$$

where  $F_0$  and  $F$  represent the fluorescence intensity in absence and in the presence of quencher, respectively.  $K_q$  is the quenching rate constant of the biomolecules,  $K_{sv}$  is the Stern–Volmer quenching constant,  $\tau_0$  is the average life time of the molecule without quencher ( $\tau_0 = 10^{-8}$  s) and  $[Q]$  is the concentration of the quencher. The plot of  $F_0/F$  versus  $[Q]$  for the quenching of fluorescence of HSA in the presence of complex **3.1** is depicted in **Figure 3.18**.  $K_{sv}$  and  $K_q$  values have been calculated to be  $5.95 \times 10^4$  M<sup>-1</sup> and  $5.95 \times 10^{12}$  M<sup>-1</sup> s<sup>-1</sup>, respectively. It indicates that the quenching rate constant of the biomolecules is bigger than that their limiting diffusion constant ( $2.0 \times 10^{10}$  M<sup>-1</sup> s<sup>-1</sup>) implying quenching occurs due to a particular interaction between the nickel complex and the protein molecule.<sup>3.45</sup>

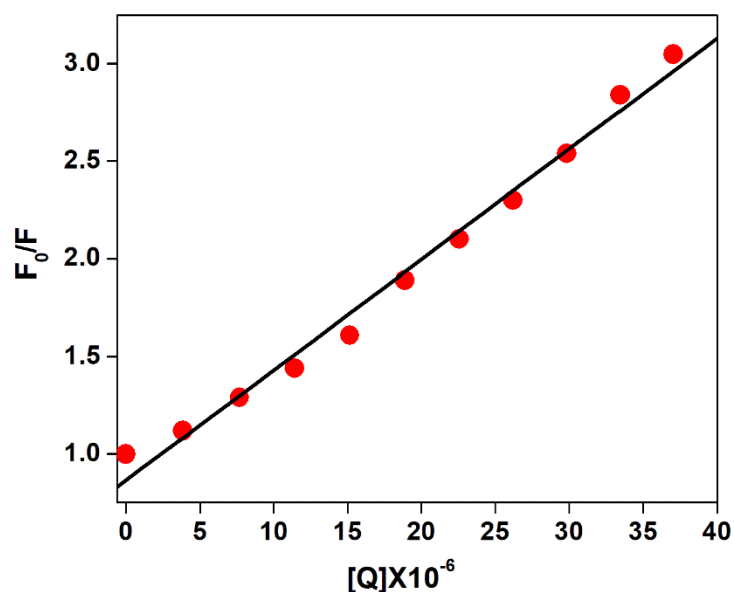


**Figure 3.18:** A plot of  $F_0/F$  versus  $[Q]$ .  $F_0$  and  $F$  are the fluorescence intensities of HSA in absence and in the presence of quencher and  $[Q]$  is the concentration of quencher.

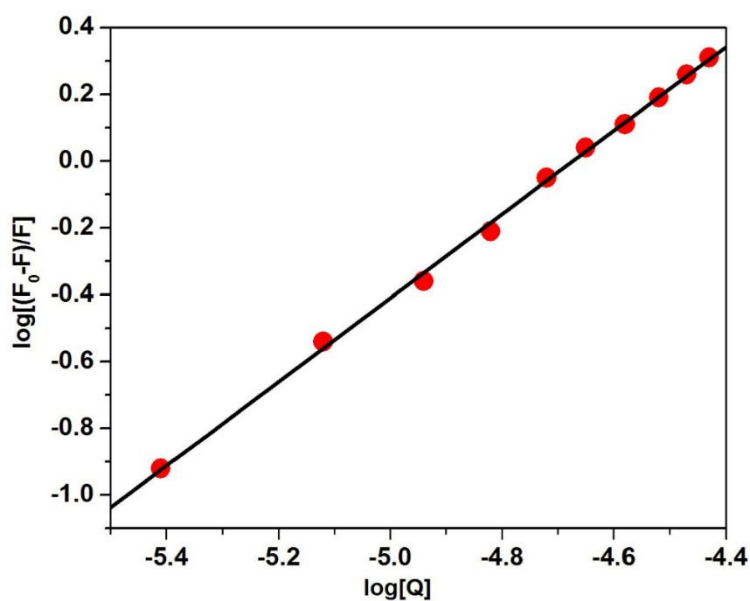


**Figure 3.19:** A plot of  $\log[(F_0-F)/F]$  versus  $\log[Q]$ .  $F_0$  and  $F$  are the fluorescence intensities of HSA in absence and in the presence of quencher and  $[Q]$  is the concentration of quencher.

Now, the Scatchard equation has been used to evaluate the binding constant and number of binding sites<sup>3,46</sup>:

$$\log \frac{F_0 - F}{F} = \log K + n \log [Q]$$

where,  $F_0$  and  $F$  are the fluorescence intensity of HSA in absence and in the presence of a quencher, respectively  $K$  is the binding constant and  $n$  is the number of binding sites. From the plot of  $\log[(F_0 - F)/F]$  vs.  $\log[Q]$  both  $K$  and  $n$  can be determined from the intercept on Y-

axis and the slope, respectively (**Figure 3.19**). The binding constant and the number of binding sites have been calculated to be  $7.16 \times 10^5 \text{ M}^{-1}$  and 1.25, respectively, which are comparable to those observed for previously reported binding constant<sup>3.10a-b</sup>. The value of n is about 1 which suggests that the complex **3.1** is bonded to HSA in 1:1 ratio.

### 3.3.4.3. Energy transfer mechanism and binding distance between complex **3.1** and HSA

Fluorescence energy transfer happens because of overlapping of the emission spectrum of HSA, which acts as the donor, with the absorption spectrum of complex **3.1**, which behaves as the acceptor (**Figure 3.20**). The extent of energy transfer depends on several factors such as the success of the overlap between emission spectrum of the donor and absorption spectrum of the acceptor, orientation of transition dipole and the distance between the donor and acceptor (**Figure 3.21**). Quenching of fluorescence of Trp residue occurs in the presence of the Ni(II) complex via Forster resonance energy transfer (FRET) mechanism.

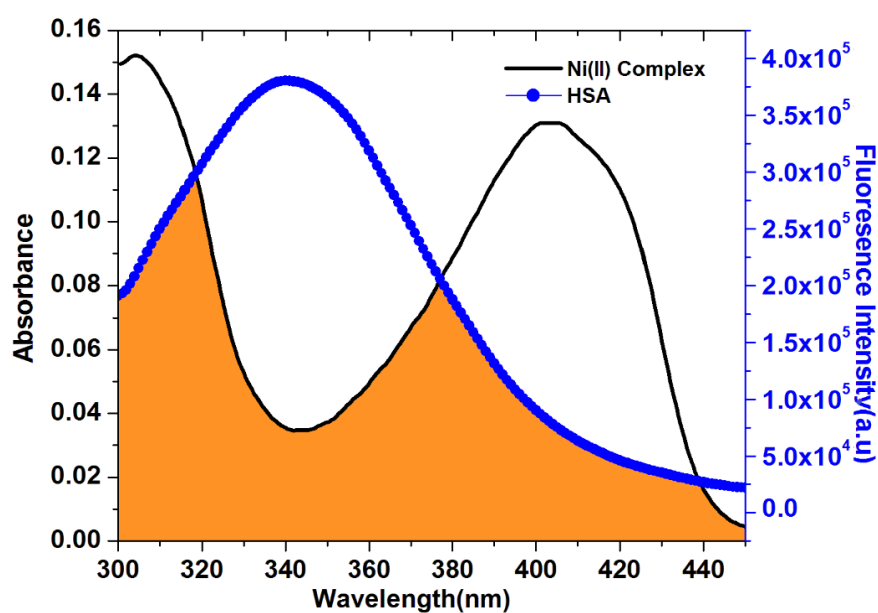


**Figure 3.20:** Overlap of the fluorescence spectrum of HSA and the absorbance spectrum of complex **3.1**,  $[\text{HSA}] = [\text{complex } \mathbf{3.1}] = 4.0 \times 10^{-5} \text{ M}$ .

Efficiency of energy transfer (E) can be determined by the following equation:<sup>3.47</sup>

$$E = 1 - \frac{F}{F_0} = \frac{R_0^6}{R_0^6 + r^6}$$

where  $F_0$  and  $F$  represent the fluorescence intensity of HSA in absence and in the presence a quencher, respectively,  $r$  is distance between the acceptor and the donor, and  $R_0$  is the critical distance at 50% transfer efficiency.  $R_0$  can be determined with the help of the following equation:<sup>3.48</sup>



$$R_0^6 = 8.78 \times 10^{-25} K^2 n^{-4} \phi J$$

where  $K^2$  represents spatial orientation factor between the emission dipole and absorption dipole,  $n$  is refractive index of the medium,  $\phi$  is emission quantum yield of the donor, and  $J$  is the overlap integral of emission spectrum of donor and absorption spectrum of acceptor.  $J$  can be evaluated by the following equation:<sup>3.49</sup>

$$J = \frac{\int_0^\infty F(\lambda) \epsilon(\lambda) \lambda^4 d\lambda}{\int_0^\infty F(\lambda) d\lambda}$$

where  $F(\lambda)$  is the proper fluorescence intensity of the donor at wavelength,  $\lambda$ , and  $\epsilon(\lambda)$  represents molar absorption coefficient of the acceptor at wavelength,  $\lambda$ . Under the experimental conditions, the value of  $K^2$  is  $2/3$ ,  $n$  is 1.36,  $\phi$  is 0.15 for a solution with haphazard orientation as in present case. The value of  $J$  has been determined to be  $7 \times 10^{-14}$  (from the graph),  $R_0$  has been calculated to be 3.48 nm,  $E$  as 0.47 and  $r$  as 3.55 nm. The donor (HSA) to acceptor (complex **3.1**) distance ( $r$ ) is less than 7 nm which indicates that the energy transfer from tryptophan residue of HSA to the metal complex occurs with high possibility.<sup>3.50</sup> These results are in accordance with the static quenching interaction observed between HSA and complex **3.1**.<sup>3.45</sup>

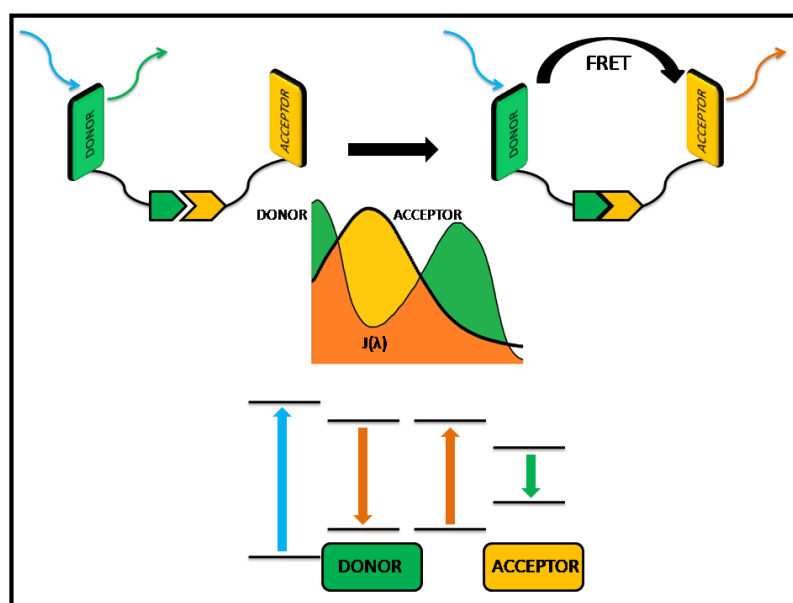


**Figure 3.21:** Schematic depiction of the fluorescence resonance energy transfer mechanism.

#### 3.3.4.4. IR spectral studies

IR spectrum of proteins has been generally used to investigate any alteration in conformation in the structure of proteins induced by a possible candidate as a drug. The IR spectra at the mid IR frequency bands of proteins usually exhibit a number of amide bands attributed to different stretching vibrations of the peptide moieties. Here the spectrum has been

obtained by subtracting the absorption of Tris buffer from the spectrum of HSA solution (Figure 3.22).

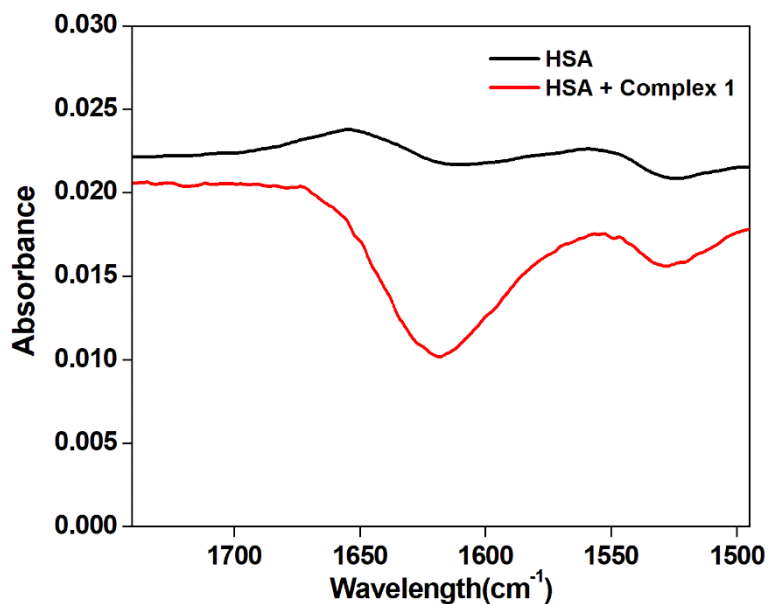


**Figure 3.22:** FTIR spectra of HSA and HSA with complex **3.1**.

The protein amide I band, which mainly appears due to C=O stretching and amide II band, which is due to C–N stretching coupled with N–H bending mode, bear a relationship with the secondary structure of proteins. However, the former one is more sensitive to the perturbation of protein secondary structure than rest of its part. As depicted in **Figure 3.22**, upon interaction with complex **3.1**, the peak position of amide I band is shifted from 1654 to 1674  $\text{cm}^{-1}$  and that of amide II band from 1557 to 1553  $\text{cm}^{-1}$ . These changes in the IR spectra indicate that complex **3.1** has been able to alter secondary structure of HSA while interacting.

### 3.3.4.5. 3D fluorescence spectral studies

These conformational and micro-environmental changes of HSA induced by complex **3.1** have further been monitored by 3D fluorescence spectroscopy of HSA in the absence and in the presence of the complex **3.1**. The 3D fluorescence spectra of HSA and complex **3.1**–HSA system are shown in **Figure 3.23**. Peak A represents a Rayleigh scattering peak ( $\lambda_{\text{ex}} = \lambda_{\text{em}}$ ) while Peak B ( $\lambda_{\text{ex}} = 280 \text{ nm}$ ,  $\lambda_{\text{em}} = 350 \text{ nm}$ ) primarily shows spectral behaviour of tryptophan residue. On the other hand, Peak C indicates the second-ordered scattering peak ( $\lambda_{\text{em}} \approx 2 \lambda_{\text{ex}}$ ).<sup>3,48</sup> It has been observed from **Figure 3.23** that both the fluorescence intensities of peaks A and B have been quenched appreciably and the emission maximum peaks alter. These facts indicate that the interaction of complex **3.1** with HSA induces some conformational and micro environmental changes in HSA. These results are in accordance with that obtained from UV–vis, fluorescence and CD spectral analysis.

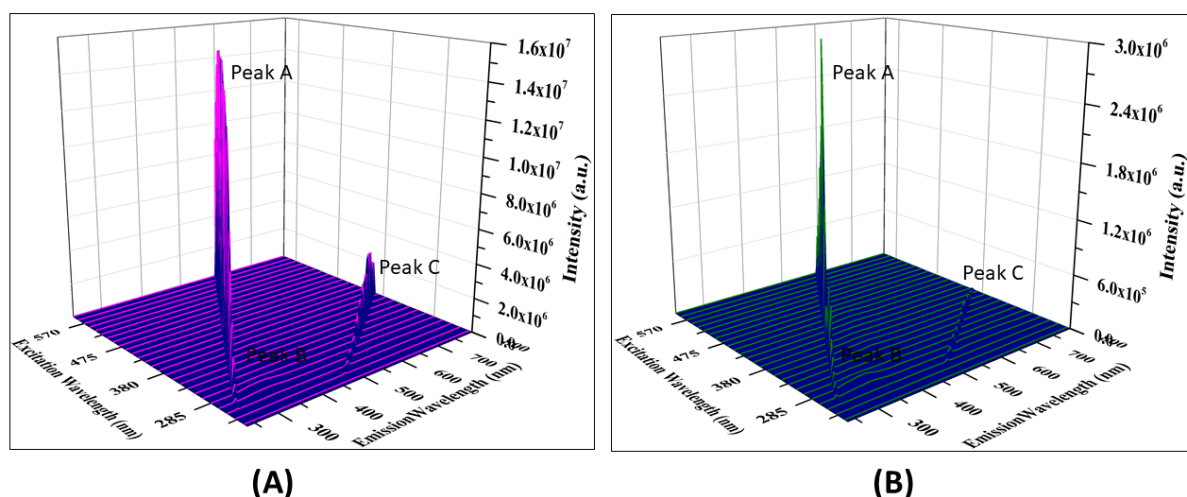


**Figure 3.23:** 3D fluorescence spectra of (A) HSA and (B) HSA-complex **3.1** conjugate system. [HSA] = [Complex **3.1**] =  $1.7 \times 10^{-5}$  M, pH 7.2, at room temperature.

### 3.3.4.6. CD spectral studies on changes of the HSA conformation with complex **3.1**

To study effect of complex **3.1** binding on the secondary structure of HSA, CD measurement has been carried out in the presence of the Ni(II) complex at different concentrations. The CD spectrum of the protein displays two negative bands at 208 and 219 nm which may be assigned to  $\pi \rightarrow \pi^*$  and  $n \rightarrow \pi^*$  transfers, respectively, for the peptide bond (**Figure 3.24**).

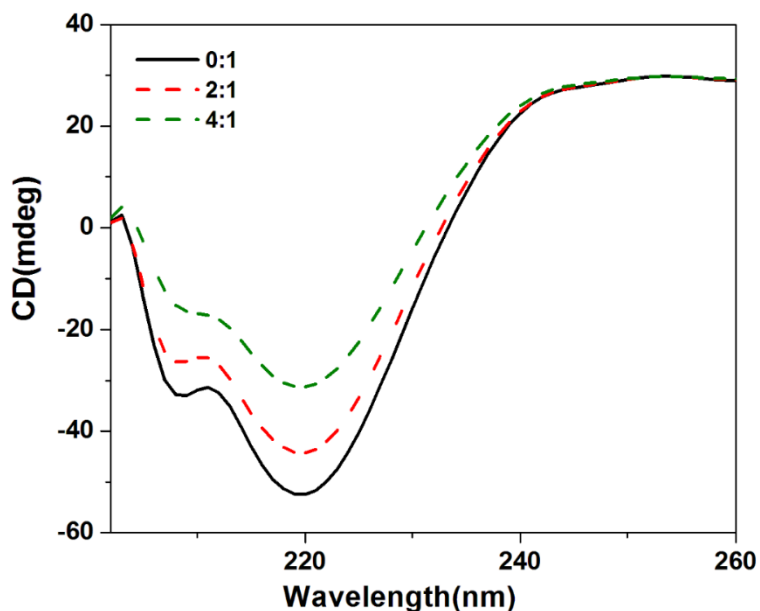


**Figure 3.24:** CD spectra of secondary structures of HSA in the absence and presence of the Ni(II) complex: (a)  $1.2 \times 10^{-5}$  M HSA; (b)  $1.2 \times 10^{-5}$  M HSA +  $2.4 \times 10^{-5}$  M complex **3.1**; (c)  $1.2 \times 10^{-5}$  M HSA +  $4.8 \times 10^{-5}$  M complex **3.1**, pH 7.2, at room temperature.

These are typical characteristic of  $\alpha$ -helix structure of the protein.<sup>3.51</sup> The CD signal of the protein molecule enhances with the increase in concentration of complex **3.1** as the helical

secondary structure of HSA is destroyed to some extent in the presence of the complex. This suggests a considerable amount changes in the conformation of HSA.<sup>3.52</sup> However, spectral pattern of HSA before and after addition of complex **3.1** is similar that indicates the predominant presence of  $\alpha$ -helical structure in HSA.

#### 3.3.4.7. Oxidative damage of HSA by complex **3.1**

Oxidative damage of HSA has been studied with different concentrations of the protein and complex **3.1**.<sup>3.53</sup> HSA exhibits remarkable degradation after incubation with complex **3.1**, for 30 min, at 37 °C in the presence of H<sub>2</sub>O<sub>2</sub>. It is indicated by a continuum of protein fragments at SDS–PAGE in 0.8% acrylamide gel (**Figure 3.25**). Clear and thick protein band is observed at the expected molecular weight range (around 66 kDa). As shown in **Figure 3.25**, it is observed that the control condition (Lane 1) does not show any apparent cleavage, while upon gradual addition of complex **3.1** (40-100  $\mu$ M), HSA displays its proficient cleavage activity with appreciable smearing or fading of the band. Possibly nonspecific binding of the nickel complex with the protein results in the fading out of the band and leads to very small fragments.<sup>3.54</sup>

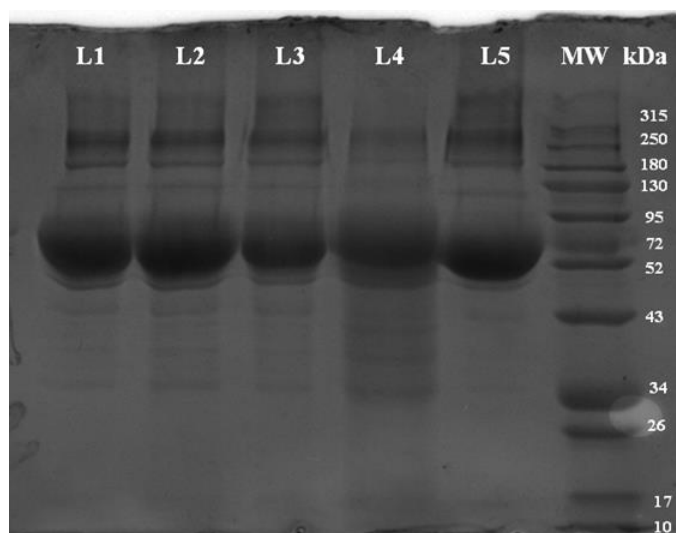


**Figure 3.25:** SDS–PAGE electrophoresis in 0.8% polyacrylamide gel of HSA fragmentation, in the presence of complex **3.1**, treated with H<sub>2</sub>O<sub>2</sub>, for 30 min at 37 °C, in Tris buffer 100 mM, pH 7.2, Lane 1:75  $\mu$ M HSA, Lane 2: 75 $\mu$ M HSA and 100 mM H<sub>2</sub>O<sub>2</sub>, Lane 3: 75  $\mu$ M HSA, 100 mM H<sub>2</sub>O<sub>2</sub> and 40  $\mu$ M complex **3.1**, Lane 4: 75  $\mu$ M HSA, 100 mM H<sub>2</sub>O<sub>2</sub> and 80  $\mu$ M complex **3.1**, Lane 5: 75  $\mu$ M HSA, 100 mM H<sub>2</sub>O<sub>2</sub> and 100  $\mu$ M complex **3.1**.

### 3.3.5. Cytotoxicity evaluation

#### 3.3.5.1. MTT assay

MTT assay has been performed to examine the ability of complex **3.1** to hinder cell growth and induce cell death in both lung carcinoma and normal lung fibroblast cell line. The

cytotoxic effect of complex **3.1** has been investigated after 12 h of treatment on A549 (lung carcinoma) and WI-38 (normal lung fibroblast) by using MTT assay. As shown in **Figure 3.26**, cell survivability has significantly ( $p < 0.0002$ , 40-200  $\mu\text{M}$ ) decreased in a dose dependent manner in carcinoma cell line. In A549 cells proliferation has been significantly inhibited by complex **3.1** with  $\text{LD}_{50}$  value of 69.82, whereas, in normal fibroblast WI-38 cells proliferation, the  $\text{LD}_{50}$  value is 104. Since, complex **3.1** shows significant cytotoxicity towards A549 cells, and less toxicity to WI-38, suggesting potential anticancer drug for lung carcinoma.

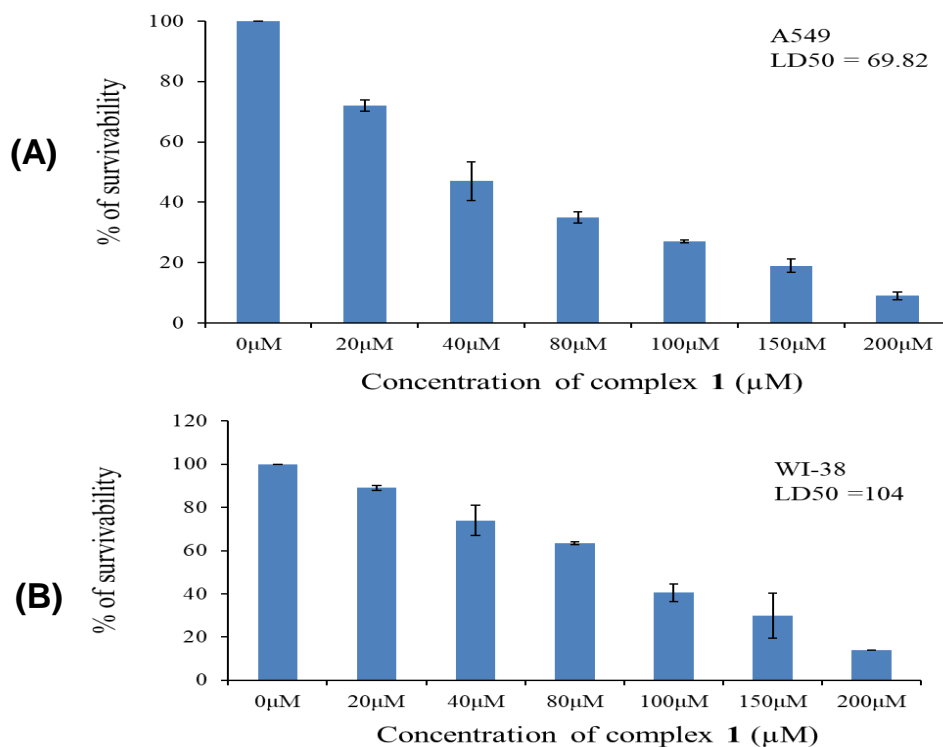


**Figure 3.26:** Effect of complex **3.1** on viability of (A) lung carcinoma (A549) and (B) normal lung fibroblast (WI-38). Cells were treated with different concentration (0-200  $\mu\text{M}$ ) of complex **3.1** for 12 h. Cell viability was measured by MTT assay. Data represented as mean  $\pm$  SE of three independent experiments made in three replicates.

### 3.3.6. Apoptosis evaluation

#### 3.3.6.1. Apoptotic nuclear morphology study by DAPI staining

Apoptotic morphology has been performed in cells treated with complex **3.1** at their respective  $\text{LD}_{50}$  dose for 12 h and 24 h by DAPI staining. It reveals that the untreated cells exhibit no nucleus shrinking or polynuclear fragmentations. However, clear polynuclear fragmentation as well as nucleus shrinking has been noticed in cells treated with the metal complex (**Figure 3.27**). It has been estimated that around 52% (40  $\mu\text{M}$ ) and 57% (70  $\mu\text{M}$ ) apoptotic cells have been observed in 24 h in complex **3.1** treated A549 cells.

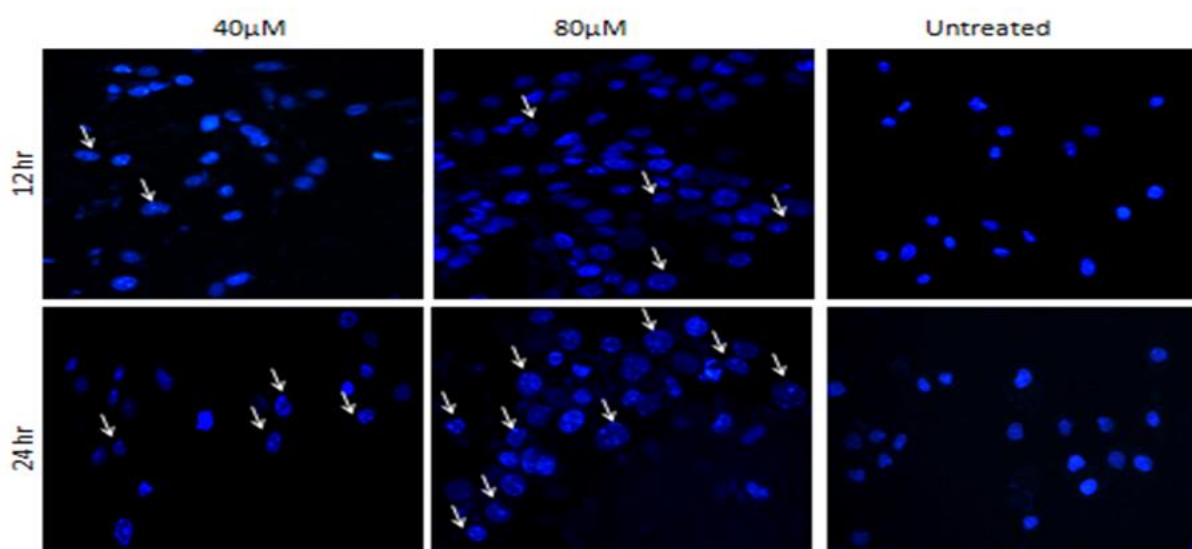


**Figure 3.27:** Apoptotic nuclear morphology study by DAPI staining in A549 cell.

### 3.3.6.2. Treatment of complex 3.1 in A549 promotes apoptosis

We have evaluated the expression of apoptotic marker cleaved caspase-3 and antiapoptotic protein Bcl-2 in the total cellular extract of 12 h complex 3.1 treated A549 cell line. It has been found that the expression of cleaved caspase-3 has been increased in a dose dependent manner while the expression of Bcl-2 decreases in the same set of experiments (**Figure 3.28**). Thus, this fact indicates that complex 3.1 induces apoptosis by downregulating Bcl-2 and upregulation of caspase-3 activity, which leads to activation of caspase-3. Upregulation of caspase-3 leads to successful apoptosis and subsequent cell death.<sup>3.55</sup>

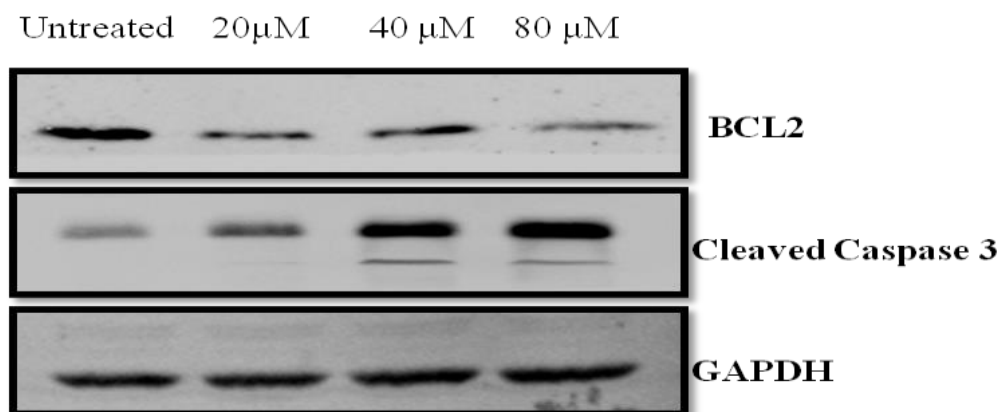


**Figure 3.28:** Western blot of apoptotic protein Bcl2, cleaved Caspase 3 and loading control GAPDH. Lane 1: Untreated A549 cell, lane 2: 20 µM of complex 3.1 treated A549 cell, lane 3: 40 µM of complex 3.1 treated A549 cell, lane 4: 80 µM of complex 3.1 treated A549 cell. This result suggests upregulation of apoptotic pathway upon treatment with complex 3.1 in lung carcinoma cell line.

### 3.4. Conclusions

A mononuclear Ni(II) complex (Complex **3.1**) with 1-((2-piperidin-1-yl)ethylimino)methyl)naphthalene-2-ol as the ligand has been synthesized and characterized. It interacts with DNA and binds mainly with minor groove. Several studies indicate that complex **3.1** is able to bind with human serum albumin efficiently. In this present study, we explore whether the nickel complex has any tumor suppressive function in lung cancer cell line (A549). To attain this aim, the lung carcinoma cells have been treated with different concentrations of nickel complex. The study shows that the mononuclear Ni(II) complex exhibits selective cytotoxicity towards A549 cell but it does not kill normal healthy cell (WI-38). Thus, it could be used as a potential anti-cancer drug. In this study we have shown that the complex can induce apoptosis in lung carcinoma cell by downregulating Bcl2 and upregulation of caspase-3 activity. We have also observed higher percentage of apoptotic bodies in A549 nucleus compared to normal fibroblast which is a major characteristic feature of apoptosis. Thus, this Ni(II) complex can bring about cell death and pave the way for further evaluation as a potential therapeutic agent. These findings suggest that this nickel complex might be a tumor suppressor and a potential target for lung carcinoma. In the previous study with Cu-complex.<sup>3,19</sup> It has been observed that the complex was involved in intercalative binding with DNA whereas in the present study, complex **3.1** involves in minor groove binding. Both of the complexes can bind HSA with same efficiency. In the present study it has been established that the complex exhibits selective cytotoxicity towards cancer cell whereas it is not harmful for normal cell indicating its tumor suppressing ability.

### 3.5. References

- 3.1 (a) K.E. Erkkila, D.T. Odom, J.K. Barton, *Chem. Rev.* **1999**, *99*, 2777–2796;  
(b) C. Santini, M. Pellei, V. Gandin, M. Porchia, F. Tisato, C. Marzano, *Chem. Rev.* **2014**, *114*, 815–862.
- 3.2 (a) A. Erdem, M. Ozsoz, *Electroanalysis* **2002**, *14*, 965–974;  
(b) H.J. Lozano, N. Busto, G. Espino, A. Carbayo, J.M. Leal, J.A. Platts, B. García, *Dalton Trans.* **2017**, *46*, 3611–3622;  
(c) S. Ambika, S. Arunachalam, R. Arunb, K. Premkumar, *RSC Adv.* **2013**, *3*, 16456-16468.
- 3.3 (a) B. Rosenberg, L. Vancamp, J. E. Trosko, V. H. Mansour, *Nature* **1969**, *222*, 385–386;

- (b) B. Rosenberg, L. Vancamp, T. Krigas, *Nature* **1965**, 205, 698–699;
- (c) B. Rosenberg, E. Renshaw, L. Vancamp, J. Hartwick, J. Drobnik, *J. Bacteriol.* **1967**, 93, 716-721;
- (d) L. Kelland, *Nat. Rev. Cancer* **2007**, 7, 573–584.
- 3.4 Y.F. Sun, H. Wu, G.Q. Zhao, Y. Shi, *Luminescence* **2015**, 30, 79-85.
- 3.5 P. Krishnamoorthy, P. Sathyadevi, R.R. Butorac, A.H. Cowley, N.S.P. Bhuvanesh, N. Dharmaraj, *Dalton Trans.* **2012**, 41, 4423-4436.
- 3.6 (a) E. Denkhaus, K. Salnikow, *Crit. Rev. Oncol. Hemat.* **2002**, 42, 35 -56;
- (b) J. G. Muller, L. A. Kayser, S. J. Paikoff, V. Duarte, N. Tang, R. J. Perez, S. E. Rokita, C. J. Burrows, *Coord. Chem. Rev.* **1999**, 185-186, 761 -774;
- (c) G. Barone, A. Terenzi, A. Lauria, A. M. Almerico, J. M. Leal, N. Busto, B. García, *Coord. Chem. Rev.* **2013**, 257, 2848 -2862.
- 3.7 (a) B. Fei, W. Li, W. Xu, J. Long, Q. Liu, W. Sun, C.E. Anson, A.K. Powell, *Eur. J. Inorg. Chem.* **2013**, 5919–5927;
- (b) J. Patole, D. Shingnapurkar, S. Padhye, C. Ratledge, *Bioorg. Med. Chem. Lett.* **2006**, 16, 1514–1517;
- (c) Z.H. Chohan, *Appl. Organomet. Chem.* **2002**, 16, 17-20;
- (d) G. Ceyhan, M. Kose, M. Tumer, I. Demirtas, A. Yaglioglu, V. McKee, *J. Lumin.* **2013**, 143, 623-634.
- 3.8 (a) J. G. Deng, G. Su, P. Chen, Y. Du, Y. Gou, Y. Liu, *Inorg. Chim. Acta* **2018**, 471, 194 -202;
- (b) G. Kalaiarasi, Ruchi Jain, H. Puschman, S. P. Chandrika, K. Preethi, R. Prabhakaran, *New J. Chem.* **2017**, 41, 2543-2560.
- 3.9 R. R. Kumar, M. K. M. Subarkhan, R. Ramesh, *RSC Adv.* **2015**, 5, 46760 -46773.
- 3.10 (a) Y. Li, Z. Yang, M. Zhou, Y. Li, *RSC Adv.* **2017**, 7, 49404-49422;
- (b) Y. Li, Y. Li, Z. Yang, F. Meng, N. Wang, M. Zhou, Z. Xia, Q. Gong, Q. Gao, *New J. Chem.* **2019**, 46, 8024 -8043;
- (c) A. C. Ekennia, E. C. Ibezim, O. C. Okpareke, C. U. Ibeji, C. J.O. Anarado, I. Babahan, B. Coban, B. Abulhasanov, F. Cömert, O. T. Ujam, *Appl. Organometal. Chem.* **2019**, 33, e4913.
- 3.11 L. Zarei, Z. Asadi, M. Dusek, V. Eigner, *J. Photochem. Photobiol. A* **2019**, 374,145 -160.
- 3.12 A.-N. M.A. Alaghaz, S.A.A. Abdulmani, *Appl. Organometal. Chem.* **2019**, 33, e5135.



- 3.13 R. L.B. Alanazi, M. Zaki, W. A. Bawazir, *J. Mol. Struct.* **2021**, *1246*, 131203.
- 3.14 C.-N. Ko, G. Li, C.-H. Leung, D.-L. Ma, *Coord. Chem. Rev.* **2019**, *381*, 79 -103.
- 3.15 Y. Xia, C.-D. Fan, B.-X. Zhao, J. Zhao, D.-S. Shin, J.-Y. Miao, *Eur. J. Med. Chem.* **2008**, *43*, 2347-2353.
- 3.16 C. D. Fan, H. Su, J. Zhao, B. X. Zhao, S. L. Zhang, J. Y. Miao, *Eur. J. Med. Chem.* **2010**, *45*, 1438 -1446.
- 3.17 T. T.-H. Fong, C.-N. Lok, C. Y.-S. Chung, Y.-M. E. Fung, P.-K. Chow, P.-K. Wan, C.-M. Che, *Angew. Chem. Int. Ed.* **2016**, *55*, 11935-11939.
- 3.18 A. Bhattacharjee, S. Das, B. Das, P. Roy, *Inorg. Chim. Acta* **2021**, *514*, 119961.
- 3.19 APEX-II, SAINT and SADABS, Bruker AXS Inc., Madison, WI, **2008**.
- 3.20 G. M. Sheldrick, *Acta Crystallogr., Sect. A: Fundam. Crystallogr.* **2015**, *71*, 3.
- 3.21 G. M. Sheldrick, *Acta Crystallogr., Sect. C: Cryst. Struct. Commun.* **2015**, *71*, 3.
- 3.22 B. Selvakumar, V. Rajendiran, P.U. Maheswari, H. Stoeckli-Evans, M. Palaniandavar, *J. Inorg. Biochem.* **2006**, *100*, 316 -330.
- 3.23 Y. Gultneh, A.R. Khan, D. Blaise, S. Chaudhry, B. Ahvazi, B.B. Marvey, R.J. Butcher, *J. Inorg. Biochem.* **1999**, *75*, 7 -18.
- 3.24 M. Zaki, M. Afzal, M. Ahmad, S. Tabassuma, *J. Photochem. Photobiol. B* **2016**, *161*, 318 -327.
- 3.25 D. Ghosh, V. A. Bohr, P. Karmakar, *DNA Repair* **2019**, *79*, 22-31.
- 3.26 D. Laha, A. Pramanik, S. Chattopadhyay, S.K. Dash, S. Roy, P. Pramanik, P. Karmakar, *RSC Adv.* **2015**, *5*, 68169-68178.
- 3.27 S. Anbu, M. Kandaswamy, B. Varghese, *Dalton Trans.* **2010**, *39*, 3823 -3832.
- 3.28 L. Yang, D. R. Powell, R. P. Houser, *Dalton Trans.* **2007**, 955 -964.
- 3.29 (a) A. Bhattacharjee, S. Dey, P. Roy, *Inorg. Chim. Acta* **2019**, *490*, 93–103;  
(b) S. Halder, J. Mondal, J. Ortega-Castro, A. Frontera, P. Roy, *Dalton Trans.* **2017**, *46*, 1943 –1950;  
(c) J. Chakraborty, M. Nandi, H. Mayer-Figge, W. S. Sheldrick, L. Sorace, A. Bhaumik, P. Banerjee, *Eur. J. Inorg. Chem.* **2007**, 5005 -5009.
- 3.30 K. Ghosh, S. Dey, S. Halder, A. Bhattacharjee, C. Rizzoli, P. Roy, *J. Mol. Struct.* **2016**, *1118*, 325 -334.
- 3.31 A. Kurutos, I. Orehovec, A. T. Paic, I. Crnolatac, L. Horvat, N. Gadjev, I. Piantanida, T. Deligeorgiev, *Dyes Pigm.* **2018**, *148*, 452-459.

- 3.32 (a) J. Rajesh, A. Gubendran, G. Rajagopal, P. Athappan, *J. Mol. Struct.* **2012**, *1010*, 169-178;  
(b) N. Revathi, M. Sankarganesh, J. Rajesh, J. D. Raja, *J. Fluoresc.* **2017**, *27*, 1801 – 1814.
- 3.33 S. Sujatha, S. Balasubramanian, B. Varghese, M. Jayaprakashvel, N. Mathivanan, *Inorg. Chim. Acta* **2012**, *386*, 109-115.
- 3.34 A. Wolfe, G.H. Shimer, T. Meehan, *Biochemistry* **1987**, *26*, 6392-6396.
- 3.35 Q. Wei, J. Dong, P. Zhao, M. Li, F. Cheng, J. Kong, L. Li, *J. Photochem. Photobiol. B* **2016**, *161*, 355-367.
- 3.36 M. E. K. Wahba, N. El-Enany, F. Belal, *Anal. Methods* **2015**, *7*, 10445-10451.
- 3.37 J.A. Pachter, C.H. Huang, V.H. DuVernay Jr., A.W. Prestayko, S.T. Crooke, *Biochemistry* **1982**, *21*, 1541-1547.
- 3.38 S. Tabassum, A. Asim, F. Arjmand, M. Afzal, V. Bagchi, *Eur. J. Med. Chem.* **2012**, *58*, 308-316.
- 3.39 P. Daroui, S. D. Desai, T.-K. Li, A. A. Liu, L. F. Liu, *J. Biol. Chem.* **2004**, *279*, 14587-14594.
- 3.40 E. Trotta, N.D. Grosso, M. Erba, M. Paci, *Biochemistry* **2000**, *39*, 6799–6808.
- 3.41 P. Wittung, P. Nielsen, B. Norden, *J. Am. Chem. Soc.* **1996**, *118*, 7049 –7054.
- 3.42 J.J. Stephanos, *J. Inorg. Biochem.* **1996**, *62*, 155-169.
- 3.43 Y. Lu, Q. Feng, F. Cui, W. Xing, G. Zhang, X. Yao, *Bioorg. Med. Chem. Lett.* **2010**, *20*, 6899-6904.
- 3.44 J.R. Lakowicz, G. Weber, *Biochemistry* **1973**, *12*, 4171- 4179.
- 3.45 B. Valeur, J.C. Brochon, *New Trends in Fluorescence Spectroscopy*, 6th ed., Springer, Berlin, 1999.
- 3.46 S. Naveenraj, S. Anandan, *J. Photochem. Photobiol. C* **2013**, *14*, 53-71.
- 3.47 T. Forster, in *Modern Quantum Chemistry: O. Sinanoglu (Ed.)*, Modern Quantum Chemistry, vol. 3, Academic, New York, 1996, pp. 93-137.
- 3.48 X.-B. Fu, G.-T. Weng, D.-D. Liu, X.-Y. Le, *J. Photochem. Photobiol. A* **2014**, *276*, 83 -95.
- 3.49 S. Tabassum, M. Zaki, M. Ahmad, M. Afzal, S. Srivastav, S. Srikrishna, F. Arjmand, *Eur. J. Med. Chem.* **2014**, *83*, 141-154.
- 3.50 C. Li, F. Cui, R. Mao, R. Huo, G. Qu, *Org. Biomol. Chem.* **2012**, *10*, 869-875.

- 3.51 Y.Q. Wang, X.Y. Wang, J. Wang, Y.M. Zhao, W.J. He, Z.J. Guo, *Inorg. Chem.* **2011**, *50*, 12661–12668.
- 3.52 B. Ahmad, S. Parveen, R.H. Khan, *Biomacromolecules* **2006**, *7*, 1350-1356.
- 3.53 S. Tabassum, W.M. Al-Asbahy, M. Afzal, F. Arjmand, R.H. Khan, *Mol. Biosyst.* **2012**, *8*, 2424-2433.
- 3.54 S. Tanimoto, D. Takahashi, K. Toshima, *Chem. Commun.* **2012**, *48*, 7659-7671.
- 3.55 (a) N. Rainey, L. Motte, B.B. Aggarwal, P.X. Petit, *Cell Death Dis.* **2015**, *6*, e2003;  
(b) U. Banik, S. Parasuraman, A.K. Adhikary, N.H. Othman, *J. Exp. Clin. Cancer Res.* **2017**, *36*, 98;  
(c) K. Pal, S. Roy, P. K. Parida, A. Dutta, S. Bardhan, S. Das, K. Jana, P. Karmakar, *Mater. Sci. Engg. C* **2019**, *95*, 204 -216.

# Chapter 4

## **Dinuclear Copper(II) Complexes with N,O Donor Ligands: Partial Ligand Hydrolysis and Alcohol Oxidation Catalysis**

### **Abstract**

Two copper(II) complexes  $[\text{Cu}_2(\text{L}^1)_2]$  (**4.1**) and  $[\text{Cu}_2(\text{L}^2)_2]$  (**4.2**) where  $\text{H}_2\text{L}^1=2$ -hydroxy-3-((3-hydroxy-2,2-dimethylpropylimino) methyl)-5-methylbenzaldehyde and  $\text{H}_2\text{L}^2=2$ -hydroxy-3-(((1-hydroxypropan-2-yl)imino)methyl)-5-methylbenzaldehyde have been synthesized and used as catalysts in alcohol oxidation. 2,6-Diformyl-4-methylphenol (DFP) based Schiff-base ligands, 3,3'-(2-hydroxy-5-methyl-1,3-phenylene)bis(methan-1-yl-1-ylidene)bis(azan-1-yl-1-ylidene)bis(2,2-dimethylpropan-1-ol) ( $\text{H}_3\text{L}'$ ) and 2,2'-(((2-hydroxy-5-methyl-1,3-phenylene)bis(methanylylidene))bis(azanylylidene))bis(propan-1-ol) ( $\text{H}_3\text{L}''$ ), undergo partial hydrolysis to convert one of the azomethine groups to aldehyde group to give  $\text{H}_2\text{L}^1$  and  $\text{H}_2\text{L}^2$ , and then react with copper(II) acetate to yield complex **4.1** and **4.2**, respectively. These complexes have been characterized by standard methods such as elemental analysis, room temperature magnetic studies, FT-IR, UV-vis, ESI-mass spectral analyses, cyclic voltammogram, etc. The structures of dinuclear complexes with modified ligands have been confirmed by single crystal X-ray diffraction analysis. Complex **4.1** and **4.2** have been used as catalysts for the oxidation of benzyl alcohol, 4-methyl benzyl alcohol, 4-methoxy benzyl alcohol, 4-nitro benzyl alcohol and 4-bromo benzyl alcohol to the corresponding aldehyde as the sole product. Efficiency of the catalyst depends on the chain length and substitution on the chain of the ligand.

## 4.1 Introduction

Attention on metal Schiff-base complexes is high among the researchers for last few decades. Appropriate coordination environment can easily be incorporated into the Schiff-base ligands by the judicious choice of the starting amine and aldehyde/keto compounds. These ligands stabilize different oxidation states of the transition metal ions offering opportunity to use such complexes in the diverse field of applications such as catalysis, redox processes, etc.<sup>4.1,4.2</sup> Apart from this, transition metal complexes were applied in the field of magnetism, biological sciences, optoelectronics, sensing, etc.<sup>4.3-4.6</sup> The Schiff-base ligands derived from 2,6-diformyl-4-methylphenol (DFP) are useful in the preparation of dinuclear or multinuclear transition metal complexes because phenoxy oxygen atom of DFP unit acts as the binucleating bridging center.<sup>4.7</sup> Depending on transition metal ions, reaction conditions and bridging ligands, di-,<sup>4.8</sup> tri-,<sup>4.9</sup> tetra-,<sup>4.7d-e,4.10</sup> penta-,<sup>4.10b</sup> hexa-,<sup>4.7e,4.11</sup> hepta-<sup>4.8a</sup> or higher nuclear transition metal complexes<sup>4.12</sup> were obtained with the Schiff-base ligands of DFP which found different applications. Copper(II) complexes with Schiff-base ligands were used as the catalyst in different oxidation reactions<sup>4.13</sup> such as oxidation of alkane,<sup>4.14</sup> alkene,<sup>4.15</sup> sulfide,<sup>4.16</sup> catechol<sup>4.17</sup>, alcohol<sup>4.18</sup> etc. Pombeiro et al. reported a landmark work on copper catalyzed oxidation of cyclohexane.<sup>4.14a</sup> After that a number of copper complexes were employed as the catalyst for such oxidation reactions.<sup>4.19</sup> The products of cycloalkane oxidation are, primarily, cycloalkanol and cycloalkanone. Alkene has been converted to corresponding epoxide as the main product by copper complex as the catalyst using various oxidants such as hydrogen peroxide, tert.-butyl hydroperoxide, molecular oxygen, etc.<sup>4.15</sup> Epoxides are important building blocks for several fine organic materials. Apart from oxidation of these substrates, dimethyl ether has been synthesized from syngas using copper-based catalyst.<sup>4.20</sup> Click reaction yields different triazoles from azides. This reaction is catalyzed by copper(I) compounds in homogeneous as well as in heterogeneous media.<sup>4.21</sup> Copper compounds catalyze several C–C, C–X (where X is B, Si and F) bond-formation reactions where unactivated alkyl electrophiles have been used as the substrates.<sup>4.22</sup>

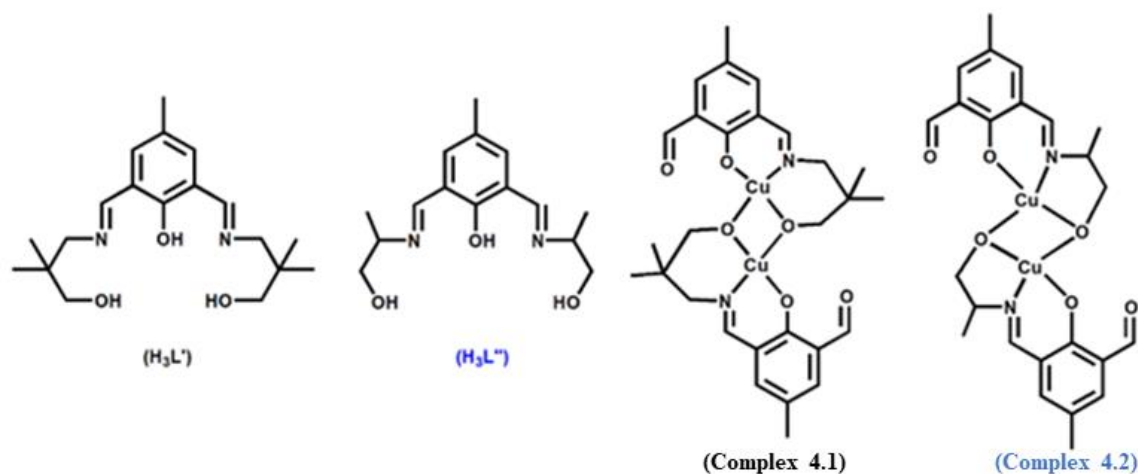
Oxidation of alcohol is important in organic chemistry as it offers transformation of alcohol to aldehyde group. Alcohol oxidation is generally achieved in the presence of stoichiometric amounts of metal containing toxic and/or hazardous oxidizing agents.<sup>4.23</sup> Work up procedure to achieve the target oxidized compounds requires huge labor. Thus, the use of appropriate catalyst for such transformation is an alternative option in terms of economy and environmental pollution. In this respect, it may be suitable to mention galactose oxidase

(GO).<sup>4.24</sup> It is a fungal enzyme and catalyzes the oxidation of various primary alcohols to the corresponding aldehyde solely with the reduction of dioxygen to H<sub>2</sub>O<sub>2</sub>.<sup>4.25</sup> It has one copper atom with square pyramidal geometry at the active site.

Aerobic oxidation of alcohols has been achieved by different metals as the catalyst. Abdel-Rahman et al. reported some Cu(II)-Schiff base complexes as the catalyst for oxidation of alcohol under different reaction conditions.<sup>4.26</sup> Zhan and co-workers reported some mononuclear copper(II) complexes with ligands containing phenol derivatives and used them in the aerobic oxidation of benzyl alcohol.<sup>4.27</sup> Sulfonated Schiff base copper(II) complexes were used as the catalyst for the oxidation of primary and secondary alcohols.<sup>4.28</sup> One mononuclear copper (II) complex with non-innocent aminophenol based ligand has been reported as biomimetic model for galactose oxidase enzyme.<sup>4.29</sup> We have also utilized some copper(II)-Schiff base complexes as the catalyst for the oxidation of different benzyl alcohols.<sup>4.30</sup> The oxidation of primary alcohols to the corresponding aldehydes in the presence of CuI OTf or CuII(OTf)<sub>2</sub> as metal sources, 2,2'-bipyridine as ligand, N-methylimidazole as base and 2,2,6,6-tetramethylpiperidine-1-oxyl (TEMPO) as the co-catalyst has been studied by different groups<sup>4.31</sup> to establish the mechanism of the oxidation reaction. Amongst the reported catalytic systems, TEMPO has been used as a co-catalyst in almost every system. However, there are some problems with the processes, for example, reaction conditions, recyclability of the catalyst, catalyst loading, chemo-/stereo-selectivity, etc. Thus, attempts for better catalysts to overcome such challenges are continuing.

Synthesis, characterization, and catalytic properties of two dinuclear complexes, [Cu<sup>2</sup>(L<sup>1</sup>)<sub>2</sub>] (**4.1**) and [Cu<sup>2</sup>(L<sup>2</sup>)<sub>2</sub>] (**4.2**) where H<sub>2</sub>L<sup>1</sup>=2-hydroxy-3-((3-hydroxy-2,2-dimethylpropylimino)methyl)-5-methylbenzaldehyde and H<sub>2</sub>L<sup>2</sup>=(E)-2-hydroxy-3-(((1-hydroxypropan-2-yl)imino)methyl)-5-methylbenzaldehyde have been reported here (**Scheme 4.1**). Complex **4.1** and **4.2** have been synthesized under mild conditions. H<sub>2</sub>L<sup>1</sup> is the product of partial hydrolysis of 3,3'-(2-hydroxy-5-methyl-1,3-phenylene)bis(methan-1-yl-1-ylidene)bis(azan-1-yl-1-ylidene)bis(2,2-dimethylpropan-1-ol) (H<sub>3</sub>L') and H<sub>2</sub>L<sup>2</sup> is obtained by partial hydrolysis of 2,2'-(((2-hydroxy-5-methyl-1,3-phenylene)bis(methanylylidene))bis(azanylylidene))bis(propan-1-ol) (H<sub>3</sub>L''). It is documented that Cu(II) can convert the ligand to its oxidized products on several occasions.<sup>4.32</sup> Cu(II) catalyzed partial hydrolysis of imine group of some Schiff-base ligands has been reported.<sup>4.33</sup> However, partial modification of DFP based ligands have been reported with metal ions generally other than Cu(II) ion.<sup>4.7e,4.8,4.9,4.11b</sup> In this report, two dinuclear copper(II) complexes with partially hydrolyzed

DFP based ligands have been used as the catalysts for the oxidation of some benzyl alcohols in the presence of tert-butyl hydroperoxide (TBHP) as the oxidant.



**Scheme 4.1:** Structures of (H<sub>3</sub>L'), (H<sub>3</sub>L''), complex **4.1** and **4.2**.

## 4.2. Experimental Section

### 4.2.1. Materials and physical methods

3-Amino-2,2-dimethyl-1-propanol, DL-2-amino-1-propanol, copper(II) acetate monohydrate were purchased from Sigma Aldrich and were used without further purification. Other reagents were obtained from commercial sources and used as received. 2,6-diformyl-4-methylphenol was synthesized following a published procedure.<sup>4,34</sup> Elemental analyses (carbon, hydrogen and nitrogen) were performed using a Perkin–Elmer 2400C elemental analyzer. FT-IR spectrum was obtained on a Perkin Elmer spectrometer (Spectrum Two) with the sample by using the attenuated total reflectance (ATR) technique. The UV-visible spectral measurement was done in Agilent 8453 diode array spectrophotometer. Electrochemical studies of the complexes were carried out in dimethylformamide (DMF) using tetrabutylammonium perchlorate (TBAP) as supporting electrolyte and all experiments were carried out at room temperature. A typical cyclic voltammogram (CV) was obtained by using a glassy carbon as working electrode, Pt as supporting electrode and saturated Ag/AgCl as reference electrode. Scan rate was set as 25 mV/s. Solutions of complex **1** and **2** were prepared freshly before use, and argon was passed through the solution for 15 min before recording CV to remove dissolved O<sub>2</sub>, if any. Analysis of reaction mixture of catalytic reactions was performed with a Shimadzu made next generation high speed gas chromatography system (model: GC-2025 AF) equipped with a fused silica capillary column and an FID detector. All experiments were carried out at room temperature in air unless reported otherwise.

**CAUTION:** Organic perchlorates are potentially explosive. Only small amount of the perchlorate salt should be handled with care.

## 4.2.2. Synthesis

### 4.2.2.1. Synthesis of 3,3'-(2-hydroxy-5-methyl-1,3-phenylene)bis(methan-1-yl-1-ylidene)bis(azan-1-yl-1-ylidene)bis(2,2-dimethylpropan-1-ol) ( $H_3L'$ )

3-Amino-2,2-dimethyl-1-propanol (0.5 mmol, 0.052 g) was added to an acetonitrile solution (10 mL) of 2,6-diformyl-4-methylphenol (0.25 mmol, 0.041 g) under stirring condition. The mixture was stirred for 30 min. Then, the resulting solution was refluxed for 3 h. The color of the mixture turned yellow. The mixture was then cooled and filtered to remove any undissolved material. Yellow colored product of  $H_3L'$  was obtained from the slow evaporation of the solvent.

Data for  $H_3L'$ : yield (0.073 g, 87%); C, H, N analysis: anal. calc. for  $C_{19}H_{30}N_2O_3$ : C, 68.23; H, 9.04; N, 8.38; found: C, 68.04; H, 8.95; N, 8.28%.  $^1H$  NMR (400 MHz,  $CDCl_3$ ;  $\delta$  ppm, TMS): 10.39 (1H, s), 8.56 (2H, s), 7.51 (2H, s), 4.93 (2H, s), 3.52 (4H, s), 3.49 (4H, s), 2.30 (3H, s), 1.00 (12H, s); ESI-MS<sup>+</sup> ( $m/z$ ): 335.18 [ $(H_3L' + H^+)$ ].

### 4.2.2.2. Synthesis of 2,2'-(((2-hydroxy-5-methyl-1,3-phenylene)bis(methanylylidene))bis(azanylylidene))bis(propan-1-ol) ( $H_3L''$ )

$H_3L''$  was obtained following the same synthetic procedure which was used for the synthesis of  $H_3L'$  except DL-2-amino-1-propanol (0.5 mmol, 0.038 g) was used in place of 3-amino-2,2-dimethyl-1-propanol (0.5 mmol, 0.052 g).

Data for  $H_3L''$ : yield (0.139 g, 90%); C, H, N analysis: anal. calc. for  $C_{15}H_{22}N_2O_3$ : C, 64.73; H, 7.97; N, 10.06; found: C, 64.54; H, 7.88; N, 10.28%.  $^1H$  NMR (400 MHz,  $CDCl_3$ ;  $\delta$  ppm, TMS): 10.47 (1H, s), 8.42 (2H, s), 7.28 (2H, s), 5.27 (2H, s), 3.71 (4H, d,  $J = 2.4$ ), 3.10 (4H, m), 2.30 (3H, s), 1.23 (6H, s); ESI-MS<sup>+</sup> ( $m/z$ ): 279.13 [ $(H_3L'' + H^+)$ ].

### 4.2.2.3. Synthesis of $[Cu_2(L^1)_2]$ (**4.1**)

To an aqueous solution (5.0 mL) of copper(II) acetate monohydrate (0.5 mmol, 0.100 g), an acetonitrile solution (10.0 mL) of  $H_3L'$  (0.5 mmol, 0.167 g) was added dropwise while stirring was continued. The mixture was stirred for another 1 h. The mixture was then filtered to remove suspended material and/or precipitate, if any. Green single crystals of complex **4.1** suitable for X-ray diffraction analysis were obtained on slow evaporation of the solvent within few days.

Data for **4.1**: yield (0.202 g, 65%); C, H, N analysis: anal. calc. for  $C_{28}H_{34}Cu_2N_2O_6$ : C, 54.10; H, 5.51; N, 4.51; found: C, 54.00; H, 5.57; N, 4.32%.



#### 4.2.2.4 Synthesis of [Cu<sub>2</sub>(L<sup>2</sup>)<sub>2</sub>] (4.2)

Complex **4.2** was synthesized following the same synthetic procedure which was used for the synthesis of complex **4.1** except H<sub>3</sub>L'' (0.5 mmol, 0.139 g) was used in place of H<sub>3</sub>L' (0.5 mmol, 0.167 g).

Data for **4.2**: yield (0.164 g, 58%); C, H, N analysis: anal. calc. for C<sub>24</sub>H<sub>26</sub>Cu<sub>2</sub>N<sub>2</sub>O<sub>6</sub>: C, 50.97; H, 4.63; N, 4.95; found: C, 50.90; H, 4.57; N, 4.82%.

#### 4.2.3. X-ray data collection and structure determination

Details of the data collection and refinement parameters for complex **4.1** and **4.2** are summarized in **Table 4.1**. The single crystal X-ray diffraction experiments were performed on a Bruker APEX-II CCD diffractometer using graphite monochromated Mo K $\alpha$  radiation at 298 K. The data integration was carried out with SAINT program<sup>4.35</sup> and the absorption correction was done using SADABS. The structures of complexes **1** and **2** were solved by SHELXS 97<sup>4.36</sup> using the Patterson method with the successive Fourier and difference Fourier synthesis. Full matrix least-squares refinements were done on F<sup>2</sup> using SHELXL-97 with anisotropic displacement parameters for all of the non-hydrogen atoms.<sup>4.37</sup> All of the hydrogen atoms were fixed geometrically by HFIX command and placed in ideal positions. Calculations were performed using SHELXL 97, SHELXS 97, PLATON v1.15,<sup>4.38</sup> ORTEP-3v2<sup>4.39</sup> and WinGX system Ver-1.80.<sup>4.40</sup>

CCDC 2050745 and CCDC 2050742 contain the supplementary crystallographic data of complexes **4.1** and **4.2**, for this paper. These data can be obtained free of charge from the Cambridge Crystallographic Data Centre *via* [www.ccdc.cam.ac.uk/data\\_request/cif](http://www.ccdc.cam.ac.uk/data_request/cif).

#### 4.2.4. Alcohol oxidation procedure

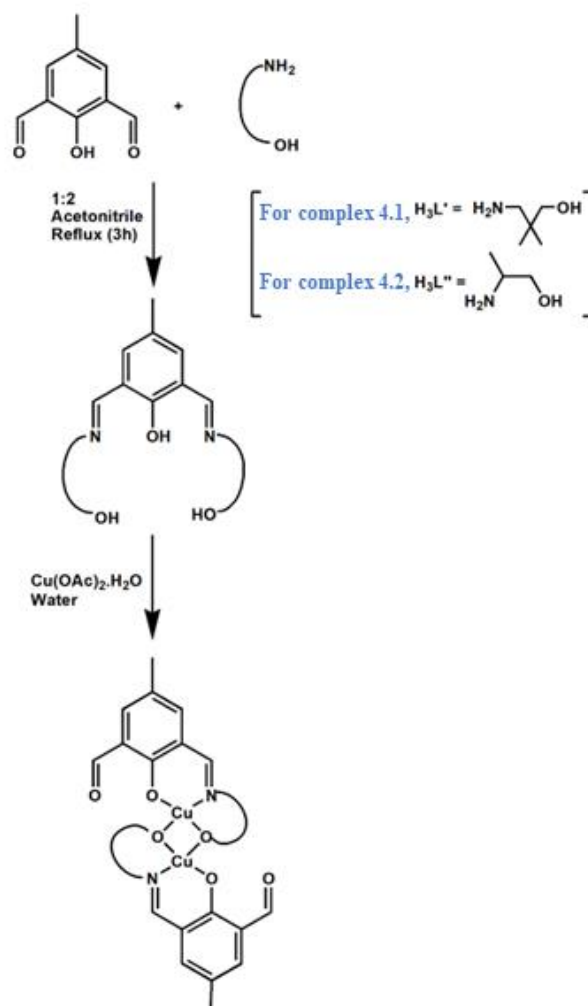
Oxidation of benzyl alcohol, 4-methyl benzyl alcohol, 4-methoxy benzyl alcohol, 4-nitro benzyl alcohol and 4-bromo benzyl alcohol was performed by using TBHP as the oxidant in the presence of complexes **4.1** and **4.2** as catalyst at 343 K. Typically, 0.5 mmol of the substrate (alcohol) in 8.0 mL of acetonitrile was taken in a two necked round-bottomed flask fitted with a condenser. 0.025 mmol of catalyst was added to it. The catalytic reaction was started as soon as 0.5 mmol of *tert*-butyl hydroperoxide was added to the mixture under stirring condition. The temperature of the reaction mixture was kept constant using a thermostat. Aliquots from the mixture were collected after 2 h and 4 h, and then every 4 h upto 24 h. The collected mixtures were analyzed by the gas chromatography. The substrate and product(s) were identified by the comparison with known standards.

Blank experiments for all of the substrates were carried out in absence of any catalyst under the same experimental conditions.

### 4.3. Results and discussion

#### 4.3.1. Synthesis of $H_3L'$ , $H_3L''$ , complex 4.1 and complex 4.2

Complex 4.1 and 4.2 were synthesized following the route as depicted in Scheme 4.2. First ligands,  $H_3L'$  and  $H_3L''$  were been synthesized by 1:2 condensation between DFP and the respective amine, characterized and thought to get multinuclear copper(II) complexes where phenolic oxygen atom could act as the bridge.



**Scheme 4.2:** Synthetic route to complex 4.1 and 4.2

Both  $H_3L'$  and  $H_3L''$  have been characterized by elemental analysis,  $^1H$  NMR and ESI mass spectral analysis. ESI-mass spectrometric measurements were performed with methanolic solutions of  $H_3L'$  and  $H_3L''$ . Mass spectrum of  $H_3L'$  shows the  $m/z$  peak at 335.18, which may be attributed to the presence of  $[H_3L' + H^+]$  species (Figure 4.1). For  $H_3L''$ , the  $m/z$  peak at 279.13 may be attributed to the presence of  $[H_3L'' + H^+]$  (Figure 4.2).

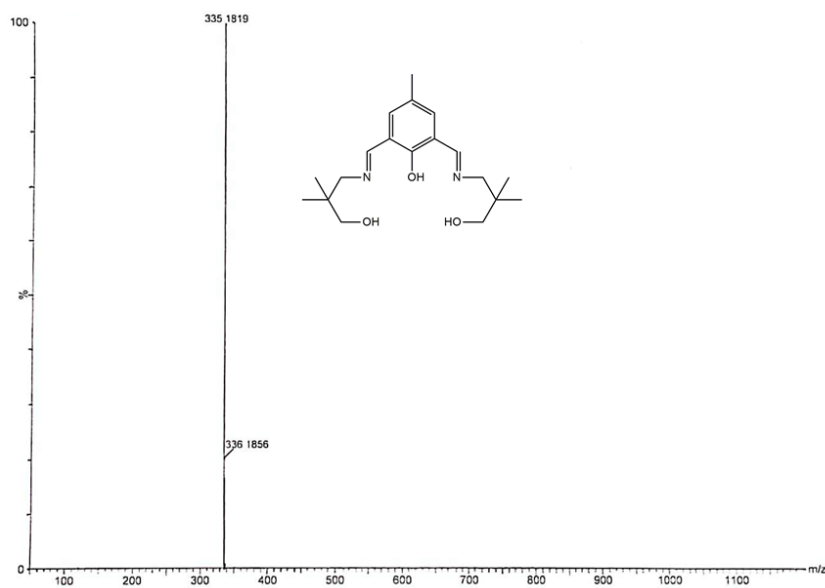


**Figure 4.1:** ESI mass spectrum of H<sub>3</sub>L' in methanol.

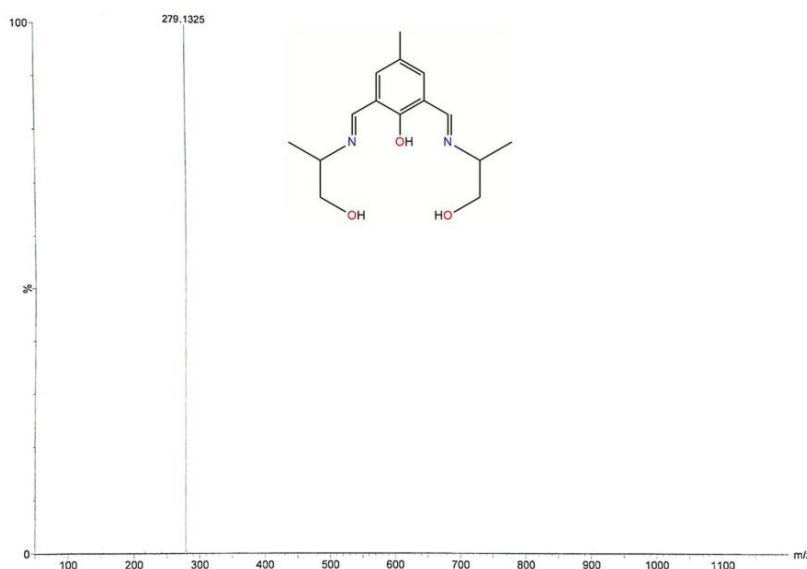


**Figure 4.2:** ESI mass spectrum of H<sub>3</sub>L'' in methanol.

<sup>1</sup>H NMR spectra of H<sub>3</sub>L' and H<sub>3</sub>L'' were recorded in CDCl<sub>3</sub> (Figure 4.3 and 4.4). Signals for phenolic proton of H<sub>3</sub>L' and H<sub>3</sub>L'' appear at 10.39 and 10.47 ppm, respectively. Peaks at 8.56 and 8.42 ppm may be attributed to the imine protons of H<sub>3</sub>L' and H<sub>3</sub>L'', respectively. The aromatic protons of H<sub>3</sub>L' appear at 7.51 ppm. Signal for aromatic protons of H<sub>3</sub>L'' emerges at 7.28 ppm. Peak of H<sub>3</sub>L' at 4.93 ppm may appear due to the presence of alcoholic protons. Alcoholic protons of H<sub>3</sub>L'' give signal at 5.27 ppm. Methylene protons of H<sub>3</sub>L' appear at 3.52 and 3.48 ppm whereas signals for the other compound appear at 3.71 and 3.10 ppm. Peaks at 2.30 and 1.00 ppm may be attributed to the various methyl protons of H<sub>3</sub>L'. Signals for methyl protons of H<sub>3</sub>L'' appear at 2.80 and 1.23 ppm.

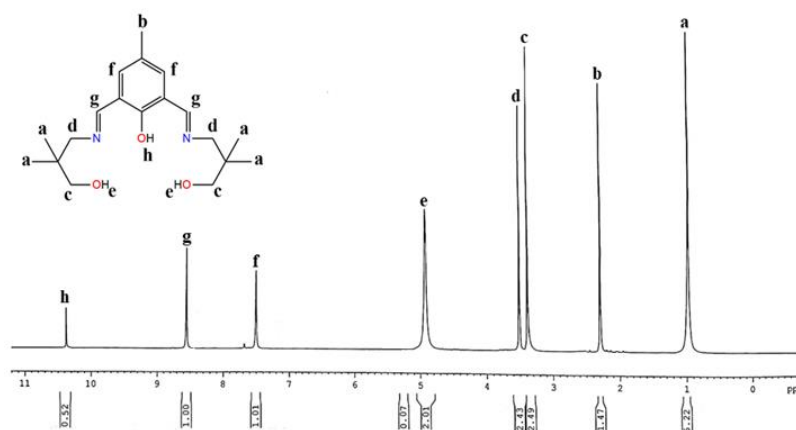


**Figure 4.3:**  $^1\text{H}$  NMR spectrum of  $\text{H}_3\text{L}'$  in  $\text{CDCl}_3$ .

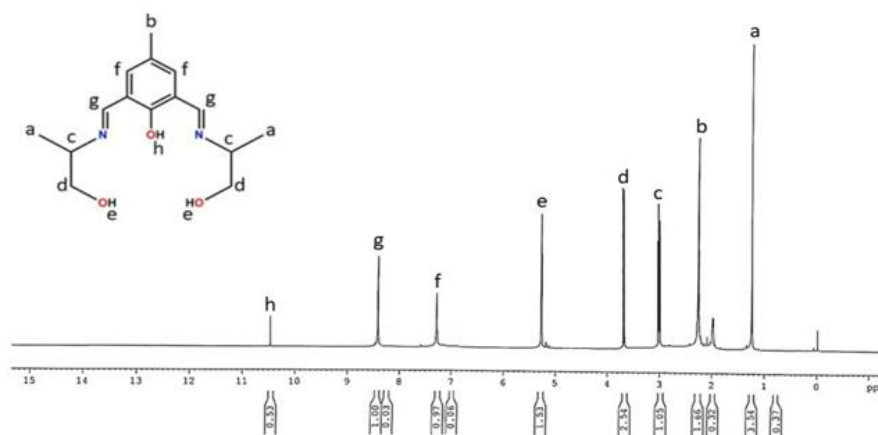
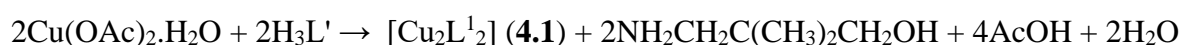
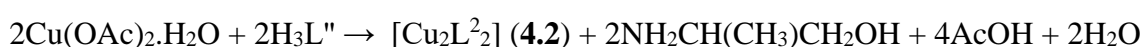


**Figure 4.4:**  $^1\text{H}$  NMR spectrum of  $\text{H}_3\text{L}''$  in  $\text{CDCl}_3$ .

However, during the synthesis of complex **4.1** and complex **4.2**, the ligand modification has been noticed for both the cases. Partial hydrolysis of  $\text{H}_3\text{L}'$  and  $\text{H}_3\text{L}''$  leads to the generation of  $\text{H}_2\text{L}^1$  and  $\text{H}_2\text{L}^2$ , respectively, where one of the imine bonds of the ligand has been converted to aldehyde group. Schiff-base ligands derived from DFP tend to undergo partial hydrolysis. In previous studies, partial hydrolysis of azomethine bond occurred in the presence of  $\text{Ni}^{2+}$  ion<sup>4.11d</sup> as well as  $\text{Zn}^{2+}$  ion.<sup>4.9</sup> Reaction between  $\text{H}_3\text{L}'$  and copper(II) acetate gives complex **4.1** without adding any external base to deprotonate the phenolic oxygen atom. Overall reaction may be written as:



Similar reaction occurs between  $\text{H}_3\text{L}''$  and copper(II) acetate to produce complex **4.2**.



### 4.3.2. Crystal structures of complex 4.1 and 4.2

Complex **4.1** crystallizes in the P-1 space group, whereas complex **4.2** crystallizes in the P 21/n space group. Perspective views of the molecules are shown in **Figure 4.5**. Selected bond angles and bond lengths are listed in **Table 4.2**. Both of the complexes consist of two deprotonated dianions of the partially hydrolyzed ligand,  $H_2L^1$  for complex **4.1** and  $H_2L^2$  for complex **4.2**, and two copper atoms. Both the copper atoms are in a tetracoordinated environment. Each copper in **4.1** and **4.2** is coordinated with one phenolic oxygen atom (O2), two alcoholic oxygen atoms (O3, O3a) and one nitrogen atom (N1) from the ligands,  $H_2L^1$  and  $H_2L^2$ , respectively. The metal center in both the cases is in a distorted square planar geometry. O2, N1, O3 and O3a form the square plane and Cu1 is slightly out the mean plane by a distance of 0.034 Å. The smaller donor-metal-donor angle around Cu1 deviates from 90° for both the cases. The O3—Cu1—O3<sup>a</sup> angle is 77.49° and 82.9° for complex **4.1** and **4.2**, respectively while the O3—Cu1—N1 angle is 96.14° and 84.2° for complex **4.1** and **4.2**, respectively. The larger donor-metal-donor angle around Cu1 also shifts from ideal 180° for both the complexes. The O2—Cu1—O3 angles are 161.78° for complex **4.1**, 178.3° for complex **2** while O3<sup>a</sup>—Cu1—N1 angles are 166.97° for complex **4.1** and 161.0° for complex **4.2**.

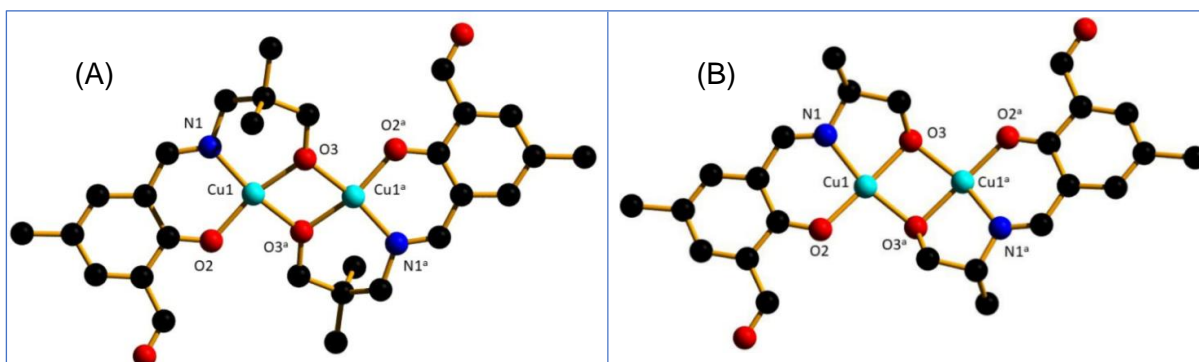


**Figure 4.5:** Perspective views of (A) complex **4.1** and (B) complex **4.2**. Hydrogen atoms have been omitted for clarity. Symmetry code: (a) 1-x, 2-y, 1-z (for complex **4.1**) and (a) 1-x, 1-y, 1-z (for complex **4.2**).

For five coordinate complex, trigonal bipyramidal or square pyramidal geometry is ascertained from the value of trigonal index parameter ( $\tau$  parameter).<sup>4.41</sup> However, for four coordinate complex, Houser *et al.* introduced four-coordinate  $\tau_4$  index to find the geometry around the metal center with the following formula<sup>4.42</sup>

$$\tau_4 = \frac{360^\circ - (\alpha + \beta)}{141^\circ}$$

where  $\alpha$  and  $\beta$  are the two largest angles in the four-coordinate species. When the value of  $\tau_4$  is 1.00, the geometry is perfect tetrahedral. For the perfect square planar geometry, it is

0.00. Other values indicate different seesaw geometry. The values of four-coordinate  $\tau_4$  index have been calculated to be 0.037 and 0.123 for complex **4.1** and **4.2**, respectively. These indicate that there is almost perfect square planar geometry around metal center in complex **4.1**. For complex **4.2**,  $\tau_4$  index indicate the fluctuation of square planar geometry. The donor metal bond distances are in the range of 1.8821 and 1.9302 Å. The metal-metal bond distances are 2.989 Å for complex **4.1** and 2.902 Å for complex **4.2** which are significantly short.

**Table 4.1:** Crystal data of complex **4.1** and **4.2**

	Complex <b>4.1</b>	Complex <b>4.2</b>
Formula	C <sub>28</sub> H <sub>34</sub> Cu <sub>2</sub> N <sub>2</sub> O <sub>6</sub>	C <sub>48</sub> H <sub>52</sub> Cu <sub>4</sub> N <sub>4</sub> O <sub>12</sub>
Formula weight	621.65	1131.14
<i>T</i> (K)	273(2)	273(2)
Crystal color	green	brown
Crystal system	triclinic	monoclinic
Space group	<i>P</i> -1	<i>P</i> 21/ <i>n</i>
<i>a</i> (Å)	8.6604(8)	8.6854(19)
<i>b</i> (Å)	8.8110(8)	19.464(4)
<i>c</i> (Å)	9.7276(8)	14.341(3)
$\alpha$ (°)	85.215(2)	90
$\beta$ (°)	81.477(2)	98.198(6)
$\gamma$ (°)	67.376(2)	90
<i>V</i> (Å <sup>3</sup> )	677.31(10)	2399.7(9)
<i>Z</i>	1	2
Crystal dimensions (mm)	0.4 × 0.2 × 0.1	0.18 × 0.10 × 0.07
<i>F</i> (0 0 0)	322.0	1160
<i>D<sub>c</sub></i> (g cm <sup>-3</sup> )	1.524	1.566
$\lambda$ (Mo K $\alpha$ ) (Å)	0.71073	0.71073
$\theta$ Range (°)	2.51- 27.10	1.776 - 26.921
Reflection collected/ unique/observed	23375, 2969, 2776	15848, 5194, 1623
Absorption correction	multi-scan	empirical

	Complex <b>4.1</b>	Complex <b>4.2</b>
$R_{\text{int}}$	0.0240	0.0946
Final $R_1$ index [ $I > 2\sigma(I)$ ]	0.0266	0.2137
Final $wR_2$ index (all reflections)	0.0719	0.2350
Goodness-of-fit	1.09	1.001

**Table 4.2:** Selected bond lengths (Å) and bond angles (°) of complex **4.1** and **4.2**

Complex <b>4.1</b>		Complex <b>4.2</b>	
Cu1—N1	1.9302(14)	Cu1—N1	1.898(10)
Cu1—O2	1.8821(13)	Cu1—O2	1.890(8)
Cu1—O3	1.9099(13)	Cu1—O3	1.947(8)
Cu1—O3 <sup>a</sup>	1.9218(13)	Cu1—O3 <sup>a</sup>	1.985(7)
Cu1—Cu1 <sup>a</sup>	2.9887(4)	Cu1—Cu1 <sup>a</sup>	2.902
O2—Cu1—O3	161.78(6)	O2—Cu1—O3	178.3(4)
O2—Cu1—O3 <sup>a</sup>	93.28(5)	O2—Cu1—O3 <sup>a</sup>	97.0(3)
O3—Cu1—O3 <sup>a</sup>	77.49(6)	O3—Cu1—O3 <sup>a</sup>	82.9(3)
O2—Cu1—N1	95.79(6)	O2—Cu1—N1	95.4(4)
O3—Cu1—N1	96.14(6)	O3—Cu1—N1	84.2(4)
O3 <sup>a</sup> —Cu1—N1	166.97(6)	O3 <sup>a</sup> —Cu1—N1	161.0(4)
O2—Cu1—Cu1 <sup>a</sup>	130.08(4)	O2—Cu1—Cu1 <sup>a</sup>	138.29
O3—Cu1—Cu1 <sup>a</sup>	38.89(4)	O3—Cu1—Cu1 <sup>a</sup>	96.8(3)
O3 <sup>a</sup> —Cu1—Cu1 <sup>a</sup>	38.60(4)	O3 <sup>a</sup> —Cu1—Cu1 <sup>a</sup>	94.7(3)
N1—Cu1—Cu1 <sup>a</sup>	134.02(4)	N1—Cu1—Cu1 <sup>a</sup>	138.29
Cu1—O3—Cu1 <sup>a</sup>	102.52(—)	Cu1—O3—Cu1 <sup>a</sup>	96.8(3)

Symmetry code: (a) 1-x, 2-y, 1-z for complex **4.1** (a) 1-x, 1-y, 1-z for complex **4.2**.

### 4.3.3. Room temperature magnetic moment determination

Room temperature magnetic susceptibility of complex **4.1** and **4.2** were determined with the powder samples using the Guoy Balance Method. The effective magnetic moment has been determined to be 1.96 and 2.26 BM per dimer for complex **4.1** and **4.2**, respectively ( $X_{\text{MT}}$  values are 0.5 and 0.6 emu K mol<sup>-1</sup> per two copper atoms for complex **4.1** and **4.2**, respectively).

Both the complexes show lower magnetic moment value than the calculated value, which is 2.83 BM for two copper atoms, indicating partial spin pairing by antiferromagnetic interaction in the complexes at room temperature.

#### 4.3.4. UV-vis spectral studies

The electronic spectra of complex **4.1** and **4.2** were recorded in dimethylformamide (DMF) at room temperature (**Figure 4.6** and **4.7**). For an octahedral geometry, the expected  ${}^2T_{2g}$  to  ${}^2E_g$  transition takes place at around 800 nm. This band will undergo a significant blue shift when the octahedral geometry changes to a square pyramidal and square planar structure.<sup>4.43</sup> The absorption band observed in the range 542–694 nm corresponds to the *d-d* transitions (Inset of Fig. s5 and s6). On the basis of the crystal structures of complex **4.1** and **4.2**, the geometry around each copper(II) center is assumed to have a square-planar geometry. The observed *d-d* transitions around 600 nm also indicate the square planar Cu(II) centers. These are weaker in intensity as they are Laporte forbidden. Moreover, both the complexes are centro-symmetric which allows very little mixing of *d* and *p* orbitals. The medium intensity bands appear in the range 330–450 nm for complex **4.1** and 334–452 nm for **4.2**.<sup>4.44</sup> The strong bands at ~415 nm for both the complexes are due to the phenolate-to-copper(II) ligand-to-metal charge transfer (LMCT) (transfer occurs from the MO with ligand-like character to the metal-like one) and other band may be due to the intra-ligand charge transfer transitions.<sup>4.44</sup>

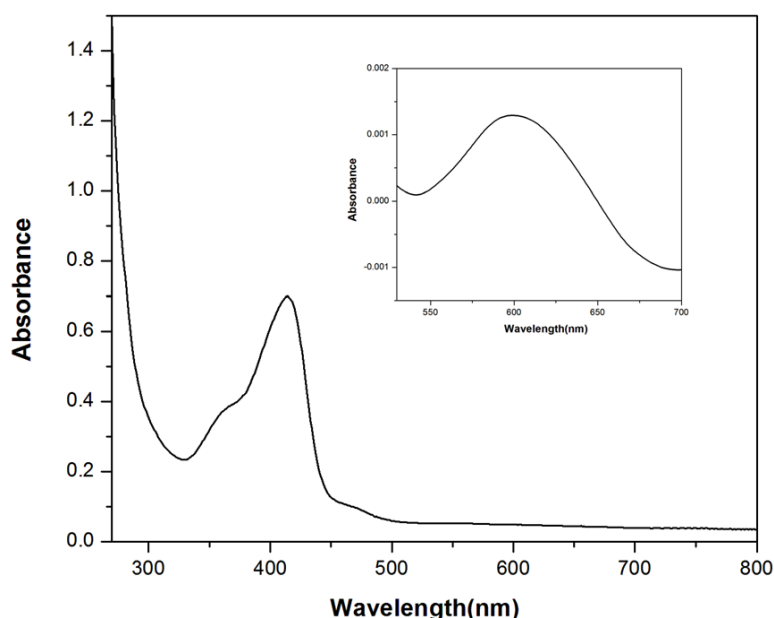


**Figure 4.6:** UV-vis spectrum of complex **4.1** in DMF.



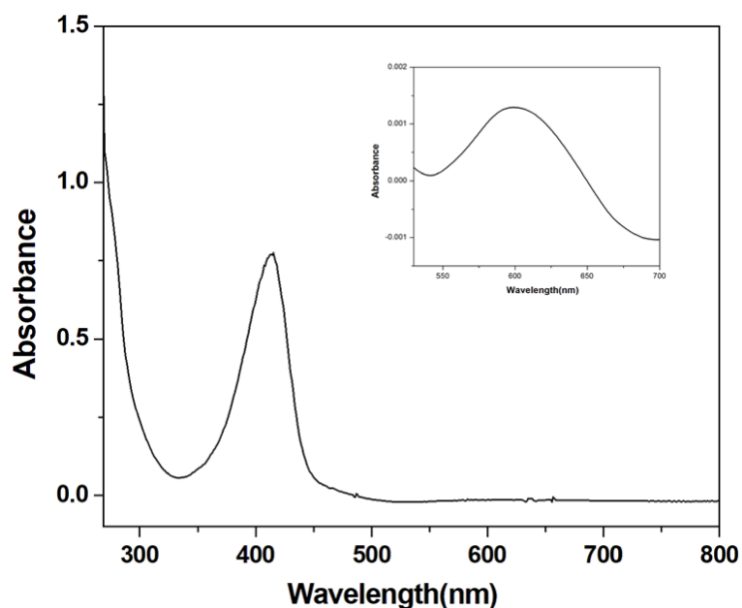


**Figure 4.7:** UV-vis spectrum of complex **4.2** in DMF.

#### 4.3.5. FT-IR spectral studies

FT-IR spectra of complex **4.1** and **4.2** were obtained with powder samples by ATR technique. In the IR spectra of the complexes (**Figure 4.8** and **4.9**), the presence of hydrocarbon part (methyl and methylene groups) of the complexes have been evidenced from the appearance of the unsymmetrical and symmetrical frequencies at the region of  $2800\text{--}3000\text{ cm}^{-1}$ . The sharp band at around  $1670\text{ cm}^{-1}$  may be attributed to the presence of aldehyde group of  $\text{H}_2\text{L}^1$  and  $\text{H}_2\text{L}^2$  species. Another intense band at around  $1625\text{ cm}^{-1}$  is due to the presence of the stretching vibration of the azomethine group ( $\text{C}=\text{N}$  moiety). These observed bands explain the structural similarities between the complex **4.1** and complex **4.2**.

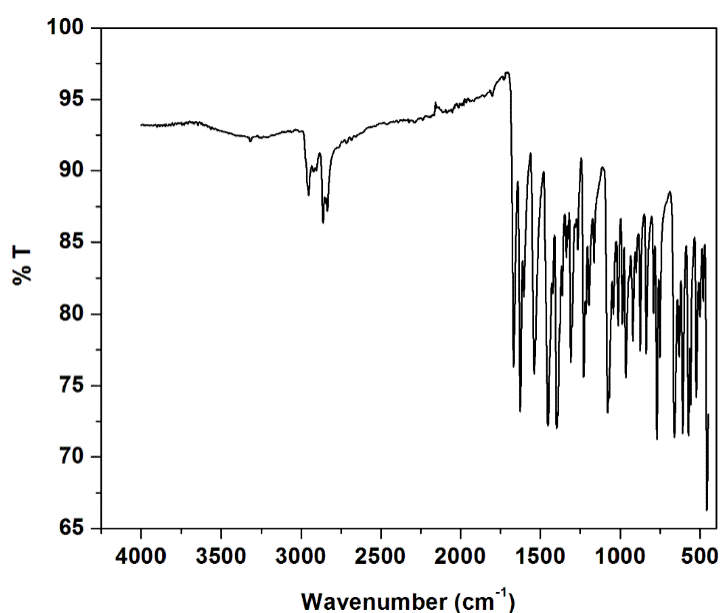


**Figure 4.8:** FT-IR spectrum of complex **4.1**.

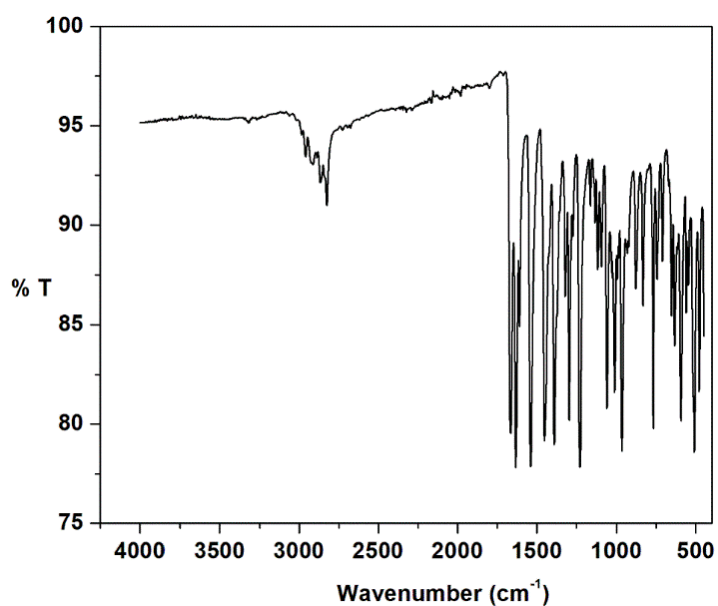


Figure 4.9: FT-IR spectrum of complex 4.2.

#### 4.3.6. Mass spectral studies

ESI-mass spectra of complex 4.1 and 4.2 were obtained in methanol (Figure 4.10 and 4.11).

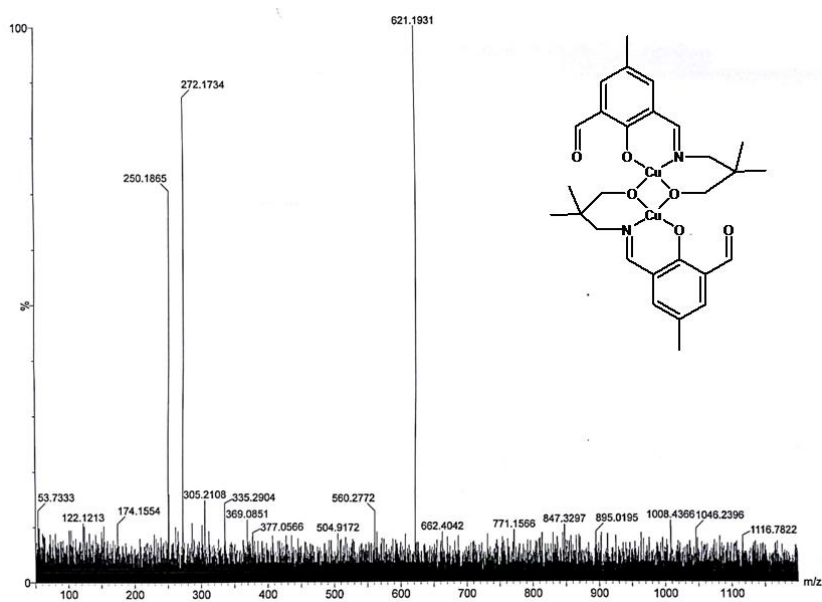
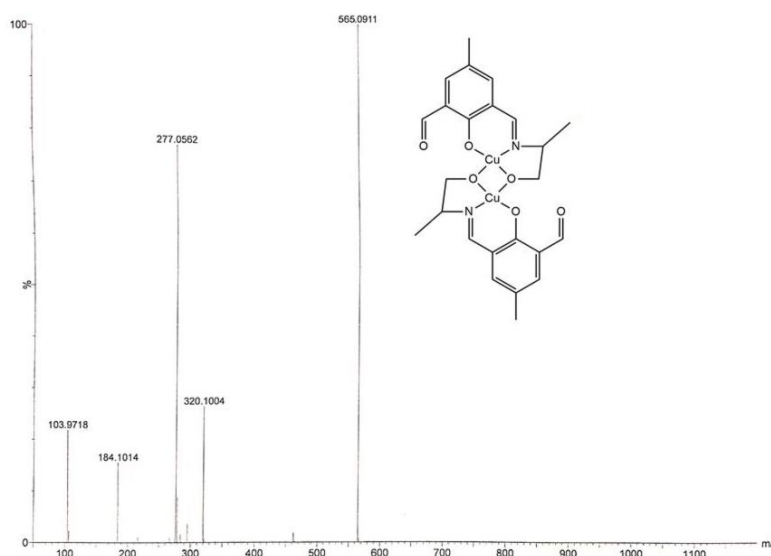


Figure 4.10: ESI mass spectrum of complex 4.1 in methanol.

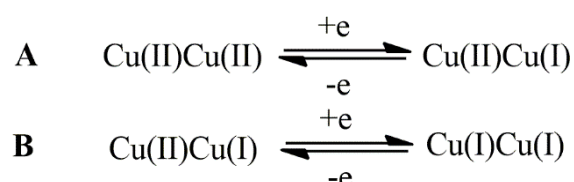


**Figure 4.11:** ESI mass spectrum of complex **4.2** in methanol

As indicated by the spectra, both the complexes have been found to exist mainly as dinuclear copper(II) species in the solution. Mass spectrum of complex **4.1** shows an  $m/z$  peak at 621.19 which may be attributed to the  $[\text{Cu}_2(\text{L}^1)_2 + \text{H}^+]$  species (calculated value: 621.11). The complex undergoes fragmentation to show the presence of the partially hydrolyzed ligand,  $\text{H}_2\text{L}^1$ . Two other significant  $m/z$  peaks are observed at 272.17 and 250.18. These peaks may be assigned to the presence of  $[\text{H}_2\text{L}^1 + \text{Na}^+]$  and  $[\text{H}_2\text{L}^1 + \text{H}^+]$ , respectively (calculated values: 272.13 and 250.14). Mass spectrum of complex **4.2** shows an  $m/z$  peak at 565.09 which may be attributed to the existence of  $[\text{Cu}_2(\text{L}^2)_2 + \text{H}^+]$  species (calculated value: 565.05).

#### 4.3.7. Electrochemical studies

Electrochemical studies of complex **4.1** and **4.2** were carried out in DMF using TBAP as supporting electrolyte. Both the dinuclear Cu(II) complexes exhibit two pairs of redox events which indicate the electronic communication present between the two metal ions of these two dinuclear Cu(II) complexes (Figure 4.12). These redox processes involved between two metal centers can be expressed as



The first pair of oxidation-reduction peaks corresponding to oxidation-reduction couples, i.e.  $\text{Cu(II)Cu(I)/Cu(I)Cu(I)}$  **B**,  $E_{pa1} = -1.48$  V for complex **4.1** and  $-1.20$  V for complex **4.2**,  $E_{pc1} = -1.50$  V for complex **4.1** and  $-1.43$  V for complex **4.2**, the average formal

potential [ $E_{1/2} = (E_{pa1} + E_{pc1})/2$ ] is  $-1.49$  V for complex **4.1** and  $-1.31$  V for complex **4.2**. The second pair of oxidation-reduction peaks corresponding to oxidation-reduction couples, *i.e.* Cu(II)Cu(II)/Cu(II)Cu(I) **A**,  $E_{pa2} = -0.96$  V for complex **4.1** and  $-0.83$  V for complex **4.2**,  $E_{pc2} = -1.08$  V for complex **4.1** and  $-1.06$  V for complex **4.2**, the average formal potential [ $E_{1/2} = (E_{pa2} + E_{pc2})/2$ ] is  $-1.02$  V for complex **4.1** and  $-0.95$  V for complex **4.2**. The peak observed at  $-0.5$  V for complex **4.2** may be assigned to the ligand reduction event.

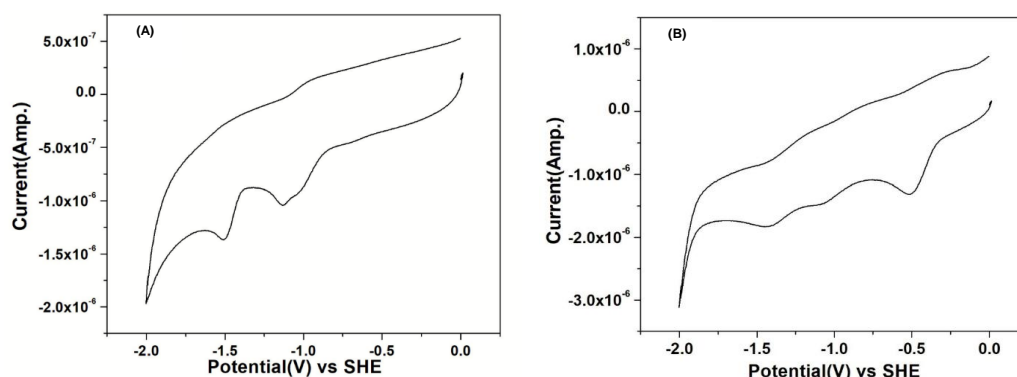


**Figure 4.12:** Cyclic voltammogram of (A) complex **4.1** and (B) complex **4.2** in DMF. Conditions: 0.1 M [n-Bu<sub>4</sub>N]ClO<sub>4</sub> as supporting electrolyte, glassy carbon as working electrode and Ag/AgCl as reference electrode (scan rate: 25 mV/s).

The stability of the mixed-valence Cu(II)Cu(I) species can be expressed in terms of the comproportionation constant,  $K_{con}$ ,

$$K_{con} = \frac{[Cu(II)Cu(I)]^2}{[Cu(II)Cu(I)][Cu(I)Cu(I)]} = \exp [nF(\Delta E_{1/2}^0)/RT]$$

where,  $\Delta E_{1/2}^0 = E_{1/2}^0 (A) - E_{1/2}^0 (B)$

The larger the separation between the potentials of the couple, the greater the stability of the mixed-valence species with respect to comproportionation. The values of  $\Delta E_{1/2}^0$  for complex **4.1** and **4.2** are 0.23 and 0.18 V, respectively whereas values of  $K_{con}$  for complex **4.1** and **4.2** have been determined as  $9.5 \times 10^3$  and  $1.1 \times 10^3$ , respectively.

The values imply the stability of the mixed valence state Cu(II)Cu(I) are comparable with those of the literature.<sup>4.45</sup> It has been reported that  $\Delta E_{1/2}^0$  separation value of non-interacting metal centers, which are in similar chemical environments, is not larger than 50 mV.<sup>4.46</sup> Thus, the cyclic voltammograms indicate significant copper-copper coupling present in these two dinuclear complexes which has also been observed in several other dinuclear metal complexes.<sup>4.47</sup>

The cyclic voltammograms of complex **4.1** and complex **4.2** were also recorded at different potential scan rates to show that the current is diffusion controlled, whereas the current

ratio of the first to second waves increases with an increase in the potential scan rate (Figure 4.13 and 4.14).

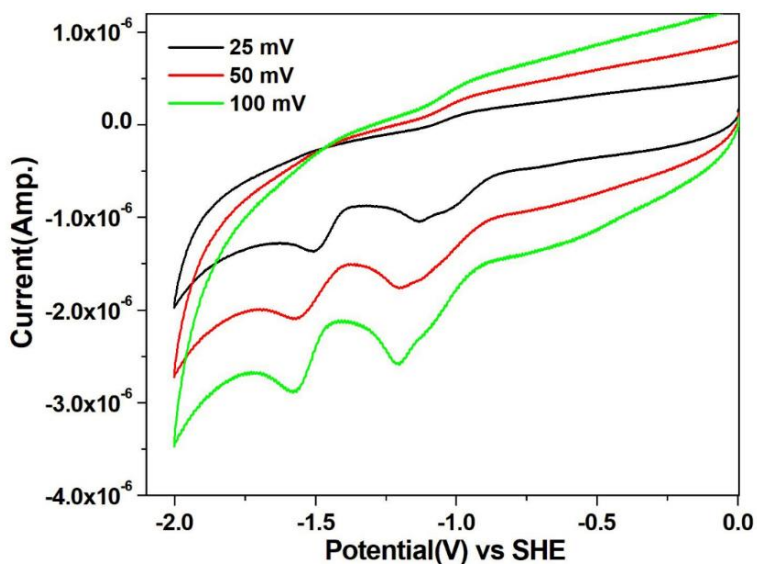


**Figure 4.13:** Scan rate dependence of  $10^{-4}$  M solution of complex **4.1**, at scan rates from 25 to 100 mV/s in DMF solutions with 0.1M  $[n\text{-Bu}_4\text{N}](\text{ClO}_4)$  as supporting electrolyte.

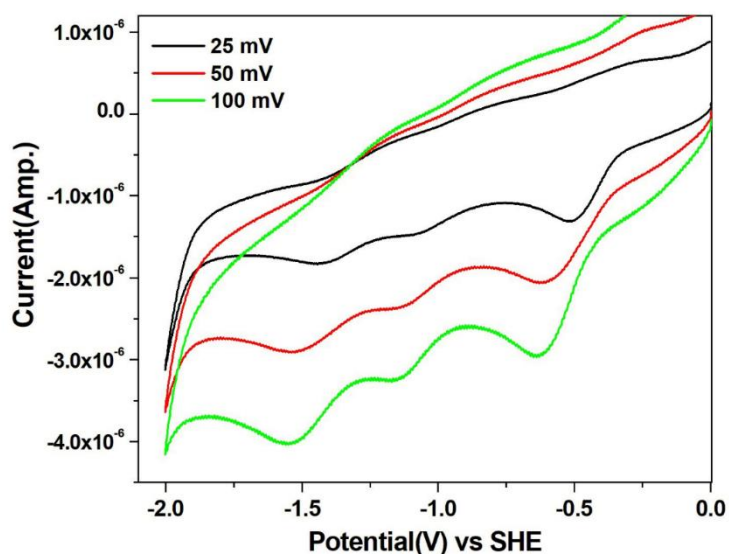


**Figure 4.14:** Scan rate dependence of  $10^{-4}$  M solution of complex **4.2**, at scan rates from 25 to 100 mV/s in DMF solutions with 0.1 M  $[n\text{-Bu}_4\text{N}](\text{ClO}_4)$  as supporting electrolyte.

#### 4.3.8. Alcohol oxidation studies

Complex **4.1** and **4.2** have been used as catalyst for the oxidation of benzyl alcohols with TBHP as the oxidant at 343 K. The complex shows galactose oxidase mimicking activity *i.e.* it acts as the catalyst for the oxidation of benzyl alcohols. The substrates used here are

benzyl alcohol, 4-methyl benzyl alcohol, 4-methoxy benzyl alcohol, 4-nitro benzyl alcohol and 4-bromo benzyl alcohol. The corresponding aldehyde has been obtained as the sole product. The results of the oxidation reactions are given in **Table 4.3**. The results indicate moderate ability of the catalyst towards the conversion of benzyl alcohol to the corresponding aldehyde. Yield of the transformation for each of the substrate is remarkably high in comparison to the corresponding blank experiments signifying the relevance of the presence of the copper complex. The optimized conditions have been found by varying different parameters for the catalytic reaction.

**Table 4.3:** Oxidation<sup>a</sup> of primary alcohol with complexes **4.1** and **4.2**

Substrate	Product	Yield <sup>b</sup> in %, (TON <sup>c</sup> )		
		Complex <b>4.1</b>	Complex <b>4.2</b>	Blank <sup>d</sup>
Benzyl alcohol	Benzaldehyde	72 (14.0)	50 (10.0)	9
4-Methylbenzyl alcohol	4-Methyl benzaldehyde	73 (14.6)	51 (10.2)	10
4-Methoxybenzyl alcohol	4-Methoxy benzaldehyde	81 (16.2)	62 (12.4)	9
4-Nitrobenzyl alcohol	4-Nitro benzaldehyde	59 (11.8)	35 (7.0)	10
4-Bromobenzyl alcohol	4-Bromo benzaldehyde	61 (12.2)	38 (7.6)	7

<sup>a</sup> Oxidant: TBHP; temperature: 343 K; solvent: acetonitrile;

<sup>b</sup> Yield calculated after 24 h

<sup>c</sup> TON: turnover number = number of moles of product/number of moles of catalyst

<sup>d</sup> Oxidation reaction without any complex under identical conditions

In order to investigate the role of the solvent, the oxidation of benzyl alcohol has been carried out in different solvents and the results of the reactions are given in **Table 4.4**. Reaction in water shows poor conversions (9%) probably because of the low solubility of the catalysts in this solvent, hence the yield is similar to that obtained during the blank experiments (Table 1, entry 3). When acetonitrile is used, the catalytic reaction produces the highest yield. Hence acetonitrile has been selected as solvent for all the oxidation reactions. Another possible explanation for the higher yield of the catalysis in CH<sub>3</sub>CN may be found in the inclination of the solvent to stabilize the intermediate Cu(I) species *via* coordination.

**Table 4.4:** Oxidation of benzyl alcohol in various solvents using complex **4.1** as the catalyst

Entry	Catalyst	Yield(%) in Acetonitrile	Yield(%) in DCM	Yield(%) in Water	Yield(%) in DMF
-------	----------	-----------------------------	--------------------	----------------------	--------------------

1	Complex <b>4.1</b>	72	22	9	17
---	-----------------------	----	----	---	----

In order to check the role of the oxidant, the oxidation of benzyl alcohol has been performed in the presence of different oxidants. The results are shown in **Table 4.5**. It is clear from the table the TBHP is far better oxidant to convert the benzyl alcohol in comparison to the other oxidants.

**Table 4.5:** Oxidation of benzyl alcohol in the presence of different oxidant using complex **4.1** as the catalyst

Entry	Catalyst	Yield(%) in presence of TBHP	Yield(%) in presence of H <sub>2</sub> O <sub>2</sub>	Yield(%) in presence of NaOCl
<b>1</b>	Complex <b>4.1</b>	72	3	7

The effect of temperature on the reaction yield has also been examined. At room temperature, the reaction proceeds slowly and produces small amount of the aldehyde. The maximum yield has been obtained at 343 K. So, the reaction has been carried out at this temperature. Higher temperature may destroy the copper complex showing lower yield of catalytic reaction.

Oxidation of benzyl alcohol has been carried out in the presence of various amounts of the catalyst to check whether amount of the catalyst has any significant effect on yield of the catalytic reactions. The results, however, indicate that it does not affect the reaction yield considerably. Thus, for all the substrates, a 1:20 catalyst/substrate ratio has been maintained.

Substrate variation has been done by introducing an electron donating or an electron withdrawing group in the aromatic ring of benzyl alcohol. The effect of these groups has been observed on the yield of the reaction (**Table 4.3**). It has been found that the yield of oxidation is increased with incorporation of electron donating groups. The highest yield has been obtained with methoxy benzyl alcohol and the yield of the reaction is 81% with complex **4.1** and 62% with **4.2**. Another substrate with electron donating (4-methylbenzyl alcohol with yield of 73% with complex **4.1** and 51% with **4.2**) shows marginally higher yield than the unsubstituted substrate with both the catalysts (benzyl alcohol with yield of 72% for complex **4.1** and 50% for **4.2**). However, the presence of a bromo or nitro group in the aromatic ring decreases the yield of the corresponding alcohol formation. The yields with bromobenzyl

alcohol and nitrobenzyl alcohol are 61% and 59%, respectively for complex **4.1**, and 35% and 38%, respectively for complex **4.2**.

Aliquots from the catalytic reaction mixture have been collected after 2 h and 4 h, and then every 4 h upto 24 h and analyzed in the GC to check the progress of the reaction. Plots of time vs. yield for complex **1** and **2** are shown in **Figure 4.15** and **4.16**, respectively. It is evident that yield of the reaction increases with passage of time for all the substrates, the maximum being observed after 24 h of reaction. With the passage of time, the conversion of benzyl alcohols is also increased. It has been found that it reaches saturation after 24 h of the reaction.

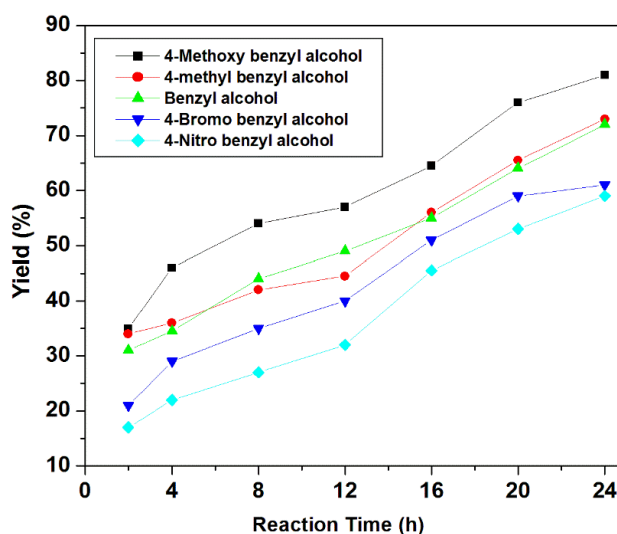


**Figure 4.15:** Plot of time vs. yield of aldehyde formation in the presence of complex **4.1** as the catalyst.

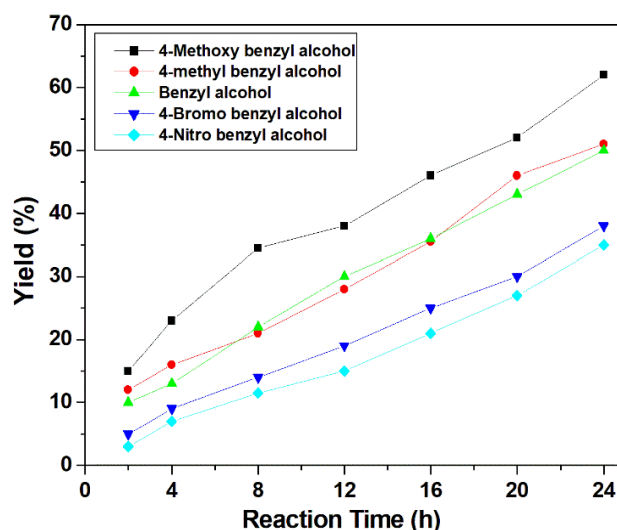


**Figure 4.16:** Plot of time vs. yield of aldehyde formation in the presence of complex **4.2** as the catalyst.

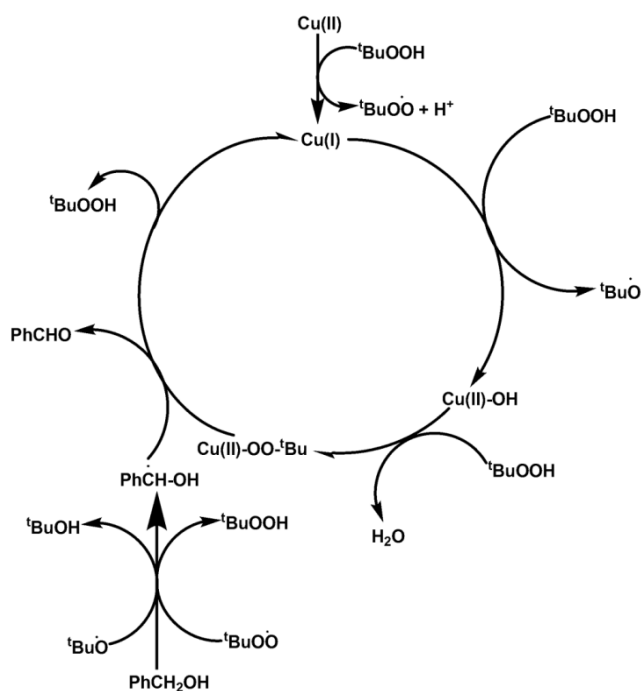
Blank reactions with all the substrates have been performed under the same experimental conditions but without any complex. It is to be noted that in case of blank reaction,



the reaction proceeds very slowly and conversion is very poor (**Table 4.3**, entry 3). It takes longer time for the conversion of benzyl alcohol into the aldehyde. In other words, when we compare yield of a particular reaction in the same duration of time, *e.g.*, 4 h, with and without catalyst, there is almost no conversion of alcohol to corresponding aldehyde in the initial time frame while the presence of copper complex as catalyst increases the yield of aldehyde manifold. These facts signify the importance of the copper(II) complex as catalysts.

We have tried to recover complex **4.1** and **4.2** after the catalytic reaction aiming to use it as catalyst for another reaction. However, attempts seem to be unsuccessful. The compound has been collected and dried after the catalytic reaction and characterized by IR spectroscopy attempting to find out the resemblance with the original catalyst. However, the spectrum of the material recovered is different from that of complexes. It indicates considerable decomposition of the complex and reuse of it as catalyst is inhibited.

A possible mechanistic pathway for the oxidation of the benzyl alcohols by the copper complex may be proposed based on the present work and results that were obtained from earlier studies (**Scheme 4.3**).<sup>4.48</sup> To explore the species responsible for the catalytic reaction, we have recorded the UV-vis spectra of complex **4.1** in absence and in the presence of TBHP in the range 250-800 nm in acetonitrile as this solvent has also been used in the catalytic reactions (**Figure 4.17**). Free complex **4.1** exhibits a sharp band at 410 nm which may be attributed to the phenolate-to-copper(II) ligand-to-metal charge transfer (LMCT). There are changes in the spectrum after addition of TBHP to the solution of the metal complex. Complex **4.1** shows a band at 379 nm which may be attributed to the shifting of charge transfer transition band position. It exhibits broad peak with a shoulder near 410-420 nm indicating the presence of peroxocopper(II) species<sup>4.2d</sup> which may be generated during the catalytic process, and thus it may act as the active species responsible for the transformation of the substrate. The alcohol oxidation is believed to proceed mainly *via* a radical mechanism, which involves both carbon- and oxygen-centered radicals.<sup>4.49</sup> Reaction between the catalyst and TBHP may produce tBuO<sup>•</sup> radical and Cu(I) species. The Cu(I) may be converted to the corresponding Cu(II)-OOBu<sup>t</sup> species which has been detected by UV-vis measurement. A radical on benzyl alcohol may be generated by the action of TBHP on it. That radical and metal peroxo species produces the corresponding aldehyde.



**Scheme 4.3:** Possible mechanism of benzyl alcohol oxidation

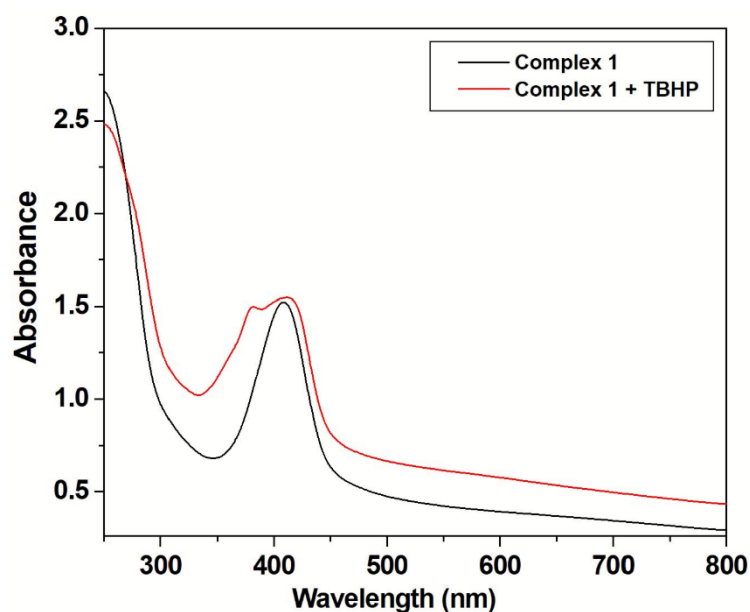


**Figure 4.17:** UV-Vis spectra of complex **4.1** in absence (black) and in the presence of TBHP (red) in acetonitrile

It is clear from the electrochemical studies that the onset potential values for the reduction of Cu(II) to Cu(I) are  $-0.86$  V and  $-0.91$  V for complex **4.1** and **4.2** respectively, indicating that the reduction of metal center is easier for complex **4.1** than in **4.2**. As discussed in the possible mechanism, formation of Cu(I) is necessary in the catalytic reaction. Thus, the system, where formation of Cu(I) is more feasible, should be more efficient in the oxidation reaction. Therefore, results obtained in electrochemical and catalytic studies corroborate perfectly establishing complex **4.1** is better catalyst than the complex **4.2**.

Comparison of some copper compounds<sup>4.30,4.50</sup> acting as catalyst for the oxidation of benzyl alcohol has been made on few aspects of the catalytic reactions (**Table 4.6**). Most of the catalytic reactions have been carried out in organic solvent such as acetonitrile, dichloromethane, *etc.* The reactions have been carried out at room temperature as well as in elevated temperature. In the present study, temperature for oxidation has been set at 70 °C. Time of reaction varies from 1 h to 24 h. Yield of the reaction is in the range of 50% to 100%. Turn over number reported in these studies is in the range of 6.6 to 684. The discussion and results summarized in **Table 4.6** indicate that complex **4.1** and **4.2** are moderate in their ability to produce the corresponding aldehyde solely from the benzyl alcohols.

**Table 4.6:** Benzyl alcohol oxidation catalyzed by selected copper complexes

Entry	Catalyst	Solvent	Additive	Temp. (°C)	Time	Yield	TON	Ref.
1	0.025 mmol [Cu <sub>3</sub> (L <sub>2</sub> ) <sub>2</sub> Cl <sub>4</sub> ]	CH <sub>3</sub> CN	0.5 mmol TBHP	R.T.	14 h	70	14	[30]
2	1 mol% of Cu (bisISQ)	CH <sub>2</sub> Cl <sub>2</sub>	0.9 eqt. methoxide	R.T.	15 h	66	66	[43a]
3	5 mol% of Cu(DBED)	CH <sub>2</sub> Cl <sub>2</sub>	20 mol% NMI or DMAP	R.T.	1 h	94	18.8	[43b]
4	5 mol% of Cu(salan)	Toluene	5 mol% TEMPO	100 °C	10 h	99	20	[43c]
5	4 mol% of Cu(APIP)	CH <sub>3</sub> CN	0.2 M KOH	R.T.	5 h	100	25	[43d]
6	15 mol% of Cu(Cl <sub>4</sub> -salan)	TFT	5 mol% TEMPO, 0.4 M CsCO <sub>3</sub>		12 h	100	6.6	[43e]
7	0.1 mol% of Cu(salendisil oxane) <sub>1</sub>	CH <sub>3</sub> CN: H <sub>2</sub> O (1:1)	5 mol% TEMPO, 0.1 M K <sub>2</sub> CO <sub>3</sub>	50 °C	24 h	68	684	[43f]
8	1 mol% of Cu(Salqu) <sup>a</sup>	CH <sub>2</sub> Cl <sub>2</sub>	1 eqt TBHP	70 °C	1 h	88	88	[43g]
9	Catalyst 1	CH <sub>3</sub> CN	0.5 mmol TBHP	70 °C	24 h	72	14	Present work

10	Catalyst 2	CH <sub>3</sub> CN	0.5 mmol	70 °C	24 h	50	10	Present work
----	------------	--------------------	----------	-------	------	----	----	--------------

#### 4.4 Conclusions

Two dinuclear copper(II) complexes, [Cu<sub>2</sub>(L<sup>1</sup>)<sub>2</sub>] (**4.1**) and [Cu<sub>2</sub>(L<sup>2</sup>)<sub>2</sub>] (**4.2**) where H<sub>2</sub>L<sup>1</sup> = 2-hydroxy-3-((3-hydroxy-2,2-dimethylpropylimino)methyl)-5-methylbenzaldehyde and H<sub>2</sub>L<sup>2</sup> = 2-hydroxy-3-(((1-hydroxypropan-2-yl)imino)methyl)-5-methylbenzaldehyde have been synthesized and characterized. 3,3'-(2-Hydroxy-5-methyl-1,3-phenylene)bis(methan-1-yl-1-ylidene)bis(azan-1-yl-1-ylidene)bis(2,2-dimethylpropan-1-ol) (H<sub>3</sub>L<sup>1</sup>) and 2,2'-(((2-hydroxy-5-methyl-1,3-phenylene)bis(methanylylidene))bis(azanylylidene))bis(propan-1-ol) (H<sub>3</sub>L<sup>2</sup>) have been aimed to synthesize multinuclear complexes with Cu(II) but both the ligands undergo partial hydrolysis to yield H<sub>2</sub>L<sup>1</sup> and H<sub>2</sub>L<sup>2</sup>, respectively and then copper(II) species coordinate with the modified ligands to produce complex **4.1** and **4.2**. Ligand used for complex **4.1** has longer side arm with branched alkyl groups. However, variation in chain length and presence of methyl group(s) here do not have any influence on partial hydrolysis of ligands during the synthesis of the complexes. DFP based ligands with azomethine linkage on both side arms undergo ligand modification in the presence of different metal ions during the synthesis of metal complexes many a times; however, the ligand modification *i.e.* partial hydrolysis of azomethine linkage does not occur in the presence of copper(II) ion often. More examples may give the idea about the conditions under which the ligand modification occurs. Complex **4.1** and **4.2** were obtained after partial hydrolysis of DFP based ligand and used effectively as catalyst in oxidation of different benzyl alcohols. With different substituents on benzyl alcohol, yield of the formation of the corresponding aldehyde as the sole product varies. Efficiency of complex **4.2** as catalyst is lower in comparison to that of complex **4.1** although in both the complexes, copper atoms exist in similar coordination environment. Variation in chain length and the presence of methyl group have effect on the efficiency of the complexes as catalyst in such oxidation reactions.

#### 4.5 References

- 4.1 (a) T. F. S. Silva, L. M. D. R. S. Martins, *Molecules* **2020**, *25*, 748;
- (b) C. Wei, Y. He, X. Shi, Z. Song, *Coord. Chem. Rev.* **2019**, *385*, 1-19;
- (c) R.-P. Ye, L. Lin, Q. Li, Z. Zhou, T. Wang, C. K. Russell, H. Adidharma, Z. Xu, Y.-G. Yao, M. Fan, *Catal. Sci. Technol.* **2018**, *8*, 3428-3449;
- (d) C. Du, X. Gao, W. Chen, *Chinese J. Catal.* **2016**, *37*, 1049-1061.

- 4.2 (a) M. Nasibipour, E. Safaei, G. Wrzeszcz, A. Wojtczak, *New J. Chem.* **2020**, *44*, 4426-4439;
- (b) A. J. McNeece, K. Jesse, J. Xie, A. S. Filatov, J. S. Anderson, *J. Am. Chem. Soc.* **2020**, *142*, 10824-10832;
- (c) X.-Y. Yu, Q.-Q. Zhao, J. Chen, J.-R. Chen, W.-J. Xiao, *Angew. Chem. Int. Ed.* **2018**, *57*, 15505-15509;
- (d) J. Reim, R. Werner, W. Haase, B. Krebs, *Chem. Eur. J.* **1998**, *4*, 289-298.
- 4.3 (a) A. Bhanja, R. Herchel, Z. Trávníček, D. Ray, *Inorg. Chem.* **2019**, *58*, 12184-12198;
- (b) X. Liu, C. Manzur, N. Novoa, S. Celedón, D. Carrillo, J.-R. Hamon, *Coord. Chem. Rev.* **2018**, *357*, 144-172.
- 4.4 (a) A. Bhattacharjee, S. Das, B. Das, P. Roy, *Inorg. Chim. Acta* **2021**, *514*, 119961;
- (b) A. Arunadevi, N. Raman, *J. Coord. Chem.* **2020**, *73*, 2095-2116;
- (c) R. Golbedaghi, A. M. Tabanez, S. Esmaeili, R. Fausto, *Appl. Organomet. Chem.* **2020**, *34*, e5884; (
- d) M.A. Malik, O.A. Dar, P. Gull, M.Y. Wani, A.A. Hashmi, *Med. Chem. Commun.* **2018**, *9*, 409-436.
- 4.5 (a) G. He, X. Hua, N. Yang, L. Li, J. Xu, L. Yang, Q. Wang, L. Ji, *Bioorg. Chem.* **2019**, *91*, 103176;
- (b) T. H. Sanatkar, A. Khorshidi, E. Sohoul, J. Janczak, *Inorg. Chim. Acta* **2020**, *506*, 119537;
- (c) S. Das, Y. Sarkar, S. Mukherjee, J. Bandyopadhyay, S. Samanta, P.P. Parui, A. Ray, *Sens. Actuators B* **2015**, *209*, 545-554.
- 4.6 (a) G. Li, D. Zhu, X. Wang, Z. Su, Martin R. Bryce, *Chem. Soc. Rev.* **2020**, *49*, 765-838;
- (b) A. Sakthivel, K. Jeyasubramanian, B. Thangagiri, J. Dhiveethu Raja, *J. Mol. Struct.* **2020**, *1222*, 128885;
- (c) Â. de Fátima, C. de Paula Pereira, C. R. S. D. G. Olímpio, B. G. de Freitas Oliveira, L. L. Franco, P. H. C. da Silva, *J. Adv. Res.* **2018**, *13*, 113-126.
- 4.7 (a) P. Roy, *Coord. Chem. Rev.* **2021**, *427*, 213562;
- (b) M. S. Jana, S. Dey, J. L. Priego, R. Jiménez-Aparicio, T. K. Mondal, P. Roy, *Polyhedron* **2013**, *59*, 101-106;

- (c) P. Roy, M. Nandi, M. Manassero, M. Ricc , M. Mazzani, A. Bhaumik, P. Banerjee, *Dalton Trans.* **2009**, 9543-9554;
- (d) T. S. Mahapatra, A. Bauz , D. Dutta, S. Mishra, A. Frontera, D. Ray, *ChemistrySelect* **2016**, *1*, 64-75;
- (e) M. Pait, A. Bauz , A. Frontera, E. Colacio, D. Ray, *Inorg. Chem.* **2015**, *54*, 4709–4723.
- 4.8 (a) A. K. Ghosh, A. Bauz , V. Bertolasi, A. Frontera, D. Ray, *Polyhedron* **2013**, *53*, 32-39;
- (b) M. Pait, A. Sarkar, E. Colacio, D. Ray, *Proc. Natl. Acad. Sci., India, Sect. A Phys. Sci.* **2014**, *84*, 189-196.
- 4.9 A. Sarkar, A. K. Ghosh, V. Bertolasi, D. Ray, *Dalton Trans.* **2012**, *41*, 1889-1896.
- 4.10 (a) P. Roy, M. Manassero, *Dalton Trans.* **2010**, *39*, 1539-1545;
- (b) S. Halder, S. Dey, C. Rizzoli, P. Roy, *Polyhedron* **2014**, *78*, 85-93.
- 4.11 (a) P. Roy, K. Dhara, M. Manassero, J. Ratha, P. Banerjee, *Inorg. Chem.* **2007**, *46*, 6405-6412;
- (b) D. Mandal, V. Bertolasi, J. Ribas-Ari o, G. Arom , D. Ray, *Inorg. Chem.* **2008**, *47*, 3465-3467.
- 4.12 K. Dhara, S. Karan, J. Ratha, P. Roy, G. Chandra, M. Manassero, B. Mallik, P. Banerjee, *Chem. Asian J.* **2007**, *2*, 1091-1100.
- 4.13 (a) T. Punniyamurthy, L. Rout, *Coord. Chem. Rev.* **2008**, *252*, 134-154;
- (b) K.C. Gupta, A.K. Sutar, *Coord. Chem. Rev.* **2008**, *252*, 1420-1450;
- (c) K.C. Gupta, A.K. Sutar, C.-C. Lin, *Coord. Chem. Rev.* **2009**, *253*, 1926-1946.
- 4.14 (a) A.M. Kirillov, M.N. Kopylovich, M.V. Kirillova, M. Haukka, M.F.C.G. da Silva, A.J.L. Pombeiro, *Angew. Chem.* **2005**, *117*, 4419-4423;
- (b) P. Roy, K. Dhara, M. Manassero, P. Banerjee, *Eur. J. Inorg. Chem.* **2008**, 4404-4412;
- (c) G.B. Shul'pin, *J. Mol. Catal. A* **2002**, *189*, 39-66;
- (d) G.B. Shul'pin, Y.N. Kozlov, L.S. Shul'pina, A.R. Kudinov, D. Mandell, *Inorg. Chem.* **2009**, *48*, 10480–10482;
- (e) M. Nandi, P. Roy, *Indian J. Chem.* **2013**, *52A*, 1263-1268;
- (f) D. D. Mal, S. Khilari, D. Pradhan, *Green Chem.* **2018**, *20*, 2279-2289.
- 4.15 (a) Z.-L. Li, G.-C. Fang, Q.-S. Gu, X.-Y. Liu, *Chem. Soc. Rev.* **2020**, *49*, 32-48;
- (b) R. Sadasivan, A. Patel, *Inorg. Chim. Acta* **2020**, *510*, 119757.

- 4.16 T. Tamoradi, M. Ghadermazi, A. Ghorbani-Choghamarani, *Catal. Lett.* **2018**, *148*, 857-872.
- 4.17 (a) K. Moschovitis, C.N. Banti, N. Kourkoumelis, E.E. Moushi, T. Lazarides, S.K. Hadjikakou, *Inorg. Chim. Acta* **2020**, *500*, 119209;  
(b) N. Beyazit, D. Çakmak, C. Demetgül, *Tetrahedron* **2017**, *73*, 2774-2779.
- 4.18 (a) S. Hazra, L. M. D. R. S. Martins, M. F. C. G. da Silva, A. J. L. Pombeiro, *RSC Adv.* **2015**, *5*, 90079-90088;  
(b) A. Jehdaramarn, S. Pornsuwan, P. Chumsaeng, K. Phomphrai, P. Sangtrirutnugul, *New J. Chem.* **2018**, *42*, 654-661.
- 4.19 (a) A.M. Kirillov, M. V. Kirillova, A.J.L. Pombeiro, *Coord. Chem. Rev.* **2012**, *256*, 2741 -2759;  
(b) L. S. Shul'pina , M. M. Vinogradov, Y. N. Kozlov, Y. V. Nelyubina, N. S. Ikonnikov, G. B. Shul'pin, *Inorg. Chim. Acta* **2020**, *512*, 119889.
- 4.20 (a) S. Asthana, C. Samanta, A. Bhaumik, B. Banerjee, R. K. Voolapalli, B. Saha, *J. Catal.* **2016**, *334*, 89-101;  
(b) S. Tian, M. Tan, Q. Ma, X. Wu, C. Luan, Y. Fang, H. Li, G. Yang, N. Tsubaki, Y. Tan, *Ind. Eng. Chem. Res.* **2020**, *59*, 11087–11097.
- 4.21 (a) M. Meldal, F. Diness, *Trends, Chem.* **2020**, *2*, 569;  
(b) L. Liang, D. Astruc, *Coord. Chem. Rev.* **2011**, *255*, 2933-2945;  
(c) S. Roy, T. Chatterjee, M. Pramanik, A. Singha Roy, A. Bhaumik, S. M. Islam, *J. Mol. Catal. A* **2014**, *386*, 78-85.
- 4.22 L.-J. Cheng, N. P. Mankad, *Chem. Soc. Rev.* **2020**, *49*, 8036-8064.
- 4.23 J. March in *Advance Organic Chemistry; Reaction, Mechanisms and Structure*, 4th edn., John Wiley & Sons, New York, **1992**.
- 4.24 (a) S. Itoh, M. Taki, S. Takayama, S. Nagatomo, T. Kitagawa, N. Sakurada, R. Arakawa, S. Fukuzumi, *Angew. Chem. Int. Ed.* **1999**, *38*, 2774-2776;  
(b) H. Oshita, Y. Shimazaki, *Chem. Eur. J.* **2020**, *26*, 8324-8340.
- 4.25 J. P. Klinman, *Chem. Rev.* **1996**, *96*, 2541–2562.
- 4.26 L. H. Abdel-Rahman, A. M. Abu-Dief, M. S. S. Adam, S. K. Hamdan, *Catal. Lett.* **2016**, *146*, 1373-1396.
- 4.27 G. Zhan, W. Zhong, Z. Wei, Z. Liu, X. Liu, *Dalton Trans.* **2017**, *46*, 8286-8297.
- 4.28 S. Hazra, L. M.D.R.S. Martins, M. F. C. G. da Silva, A.J.L. Pombeiro, *Inorg. Chim. Acta* **2017**, *455*, 549-556.

- 4.29 E. Safaei, H. Bahrami, A. Pevec, B. Kozlevčar, Z. Jagličić, *J. Mol. Struct.* **2017**, *1133*, 526-533.
- 4.30 A. Bhattacharjee, S. Halder, K. Ghosh, C. Rizzoli, P. Roy, *New J. Chem.* **2017**, *41*, 5696-5706.
- 4.31 (a) Z. Liu, Z. Shen, N. Zhang, W. Zhong, X. Liu, *Catal. Lett.* **2018**, *148*, 2709-2718;  
(b) J. Rabeah, U. Bentrup, R. Stöber, A. Brückner, *Angew. Chem. Int. Ed.* **2015**, *54*, 11791-11794;  
(c) B. L. Ryland, S. D. McCann, T. C. Brunold, S. S. Stahl, *J. Am. Chem. Soc.* **2014**, *136*, 12166-12173;  
(d) J. M. Hoover, B. L. Ryland, S. S. Stahl, *J. Am. Chem. Soc.* **2013**, *135*, 2357-2367;  
(e) J. M. Hoover, B. L. Ryland, S. S. Stahl, *ACS Catal.* **2013**, *3*, 2599-2605.
- 4.32 (a) R. R. Koner, M. Ray, *Inorg. Chem.* **2008**, *47*, 9122-9124;  
(b) O. Das, S. Paria, T. K. Paine, *Tetrahedron Lett.* **2008**, *49*, 5924-5927.
- 4.33 (a) F. Conan, J.-M. Kerbaol, M. M. Kubicki, E. Vigier, Y. L. Mest, J. S. Pala, *Inorg. Chim. Acta* **2002**, *336*, 87-90;  
(b) R. Gupta, R. Mukherjee, *Inorg. Chim. Acta* **1997**, *263*, 133-137;  
(c) D. E. Fenton, G. P. Westwood, A. Bashall, M. McPartlin, I. J. Scowen, *J. Chem. Soc. Dalton Trans.* **1994**, 2213-2214.
- 4.34 R. R. Gagne, C. L. Spiro, T. J. Smith, C. A. Hamann, W. R. Thies, A. K. Schiemke, *J. Am. Chem. Soc.* **1981**, *103*, 4073-4081.
- 4.35 APEX-II, SAINT and SADABS, Bruker AXS Inc., Madison, WI, **2008**.
- 4.36 G. M. Sheldrick, *Acta Crystallogr., Sect. A: Fundam. Crystallogr.* **2015**, *71*, 3-8.
- 4.37 G. M. Sheldrick, *Acta Crystallogr., Sect. C: Cryst. Struct. Commun.* **2015**, *71*, 3-8.
- 4.38 A. L. Spek, *Acta Crystallogr., Sect. D: Biol. Crystallogr.* **2009**, *65*, 148-155.
- 4.39 L. J. Farrugia, *J. Appl. Crystallogr.* **1997**, *30*, 565.
- 4.40 L. J. Farrugia, *J. Appl. Crystallogr.* **1999**, *32*, 837-838.
- 4.41 A.W. Addison, T. N. Rao, J. Reedijk, J. van Rijn, G. C. Verschoor, *J. Chem. Soc., Dalton Trans.* **1984**, 1349-1356.
- 4.42 L. Yang, D. R. Powell, R. P. Houser, *Dalton Trans.* **2007**, 955-964.
- 4.43 (a) L. Sacconi, M. Ciampolini, *J. Chem. Soc.* **1964**, 276-280;  
(b) A. B. P. Lever, *Inorganic Electronic Spectroscopy*, Elsevier, New York, **1968**.
- 4.44 (a) A. B. P. Lever, *Inorganic Electronic Spectroscopy*, Elsevier, Amsterdam, **1984**; pp. 553-572;



- (b) C. T. Yang, B. Moubaraki, K. S. Murray, J. D. Ranford, J. J. Vittal, *Inorg. Chem.* **2001**, *40*, 5934–5941;
- (c) W. Mazurek, B. J. Kennedy, K. S. Murray, M. J. O'Connor, J. R. Rodger, M. R. Snow, A. G. Wedd, P. R. Zwak, *Inorg. Chem.* **1985**, *24*, 3258–3264;
- (d) R. C. Holz, J. M. Brink, F. T. Gobena, C. J. O'Connor, *Inorg. Chem.* **1994**, *33*, 6086–6092.
- 4.45 S. K. Mandal, L. K. Thompson, K. Nag, J. -P. Charland, E. G. Gabe, *Inorg. Chem.* **1987**, *26*, 1391–1395.
- 4.46 F. Ammar, J. M. Saveant, *J. Electroanal. Chem.* **1973**, *47*, 115-125.
- 4.47 (a) R.N. Patel, *Inorg. Chim. Acta* **2010**, *363*, 3838-3846;
- (b) H. Hadadzadeh, S.J.A. Fatemi, S.R. Hosseinian, H.R. Khavasi, R. Pöttgen, *Polyhedron* **2008**, *27*, 249-254;
- (c) S. K. Verma, V.K. Singh, *J. Coord. Chem.* **2015**, *68*, 1072-1087;
- (d) R.N. Patel, D.K. Patel, K.K. Shukla, Y. Singh, *J. Coord. Chem.* **2013**, *66*, 4131-4143.
- 4.48 (a) J. K. Kochi, *Tetrahedron* **1962**, *18*, 483-497;
- (b) J. K. Kochi, *J. Am. Chem. Soc.* **1962**, *84*, 1572-1579;
- (c) G. Rothenberg, L. Feldberg, H. Wiener, Y. Sasson, *J. Chem. Soc. Perkin Trans.* **1998**, *2*, 2429-2434.
- 4.49 (a) I. Timokhin, C. Pettinari, F. Marchetti, R. Pettinari, F. Condello, S. Galli, E. C. B. A. Alegria, L. M. D. R. S. Martins, A. J. L. Pombeiro, *Cryst. Growth Des.* **2015**, *15*, 2303-2317;
- (b) A. Sabbatini, L. M. D. R. S. Martins, K. T. Mahmudov, M. N. Kopylovich, M. G. B. Drew, C. Pettinari, A. J. L. Pombeiro, *Catal. Commun.* **2014**, *48*, 69-72;
- (c) M. N. Kopylovich, Y. Y. Karabach, M. F. C. G. da Silva, P. J. Figiel, J. Lasri, A. J. L. Pombeiro, *Chem. Eur. J.* **2012**, *18*, 899-914;
- (d) R. R. Fernandes, J. Lasri, M. F. C. G. da Silva, J. A. L. Silva, J. J. R. F. da Silva, A. J. L. Pombeiro, *J. Mol. Catal. A* **2011**, *351*, 100-111.
- 4.50 (a) C. Mukherjee, T. Weyhermüller, E. Bothe, P. Chaudhuri, *Inorg. Chem.* **2008**, *47*, 11620–11632;
- (b) B. Xu, J.-P. Lumb, B.A. Arndtsen, *Angew. Chem. Int. Ed.* **2015**, *54*, 4208-4211;
- (c) S. Velusamy, A. Srinivasan, T. Punniyamurthy, *Tetrahedron Lett.* **2006**, *47*, 923-926;

- (d) Z. Alaji, E. Safaei, L. Chiang, R.M. Clarke, C. Mu, T. Storr, *Eur. J. Inorg. Chem.* **2014**, 6066-6074;
- (e) E. Safaei, L. Hajikhanmirzaei, B. Karimi, A. Wojtczak, P. Cotic, Y.I. Lee, *Polyhedron* **2016**, *106*, 153-162;
- (f) A. Soroceanu, M. Cazacu, S. Shova, C. Turta, J. Kozisek, M. Gall, M. Breza, P. Rapta, T.C.O. Mac Leod, A.J.L. Pombeiro, J. Tesler, A.A. Dobrov, V.B. Arion, *Eur. J. Inorg. Chem.* **2013**, 1458-1474;
- (g) K.C. Weerasiri, A.E.V. Gorden, *Eur. J. Org. Chem.* **2013**, 1546-1550.

## Chapter 5

### **Mononuclear nickel(II) complexes as electrocatalyst in hydrogen evolution reactions: Effect of alkyl side chain length**

#### **Abstract**

Three mononuclear Ni(II) complexes, namely,  $[\text{Ni}(\text{L}^1)_2]$  (**5.1**),  $[\text{Ni}(\text{L}^2)_2]$  (**5.2**) and  $[\text{Ni}(\text{L}^3)_2]$  (**5.3**) where  $\text{HL}^1 = 1-((4\text{-hydroxybutylimino)methyl)naphthalen-2-ol}$ ,  $\text{HL}^2 = 1-((5\text{-hydroxypentylimino)methyl)naphthalen-2-ol}$  and  $\text{HL}^3 = 1-((6\text{-hydroxyhexylimino)methyl)naphthalen-2-ol}$  have been reported here as the electrocatalyst for hydrogen evolution reaction (HER). Complexes **5.1**, **5.2** and **5.3** have been characterized by various standard analytical methods. Single crystal X-ray structure analysis reveals that nickel is in square planar geometry in all the complexes. These complexes act as efficient electrocatalyst in HER using acetic acid (AA) and trifluoroacetic acid (TFA) as the proton source in DMF. Controlled-potential electrolysis experiments show that these complexes are capable of reducing proton of AA and TFA to produce  $\text{H}_2$ . Control experiments show that the complexes are essential for improved production of hydrogen. Theoretical calculations were performed to support the mechanism of HER and to check the effect of chain lengths on the catalytic activity. The catalytic activity runs in the order of complex **5.1**>**5.2**>**5.3**.

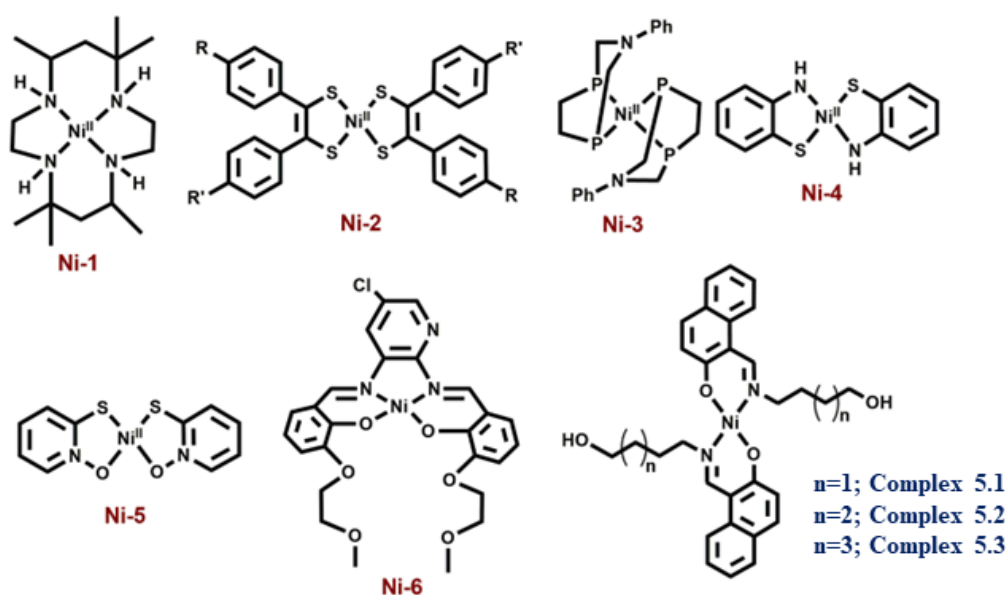
## 5.1 Introduction

The need for the development and improvement of secure, sustainable and eco-friendly energy resources is one of the most vital scientific and technical challenges in the present century due to the finite resources of fossil fuels. It is common to use fossil fuel that releases greenhouse gas, carbon dioxide into the environment resulting in global warming. In this respect, hydrogen may be considered as a potential candidate for use as an apt energy carrier. The reaction by which molecular hydrogen is produced by two protons via the two-electron reduction is known as the hydrogen evolution reaction (HER).<sup>5.1</sup>

To design an efficient and suitable catalyst for HERs, few things such as low price of the metal, metal with labile oxidation states, coordination sites are to be kept in mind. Platinum has been established as an efficient catalyst for the production of hydrogen.<sup>5.2</sup> However, it is available in limited quantity and highly expensive. Thus, its extensive use as the catalyst is restricted. Therefore, alternatives are being investigated with much cheaper earth-abundant metals as the catalyst. There are reports of different transition metal complexes<sup>5.3</sup> with Fe,<sup>5.4</sup> Mn,<sup>5.5</sup> Cu,<sup>5.6</sup> Co<sup>5.7</sup> and Ni<sup>5.8</sup> as the electrocatalysts for HERs. Various compounds of nickel and cobalt have also been used as the electrocatalysts for water splitting, hydrogen generation, and carbon dioxide reduction, showing their efficient role as electrocatalysts.<sup>5.9</sup> Due to their inherent better ability towards hydrogen evolution, complexes of cobalt and nickel gain intense interest of researchers as high-performance catalysts.<sup>5.10</sup> Moreover, Ni(II) system are abundant in earth<sup>5.11</sup> and have relevance to biology.<sup>5.12</sup> Typically, the hydrogen evolution reaction is operated via metal-centred route, and involves a metal hydride. However, the electrocatalysts consisting of earth-abundant elements are rarely prevailing for HERs in pure aqueous conditions. In most of the cases, organic acids have been used as the substrate in organic media with metal complexes as electrocatalysts.

Nickel(II) complexes with square planar geometry have been used as catalyst for HERs. Ligands with different donor atoms were designed to get various types of Ni(II) complexes. Generally, NiN<sub>4</sub>, NiS<sub>4</sub>, NiP<sub>4</sub>, NiN<sub>2</sub>S<sub>2</sub> and NiS<sub>2</sub>O<sub>2</sub> cores have been employed in such catalytic reactions (**Scheme 5.1**). Fisher and Eisenberg reported a nickel(II) complex involving a macrocycle with a NiN<sub>4</sub> core as the ligand, as an electrocatalyst for reduction of carbon dioxide into carbon monoxide and hydrogen as the major products.<sup>5.13</sup> After that, a number of complexes with N<sub>4</sub>-donor atoms have been reported in the literature for the same. Mitsopoulou *et al.* reported three Ni(II) diphenyl-1,2-dithiolene complexes with different substituents on the benzene ring having NiS<sub>4</sub> core for this purpose and showed the effects of the substituents on

the results.<sup>5.14</sup> Helm and coworkers used a mononuclear nickel(II) complex with two seven membered cyclic diphosphine ligands having P donor atoms as an highly efficient electrocatalyst for the hydrogen generation.<sup>5.15</sup> Bergamini and Natali reported a nickel(II) bis(diphosphine) complex as a catalyst for the HER in homogeneous media as well as in heterogeneous media.<sup>5.16</sup> Eisenberg *et al.* reported a series of nickel complexes with two ligands of N,S or O,S donor sites having square planar coordination for hydrogen evolution with a high turnover number and high stability under conditions of hydrogen production.<sup>5.17</sup> In comparison to these square planar Ni(II) complexes, very limited number of articles describe the NiN<sub>2</sub>O<sub>2</sub> core as the electrocatalyst for hydrogen evolution. Soo *et al.* reported NiN<sub>2</sub>O<sub>2</sub> core as an electrocatalyst for the HER. The presence of alkali metals in the second sphere ether appendages actually increased the hydrogen evolution.<sup>5.18</sup> The same group has recently reported another nickel complex with NiO<sub>2</sub>N<sub>2</sub> core with different ligand backbones for hydrogen evolution with TONs up to 3880.<sup>5.19</sup>



**Scheme 5.1:** Different types of mononuclear nickel complexes with NiN<sub>4</sub> (**Ni-1**),<sup>5.12</sup> NiS<sub>4</sub> (**Ni-2**),<sup>5.13</sup> NiP<sub>4</sub> (**Ni-3**),<sup>5.14</sup> NiS<sub>2</sub>N<sub>2</sub> (**Ni-4**),<sup>5.16</sup> NiS<sub>2</sub>O<sub>2</sub> (**Ni-5**)<sup>5.16</sup> and NiN<sub>2</sub>O<sub>2</sub> (**Ni-6**)<sup>5.17</sup> core for hydrogen evolution reaction.

The electro-catalytic behavior for HER of three neutral, monomeric Ni(II) complexes, [Ni(L<sup>1</sup>)<sub>2</sub>] (**5.1**), [Ni(L<sup>2</sup>)<sub>2</sub>] (**5.2**) and [Ni(L<sup>3</sup>)<sub>2</sub>] (**5.3**), where HL<sup>1</sup> = 1-((4-hydroxybutylimino)methyl)naphthalen-2-ol, HL<sup>2</sup> = 1-((5-hydroxypentylimino)methyl)naphthalen-2-ol and HL<sup>3</sup> = 1-((6-hydroxyhexylimino)methyl)naphthalen-2-ol is reported here. Complexes **5.1**, **5.2** and **5.3** have been synthesized easily and characterized by several standard methods including single crystal

X-ray diffraction analysis. All of these complexes have been used as electrocatalyst for the reduction of proton in DMF with acetic acid (AA) and trifluoroacetic acid (TFA) as the proton source. Here, we aim to make the variation in the ligand chain length of the complexes and to compare the electro-catalytic results obtained under identical conditions. Some theoretical calculations have been performed with insight in hydrogen evolution mechanism and effect of chain lengths of the ligands on the results.

## 5.2 Experimental Section

### 5.2.1 Materials and physical methods

2-Hydroxy-1-naphthaldehyde, 4-Amino-1-butanol, 5-Amino-1-pentanol, 6-Amino-1-hexanol and nickel(II) perchlorate hexahydrate were purchased from Sigma Aldrich and were used without any purification. Other reagents and solvents were obtained from different commercial sources and used without any purification. Elemental analyses of complexes **5.1**, **5.2** and **5.3** were performed using a Perkin–Elmer 2400C elemental analyzer.  $^1\text{H}$  NMR spectra of three Schiff-base ligands, complexes **5.1**, **5.2** and **5.3** were recorded on Bruker 400 MHz spectrometer. FT-IR spectra of complexes **5.1**, **5.2** and **5.3** were measured on a Perkin Elmer spectrometer (Spectrum Two) with the samples by using ATR method. The UV-visible spectral measurements of complexes **5.1**, **5.2** and **5.3** were done in Agilent 8453 diode array spectrophotometer. Cyclic voltammograms were obtained on an electrochemical analyzer (CHI 600C, CH Instruments,) under air-free conditions using a conventional three-electrode cell in which a glassy carbon electrode was the working electrode, a saturated Ag/AgCl electrode was the reference electrode, and platinum wire was the auxiliary electrode. The surface area of the glassy carbon working electrode is  $0.07\text{ cm}^2$ . The gas evolved during bulk electrolysis was detected by using GC instrument of model no. 7890B (G3440B), serial no. CN14333203 fitted with TCD. 500  $\mu\text{l}$  gas was syringed out by a gas tight syringe from the head space and was injected into the inlet of the GC.

### 5.2.2 Synthesis of Complexes **5.1**, **5.2** and **5.3** as the catalyst

#### 5.2.2.1 Synthesis of 1-((4-hydroxybutylimino)methyl)naphthalen-2-ol ( $\text{HL}^1$ ), 1-((5-hydroxypentylimino)methyl)naphthalen-2-ol ( $\text{HL}^2$ ) and 1-((6-hydroxyhexylimino)methyl)naphthalen-2-ol ( $\text{HL}^3$ )

All of the ligands, namely  $\text{H}_2\text{L}^1$ ,  $\text{H}_2\text{L}^2$  and  $\text{H}_2\text{L}^3$ , were synthesized following a general synthetic procedure. Typically, 0.3 mmol of respective amino alcohol (0.027 g for 4-amino-1-butanol, 0.031 g for 5-amino-1-pentanol and 0.035 g for 6-amino-1-hexanol) was added to an acetonitrile solution of 2-hydroxy-1-naphthaldehyde (0.3 mmol, 0.0516 g) dropwise under

stirring condition. Stirring was continued for another 30 min. The mixture was then refluxed for 4 h when the color of the reaction mixture became yellow. The mixture was then cooled to room temperature. It was filtered to remove solid material, if any. Solid products were obtained after few days on slow evaporation of acetonitrile.

Data for **HL**<sup>1</sup>: Yield = 0.068 g, 92%; anal. calc. (%) for C<sub>15</sub>H<sub>17</sub>NO<sub>2</sub>: C, 74.05; H, 7.04; N, 5.76. Found: C, 73.97; H, 6.96; N, 5.79; <sup>1</sup>H NMR (400 MHz, DMSO-d<sub>6</sub>, δ ppm, TMS) 14.13 (1H, s), 9.08 (1H, s), 8.07 (1H, d, J = 8.4 Hz), 7.71 (1H, d, J = 9.2 Hz), 7.62 (1H, d, J = 7.6 Hz), 7.42 (1H, m), 7.19 (1H, t, J = 7.2 Hz), 6.72 (1H, d, J = 9.2 Hz), 4.51 (1H, s), 3.66 (2H, t, J = 4.4 Hz), 3.45 (2H, t, J = 4.4 Hz), 1.72 (2H, m), 1.54 (2H, m); ESI-MS<sup>+</sup> (*m/z*): 244.23 [(HL<sup>1</sup> + H<sup>+</sup>)].

Data for **HL**<sup>2</sup>: Yield = 0.070 g, 90%; anal. calc. (%) for C<sub>16</sub>H<sub>19</sub>NO<sub>2</sub>: C, 74.68; H, 7.44; N, 5.44. Found: C, 74.57; H, 7.36; N, 5.39; <sup>1</sup>H NMR (400 MHz, DMSO-d<sub>6</sub>, δ ppm, TMS) 14.13 (1H, s), 9.09 (1H, s), 8.06 (1H, d, J = 8.0 Hz), 7.71 (1H, d, J = 9.2 Hz), 7.62 (1H, d, J = 7.6 Hz), 7.42 (1H, t, J = 7.6 Hz), 7.18 (1H, t, J = 7.2 Hz), 6.72 (1H, d, J = 9.2 Hz), 4.33 (1H, s), 3.65 (2H, t, J = 6.8 Hz), 3.42 (2H, t, J = 6.0 Hz), 1.49 (2H, m), 1.29 (2H, m); ESI-MS<sup>+</sup> (*m/z*): 258.11 [(HL<sup>2</sup> + H<sup>+</sup>)].

Data for **HL**<sup>3</sup>: Yield = 0.069 g, 85%; anal. calc. (%) for C<sub>17</sub>H<sub>21</sub>NO<sub>2</sub>: C, 75.25; H, 7.80; N, 5.16. Found: C, 75.17; H, 7.76; N, 5.29; <sup>1</sup>H NMR (400 MHz, DMSO-d<sub>6</sub>, δ ppm, TMS) 14.12 (1H, s), 9.08 (1H, s), 8.06 (1H, d, J = 8.4 Hz), 7.70 (1H, d, J = 9.2 Hz), 7.61 (1H, d, J = 8.0 Hz), 7.41 (1H, t, J = 7.2 Hz), 7.18 (1H, t, J = 7.6 Hz), 6.71 (1H, d, J = 9.2 Hz), 4.36 (1H, s), 3.63 (2H, t, J = 7.2 Hz), 3.39 (2H, t, J = 6.0 Hz), 1.67 (2H, m), 1.33 (2H, m); ESI-MS<sup>+</sup> (*m/z*): 272.13 [(HL<sup>3</sup> + H<sup>+</sup>)].

#### 5.2.2.2 Synthesis of [Ni(L<sup>1</sup>)] (5.1)

HL<sup>1</sup> (0.6 mmol, 0.146 g) in 5.0 mL of acetonitrile was added to a solution of nickel(II) perchlorate hexahydrate (0.3 mmol, 0.1097g) in acetonitrile (5.0 mL) slowly under continuous stirring condition. The mixture was stirred till it turned greenish. Then, it was refluxed for one hour. Color of the solution changed to dark green. The mixture was then cooled to room temperature and filtered to remove solid material, if any. The filtrate was kept in beaker under ambient condition for slow evaporation. Green crystals of complex **5.1** suitable for single crystal X-ray diffraction were produced after few days.

Data for **5.1**: Yield, 0.094 g, 58%; anal. calc. for C<sub>30</sub>H<sub>31</sub>NiN<sub>2</sub>O<sub>4</sub>: C, 66.45; H, 5.76; N, 5.17; found: C, 66.33; H, 5.80; N, 5.06%. <sup>1</sup>H NMR (400 MHz, DMSO-d<sub>6</sub>, δ ppm, TMS) 9.11 (1H, s), 8.12 (1H, d, J = 8.4 Hz), 7.83 (1H, d, J = 8.8 Hz), 7.74 (1H, d, J = 8.0 Hz), 7.50 (1H, t, J =

7.6 Hz), 7.25 (1H, t,  $J = 7.2$  Hz), 6.82 (1H, d,  $J = 8.8$  Hz), 4.45 (1H, s), 4.17 (2H, t,  $J = 5.2$  Hz), 3.50 (2H, t,  $J = 5.6$  Hz), 1.97 (2H, m), 1.65 (2H, m).

### 5.2.2.3 Synthesis of [Ni(L<sup>2</sup>)] (5.2) and [Ni(L<sup>3</sup>)] (5.3)

Complexes **5.2** and **5.3** were synthesized following the method used for the synthesis of complex **5.1**. HL<sup>2</sup> (0.6 mmol, 0.154 g) and HL<sup>3</sup> (0.6 mmol, 0.163 g) were used for complexes **5.2** and **5.3**, respectively, in place of HL<sup>1</sup>.

Data for **5.2**: yield, 0.106 g, 62%; anal. calc. for C<sub>32</sub>H<sub>36</sub>NiN<sub>2</sub>O<sub>4</sub>: C, 67.27; H, 6.35; N, 4.90; found: C, 67.20; H, 6.26; N, 5.05%. <sup>1</sup>H NMR (400 MHz, DMSO-d<sub>6</sub>,  $\delta$  ppm, TMS) 9.15 (1H, s), 8.12 (1H, d,  $J = 8.8$  Hz), 7.85 (1H, d,  $J = 8.8$  Hz), 7.74 (1H, d,  $J = 8.0$  Hz), 7.48 (1H, t,  $J = 7.6$  Hz), 7.27 (1H, t,  $J = 7.2$  Hz), 6.80 (1H, d,  $J = 8.8$  Hz), 4.35 (1H, s), 4.24 (2H, t,  $J = 5.2$  Hz), 3.43 (2H, t,  $J = 5.2$  Hz), 1.94 (2H, m), 1.52 (2H, m).

Data for **5.3**: yield, 0.104 g, 58%; anal. calc. for C<sub>34</sub>H<sub>40</sub>NiN<sub>2</sub>O<sub>4</sub>: C, 68.13; H, 6.73; N, 4.67; found: C, 68.05; H, 6.80; N, 4.58%. <sup>1</sup>H NMR (400 MHz, DMSO-d<sub>6</sub>,  $\delta$  ppm, TMS) 9.12 (1H, s), 8.11 (1H, d,  $J = 8.0$  Hz), 7.89 (1H, d,  $J = 8.8$  Hz), 7.74 (1H, d,  $J = 7.2$  Hz), 7.50 (1H, t,  $J = 7.2$  Hz), 7.25 (1H, t,  $J = 8.0$  Hz), 6.79 (1H, d,  $J = 8.8$  Hz), 4.32 (1H, s), 3.38 (2H, t,  $J = 5.2$  Hz), 3.33 (2H, t,  $J = 6.4$  Hz), 2.29 (2H, m), 1.48 (2H, m).

**CAUTION:** Nickel(II) perchlorate hexahydrate can be explosive on heating. Thus, the perchlorate salts should be handled with care.

### 5.2.3 X-ray data collection and structure determination

Data collection and refinement parameters for complexes **5.1**, **5.2** and **5.3** are given as summary in **Table 5.1**. The X-ray diffraction experiments were performed on a BRUKER D8 QUEST CCD diffractometer for **5.1** and on a Bruker APEX-II CCD diffractometer for **5.2** and **5.3** using graphite monochromated Mo  $K\alpha$  radiation at 294(2) K. Data processing was done with Bruker *APEX2* and *SAINT* packages.<sup>5,20</sup> Absorption corrections, which are based on multi-scans using the *SADABS* software,<sup>5,20</sup> were applied to intensity data. The structures of complexes **5.1**, **5.2** and **5.3** were solved by direct methods utilizing SHELXT<sup>5,21</sup> and refined with full-matrix least-squares on  $F^2$  on all unique reflections employing SHELXL-2014/7.<sup>5,22</sup> All the non-hydrogen atoms of all of three complexes were refined anisotropically. The crystals selected for the single crystal X-ray diffraction analysis of complexes **5.1** and **5.3** were refined as merohedral twin in both the complexes with a fractional contribution of minor component of 0.18(3) and 0.03(2), respectively. In complex **5.1**, quality of crystal was poor. Poor quality as well as the presence of twinning in **5.1** may account for the limited overall precision of its structure, high residual peaks and the relatively high values of R and wR<sub>2</sub> parameters.

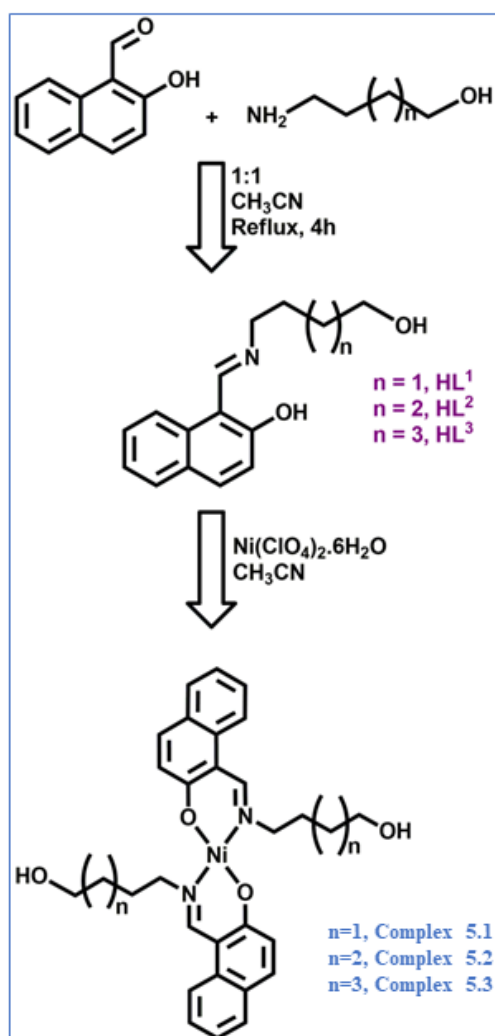


CCDC 2062677, 2062678 and 2062679 contain the supplementary crystallographic data for complexes **5.1**, **5.2** and **5.3**, respectively.

## 5.3 Results and Discussion

### 5.3.1 Synthesis of ligands and their characterization by ESI mass and $^1\text{H}$ spectral analysis

1-((4-Hydroxybutylimino)methyl)naphthalen-2-ol ( $\text{HL}^1$ ), 1-((5-hydroxypentylimino)methyl)naphthalen-2-ol ( $\text{HL}^2$ ) and 1-((6-hydroxyhexylimino)methyl)naphthalen-2-ol ( $\text{HL}^3$ ) were synthesized by Schiff-base condensation reaction between 2-hydroxy-1-naphthaldehyde and the respective amine in 1:1 ratio in acetonitrile with high yield (**Scheme 5.2**). Complexes **5.1**, **5.2** and **5.3** were obtained by the reactions between the ligands and nickel(II) perchlorate hexahydrate in 2:1 ratio without addition of any external base.



**Scheme 5.2:** Synthetic route to Complexes **5.1**, **5.2** and **5.3**.

ESI-mass spectrometric measurements of HL<sup>1</sup>, HL<sup>2</sup> and HL<sup>3</sup> were performed with their methanolic solutions (**Figure 5.1-5.3**). Mass spectrum of HL<sup>1</sup> shows an *m/z* peak at 244.23 which may be attributed to the [HL<sup>1</sup> + H<sup>+</sup>] species (calculated value 244.31). The *m/z* peak at 258.11 may be assigned to the presence of [HL<sup>2</sup> + H<sup>+</sup>] species (calculated value 258.15). Mass spectrum of HL<sup>3</sup> shows *m/z* peak at 272.13 may be due to the presence of [HL<sup>3</sup> + H<sup>+</sup>] (calculated value 272.17).

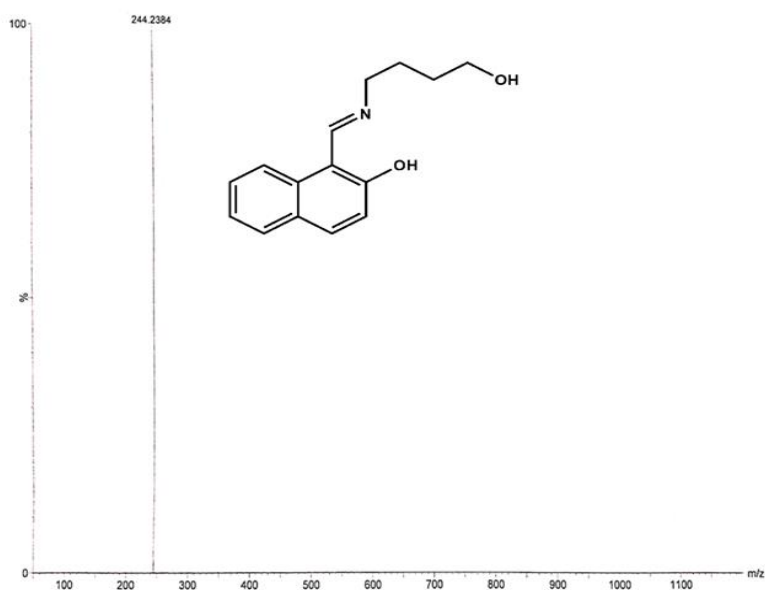


**Figure 5.1:** Mass spectrum of HL<sup>1</sup> in methanol.

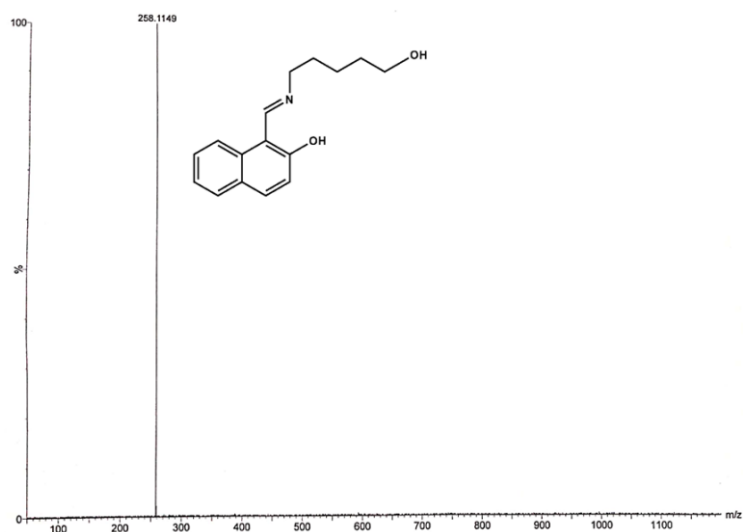


**Figure 5.2:** Mass spectrum of HL<sup>2</sup> in methanol.

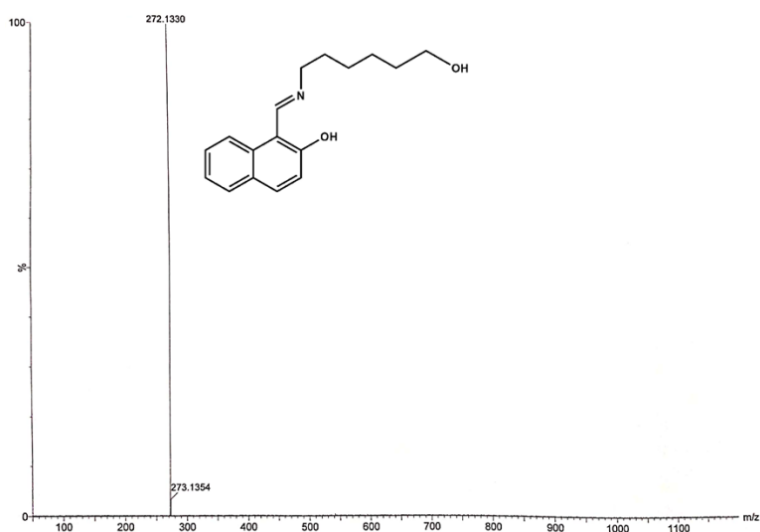


**Figure 5.3:** Mass spectrum of HL<sup>3</sup> in methanol.

These ligands were further characterized by <sup>1</sup>H NMR spectral studies (**Figure 5.4-5.6**). Spectra were obtained in DMSO-d<sub>6</sub>. NMR spectral studies support the formation of the Schiff-base ligands. All of these compounds show a peak at around 14.1 ppm which indicates the presence of phenolic OH group. The peak at around 9.0 ppm in all the ligands may be due to the presence of imine proton indicating formation of Schiff-base compounds. Signals for aromatic protons for all of the ligands appear in the appropriate positions. Signals for methylene protons also appear in their usual positions. All of these analyses support formation of the Schiff-base ligands.

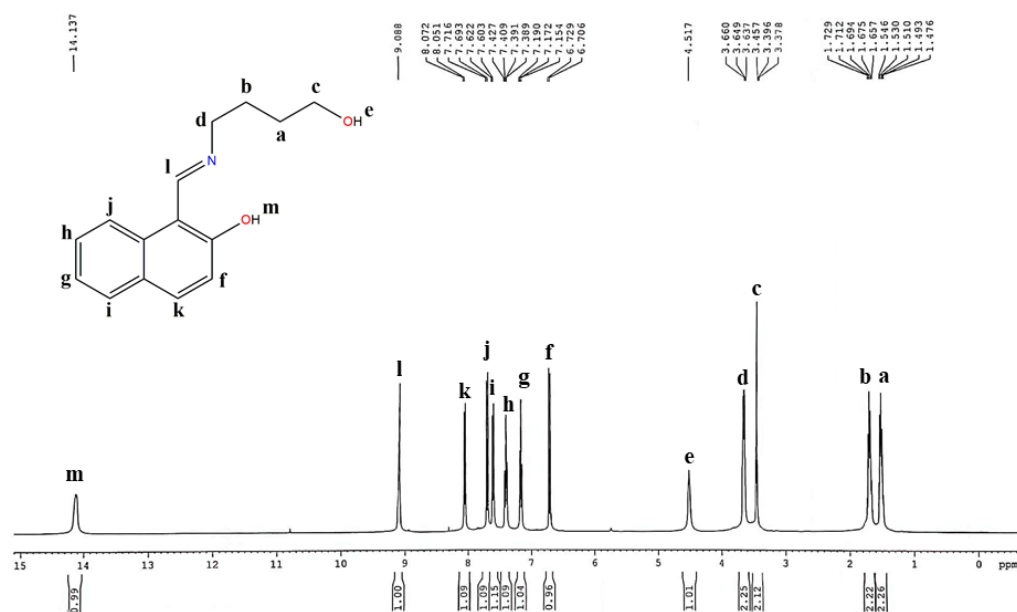


**Figure 5.4:** <sup>1</sup>H NMR spectrum of HL<sup>1</sup> in DMSO-d<sub>6</sub>.

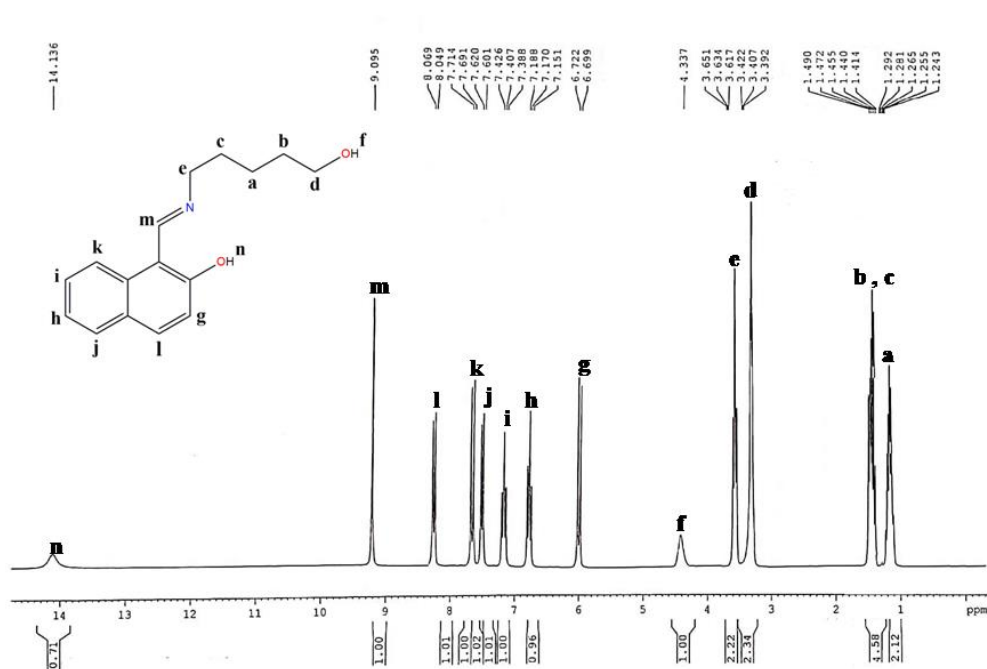


Figure 5.5:  $^1\text{H}$  NMR spectrum of  $\text{HL}^2$  in  $\text{DMSO-d}_6$ .

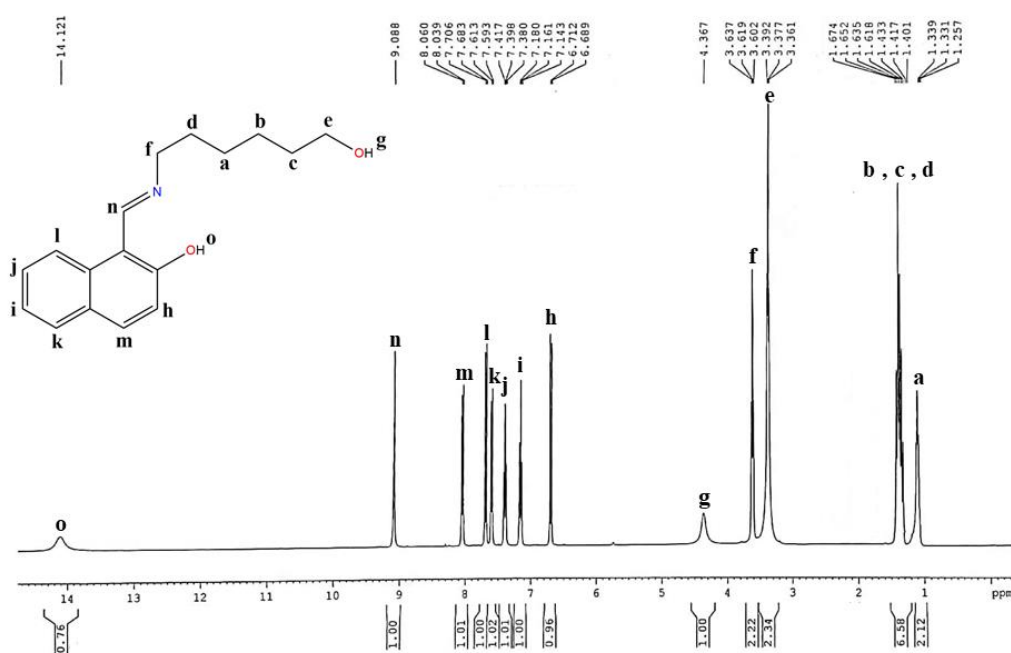


Figure 5.6:  $^1\text{H}$  NMR spectrum of  $\text{HL}^3$  in  $\text{DMSO-d}_6$ .

### 5.3.2 Characterization of complexes 5.1, 5.2 and 5.3

#### 5.3.2.1 Crystal structures of complexes 5.1, 5.2 and 5.3

Single crystals of complexes **5.1**, **5.2** and **5.3** were obtained on slow evaporation of their acetonitrile solution. Complex **5.1** crystallizes in monoclinic system and  $P 2_1/c$  space group. But both complexes **5.2** and **5.3** crystallize in triclinic system and  $P-1$  space group. Asymmetric

unit consists of one nickel centre and a pair of ligands for all of the complexes (**Figure 5.7**). All of complexes **1**, **2** and **3** are mononuclear complex (**Figure 5.8-5.10**). Selected bond lengths and bond angles are listed in **Table 5.2**. All of these complexes may be summarized as NiO<sub>2</sub>N<sub>2</sub> core. For all of the complexes, Ni atom is coordinated to N and O donor atoms from a ligand and another set of N and O donor atoms from a different ligand. Ni atom is in a square planar geometry. Apart from hydroxyl alkyl chain, rest of the molecule is planar. For complex **5.1**, angles O1-Ni1-O1<sup>a</sup> and N1-Ni1-N1<sup>a</sup> are 180° whereas other donor-metal-donor angles range from 87.86 to 92.14°. While other donor-metal-donor angles vary from 87.82 to 92.18° in complex **5.2**. For complex **5.3**, donor-metal-donor angles vary from 88.44 to 91.56°.

For other two complexes, all of the large donor-metal-donor angles 180°. For a four-coordinate complex, Houser and co-workers proposed the four-coordinate  $\tau_4$  index to ascertain the geometry around the metal center. The value four-coordinate  $\tau_4$  index is obtained using the following formula<sup>5.23</sup>

$$\tau_4 = \frac{360^\circ - (\alpha + \beta)}{141^\circ}$$

where  $\alpha$  and  $\beta$  are the two largest donor-metal-donor angles in a tetra-coordinated complex. For a tetrahedral geometry, the value of  $\tau_4$  is 1.00 while for an ideal square planar arrangement, it is 0.00. As two largest donor-metal-donor angles are 180° for all of these three complexes, the values of four-coordinate  $\tau_4$  index come out as 0.00 for all the complexes. This fact indicates that there exists the perfect square planar geometry around nickel atom in the complexes **5.1**, **5.2** and **5.3**. The O-Ni bond distances are close to 1.82 Å and the O-Ni bond distances are about 1.91 Å. These values are in agreement with the published results.<sup>5.24</sup>

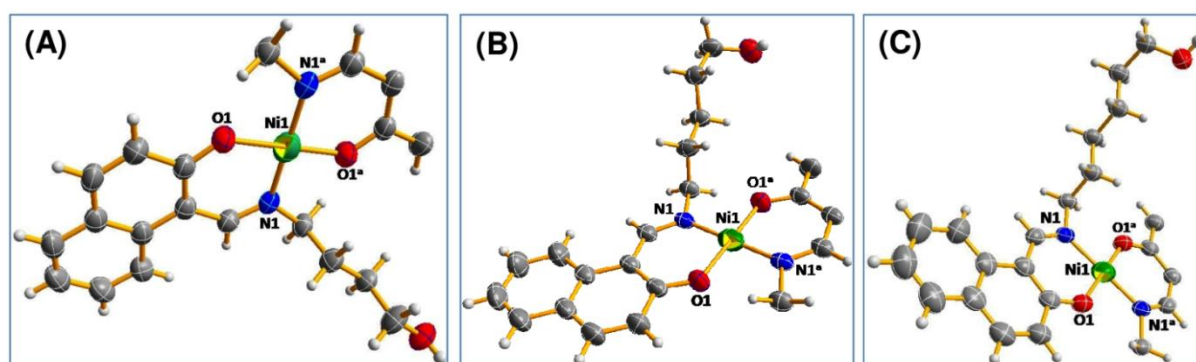


**Figure 5.7:** A perspective view of (A) complex **5.1**, (B) Complex **5.2** and (C) Complex **5.3** with displacement ellipsoids drawn at the 50% probability level.

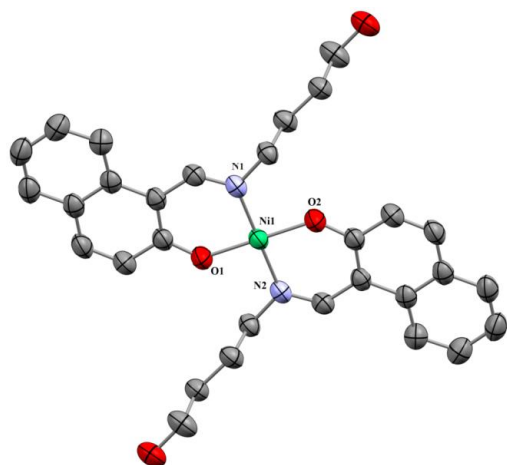


**Figure 5.8:** A perspective view of complex **5.1** with displacement ellipsoids drawn at the 50% probability level. Symmetry code; (a)  $-x, 1-y, 1-z$

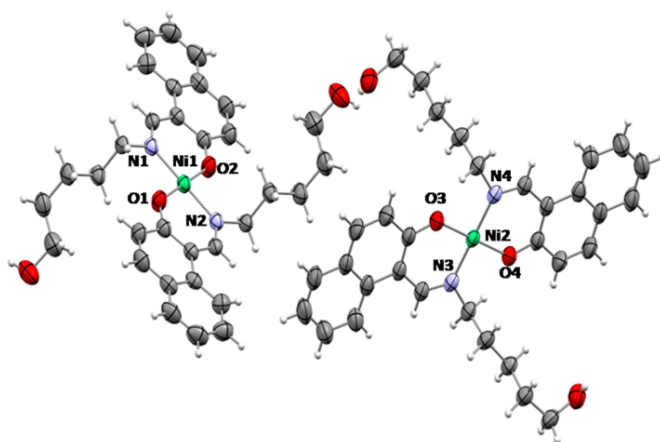


**Figure 5.9:** A perspective view of complex **5.2** with displacement ellipsoids drawn at the 50% probability level. Symmetry code; (a)  $-x, 1-y, 1-z$

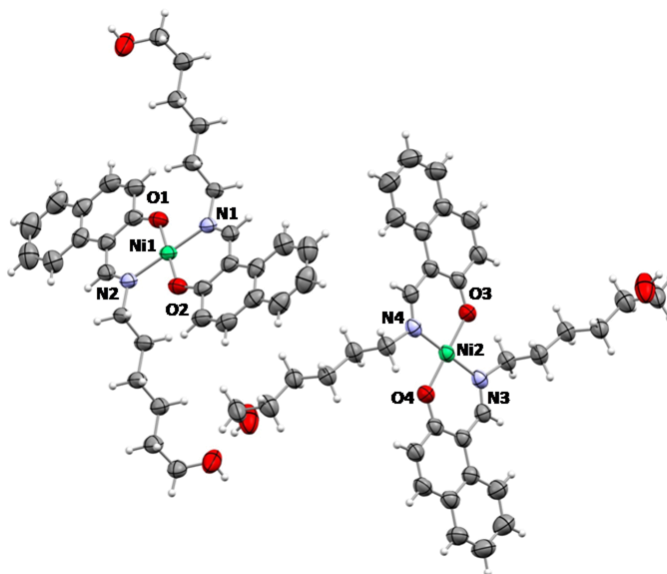


**Figure 5.10:** A perspective view of complex **5.3** with displacement ellipsoids drawn at the 50% probability level. Symmetry code; (a)  $1-x, -y, 2-z$

**Table 5.1:** Crystal data of complexes **5.1**, **5.2** and **5.3**

Complex	<b>5.1</b>	<b>5.2</b>	<b>5.3</b>
Formula	$C_{30}H_{31}N_2Ni_1O_4$	$C_{32}H_{36}N_2Ni_1O_4$	$C_{34}H_{40}N_2Ni_1O_4$
Formula weight	542.26	571.32	599.39
$T$ (K)	298(2)	298(2)	298(2)
Crystal color	Green	green	green
Crystal system	monoclinic	triclinic	triclinic
Space group	$P 21/c$	$P -1$	$P -1$
$a$ (Å)	10.7840(8)	4.9186(4)	5.1838(7)

Complex	5.1	5.2	5.3
$b$ (Å)	4.9890(4)	16.7080(14)	16.905(2)
$c$ (Å)	23.8099(18)	16.9064(14)	17.141(2)
$\alpha$ (°)	90	86.436(3)	84.192(5)
$\beta$ (°)	90.846(2)	84.966(2)	87.843(4)
$\gamma$ (°)	90	89.509(2)	89.703(4)
$V$ (Å <sup>3</sup> )	1280.87(17)	1381.3(2)	1493.3(3)
$Z$	2	2	2
Crystal dimensions (mm)	0.40 × 0.26 × 0.13	0.41 × 0.23 × 0.12	0.46 × 0.29 × 0.16
$F(0\ 0\ 0)$	570.0	604.0	636.0
$D_c$ (g cm <sup>-3</sup> )	1.406	1.374	1.333
$\lambda$ (Mo K $\alpha$ ) (Å)	0.71073	0.71073	0.71073
$\theta$ Range (°)	2.53- 27.11	2.65- 27.25	2.39- 27.00
Reflection collected/ unique/observed	29207, 2837, 2507	70198, 6202, 5565	78729, 6626, 5259
Absorption correction	multi-scan	multi-scan	multi-scan
$R_{\text{int}}$	0.0306	0.0320	0.0350
Final $R_1$ index [ $I > 2\sigma(I)$ ]	0.0352	0.0348	0.0498
Final $wR_2$ index (all reflections)	0.1324	0.1024	0.1397
Goodness-of-fit	1.166	1.022	0.925

**Table 5.2:** Selected bond lengths (Å) and bond angles (°) of complexes **5.1**, **5.2** and **5.3**.

<b>Complex 5.1</b>	
Ni1–O1	1.8261
Ni1–O1 <sup>a</sup>	1.8261
Ni1–N1	1.9106
Ni1–N1 <sup>a</sup>	1.9106
O1–Ni1–O1 <sup>a</sup>	180.00

O1 <sup>a</sup> -Ni1-N1 <sup>a</sup>	92.14
O1 <sup>a</sup> -Ni1-N1	87.86
O1-Ni1-N1 <sup>a</sup>	87.86
O1-Ni1-N1	92.14
N1-Ni1-N1 <sup>a</sup>	180.00
<b><u>Complex 5.2</u></b>	
Ni1-O1	1.8226
Ni1-O1 <sup>a</sup>	1.8226
Ni1-N1	1.9164
Ni1-N1 <sup>a</sup>	1.9164
O1-Ni1-O1 <sup>a</sup>	180.00
O1-Ni1-N1	92.13
O1-Ni1-N1 <sup>a</sup>	87.87
O1 <sup>a</sup> -Ni1-N1	87.87
O1 <sup>a</sup> -Ni1-N1 <sup>a</sup>	92.13
N1-Ni1-N1 <sup>a</sup>	180.00
<b><u>Complex 5.3</u></b>	
Ni1-O1 <sup>a</sup>	1.8310
Ni1-O1	1.8310
Ni1-N1 <sup>a</sup>	1.9162
Ni1-N1	1.9162
O1-Ni1-O1 <sup>a</sup>	180.00
O1-Ni1-N1 <sup>a</sup>	88.44
O1-Ni1-N1	91.56
O1 <sup>a</sup> -Ni1-N1 <sup>a</sup>	91.56
O1 <sup>a</sup> -Ni1-N1	88.44
N1-Ni1-N1 <sup>a</sup>	180.00

### 5.3.2.2 ESI-mass, FT-IR, UV-vis and <sup>1</sup>H NMR spectral characterization of the complexes

ESI-mass spectra of complexes **5.1**, **5.2** and **5.3** were obtained with their methanolic solutions (**Figure 5.11-5.13**). All of them behave similarly. Mass spectrum of **5.1** exhibits an  $m/z$  peak at 565.0727 which may be attributed to the  $[\text{Ni}(\text{L}^1)_2 + \text{Na}^+]$  species (calculated value 565.16). This indicates that the complex exists mainly as mononuclear nickel(II) species in solution. For complex **5.2**, an  $m/z$  peak appears at 593.10 which may be assigned to the  $[\text{Ni}(\text{L}^2)_2$



+ Na<sup>+</sup>] (calculated value 565.19). Similarly, *m/z* peak at 621.14 of complex **5.3** appear due to the presence of [Ni(L<sup>3</sup>)<sub>2</sub> + Na<sup>+</sup>] species (calculated value 621.22).<sup>5.25</sup>

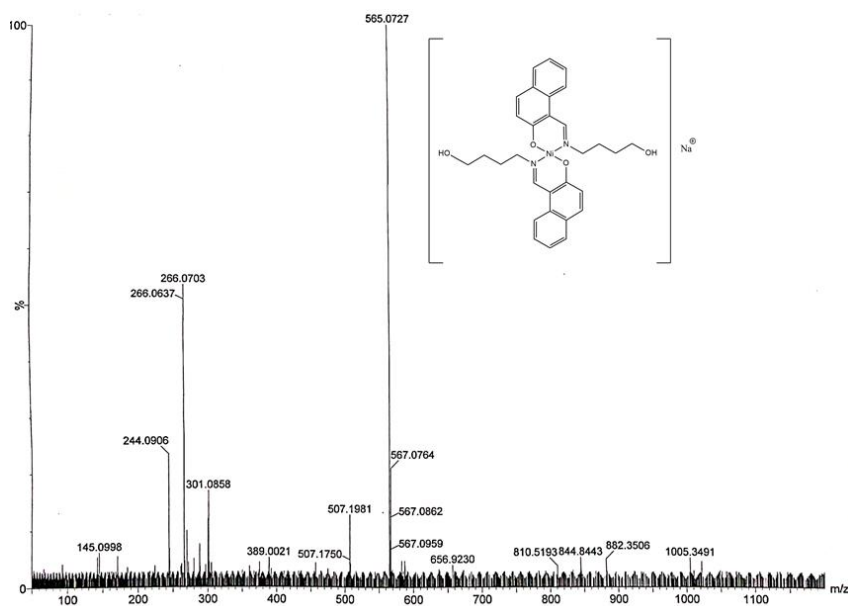


**Figure 5.11:** Mass spectrum of Complex **5.1** in methanol.

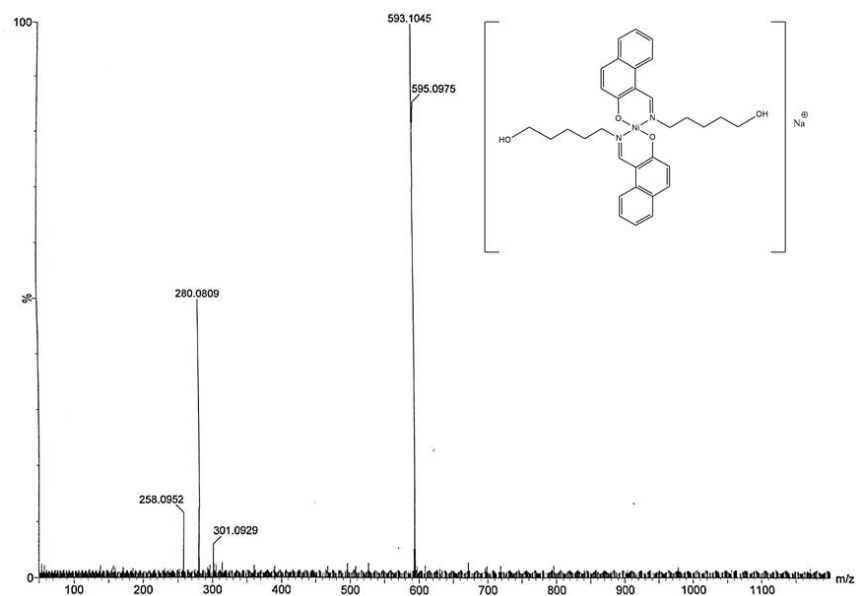


**Figure 5.12:** Mass spectrum of Complex **5.2** in methanol.

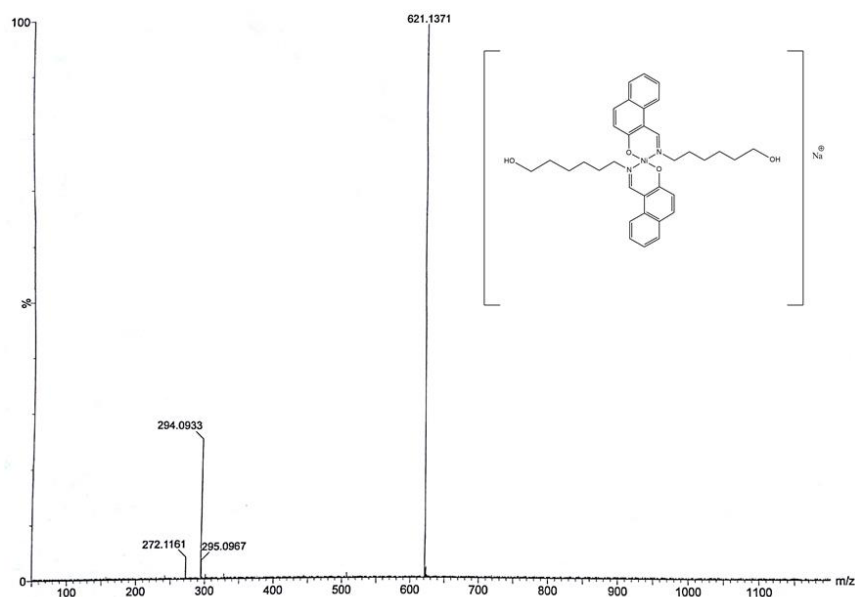


**Figure 5.13:** Mass spectrum of Complex **5.3** in methanol.

FT-IR spectra of complexes **5.1**, **5.2** and **5.3** were recorded with solid sample using ATR technique (**Figure 5.14-5.16**). In the IR spectra, a broad band appears at  $3536\text{ cm}^{-1}$ ,  $3316\text{ cm}^{-1}$  and  $3272\text{ cm}^{-1}$  for complexes **5.1**, **5.2** and **5.3**, respectively. The peaks have assigned to O–H stretching for the presence of hydroxyl group in the ligand part of the complexes. The presence of methylene group in the complexes has been evidenced by the appearance of unsymmetrical and symmetrical frequencies of  $\nu_{\text{C-H}}$  in the range of  $2800\text{--}3000\text{ cm}^{-1}$ . In the IR spectra of complexes **5.1**, **5.2** and **5.3**, the intense bands appeared at  $1657\text{ cm}^{-1}$ ,  $1658\text{ cm}^{-1}$  and  $1642\text{ cm}^{-1}$  respectively. These may be attributed to the presence of the C=N moiety in the complexes. The conclusive evidence for the formation of Ni–N and Ni–O bonds in the IR spectra of these complexes is also observed with characteristic bands. These bands support the fact that the metal ion has been effectively coordinated to the four coordinating heteroatoms (NONO). These data are also supported by the literature.<sup>5.26</sup>

Complex	$\nu(\text{cm}^{-1})$	Assigned for
5.1	3536	O–H stretching
5.2	3316	
5.3	3272	
5.1	2939	aromatic C–H bond
5.2	2933	
5.3	2934	
5.1	2855	aliphatic C–H bond
5.2	2854	
5.3	2851	

5.1	1657	azomethine e group
5.2	1658	
5.3	1642	
5.1	486	metal- nitrogen
5.2	485	
5.3	479	
5.1	562	metal- oxygen
5.2	534	
5.3	532	

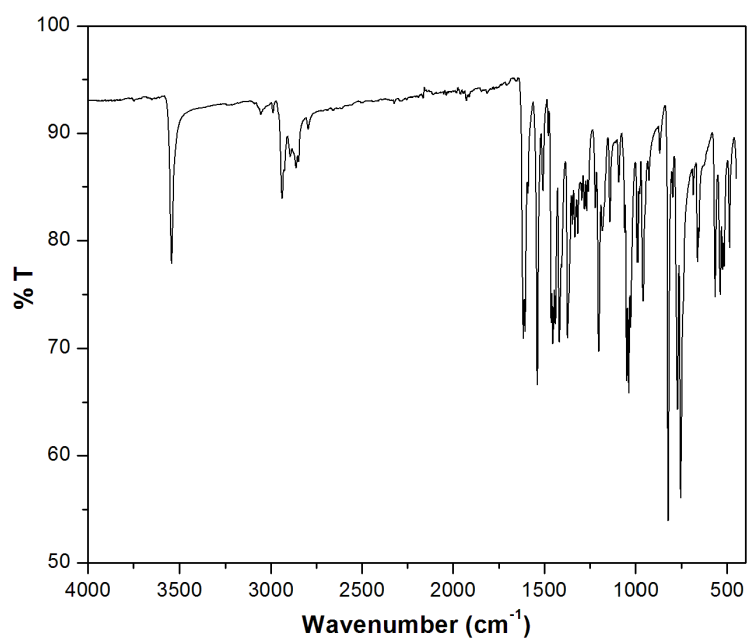


**Figure 5.14:** FT-IR spectrum of Complex 5.1.

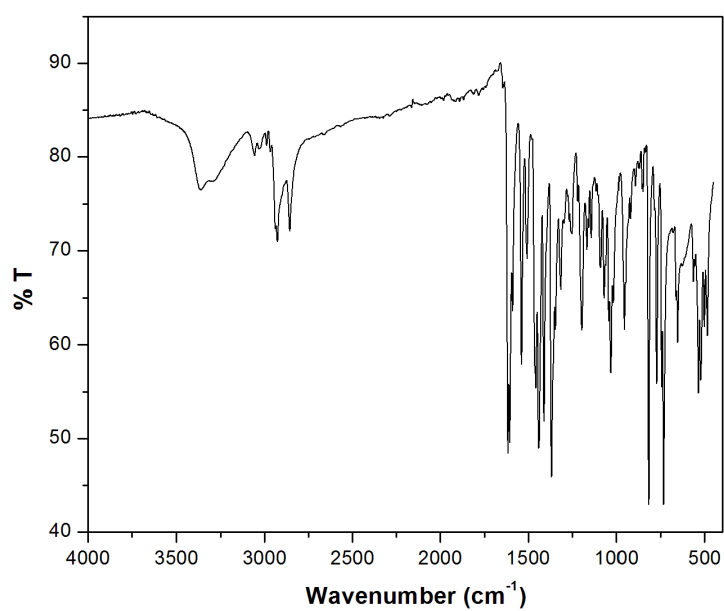


**Figure 5.15:** FT-IR spectrum of Complex 5.2.

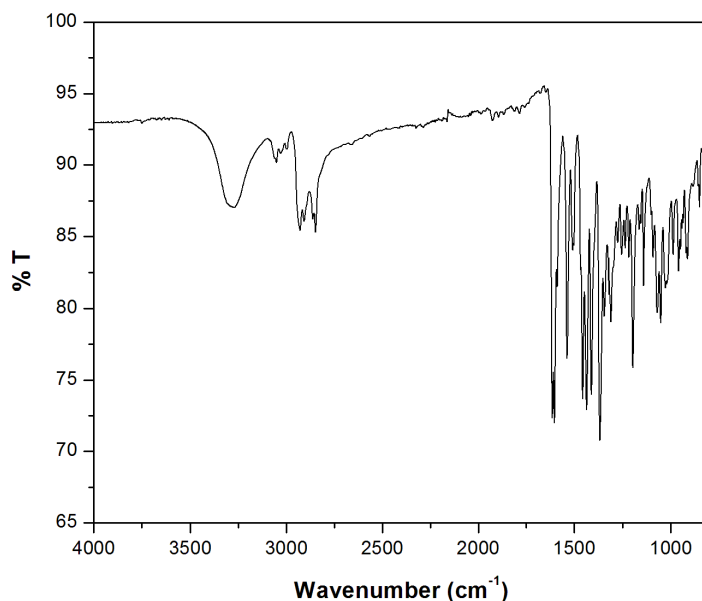


**Figure 5.16:** FT-IR spectrum of Complex 5.3.

The UV-vis spectra of complexes 5.1, 5.2 and 5.3 were recorded in the range of 200–800 nm in DMF at room temperature (Figure 5.17-5.19). Electronic spectra of these complexes are grossly similar in nature. A broad band at around 600 nm was observed for each of the complexes which may be attributed to the  $d-d$  transition. These are weak in intensity as they are Laporte forbidden.<sup>5.27</sup> The bands at 275 nm for complex 5.1, 279 nm for complex 5.2 and 274 nm for complex 5.3 may be assigned to  $\pi-\pi^*$  transitions of phenolic chromophore. The bands between 300 and 500 nm may be assigned of  $\pi-\pi^*$  transition of the azomethine chromophore and the benzene ring and  $n-\pi^*$  transition of the azomethine chromophore.<sup>5.28</sup> The higher intensity charge-transfer transition has been observed at a wavelength near 420 nm for all three complexes. These are attributed to  $O^-$  (of naphthalen-1-olate)  $\rightarrow Ni(II)$ ,  $N(\text{amino}) \rightarrow Ni(II)$  LMCT and intra-ligand charge transfer transitions.<sup>29</sup> All of these bands corroborates to the structure of the complexes (Table 5.3).

**Table 5.3:** Assignment of different UV-vis spectral bands of Complexes 5.1, 5.2 and 5.3

Complex	$\pi-\pi^*$ (phenolic chromop -hore)	$\epsilon$ ( $M^{-1}$ $cm^{-1}$ )	$\pi-\pi^*$ (C=N and benzene ring)	$\epsilon$ ( $M^{-1}$ $cm^{-1}$ )	$n-\pi^*$ (C=N)	$\epsilon$ ( $M^{-1}$ $cm^{-1}$ )	LM CT	$\epsilon$ ( $M^{-1}$ $cm^{-1}$ )	$d-d$	$\epsilon$ ( $M^{-1}$ $cm^{-1}$ )
5.1	275	10500	312	4000	348	2000	424	1500	600	30
5.2	279	9500	310	5700	345	2500	420	1800	596	30
5.3	274	9600	307	4200	347	2000	421	1900	592	30

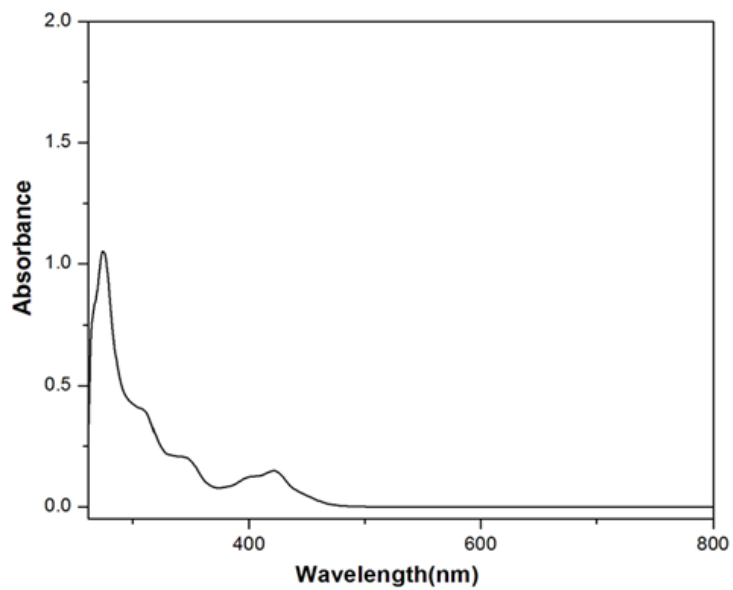


**Figure 5.17:** UV-vis spectrum of complex 5.1

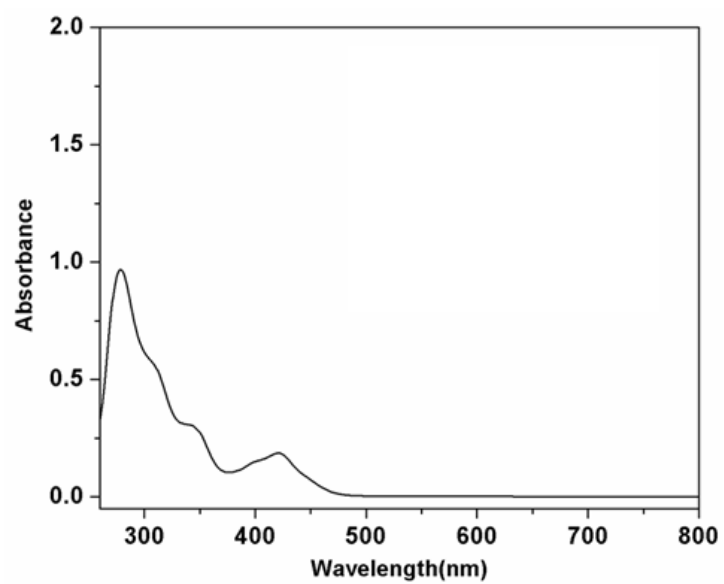


**Figure 5.18:** UV-vis spectrum of complex 5.2 in DMF

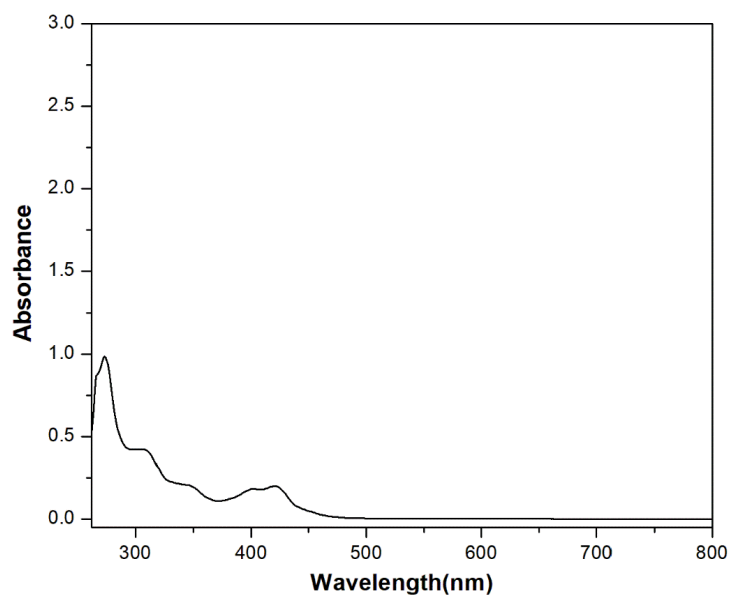


**Figure 5.19:** UV-vis spectrum of complex **5.3** in DMF

$^1\text{H}$  NMR spectra of complexes **5.1**, **5.2** and **5.3** were obtained in  $\text{DMSO-d}_6$  (Figure 5.20-5.22). Behavior of all the ligands in the presence of  $\text{Ni}^{2+}$  is grossly similar.

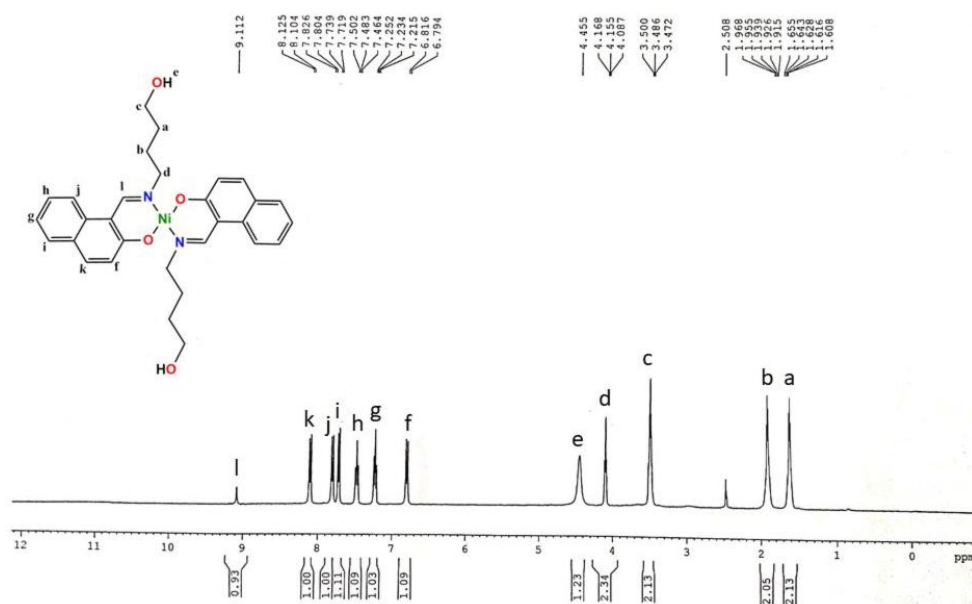


**Figure 5.20:**  $^1\text{H}$  NMR spectrum of complex **5.1** in  $\text{DMSO-d}_6$ .

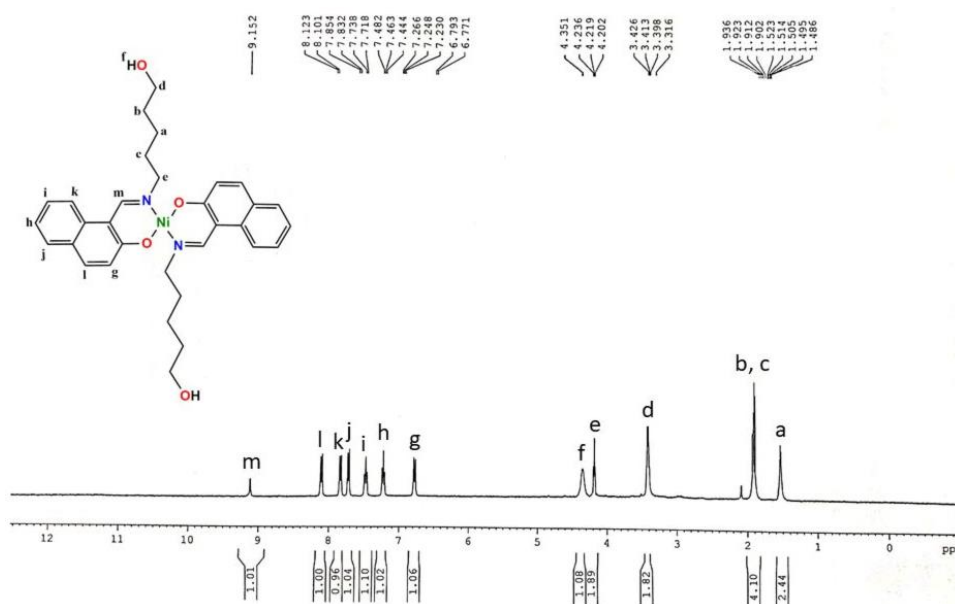


**Figure 5.21:**  $^1\text{H}$  NMR spectrum of complex 5.2 in  $\text{DMSO-d}_6$ .

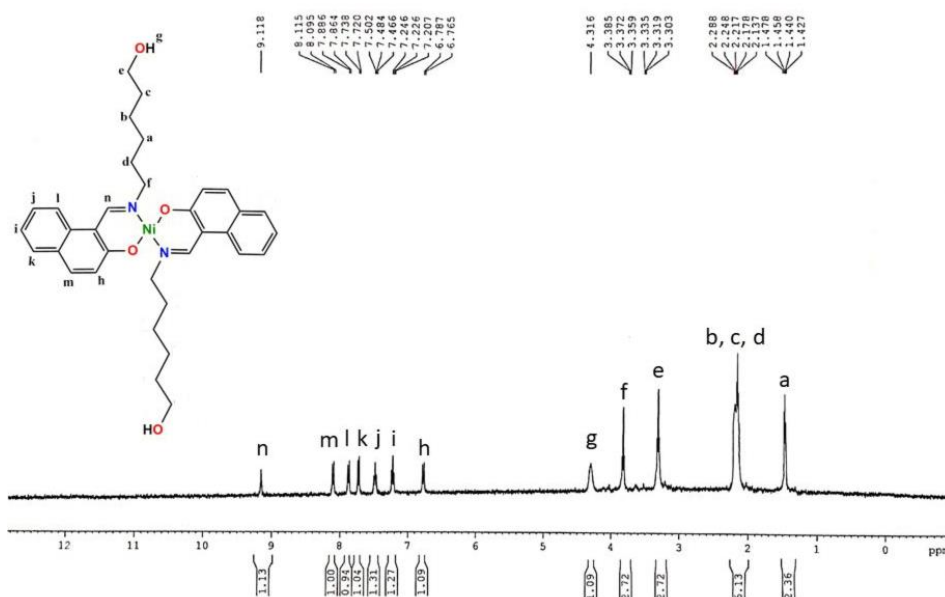


**Figure 5.22:**  $^1\text{H}$  NMR spectrum of complex 5.3 in  $\text{DMSO-d}_6$ .

All of these complexes are square planar in geometry and metal ion in the complex does not possess any unpaired electron. Peak for phenolic OH at  $\sim 14$  ppm is absent in the NMR spectra of all the complexes. This indicates that phenolic OH group is deprotonated during complex formation and then, coordinated to the metal center. The signal for imine proton at  $\sim 8$  ppm in the ligands undergoes a shift to  $\sim 9$  ppm for all the complexes confirming complex formation through azomethine nitrogen atom. Signals for aromatic protons shift towards higher  $\delta$  values. All other peaks appear in their usual positions. The fact indicates that all of the complexes remain the same in  $\text{DMSO}$  solution.<sup>5.25</sup>

### 5.3.2.3 Electrochemistry

#### 5.3.2.3.1 Cyclic voltammetric studies

As shown in **Figure 5.23(A-C)**, cyclic voltammograms of complexes **5.1**, **5.2** and **5.3**, respectively were recorded in air-free DMF containing 0.1 M tetrabutylammonium bromide in the range of  $-2$  V versus  $\text{Fc}/\text{Fc}^+$  to  $+2$  V versus  $\text{Fc}/\text{Fc}^+$ . An important feature of these cyclic voltammograms is the nickel(II)–nickel(I) redox couple with a cathodic peak potential ( $E_{\text{pc}}$ ) at  $-1.48$ ,  $-1.51$ ,  $-1.52$  V versus  $\text{Fc}/\text{Fc}^+$  for complexes **5.1**, **5.2** and **5.3**, respectively while an anodic peak potential ( $E_{\text{pa}}$ ) of  $-0.77$ ,  $-0.68$  and  $-0.74$  V versus  $\text{Fc}/\text{Fc}^+$  for complexes **5.1**, **5.2** and **5.3**, respectively.<sup>5.30</sup> Considering the reduction sweep, initially, an irreversible event is observed at  $-0.85$ ,  $-0.76$  and  $-0.73$  V versus  $\text{Fc}/\text{Fc}^+$  for complexes **5.1**, **5.2** and **5.3**, respectively, due to the electrochemically irreversible Ni(III)/Ni(II) reductive response.<sup>5.31</sup> While another quasi reversible redox event observed for each of the complexes at  $0.5$  V versus  $\text{Fc}/\text{Fc}^+$  appear for the solvent DMF. The nature of the voltammograms of the complexes scanned over the presently important region of potential of reversible Ni(II/I) couple ( $-2$  V versus  $\text{Fc}/\text{Fc}^+$  to  $+0.6$  V versus  $\text{Fc}/\text{Fc}^+$ ) has been shown at the insets of **Figure 5.23**. In **Figure 5.23(D)**, cyclic voltammogram of ferrocene is presented in DMF solution on the same working electrode. The  $E_{1/2}$  value obtained ( $0.535$  V versus aqueous  $\text{AgCl}/\text{Ag}$ ,  $\text{Cl}^-$  electrode or  $0.559$  V versus nHE) is very near to the literature value.<sup>5.32</sup>

#### [Calculation of $E_{1/2}$ with respect to nHE of $\text{Fc}/\text{Fc}^+$

$E$  vs. nHE = [value obtained against  $\text{Ag}/\text{AgCl}$ ,  $\text{Cl}^-$  +  $0.224$  V (Potential of  $\text{Ag}/\text{AgCl}$ ,  $\text{Cl}^-$  electrode) –  $0.200$  V (Liquid junction potential of saturated aqueous KCl solution with DMF)]  
 =  $[0.535 + 0.224 - 0.200]$  V =  $0.559$  V]

The current response of the redox events at  $-1.48$ ,  $-1.51$ ,  $-1.52$  V versus  $\text{Fc}/\text{Fc}^+$  for the complexes **5.1**, **5.2** and **5.3**, respectively at multiple scan rates from  $0.02$  to  $0.15$  V/s were used to construct Cottrell plot. The plots show linear dependence of the current response on the square root of the scan rate (**Figure 5.24**). This indicates that for the three complexes, the reduction is diffusion limited with a diffusion coefficient of  $1.07 \times 10^{-5}$  for complex **5.1**,  $0.77 \times 10^{-5}$  for complex **5.2** and  $0.72 \times 10^{-5}$  for complex **5.3**. It has been observed that the catalytic to peak current ratio ( $i_{\text{cat}}/i_{\text{p}}$ ) increases for all the three complexes with increasing acid concentration (**Figure 5.25**).



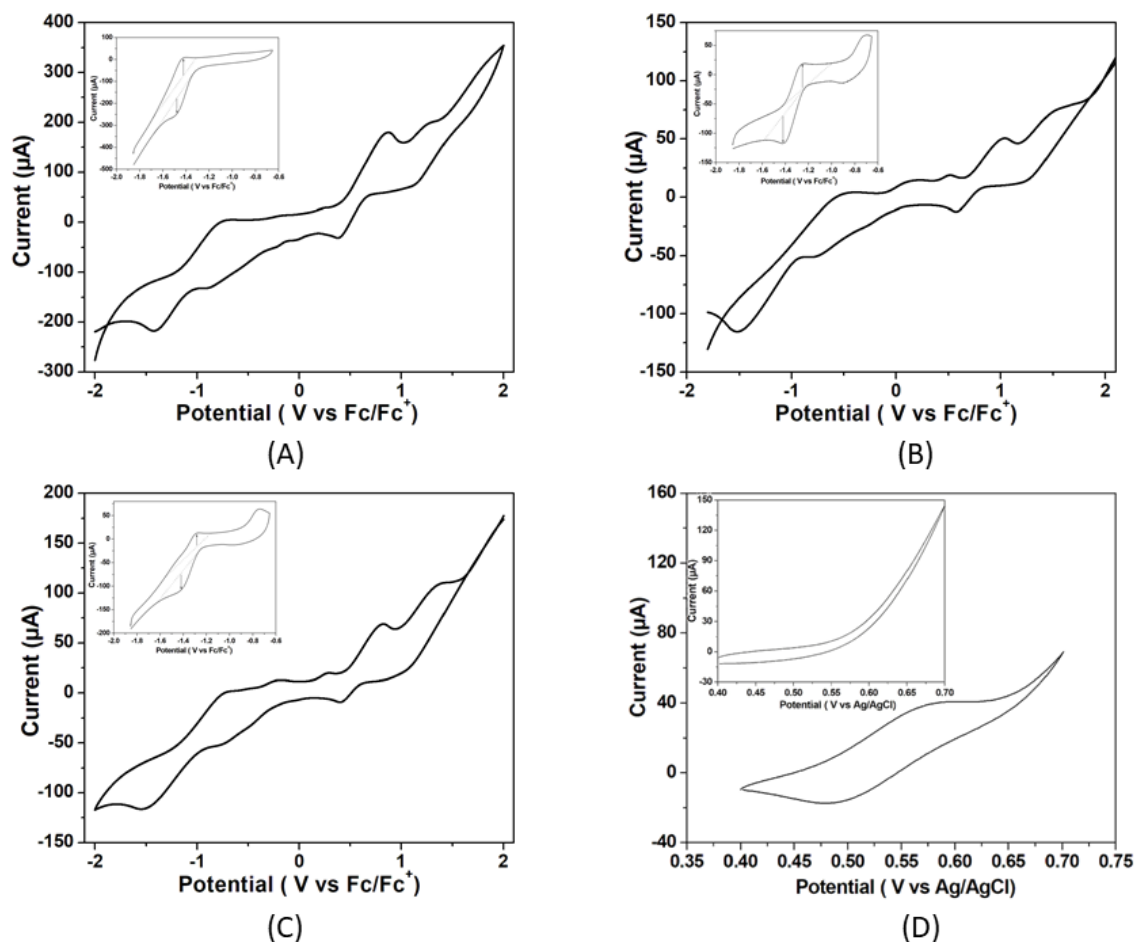


**Figure 5.23:** Cyclic voltammograms of 5.36  $\mu\text{M}$  of (A) complex **5.1**, (B) complex **5.2** (C) complex **5.3** and (D) ferrocene (Inset: Cyclic voltammograms scanned over the presently important region of potential of reversible Ni(II/I) couple) in air free DMF solutions with 0.1 M of  $[\text{n-Bu}_4\text{N}]\text{Br}$  as supporting electrolyte at a scan rate of 50 mV/s. Here ferrocene is the internal standard.

#### Determination of Diffusion Coefficient (D) for complex **5.1**, **5.2** and **5.3**

Using the Randles-Sevcik equation,

$$i_p = 0.4463 \left( \frac{n^3 F^3}{RT} \right)^{1/2} A[\text{cat}](Dv)^{1/2}$$

Where,  $i_p$  = Peak current (amperes),  $n$  = Number of electrons transferred in a redox cycle,  $F$  = Faraday's constant (96485 C/mol),  $R$  = Universal gas constant (8.314 J.K<sup>-1</sup>.mol<sup>-1</sup>),  $T$  = Absolute temperature (298 K),  $A$  = The electrode surface area in working (0.07 cm<sup>2</sup>),  $C$  = Molar concentration of redox-active species (mol/cm<sup>3</sup>),  $D$  = The diffusion coefficient (cm<sup>2</sup>/s),  $v$  = Scan rate in V/s.

Plotting peak current ( $i_p$ ) versus the square root of the scan rate ( $v$ )<sup>1/2</sup>

$$\text{Slope} = 0.4463 \left( \frac{n^3 F^3}{RT} \right)^{1/2} A[\text{cat}](D)^{1/2}$$

Complex	Slope	Diffusion coefficient (cm <sup>2</sup> /s)
5.1	1.31 X 10 <sup>-5</sup>	1.07 X 10 <sup>-5</sup>
5.2	1.11 X 10 <sup>-5</sup>	0.77 X 10 <sup>-5</sup>
5.3	1.08 X 10 <sup>-5</sup>	0.72 X 10 <sup>-5</sup>

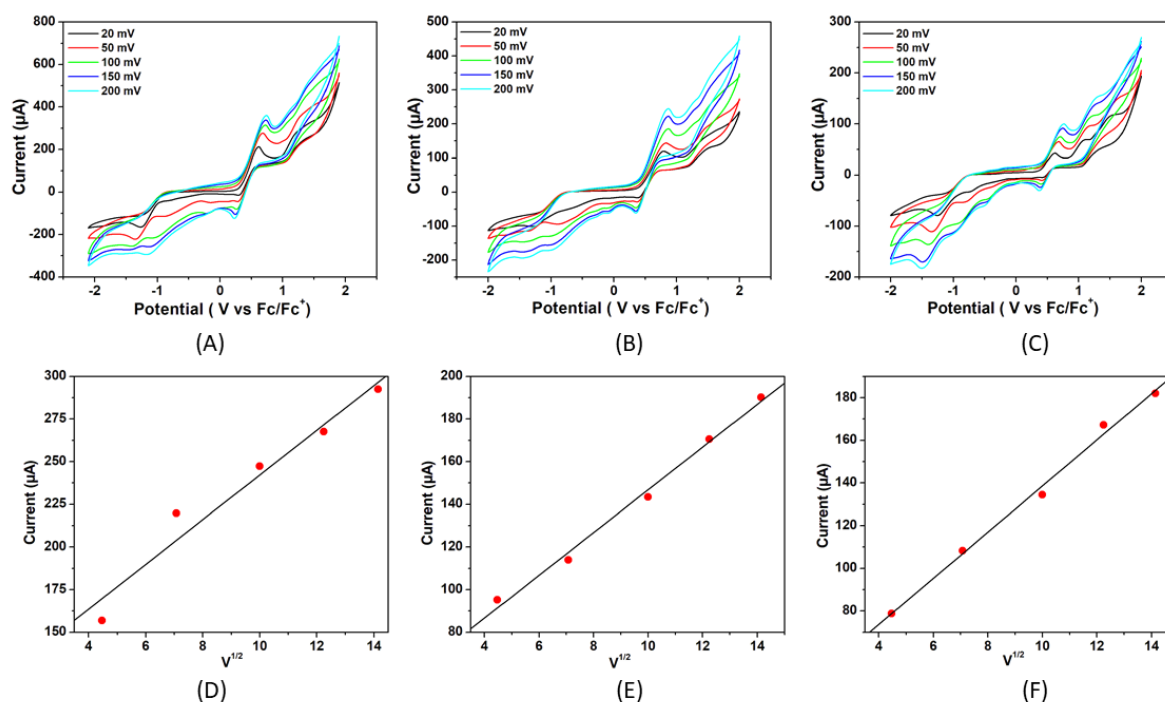


**Figure 5.24:** Scan rate dependence of precatalytic waves for 5.36  $\mu\text{M}$  solutions of complexes (A) **5.1**, (B) **5.2** and (C) **5.3** at scan rate from 20 to 200 mV/s in air free DMF solutions with 0.1M [n-Bu<sub>4</sub>N]Br as supporting electrolyte and Cottrell plot of peak current versus the square root of scan rate for complexes (D) **5.1**, (E) **5.2** and (F) **5.3**.

The electrochemical properties of three nickel(II) complexes with salen type ligands were influenced by the presence of different substituents of the imine linkage.<sup>5.33</sup> Ren and co-workers showed that the electrochemical reduction ability of nickel(II) complexes with cyclam ligands from H<sup>+</sup> to H<sub>2</sub> are dependent on the substituents on the macrocyclic ligands.<sup>5.34</sup> Thus, it is expected that changes in chain length of ligands in the Ni(II) complexes in the present study could influence Ni(II)/Ni(I) potentials of the complexes.

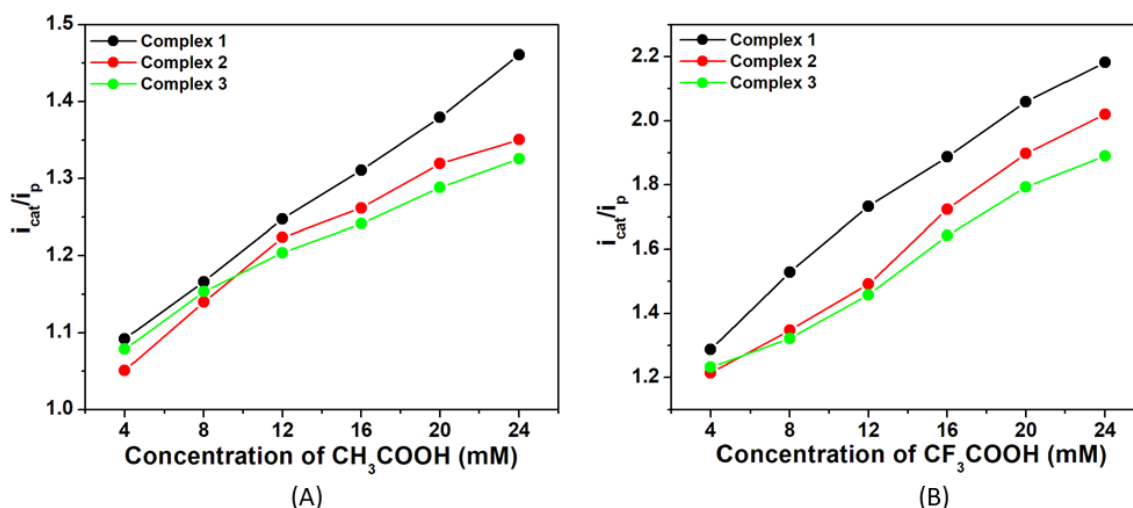


**Figure 5.25:** Plot of  $i_{cat}/i_p$  vs [Acid] for 5.36  $\mu\text{M}$  of complexes **5.1**, **5.2** and **5.3**.

### 5.3.2.3.2 Electrocatalytic Hydrogen Evolution in DMF: CV Studies

The performance of these three mononuclear Ni(II) complexes as effective electrocatalysts for the HER has been assessed under various conditions in which the proton source ( $\text{CH}_3\text{COOH}$  or  $\text{CF}_3\text{COOH}$ ) has been systematically varied.

To determine activity of complexes **5.1**, **5.2** and **5.3** as electrocatalyst, first, cyclic voltammograms of the complexes were recorded in the presence of acetic acid ( $\text{pK}_a = 13.5$ ) in DMF.<sup>5.35</sup> The addition of  $\text{CH}_3\text{COOH}$  aliquots from 0.00 to 24.00 mM to the solutions of complexes **5.1**, **5.2** and **5.3** in DMF triggers the systematic increase in catalytic current ( $i_{cat}$ ) near at  $-1.48$ ,  $-1.51$ ,  $-1.52$  V, respectively, versus  $\text{Fc}/\text{Fc}^+$  (**Figure 5.26**).

The onset potentials for the reduction of hydrogen ion in the presence of the three complexes studied are  $-1.13$  V,  $-1.15$  V and  $-1.20$  V versus  $\text{Fc}/\text{Fc}^+$ , respectively, indicating the catalytic activity is in the order: Complex **5.1** > Complex **5.2** > Complex **5.3**.

The electrocatalytic activity of these complexes has been accessed using trifluoroacetic acid ( $\text{pK}_a = 6.0$ ) in DMF as a proton source.<sup>5.35</sup> As shown in **Figure 5.27**, there is an increase in the catalytic current ( $i_{cat}$ ) near at  $-1.48$ ,  $-1.51$ ,  $-1.52$  V versus  $\text{Fc}/\text{Fc}^+$  for complexes **5.1**, **5.2** and **5.3** respectively upon successive addition of  $\text{CF}_3\text{COOH}$  (0.00 to 24.00 mM). For all the three complexes, the peak current increases and the peak potential is shifted towards less negative potential (anodically) with increase of acid concentration in the solution. This signifies that the greater diffusion of proton from bulk solution to the electrode surface makes the reduction process much easier at high concentration of acid. Notably for all the three complexes, the sequence of peak currents which also represent their catalytic activity at any particular acid concentration is the same as the order of post peak current values which decrease sharply with the decreased potential due to increased hydrogen evolution.

This rise in current in both the cases can be attributed to the generation of  $H_2$  from catalytic reduction of protons. Reduction potentials of these complexes slightly change towards more anodic values with the sequential enhancements in concentration of the acid. Over potential for hydrogen evolution has been calculated following the methods reported by Fourmond et al.<sup>5,35</sup> from the theoretical half wave potential,  $E_{1/2}^T$ , based on the expression found in the supporting document and the experimental potential  $E_{cat/2}$  (**Equation 5.1**).

$$\text{Over potential}(\eta) = |E_{1/2}^T - E_{cat/2}| \dots \dots \dots (5.1)$$

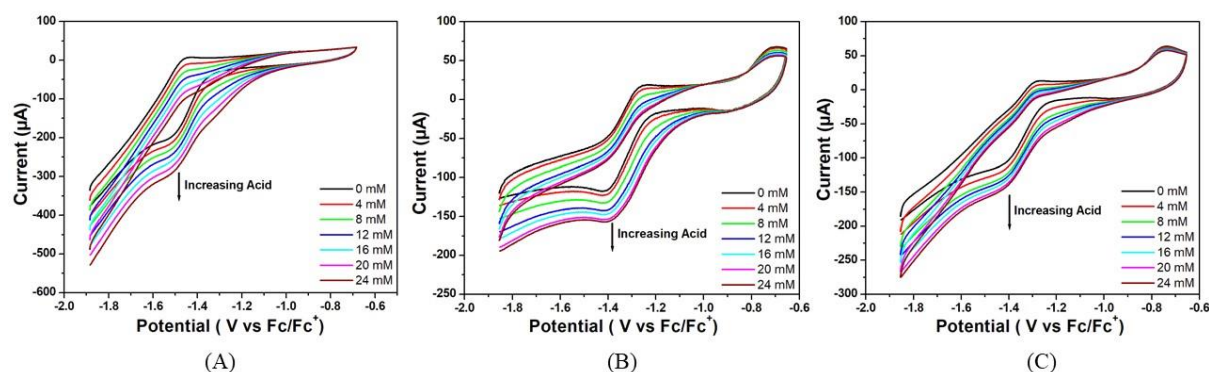


**Figure 5.26:** Cyclic voltammograms of (A) complex **5.1**, (B) complex **5.2** and (C) complex **5.3** ( $5.36 \mu\text{M}$ ) in the absence of acetic acid (black trace) and in the presence of varying concentration of acetic acid in air free DMF. Conditions:  $25 \text{ }^\circ\text{C}$ ,  $0.1 \text{ M}$   $[\text{n-Bu}_4\text{N}]\text{Br}$  as supporting electrolyte, scan rate =  $50 \text{ mV/s}$ , glassy carbon working electrode, Pt wire counter electrode and the potential is referenced against  $\text{Fc/Fc}^+$ .

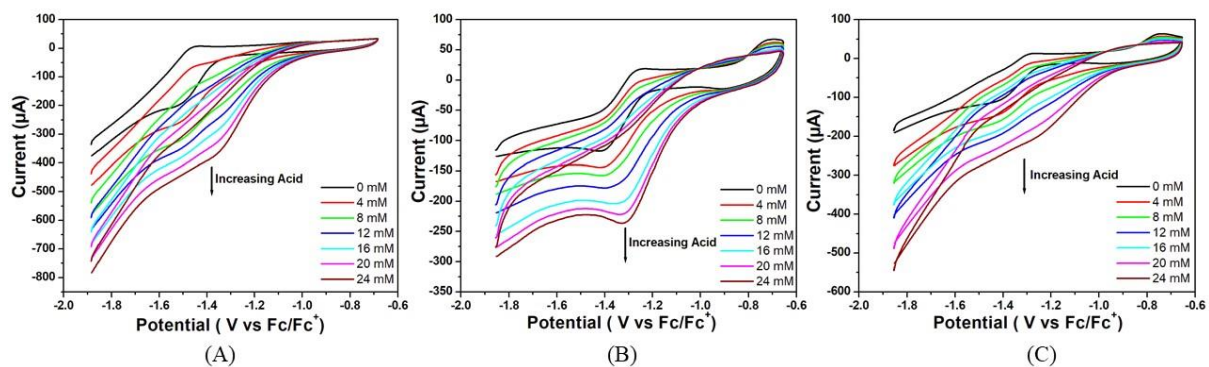


**Figure 5.27:** Cyclic voltammograms of (A) complex **5.1**, (B) complex **5.2** and (C) complex **5.3** ( $5.36 \mu\text{M}$ ) in absence of trifluoroacetic acid (black trace) and in the presence of varying concentration of trifluoroacetic acid in air free DMF. Conditions:  $25 \text{ }^\circ\text{C}$ ,  $0.1 \text{ M}$   $[\text{n-Bu}_4\text{N}]\text{Br}$  as supporting electrolyte, scan rate =  $50 \text{ mV/s}$ , glassy carbon working electrode, Pt wire counter electrode and the potential is referenced against  $\text{Fc/Fc}^+$ .

Based on Eq. 5.1, this reduction occurs at an over potential of  $-0.52$  V,  $-0.55$  V and  $-0.56$  V for complexes **5.1**, **5.2** and **5.3**, respectively for the former case where acetic acid is the proton source. The corresponding values are  $-0.22$  V,  $-0.23$  V and  $-0.24$  V for complexes **5.1**, **5.2** and **5.3**, respectively, for the latter case, where trifluoroacetic acid is the proton source.

**Over potential Calculations:**

Calculations of  $E_{1/2}^T (= E_{ref})$  and  $\eta$  using  $E_{H^+/H_2}^0$ ,  $pK_a$ ,  $\epsilon_D$  and  $C_{H_2}^0$  using Fourmond’s approach (**Equation 5.2**).

$$E_{1/2}^T = E_{H^+/H_2}^0 - 2.303 \frac{RT}{F} pK_a + \epsilon_D - \frac{RT}{2F} \ln \frac{C_0}{C_{H_2}^0} \dots\dots\dots(5.2)$$

$E_{1/2}^T$  for Complexes **5.1**, **5.2**, **5.3** with 24.00 mM  $CH_3COOH$  in DMF

$$E_{1/2}^T = (-0.62) - 2.303 \frac{8.314 \times 298}{96485} 13.5 + 0.04 - \frac{8.314 \times 298}{2 \times 96485} \ln \frac{24}{1.9}$$

$$E_{1/2}^T = -1.41 \text{ vs } Fc^+/Fc$$

Complex	Overpotential
5.1	$-1.41 - (-0.888) = -0.52$
5.2	$-1.41 - (-0.853) = -0.55$
5.3	$-1.41 - (-0.849) = -0.56$

$E_{1/2}^T$  for Complexes **5.1**, **5.2**, **5.3** with 24.00 mM  $CF_3COOH$  in DMF

$$E_{1/2}^T = (-0.62) - 2.303 \frac{8.314 \times 298}{96485} 6.0 + 0.04 - \frac{8.314 \times 298}{2 \times 96485} \ln \frac{24}{1.9}$$

$$E_{1/2}^T = -0.96 \text{ vs } Fc^+/Fc$$

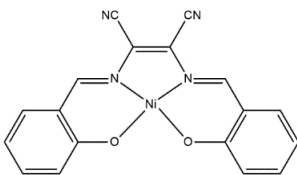
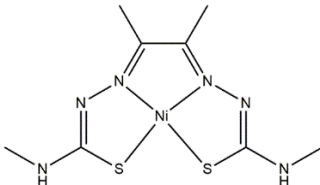
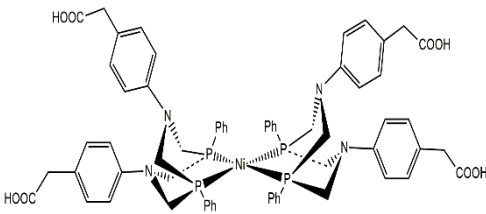
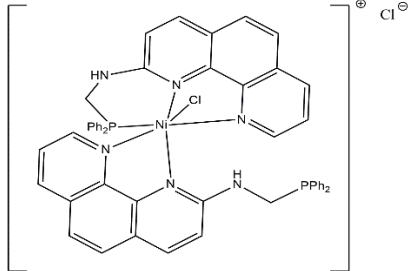
Complex	Overpotential
5.1	$-0.96 - (-0.733) = -0.22$
5.2	$-0.96 - (-0.723) = -0.23$
5.3	$-0.96 - (-0.713) = -0.24$

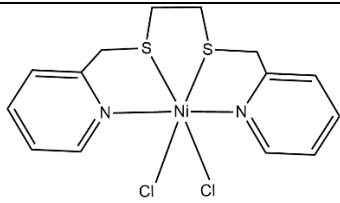
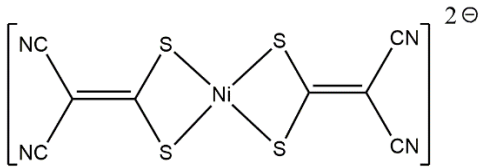
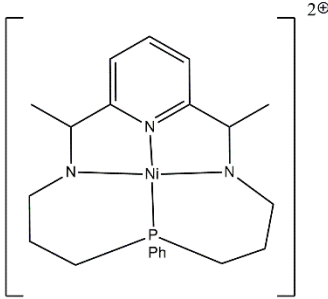
In both the cases, the catalytic activity of the three homogeneous catalysts as obtained from the overpotential value is in the order: Complex **5.1** > Complex **5.2** > Complex **5.3**. Moreover, the large difference in overpotential for each complex for the two proton sources is expected for the increased diffusion of proton in the latter case.

A table has been given in supporting information where few of recently published Ni(II) complexes<sup>5.8b,c, 5.37</sup> are listed with their overpotential values (**Table 5.4**). In most of the cases, the medium of experiment was organic. Proton source varies as acetic acid, trifluoroacetic acid, perchloric acid or buffer solution. If we look into the values of overpotential, they are in range

of few mV. While comparing with the other reported overpotential values for the electrocatalytic hydrogen evolution catalysed by nickel complexes as enlisted in the table, it can be concluded that these three nickel(II) complexes are more effective in this field.

**Table 5.4:** Few parameters of recently published complexes used for hydrogen evolution reaction

Entry	Complex	Medium	Source	Overpotential (V)
1	 (Int. J. Hydrogen Energy <b>2014</b> , 39, 10980)	DMF	CH <sub>3</sub> COOH	0.320
2	 (Inorg. Chem. <b>2018</b> , 57, 21, 13486)	DMF	CH <sub>3</sub> COOH CF <sub>3</sub> COOH	0.85 -----
3	 (Dalton Trans., <b>2019</b> , 48, 14653)	ACN ACN	CH <sub>3</sub> COOH CF <sub>3</sub> COOH	0.53 0.67 0.93
4	 (Inorg. Chem. <b>2020</b> , 59, 1038)		H <sub>2</sub> -saturated basic (1.0 M KOH)	0.364

5		Neutral buffer	0.837
	( <i>Int. J. Hydrogen Energy</i> <b>2018</b> , 43, 19047)		
6		Neutral buffer	0.837.6
	( <i>Applied Catalysis B</i> <b>2017</b> , 219, 353–361)		
7		ACN HClO <sub>4</sub>	1.07
	( <i>ACS Catal.</i> <b>2015</b> , 5, 356–364)		
8	Complex <b>5.1</b> (Present study)	DMF CH <sub>3</sub> COOH CF <sub>3</sub> COOH	0.52 0.22
9	Complex <b>5.2</b> (Present study)	DMF CH <sub>3</sub> COOH CF <sub>3</sub> COOH	0.55 0.23
10	Complex <b>5.3</b> (Present study)	DMF CH <sub>3</sub> COOH CF <sub>3</sub> COOH	0.56 0.24

The stability of all three complexes have been checked by repeated cyclic voltammetry (CV) studies upto 65 cycles using TFA as proton source (**Figure 5.28**). It has been observed that no new peaks are generated in the CV and also the colour of the solution remains the same during the study. In all cases, the reduction peak current increases continuously and reaches almost steady value at the 55<sup>th</sup> cycle. The peak current with respect to the lowest amount is increased by 12% for complex **5.1**, 14% for complex **5.2**, 28% for complex **5.3**. The current of complex **5.1** is always greater than the rest two complexes. The increase in current during repeated cyclic voltammetric operation might be due to the cleansing of the fine surface of the electrode and opening up of new channels by initial H<sup>+</sup> ion penetration at the metal centre and associated H<sub>2</sub> evolution. Thus, more active sites of the electrode surface are created for further

reaction. Greater the size of the alkyl group, greater is the initial prevention of  $H^+$  for approaching towards metal centre for reduction. On application of the negative potential the proton penetrates through the barrier and creates new channels for further reaction. Since the initial barrier varies in the order complex **5.3** > complex **5.2** > complex **5.1**, the increase in the peak current on cycling is in the reverse order.

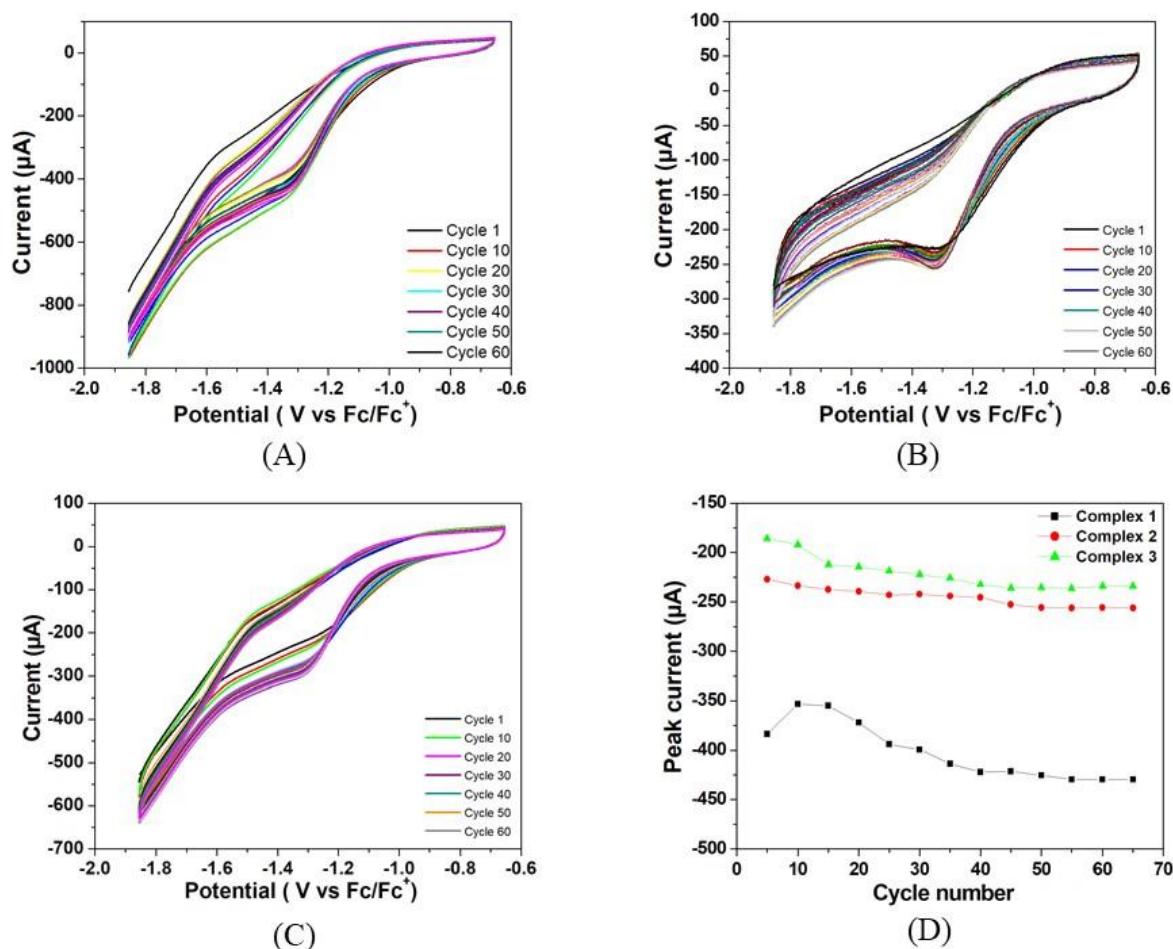


**Figure 5.28:** Repeated cyclic voltammetry studies of (A) complex **5.1**, (B) complex **5.2**, (C) complex **5.3**. (D) Peak current vs. cycle number profiles for all the three complexes.

### 5.3.2.3.3 Electrocatalytic Hydrogen Evolution: CPE Studies

Further evidence for the electrocatalytic activity of these mononuclear nickel(II) complexes for HER was evaluated in DMF by conducting Controlled-potential electrolysis (CPE) experiments over a period of 1 hour, as in **Figure 5.29**, **Figure 5.30**. **Figure 5.29** shows the total charge of bulk electrolysis of a 5.36 μM of complex **5.1**, **5.2** and **5.3** separately in DMF solution in the presence of acetic acid (24 mM). At an applied potential of -1.5 V versus Fc/Fc<sup>+</sup> the maximum charge reached during 1 hour of electrolysis are 0.73 C for complex **5.1**, 0.51 C for complex **5.2** and 0.44 C for complex **5.3**, accompanied by gas bubble appearing on the electrode (**Figure 5.31**).



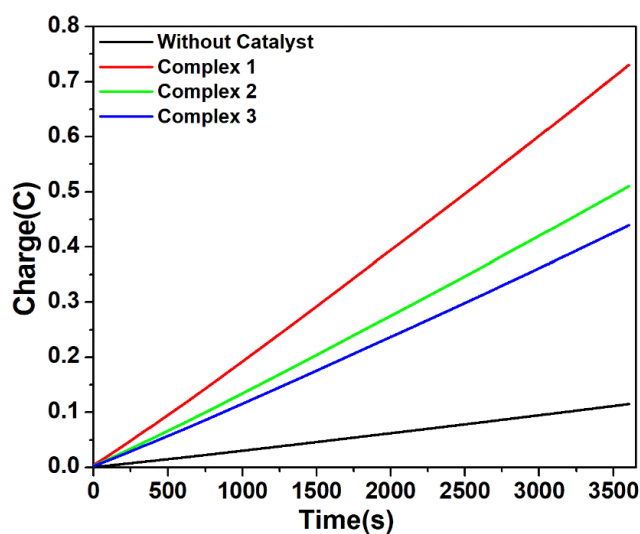


**Figure 5.29:** Charge build up vs time plots in the CPE (controlled potential electrolysis) experiment of complex **5.1** (red), complex **5.2** (green), complex **5.3** (blue) and without catalyst (black) at potential -1.5 V versus Fc/Fc<sup>+</sup>. Conditions: 5.36  $\mu$ M complex in air free DMF with 0.1 M [n-Bu<sub>4</sub>N]Br as supporting electrolyte and 24 mM CH<sub>3</sub>COOH as proton source.

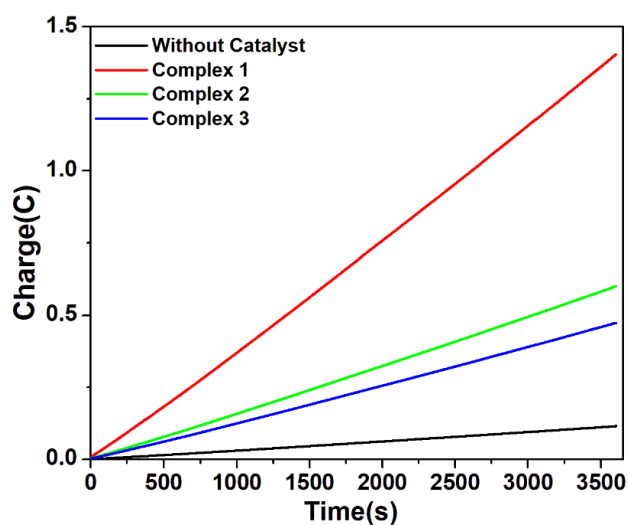


**Figure 5.30:** Charge build up vs time plots in the CPE (controlled potential electrolysis) experiment of complex **5.1** (red), complex **5.2** (green), complex **5.3** (blue) and without catalyst (black) at potential -1.5 V versus Fc/Fc<sup>+</sup>. Conditions: 5.36  $\mu$ M complex in air free DMF with 0.1 M [n-Bu<sub>4</sub>N]Br as supporting electrolyte and 24 mM CF<sub>3</sub>COOH as proton source.



**Figure 5.31:** Photograph of the customized, one-compartment, three-neck cell with a glassy carbon working electrode.  $\text{H}_2$  gas bubbles are appeared on the surface of the working electrode.

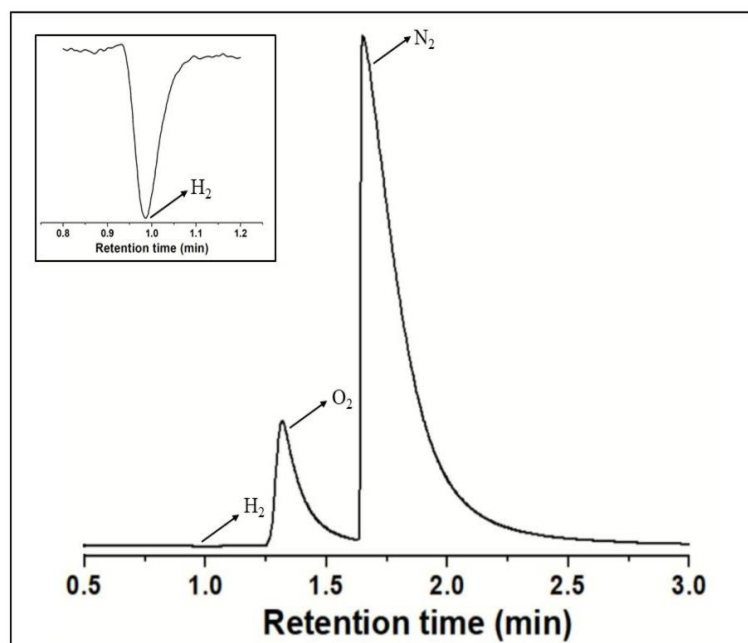


**Figure 5.32** Gas chromatogram of the headspace gas obtained after bulk electrolysis of a  $\text{N}_2$  saturated 0.5 mM solution of complex **5.1** containing 24 mM TFA. The headspace gas was analyzed after 30 min of electrolysis. Inset: Detection region of evolved  $\text{H}_2$  gas.

However, when the CPE experiments were done with  $5.36 \mu\text{M}$  of complexes **5.1**, **5.2** and **5.3** separately in DMF solution in the presence of trifluoroacetic acid (24 mM) the same trend was obtained (**Figure 5.30**). At an applied potential of  $-1.50 \text{ V}$  versus  $\text{Fc}/\text{Fc}^+$ , the maximum charge reached 1.41 C for complex **5.1**, 0.61 C for complex **5.2** and 0.49 C for complex **5.3** during 1 hour of electrolysis. CPE experiments under the same potential with a catalyst-free solution gave only a charge of 0.11 C, showing that complex **5.1** is again more effective than the rest

two complexes in hydrogen production under such conditions. This study suggests that all these three complexes are capable of catalysing the reduction of protons from acid to H<sub>2</sub>. The evolution of H<sub>2</sub> gas has been confirmed by the use of gas chromatography (**Figure 5.32**). The Turn over number (TON) and Faradic efficiency were calculated for all the complexes (**Table 5.5, 5.6**) and the result of CPE experiments is enlisted in **Table 5.8**.

**Table 5.5:** TON Calculations

Complex in DMF	Proton source	$q_{\text{total}}=q_{\text{cat}} - q_{\text{blank}}$	Theoretical moles of hydrogen produced = $\frac{q_{\text{total}} (1 \text{ mol } e^- / 96485 \text{ C})}{2 \text{ mol } e^-} \times (1 \text{ mol } H_2)$	Moles of catalyst used	TON = $\frac{\text{Theoretical moles of } H_2}{\text{Moles of catalyst used}}$
5.1	Acetic acid	0.62	$3.21 \times 10^{-6}$	$1.34 \times 10^{-7}$	23.95
5.2	Acetic acid	0.40	$2.07 \times 10^{-6}$		15.45
5.3	Acetic acid	0.33	$1.71 \times 10^{-6}$		12.76
5.1	Trifluoroacetic acid	1.30	$6.74 \times 10^{-6}$		50.30
5.2	Trifluoroacetic acid	0.50	$2.59 \times 10^{-6}$		19.33
5.3	Trifluoroacetic acid	0.38	$1.97 \times 10^{-6}$		14.70

**Faradaic Efficiency**

$$\text{Faradaic Efficiency} = \frac{\text{Quantified moles of } H_2}{\text{Theoretical moles of } H_2} \times 100\%$$

**Table 5.6:** Calculations of Faradaic Efficiency

Complex	Proton Source	Quantified moles of H <sub>2</sub>	Theoretical moles of H <sub>2</sub> (X 10 <sup>-6</sup> )	Faradaic Efficiency (%)
5.1	Acetic Acid	2.17	3.21	67.56
5.2		1.01	2.07	48.64
5.3		0.71	1.71	41.35
5.1		5.51	6.74	81.78

5.2	Trifluoroacetic	1.59	2.59	61.41
5.3	acid	1.17	1.97	59.58

The turnover frequency (TOF) for hydrogen evolution using all the three complexes **5.1**, **5.2** and **5.3** as electrocatalysts was estimated using the foot-of-the-wave analysis (FOWA).<sup>5.37</sup> FOWA has been considered near the foot of the catalytic wave where the catalytic wave does not get affected much by phenomenon like substrate consumption, diffusion and shape of CV is dominated mainly by catalytic phenomenon.<sup>5.38</sup> The  $i_{cat}/i_p$  was plotted against  $1/(1 + \exp [(F/RT)(E-E_{1/2})])$  for both the complexes as given in **Figure 5.33**, **5.34** and the obtained TOF values are given in the **Table 5.7**.

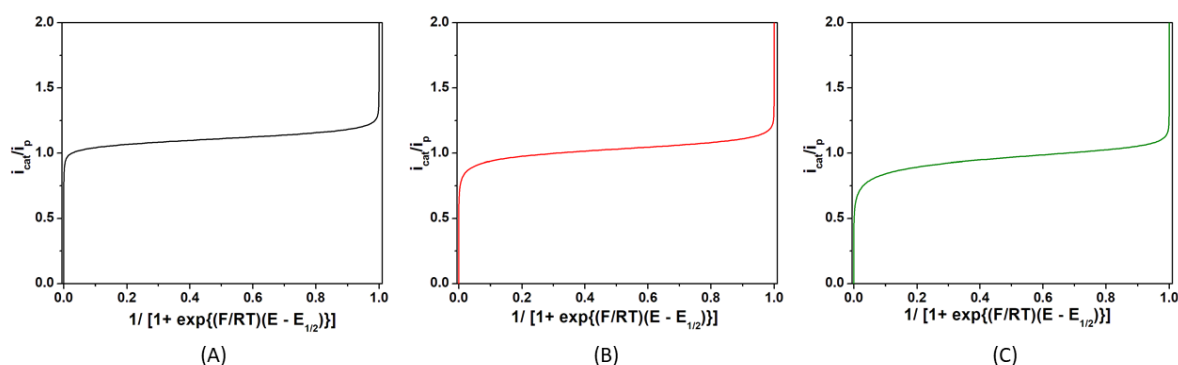


**Figure 5.33:** Plot of  $i_{cat}/i_p$  vs.  $1/(1+\exp[(F/RT)(E-E_{1/2})])$  using FOWA of 5.36  $\mu\text{M}$  of (A) complex **5.1** (B) complex **5.2** and (C) complex **5.3** with 24 mM  $\text{CH}_3\text{COOH}$  in DMF.

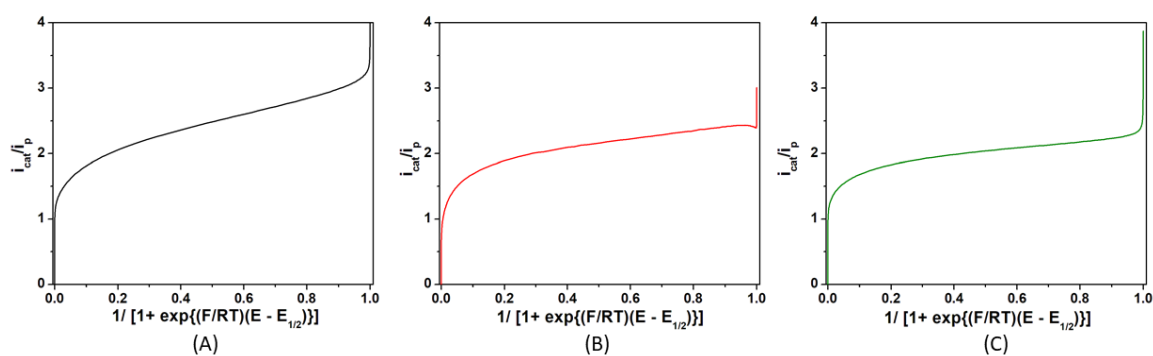


**Figure 5.34:** Plot of  $i_{cat}/i_p$  vs.  $1/(1+\exp[(F/RT)(E-E_{1/2})])$  using FOWA of 5.36  $\mu\text{M}$  of (A) complex **5.1** (B) complex **5.2** and (C) complex **5.3** with 24 mM  $\text{CF}_3\text{COOH}$  in DMF.

### TOF Calculations:

For homogenous, diffusion controlled process the peak current can be given by Randle Sevcik equation

$$i_p = 0.4463FSC_p^0 \sqrt{\frac{FvD}{RT}} \dots\dots\dots(5.3)$$

$$i_{cat} = \frac{2FSC_p^0 \sqrt{\frac{FvD}{RT}}}{1 + \exp\left[\frac{F}{RT}(E-E_{1/2})\right]} \dots\dots\dots(5.4)$$

Where, F is the Faraday’s constant, S is the surface of electrode, C<sub>p</sub><sup>0</sup> is the concentration of the complex in solution, D is the diffusion coefficient, E<sub>1/2</sub> the half-wave potential of the redox couple triggering catalysis, R is the gas constant and T is the absolute temperature. Combining the equation (5.3) and (5.4) we get the equation (5.5). The plot of i<sub>cat</sub>/i<sub>p</sub> vs 1/(1+exp[(F/RT)(E-E<sub>1/2</sub>)] gives access of the observed rate constant (k<sub>obs</sub>).

$$\frac{i_{cat}}{i_p} = \frac{2}{0.4463} \sqrt{\frac{RT(K_{obs})}{Fv}} \frac{1}{1 + \exp\left[\frac{F}{RT}(E-E_{1/2})\right]} \dots\dots\dots(5.5)$$

$$Slope = \frac{2}{0.4463} \sqrt{\frac{RT(K_{obs})}{Fv}} \dots\dots\dots(5.6)$$

**Table 5.7:** TOF Calculations

Complex	Proton Source	Slope	K <sub>obs</sub> (s <sup>-1</sup> )	C <sub>H</sub> <sup>0</sup> (M)	K <sub>cat</sub> = (K <sub>obs</sub> / C <sub>H</sub> <sup>0</sup> ) (M <sup>-1</sup> s <sup>-1</sup> )	TOF (s <sup>-1</sup> )
5.1	Acetic Acid	2.48	6.03	0.024	251.25	251.25
5.2		1.81	3.21		133.75	133.75
5.3		1.51	2.23		92.92	92.92
5.1	Trifluoroacetic acid	3.23	10.24		426.67	426.67
5.2		2.15	4.53		188.75	188.75
5.3		1.76	3.04		126.67	126.67

**Table 5.8:** Results of CPE experiments with complexes **5.1**, **5.2** and **5.3**.

Complex	Solvent	Proton Source	q (C)	n (X 10 <sup>-6</sup> )	TON	TOF (s <sup>-1</sup> )	Faradic efficiency (%)
5.1	DMF	Acetic acid	0.62	3.21	23.95	251.25	67.56
5.2			0.40	2.07	15.45	133.75	48.64

5.3			0.33	1.71	12.76	92.92	41.35
5.1		Trifluoroacetic acid	1.30	6.74	50.30	426.67	81.78
5.2	0.50		2.59	19.33	188.75	61.41	
5.3	0.38		1.97	14.70	126.67	59.58	

**5.3.2.3.4 Determination of the reaction mechanism of HER using Tafel analysis**

Tafel analysis is generally employed to understand the catalytic kinetics of hydrogen evolution reactions (Figure 5.35). Tafel slope is regarded as an inherent property of electrocatalyst and evaluated by the rate limiting step for HER. Its analysis is vital for enlightening the mechanism of HER. According to Tafel equation,

$$\eta = a + b \log i \dots\dots\dots(5.7)$$

where  $\eta$  = overpotential,  $a$  = constant,  $b$  = Tafel slope and  $i$  = measured current density.

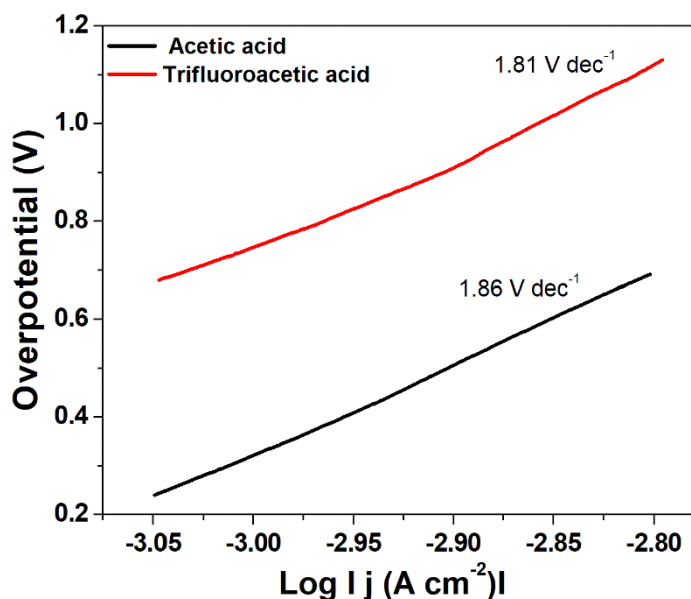


**Figure 5.35:** Tafel plot for hydrogen evolution catalysed by complex 1 using trifluoroacetic acid (Red line) and acetic acid (Black line) as the acid source.

A low  $\eta$  value corresponds to a large exchange current density ( $i_0$ , current density at  $\eta = 0$ ), whereas, a low  $b$  value indicates better hydrogen evolution and hence a better catalytic activity.<sup>5.40</sup> In the present case, the determined Tafel slopes for complex 5.1 are 1.81 V dec<sup>-1</sup> and 1.86 V dec<sup>-1</sup> for the acid sources trifluoroacetic acid and acetic acid, respectively indicating trifluoroacetic acid will lead to a faster increase of reaction rate (fast proton discharge kinetics on working electrode) with increasing potential.

### 5.3.2.3.5 Electrocatalytic Hydrogen Evolution: Control Experiments

To confirm the role of these three nickel complexes in HER and to ascertain the hydrogen evolution not due to complex adsorbed on the surface or degradation products of the complex, different control experiments have been done. First, blank CVs have been recorded with  $\text{CH}_3\text{COOH}$  or  $\text{CF}_3\text{COOH}$  and without the addition of these complexes showing lower measurable current at potentials associated with hydrogen evolution (**Figure 5.36** and **5.37**).

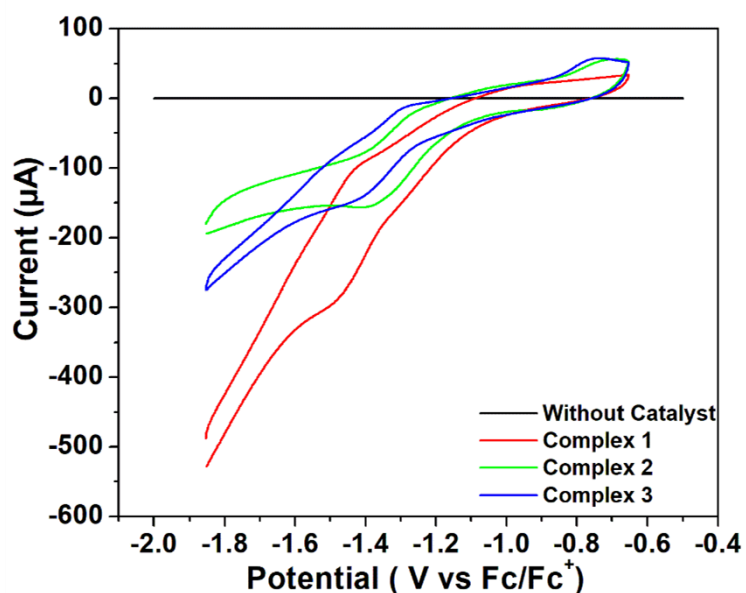


**Figure 5.36:** CVs showing blank DMF with 24 mM  $\text{CH}_3\text{COOH}$  added (black) and with 24 mM  $\text{CH}_3\text{COOH}$  in the presence of 5.36  $\mu\text{M}$  complex **5.1** (red), complex **5.2** (green), complex **5.3** (blue). Conditions: room temperature, 0.1 M  $[\text{n-Bu}_4\text{N}]\text{Br}$  as supporting electrolyte, scan rate = 50 mV/s, glassy carbon working electrode, Pt wire counter electrode and the potential is referenced against  $\text{Fc}/\text{Fc}^+$ .

A series of CVs were obtained with complexes **5.1**, **5.2** and **5.3** in DMF with acid as the substrate to confirm HER activity. Then, the glassy carbon working electrode was withdrawn from the solution and washed thoroughly with the deionized water but it was not polished. It is pertinent to mention that upon immersion of this electrode into a fresh set of acid solution and electrolyte, no catalytic current was observed on sweeping the potential in the cathodic region. This fact shows HER activity is not because of a film of catalyst compound and also not because of its degraded product which could be strongly adsorbed on electrode surface.

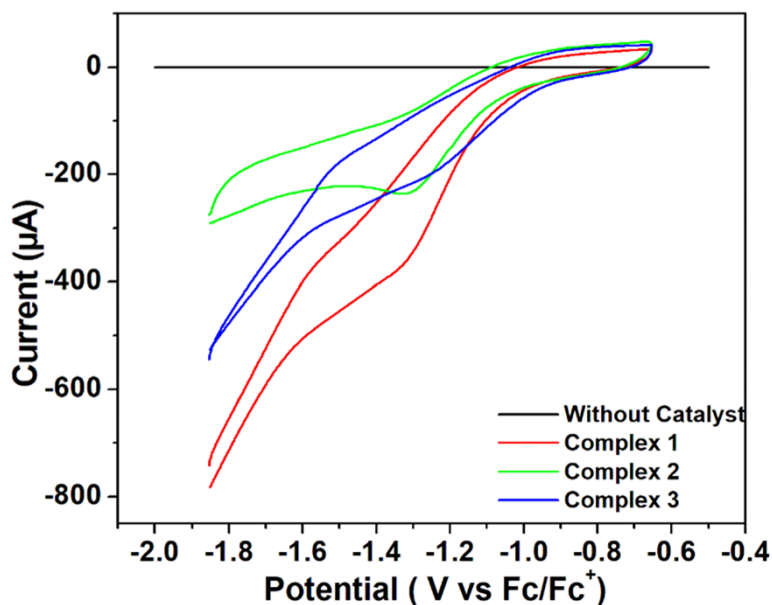


**Figure 5.37:** CVs showing blank DMF with 24 mM  $\text{CF}_3\text{COOH}$  added (black) and with 24 mM  $\text{CH}_3\text{COOH}$  in the presence of 5.36  $\mu\text{M}$  complex **5.1** (red), complex **5.2** (green), complex **5.3** (blue). Conditions: room temperature, 0.1 M  $[\text{n-Bu}_4\text{N}]\text{Br}$  as supporting electrolyte, scan rate = 50 mV/s, glassy carbon working electrode, Pt wire counter electrode and the potential is referenced against  $\text{Fc}/\text{Fc}^+$ .

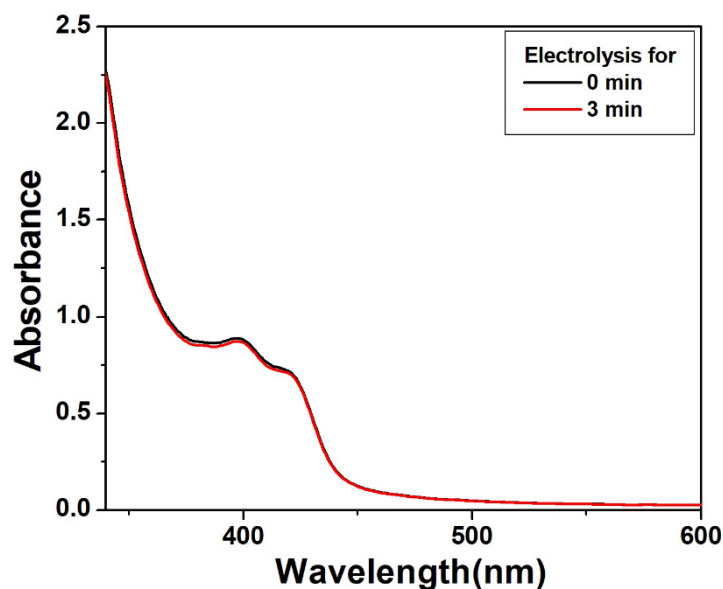


**Figure 5.38:** UV-Vis spectra of complex **5.1** in DMF during electrolysis under  $-1.50$  V versus  $\text{Fc}/\text{Fc}^+$ .

As shown in **Figure 5.38**, the electrolysis did not show appearance of any new bands. These results indicate that complex **5.1** is stable during electrocatalysis for the hydrogen production.



### 5.3.2.4 Computational analysis of catalysts and intermediates by DFT-D4

All the complexes were initially optimized by DFT-D4 analysis with def2-TZVP for metal center and def2-SVP for other atoms with solvent model COSMO (water) and B3LYP.<sup>5,41</sup> The comparison of the bond length between the geometry optimized structure and X-ray analysis data has been tabulated in supporting information (**Table 5.9**). Theoretically calculated UV-vis spectra of complexes **5.1** and **5.2** are given in Figure 5.39.

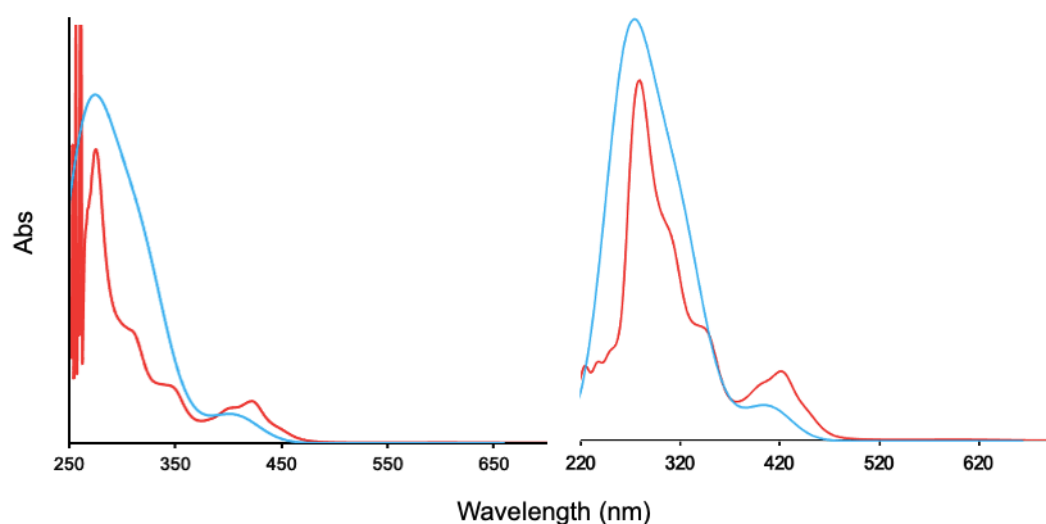


**Figure 5.39:** TDDFTUV-Vis spectra of (A) complex 5.1 and (B) complex 5.2 (blue: calculated and red: experimental).

**Table 5.9:** Bond length comparison of complex **5.1**, **5.2** and **5.3** as obtained from X-ray analysis with DFT calculation.

Bond	X-ray	DFT
<b>Complex 5.1</b>		
Ni01-O002	1.83	1.85
Ni01-N004	1.91	1.92
Ni01-O002	1.83	1.85
Ni01-N004	1.91	1.92
<b>Complex 5.2</b>		
Ni01-O003	1.82	1.85
Ni01-N1	1.92	1.92
Ni01-O003	1.82	1.85
Ni01-N1	1.92	1.92

## Complex 5.3

Ni01-O005	1.83	1.85
Ni01-N004	1.92	1.92
Ni01-O005	1.83	1.85
Ni01-N004	1.92	1.92

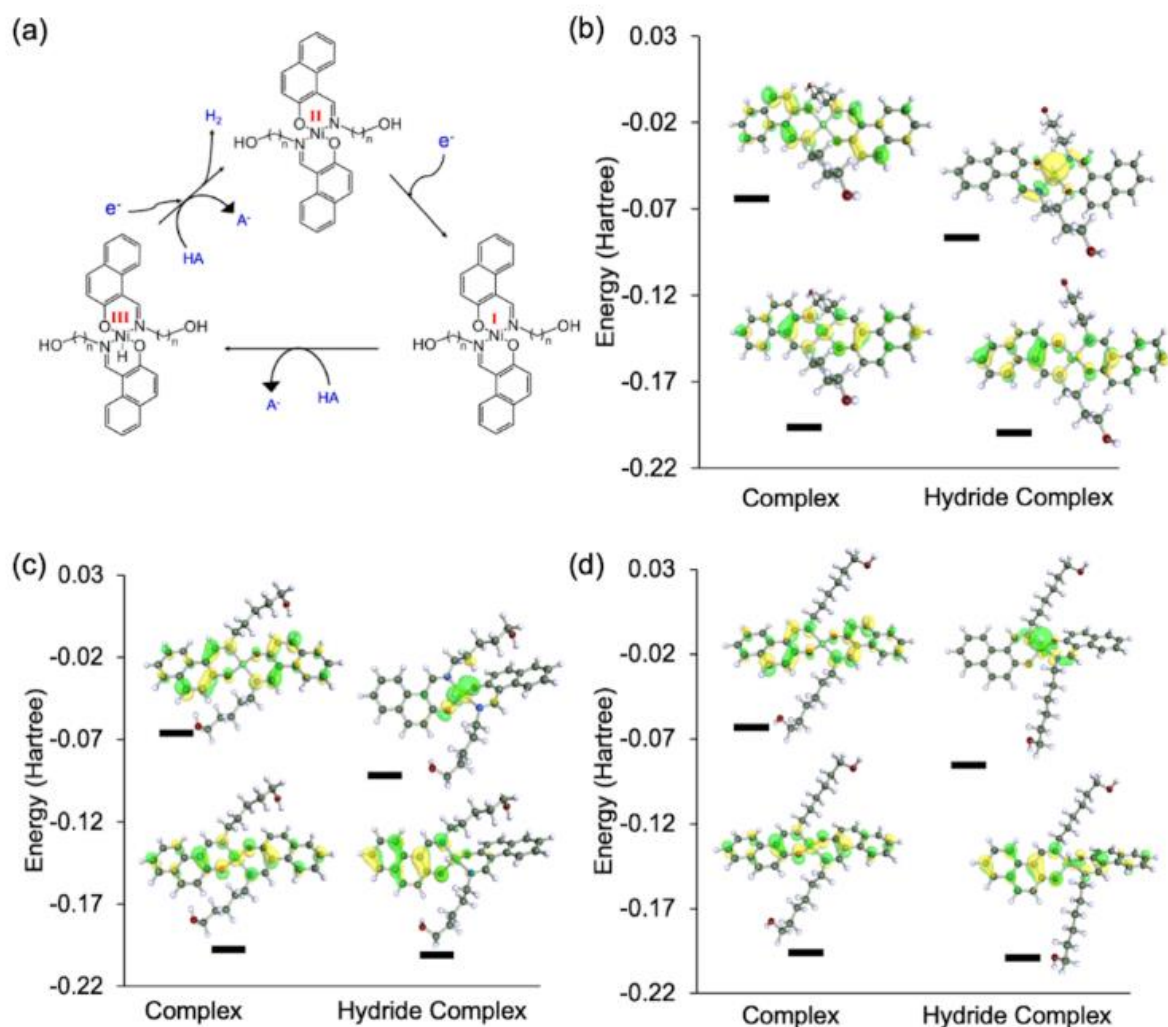


**Figure 5.40:** (a) Plausible mechanistic pathway of HER by complexes 5.1, 5.2 and 5.3 ( $n = 4, 5$  and  $6$ ); (b-d) HOMO-LUMO electronic distribution for complexes 5.1, 5.2 and 5.3 and their hydride complex derivative.

Mechanistic pathways are reportedly known in literature, based on different reports we propose the plausible mechanism as depicted in Figure 5.40a. The pristine catalyst with Ni(II) center reduced first to Ni(I), which then undergoes an oxidative protonation to form a hydride complex  $\{Ni(III)-H\}$  (Table 5.10-5.21). As per the report of Cao et al.,<sup>5.42</sup> this Ni(III)-H hydride complex either reacts with a proton to produce  $H_2$  and Ni(III) complex (heterolytic route), or

is further reduced to Ni(II)-H. This Ni(II)-H can react with a proton to give Ni(II) and H<sub>2</sub>, or react with another Ni(II)-H to produce H<sub>2</sub> and 2 molecules of Ni(I) complex. Another way is Ni(III)-H went through bimolecular hydrolysis to produce H<sub>2</sub> and original starting Ni(II) complex. This concludes that once the hydride complex formed, can liberate hydrogen and by simultaneous reduction gets back to the initial catalyst to continue the cycle.<sup>5.42,5.43</sup> This suggests the key intermediate is Ni(III)-H complexes in a mechanistic cycle of HER. In this work, we wanted to model those complexes and to understand about their geometries, which in one hand helps to understand the present outcome and on the other hand can suggest altered geometries for future development. Therefore, we took aid of DFT calculation that helps to understand an interesting trend in dipole moment (Table 5.21), where the highest value has been obtained for complex 5.1. Indeed, we hypothesize one reason of showing better catalytic activity for complex 5.1 can be associated with higher dipole moment that possibly helps in forming the hydride complex leading to catalysis.<sup>5.42,5.43,5.44</sup> To understand the geometry of the hydride intermediates, it was calculated at the level of B3LYP+ COSMO(H<sub>2</sub>O) +def2TZVP(Ni)+ def2-SVP(C,H,N,O) which reveals a distorted penta-coordination network for the Ni(III) centre in the complexes. Metal centres of catalysts (Complexes 5.1, 5.2 and 5.3) comprises the HOMO density whereas for hydride complexes the metal centres in LUMO comprises the density as obtained from the examined frontier molecular orbitals (Figure 5.40b-d). Thus, from DFT calculation, we understood shorter aliphatic substitution gives higher dipole moment that could have an influence in higher catalytic activity. Another aspect that originates from DFT calculation regarding future development, is to keep an aromatic group at the end of the aliphatic chain for aromatic interaction with adjacent aromatic group for complex 5.2. As we observed for complex 5.2 and its hydride derivative, the aliphatic group is finally inclined towards the aromatic groups. However, for complex 5.1 and 5.3 such observation was not seen. This possibly suggests an optimum chain length for inclination, here substitution with an aromatic group could give higher stability of the complex, eventually better catalytic activity.

**Table 5.10:** Geometry optimized coordinates of complex 5.1.

total energy = -3079.28092039001 Hartree

69

Ni	-0.1812	2.49708	11.9076	O	-0.175	0.97759	12.9577
O	5.81704	5.20315	8.50062	N	1.56833	2.46454	12.0849
C	3.48824	3.23931	10.7134	C	1.96554	2.04938	13.2543
C	2.05075	0.65895	15.3227	C	4.0978	4.42914	9.97133

C	1.56124	0.87998	13.9719	C	0.75976	-0.113	13.3319
C	1.77205	-0.5859	15.9719	C	2.24853	3.63734	11.52
C	0.52039	-1.3557	14.0211	C	1.00433	-1.576	15.2786
C	2.79371	1.62125	16.0586	C	2.24591	-0.83	17.2846
C	2.98014	0.12358	17.9676	C	5.31819	4.04255	9.14873
C	3.24921	1.35953	17.3418	O	0.84157	2.33004	9.34968
O	-4.9849	-0.2536	15.2039	N	-1.5033	1.12402	10.2526
C	-2.9085	0.9695	12.3116	C	-1.8969	1.49635	9.06739
C	-1.8713	2.65858	6.86241	C	-3.745	0.02824	13.1797
C	-1.1955	2.27385	8.09155	C	0.18315	2.59806	8.27876
C	-1.1256	3.30885	5.82724	C	-2.3964	0.2759	11.0473
C	0.89193	3.244	7.20116	C	0.26556	3.57863	6.03564
C	-3.2544	2.43743	6.61956	C	-1.7577	3.68504	4.61648
C	-3.1035	3.44008	4.40685	C	-4.233	0.69259	14.4588
C	-3.8516	2.81267	5.42565	H	6.59306	4.94929	7.97447
H	3.19285	2.46343	9.99092	H	4.23537	2.79312	11.3957
H	2.74103	2.66439	13.7267	H	3.34429	4.87222	9.29383
H	4.38922	5.22209	10.6844	H	2.53195	4.32349	12.3374
H	1.54007	4.15885	10.8645	H	-0.0745	-2.1069	13.497
H	0.80109	-2.5236	15.786	H	3.00831	2.59986	15.6288
H	2.01687	-1.7922	17.7515	H	3.34132	0.07244	-18.98
H	6.08873	3.59634	9.81062	H	5.03548	3.26578	8.40879
H	3.81761	2.12653	17.8748	H	-5.2973	0.17681	16.0167
H	-2.0473	1.33643	12.8947	H	-3.5023	1.85621	12.0241
H	-2.8847	1.12733	8.77077	H	-3.1453	-0.8596	13.4533
H	-4.6216	-0.3405	12.6159	H	-3.2491	-0.0354	10.4192
H	-1.8339	-0.6236	11.3359	H	1.95035	3.45926	7.36465
H	0.82395	4.07306	5.2353	H	-3.8834	1.97679	7.38175
H	-1.1575	4.17809	3.8466	H	-3.5838	3.73394	3.47032
H	-4.8497	1.57962	14.207	H	-3.3627	1.0559	15.0435
H	-4.9187	2.62442	5.27911	H	-0.6476	2.82743	11.5658

**Table 5.11:** geometry optimized coordinates of complex **5.2**.

total energy = -3157.79871580081 Hartree

75

Ni	0.81658	8.86776	8.40531	O	-0.6262	8.06544	7.5644
O	3.95755	14.4013	9.69221	H	3.37502	13.9255	10.3085
N	1.5672	9.35221	6.70242	C	0.32014	7.70431	5.39508
C	-0.6478	7.48331	6.40592	C	1.7847	11.7956	7.05894
H	1.1844	11.5898	7.96037	H	1.07353	12.1068	6.27222
C	1.28828	8.74439	5.58923	H	1.81967	9.09657	4.69744

C	0.24614	6.98541	4.14023	C	2.77613	12.9175	7.37611
H	3.56187	12.5179	8.03822	H	3.28761	13.2548	6.45509
C	2.48171	10.4963	6.6411	H	2.88828	10.5861	5.61935
H	3.31457	10.3018	7.32901	C	-1.7475	6.59792	6.12849
H	-2.5073	6.4785	6.90193	C	2.12846	14.1153	8.07886
H	1.49832	14.6911	7.37658	H	1.44678	13.7484	8.87198
C	-0.8485	6.09155	3.91247	C	3.14222	15.0571	8.72603
H	3.83714	15.4583	7.96842	H	2.61332	15.9191	9.18001
C	-1.8377	5.93611	4.93417	H	-2.6831	5.2686	4.74234
C	1.21685	7.10738	3.10983	H	2.08611	7.75155	3.24733
C	-0.945	5.37995	2.69031	H	-1.7931	4.70522	2.5434
C	0.01044	5.53092	1.70137	H	-0.0704	4.97898	0.7617
C	1.09955	6.40295	1.92206	H	1.86569	6.52083	1.15097
O	2.26079	9.66691	9.24715	O	-2.3276	3.34285	7.12199
H	-1.7426	3.8179	6.50742	N	0.064	8.38707	10.1087
C	1.3077396	10.0411	11.4112	C	2.28008	10.2545	10.4029
C	-0.1548	5.94269	9.75815	H	0.4463	6.14635	8.85679
H	0.55527	5.63227	10.5461	C	0.33933	9.00075	11.2195
H	-0.1946	8.65326	12.1117	C	1.37785	10.7672	12.662
C	-1.1474	4.82148	9.442	H	-1.9329	5.22158	8.77985
H	-1.6591	4.48532	10.3633	C	-0.851	7.24354	10.1726
H	-1.2581	7.15666	11.1945	H	-1.6835	7.43667	9.48389
C	3.38179	11.1372	10.6808	H	4.14543	11.2497	9.91012
C	-0.5014	3.62254	8.73964	H	0.12584	3.04447	9.44268
H	0.18288	3.98827	7.94817	C	2.47431	11.6589	12.8898
C	-1.5164	2.68404	8.08951	H	-2.2143	2.28443	8.84519
H	-0.989	1.82081	7.63621	C	3.46894	11.805	11.872
H	4.31608	12.4701	12.0644	C	0.40143	10.6547	13.688
H	-0.4693	10.0126	13.5498	C	2.5669	12.3775	14.1081
H	3.41657	13.0503	14.2554	C	1.60583	12.2359	15.093
H	1.68362	12.7934	16.0296	C	0.51485	11.3662	14.8719
H	-0.2558	11.2559	15.6397				

**Table 5.12:** geometry optimized coordinates of complex **5.2**-hydride.

total energy = -3158.33873725985 Hartree

76

Ni	0.75322	8.82676	8.09104	O	0.67918	6.97236	7.38204
O	3.59636	14.0832	10.5173	N	1.47017	9.48059	6.44912
C	0.73879	7.6104	5.05716	C	0.45968	6.71304	6.13712
C	1.43622	11.7148	7.49925	C	1.35371	8.88568	5.30422
C	0.46993	7.20481	3.68831	C	2.31076	12.8095	8.11267

C	2.19925	10.7399	6.5931	C	-0.0761	5.41112	5.82322
C	1.57234	13.6027	9.19517	C	-0.0508	5.896	3.4304
C	2.44044	14.6407	9.90408	C	-0.314	5.02572	4.53522
C	0.68195	8.04789	2.56258	C	-0.3141	5.47747	2.10244
C	-0.0782	6.31731	1.02858	C	0.42252	7.61463	1.27149
O	2.51692	8.93575	8.99331	O	-1.8628	2.83885	7.71557
N	-0.1051	8.60426	9.79244	C	1.56613	9.96646	10.9455
C	2.64428	9.64409	10.0651	C	-0.7172	6.23888	10.1341
C	0.32921	9.24147	10.837	C	1.77215	10.8874	12.0404
C	-1.7222	5.17539	9.69078	C	-1.2264	7.67379	9.92146
C	3.96086	10.1237	10.4033	C	-1.2066	3.74842	9.90657
C	3.08693	11.3901	12.3	C	-1.9902	2.69308	9.12829
C	4.16805	10.9559	11.4661	C	0.71467	11.3593	12.8625
C	3.29953	12.3108	13.358	C	2.24795	12.7451	14.147
C	0.94691	12.261	13.8899	H	3.31335	13.3982	11.1467
H	0.98543	11.1442	8.33525	H	0.585	12.151	6.94812
H	1.79338	9.4095	4.4465	H	3.20603	12.3495	8.56448
H	2.67194	13.4958	7.32376	H	2.39326	11.18	5.59968
H	3.17182	10.5062	7.05757	H	-0.3037	4.75128	6.66223
H	0.6954	14.1184	8.76202	H	1.17492	12.8981	9.95113
H	2.81385	15.3837	9.17858	H	1.82747	15.1883	10.6483
H	-0.728	4.0342	4.32912	H	1.04513	9.06723	2.69583
H	-0.712	4.47129	1.94279	H	-0.2831	5.98706	0.00728
H	0.60251	8.29364	0.43351	H	-0.9451	2.63198	7.4722
H	0.1991	6.11339	9.53854	H	-0.4432	6.1028	11.1968
H	-0.2843	9.16326	11.7459	H	-1.9316	5.32116	8.61623
H	-2.6858	5.30353	10.2201	H	-1.8769	7.98719	10.7574
H	-1.8123	7.72353	8.99267	H	4.78181	9.81545	9.7526
H	-1.2298	3.49206	10.9819	H	-0.1446	3.68523	9.5978
H	-3.0688	2.78438	9.34279	H	-1.6749	1.67915	9.4422
H	5.17387	11.3273	11.6813	H	-0.31	11.0356	12.6731
H	4.31368	12.6789	13.5365	H	2.42008	13.4589	14.9559
H	0.10829	12.6085	14.4991	H	-0.5539	9.12658	7.5208

**Table 5.13:** geometry optimized coordinates of complex **5.3**.

total energy = -3236.30986835935 Hartree

81

Ni	2.95928	9.31574	8.51538	O	1.3248	9.13269	7.67542
N	2.7242	11.2208	8.6361	O	3.98473	10.8407	16.2813
H	3.65631	10.6395	17.1731	C	1.90307	11.8979	7.88913
H	1.89608	12.9834	8.04085	C	-1.0287	10.3171	5.23754

H	-1.8094	9.91315	4.58668	C	-0.7598	11.7217	5.18624
C	3.43479	11.9236	13.5726	H	2.38373	12.2392	13.7197
H	3.45138	10.8276	13.7058	C	4.30951	12.5697	14.6508
H	5.35969	12.2469	14.5198	H	4.29915	13.6691	14.534
C	3.87486	12.2425	16.0724	H	4.51086	12.7972	16.7918
H	2.8298	12.5814	16.2287	C	0.50388	13.6621	5.94697
H	1.28424	14.1224	6.55369	C	3.01142	11.6105	11.0723
H	1.9542	11.9096	11.1969	H	3.04924	10.5152	11.1959
C	0.98032	11.3786	6.92429	C	3.46854	11.9687	9.65538
H	3.33172	13.0501	9.48226	H	4.53453	11.7337	9.54578
C	0.70779	9.98796	6.92225	C	3.87507	12.2728	12.1483
H	3.85571	13.3715	12.0162	H	4.92825	11.9644	12.0071
C	0.25622	12.2655	6.03611	C	-0.3328	9.48353	6.06811
H	-0.5384	8.41199	6.10344	C	-1.4829	12.5682	4.3088
H	-2.2529	12.1241	3.67156	C	-0.2196	14.4701	5.08381
H	-0.002	15.5409	5.04276	C	-1.2252	13.9264	4.2543
H	-1.7876	14.5721	3.57529	O	4.59529	9.49687	9.35361
N	3.19366	7.4101	8.3967	O	1.96439	7.80218	0.74771
H	2.29173	8.00483	-0.1441	C	4.00774	6.73338	9.1514
H	4.01454	5.64741	9.00233	C	6.92833	8.31628	11.8135
H	7.70714	8.72049	12.4664	C	6.65157	6.91358	11.8725
C	2.50496	6.7142	3.4561	H	3.55651	6.39847	3.31275
H	2.48928	7.81045	3.32426	C	1.63435	6.0698	2.37349
H	0.58358	6.39201	2.50143	H	1.6447	4.97023	2.48833
C	2.07379	6.39996	0.95405	H	1.44022	5.84674	0.23142
H	3.11943	6.06152	0.80055	C	5.3819	4.97499	11.1167
H	4.60245	4.51533	10.5083	C	2.91803	7.02373	5.95869
H	3.97592	6.72566	5.8374	H	2.87978	8.11929	5.83729
C	4.92448	7.25431	10.1213	C	2.45559	6.66223	7.37299
H	2.59377	5.58087	7.54504	H	1.3886	6.89499	7.47814
C	5.20364	8.64359	10.1163	C	2.05881	6.36318	4.87811
H	2.07749	5.26422	5.00866	H	1.0051	6.67156	5.01547
C	5.63803	6.36962	11.0198	C	6.24199	9.14805	10.9731
H	6.45364	10.2182	10.9319	C	7.36447	6.06889	12.7601
H	8.13276	6.51301	13.3993	C	6.0955	4.16881	11.9896
H	5.87164	3.09958	12.0366	C	7.09893	4.71254	12.8218
H	7.65348	4.06832	13.5086				

**Table 5.14:** geometry optimized coordinates of complex **5.3**-hydride.

total energy = -3236.84578928266 Hartree

Ni	3.062261	9.716201	8.387695	C	7.206121	4.759248	12.40189
O	2.367919	9.819575	6.525832	H	3.492779	9.85499	17.05049
N	2.767368	11.59547	8.635995	H	1.881565	13.36745	8.210137
O	3.8169	10.23684	16.21834	H	-0.28156	11.14275	3.179288
C	1.991089	12.32581	7.887327	H	2.094077	11.79381	13.79314
C	0.158471	11.36317	4.156379	H	3.329418	10.53318	13.65838
C	-0.18841	12.59694	4.795592	H	5.009542	12.06913	14.75241
C	3.181683	11.62769	13.66929	H	3.753555	13.31127	14.91695
C	3.919921	12.21909	14.87381	H	4.015691	12.15036	17.03305
C	3.496117	11.62195	16.2081	H	2.406795	11.77397	16.35482
C	-0.01207	14.12696	6.679114	H	0.363	14.4017	7.665157
C	2.895189	11.63159	11.13012	H	1.809508	11.81744	11.22369
C	1.307911	11.96206	6.682756	H	3.031537	10.53654	11.11837
C	3.394312	12.21503	9.806234	H	3.20509	13.30237	9.780786
C	1.594697	10.72143	6.034728	H	4.478969	12.05209	9.729603
C	3.637821	12.21854	12.33271	H	3.504834	13.31725	12.35151
C	0.382507	12.90319	6.072764	H	4.722999	12.04087	12.20785
C	1.005847	10.46781	4.742311	H	1.262443	9.522063	4.259261
C	-1.08903	13.49941	4.177788	H	-1.50541	13.23364	3.201975
C	-0.89341	14.99623	6.054301	H	-1.17129	15.92767	6.555244
C	-1.44042	14.68963	4.790036	H	-2.13649	15.38011	4.307467
O	4.857251	9.807651	9.20478	H	2.673889	5.712443	0.029908
N	3.131214	7.805439	8.375819	H	3.783121	6.007021	9.046792
O	2.279006	5.97517	0.877514	H	8.236702	8.657655	11.89585
C	3.940831	7.090843	9.104306	H	3.108901	5.035206	3.971593
C	7.340066	8.350417	11.34965	H	2.744811	6.660168	3.371733
C	6.906561	6.990777	11.4657	H	0.421497	5.91579	2.748261
C	2.290621	5.769261	3.840489	H	0.787603	4.283816	3.340268
C	1.240978	5.186096	2.890066	H	0.993198	4.328859	0.920503
C	1.792271	4.805999	1.523451	H	2.603269	4.058392	1.645111
C	5.332346	5.217317	10.91775	H	4.433713	4.84634	10.42478
C	2.769119	6.730771	6.160202	H	3.597413	6.011466	6.30055
C	5.025908	7.530313	9.927379	H	3.195291	7.645927	5.720635
C	2.174035	7.083657	7.526493	H	1.848545	6.164752	8.045927
C	5.464512	8.887431	9.872303	H	1.295187	7.725176	7.385568
C	1.721708	6.14445	5.211332	H	1.258452	5.251448	5.673396
C	5.736733	6.570131	10.75553	H	0.905801	6.880374	5.078087
C	6.6576	9.256951	10.59016	H	6.982485	10.29652	10.50997
C	7.620538	6.073411	12.27596	H	8.510155	6.427328	12.80451
C	6.048532	4.336606	11.71394	H	5.704432	3.303474	11.8125

**Table 5.15:** Summary of Natural Population Analysis for complex 5.1.



## Natural Population

Natural -----

Atom No	Charge	Core	Valence	Rydberg	Total
1 ni	0.96584	17.9956	9.0016	0.03699	27.0342
2 o	-0.7376	1.99971	6.72504	0.01282	8.73757
3 o	-0.7742	1.99978	6.76384	0.01057	8.77419
4 h	0.46969	0	0.52874	0.00157	0.53031
5 n	-0.556	1.9992	5.53384	0.02297	7.55602
6 c	-0.4232	1.99912	4.40941	0.01468	6.42321
7 h	0.21476	0	0.78132	0.00393	0.78524
8 h	0.21218	0	0.78463	0.00319	0.78782
9 c	0.17229	1.99906	3.80414	0.02451	5.82771
10 h	0.20359	0	0.79414	0.00227	0.79641
11 c	-0.0262	1.99888	4.01154	0.01573	6.02615
12 c	-0.4365	1.99914	4.4227	0.01463	6.43647
13 h	0.2074	0	0.78829	0.00431	0.7926
14 h	0.21062	0	0.78526	0.00412	0.78938
15 c	-0.2165	1.99882	4.20069	0.01701	6.21652
16 c	0.43659	1.99877	3.53154	0.03311	5.56341
17 c	-0.0975	1.99884	4.08294	0.01571	6.0975
18 c	-0.1935	1.99911	4.17537	0.01906	6.19353
19 h	0.2044	0	0.79308	0.00252	0.7956
20 h	0.22958	0	0.76666	0.00376	0.77042
21 c	-0.2654	1.9989	4.24854	0.01794	6.26538
22 h	0.2316	0	0.76606	0.00234	0.7684
23 c	-0.1582	1.99893	4.14273	0.01653	6.15819
24 h	0.23213	0	0.7659	0.00197	0.76787
25 c	-0.223	1.99894	4.2085	0.01559	6.22303
26 h	0.22399	0	0.77396	0.00205	0.77601
27 c	-0.1876	1.99893	4.17194	0.01673	6.1876
28 h	0.22761	0	0.77048	0.00191	0.77239
29 c	-0.2414	1.99894	4.22584	0.01662	6.24139
30 h	0.2291	0	0.76923	0.00167	0.7709
31 c	-0.0163	1.99914	3.99987	0.01733	6.01634
32 h	0.17156	0	0.82568	0.00276	0.82844
33 h	0.17131	0	0.82585	0.00284	0.82869
34 c	-0.2072	1.99895	4.19169	0.01651	6.20715
35 h	0.22884	0	0.76945	0.00171	0.77116
36 o	-0.7376	1.99971	6.72507	0.0128	8.73757
37 o	-0.7742	1.99978	6.76388	0.01057	8.77422
38 h	0.46972	0	0.52872	0.00157	0.53028
39 n	-0.5558	1.9992	5.53361	0.02297	7.55578
40 c	-0.4232	1.99912	4.4094	0.01467	6.42319

41 h	0.2148	0	0.78126	0.00393	0.7852
42 h	0.21213	0	0.78467	0.0032	0.78787
43 c	0.1724	1.99906	3.80404	0.0245	5.8276
44 h	0.20365	0	0.79408	0.00227	0.79635
45 c	-0.0262	1.99888	4.01156	0.01573	6.02617
46 c	-0.4365	1.99914	4.42271	0.01464	6.43648
47 h	0.20741	0	0.78826	0.00432	0.79259
48 h	0.21059	0	0.78529	0.00412	0.78941
49 c	-0.2164	1.99882	4.2006	0.01702	6.21643
50 c	0.43627	1.99877	3.53185	0.03312	5.56373
51 c	-0.0975	1.99884	4.08291	0.01571	6.09746
52 c	-0.1935	1.99911	4.17532	0.01905	6.19348
53 h	0.20442	0	0.79306	0.00252	0.79558
54 h	0.22947	0	0.76676	0.00377	0.77053
55 c	-0.2655	1.9989	4.24867	0.01796	6.26553
56 h	0.23157	0	0.76608	0.00234	0.76843
57 c	-0.1581	1.99893	4.14259	0.01653	6.15805
58 h	0.23213	0	0.7659	0.00197	0.76787
59 c	-0.2231	1.99894	4.20851	0.01559	6.22305
60 h	0.22401	0	0.77394	0.00205	0.77599
61 c	-0.1876	1.99893	4.17194	0.01673	6.18759
62 h	0.22762	0	0.77047	0.00191	0.77238
63 c	-0.2414	1.99894	4.22585	0.01662	6.2414
64 h	0.2291	0	0.76923	0.00167	0.7709
65 c	-0.0163	1.99914	3.99987	0.01732	6.01634
66 h	0.17165	0	0.82559	0.00276	0.82835
67 h	0.17123	0	0.82593	0.00284	0.82877
68 c	-0.2072	1.99895	4.19169	0.01651	6.20715
69 h	0.22884	0	0.76945	0.00171	0.77116

\* Total \*      -0.00000    89.96186    195.27925    0.75889    286.0000

**Table 5.16:** Summary of Natural Population Analysis for complex **5.1**-hydride.  
Natural Population

Natural -----

Atom No	Charge	Core	Valence	Rydberg	Total
1 ni	1.06646	17.99438	8.89038	0.04878	26.93354
2 o	-0.79076	1.99973	6.77573	0.0153	8.79076
3 o	-0.77423	1.99978	6.76388	0.01057	8.77423
4 n	-0.55579	1.9992	5.53234	0.02425	7.55579
5 c	-0.42315	1.99912	4.41023	0.01381	6.42315
6 c	0.17486	1.99905	3.80108	0.025	5.82514
7 c	-0.02562	1.99888	4.01094	0.0158	6.02562

8 c	-0.43823	1.99914	4.42428	0.01481	6.43823
9 c	-0.21373	1.99882	4.19794	0.01697	6.21373
10 c	0.45208	1.99881	3.51381	0.0353	5.54792
11 c	-0.0968	1.99884	4.08219	0.01577	6.0968
12 c	-0.19477	1.99912	4.17623	0.01943	6.19477
13 c	-0.26835	1.9989	4.25146	0.01799	6.26835
14 c	-0.15674	1.99893	4.14127	0.01654	6.15674
15 c	-0.22222	1.99894	4.20774	0.01554	6.22222
16 c	-0.18785	1.99893	4.17215	0.01677	6.18785
17 c	-0.23999	1.99894	4.22442	0.01664	6.23999
18 c	-0.01631	1.99914	3.99993	0.01724	6.01631
19 c	-0.20652	1.99895	4.19106	0.01651	6.20652
20 o	-0.77833	1.99973	6.76343	0.01517	8.77833
21 o	-0.77422	1.99978	6.76387	0.01057	8.77422
22 n	-0.5515	1.99919	5.5285	0.0238	7.5515
23 c	-0.42467	1.99912	4.4113	0.01426	6.42467
24 c	0.17825	1.99905	3.79795	0.02474	5.82175
25 c	-0.0255	1.99889	4.01085	0.01577	6.0255
26 c	-0.43701	1.99914	4.42318	0.01468	6.43701
27 c	-0.21992	1.99883	4.20408	0.01701	6.21992
28 c	0.45323	1.99882	3.51258	0.03537	5.54677
29 c	-0.09852	1.99884	4.08392	0.01576	6.09852
30 c	-0.19473	1.99911	4.17628	0.01935	6.19473
31 c	-0.26894	1.9989	4.25196	0.01808	6.26894
32 c	-0.15822	1.99893	4.14276	0.01654	6.15822
33 c	-0.2237	1.99894	4.20927	0.01549	6.2237
34 c	-0.18784	1.99893	4.17216	0.01676	6.18784
35 c	-0.24152	1.99894	4.22593	0.01666	6.24152
36 c	-0.01667	1.99915	4.00022	0.0173	6.01667
37 c	-0.20696	1.99895	4.19149	0.01651	6.20696
38 h	0.46969	0	0.52874	0.00157	0.53031
39 h	0.22531	0	0.77027	0.00442	0.77469
40 h	0.2086	0	0.78863	0.00276	0.7914
41 h	0.20323	0	0.79435	0.00242	0.79677
42 h	0.20769	0	0.78778	0.00453	0.79231
43 h	0.20983	0	0.78601	0.00416	0.79017
44 h	0.20882	0	0.78858	0.0026	0.79118
45 h	0.2276	0	0.76956	0.00284	0.7724
46 h	0.23237	0	0.76504	0.00259	0.76763
47 h	0.23178	0	0.7662	0.00202	0.76822
48 h	0.22306	0	0.77482	0.00212	0.77694
49 h	0.22777	0	0.77032	0.00191	0.77223
50 h	0.22924	0	0.7691	0.00166	0.77076
51 h	0.17179	0	0.82547	0.00274	0.82821

52 h	0.17092	0	0.82636	0.00272	0.82908
53 h	0.22894	0	0.76935	0.00171	0.77106
54 h	0.47003	0	0.52841	0.00156	0.52997
55 h	0.21648	0	0.78016	0.00336	0.78352
56 h	0.21358	0	0.78326	0.00317	0.78642
57 h	0.20263	0	0.79503	0.00233	0.79737
58 h	0.20933	0	0.78633	0.00434	0.79067
59 h	0.21082	0	0.78509	0.0041	0.78918
60 h	0.20868	0	0.78879	0.00253	0.79132
61 h	0.23078	0	0.76518	0.00405	0.76922
62 h	0.22832	0	0.769	0.00267	0.77168
63 h	0.2316	0	0.76639	0.00201	0.7684
64 h	0.22283	0	0.77505	0.00212	0.77717
65 h	0.22751	0	0.77057	0.00192	0.77249
66 h	0.22898	0	0.76936	0.00167	0.77102
67 h	0.17227	0	0.82498	0.00275	0.82773
68 h	0.17112	0	0.82611	0.00277	0.82888
69 h	0.22871	0	0.76958	0.00172	0.77129
70 h	-0.05587	0	1.0533	0.00257	1.05587

**Table 5.17:** Summary of Natural Population Analysis for complex 5.2.

Natural Population

Natural -----

Atom No	Charge	Core	Valence	Rydberg	Total
1 ni	0.96856	17.99558	8.99989	0.03596	27.03144
2 o	-0.73833	1.99971	6.7259	0.01272	8.73833
3 o	-0.77415	1.99979	6.76364	0.01073	8.77415
4 h	0.45912	0	0.53889	0.00199	0.54088
5 n	-0.55235	1.9992	5.53011	0.02303	7.55235
6 c	-0.21323	1.99882	4.19739	0.01702	6.21323
7 c	0.43505	1.99876	3.53299	0.0332	5.56495
8 c	-0.41799	1.99912	4.40419	0.01468	6.41799
9 h	0.21096	0	0.78528	0.00376	0.78904
10 h	0.21163	0	0.78531	0.00306	0.78837
11 c	0.17278	1.99906	3.80371	0.02445	5.82722
12 h	0.20504	0	0.79271	0.00225	0.79496
13 c	-0.0255	1.99888	4.01085	0.01577	6.0255
14 c	-0.41996	1.99913	4.40537	0.01546	6.41996
15 h	0.20739	0	0.78753	0.00508	0.79261
16 h	0.2108	0	0.78641	0.00279	0.7892
17 c	-0.19406	1.99911	4.17587	0.01908	6.19406
18 h	0.20533	0	0.79222	0.00245	0.79467

---

19 h	0.22825	0	0.76817	0.00358	0.77175
20 c	-0.26885	1.9989	4.25108	0.01888	6.26885
21 h	0.23541	0	0.762	0.00259	0.76459
22 c	-0.44439	1.99914	4.4329	0.01235	6.44439
23 h	0.22127	0	0.77601	0.00272	0.77873
24 h	0.20283	0	0.79377	0.0034	0.79717
25 c	-0.09556	1.99884	4.08084	0.01589	6.09556
26 c	-0.02363	1.99914	4.00544	0.01904	6.02363
27 h	0.18864	0	0.80896	0.0024	0.81136
28 h	0.17868	0	0.81881	0.00251	0.82132
29 c	-0.18009	1.99892	4.16421	0.01696	6.18009
30 h	0.23414	0	0.76364	0.00222	0.76586
31 c	-0.22215	1.99894	4.20754	0.01567	6.22215
32 h	0.22445	0	0.77352	0.00203	0.77555
33 c	-0.18743	1.99893	4.17178	0.01673	6.18743
34 h	0.2283	0	0.7698	0.00191	0.7717
35 c	-0.23959	1.99894	4.22403	0.01662	6.23959
36 h	0.22948	0	0.76885	0.00167	0.77052
37 c	-0.20597	1.99895	4.19053	0.01649	6.20597
38 h	0.22935	0	0.76895	0.00171	0.77065
39 o	-0.73816	1.99971	6.72574	0.01271	8.73816
40 o	-0.77409	1.99979	6.76358	0.01073	8.77409
41 h	0.45914	0	0.53887	0.002	0.54086
42 n	-0.55233	1.9992	5.5301	0.02303	7.55233
43 c	-0.21316	1.99882	4.19731	0.01703	6.21316
44 c	0.43489	1.99876	3.53313	0.03322	5.56511
45 c	-0.41797	1.99912	4.40418	0.01467	6.41797
46 h	0.21104	0	0.78519	0.00377	0.78896
47 h	0.2116	0	0.78534	0.00306	0.7884
48 c	0.17273	1.99906	3.80377	0.02444	5.82727
49 h	0.20528	0	0.79247	0.00224	0.79472
50 c	-0.0255	1.99888	4.01084	0.01578	6.0255
51 c	-0.41996	1.99913	4.40538	0.01545	6.41996
52 h	0.20731	0	0.78761	0.00508	0.79269
53 h	0.21081	0	0.7864	0.00279	0.78919
54 c	-0.19399	1.99911	4.1758	0.01908	6.19399
55 h	0.20533	0	0.79222	0.00245	0.79467
56 h	0.22811	0	0.76831	0.00358	0.77189
57 c	-0.2686	1.9989	4.25082	0.01889	6.2686
58 h	0.23533	0	0.7621	0.00257	0.76467
59 c	-0.44444	1.99914	4.43295	0.01235	6.44444
60 h	0.22131	0	0.77597	0.00272	0.77869
61 h	0.20286	0	0.79375	0.0034	0.79714
62 c	-0.09554	1.99884	4.08082	0.01589	6.09554

---

63 c	-0.02364	1.99914	4.00546	0.01904	6.02364
64 h	0.18859	0	0.80901	0.0024	0.81141
65 h	0.17868	0	0.8188	0.00251	0.82132
66 c	-0.18041	1.99892	4.1645	0.01698	6.18041
67 h	0.23414	0	0.76365	0.00221	0.76586
68 c	-0.22214	1.99894	4.20753	0.01568	6.22214
69 h	0.22448	0	0.77349	0.00203	0.77552
70 c	-0.18751	1.99893	4.17185	0.01673	6.18751
71 h	0.22828	0	0.76981	0.00191	0.77172
72 c	-0.23957	1.99894	4.22401	0.01662	6.23957
73 h	0.22949	0	0.76884	0.00166	0.77051
74 c	-0.20596	1.99895	4.19051	0.01649	6.20596
75 h	0.22935	0	0.76894	0.00171	0.77065

\* Total \*      0.00000    93.96014    207.23812    0.80174    302.00000

**Table 5.18:** Summary of Natural Population Analysis for complex **2**-hydride.  
Natural Population

Atom No	Charge	Core	Valence	Rydberg	Total
1 ni	1.08871	17.9945	8.86569	0.05113	26.9113
2 o	-0.7509	1.99973	6.73714	0.01401	8.75088
3 o	-0.7798	1.99978	6.76951	0.01055	8.77983
4 n	-0.5459	1.99917	5.52233	0.02436	7.54586
5 c	-0.2244	1.99883	4.20854	0.01707	6.22444
6 c	0.44421	1.99881	3.52138	0.0356	5.55579
7 c	-0.4116	1.99911	4.39796	0.01453	6.4116
8 c	0.18764	1.99904	3.78899	0.02433	5.81236
9 c	-0.0256	1.99888	4.01098	0.01574	6.0256
10 c	-0.418	1.99913	4.40267	0.01618	6.41798
11 c	-0.1974	1.99913	4.17893	0.01936	6.19741
12 c	-0.2675	1.99889	4.25035	0.01826	6.26749
13 c	-0.4429	1.99913	4.43128	0.0125	6.4429
14 c	-0.0988	1.99884	4.08416	0.01577	6.09877
15 c	-0.0258	1.99913	4.00733	0.01936	6.02582
16 c	-0.1596	1.99892	4.14414	0.01653	6.1596
17 c	-0.2249	1.99894	4.21048	0.01551	6.22493
18 c	-0.188	1.99893	4.17237	0.01675	6.18804
19 c	-0.2427	1.99894	4.22712	0.01667	6.24272
20 c	-0.2074	1.99895	4.19191	0.01653	6.20739
21 o	-0.7883	1.99974	6.77422	0.0143	8.78825
22 o	-0.7755	1.99979	6.7649	0.01085	8.77553

---

23 n	-0.5663	1.9992	5.54186	0.02527	7.56633
24 c	-0.2286	1.99879	4.21241	0.01739	6.22859
25 c	0.43775	1.9988	3.5265	0.03695	5.56225
26 c	-0.4213	1.99911	4.40861	0.01353	6.42125
27 c	0.17538	1.99904	3.80075	0.02483	5.82462
28 c	-0.0261	1.99885	4.01088	0.01631	6.02605
29 c	-0.4191	1.99914	4.40457	0.01542	6.41913
30 c	-0.1903	1.99913	4.1714	0.01981	6.19034
31 c	-0.2654	1.99887	4.24809	0.01848	6.26544
32 c	-0.4429	1.99914	4.43086	0.01289	6.44289
33 c	-0.1258	1.99884	4.1101	0.01688	6.12582
34 c	-0.0237	1.99914	4.00565	0.01893	6.02372
35 c	-0.1657	1.99892	4.14928	0.01749	6.16569
36 c	-0.2212	1.99893	4.2065	0.01576	6.22119
37 c	-0.2061	1.99892	4.18932	0.01781	6.20606
38 c	-0.2358	1.99893	4.21993	0.0169	6.23576
39 c	-0.2018	1.99895	4.18635	0.01651	6.20182
40 h	0.46667	0	0.53103	0.0023	0.53333
41 h	0.18823	0	0.80746	0.0043	0.81177
42 h	0.22268	0	0.77422	0.0031	0.77732
43 h	0.20643	0	0.79135	0.00222	0.79357
44 h	0.21195	0	0.78312	0.00493	0.78805
45 h	0.2133	0	0.78389	0.00281	0.7867
46 h	0.21718	0	0.7805	0.00233	0.78282
47 h	0.22551	0	0.77086	0.00364	0.77449
48 h	0.22388	0	0.77087	0.00525	0.77612
49 h	0.22015	0	0.77703	0.00282	0.77985
50 h	0.2031	0	0.79294	0.00397	0.7969
51 h	0.1892	0	0.80845	0.00235	0.8108
52 h	0.17804	0	0.8194	0.00256	0.82196
53 h	0.22991	0	0.76795	0.00213	0.77009
54 h	0.22274	0	0.77516	0.0021	0.77726
55 h	0.22729	0	0.77079	0.00192	0.77271
56 h	0.22873	0	0.7696	0.00167	0.77127
57 h	0.22844	0	0.76984	0.00172	0.77156
58 h	0.46486	0	0.53338	0.00176	0.53514
59 h	0.22858	0	0.76722	0.0042	0.77142
60 h	0.20776	0	0.78942	0.00282	0.79224
61 h	0.21125	0	0.78635	0.0024	0.78875
62 h	0.20971	0	0.78527	0.00501	0.79029
63 h	0.20702	0	0.79014	0.00284	0.79298
64 h	0.21114	0	0.78635	0.00251	0.78886
65 h	0.21925	0	0.77831	0.00244	0.78075
66 h	0.23587	0	0.76147	0.00266	0.76413

---

67 h	0.21817	0	0.77904	0.00278	0.78183
68 h	0.20426	0	0.79218	0.00356	0.79574
69 h	0.18801	0	0.80959	0.00241	0.81199
70 h	0.18133	0	0.81638	0.00229	0.81867
71 h	0.23614	0	0.7618	0.00206	0.76386
72 h	0.22762	0	0.77042	0.00195	0.77238
73 h	0.23399	0	0.76405	0.00196	0.76601
74 h	0.23164	0	0.76671	0.00165	0.76836
75 h	0.23098	0	0.76731	0.0017	0.76902
76 h	-0.0696	0	1.0684	0.00115	1.06955

-----  
 \* Total \*      0.00000    93.95900    208.20372    0.83728    303.00000

**Table 5.19:** Summary of Natural Population Analysis for complex **5.3**.

Natural Population

Natural -----

Atom No	Charge	Core	Valence	Rydberg	Total
1 ni	0.96653	17.9956	9.00081	0.03709	27.0335
2 o	-0.7376	1.99971	6.72507	0.0128	8.73758
3 n	-0.555	1.99921	5.53276	0.02301	7.55498
4 o	-0.777	1.99978	6.76646	0.01074	8.77697
5 h	0.46897	0	0.52956	0.00146	0.53103
6 c	0.17126	1.99906	3.80511	0.02457	5.82874
7 h	0.20288	0	0.79484	0.00228	0.79712
8 c	-0.1589	1.99893	4.14342	0.01654	6.15889
9 h	0.23183	0	0.7662	0.00198	0.76817
10 c	-0.0977	1.99884	4.08308	0.01572	6.09765
11 c	-0.4131	1.99915	4.39852	0.01545	6.41313
12 h	0.20349	0	0.79346	0.00305	0.79651
13 h	0.21013	0	0.78568	0.00419	0.78987
14 c	-0.4345	1.99915	4.42154	0.0138	6.43448
15 h	0.20618	0	0.78975	0.00407	0.79382
16 h	0.21557	0	0.78205	0.00238	0.78443
17 c	-0.0211	1.99915	4.00414	0.01777	6.02107
18 h	0.17641	0	0.82111	0.00248	0.82359
19 h	0.17047	0	0.8266	0.00292	0.82953
20 c	-0.2225	1.99894	4.20795	0.01561	6.2225
21 h	0.22356	0	0.77437	0.00207	0.77644
22 c	-0.4172	1.99912	4.40331	0.01474	6.41718
23 h	0.20912	0	0.78781	0.00307	0.79088
24 h	0.2129	0	0.78338	0.00373	0.7871
25 c	-0.2166	1.99882	4.20077	0.01704	6.21662
26 c	-0.1947	1.99911	4.17655	0.01899	6.19465



---

27 h	0.20318	0	0.79429	0.00253	0.79682
28 h	0.22935	0	0.76685	0.0038	0.77065
29 c	0.43597	1.99877	3.53212	0.03314	5.56403
30 c	-0.4087	1.99914	4.3958	0.01371	6.40866
31 h	0.2059	0	0.79114	0.00296	0.7941
32 h	0.20454	0	0.7923	0.00315	0.79546
33 c	-0.0263	1.99888	4.01166	0.01572	6.02626
34 c	-0.2647	1.9989	4.24792	0.01788	6.26469
35 h	0.23168	0	0.766	0.00232	0.76832
36 c	-0.1876	1.99893	4.17194	0.01676	6.18763
37 h	0.22746	0	0.77063	0.00191	0.77254
38 c	-0.2074	1.99895	4.19196	0.01648	6.20739
39 h	0.22874	0	0.76955	0.00171	0.77126
40 c	-0.2417	1.99894	4.22615	0.0166	6.24169
41 h	0.22903	0	0.7693	0.00167	0.77097
42 o	-0.7376	1.99971	6.72513	0.01277	8.73761
43 n	-0.5547	1.99921	5.53247	0.02301	7.55468
44 o	-0.7771	1.99978	6.7666	0.01073	8.77711
45 h	0.46904	0	0.5295	0.00146	0.53096
46 c	0.1714	1.99906	3.80499	0.02455	5.8286
47 h	0.20298	0	0.79474	0.00228	0.79702
48 c	-0.1587	1.99893	4.14324	0.01654	6.15872
49 h	0.2318	0	0.76623	0.00198	0.7682
50 c	-0.0976	1.99884	4.08308	0.01572	6.09764
51 c	-0.4131	1.99915	4.39853	0.01545	6.41313
52 h	0.20354	0	0.79341	0.00305	0.79646
53 h	0.21006	0	0.78575	0.00419	0.78994
54 c	-0.4345	1.99915	4.42155	0.01379	6.43449
55 h	0.20618	0	0.78975	0.00407	0.79382
56 h	0.21561	0	0.78201	0.00238	0.78439
57 c	-0.0211	1.99915	4.00417	0.01777	6.02108
58 h	0.1765	0	0.82102	0.00248	0.8235
59 h	0.17046	0	0.82662	0.00293	0.82954
60 c	-0.2226	1.99894	4.20801	0.01561	6.22256
61 h	0.22362	0	0.77431	0.00206	0.77638
62 c	-0.4172	1.99912	4.40328	0.01474	6.41715
63 h	0.2091	0	0.78782	0.00308	0.7909
64 h	0.21293	0	0.78333	0.00374	0.78707
65 c	-0.2165	1.99882	4.20068	0.01704	6.21654
66 c	-0.1946	1.99911	4.17654	0.01898	6.19463
67 h	0.20323	0	0.79424	0.00253	0.79677
68 h	0.22922	0	0.76697	0.00381	0.77078
69 c	0.43568	1.99877	3.5324	0.03315	5.56432
70 c	-0.4087	1.99914	4.39581	0.01372	6.40866

---

71 h	0.20589	0	0.79115	0.00296	0.79411
72 h	0.20455	0	0.7923	0.00316	0.79545
73 c	-0.0263	1.99888	4.0117	0.01572	6.02631
74 c	-0.2647	1.9989	4.24794	0.01789	6.26473
75 h	0.23161	0	0.76607	0.00232	0.76839
76 c	-0.1876	1.99893	4.17193	0.01676	6.18762
77 h	0.22746	0	0.77063	0.00191	0.77254
78 c	-0.2074	1.99895	4.19195	0.01649	6.20739
79 h	0.22875	0	0.76954	0.00171	0.77125
80 c	-0.2417	1.99894	4.22618	0.01661	6.24172
81 h	0.22903	0	0.7693	0.00167	0.77097

\* Total \*      0.00000    97.95850    219.20283    0.83868    318.00000

**Table 5.20:** Summary of Natural Population Analysis for complex **5.3**-hydride.  
Natural Population

Natural	-----				
1 ni	1.06583	17.9944	8.89065	0.04911	26.9342
2 o	-0.7757	1.99973	6.76089	0.01505	8.77567
3 n	-0.5493	1.99919	5.52623	0.0239	7.54932
4 o	-0.7778	1.99978	6.76734	0.01072	8.77783
5 c	0.17777	1.99905	3.7984	0.02478	5.82223
6 c	-0.1588	1.99892	4.14335	0.01655	6.15882
7 c	-0.0988	1.99884	4.08418	0.01577	6.09879
8 c	-0.4132	1.99915	4.3987	0.01539	6.41324
9 c	-0.435	1.99915	4.42204	0.01386	6.43504
10 c	-0.0214	1.99915	4.00453	0.01775	6.02143
11 c	-0.2239	1.99894	4.20948	0.0155	6.22392
12 c	-0.4188	1.99912	4.40528	0.01436	6.41876
13 c	-0.2209	1.99883	4.20495	0.01707	6.22085
14 c	-0.1955	1.99911	4.177	0.01937	6.19547
15 c	0.45223	1.99882	3.51347	0.03548	5.54777
16 c	-0.409	1.99915	4.39593	0.01387	6.40895
17 c	-0.0257	1.99889	4.011	0.01579	6.02567
18 c	-0.2695	1.9989	4.25242	0.01813	6.26945
19 c	-0.1881	1.99893	4.17239	0.01674	6.18805
20 c	-0.2074	1.99895	4.19185	0.01654	6.20735
21 c	-0.242	1.99894	4.22639	0.01668	6.24201
22 o	-0.793	1.99973	6.77784	0.01543	8.793
23 n	-0.5549	1.99921	5.53128	0.02439	7.55487
24 o	-0.7772	1.99978	6.76665	0.01072	8.77715
25 c	0.1744	1.99905	3.8016	0.02495	5.8256
26 c	-0.1569	1.99893	4.14144	0.01652	6.15689
27 c	-0.0968	1.99884	4.08223	0.01572	6.09679

---

28 c	-0.4127	1.99915	4.39818	0.01538	6.41272
29 c	-0.4344	1.99915	4.42137	0.01385	6.43436
30 c	-0.0211	1.99915	4.00422	0.01777	6.02114
31 c	-0.222	1.99894	4.20759	0.01549	6.22202
32 c	-0.4176	1.99912	4.40469	0.01383	6.41764
33 c	-0.2134	1.99883	4.19765	0.01691	6.21338
34 c	-0.1956	1.99912	4.17705	0.01946	6.19562
35 c	0.45129	1.99881	3.51465	0.03525	5.54871
36 c	-0.4103	1.99915	4.39722	0.0139	6.41027
37 c	-0.0259	1.99888	4.01125	0.01575	6.02588
38 c	-0.2673	1.9989	4.25042	0.01798	6.2673
39 c	-0.1878	1.99893	4.17217	0.01674	6.18784
40 c	-0.2067	1.99895	4.19128	0.01651	6.20674
41 c	-0.24	1.99894	4.22445	0.01663	6.24001
42 h	0.46952	0	0.52903	0.00145	0.53048
43 h	0.20255	0	0.79511	0.00234	0.79745
44 h	0.23151	0	0.76647	0.00202	0.76849
45 h	0.20414	0	0.79281	0.00304	0.79586
46 h	0.20935	0	0.78642	0.00423	0.79065
47 h	0.20633	0	0.78959	0.00408	0.79367
48 h	0.2161	0	0.78153	0.00237	0.7839
49 h	0.17675	0	0.82078	0.00247	0.82325
50 h	0.17106	0	0.82602	0.00291	0.82894
51 h	0.22291	0	0.77499	0.00211	0.77709
52 h	0.21118	0	0.78577	0.00305	0.78882
53 h	0.21394	0	0.78284	0.00322	0.78606
54 h	0.2074	0	0.79007	0.00253	0.7926
55 h	0.23018	0	0.76582	0.004	0.76982
56 h	0.20615	0	0.79089	0.00296	0.79385
57 h	0.20663	0	0.79023	0.00314	0.79337
58 h	0.2282	0	0.76913	0.00266	0.7718
59 h	0.22735	0	0.77073	0.00192	0.77265
60 h	0.22849	0	0.76979	0.00172	0.77151
61 h	0.22878	0	0.76956	0.00166	0.77122
62 h	0.46913	0	0.52942	0.00146	0.53087
63 h	0.20329	0	0.7943	0.00241	0.79671
64 h	0.23176	0	0.76622	0.00202	0.76824
65 h	0.2037	0	0.79326	0.00304	0.7963
66 h	0.20932	0	0.7866	0.00408	0.79068
67 h	0.206	0	0.78994	0.00406	0.794
68 h	0.21566	0	0.78196	0.00237	0.78434
69 h	0.17663	0	0.8209	0.00247	0.82337
70 h	0.17049	0	0.82659	0.00292	0.82951
71 h	0.22299	0	0.77488	0.00213	0.77701

---

72 h	0.20625	0	0.7911	0.00265	0.79375
73 h	0.22333	0	0.77241	0.00426	0.77667
74 h	0.20842	0	0.78898	0.00261	0.79158
75 h	0.2258	0	0.77144	0.00275	0.7742
76 h	0.20519	0	0.7918	0.00301	0.79481
77 h	0.20478	0	0.79187	0.00335	0.79522
78 h	0.23233	0	0.76509	0.00258	0.76767
79 h	0.22779	0	0.7703	0.00191	0.77221
80 h	0.22891	0	0.76938	0.00171	0.77109
81 h	0.22928	0	0.76905	0.00166	0.77072
82 h	-0.0569	0	1.05434	0.00252	1.05686

\* Total \*      -0.00000    97.95747    220.17710    0.86543    319.00000

**Table 5.21:** Dipole moment of complexes (5.1, 5.2 and 5.3)

Complex	\$dipole from dscf				
<b>5.1</b>	x	-0.00594651188212	y	0.00130130527805	z -0.01100192940339
	a.u.				
	dipole   = 0.0319592898 debye				
Complex	\$dipole from dscf				
<b>5.2</b>	x	-0.00445480443091	y	0.00240391006082	z 0.00209883938714
	a.u.				
	dipole   = 0.0139285960 debye				
Complex	\$dipole from dscf				
<b>5.3</b>	x	-0.00320946676061	y	0.00006161043984	z 0.00221978258378
	a.u.				
	dipole   = 0.0099200225 debye				

## 5.4 Conclusions

In summary, we have been successful to synthesize three mononuclear nickel(II) with similar N,O donor ligands and characterized them by several standard methods. These complexes have been found to be active electrocatalyst for hydrogen evolution reaction using acetic acid and trifluoroacetic acid as the substrates in DMF. TOF values of these catalysts decrease with the increase in chain length of hydroxyalkyl group. The Ni(II) centres in these complexes is reduced Ni(I) species and then converted to Ni(III)-hydride which ultimately generates hydrogen and returns to Ni(II) state. This possible mechanism has been supported by theoretical calculations. Thus, in this study, it has been shown that the length of alkyl side chain

has significant effect in catalytic ability in HER reaction and can be judiciously designed to get optimized efficiency.

## 5.5 References

- 5.1 J.-W. Wang, W.-J. Liu, D.-C. Zhong, T.-B. Lu, *Coord. Chem. Rev.* **2019**, *378*, 237–261.
- 5.2 (a) M. G. Pfeffer, T. Kowacs, M. Wächtler, J. Guthmuller, B. Dietzek, J. G. Vos, S. Rau, *Angew. Chem. Int. Ed.* **2015**, *54*, 6627–6631;  
(b) H. Ozawa, M.-A. Haga, K. Sakai, *J. Am. Chem. Soc.* **2006**, *128*, 4926–4927;  
(c) D. Liu, X. Li, S. Chen, H. Yan, C. Wang, C. Wu, Y. A. Haleem, S. Duan, J. Lu, B. Ge, P. M. Ajayan, Y. Luo, J. Jiang, L. Song, *Nat. Energy.* **2019**, *4*, 512–518;  
(d) K.Zeng, D. K.Zhang, *Prog. Energy Combust. Sci.* **2010**, *36*, 307–326;  
(e) A. Lasia, Hydrogen evolution reaction. In *Handbook of Fuel Cells*; John Wiley & Sons: New York, **2010**;  
(f) J. K.Nørskov, T. Bligaard, A. Logadottir, J. R. Kitchin, J. G. Chen, S. Pandalov, U. Stimming, *J. Electrochem. Soc.* **2005**, *152*, J23–J26;  
(g) J. Greeley, T. F. Jaramillo, J. Bonde, I. Chorkendorff, J. K. Nørskov, *Nat. Mater.* **2006**, *5*, 909–913.
- 5.3 (a) K. E. Dalle, J. Warnan, J. J. Leung, B. Reuillard, I. S. Karmel, E. Reisner, *Chem. Rev.* **2019**, *119*, 2752–2875;  
(b) L. Tong, L. Duan, A. Zhou, R. P. Thummel, *Coord. Chem. Rev.* **2020**, *402*, 213079;
- 5.4 T. Agarwal, S. Kaur-Ghumaan, *Coord. Chem. Rev.* **2019**, *397*, 88–219;
- 5.5 M.D. Sampson, C.P. Kubiak, *Inorg. Chem.* **2015**, *54*, 6674–6676;
- 5.6 (a) A.Z. Haddad, S.P. Cronin, M.S. Mashuta, R.M. Buchanan, C.A. Grapperhaus, *Inorg. Chem.* **2017**, *56*, 11254–11265;  
(b) P. Zhang, M. Wang, Y. Yang, T. Yao, L. Sun, *Angew. Chem. Int. Ed.* **2014**, *53*, 13803–13807.
- 5.7 (a) N. Queyriaux, D. Sun, J. Fize, J. Pécaut, M.J. Field, M. Chavarot-Kerlidou, V. Artero, *J. Am. Chem. Soc.* **2020**, *142*, 274–282;  
(b) T. Straistari, R. Hardré, J. Fize, S. Shova, M. Giorgi, M. Réglie, V. Artero, M. Orto, *Chem. Eur. J.* **2018**, *24*, 8779 – 8786,;  
(c) N. Kaeffer, M. Chavarot-Kerlidou, V. Artero, *Acc. Chem. Res.* **2015**, *48*, 1286–1295.

- 5.8 (a) T. Fogeron, T. K. Todorova, J.-P. Porcher, M. Gomez-Mingot, L.-M. Chamoreau, C. Mellot-Draznieks, Y. Li, M. Fontecave, *ACS Catal.* **2018**, *8*, 2030–2038;  
(b) G. Bergamini, M. Natali, *Dalton Trans.* **2019**, *48*, 14653–14661;  
(c) Y.-P. Zhang, M. Zhang, X.-R. Chen, C. Lu, D. J. Young, Z.-G. Ren, J.-P. Lang, *Inorg. Chem.* **2020**, *59*, 1038–1045;  
(d) R. Shen, J. Xie, Q. Xiang, X. Chen, J. Jiang, X. Li, *Chinese J. Catal.* **2019**, *40*, 240–288;  
(e) D. Jana, H. K. Kolli, S. Sabnam, S. K. Das, *Chem. Commun.* **2021**, *57*, 9910–9913;  
(f) Soumalya Sinha, Giang N. Tran, Hanah Na and Liviu M. Mirica, *Chem. Commun.* **2022**, *58*, 1143–1146;  
(g) A. Cabrera-García, V. Blay, R. Blay-Roger, Á. G. Ravelo, J. González-Platas, M. C. Arévalo, J. Sanchiz, P. Martín-Zarza, *Chem. Eng. J.* **2021**, *420*, 130342.
- 5.9 (a) P. Bhanja, B. Mohanty, S. Chongdar, A. Bhaumik, B. K. Jena, S. Basu, *ACS Appl. Energy Mater.* **2022**, *5*, 3558–3567;  
(b) S. Bhattacharjee, S. Bera, R. Das, D. Chakraborty, A. Basu, P. Banerjee, S. Ghosh, A. Bhaumik, *ACS Appl. Mater. Interfaces* **2022**, *14*, 20907–20918;  
(c) H. Xu, H. Shang, C. Wang, Y. Du, *Coord. Chem. Rev.* **2020**, *418*, 213374;  
(d) J. Mohammed-Ibrahim, X. Sun, *J. Energy Chem.* **2019**, *34*, 111–160.
- 5.10 R.M. Bullock, A.M. Appel, M.L. Helm, *Chem. Commun.* **2014**, *50*, 3125–3143.
- 5.11 J.W. Morgan, E. Anders, *Proc. Natl. Acad. Sci. U.S.A.* **1980**, *77*, 6973–6977.
- 5.12 J. Fessler, J.-H. Jeoung, H. Dobbek, *Angew. Chem. Int. Ed.* **2015**, *54*, 8560–8564.
- 5.13 B. J. Fisher, R. Eisenberg, *J. Am. Chem. Soc.* **1980**, *102*, 7361–7363.
- 5.14 A. Zarkadoulas, M. J. Field, C. Papatriantafyllopoulou, J. Fize, V. Artero, C.A. Mitsopoulou, *Inorg. Chem.* **2016**, *55*, 432–444.
- 5.15 M. L. Helm, M. P. Stewart, R. M. Bullock, M. R. DuBois, D. L. DuBois, *Science* **2011**, *333*, 863–866.
- 5.16 G. Bergamini, M. Natali, *Dalton Trans.* **2019**, *48*, 14653–14661.
- 5.17 A. Das, Z. Han, W.W. Brennessel, P.L. Holland, R. Eisenberg, *ACS Catal.* **2015**, *5*, 1397–1406.
- 5.18 H. Shao, S. K. Muduli, P.D. Tran, H.S. Soo, *Chem. Commun.* **2016**, *52*, 2948–2951.
- 5.19 X. Li, Ho, H. Shao, Y.Y. Ng, R. Ganguly, Y. Lu, H.S. Soo, *Inorg. Chem.* **2019**, *58*, 1469–1480.
- 5.20 APEX-II, SAINT and SADABS, Bruker AXS Inc., Madison, WI, **2008**.

- 5.21 G. M. Sheldrick, *Acta Crystallogr., Sect. A: Fundam. Crystallogr.* **2015**, 71, 3.
- 5.22 G. M. Sheldrick, *Acta Crystallogr., Sect. C: Cryst. Struct. Commun.* **2015**, 71, 3.
- 5.23 L. Yang, D.R. Powell, R.P. Houser, *Dalton Trans.* **2007**, 9, 955–964.
- 5.24 (a) S. Halder, J. Mondal, J. Ortega-Castro, A. Frontera, P. Roy, *Dalton Trans.* **2017**, 46, 1943–1950;  
(b) A. Bhattacharjee, S. Dey, P. Roy, *Inorg. Chim. Acta* **2019**, 490, 93–103.
- 5.25 D. L. Pavia, G. M. Lampman, G. S. Kriz and J. R. Vyvyan, Introduction to spectroscopy, 5<sup>th</sup> edition, Cengage Learning, Stamford, USA, 2015.
- 5.26 (a) M. F.-Mehrdadi, H. Kargar, R. B.-Ardakani, M. Ashfaq, K. S. Munawar, M. N. Tahir, *J. Mol. Struct* **2022**, 1251, 132037;  
(b) G. R. Reddy, S. Balasubramanian, K. Chennakesavulu, *J. Mater. Chem. A* **2014**, 2, 15598–15610;  
(c) A. D. Khalaji, M. Nikookar, D. Das, *J Therm Anal Calorim* **2014**, 115, 409–417;  
(d) S. N. Shukla, P. Gaur, M. L. Raidas, B. Chaurasia, *J. Mol. Struct* **2020**, 1202, 127362;  
(e) H. Kargar, A. A. Ardakani, M. N. Tahir, M. Ashfaq, K. S. Munawar, *J. Mol. Struct* **2021**, 1229, 129842.
- 527 (a) S. Chattopadhyay, M.S. Ray, S. Chaudhuri, G. Mukhopadhyay, G. Bocelli, A. Cantoni, A. Ghosh, *Inorg. Chem. Acta* **2006**, 359, 1367–1375;  
(b) M.S. Ray, S. Chaudhuri, L. Right, G. Bocelli, G. Mukhopadhyay, A. Ghosh, *Polyhedron* **2003**, 22, 617–624.
- 5.28 (a) B.S. Garg, D.N. Kumar, *Spectrochim. Acta Part A* **2003**, 59, 229–234;  
(b) A. Anthonysamy, S. Balasubramanian, *Inorg. Chem. Commun.* **2005**, 8, 908–911.
- 5.29 M. Salehi, F. Rahimifar, M. Kubicki, A. Asadi, *Inorganica Chimica Acta* **2016**, 443, 28–35.
- 5.30 A. Ourari, Y. Ouennoughi, D. Aggoun, M.S. Mubarak, E. M. Pasciak, D.G. Peters, *Polyhedron* **2014**, 67, 59–64.
- 5.31 L.-Q. Chai, H.-S. Zhang, J.-J. Huang, Y.-L. Zhang, *Spectrochim. Acta A* **2015**, 137, 661–669.
- 5.32 J. Datta, S. Bhattacharya, K.K. Kundu, *Aust. J. Chem.* **1983**, 36, 1779–1784.
- 5.33 C. Chen, X. Li, F. Deng, J. Li, *RSC Adv.* **2016**, 6, 79894–79899.
- 5.34 T.D. Cook, S.F. Tyler, C.M. McGuire, M. Zeller, P. E. Fanwick, D.H. Evans, D.G. Peters, T. Ren, *ACS Omega* **2017**, 2, 3966–3976.

- 5.35 V. Fourmond, P.-A. Jacques, M. Fontecave, V. Artero, *Inorg. Chem.* **2010**, *49*, 10338–10347.
- 5.36 (a) V. Fourmond, S. Canaguier, B. Golly, M. J. Field, M. Fontecave, V. Artero, *Energy Environ. Sci.* **2011**, *4*, 2417–2427;  
(b) G. A. N. Felton, R. S. Glass, D. L. Lichtenberger, D. H. Evans, *Inorg. Chem.* **2006**, *45*, 9181–9184.
- 5.37 (a) J.-P. Cao, T. Fang, L.-Z. Fu, L.-L. Zhou, S. Zhan, *Int. J. Hydrog. Energy* **2014**, *39*, 10980–10986;  
(b) R. Jain, A.A. Mamun, R.M. Buchanan, P.M. Kozlowski, C.A. Grapperhaus, *Inorg. Chem.* **2018**, *57*, 13486–13493;  
(c) G. Bergamini, M. Natali, *Dalton Trans.* **2019**, *48*, 14653–14661;  
(d) Y.-P. Zhang, M. Zhang, X.-R. Chen, C. Lu, D. J. Young, Z.-G. Ren, J.-P. Lang, *Inorg. Chem.* **2020**, *59*, 1038–1045;  
(e) J.-M. Lei, S.-P. Luo, S.-Z. Zhan, *Int. J. Hydrog. Energy* **2018**, *43*, 19047–19056;  
(f) Q.-X. Peng, D. Xue, S.-Z. Zhan, C.-L. Ni, *Appl. Catal. B* **2017**, *219*, 353–361;  
(g) L. Chen, G. Chen, C.-F. Leung, S.-M. Yiu, C.-C. Ko, E.A. Mallart, M. Robert, T.-C. Lau, *ACS Catal.* **2015**, *5*, 356–364.
- 5.38 (a) C. Costentin, S. Drouet, M. Robert, J.-M. Saveant, *J. Am. Chem. Soc.* **2012**, *134*, 11235–11242;  
(b) C. Costentin, M. Robert, J.-M. Saveant, *Chem. Soc. Rev.* **2013**, *42*, 2423–2436;  
(c) C. Costentin, J.-M. Saveant, Multielectron, *ChemElectroChem* **2014**, *1*, 1226–1236;  
(d) R. J. DiRisio, J. E. Armstrong, M. A. Frank, W. R. Lake, W. R. McNamara, *Dalton Trans* **2017**, *46*, 10418–10425.
- 5.39 N. Elgrishi, M.B. Chambers, M. Fontecave, *Chem. Sci.* **2015**, *6*, 2522–2531.
- 5.40 (a) V. S. Thoi, Y. Sun, J. R. Long, C. J. Chang, *Chem. Soc. Rev.* **2013**, *42*, 2388–2400;  
(b) M. Zeng, Y. Li, *J. Mater. Chem. A* **2015**, *3*, 14942–14962;  
(c) X. Zou, Y. Zhang, *Chem. Soc. Rev.* **2015**, *44*, 5148–5180.
- 5.41 (a) TURBOMOLE, Version 7.3, a development of University of Karlsruhe and Forschungszentrum Karlsruhe GmbH, 1989–2007;  
(b) E. Caldeweyher, C. Bannwarth, S. Grimme, *J. Chem. Phys.* **2017**, *147*, 34112.
- 5.42 Y. Han, H. Fang, H. Jing, H. Sun, H. Lei, W. Lai, R. Cao, *Angew. Chem. Int. Ed.* **2016**, *55*, 5457–5462.



- 5.43 K. Majee, J. Patel, S. Rai, B. Das, B. Panda, S. K. Padhi, *Phys. Chem. Chem. Phys.* **2016**, *18*, 21640-21650.
- 5.44 N. Villegas-Escobar, D.E. Ortega, D. Cortes-Arriagada, R. Duran, D. Yepes, S. Gutierrez-Oliva, A. Toro-Labbe, *J. Phys. Chem. C* **2017**, *121*, 12127–12135.

# Chapter 6

## **Mononuclear nickel and copper complexes as electrocatalyst for generation of hydrogen from acetic acid**

### **Abstract**

Ever increasing use of conventional energy and demand of clean renewable energy inspires many researchers to produce effective systems for hydrogen generation. Herein we report two mononuclear complexes, [NiL] (Complex **6.1**) and [CuL] (Complex **6.2**), where H<sub>2</sub>L is 1,1'-(1E,1'E)-(propane-1,2-diylbis(azan-1-yl-1-ylidene))bis(methan-1-yl-1-ylidene)dinaphthalen-2-ol, as electrocatalyst for hydrogen evolution reaction using acetic acid as the substrate. Both of the complexes have been synthesized under mild conditions and characterized by several methods. Single crystal X-ray structure of Complex **6.1** shows square planar geometry around nickel center. These complexes have effectively been used to reduce proton to generate hydrogen. Different control experiments have been carried out to understand the role of these catalysts and find their relevance in this regard. Turnover frequency (TOF) values for **6.1** and **6.2** have been determined as 653.1 and 777.5 s<sup>-1</sup>, respectively. Hydrogen is evolved via reduction of metal center followed by formation of metal hydride species.

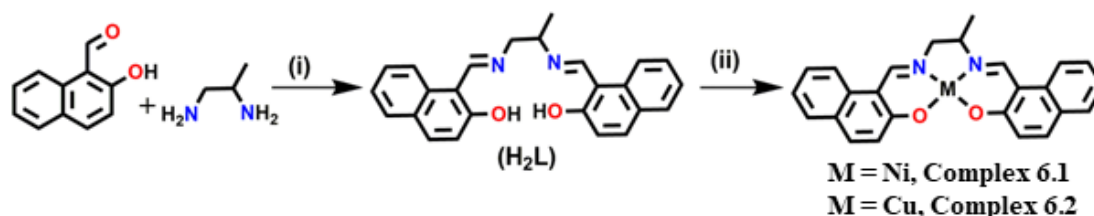
## 6.1 Introduction

The dramatic increase in the efforts to develop clean and renewable energy is observed now-a-days to address the problems of increasing worldwide demand for energy and the low abundance of conventional fuels.<sup>6.1</sup> Majority of worldwide consumed energy is derived from fossil fuel, which causes higher emissions of CO<sub>2</sub> to the environment resulting into the greenhouse effect.<sup>6.2</sup> Present renewable energy sources such as solar, wind or geothermal energy exhibit low efficiency in energy delivery due to their temporal and spatial intermittencies limiting their application on regular basis.<sup>6.3</sup> A perspective solution of this problem is the storage of the energy obtained from these diluted sources via the conversion of electricity to chemical energy by electrolysis of water. In this context, the most promising fuel candidate is hydrogen owing to its high gravimetric energy density, relatively high abundance, and zero emission during consumption.<sup>6.4</sup>

The electrocatalytic hydrogen evolution reaction (HER), a half reaction as well as the vital step of water electrolysis to H<sub>2</sub> production, become the appealing subject of extensive study over the past decades. Even though HER involves simple reactants and only two electrons for each hydrogen molecule, the multiple elemental reactions provide an accumulation of energy barriers resulting in slow kinetics.<sup>6.5</sup> This has led to the development of molecular catalysts which can play significant roles in expediting the reactions. Among all HER catalysts, platinum-based catalysts stand out first with almost no overpotential at the onset and rapid current increase over voltage increment.<sup>6.6</sup> But its large-scale utilization as the catalyst is restricted due to its scarcity and high cost. Thus, it promotes the development of alternative molecular catalysts involving more abundant metals with high activity and durability.<sup>6.7</sup> In this context, molecular catalysts involving Ni<sup>6.8</sup> and Cu<sup>6.9</sup> are worth mentioning. Many of these complexes show impressive TOFs in organic solvents and are supported by ligands such as N<sub>2</sub>P<sub>2</sub> core,<sup>6.10</sup> macrocyclic oximes,<sup>6.11</sup> polypyridines,<sup>6.12</sup> thiolates<sup>6.13</sup> and porphyrins.<sup>6.14</sup> The structural studies suggest that when a basic nitrogen or oxygen atom is incorporated into the backbone of the dithiolate ligand,<sup>6.15</sup> the amine<sup>6.16</sup> or oxygen<sup>6.17</sup> cofactor facilitates the cleavage/formation of the hydrogen-hydrogen bond and the transfer of protons to and from the distal metal center.<sup>6.17</sup>

In this chapter, the electrocatalytic proton reduction reaction (or HER) by two neutral, monomeric transition metal complexes, [ML] (M = Ni, Complex **6.1**; M = Cu, Complex **6.2**; H<sub>2</sub>L=1,1'-(1E,1'E)-(propane-1,2-diylbis(azan-1-yl-1-ylidene))bis(methan-1-yl-1-ylidene)dinaphthalen-2-ol) with a tetradentate Schiff-base ligand are being reported (**Scheme**

**6.1).** They have been synthesized by conventional method and characterized by several standard methods. These have been used as electrocatalyst to generate hydrogen from acetic acid. The purpose of this study is to examine the effect of change of metal centre on the generation of hydrogen evolution reaction. So, Ni- and Cu- complexes have been selected.



**Scheme 6.1:** Synthetic route to Complex **6.1** and **6.2**. (i) 2-Hydroxy-1-naphthaldehyde:1,2-diaminopropane = 2:1, Refluxed in acetonitrile for 3 h; (ii)  $H_2L$ : Metal salt = 1:1, Refluxed in acetonitrile for 1 h,  $Ni(ClO_4)_2$  for Complex **6.1** and  $Cu(NO_3)_2$  for Complex **6.2**.

## 6.2 Experimental Section

### 6.2.1 Materials and physical methods

2-Hydroxy-1-naphthaldehyde, 1,2-diaminopropane, nickel(II) perchlorate hexahydrate and copper(II) nitrate trihydrate were purchased from Sigma Aldrich and were used as received. Other reagents and solvents were used without any purification after purchasing from different commercial sources. Elemental analyses of Complex **6.1** and **6.2** were performed using a Perkin–Elmer 2400C elemental analyzer.  $^1H$  NMR spectrum of the Schiff-base ligand,  $H_2L$ , was recorded on Bruker 400 MHz spectrometer. The UV-visible spectral measurements of Complex **6.1** and **6.2** were done in Agilent 8453 diode array spectrophotometer. FT-IR spectra of the ligand and the complexes were measured on a Perkin Elmer spectrometer (Spectrum Two) with the samples by using ATR method. Cyclic voltammograms (CVs) were obtained on a computer supported potentiostat (AUTOLAB company) under air-free conditions employing the usual three-electrode cell. Here, a graphite electrode was used as a working electrode, a saturated Ag/AgCl electrode was used a reference electrode and platinum wire was considered as the auxiliary electrode. The surface area of the working electrode was measured to be  $0.12\text{ cm}^2$ . Gas chromatography (Model no. 7890B (G3440B), serial no. CN14333203 fitted with TCD) was used to detect the gas during bulk electrolysis.  $500\ \mu\text{L}$  gas was collected from the head space with the help of a gas tight syringe and was injected through the inlet of the gas chromatography. Faradaic efficiency was determined using an inverted burette in which the

evolved gas displaced the volume of the solvent. By applying the conversion factor of 1 mol of gas corresponds to 22.4 L, the evolved moles of hydrogen can be quantified.

*CAUTION: Perchlorate salts are potentially explosive. Small amount of the salt should be handled with care.*

## 6.2.2 Syntheses of ligand and complexes

### 6.2.2.1 Synthesis of 1,1'-(1E,1'E)-(propane-1,2-diylbis(azan-1-yl-1-ylidene))bis(methan-1-yl-1-ylidene)dinaphthalen-2-ol (**H<sub>2</sub>L**)

1,2-Diaminopropane (0.3 mmol, 25.56  $\mu$ L) was added to an acetonitrile solution of 2-hydroxy-1-naphthaldehyde (0.3 mmol, 0.052 g) dropwise under stirring condition. Stirring was continued for 30 min. The color of the reaction mixture turned yellow and it was then refluxed for 3 h. The mixture was then cooled to room temperature and was filtered. Solid product was obtained after few days on slow evaporation of acetonitrile. Data for **H<sub>2</sub>L**: Yield = 0.103 g, 90%; anal. calc. (%) for C<sub>25</sub>H<sub>22</sub>N<sub>2</sub>O<sub>2</sub>: C, 78.51; H, 5.80; N, 7.32. Found: C, 78.43; H, 5.76; N, 7.19; <sup>1</sup>H NMR (400 MHz, DMSO-d<sub>6</sub>,  $\delta$  ppm, TMS) 14.46 (2H, s), 9.15 (2H, s), 7.74 (2H, d, J = 6 Hz), 7.63 (2H, d, J = 8 Hz), 7.43 (2H, d, J = 7.2 Hz), 7.21 (2H, t, J = 8.0 Hz), 6.80 (2H, t, J = 9.2 Hz), 6.70 (2H, d, J = 7.2 Hz), 4.12 (2H, d, J = 3.6 Hz), 3.98 (1H, m), 1.44 (3H, d, J = 6.4 Hz); ESI-MS<sup>+</sup> (*m/z*): 405.08 [(H<sub>2</sub>L + Na<sup>+</sup>)].

### 6.2.2.2 Synthesis of [Ni(L)] (**6.1**)

A solution of nickel(II) perchlorate hexahydrate (0.3 mmol, 0.1097 g) in acetonitrile (5.0 mL) was added dropwise to 5.0 mL acetonitrile solution of H<sub>2</sub>L (0.3 mmol, 0.115 g) under continuous stirring condition. The mixture was stirred till it turned greenish. Then, it was refluxed for 1 h. Color of the solution changed to dark green. The mixture was then cooled to room temperature and filtered to remove solid material, if any. The filtrate was kept in beaker under ambient condition for slow evaporation. Green crystals of Complex **6.1** suitable for single crystal X-ray diffraction were produced after four to five days. Data for **6.1**: Yield, 0.086 g, 65%; anal. calc. for C<sub>25</sub>H<sub>20</sub>NiN<sub>2</sub>O<sub>2</sub>: C, 68.38; H, 4.59; N, 6.38; found: C, 68.33; H, 4.45; N, 6.30%. ESI-MS<sup>+</sup> (*m/z*): 440.11 [(Ni(L) + H<sup>+</sup>)].

### 6.2.2.3 Synthesis of [Cu(L)] (**6.2**)

To 5.0 mL acetonitrile solution of H<sub>2</sub>L (0.3 mmol, 0.115 g), an acetonitrile solution (5.0 mL) of copper(II) nitrate trihydrate (0.3 mmol, 0.0725 g) was added dropwise under continuous stirring condition. The mixture was stirred for another 30 min. Then, it was refluxed for 1 h. The mixture was then filtered to remove suspended material and/or precipitate, if any. Green crystalline product was obtained on slow evaporation of the solvent within few days. Data for

**6.2:** Yield, 0.063 g, 72%; anal. calc. for  $C_{25}H_{20}CuN_2O_2$ : C, 67.63; H, 4.54; N, 6.31; found: C, 67.53; H, 4.46; N, 6.36%. ESI-MS<sup>+</sup> ( $m/z$ ): 444.10 [(Cu(L) + H<sup>+</sup>)].

### 6.2.3 X-ray data collection and structure determination

Data collection and refinement parameters for Complex **6.1** are summarized in **Table 6.1**. Single crystal data collections were performed with an automated Bruker D8 VENTURE diffractometer using graphite monochromatized Mo K $\alpha$  radiation. The spots were measured using 10 s counting time. Unit cell parameters were determined from least-squares refinement of setting angles with  $\theta$  in the range  $2.29 \leq \theta \leq 26.32^\circ$ . Data were processed using the Bruker SAINT package.<sup>6,18</sup> Absorption corrections based on multi scans using the SADABS software were applied to all intensity data. The structures were solved by direct methods using SHELXT<sup>6,19</sup> and refined by full-matrix least-squares techniques on  $F^2$  using the SHELXS-2014/7 program.<sup>6,20</sup> The absorption corrections were done by the multi-scan technique. All data were corrected for Lorentz and polarization effects, and the non-hydrogen atoms were refined anisotropically.

## 6.3 Results and discussion

### 6.3.1 Synthesis and characterization of the ligand

Ligand, **H<sub>2</sub>L**, has been synthesized by a typical Schiff base condensation reaction between two equivalents of 2-hydroxy-1-naphthaldehyde and one equivalent of 1,2-diaminopropane in acetonitrile (**Scheme 1**). The product has been obtained in high yield. One equivalent of **H<sub>2</sub>L** has been allowed to react with one equivalent of metal salts (Ni(ClO<sub>4</sub>)<sub>2</sub> for Complex **6.1** and Cu(NO<sub>3</sub>)<sub>2</sub> for Complex **6.2**) to produce the mononuclear transition metal complexes without adding any external base for the deprotonation of phenolic OH groups. Metal complexes are also obtained in good yield.

**H<sub>2</sub>L** has been characterized by a number of standard techniques such as elemental analysis, mass spectrometry, FT-IR and <sup>1</sup>H NMR spectral analysis. ESI-mass spectrum of the ligand has been obtained with methanolic solution (**Figure 6.1**). Mass spectrum exhibits the most intense peak at an  $m/z$  value of 405.08 which may be attributed to the [**H<sub>2</sub>L**+ Na<sup>+</sup>] species (calculated value: 405.16). This supports the formation of the Schiff base ligand.

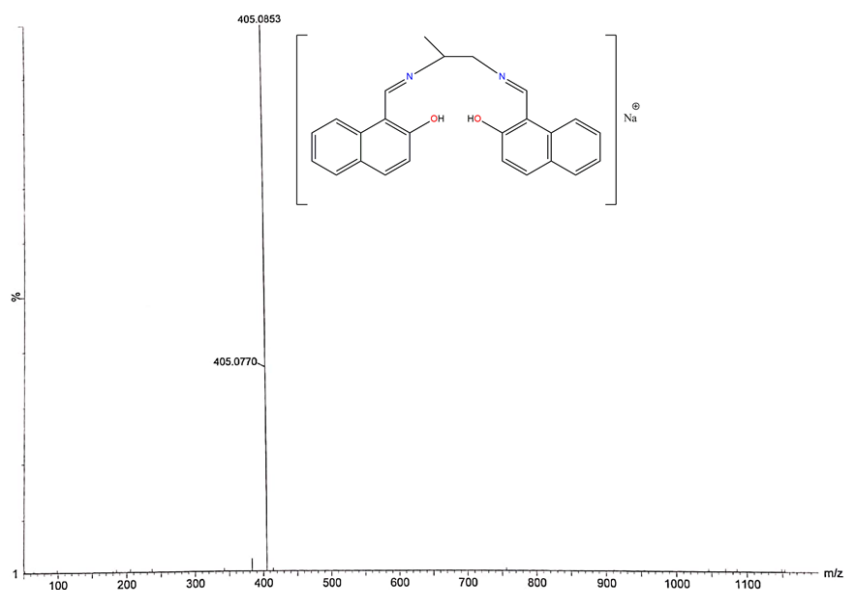


**Figure 6.1:** Mass spectrum of  $H_2L$  in methanol.

The FTIR spectrum of the ligand,  $H_2L$ , exhibits a broad band at  $3420\text{ cm}^{-1}$  due to O–H stretching indicating the presence of hydroxyl group (Figure 6.2). Considering the hydrocarbon part, for aromatic C–H bond,  $\nu_{C-H}$  is observed at  $3044\text{ cm}^{-1}$ , whereas the band observed at  $2953\text{ cm}^{-1}$  may be assigned to  $\nu_{C-H}$  for aliphatic C–H bond. An intense band around  $1609\text{ cm}^{-1}$  is also observed due to the stretching vibration of the azomethine group. These bands strongly support the formation and structure of the Schiff base ligand.

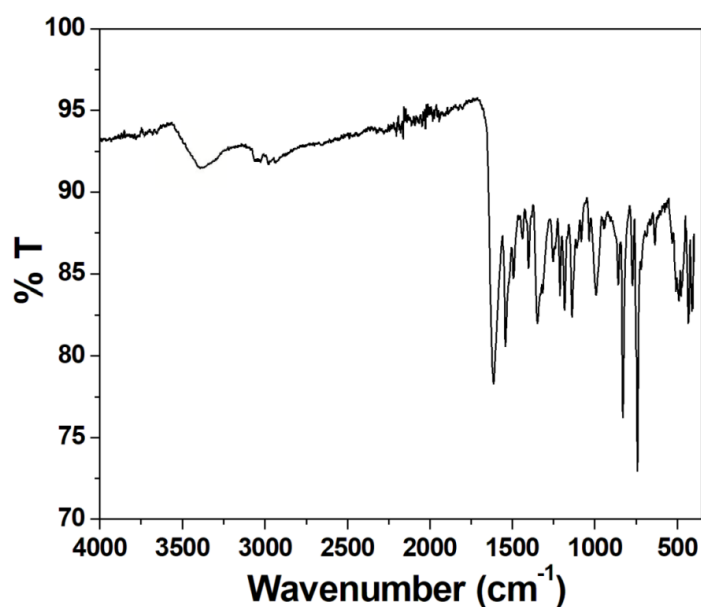


**Figure 6.2:** FTIR spectrum of  $H_2L$ .

The ligand has further been characterized by  $^1H$  NMR spectral studies (Figure 6.3). Spectrum has been obtained in  $DMSO-d_6$ . It shows a peak at  $14.46\text{ ppm}$  which indicates the presence of phenolic OH group. The peak at  $9.15\text{ ppm}$  may be due to the presence of imine

proton indicating formation of the Schiff-base compound. Signals for aromatic protons (7.74–6.70 ppm) and methylene protons (4.12 ppm) appear in the appropriate positions. Signal for methyl protons appears at 1.44 ppm. Thus, NMR spectral study confirms the formation of **H<sub>2</sub>L**.

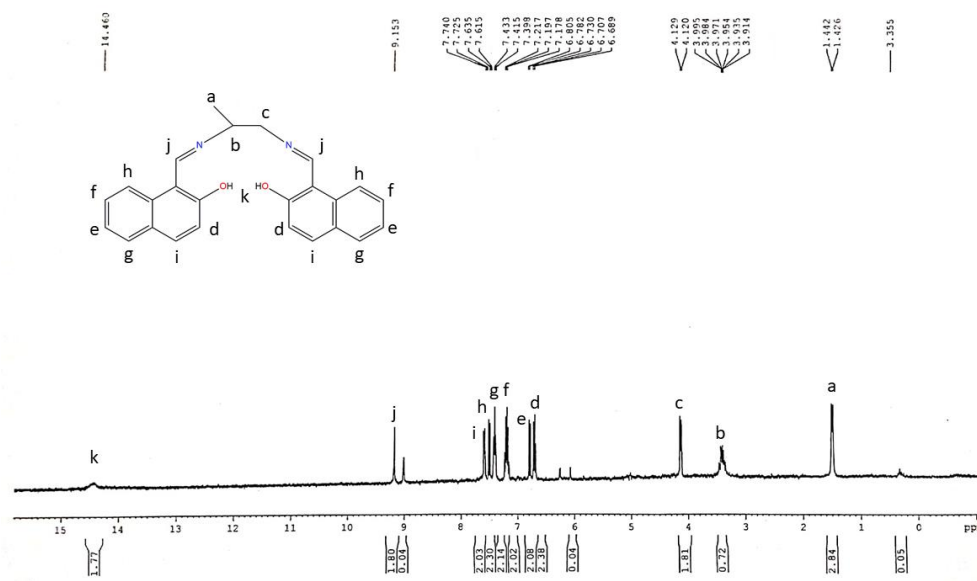


**Figure 6.3:** <sup>1</sup>H NMR spectrum of **H<sub>2</sub>L** in DMSO-d<sub>6</sub>.

## 6.3.2 Characterization of the complexes

### 6.3.2.1 Crystal structure of complex 6.1

Complex **6.1** crystallizes in the *P* 21/*n* space group from methanol. A perspective view of the complex is shown in **Figure 6.4**. Selected bond angles and bond lengths are listed in **Table 6.2**. Complex **6.1** consists of one deprotonated ligand and one nickel atom. Nickel atom is in a tetracoordinated environment. Ni1 is coordinated to four heteroatoms, two oxygen atoms (O1, O2) and two nitrogen atoms (N1, N2) of the ligand. It is almost a perfect square planar molecule as evident from the four-coordinate  $\tau_4$  index value.  $\tau_4$  index indicates tetrahedral or square planar geometry of a tetracoordinate complex and it is calculated from the following equation:<sup>6.21</sup>

$$\tau_4 = \frac{360^\circ - (\alpha + \beta)}{141^\circ}$$

here  $\alpha$  and  $\beta$  signifies the values of the two largest donor-metal-donor angles of the tetra-coordinated complex. Values of  $\tau_4$  are 1.00 and 0.00 an ideal tetrahedral geometry and square planar geometry, respectively. For Complex **6.1**, the value of  $\tau_4$  has been determined to be 0.016 indicating almost perfect square planar geometry around the metal center. Both the *trans* angles O1–Ni1–N1 and O2–Ni1–N2 are close to 180° (178.88° and 178.83° respectively) and the O–Ni–N bond angles are very close to the ideal 90°. The Ni–O and Ni–N bond lengths are also in good agreement with the literature values.<sup>6.22</sup>



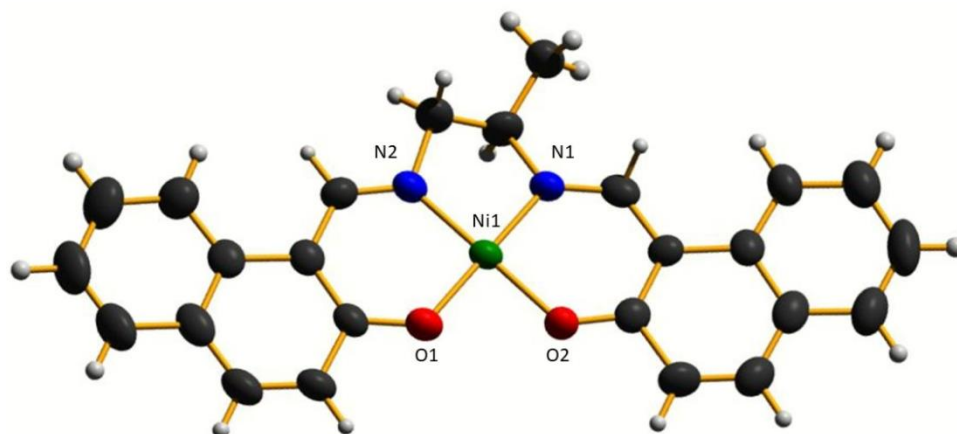


**Figure 6.4:** A perspective view of complex **6.1** with displacement ellipsoids drawn at the 50% probability level.

**Table 6.1:** Crystal data of complex **6.1**

Complex	<b>6.1</b>
Formula	$C_{25}H_{21}N_2NiO_2$
Formula weight	440.13
$T$ (K)	298(2)
Crystal color	brown
Crystal system	monoclinic
Space group	$P 21/n$
$a$ (Å)	14.4230 (12)
$b$ (Å)	8.2705 (6)
$c$ (Å)	17.6642 (15)
$\alpha$ (°)	90
$\beta$ (°)	111.738 (2)
$\gamma$ (°)	90
$V$ (Å <sup>3</sup> )	1957.2 (3)
$Z$	4
Crystal dimensions (mm)	$0.3 \times 0.2 \times 0.2$
$F(0\ 0\ 0)$	916
$D_c$ (g cm <sup>-3</sup> )	1.494
$\lambda$ (Mo $K\alpha$ ) (Å)	0.71073

$\theta$ Range (°)	2.29- 26.32
Reflection collected/ unique/observed	25059, 3986, 3153
Absorption correction	multi-scan
$R_{\text{int}}$	0.0846
Final $R_1$ index [ $I > 2\sigma(I)$ ]	0.1088
Final $wR_2$ index (all reflections)	0.2160
Goodness-of-fit	1.384

**Table 6.2:** Selected bond length (Å) and bond angles (°) of Complex **6.1**

Ni1–O2	1.847 (4)
Ni1–O1	1.843 (3)
Ni1–N1	1.833 (4)
Ni1–N2	1.837 (4)
O2–Ni1–O1	85.25 (15)
O2–Ni1–N1	93.86 (17)
O1–Ni1–N1	178.88 (17)
O2–Ni1–N2	178.83 (17)
O1–Ni1–N2	94.61 (17)
N1–Ni1–N2	86.30 (19)

### 6.3.2.2 UV-vis spectral studies

The UV-vis spectra of Complex **6.1** and **6.2** have been recorded in the range of 200–800 nm in DMF at room temperature (**Figure 6.5**). A broad band is observed at 684 nm ( $\epsilon = 13.5 \text{ M}^{-1} \text{ cm}^{-1}$ ) for Complex **6.1** and 767 nm ( $\epsilon = 15.76 \text{ M}^{-1} \text{ cm}^{-1}$ ) for Complex **6.2**, which may be attributed to the  $d-d$  transition. Since, both the complexes are almost centro-symmetric, it allows very little mixing of  $d$  and  $p$  orbitals in metal center. The bands at 270 nm ( $\epsilon = 135810 \text{ M}^{-1} \text{ cm}^{-1}$ ) for Complex **6.1** and 277 nm ( $\epsilon = 128910 \text{ M}^{-1} \text{ cm}^{-1}$ ) for Complex **6.2** may be assigned to  $n-\pi^*$  transitions of the C=N groups. Another band at 318 nm ( $\epsilon = 50550 \text{ M}^{-1} \text{ cm}^{-1}$  for complex **6.1** and  $83420 \text{ M}^{-1} \text{ cm}^{-1}$  for Complex **6.2**) for both the complexes may be attributed to ILCT (intra-ligand charge transfer). The higher intensity charge-transfer transition has been observed

at 425 nm ( $\epsilon = 14860 \text{ M}^{-1} \text{ cm}^{-1}$ ) for Complex **6.1** and 393 nm ( $\epsilon = 42350 \text{ M}^{-1} \text{ cm}^{-1}$ ) for Complex **6.2**. These are attributed to  $\text{O}^-$  (of naphthalen-1-olate)  $\rightarrow$  Metal(II), N(amino)  $\rightarrow$  Metal(II) LMCT (transfer occurs from the MO with ligand-like character to the metal-like one) transitions.

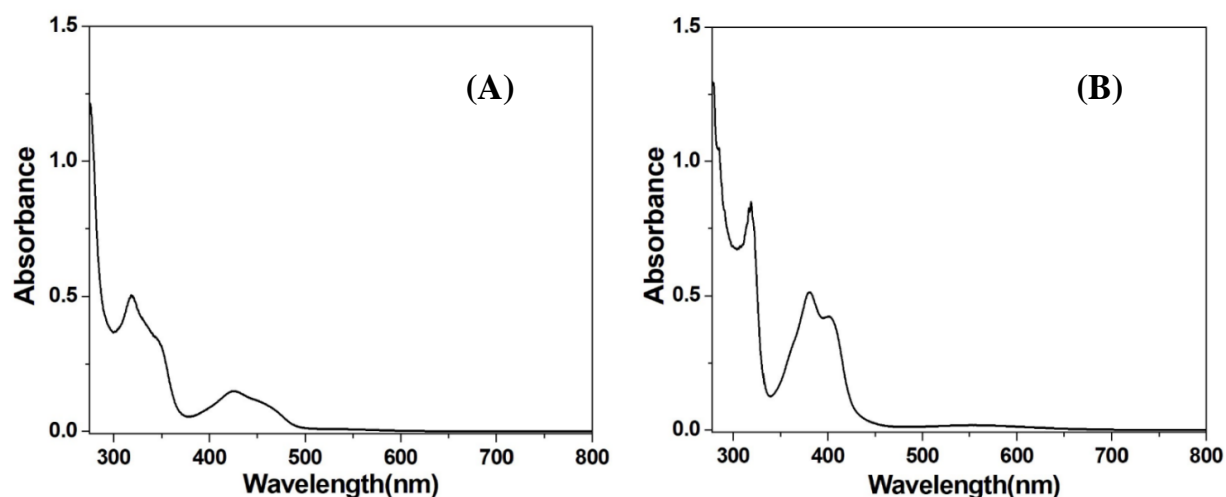


**Figure 6.5:** UV-vis spectra of (A) Complex **6.1** and (B) Complex **6.2** in DMF.

### 6.3.2.3 FTIR spectral studies

The FTIR spectra of Complex **6.1** and Complex **6.2** show typical changes for Schiff base coordination when compared with the FTIR spectrum of the corresponding ligand (**Figure 6.6** and **6.7**). The presence of hydrocarbon part has been evidenced by the appearance of characteristic unsymmetrical and symmetrical frequencies of  $\nu_{\text{C-H}}$  observed in the spectra. For aromatic C-H bond,  $\nu_{\text{C-H}}$  has been observed at  $3050 \text{ cm}^{-1}$  for Complex **6.1** and  $3061 \text{ cm}^{-1}$  for Complex **6.2** whereas the corresponding value for free ligand is  $3044 \text{ cm}^{-1}$ . The bands observed at the range of  $2964\text{--}2856 \text{ cm}^{-1}$  for Complex **6.1** and  $2980\text{--}2874 \text{ cm}^{-1}$  for Complex **6.2** may be assigned to  $\nu_{\text{C-H}}$  for aliphatic C-H bond. The corresponding peak for free  $\text{H}_2\text{L}$  appears at  $2953 \text{ cm}^{-1}$ . An intense band at  $1604 \text{ cm}^{-1}$  for Complex **6.1** and  $1613 \text{ cm}^{-1}$  for Complex **6.2** is observed due to the stretching vibration of the azomethine group. The conclusive evidence for the formation of Ni–N and Ni–O bonds in the IR spectrum of Complex **6.1** is also shown by the appearance of new bands at around  $425$  and  $590 \text{ cm}^{-1}$  which may be attributed to  $\nu_{\text{Ni-N}}$  stretching frequency and  $\nu_{\text{Ni-O}}$  stretching frequency respectively. Similarly, for Complex **6.2** the bands at  $531$  and  $413 \text{ cm}^{-1}$  give the evidence for the formation of Cu–N and Cu–O bonds, respectively. These bands suggest that the metallic ion has effectively coordinated to the four coordinating heteroatoms (ONON).

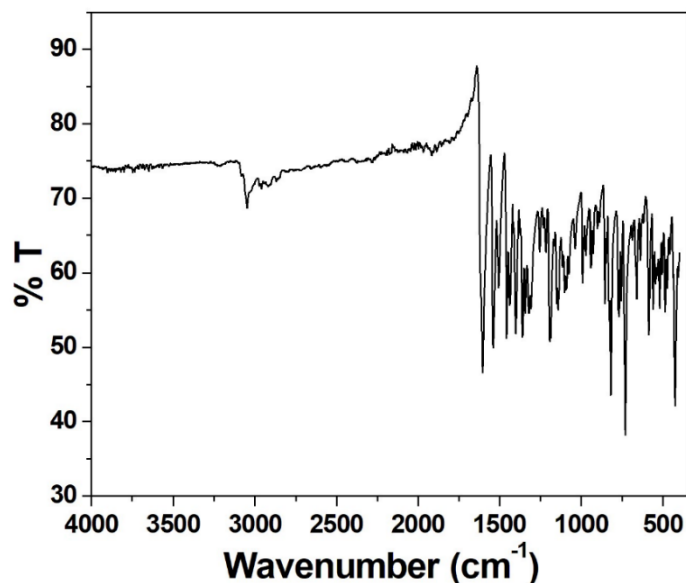


Figure 6.6: FTIR spectrum of complex 6.1.

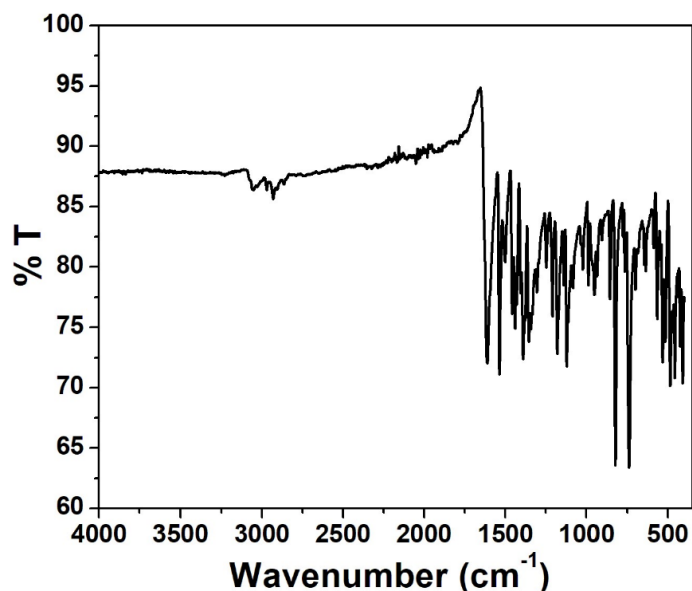
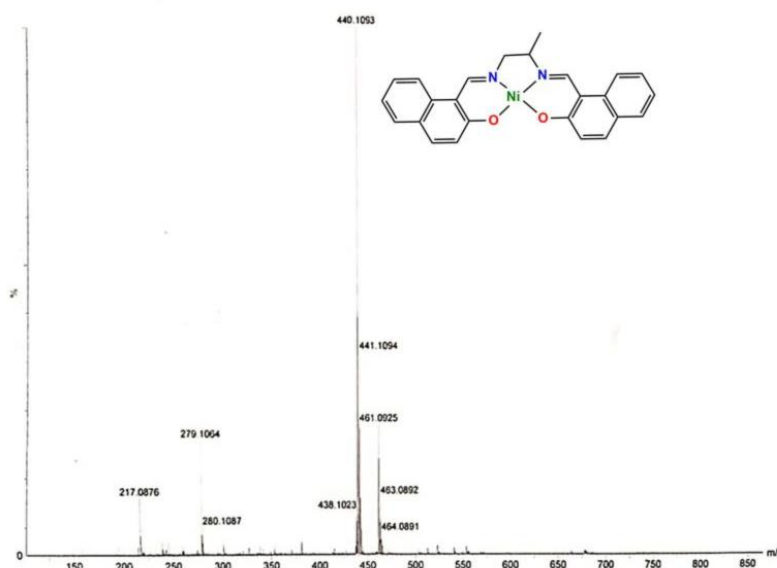


Figure 6.7: FTIR spectrum of complex 6.2.

#### 6.3.2.4 ESI-mass spectral studies

ESI-mass spectra of Complex **6.1** and **6.2** have been obtained with their methanolic solutions (Figure 6.8 and 6.9). Mass spectrum of **6.1** exhibits the most intense peak at an  $m/z$  value of 440.11 which may be attributed to the  $\{[\text{Ni}(\text{L})] + \text{H}^+\}$  species (calculated value 440.14). For Complex **6.2**, the most intense peak is observed at an  $m/z$  value of 444.10, which may be attributed to the  $\{[\text{Cu}(\text{L})] + \text{H}^+\}$  species (calculated value 444.09). The results indicate the formation of these complexes and also suggest both the complexes exist mainly as mononuclear species in methanol solution.



**Figure 6.8:** Mass spectrum of Complex **6.1** in methanol.

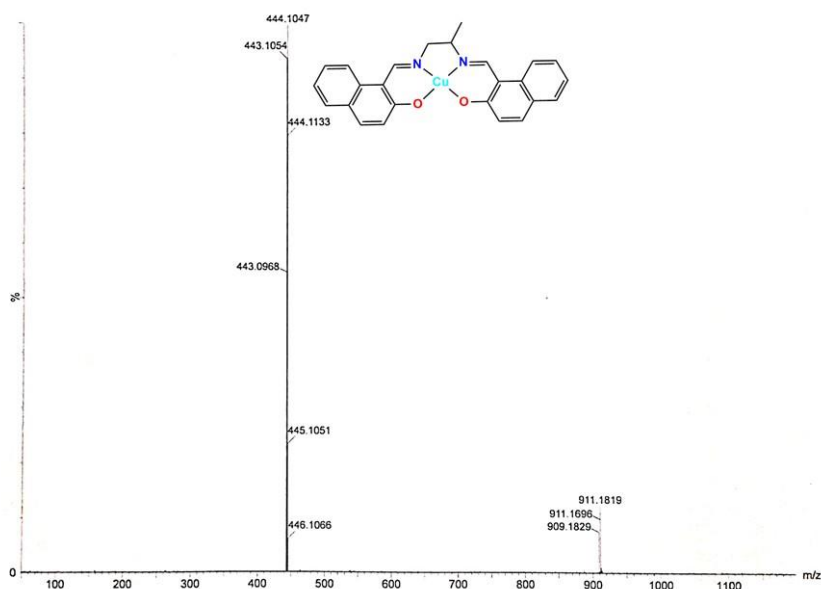


**Figure 6.9:** Mass spectrum of Complex **6.2** in methanol.

### 6.3.2.5 Electrochemistry

#### 6.3.2.5.1 Cyclic voltammetric studies

Cyclic voltammograms of both the complexes (0.5 mM) have been recorded at a scan rate of  $50 \text{ mV s}^{-1}$  in air-free DMF containing 0.1 M TBAB at a freshly polished graphite carbon electrode in the range of  $-2.0 \text{ V}$  to  $+0.5 \text{ V}$  versus  $\text{Fc}/\text{Fc}^+$  (**Figure 6.10**). For Complex **6.1**, central feature of the cyclic voltammogram is the presence of nickel(II)–nickel(I) redox couple with a cathodic peak potential ( $E_{\text{pc}}$ ) of  $-1.76 \text{ V}$  and an anodic peak potential ( $E_{\text{pa}}$ ) of  $-1.36 \text{ V}$ .<sup>6.23</sup> Another nickel(III)–nickel(II) redox couple is observed with a cathodic peak potential ( $E_{\text{pc}}$ ) of  $-1.09 \text{ V}$  and an anodic peak potential ( $E_{\text{pa}}$ ) of  $-0.84 \text{ V}$ .<sup>6.24</sup> The central feature of the cyclic

voltammogram of Complex **6.2** is the copper(II)–copper(I) redox couple with a cathodic peak potential ( $E_{pc}$ ) of -1.54 V and an anodic peak potential ( $E_{pa}$ ) of -1.01 V. When the potential window has been set to -2.0 V to +2.0 V, for both the complexes, a peak around -0.02 V appeared for the solvent DMF and another redox event for the Fc/Fc<sup>+</sup> couple is observed for each of the complexes at  $E_{1/2} = 0.5$  V (**Figure 6.10** inset).

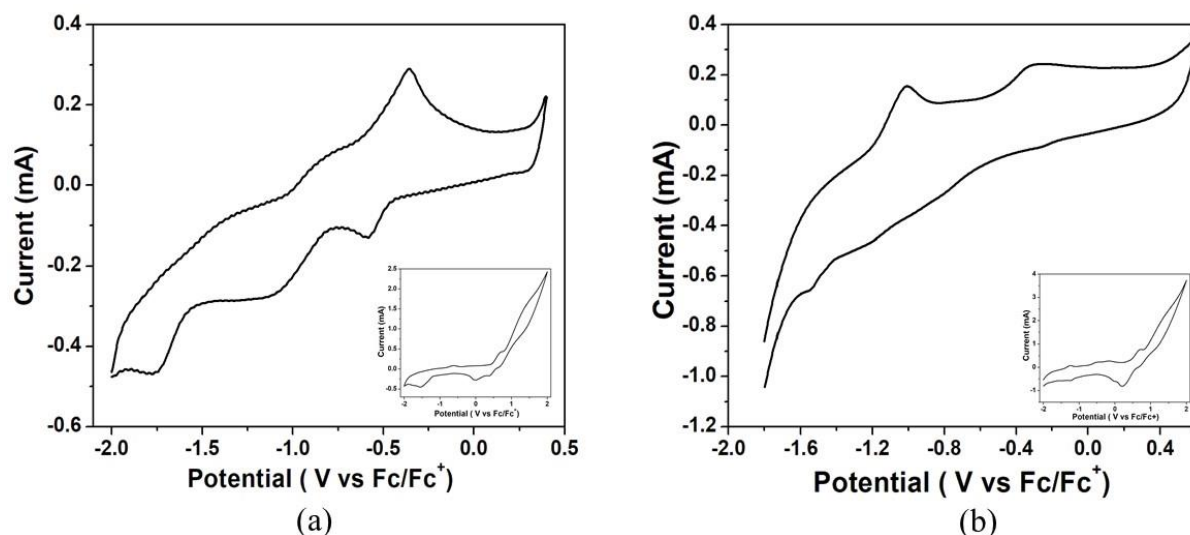


**Figure 6.10:** Cyclic voltammograms of (a) Complex **6.1** and (b) Complex **6.2** in air free DMF solutions with 0.1 M of TBAB as supporting electrolyte at a scan rate of 50 mV/s electrode in the range of -2.0 V to +0.5 V versus Fc/Fc<sup>+</sup> (Inset: Cyclic voltammograms in the -2.0 V to +2.0 V versus Fc/Fc<sup>+</sup> region).

Analyses of the cathodic current for Complex **6.1** and **6.2** in DMF at the multiple scan rates from 0.02 to 0.25 V/s have been used to construct a Cottrell plot **Figure 6.11**. The plots depict linear dependence of the current response on the square root of the scan rate (**Figure 6.11**). This indicates that for both the complexes, the reduction is diffusion limited with a diffusion coefficient of  $0.88 \times 10^{-3}$  for Complex **6.1** and  $1.57 \times 10^{-3}$  for Complex **6.2**.

#### Determination of Diffusion Coefficient (D) for complex 6.1 and complex 6.2

Using the Randles-Sevcik equation,

$$i_p = 0.4463 \left( \frac{n^3 F^3}{RT} \right)^{1/2} A[cat](Dv)^{1/2}$$

where,  $i_p$  = peak current (amperes),  $n$  = number of electrons transferred in a redox cycle,  $F$  = Faraday's constant (96485 C/mol),  $R$  = universal gas constant (8.314 J.K<sup>-1</sup>.mol<sup>-1</sup>),  $T$  = absolute temperature (298 K),  $A$  = the electrode surface area in working electrode (0.12 cm<sup>2</sup>),  $C$  = molar concentration of redox-active species (mol/cm<sup>3</sup>),  $D$  = the diffusion coefficient (cm<sup>2</sup>/s),  $v$  = scan rate in V/s.

Plotting peak current ( $i_p$ ) versus the square root of the scan rate ( $v$ )<sup>1/2</sup>

$$\text{Slope} = 0.4463 \left( \frac{n^3 F^3}{RT} \right)^{1/2} A[\text{cat}](D)^{1/2}$$

Complex	Slope	Diffusion coefficient (cm <sup>2</sup> /s)
<b>6.1</b>	0.048	$0.88 \times 10^{-3}$
<b>6.2</b>	0.064	$1.57 \times 10^{-3}$

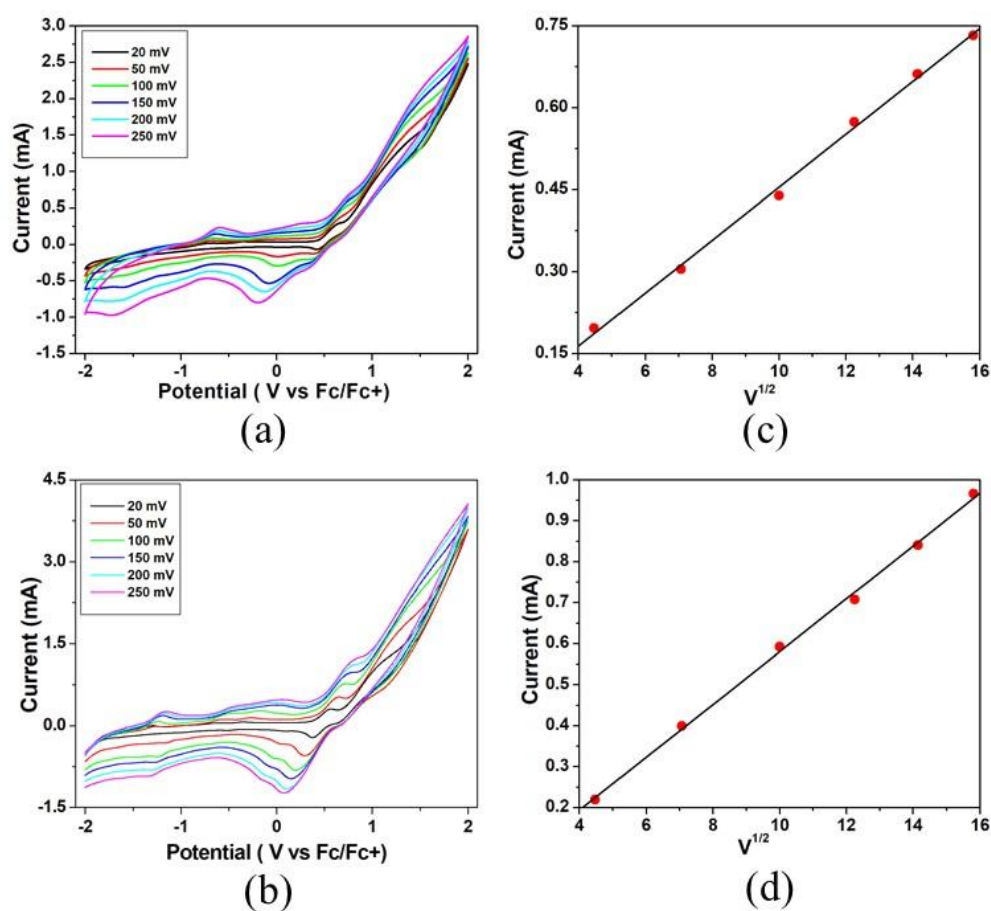


**Figure 6.11:** Scan rate dependence of precatalytic waves for 0.5 mM solutions of (a) complex **6.1** and (b) complex **6.2** at scan rate from 0.02 to 0.25 V/s in DMF solutions with 0.1M TBAB as supporting electrolyte and Cottrell plot of peak current versus the square root of scan rate for (c) complex **6.1** and (d) complex **6.2**.

### 6.3.2.5.2 Electrocatalytic Hydrogen Evolution in DMF: CV Studies

The performance of Complex **6.1** and **6.2** as effective electrocatalysts for the hydrogen evolution reaction has been investigated in DMF under nitrogen atmosphere using acetic acid as a proton source ( $pK_a = 13.5$ ).<sup>6.25</sup> The addition of  $\text{CH}_3\text{COOH}$  aliquots from 0.00 to 35.00 mM to the solutions of **6.1** and **6.2** in DMF triggers the systematic increase in catalytic current ( $i_{\text{cat}}$ )

at  $-1.76$  V and  $-1.54$  V respectively, versus  $\text{Fc}/\text{Fc}^+$  (Figure 6.12). The current enhancement occurs in the presence of both the complexes with the increase in the concentration of acid, is a signature of electro-catalytic proton reduction. It has been observed that the catalytic to peak current ratio ( $i_{\text{cat}}/i_{\text{p}}$ ) increases linearly for both the complexes with increasing acid concentration (Figure 6.13).

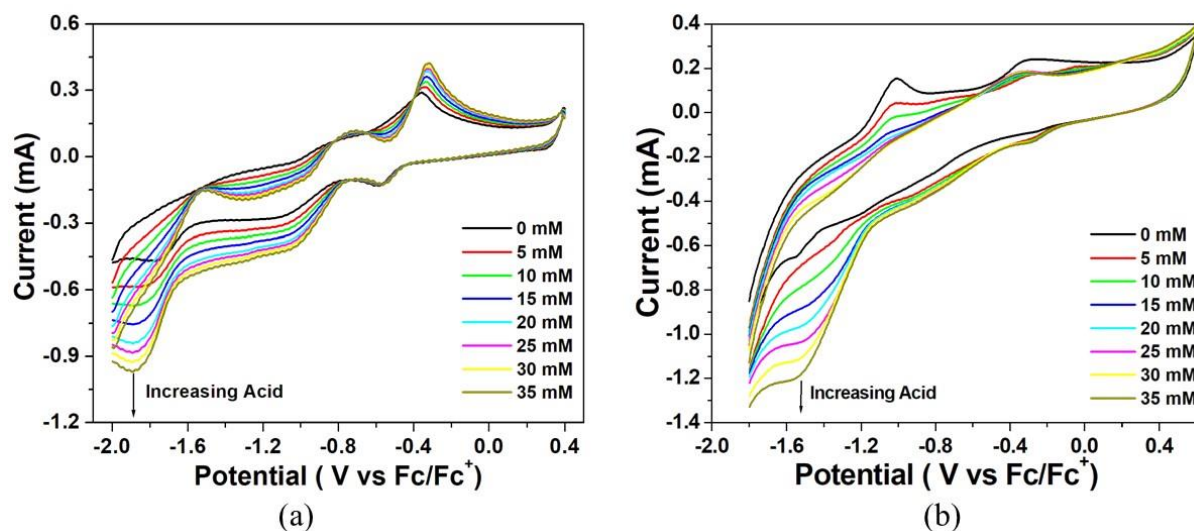


**Figure 6.12:** Cyclic voltammograms of a 0.5 mM of (a) complex 6.1 and (b) complex 6.2 in air free DMF with varying concentrations of acetic acid. Conditions: Graphite carbon working electrode, Pt counter electrode, Ag/AgCl reference electrode, 0.1 M TBAB as supporting electrolyte, scan rate of 50 mV/s. Ferrocene as an internal standard.

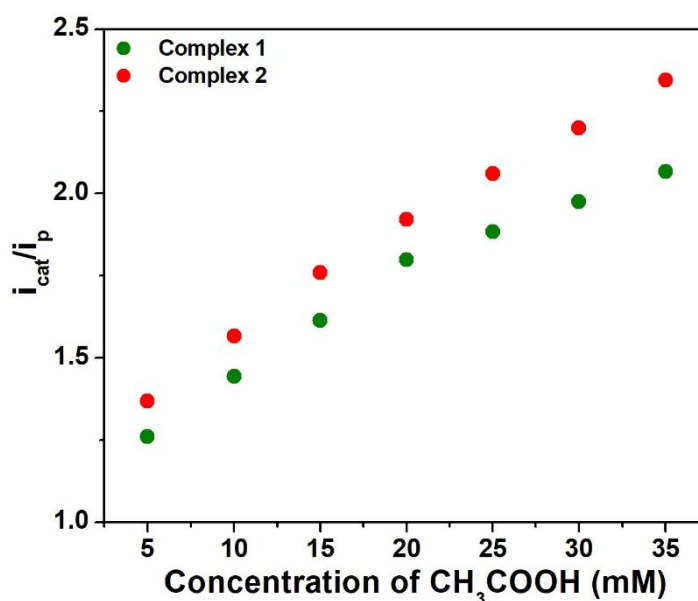


**Figure 6.13:** Plot of  $i_{\text{cat}}/i_{\text{p}}$  vs  $[\text{CH}_3\text{COOH}]$  for 0.5 mM of complex 6.1 and complex 6.2 at scan rate of  $50 \text{ mVs}^{-1}$ .



This is to note that the position of the peak is independent of the acid concentration and corresponds to a one-electron reduction of the protonated complex to complex-H.<sup>6,26</sup> Moreover, for both the complexes, the catalytic current strength at the potential corresponding to Metal(II) – Metal(I) decreases with the addition of triethylamine (TEA) (**Figure 6.14**). This finding can be attributed to the neutralization of hydrogen proton in Metal-H by TEA. These results can be attributed to the fact that the reduction of Metal(II) to Metal(I) and protonation are possibly responsible for hydrogen generation in the above electrocatalytic system.

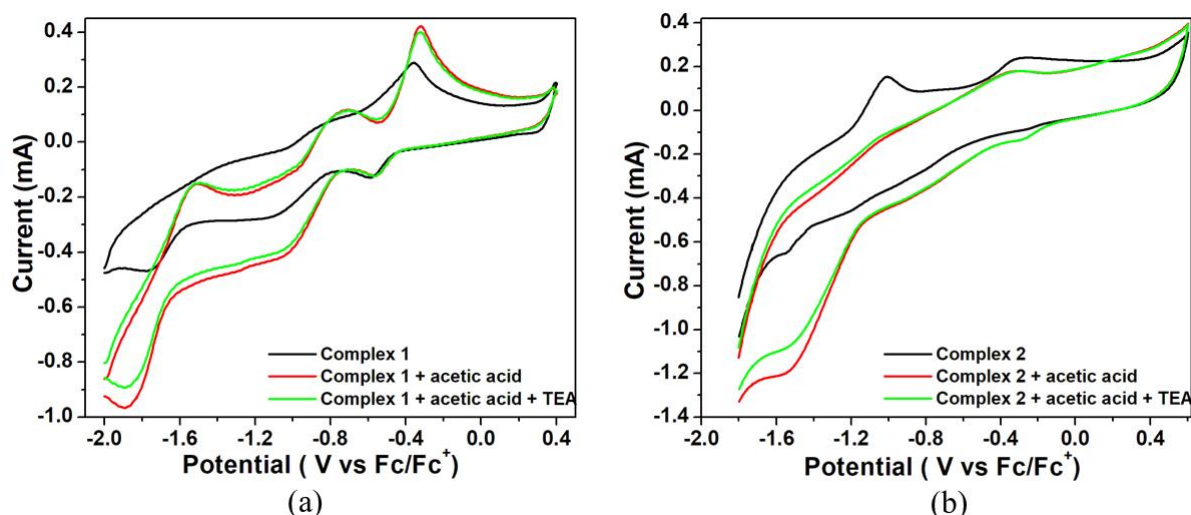
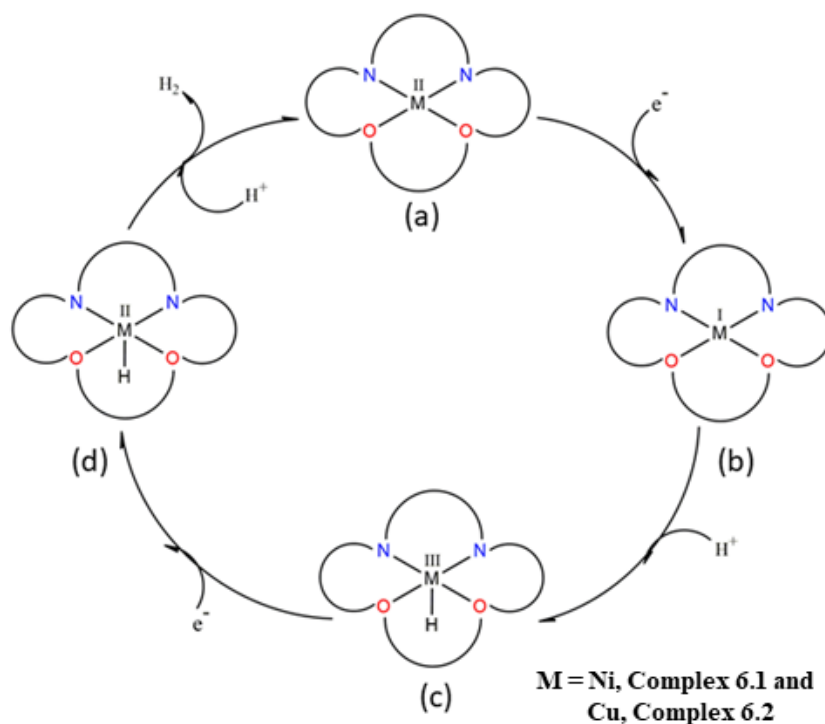


**Figure 6.14:** Cyclic voltammograms of 0.5 mM (a) complex **6.1** and (b) complex **6.2** in air free DMF (black), in presence of acetic acid (red); in presence of acetic acid and triethylamine (TEA). Conditions: Graphite carbon working electrode, Pt counter electrode, Ag/AgCl reference electrode, 0.1 M TBAB as supporting electrolyte, scan rate 50 mV/s. Ferrocene internal standard.

An electrocatalytic cycle for proton reduction to hydrogen is proposed (**Scheme 6.2**) on the basis of the above observations and literature precedent.<sup>6,27</sup> It is evident from the scheme that the Metal (I) species (b) is obtained by one-electron reduction of Metal (II) species (a). Then the introduction of hydrogen proton ( $H^+$ ) results in the formation of one Metal (III)-H species (c). Another one-electron reduction of the Metal (III)-H species leads to the formation of the Metal (II)-H species (d). Dihydrogen is afforded by further introduction of hydrogen proton ( $H^+$ ) along with the regeneration of the starting sample.



**Scheme 6.2:** A possible electrocatalytic mechanism for proton reduction to hydrogen by Complex **6.1** and **6.2**.

From the probable electrocatalytic mechanism for the reduction of proton to hydrogen in the presence of Complex **1** and **2**, it is evident that the conversion of metal(II) to metal(I) during the electrocatalytic process is an important step. This step is much more feasible for copper(II) complex than that of nickel(II) complex as  $d^9$  configuration of Cu(II) is converted to more stable configuration (Cu(I) [ $d^{10}$ ]), whereas [ $d^8$ ] configuration of Ni(II) is converted to [ $d^9$ ] configuration. Moreover, redox potential values of copper(II)–copper(I) redox couple and nickel(II)–nickel(I) redox couple also support this fact. These may be the possible reason for better catalytic activity of copper complex than nickel complex.

Over potential for hydrogen evolution has been calculated using following methods reported by Fourmond et al.<sup>6.25</sup> from the theoretical half wave potential,  $E_{1/2}^T$  and the experimental potential  $E_{\text{cat}/2}$  (**Equation 6.1**).

$$\text{Over potential}(\eta) = |E_{1/2}^T - E_{\text{cat}/2}| \dots \dots \dots (6.1)$$

Based on Equation 6.1, this reduction occurs at an over potential of 0.29 V and –0.13 V for complex **6.1** and **6.2**, respectively. Thus, the catalytic activity of the both the homogeneous catalysts as obtained from the overpotential value is in the order: Complex **6.2** > Complex **6.1**.

#### Over potential Calculations:

Calculations of  $E_{1/2}^T (= E_{\text{ref}})$  and  $\eta$  using  $E_{\text{H}^+/\text{H}_2}^0$ ,  $pK_a$ ,  $\epsilon_D$  and  $C_{\text{H}_2}^0$  using Fourmond's approach.

$$E_{1/2}^T = E_{H^+/H_2}^0 - 2.303 \frac{RT}{F} pK_a + \epsilon_D - \frac{RT}{2F} \ln \frac{C_0}{C_{H_2}^0}$$

$E_{1/2}^T$  for Complex **6.1** and **6.2** with 35mM CH<sub>3</sub>COOH in DMF

$$E_{1/2}^T = (-0.62) - 2.303 \frac{8.314 \times 298}{96485} 13.5 + 0.04 - \frac{8.314 \times 298}{2 \times 96485} \ln \frac{35}{1.9}$$

$$E_{1/2}^T = -1.41 \text{ vs } Fc^+/Fc$$

Complex	Overpotential
6.1	-1.41-(-1.70) = 0.29
6.2	-1.41-(-1.27) = -0.13

### 6.3.2.5.3 Stability analysis of the catalyst

The stability of Complex **6.1** and **6.2** have been checked by repeated cyclic voltammetry (CV) studies upto 200 cycles using acetic acid as proton source (**Figure 6.15**). It has been observed that no new peaks are generated in the CV for both the complexes and also the colour of the solutions remain the same during the study.

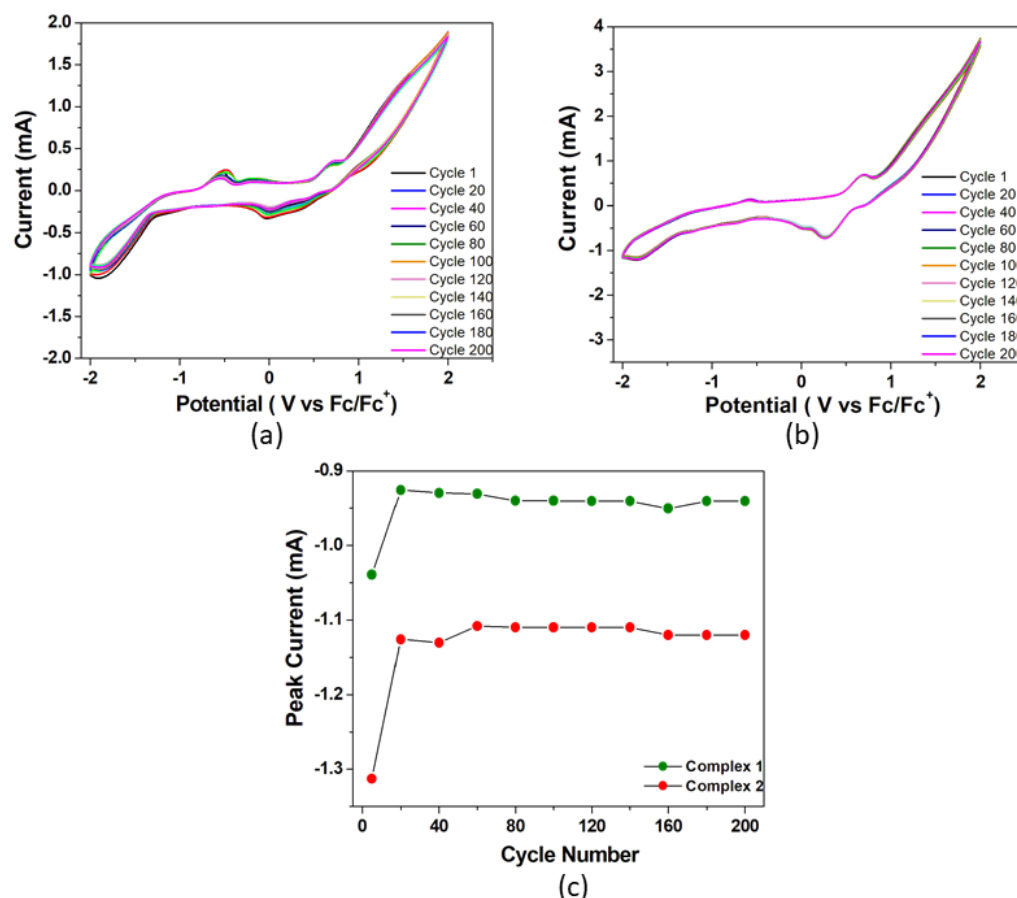


**Figure 6.15:** Repeated cyclic voltammetry studies of (a) complex **6.1** and (b) complex **6.2**, (c) Peak current vs. cycle number profiles for both the complexes.

In both cases, at first, the reduction peak current increases and reaches almost steady value after 15<sup>th</sup> cycle for Complex **6.1** and 10<sup>th</sup> cycle for Complex **6.2**. The peak current with respect to the lowest amount is increased by 10% for Complex **6.1** and 18% for Complex **6.2**. The current of Complex **6.2** is always greater than that of Complex **6.1**. The enhancement in reduction peak current during repeated cyclic voltammetric operation might be due to the cleansing of the fine surface of the electrode and opening up of new channels by initial H<sup>+</sup> ion penetration at the metal center and associated H<sub>2</sub> evolution. Thus, more active sites of the electrode surface are opened up for further reaction.

#### 6.3.2.5.4 Electrocatalytic Hydrogen Evolution: CPE Studies

Evidence for the electrocatalytic activity of **6.1** and **6.2** for HER has been evaluated in DMF by conducting Controlled-potential electrolysis (CPE) experiments over a period of 1 h. **Figure 6.16** shows the total charge of bulk electrolysis of 0.5 mM of Complex **6.1** and **6.2** separately in DMF in the presence of 35 mM of acetic acid. Results are summarized in **Table 6.3**.

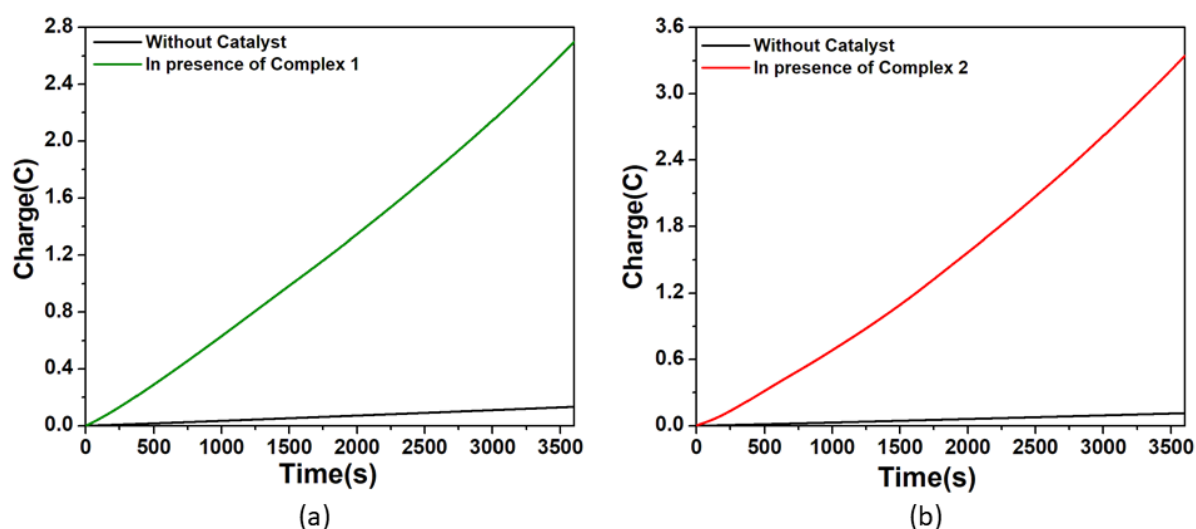


**Figure 6.16:** Charge buildup vs time plots in the CPE experiments of (a) Complex **6.1** at potential  $-1.76$  V versus  $\text{Fc}/\text{Fc}^+$  and (b) Complex **6.2** at  $-1.54$  V versus  $\text{Fc}/\text{Fc}^+$ . Conditions: 0.5 mM of the complex in air free DMF with 0.1 M TBAB as supporting electrolyte and 35 mM  $\text{CH}_3\text{COOH}$  as the proton source.

At an applied potential of  $-1.76$  V versus  $\text{Fc}/\text{Fc}^+$  for Complex **6.1** and  $-1.54$  V versus  $\text{Fc}/\text{Fc}^+$  for Complex **6.2**, the maximum charges reached during 1 h of electrolysis are 2.7 C and 3.4 C respectively, accompanied by appearance of gas bubbles on surface of the electrode (**Figure 6.17**). However, CPE experiments under the respective potentials, the solution without any catalyst gives a charge of only 0.1 C. This study suggests that both these complexes are capable of catalysing the reduction of protons from the acid to H<sub>2</sub>. Controlled-potential

electrolysis is associated with  $1.34 \times 10^{-5}$  moles of  $H_2$  produced with a turnover number (TON) of 2.7 for Complex **6.1** and  $1.71 \times 10^{-5}$  moles of  $H_2$  produced with a TON of 3.4 for Complex **6.2** (Table 6.4). Gas chromatography has been used to analyse the headspace sample and the results confirm the evolution of  $H_2$  as the gaseous product (Figure 6.18). The Faradic efficiency has been calculated for both the complexes from the ratio of moles of  $H_2$  produced in the controlled potential electrolysis to theoretical moles of  $H_2$ . The Faradic efficiency obtained for Complex **1** and **2** after 1 h of electrolysis is 66.41% and 77.77%, respectively (Table 6.5).



**Figure 6.17:** Photograph of the customized, one-compartment, three-neck cell with a graphite working electrode containing 0.5 mM of complex **6.1** in air free DMF, 35 mM acetic acid and 0.1 M TBAB as supporting electrolyte.  $H_2$  gas bubbles are appeared on the surface of the working electrode.

**Table 6.3:** Results of CPE experiments with Complex **6.1** and **6.2**.

Complex	Solvent	Acid	q (C)	n ( $\times 10^{-5}$ )	TON	TOF ( $s^{-1}$ )	Faradic efficiency (%)
<b>6.1</b>	DMF	Acetic	2.6	1.34	2.7	653.10	66.41
<b>6.2</b>		acid	3.3	1.71	3.4	777.53	77.77

**Table 6.4:** TON calculations

Complex in DMF	$q_{total} = q_{cat} - q_{blank}$	Theoretical moles of hydrogen produced = $q_{total} \times (1$	Moles of catalyst used	TON = Theoretical moles of $H_2$ / Moles of catalyst used
----------------	-----------------------------------	--	------------------------	---

		$\text{mol e}^- / 96485 \text{ C}) \times$		
		$(1 \text{ mol H}_2 / 2 \text{ mol e}^-)$		
<b>6.1</b>	2.6	$1.34 \times 10^{-5}$	$5 \times 10^{-6}$	2.7
<b>6.2</b>	3.3	$1.71 \times 10^{-5}$	$5 \times 10^{-6}$	3.4

### Calculation of Faradaic Efficiency

$$\text{Faradaic Efficiency} = \frac{\text{Quantified moles of H}_2}{\text{Theoretical moles of H}_2} \times 100\%$$

**Table 6.5:** Calculations of Faradaic Efficiency

Complex	Quantified moles of H <sub>2</sub>	Theoretical moles of H <sub>2</sub>	Faradaic Efficiency (%)
6.1	$0.89 \times 10^{-5}$	$1.34 \times 10^{-5}$	66.41
6.2	$1.33 \times 10^{-5}$	$1.71 \times 10^{-5}$	77.77

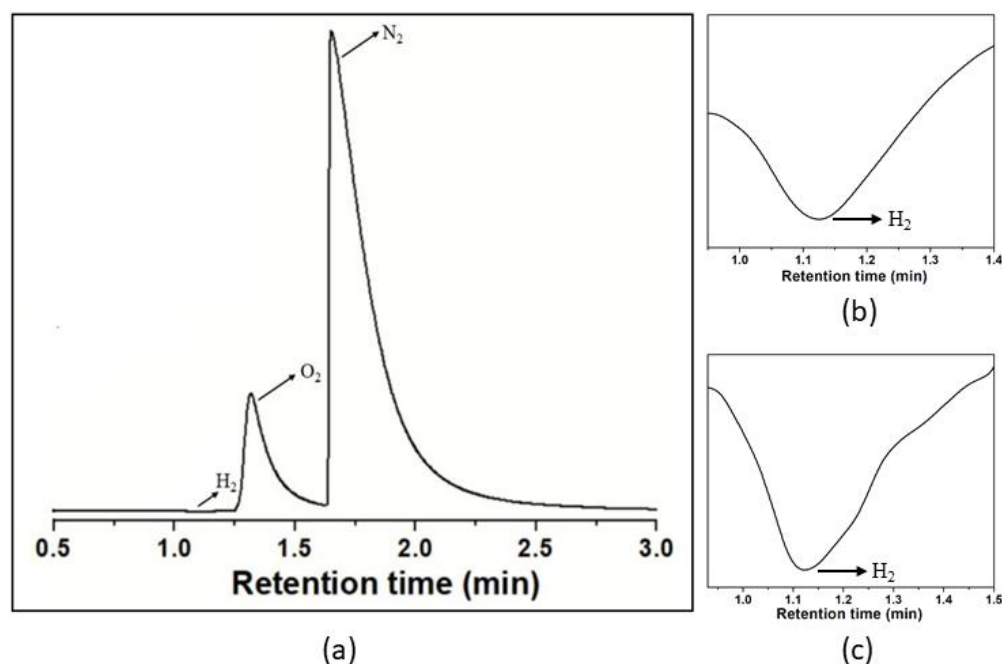


**Figure 6.18:** (a) Gas chromatogram of the headspace gas obtained after bulk electrolysis of a N<sub>2</sub> saturated 0.5 mM solution of complex **6.1** and complex **6.2** containing 35 mM acetic acid. The headspace gas was analysed after 1 hour of electrolysis. Detection region of evolved H<sub>2</sub> gas for (b) complex **6.1** and (c) complex **6.2**.

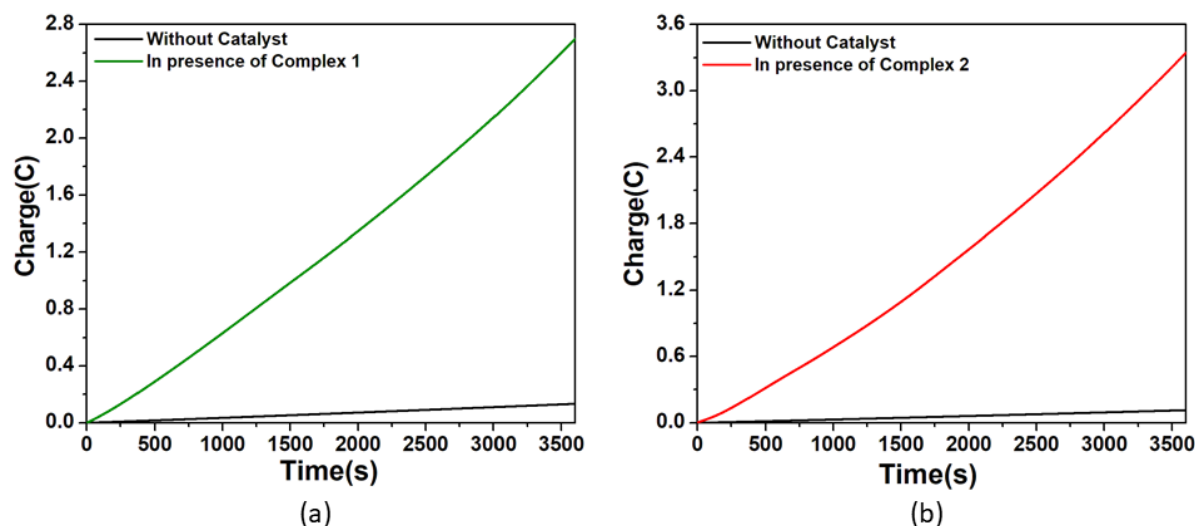


**Figure 6.19:** Charge buildup vs time plots in the CPE experiments of (a) Complex **6.1** at potential  $-1.76$  V versus  $Fc/Fc^+$  and (b) Complex **6.2** at  $-1.54$  V versus  $Fc/Fc^+$ . Conditions:  $0.5$  mM of the complex in air free DMF with  $0.1$  M TBAB as supporting electrolyte and  $35$  mM  $CH_3COOH$  as the proton source.

The turnover frequency (TOF) for hydrogen evolution using Complex **6.1** and **6.2** as electrocatalysts has been estimated using the foot-of-the-wave analysis (FOWA).<sup>6.28</sup> FOWA has been considered near the foot of the catalytic wave where the catalytic wave does not get affected much by phenomena like substrate consumption, diffusion and shape of CV is dominated mainly by catalytic phenomenon.<sup>6.29</sup> The  $i_{cat}/i_p$  has been plotted against  $1/(1 + \exp [(F/RT)(E-E_{1/2})])$  for both the complexes as given in **Figure 6.19**, which stretches a linear function at a scan rate of  $50$  mVs<sup>-1</sup>. Thus, the TOF values obtained for Complex **6.1** and **6.2** are  $653.1$  s<sup>-1</sup> and  $777.5$  s<sup>-1</sup>, respectively.

**TOF Calculations:**

For homogenous, diffusion controlled process the peak current can be given by Randle Sevcik equation

$$i_p = 0.4463FS C_p^0 \sqrt{\frac{FvD}{RT}} \dots\dots\dots(6.2)$$

$$i_{cat} = \frac{2FS C_p^0 \sqrt{\frac{FvD}{RT}}}{1 + \exp \left[ \frac{F}{RT} (E - E_{1/2}) \right]} \dots\dots\dots(6.3)$$

where, F is the Faraday’s constant, S is the surface area of electrode,  $C_p^0$  is the concentration of the complex in solution, D is the diffusion coefficient,  $E_{1/2}$  the half-wave potential of the redox couple triggering catalysis, R is the gas constant and T is the absolute

temperature. Combining the equation (6.2) and (6.3) we get the equation (6.4). The plot of  $i_{cat}/i_p$  vs  $1/(1+\exp[(F/RT)(E-E_{1/2}]$ ) (**Figure 6.20**) gives access of the observed rate constant ( $k_{obs}$ ).

$$\frac{i_{cat}}{i_p} = \frac{2}{0.4463} \sqrt{\frac{RT(K_{obs})}{Fv}} \frac{1}{1 + \exp\left[\frac{F}{RT}(E - E_{1/2})\right]} \dots\dots\dots(6.4)$$

$$Slope = \frac{2}{0.4463} \sqrt{\frac{RT(K_{obs})}{Fv}} \dots\dots\dots(6.5)$$

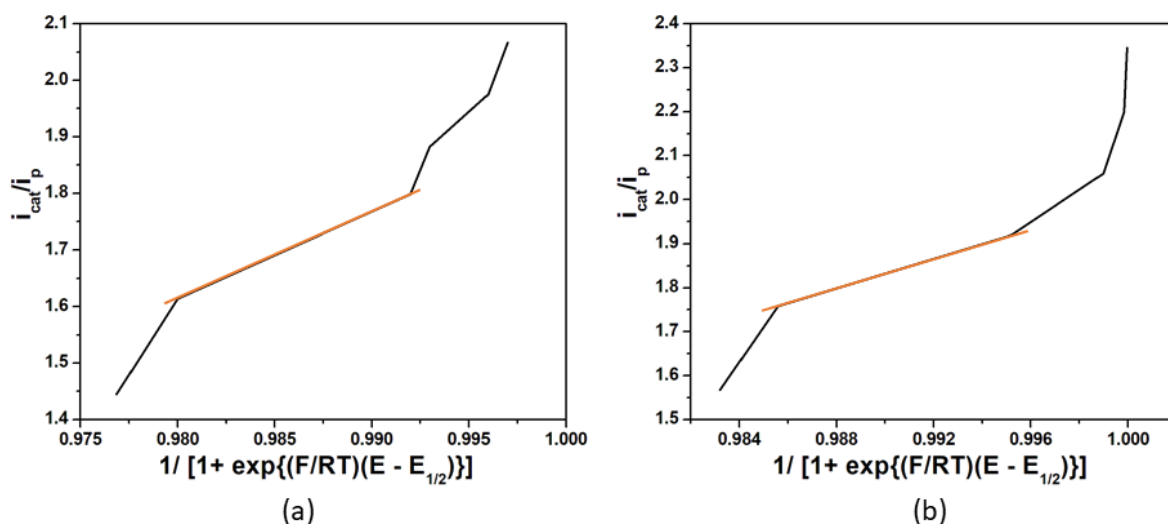


**Figure 6.20:** Plot of  $i_{cat}/i_p$  vs.  $1/(1+\exp[(F/RT)(E-E_{1/2}]$ ) using FOWA of 0.5 mM of (a) Complex **6.1** and (b) Complex **6.2** with 35 mM  $CH_3COOH$  in DMF at  $50\text{ mV s}^{-1}$ . The experimental data (black) can be fitted linearly near the foot of the catalytic wave and the slope (red) giving the access to the observed rate constant,  $k_{obs}$ .

Complex	Slope	$K_{obs}(s^{-1})$	$C_H^0(M)$	$K_{cat} = (K_{obs}/ C_H^0) (M^{-1}s^{-1})$	TOF ( $s^{-1}$ )
6.1	15.35	22.86	0.035	653.10	653.10
6.2	16.75	27.21		777.53	777.53

### 6.3.2.5.5 Electrocatalytic Hydrogen Evolution: Control Experiments

To confirm the HER observed is associated with Complex **6.1** and **6.2** in solution and not due to surface adsorbed complex or degradation products, different control experiments have been performed. First, blank CV has been collected in the presence of  $CH_3COOH$  without the addition of either Complex **6.1** or Complex **6.2** and the results show no measurable current at potentials associated with hydrogen evolution (**Figure 6.21**). Then CVs of Complex **6.1** and **6.2** in DMF with acetic acid as the substrate have been obtained to confirm HER activity. To ensure that the HER activity is due to neither because of a film of the catalyst compound nor its degradation product which could be strongly absorbed on the electrode surface, the graphite carbon working electrode has been removed from the respective solutions and washed with the



deionized water but not polished. Immersion of the electrode into a fresh working solution containing the acid and electrolyte shows no observable catalytic current in the cathodic region. Thus, the above findings strongly suggest that both the complexes are efficient electrocatalysts towards HER.

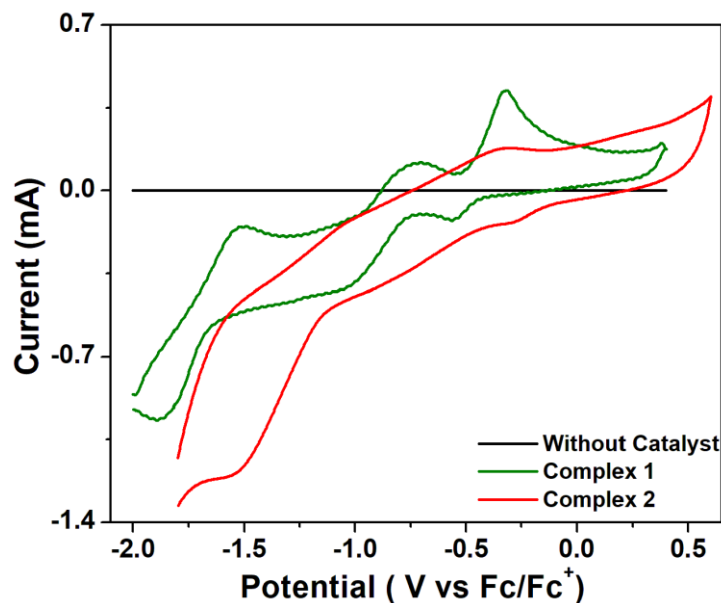


**Figure 6.21:** CVs showing blank DMF with 35 mM  $\text{CH}_3\text{COOH}$  added (black) and with 35 mM  $\text{CH}_3\text{COOH}$  in the presence of 0.5 mM complex **6.1** (green) and complex **6.2** (red). Conditions: room temperature Graphite carbon working electrode, Pt counter electrode, Ag/AgCl reference electrode, 0.1 M TBAB as supporting electrolyte, scan rate 50 mV/s. Ferrocene internal standard.

### 6.3.2.5.6 Comparative discussion

A comparative discussion has been made with the recently published results<sup>6.30</sup> with respect to the present study (**Table 6.6**). It may be noticed that for all the cases, proton source is either acetic acid or trifluoroacetic acid or both. Solvent is generally organic (except Entry 5). TOF value reported can be compared with the present study. Some of catalysts produce higher TOF values (Entry 1, 3, 4). However, many of them show lower TOFs compared to Complex **6.1** and Complex **6.2** (Entry 8). In most of the cases, Ni-complex has been used as the catalyst. Ni- and Cu-complexes with the same ligand have rarely been used as catalyst in HER.

**Table 6.6:** Values of TOF of recently published complexes used as electrocatalyst for hydrogen evolution reaction

Entry	Catalyst	Proton source	Solvent	TOF	Ref.
1	$\text{Ni}_3(\text{L}^{\text{N}_2\text{S}_2})_2$	acetic acid	acetonitrile	$3495 \text{ s}^{-1}$	[6.28a]

2	Complex 1 (Ni)	trifluoro	DMF	46 s <sup>-1</sup>	[6.28b]
	Complex 2 (Ni)	acetic acid		32 s <sup>-1</sup>	
	Complex 3 (Ni)			102 s <sup>-1</sup>	
3	NiL <sup>1</sup>	trifluoro	acetonitrile	1324 s <sup>-1</sup>	[6.28c]
		acetic acid	DMF	115 s <sup>-1</sup>	
		acetic acid	acetonitrile	4161 s <sup>-1</sup>	
			DMF	1196 s <sup>-1</sup>	
4	Complex 1 (Ni)	acetic acid	acetonitrile	63827.5 s <sup>-1</sup>	[6.28d]
	Complex 2 (Cu)			70139.5 s <sup>-1</sup>	
5	[Ni(QCl- tpy) <sub>2</sub> ]Cl <sub>2</sub>	trifluoro	DMF/ H <sub>2</sub> O	3.68 s <sup>-1</sup>	[6.28e]
		acetic acid			
6	[NiL]	acetic acid	DMF	193 s <sup>-1</sup>	[6.28f]
7	[CuL]	acetic acid	DMF	255 h <sup>-1</sup>	[6.28g]
8	Complex 6.1	acetic acid	DMF	653.1 s <sup>-1</sup>	Present study
	Complex 6.2			777.5 s <sup>-1</sup>	

## 6.4 Conclusions

Two mononuclear complexes, [NiL] designated as Complex **6.1** and [CuL] designated as Complex **6.2**, where H<sub>2</sub>L is 1,1'-(1E,1'E)-(propane-1,2-diylbis(azan-1-yl-1-ylidene))bis(methan-1-yl-1-ylidene)dinaphthalen-2-ol, were synthesized under mild conditions and characterized by different standard methods. Square planar geometry of Complex **6.1** has been confirmed from single crystal X-ray diffraction analysis. Both of the complexes have been found to be active catalyst for hydrogen evolution reaction (HER) using acetic acid as the substrate. Two metals have been used as they are earth abundant and to compare their activity as the electrocatalyst. Between two complexes, copper complex shows better catalytic activity than the nickel complex towards HER. Effort is going on to develop other metal complexes as the efficient catalyst for hydrogen generation.

## 6.5 References

- 6.1 (a) J.A. Turner, *Science* **2004**, *305*, 972-974;
- (b) T. Egeland-Eriksen, A. Hajizadeh, S. Sartori, *Int. J. Hydrog. Energy* **2021**, *46*, 31963 -31983;
- (c) C. Tarhan, M. A. Çil, *J. Energy Storage* **2021**, *40*, 102676.

- 6.2 (a) M. D. Leonard, E. E. Michaelides, D. N. Michaelides, *Renew. Energy* **2020**, *145*, 951;  
(b) Z. Wang, C. Li, K. Domen, *Chem. Soc. Rev.* **2019**, *48*, 2109-2125;  
(c) T. Yu, Y. Chen, *Sci. Total Environ.* **2019**, *655*, 865–879.
- 6.3 (a) J. Chi, H. Yu, *Chinese J. Catal.*, **2018**, *39*, 390–394;  
(b) H. B. Gray, *Nat. Chem.* **2009**, *1*, 7;  
(c) A. Kudo, Y. Miseki, *Chem. Soc. Rev.* **2009**, *38*, 253–278.
- 6.4 (a) M. Zeng, Y. Li, *J. Mater. Chem. A* **2015**, *3*, 14942-14962;  
(b) A. K. Srivastava, A. Mondal, S. Konar, S. Pal, *Dalton Trans.* **2022**, *51*, 4510–4521;  
(c) H.-F. Wang, L. Chen, H. Pang, S. Kaskel, Q. Xu, *Chem. Soc. Rev.* **2020**, *49*, 1414-1448;  
(d) N. J. Van Zee, B. Adelizzi, M. F. J. Mabesoone, X. Meng, A. Aloï, R. H. Zha, M. Lutz, I. A. W. Filot, A. R. A. Palmans, E. W. Meijer, *Nature* **2018**, *558*, 100.
- 6.5 (a) A. Lasia, Hydrogen evolution reaction. In *Handbook of Fuel Cells*; John Wiley & Sons: New York, **2010**;  
(b) N. Danilovic, R. Subbaraman, D. Strmcnik, V. R. Stamenkovic, N. M. Markovic, *J. Serb. Chem. Soc.* **2013**, *78*, 2007–2015.
- 6.6 (a) M.-R. Gao, J.-X. Liang, Y.-R. Zheng, Y.-F. Xu, J. Jiang, Q. Gao, J. Li, S.-H. Yu, *Nat. Commun.* **2015**, *6*, 5982;  
(b) L. Zhu, H. Lin, Y. Li, F. Liao, Y. Lifshitz, M. Sheng, S.-T. Lee, M. Shao, *Nat. Commun.* **2016**, *7*, 12272.
- 6.7 (a) D. Merki, X. Hu, *Energy Environ. Sci.* **2011**, *4*, 3878-3888;  
(b) D. Dolui, S. Ghorai, A. Dutta, *Coord. Chem. Rev.* **2020**, *416*, 213335;  
(c) D. Dolui, S. Khandelwal, P. Majumder, A. Dutta, *Chem. Commun.* **2020**, *56*, 8166-8181;  
(d) C.-L. Wang, H. Yang, J. Du, S.-Z. Zhan, *Int. J. Hydrog. Energy* **2021**, *46*, 32480-32489;  
(e) J. M. Gurrentz, M. J. Rose, *J. Am. Chem. Soc.* **2020**, *142*, 12, 5657–5667;  
(f) P. Bose, C. Mukherjee, A. K. Golder, *Inorg. Chem. Front.* **2019**, *6*, 1721-1728; (g) K. Kannimuthu, K. Sangeetha, S. S. Sankar, A. Karmakar, R. Madhu, S. Kundu, *Inorg. Chem. Front.* **2021**, *8*, 234-272;  
(h) K. Chen, D. Ray, M. E. Ziebel, C. A. Gaggioli, L. Gagliardi, S. C. Marinescu, *ACS Appl. Mater. Interfaces* **2021**, *13*, 29, 34419–34427;

- (i) J. Ekka, S. N. Upadhyay, F. J. Keil, S. Pakhira, *Phys. Chem. Chem. Phys.* **2022**, *24*, 265-280;
- (j) C. Li, J.-B. Baek, *ACS Omega* **2020**, *5*, 31-40; (k) T. Agarwal, S. Kaur-Ghumaan, *Coord. Chem. Rev.* **2019**, *397*, 188-219.
- 6.8 (a) D. Jana, H. K. Kolli, S. Sabnam, S. K. Das, *Chem. Commun.* **2021**, *57*, 9910-9913;
- (b) R. Jain, A. A. Mamun, R. M. Buchanan, P. M. Kozlowski, C. A. Grapperhaus, *Inorg. Chem.* **2018**, *57*, 13486-13493;
- (c) B. Devi, R. R. Koner, A. Halder, *ACS Sustainable Chem. Eng.* **2019**, *7*, 2187-2199;
- (d) J.P. Cao, T. Fang, L.Z. Fu, L.L. Zhou, S.Z. Zhan, *Int. J. Hydrog. Energy* **2014**, *39*, 10980-10986.
- 6.9 (a) A. Upadhyay, H. Meena, R. K. Jha, Kanika, S. Kumar, *Dalton Trans.* **2022**, *51*, 7284-7293;
- (b) G.-G. Luo, H.-L. Zhang, Y.-W. Tao, Q.-Y. Wu, D. Tian, Q. Zhang, *Inorg. Chem. Front.* **2019**, *6*, 343-354;
- (c) K. Chen, D. Ray, M.E. Ziebel, C. A. Gaggioli, L. Gagliardi, S. C. Marinescu, *ACS Appl. Mater. Interfaces* **2021**, *13*, 29, 34419-34427;
- (d) X. Feng, Y. Pi, Y. Song, C. Brzezinski, Z. Xu, Z. Li, W. Lin, *J. Am. Chem. Soc.* **2020**, *142*, 2, 690-695;
- (e) A. Z. Haddad, S. P. Cronin, M. S. Mashuta, R. M. Buchanan, C. A. Grapperhaus, *Inorg. Chem.* **2017**, *56*, 11254-11265;
- (f) J.P. Cao, T. Fang, L.Z. Fu, L.L. Zhou, S.Z. Zhan, *Int. J. Hydrog. Energy* **2014**, *39*, 13972-13978;
- (g) T. Fang, L.Z. Fu, L.L. Zhou, S.Z. Zhan, *Electrochim. Acta* **2015**, *161*, 388-394.
- 6.10 (a) M. L. Helm, M. P. Stewart, R. M. Bullock, M. R. DuBois, D. L. DuBois, *Science* **2011**, *333*, 863-866;
- (b) R. M. Bullock, A. M. Appel, M. L. Helm, *Chem. Commun.* **2014**, *50*, 3125-3143;
- (c) M.-H. Ho, M. O'Hagan, M. Dupuis, D. L. DuBois, R. M. Bullock, W. J. Shaw, S. Raugei, *Dalton Trans.* **2015**, *44*, 10969-10979.
- 6.11 (a) R. Gueret, C. E. Castillo, M. Rebarz, F. Thomas, M. Sliwa, J. Chauvin, B. Dautreppe, J. Pécaut, J. Fortage, M.-N. Collom, *Inorg. Chem.* **2019**, *58*, 14, 9043-9056;
- (b) A. G. Maher, M. Liu, D. G. Nocera, *Inorg. Chem.* **2019**, *58*, 7958-7968;

- (c) D. P. Estes, D. C. Grills, J. R. Norton, *J. Am. Chem. Soc.* **2014**, *136*, 17362–17365.
- 6.12 L. Tong, L. Duan, A. Zhou, R. P. Thummel, *Coord. Chem. Rev.* **2020**, *402*, 213079.
- 6.13 (a) F. Kamatsos, M. Drosou, C. A. Mitsopoulou, *Int. J. Hydrog. Energy* **2021**, *46*, 19705;  
(b) N. X. Gu, P. H. Oyala, Jonas C. Peters, *J. Am. Chem. Soc.* **2020**, *142*, 17, 7827–7835;  
(c) T. R. Simmons, G. Berggren, M. Bacchi, M. Fontecave, V. Artero, *Coord. Chem. Rev.* **2014**, *270–271*, 127–150.
- 6.14 (a) P. Chou, L. Kim, S. M. Marzouk, R. Sun, A. C. Hartnett, D. K. Dogutan, S.-L. Zheng, D. G. Nocera. *ACS Omega* **2022**, *7*, 8988-8994;  
(b) D. Khusnutdinova, B. L. Wadsworth, M. Flores, A. M. Beiler, E. A. R. Cruz, Y. Zenkov, G. F. Moore, *ACS Catal.* **2018**, *8*, 10, 9888–9898.
- 6.15 (a) J.C. Fontecilla-Camps, A. Volbeda, C. Cavazza, Y. Nicolet, *Chem. Rev.* **2007**, *107*, 4273-4303,  
(b) C. Greco, M. Bruschi, L. De Gioia, U. Ryde, *Inorg. Chem.* **2007**, *46*, 15, 5911-5921;  
(c) A.S. Pandey, T.V. Harris, L.J. Giles, J.W. Peters, R.K. Szilagyi, *J. Am. Chem. Soc.* **2008**, *130*, 13, 4533-4540;  
(d) A. Silakov, B. Wenk, E. Reijerse, W. Lubitz, *Phys. Chem. Chem. Phys.* **2009**, *11*, 6592-6599.
- 6.16 S. Ezzaher, J.F. Capon, F. Gloaguen, F.Y. Petillon, P. Schollhammer, J. Talarmin, *Inorg. Chem.* **2007**, *46*, 23, 9863-9872.
- 6.17 B.E. Barton, M.T. Olsen, T.B. Rauchfuss, *J. Am. Chem. Soc.* **2008**, *130*, 50, 16834-16835.
- 6.18 APEX-II, SAINT and SADABS, Bruker AXS Inc., Madison, WI, **2008**.
- 6.19 G. M. Sheldrick, *Acta Crystallogr., Sect. A: Fundam. Crystallogr.* **2015**, *71*, 3.
- 6.20 G. M. Sheldrick, *Acta Crystallogr., Sect. C: Cryst. Struct. Commun.* **2015**, *71*, 3.
- 6.21 L. Yang, D.R. Powell, R.P. Houser, *Dalton Trans.* **2007**, *9*, 955–964.
- 6.22 (a) A. Bhattacharjee, S. Dey, P. Roy, *Inorg. Chim. Acta* **2019**, *490*, 93-103;  
(b) S. Halder, J. Mondal, J. Ortega-Castro, A. Frontera, P. Roy, *Dalton Trans.* **2017**, *46*, 1943-1950;  
(c) S. Anbu, M. Kandaswamy, B. Varghese, *Dalton Trans.* **2010**, *39*, 3823-3832.
- 6.23 Q.-X. Peng, D. Xue, S.-Z. Zhan, C.-L. Ni, *Appl. Catal. B* **2017**, *219*, 353–361,

- 6.24 L.-Q. Chai, H.-S. Zhang, J.-J. Huang, Y.-L. Zhang, *Spectrochim. Acta A* **2015**, 137, 661-669.
- 6.25 V. Fourmond, P.-A. Jacques, M. Fontecave, V. Artero, *Inorg. Chem.* **2010**, 49, 10338–10347.
- 6.26 Z. Han, L. Shen, W.W. Brennessel, P.L. Holland, R. Eisenberg, *J. Am. Chem. Soc.* **2013**, 135, 14659–14669.
- 6.27 Y.-X. Zhang, L.-Z. Tang, Y.-F. Deng, S.-Z. Zhan, *Inorg. Chem. Commun.* **2016**, 72, 100-104.
- 6.28 (a) C. Costentin, S. Drouet, M. Robert, J.-M. Saveant, *J. Am. Chem. Soc.* **2012**, 134, 11235-11242;  
(b) C. Costentin, M. Robert, J.-M. Saveant, *Chem. Soc. Rev.* **2013**, 42, 2423–2436; (c) C. Costentin, J.-M. Saveant, *ChemElectroChem* **2014**, 1, 1226–1236;  
(d) R. J. DiRisio, J. E. Armstrong, M. A. Frank, W. R. Lake, W. R. McNamara, *Dalton Trans* **2017**, 46, 10418–10425.
- 6.29 N. Elgrishi, M.B. Chambers, M. Fontecave, *Chem. Sci.* **2015**, 6, 2522-2531.
- 6.30 (a) A. Xie, J. Zhu, G.-G. Luo, *Int. J. Hydrog. Energy* **2018**, 43, 2772; (b) F. Kamatsos, M. Drosou, C. A. Mitsopoulou, *Int. J. Hydrog. Energy* **2021**, 46, 19705;  
(c) R. Jain, A. A. Mamun, R. M. Buchanan, P. M. Kozlowski, C. A. Grapperhaus, *Inorg. Chem.* **2018**, 57, 13486–13493;  
(d) X.-S. Hong, D. Huo, W.-J. Jiang, W.-J. Long, J.-D. Leng, L. Tong, Z.-Q. Liu, *ChemElectroChem* **2020**, 7, 4956–4962;  
(e) E. Ahmad, S. Rai, S. K. Padhi, *Int. J. Hydrog. Energy* **2019**, 44, 16467;  
(f) J.-P. Cao, T. Fang, L.-Z. Fu, L.-L. Zhou, S.-Z. Zhan, *Int. J. Hydrog. Energy* **2014**, 39, 10980;  
(g) J.-P. Cao, T. Fang, L.-Z. Fu, L.-L. Zhou, S.-Z. Zhan, *Int. J. Hydrog. Energy* **2014**, 39, 13972.



## List of Publications

- 1\* Shibashis Halder, **Arpita Barma**, Corrado Rizzoli, Pritam Ghosh, Partha Roy, “Density Functional Theory Analysis of Host–Guest Interactions in Cu(II)-Based Metal–Organic Frameworks for Pesticide Detection”, *ACS Appl. Nano Mater.* **2019**, 2(9), 5469–5474.
- 2 Ananta Hazra, Ankita Roy, Aradhita Bhattacharjee, **Arpita Barma**, Partha Roy, “Quinoline based chromogenic and fluorescence chemosensor for pH: Effect of isomer”, *J. Mol. Struct.* **2020**, 1201, 127173.
- 3 Tanumoy Dhawa, Ananta Hazra, **Arpita Barma**, Kunal Pal, Parimal Karmakar, Partha Roy, “4-Methyl-2,6-diformylphenol based biocompatible chemosensors for pH: discrimination between normal cells and cancer cells”, *RSC Advances* **2020**, 10, 15501–15513.
- 4\* **Arpita Barma**, Deblina Ghosh, Parimal Karmakar, Partha Roy, “DNA/protein binding properties and tumor suppressive function of a mononuclear nickel(II) complex”, *J. Mol. Struct.* **2022**, 1250, 131687.
- 5\* **Arpita Barma**, Aradhita Bhattacharjee, Partha Roy, “Dinuclear Copper(II) Complexes with N,O Donor Ligands: Partial Ligand Hydrolysis and Alcohol Oxidation Catalysis”, *Eur. J. Inorg. Chem* **2021**, 23, 2284–2292.
- 6\* **Arpita Barma**, Malay Chakraborty, Swapan Kumar Bhattacharya, Pritam Ghosh, Partha Roy, “Mononuclear nickel(II) complexes as electrocatalyst in hydrogen evolution reactions: Effect of alkyl side chain length”, *Material Advances* **2022**, 3, 7655–7666.
- 7\* **Arpita Barma**, Malay Chakraborty, Swapan Kumar Bhattacharya, Partha Roy, “Electrocatalytic Hydrogen Evolution by Ni(II) and Cu(II) Schiff Base Complexes”, *Inorg. Chem. Commun.* (revised manuscript has been submitted).

\*Included in this thesis



# **Selected Publications**

# Density Functional Theory Analysis of Host–Guest Interactions in Cu(II)-Based Metal–Organic Frameworks for Pesticide Detection

Shibashis Halder,<sup>\*,†,‡,§</sup> Arpita Barma,<sup>†,§</sup> Corrado Rizzoli,<sup>§</sup> Pritam Ghosh,<sup>\*,||</sup> and Partha Roy<sup>\*,†,§</sup>

<sup>†</sup>Department of Chemistry, Jadavpur University, Kolkata 700 032, India

<sup>‡</sup>Department of Chemistry, Tej Narayan Banaili College, Lower Nathnagar Road, Bhagalpur, 812007 Bihar, India

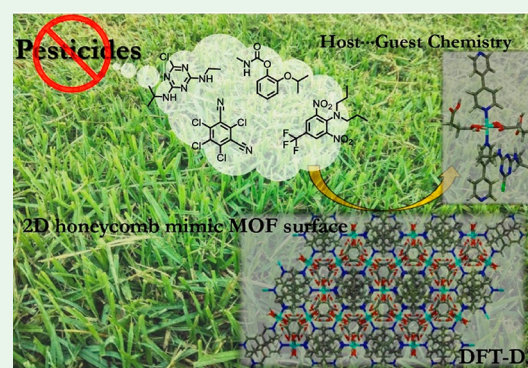
<sup>§</sup>Universita' degli Studi di Parma, Dipartimento S.C.V.S.A., Parco Area delle Scienze 17/A, I-43124 Parma, Italy

<sup>||</sup>Schulich Faculty of Chemistry, Technion-Israel Institute of Technology, Technion City, Haifa 3200008, Israel

## Supporting Information

**ABSTRACT:** A metal organic framework (MOF) (1), having the formula  $[\text{Cu}(4,4'\text{-bipy})(\text{sa})]_n$  (where 4,4'-bipy is 4,4'-bipyridine and sa is succinate dianion), has been synthesized under ambient conditions and characterized by single-crystal X-ray diffraction analysis. The surface of the MOF mimics a 2D honeycomb structure. The uncoordinated oxygen of succinate dianion has been explored for its interaction with toxic pesticides by theoretical density functional theory analysis, and it reveals the selective identification of atrazine- and dicofol-like pesticides. The rational design of  $\text{Cu}^{2+}$  MOFs with aliphatic acid is the key factor toward the identification of pesticides, as the same MOF background with  $\text{Cd}^{2+}$  does not show any significant interaction.

**KEYWORDS:** MOF, copper, DFT, chemosensor, pesticides



## INTRODUCTION

Metal–organic frameworks (MOFs) have been extensively explored during the last couple of decades in several fields,<sup>1,2</sup> especially for gas adsorption,<sup>3–7</sup> sensing,<sup>8,9</sup> catalysis,<sup>10–14</sup> molecular magnets,<sup>15–18</sup> optoelectronic devices,<sup>19–23</sup> and so on. The application of the MOF materials in wastewater treatment<sup>24,25</sup> as well as in fluorescence<sup>26,27</sup> is one of the hot topics nowadays. In recent years, MOFs have been used as chemosensors for several toxic materials owing to their robust 3D architecture and tight packing.<sup>28–34</sup> The tight skeleton of MOFs provides a rigid framework, which is, in general, stable in the presence of guest molecules. Host–guest interactions, in general, follow noncovalent  $\pi$ – $\pi$  or hydrogen-bonding interactions; as a consequence, the appropriate design of MOFs' skeletons is very important. Target-specific groups can be introduced for specific interactions toward guest moieties. Depending on the nature of the guest, the MOF's skeleton can be tuned; for example, for ionic substances, polar groups like –OH or –NH can be used, whereas for neutral substances, an aromatic  $\pi$ – $\pi$  interaction can be explored. In this respect, MOFs as sensors for ionic substances or picric acid have been extensively studied by the scientific community, and there are plenty of reports in the literature.<sup>28,29,31–34</sup> On the contrary, pesticides are another class of biologically toxic substances, where several organochlorine-, organofluorine-, or benzamide-based pesticides are known to be biohazardous owing to their toxic effect on living organisms. As of now, there are very few

reports that deal with studies on the detection of pesticides.<sup>35–41</sup>

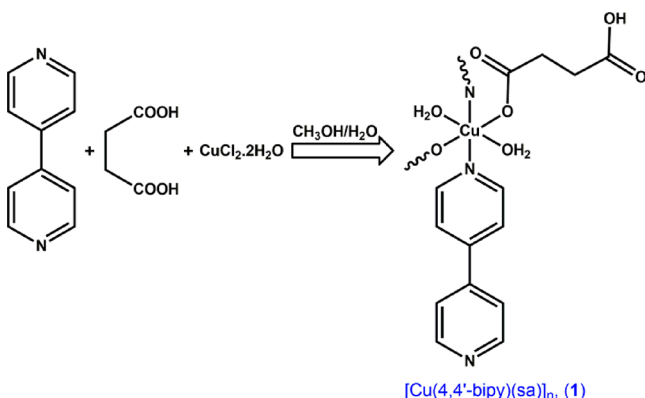
It would be advantageous to use a MOF as a host owing to its robust structure and insolubility in common solvents, and, as a consequence, it could be used for heterogeneous sensing. Such a heterogeneous phase interaction makes it possible to use the host in a reversible manner, as it has been observed that after the process of sensing, the MOF's surface could be washed with solvents and eventually could be reused.<sup>42</sup> Therefore, designing the MOF's surface has become a fundamental target for researchers.

As a first time report, we have developed a copper-based MOF with succinic acid and 4,4'-bipyridine (Scheme 1), whose X-ray structure shows that it mimics the morphological features of a 2D honeycomb-like structure. An interesting feature observed in the structure is the presence of uncoordinated C=O groups of succinate dianion, which exist as dangling entities and instigated us to explore the MOF's response to toxic pesticides by density functional theory (DFT) analysis.

**Received:** June 4, 2019

**Accepted:** August 6, 2019

**Published:** August 6, 2019

Scheme 1. Synthetic Route of the  $[\text{Cu}(4,4'\text{-bipy})(\text{sa})]_n$  (**1**)

## RESULTS AND DISCUSSION

The MOF  $[\text{Cu}(4,4'\text{-bipy})(\text{sa})]_n$  (**1**) was synthesized by the reaction of copper(II) chloride, 4,4'-bipyridine, and succinic acid in methanol/water medium through a slow diffusion process. (See the [Experimental Section](#) for details.) Needle-shaped blue crystals thus obtained were suitable for X-ray diffraction analysis. The structure of **1** was already reported in the literature,<sup>43</sup> but no discussion of the molecular and supramolecular features was included in the paper. As evident from the structure resolution, **1** is a 3D coordination polymer whose asymmetric unit consists of two water molecules and half each of a copper atom, a 4,4'-bipyridine molecule, and a succinate dianion. The copper atom and the nitrogen atoms of the bipyridine molecule lie on a two-fold axis, and the carboxylate groups of the anion act as monodentate ligands through the O1 oxygen atom. The metal adopts an elongated octahedral coordination geometry (see [Figure 1](#) and [Table S1](#) for crystallographic data), where the axial positions are occupied by the oxygen atoms (O3) of two water molecules with distances of 2.532(3) Å and an O–Cu–O angle of 177.26(9)° (see [Tables S2 and S3](#) for selected bond distances and bond angles). The equatorial plane is provided by two carbonyl oxygen atoms (O1) of succinate dianions and two

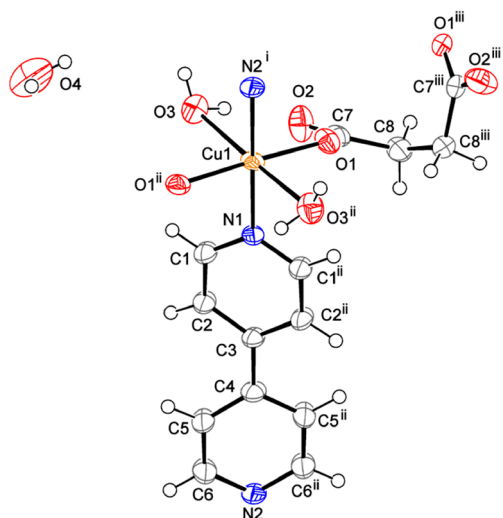


**Figure 1.** Asymmetric unit of **1** with displacement ellipsoids drawn at the 50% probability level. Only one component of the disordered water H atoms is shown. Symmetry codes: (i)  $1 + x, 1 + y, z$ ; (ii)  $y, x, 2/3 - z$ ; and (iii)  $x, 1 + x - y, 5/6 - z$ .

nitrogen atoms (N1, N2) of 4,4'-bipyridine molecules. The Cu–O1, Cu–N1, and Cu–N2 bond distances are 1.958(2), 2.020(3), and 1.999(3) Å, respectively. The equatorial N–Cu–N bond angle is 180° for symmetry requirements, whereas the O–Cu–O angle is 177.08(12)°. In the crystal, the copper atoms and the succinate dianions are linked into chains along the  $c$  axis to form left-handed helices ([Figure S1](#)), which are connected by the 4,4'-bipyridine ligands, producing a polymeric 3D network. Pairs of water molecules of crystallization are hosted inside cavities of  $\sim 82$  Å<sup>3</sup> ([Figure S2a](#)), the surface of which is delimited by the coordinated water molecules, the O2 uncoordinated carboxylate oxygen atoms, and the ethyl fragment of the succinate dianions. The topology of the framework can be described as a **qzd** (quartz-dual) “dense” net with point (Schläfli) symbol  $\{7^5 \cdot 9\}$  ([Figure S2b](#)). The 3D polymeric network is stabilized by O–H···O hydrogen-bonding interactions involving the coordinated and uncoordinated water molecules as hydrogen donors ([Table S4 and Figure S3](#)). The crystal structure, when extended in the crystallographic axis  $c$ , forms an extremely symmetrical structure with hexagons, which, upon further expansion, shows a honeycomb-like morphology ([Figure 2](#)).

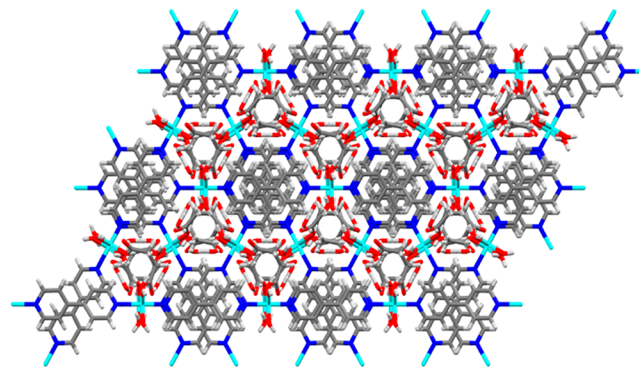
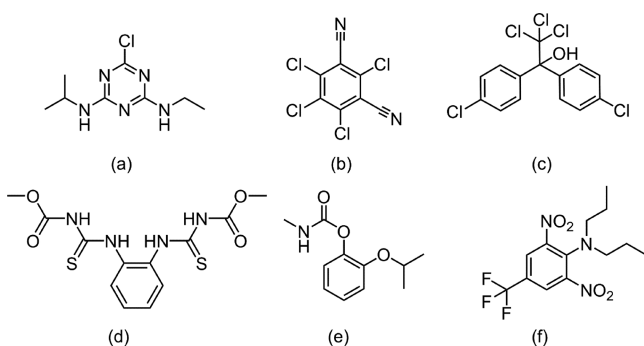


**Figure 2.** Packing diagram of **1** viewed along the  $c$  axis.

The presence of uncoordinated carbonyl groups in the structure of **1** prompted us to explore its ability as a chemosensor. The effect of coordinated water molecules could also be accounted for; however, as a structural property, the effect of the dangling oxygen of the acid groups is very interesting. With previous experience in the field of supramolecular chemistry, in this work, we have targeted rarely explored neutral analytes, that is, pesticides. Indeed, pesticides are chemicals that are used to control/kill pests, rodents, insects, fungi, or other weeds for agricultural and domestic purposes.<sup>44</sup> Therefore, pesticides are potentially toxic to living organisms, including human beings. Thus the use of these substances must be carried out following careful and thorough scientific procedures. Several pesticides are banned worldwide owing to their high toxic effect on living beings, and it is certainly severely toxic and unsafe to use and work with them. However, still, such pesticides are sometimes used by people. In this respect, we have selected a series of pesticides for our studies, for example, atrazine, chlorothalonil, dicofol, thiophanate-methyl, propoxur, and trifluralin, which are either banned or potentially toxic to mankind ([Scheme 2](#)). Because of the acute toxicity of these pesticides, DFT calculations have been used as a tool to investigate their host–guest interactions.

DFT considering the dispersion correction, that is, DFT-(D3), has been utilized for the proper monitoring of the

**Scheme 2. Molecular Structure of Pesticides: (a) Atrazine, (b) Chlorothalonil, (c) Dicofol, (d) Thiophanate-Methyl, (e) Propoxur, and (f) Trifluralin**



possible interactions between the host and the guest. Owing to the possibility of a noncovalent host–guest interaction, a dispersion correction has been considered. The def2-SVP and TZVP basis set levels have been used for nonmetallic atoms and metal ions, respectively, with the B3LYP hybrid function. Initially, the primary unit of the MOF, that is, the immediate coordination of one Cu center, was considered for the calculation, keeping in mind the computational time (Figure 3 and Tables S5 and S6). The selected bond distances of the

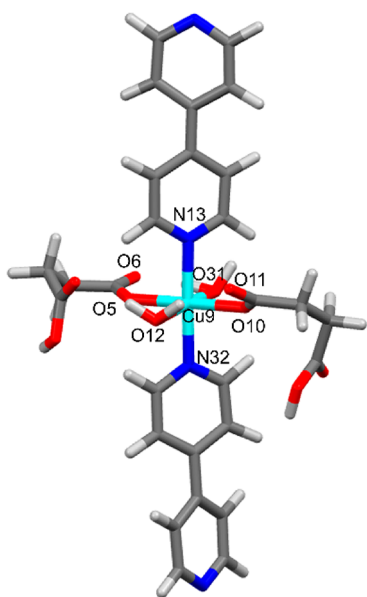


**Figure 3.** Geometry-optimized structure of the single unit of the MOF, where the immediate coordination of  $\text{Cu}^{2+}$  has been considered.

structures obtained from single-crystal X-ray diffraction analysis and DFT are of comparable values (Table S6). All guest pesticides were optimized at the same level of DFT (Tables S7–S12). Furthermore, the pesticide molecules were again optimized with the host MOF to visualize the host–guest interaction using the solvent model for water.

The geometry-optimized structures of **1** with the pesticides was carefully investigated. The uncoordinated atom of succinate dianion in **1** interacts via hydrogen-bonding interactions with  $-\text{NH}$  protons from the atrazine molecule with  $\text{O}\cdots\text{H}$  distances of 1.85 to 1.93 Å (see Figure 4a and Table S13 for coordinates). Interestingly, water molecules are

not involved in the interaction with the guest molecule, rather they stabilize the cluster by hydrogen bonding with the uncoordinated oxygen atom via the formation of a six-membered ring ( $\text{O}\cdots\text{H}$  distance: 1.69 Å). The specific interaction of the uncoordinated oxygen atom with the guest  $-\text{NH}$  group is the key factor for the formation of the stabilized host–guest adduct. It is advantageous for future work that the coordinated solvent molecule does not take any leading role in the host–guest interaction because the solvent molecules are not a part of the designed architecture. Hence, the superiority of using an aliphatic ligand like succinic acid in designing the MOF is justified. In the case of chlorothalonil, an organochlorine pesticide, we expected that ring-to-ring ( $\pi-\pi$ ) interactions might be possible because the presence of multiple chloride groups makes the ring electron-deficient and could promote a  $\pi-\pi$  interaction with bipyridine moiety. The bipyridine moiety has indeed been incorporated into the framework with this purpose. The optimized structure of **1** with chlorothalonil shows no ring-to-ring interaction as well as no hydrogen-bonding interaction between water and chlorothalonil Cl atoms. The optimized structure (see Figure 4b and Table S14 for coordinates) also reveals that the guest is situated far away from the host, which suggests the nonaffinity of the host toward this particular guest. Dicofol (see Figure 4c and Table S15 for coordinates), another example of an organochlorine miticide derived from dichlorodiphenyltrichloroethane (DDT), has been chosen for host–guest interaction studies at the level of DFT-D3. It is found that this compound can also, in principle, interact with **1** via hydrogen bonds through the  $-\text{Cl}$  and  $-\text{OH}$  groups or via  $\pi-\pi$  interactions through the aromatic rings. The optimized structure reveals that **1** participates in a very weak  $\pi-\pi$  interaction with the aromatic ring of dicofol, with a centroid-to-centroid distance of 4.37 Å. Although the interaction takes place, the presence of a bulky trichloromethane group creates a steric hindrance, preventing further closeness of the rings.

After the series of organochlorine-based pesticides, a systemically active benzimidazole fungicide, for example, thiophanate-methyl, has been chosen (see Figure 4d and Table S16 for coordinates). Its interaction with **1** consists of a hydrogen-bonding interaction between the nonligating oxygen of succinate dianion and a secondary amine of thiophanate-methyl ( $\text{H}\cdots\text{O}$  distance: 1.82 Å). Then, we chose a carbamate insecticide, propoxur (commercially known as Baygon), because it is sometimes toxic to many bird species, honeybees, or aquatic life like fish. The optimized structure showed no interaction between the host and the guest (see Figure 4e and Table S17 for coordinates). The steric hindrance of the  $-\text{CH}_3$  group adjacent to  $-\text{NH}$  perhaps does not facilitate the sensing property. Moreover, the results of the calculation suggest that the presence of the  $-\text{NH}$  moiety does not ascertain sensing, rather it strictly depends on other parameters, such as adjacent groups, steric crowding, and so on. We further moved on toward a representative of herbicides, for example, trifluralin, which contains nitro groups as well as fluorine. It was expected that nitro groups could make the ring electron-deficient, and thus  $\pi-\pi$  stacking, as it happens with dicofol, might play a vital role. However, after optimization, no trace of interaction between the host and the guest was observed (see Figure 4f and Table S18 for coordinates). Natural bond orbital (NBO) analysis of **1** and its host–guest adduct with the pesticides were executed and is tabulated in the Supporting Information (Tables S19–S25, Figures S4–S10). For example, the O2 and

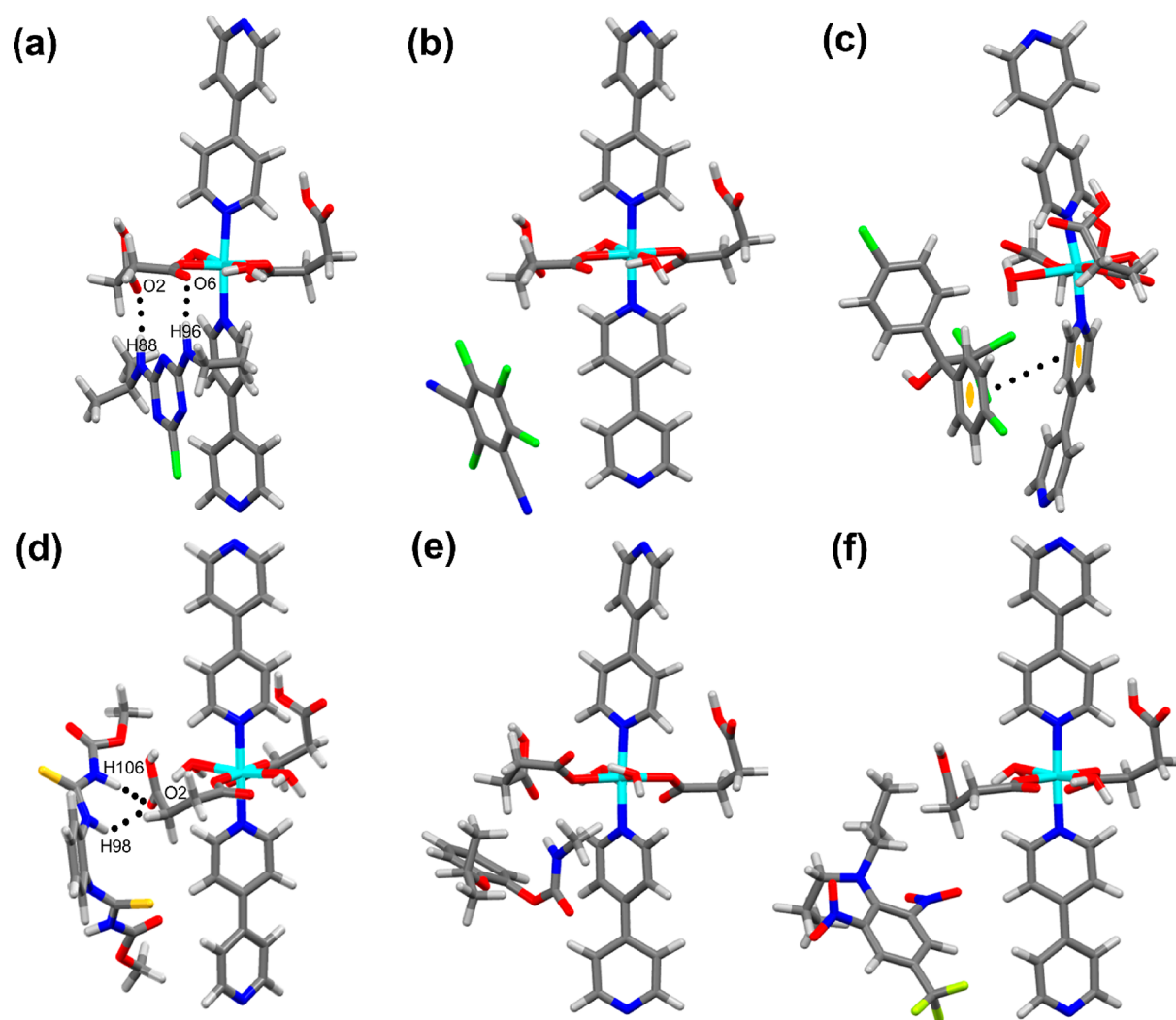


**Figure 4.** Geometry-optimized structure of (a) atrazine C **1**, (b) chlorothalonil C **1**, (c) dicofol C **1**, (d) thiophanate-methyl C **1**, (e) propoxur C **1**, and (f) trifluralin C **1**.

O6 populations from spin density are 0.00026 and  $-0.00047$  for **1**, which, after interaction with atrazine, altered to 0.00039 and  $-0.00009$ . For further verification regarding the geometry, the vibrational stretching of **1** and an adduct of **1** with atrazine were studied, and no negative vibration was found. The zero-point energy (ZPE) of the MOF and the MOF–atrazine adduct was then calculated and was found to be 1472.93 and 2083.19 kJ/mol.

The crystal structure of the Cd–MOF with the same ligands is reported in the literature and has been obtained from the Cambridge Structural Database (CSD).<sup>45</sup> The immediate coordination of the Cd–MOF was optimized (see Table S26 for coordinates) and further examined with dicofol, which primarily showed weak/no  $\pi$ – $\pi$  interaction with Cd–MOF (see Table S27 for coordinates). This shows the role of the central metal ion in making the skeleton of MOF **1** an effective chemosensor.

## CONCLUSIONS

The DFT-D3 analysis established the utility of MOF-based structurally rigid and less flexible architectures toward their applications in supramolecular noncovalent interactions. We studied geometry-optimized structures of a series of different

organochlorine-, benzamide-, carbamate-, or organofluorine-based guests with **1**. The advantage of the  $\text{Cu}^{2+}$ –MOF with aliphatic acid and 4,4'-bipyridine over its analogue of  $\text{Cd}^{2+}$  was established. The aromatic rings of bipyridine actually target the guest via a  $\pi$ – $\pi$  interaction, whereas the uncoordinated oxygen from the succinate dianion acts as an antenna toward different guests possessing secondary  $-\text{NH}$  or  $-\text{OH}$  moieties. The outcome of DFT studies clearly reveals that the coordinated water plays a role in the structural stability of the host framework by a hydrogen-bonding interaction with the adjacent uncoordinated oxygen of succinic acid. It acts as a structural cofactor toward the better stabilization of the host framework. On the contrary, the uncoordinated oxygen is the key factor for the noncovalent interaction between the host and the guest. Our group is actively engaged in the field of using MOFs as a receptor for versatile guest entities, and we expect several significant outcomes in the near future.

## EXPERIMENTAL SECTION

**Materials and Physical Methods.** 4,4'-Bipyridine, copper(II) chloride dihydrate, and succinic acid were purchased from Sigma-Aldrich and used as received. All other chemicals including solvents were of reagent grade and were used as received without further purification. Elemental analyses (carbon, hydrogen, and nitrogen)

were performed using a Perkin-Elmer 2400C elemental analyzer. The theoretical calculation was performed using the Turbomole software package [a development of University of Karlsruhe and Forschungszentrum Karlsruhe GmbH, TURBOMOLE GmbH (V 7.3), since 2007; available from <http://www.turbomole.com>] in macOS Mojave (version 10.14.4) work station.

**Synthesis of [Cu(4,4'-bipy)(sa)]<sub>n</sub> (1).** A methanolic solution (4.0 mL) of 4,4'-bipyridine (4-bpd) (1.0 mmol, 0.156 g) was added to an aqueous solution (4.0 mL) of succinic acid (1.0 mmol, 0.118 g) taken in a beaker and stirred for 30 min to mix well. CuCl<sub>2</sub> · 2H<sub>2</sub>O (1.0 mmol, 0.170 g) was dissolved in 4.0 mL of water in a separate test tube. The previously prepared mixed ligand solution was then slowly and carefully layered with the aqueous CuCl<sub>2</sub> solution using 5.0 mL of a 1:1 v/v methanol and water mixture as buffer. Blue needle-shaped crystals suitable for single-crystal X-ray diffraction analyses were obtained after a few days. The crystals were collected and washed with the methanol–water mixture and dried in vacuum (yield = 72%). Anal. calcd (%) for C<sub>14</sub>H<sub>20</sub>N<sub>2</sub>O<sub>8</sub>Cu: C, 41.19; H, 4.90; N, 6.87. Found: C, 41.12; H, 4.85; N, 6.89.

**Crystallographic Data Collection and Refinement.** A suitable blue single crystal of **1** was mounted on the tip of a glass fiber coated with commercially available super glue. X-ray single crystal data were collected at room temperature using a Bruker APEX-II diffractometer equipped with a fine-focus, sealed tube X-ray source with graphite monochromated Mo K<sub>α</sub> radiation ( $\lambda = 0.71073 \text{ \AA}$ ). The data were integrated using a SAINT program,<sup>46</sup> and absorption correction was made with SADABS. The structure was solved with the help of SHELXT,<sup>47</sup> following direct methods, and refined by full-matrix least-squares on F<sup>2</sup> using SHELXL-2018/3<sup>48</sup> with anisotropic displacement parameters for all non-hydrogen atoms. The water H atoms could be located in a difference Fourier map and were refined by constraining the O–H bond lengths and considering the H···H separations to be 0.86(1) and 1.36(2) Å, respectively, with  $U_{\text{iso}}(\text{H}) = 1.5U_{\text{eq}}(\text{O})$ . The H32 and H42 hydrogen atoms were disordered over two orientations with site occupancies of 0.5. All other H atoms were placed geometrically and refined as riding, with C–H = 0.93 to 0.97 Å and with  $U_{\text{iso}}(\text{H}) = 1.2U_{\text{eq}}(\text{C})$ . Data collection and structure refinement parameters are given in Table S18. Crystallographic data for the crystal structure of **1** in CIF format have been deposited in the Cambridge Crystallographic Data Centre (CCDC) under deposition number CCDC-1918966. The data can be obtained free of charge via [www.ccdc.cam.ac.uk/data\\_request/cif](http://www.ccdc.cam.ac.uk/data_request/cif) (or from the Cambridge Crystallographic Data Centre, 12 Union Road, Cambridge CB21EZ, U.K.).

## ■ ASSOCIATED CONTENT

### 📄 Supporting Information

The Supporting Information is available free of charge on the ACS Publications website at DOI: 10.1021/acsanm.9b01067.

Crystal data for **1**, bond distances of **1**, bond angles of **1**, coordinates of **1**, coordinates of atrazine, coordinates of chlorothalonil, coordinates of dicofol, coordinates of thiophanate-methyl, coordinates of propoxur, coordinates of trifluralin, coordinates of atrazine C **1**, coordinates of chlorothalonil C **1**, coordinates of dicofol C **1**, coordinates of thiophanate-methyl C **1**, coordinates of propoxur C **1**, coordinates of trifluralin C **1**, NBO analysis of **1**, NBO analysis of atrazine C **1**, NBO analysis of chlorothalonil C **1**, NBO analysis of dicofol C **1**, NBO analysis of thiophanate-methyl C **1**, NBO analysis of propoxur C **1**, NBO analysis of trifluralin C **1**, coordinates of Cd–MOF, coordinates of atrazine C Cd–MOF, left-handed helix of **1**, cavity in **1**, topological representation, hydrogen-bond geometry of **1**, and details of the hydrogen bonds in **1** involving the disordered water H atoms (PDF)

Crystallographic data for the crystal structure of **1** (CIF)

## ■ AUTHOR INFORMATION

### Corresponding Authors

\*E-mail: [haldershibashis@gmail.com](mailto:haldershibashis@gmail.com) (S.H.).

\*E-mail: [ppritamghosh@gmail.com](mailto:ppritamghosh@gmail.com) (P.G.).

\*E-mail: [partha.roy@jadavpuruniversity.in](mailto:partha.roy@jadavpuruniversity.in) or [proy@chemistry.jdvu.ac.in](mailto:proy@chemistry.jdvu.ac.in) (P.R.).

### ORCID

Shibashis Halder: 0000-0001-7529-8508

Arpita Barma: 0000-0003-1281-3466

Corrado Rizzoli: 0000-0002-4841-6123

Pritam Ghosh: 0000-0002-2345-8036

Partha Roy: 0000-0001-5387-5626

### Notes

The authors declare no competing financial interest.

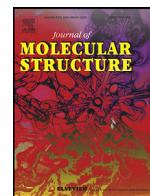
## ■ ACKNOWLEDGMENTS

P.R. acknowledges the financial support from RUSA 2.0, Jadavpur University (ref. no.: R-11/264/19, dated 08.03.2019). A.B. thanks CSIR-New Delhi for providing her a fellowship.

## ■ REFERENCES

- (1) Shimomura, S.; Kitagawa, S. Soft Porous Crystal Meets TCNQ: Charge Transfer-Type Porous Coordination Polymers. *J. Mater. Chem.* **2011**, *21*, 5537–5546.
- (2) Zhou, H.-C.; Kitagawa, S. Metal–Organic Frameworks (MOFs). *Chem. Soc. Rev.* **2014**, *43*, 5415–5418.
- (3) Mason, J. A.; Veenstra, M.; Long, J. R. Evaluating Metal–Organic Frameworks for Natural Gas Storage. *Chem. Sci.* **2014**, *5*, 32–51.
- (4) Chaemchuen, S.; Kabir, N. A.; Zhou, K.; Verpoort, F. Metal–Organic Frameworks for Upgrading Biogas via CO<sub>2</sub> Adsorption to Biogas Green Energy. *Chem. Soc. Rev.* **2013**, *42*, 9304–9332.
- (5) Liu, J.; Thallapally, P. K.; McGrail, B. P.; Brown, D. R.; Liu, J. Progress in Adsorption-Based CO<sub>2</sub> Capture by Metal–Organic Frameworks. *Chem. Soc. Rev.* **2012**, *41*, 2308–2322.
- (6) Sumida, K.; Rogow, D. L.; Mason, J. A.; McDonald, T. M.; Bloch, E. D.; Herm, Z. R.; Bae, T.-H.; Long, J. R. Carbon Dioxide Capture in Metal–Organic Frameworks. *Chem. Rev.* **2012**, *112*, 724–781.
- (7) Barea, E.; Montoro, C.; Navarro, J. A. R. Toxic Gas Removal–Metal–Organic Frameworks for the Capture and Degradation of Toxic Gases and Vapours. *Chem. Soc. Rev.* **2014**, *43*, 5419–5430.
- (8) Kreno, L. E.; Leong, K.; Farha, O. K.; Allendorf, M.; Van Duyne, R. P.; Hupp, J. T. Metal–Organic Framework Materials as Chemical Sensors. *Chem. Rev.* **2012**, *112*, 1105–1125.
- (9) Halder, S.; Mondal, J.; Ortega-Castro, J.; Frontera, A.; Roy, P. A Ni-Based MOF for Selective Detection and Removal of Hg<sup>2+</sup> in Aqueous Medium: A Facile Strategy. *Dalton Trans.* **2017**, *46*, 1943–1950.
- (10) Eddaoudi, M.; Sava, D. F.; Eubank, J. F.; Adil, K.; Guillemin, V. Zeolite-like Metal–Organic Frameworks (ZMOFs): Design, Synthesis, and Properties. *Chem. Soc. Rev.* **2015**, *44*, 228–249.
- (11) Liu, J.; Chen, L.; Cui, H.; Zhang, J.; Zhang, L.; Su, C. Y. Applications of Metal–Organic Frameworks in Heterogeneous Supramolecular Catalysis. *Chem. Soc. Rev.* **2014**, *43*, 6011–6061.
- (12) Zhang, T.; Lin, W. Metal–Organic Frameworks for Artificial Photosynthesis and Photocatalysis. *Chem. Soc. Rev.* **2014**, *43*, 5982–5993.
- (13) Dhakshinamoorthy, A.; Garcia, H. Metal–Organic Frameworks as Solid Catalysts for the Synthesis of Nitrogen-Containing Heterocycles. *Chem. Soc. Rev.* **2014**, *43*, 5750–5765.
- (14) Leenders, S. H. A. M.; Gramage-Doria, R.; De Bruin, B.; Reek, J. N. H. Transition Metal Catalysis in Confined Spaces. *Chem. Soc. Rev.* **2015**, *44*, 433–448.

- (15) Aulakh, D.; Liu, L.; Varghese, J. R.; Xie, H.; Islamoglu, T.; Duell, K.; Kung, C.-W.; Hsiung, C.-E.; Zhang, Y.; Drout, R. J.; Farha, O. K.; Dunbar, K. R.; Han, Y.; Wriedt, M. Direct Imaging of Isolated Single-Molecule Magnets in Metal–Organic Frameworks. *J. Am. Chem. Soc.* **2019**, *141*, 2997–3005.
- (16) Castells-Gil, J.; Baldovi, J. J.; Marti-Gastaldo, C.; Mínguez Espallargas, G. M. Implementation of Slow Magnetic Relaxation in a SIM-MOF Through a Structural Rearrangement. *Dalton Trans.* **2018**, *47*, 14734–14740.
- (17) Aulakh, D.; Xie, H.; Shen, Z.; Harley, A.; Zhang, X.; Yakovenko, A. A.; Dunbar, K. R.; Wriedt, M. Systematic Investigation of Controlled Nanostructuring of Mn<sub>12</sub> Single-Molecule Magnets Templated by Metal–Organic Frameworks. *Inorg. Chem.* **2017**, *56*, 6965–6972.
- (18) Mahata, P.; Draznieks, C. M.; Roy, P.; Natarajan, S. Solid State and Solution Mediated Multistep Sequential Transformations in Metal–Organic Coordination Networks. *Cryst. Growth Des.* **2013**, *13*, 155–168.
- (19) Dutta, B.; Dey, A.; Sinha, C.; Ray, P. P.; Mir, M. H. Tuning of the para-Position of Pyridyl Ligands Impacts the Electrical Properties of a Series of Cd(II) Ladder Polymers. *Dalton Trans.* **2019**, *48*, 11259.
- (20) Halder, S.; Dey, A.; Bhattacharjee, A.; Ortega-Castro, J.; Frontera, A.; Ray, P. P.; Roy, P. A Cd(II)-Based MOF as a Photosensitive Schottky Diode: Experimental and Theoretical Studies. *Dalton Trans.* **2017**, *46*, 11239–11249.
- (21) Halder, S.; Layek, A.; Ghosh, K.; Rizzoli, C.; Ray, P. P.; Roy, P. A Cd(II) Based Metal Organic Framework: a Photosensitive Current Conductor. *Dalton Trans.* **2015**, *44*, 16149–16155.
- (22) Talin, A. A.; Centrone, A.; Ford, A. C.; Foster, M. E.; Stavila, V.; Haney, P.; Kinney, R. A.; Szalai, V.; El Gabaly, F.; Yoon, H. P.; Léonard, F.; Allendorf, M. D. Tunable Electrical Conductivity in Metal–Organic Framework Thin-Film Devices. *Science* **2014**, *343*, 66–69.
- (23) Stavila, V.; Talin, A. A.; Allendorf, M. D. MOF-Based Electronic and Opto-Electronic Devices. *Chem. Soc. Rev.* **2014**, *43*, 5994–6010.
- (24) Fu, H. R.; Wang, N.; Qin, J.-H.; Han, M.-L.; Ma, L.-F.; Wang, F. Spatial Confinement of a Cationic MOF: A SC–SC Approach for High Capacity Cr(VI)-Oxyanion Capture in Aqueous Solution. *Chem. Commun.* **2018**, *54*, 11645–11648.
- (25) Zhao, Y.; Wang, L.; Fan, N.-N.; Han, M.-L.; Yang, G.-P.; Ma, L.-F. Porous Zn(II)-Based Metal–Organic Frameworks Decorated with Carboxylate Groups Exhibiting High Gas Adsorption and Separation of Organic Dyes. *Cryst. Growth Des.* **2018**, *18*, 7114–7121.
- (26) Chen, Z.; Zhang, S.; Zhang, S.; Sun, Q.; Xiao, Y.; Wang, K. Cadmium-Based Coordination Polymers from 1D to 3D: Synthesis, Structures, and Photoluminescent and Electrochemiluminescent Properties. *ChemPlusChem* **2019**, *84*, 190–202.
- (27) Guo, Y.; Feng, X.; Han, T.; Wang, S.; Lin, Z.; Dong, Y.; Wang, B. Tuning the Luminescence of Metal–Organic Frameworks for Detection of Energetic Heterocyclic Compounds. *J. Am. Chem. Soc.* **2014**, *136*, 15485–15488.
- (28) Zhai, Z.-W.; Yang, S.-H.; Cao, M.; Li, L.-K.; Du, C.-X.; Zang, S.-Q. Rational Design of Three Two-Fold Interpenetrated Metal–Organic Frameworks: Luminescent Zn/Cd-Metal–Organic Frameworks for Detection of 2,4,6-Trinitrophenol and Nitrofurazone in the Aqueous Phase. *Cryst. Growth Des.* **2018**, *18*, 7173–7182.
- (29) Senthilkumar, S.; Goswami, R.; Smith, V. J.; Bajaj, H. C.; Neogi, S. Pore Wall-Functionalized Luminescent Cd(II) Framework for Selective CO<sub>2</sub> Adsorption, Highly Specific 2,4,6-Trinitrophenol Detection, and Colorimetric Sensing of Cu<sup>2+</sup> Ions. *ACS Sustainable Chem. Eng.* **2018**, *6*, 10295–10306.
- (30) Lustig, W. P.; Mukherjee, S.; Rudd, N. D.; Desai, A. V.; Li, J.; Ghosh, S. K. Metal–Organic Frameworks: Functional Luminescent and Photonic Materials for Sensing Applications. *Chem. Soc. Rev.* **2017**, *46*, 3242–3285.
- (31) Halder, H.; Ghosh, P.; Rizzoli, C.; Banerjee, P.; Roy, P. Nitroaromatic Explosives Detection by a Luminescent Cd(II) Based Metal Organic Framework. *Polyhedron* **2017**, *123*, 217–225.
- (32) Mukherjee, S.; Desai, A. V.; Manna, B.; Inamdar, A. I.; Ghosh, S. K. Exploitation of Guest Accessible Aliphatic Amine Functionality of a Metal–Organic Framework for Selective Detection of 2,4,6-Trinitrophenol (TNP) in Water. *Cryst. Growth Des.* **2015**, *15*, 4627–4634.
- (33) Cao, L. H.; Shi, F.; Zhang, W. M.; Zang, S. Q.; Mak, T. C. W. Selective Sensing of Fe<sup>3+</sup> and Al<sup>3+</sup> Ions and Detection of 2,4,6-Trinitrophenol by a Water-Stable Terbium-Based Metal–Organic Framework. *Chem. - Eur. J.* **2015**, *21*, 15705–15712.
- (34) Ye, J.; Zhao, L.; Bogale, R. F.; Gao, Y.; Wang, X.; Qian, X.; Guo, S.; Zhao, J.; Ning, G. Highly Selective Detection of 2,4,6-Trinitrophenol and Cu<sup>2+</sup> Ions Based on a Fluorescent Cadmium-Pamoate Metal–Organic Framework. *Chem. - Eur. J.* **2015**, *21*, 2029–2037.
- (35) He, K.; Li, Z.; Wang, L.; Fu, Y.; Quan, H.; Li, Y.; Wang, X.; Gunasekaran, S.; Xu, X. A Water-stable Luminescent Metal-organic Framework for Rapid and Visible Sensing of Organophosphorus Pesticides. *ACS Appl. Mater. Interfaces* **2019**, *11*, 26250.
- (36) Vikrant, K.; Tsang, D. C. W.; Raza, N.; Giri, B. S.; Kukkar, D.; Kim, K.-H. Potential Utility of Metal–Organic Framework-Based Platform for Sensing Pesticides. *ACS Appl. Mater. Interfaces* **2018**, *10*, 8797–8817.
- (37) Yang, Q.; Wang, J.; Chen, X.; Yang, W.; Pei, H.; Hu, N.; Li, Z.; Suo, Y.; Li, T.; Wang, J. The Simultaneous Detection and Removal of Organophosphorus Pesticides by a Novel Zr-MOF Based Smart Adsorbent. *J. Mater. Chem. A* **2018**, *6*, 2184–2192.
- (38) Raj, P.; Singh, A.; Kaur, K.; Aree, T.; Singh, A.; Singh, N. Fluorescent Chemosensors for Selective and Sensitive Detection of Phosmet/Chlorpyrifos with Octahedral Ni<sup>2+</sup> Complexes. *Inorg. Chem.* **2016**, *55*, 4874–4883.
- (39) Hussein, B. H. M.; Khairy, G. M.; Kamel, R. M. Fluorescence Sensing of Phosdrin Pesticide by the Luminescent Eu(III)- and Tb(III)-Bis(Coumarin-3-Carboxylic Acid) Probes. *Spectrochim. Acta, Part A* **2016**, *158*, 34–42.
- (40) Wen, L.; Xu, X.; Lv, K.; Huang, Y.; Zheng, X.; Zhou, L.; Sun, R.; Li, D. Metal–Organic Frameworks Constructed from d-Camphor Acid: Bifunctional Properties Related to Luminescence Sensing and Liquid-Phase Separation. *ACS Appl. Mater. Interfaces* **2015**, *7*, 4449–4455.
- (41) Hou, J.; Dong, J.; Zhu, H.; Teng, X.; Ai, S.; Mang, M. A Simple and Sensitive Fluorescent Sensor for Methyl Parathion Based on L-Tyrosine Methyl Ester Functionalized Carbon Dots. *Biosens. Bioelectron.* **2015**, *68*, 20–26.
- (42) Nagarkar, S. S.; Desai, A. V.; Ghosh, S. K. Engineering Metal–Organic Frameworks for Aqueous Phase 2,4,6-Trinitrophenol (TNP) Sensing. *CrystEngComm* **2016**, *18*, 2994–3007.
- (43) Wu, S.-T.; Wu, Y.-R.; Kang, Q.-Q.; Zhang, H.; Long, L.-S.; Zheng, Z.; Huang, R.-B.; Zheng, L.-S. Chiral Symmetry Breaking by Chemically Manipulating Statistical Fluctuation in Crystallization. *Angew. Chem., Int. Ed.* **2007**, *46*, 8475–8479.
- (44) *The WHO Recommended Classification of Pesticides by Hazard and Guidelines to Classification*; World Health Organization: Geneva, Switzerland, 2009.
- (45) Zhang, J.; Li, Z. J.; Wen, Y. H.; Kang, Y.; Cheng, J. K.; Yao, Y. G. Syntheses and Crystal Structures of Two Metal Succinates Modified by Bipyridines. *Z. Anorg. Allg. Chem.* **2004**, *630*, 2731–2735.
- (46) APEX-II, SAINT, and SADABS; Bruker AXS, Inc.: Madison, WI, 2008.
- (47) Sheldrick, G. M. SHELXT - Integrated space-group and crystal-structure determination. *Acta Crystallogr., Sect. A: Found. Adv.* **2015**, *A71*, 3–8.
- (48) Sheldrick, G. M. Crystal Structure Refinement with SHELXL. *Acta Crystallogr., Sect. C: Struct. Chem.* **2015**, *C71*, 3–8.



# Synthesis and characterization of a mononuclear nickel(II) complex with N,O-donor ligand: Its DNA/HSA protein binding properties and tumor suppressive function

Arpita Barma<sup>a,†</sup>, Deblina Ghosh<sup>b,†</sup>, Parimal Karmakar<sup>b,\*</sup>, Partha Roy<sup>a,\*</sup>

<sup>a</sup> Department of Chemistry, Jadavpur University, Kolkata 700 032, India

<sup>b</sup> Department of Life Science & Bio-technology, Jadavpur University, Kolkata 700 032, India



## ARTICLE INFO

### Article history:

Received 4 August 2021

Revised 21 September 2021

Accepted 7 October 2021

Available online 9 October 2021

### Keywords:

Ni(II) complex

DNA binding

HSA binding

Selective cytotoxicity

Apoptosis

## ABSTRACT

A mononuclear Ni(II) complex,  $[\text{Ni}(\text{HL})_2]\text{Cl}_2 \cdot \text{H}_2\text{O}$  (Complex **1**), where HL = 1-((2-piperidin-1-yl)ethylimino)methyl)naphthalene-2-ol has been synthesized under mild conditions. It has been characterized by elemental analysis, cyclic voltammetry, FT-IR, UV-vis, fluorescence and mass spectral analyses. Square planar geometry of the mononuclear complex has been confirmed by single crystal X-ray diffraction analysis. Complex **1** interacts with CT DNA with a binding constant of  $3.6 \times 10^3 \text{ M}^{-1}$  which suggests electrostatic interaction between the complex and DNA. The metal complex cleaves plasmid DNA efficiently in the presence of  $\text{H}_2\text{O}_2$ . On the other hand, complex **1** binds with the carrier protein, HSA, quite efficiently with a binding constant value of  $7.16 \times 10^5 \text{ M}^{-1}$ . Cytotoxicity of the complex has been checked with lung carcinoma (A549) and normal lung fibroblast cell lines (WI-38). From MTT assay, it has been seen that the complex could inhibit the cell proliferation. Western blot analysis suggests that nickel complex is a tumor suppressor.

© 2021 Elsevier B.V. All rights reserved.

## 1. Introduction

Researchers of chemical, biological and medicinal sciences from all over the globe have been engaged to study different transition metal complexes and their interaction with DNA and proteins. DNA is the primary intracellular objective for effective designing of anticancer drugs [1]. To design effective metal based chemotherapeutic agents, the interaction of metal complexes with DNA has to be explored as these interactions can lead to damage DNA in cancer cells, which finally results in cell death. The metal complexes can interact with it via covalently or through non-covalent interactions, for example, intercalation, groove binding and electrostatic binding [2]. Use of *cis*-platin has been clinically successful to treat most aggressive solid tumors and thereafter, a number of different platinum-based complexes are being reported as antitumor agent. But the challenges for utility of *cis*-platin still remain due to its severe toxicity, intrinsic drug resistance and high cost [3]. Therefore, designing and development of effective, target specific, less

toxic and preferably non-covalently binding metal based novel anticancer drugs can trigger the apoptosis.

Human serum albumin (HSA), the most abundant proteins, acts as the most versatile transporter and disposer of various endogenous and exogenous molecules to their target organs [4]. The lack of toxicity and immunogenicity of HSA makes it ideal for drug delivery. When a drug binds to albumin, drug solubility in plasma is increased. As a result, toxicity as well as protection against oxidation of the bound drug are decreased. However, strong interaction between albumin and small molecules results formation of a stable protein–drug complex affecting the distribution, metabolism and the efficacy of the possible drugs [5]. Thus, it is imperative and important to study interaction of albumin protein and drug molecules for evaluating the therapeutic efficacy of the drug and its delivery towards the target organs.

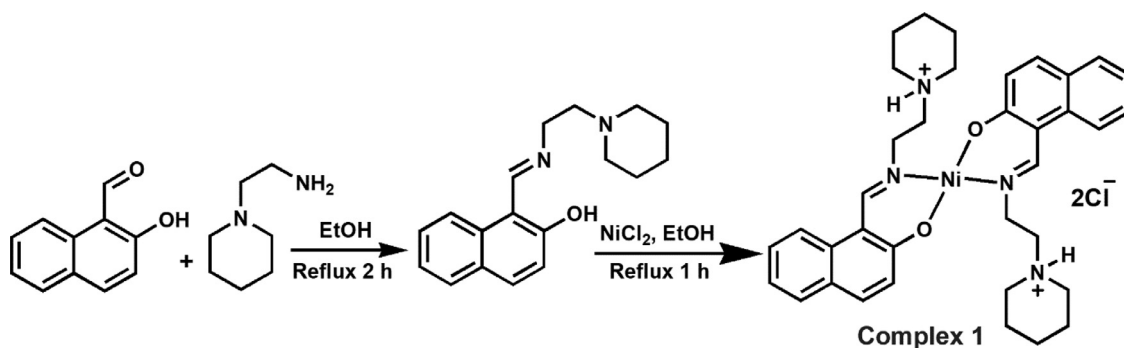
Among the transition metals, a rich and versatile chemistry of nickel with DNA has been supported by the existing literature [6]. Its flexible metal coordination behaviour, less toxicity and simple, inexpensive synthesis suggest that nickel(II) complexes are potential candidates for pharmaceutical applications [7]. The nickel(II) complexes with thiosemicarbazone [8], thiocarboxamide [9], hydrazone [10] and other ligands [11–13] have been reported for DNA interaction and/or cleavage. On the other hand, some metal complexes of copper and palladium have exhibited tumor suppression

\* Corresponding author.

E-mail addresses: [partha.roy@jadavpuruniversity.in](mailto:partha.roy@jadavpuruniversity.in), [proy@chemistry.jdvu.ac.in](mailto:proy@chemistry.jdvu.ac.in) (P. Karmakar), [proy@chemistry.jdvu.ac.in](mailto:proy@chemistry.jdvu.ac.in) (P. Roy).

† These authors contribute equally





Scheme 1. Synthesis of Complex 1

properties [14–17]. However, report on antitumor activity of nickel complexes is rare [14]. But there is continuous effort to develop more efficient nickel complexes for DNA binding and cleavage.

With these backgrounds, we report herein synthesis, characterization, DNA/HSA binding and cytotoxicity properties of a mononuclear nickel(II) complex containing piperidine unit (Scheme 1). Complex 1 has been synthesized under ambient conditions. Its interaction with DNA and human serum albumin has been extensively explored. Its cytotoxicity effect on several systems has been evaluated. Recently we have reported a mononuclear copper(II) complex with a Schiff-base ligand and explored its DNA binding, protein binding and antibacterial activities [18]. It showed effective intercalative binding and HSA could act as effective carrier of it. In continuation of the previous work, we have used here 1-(2-aminoethyl)piperidine instead of 1-cyclohexylmethanamine in anticipation to get one extra donor atom and nickel in place of copper to synthesize the complex aiming to examine the effect of these changes in its DNA and protein binding activities.

## 2. Experimental Section

### 2.1. Materials and methods

2-Hydroxy-1-naphthaldehyde, 1-(2-aminoethyl)piperidine, nickel(II) chloride hexahydrate, Human serum albumin (HSA) and Calf thymus (CT)-DNA were obtained from Sigma Aldrich and these were used without any purification. Supercoiled pUC19 plasmid DNA was received from the biotechnology laboratory. Solvents used were purchased from different commercial sources and used as received. Elemental analysis was performed on a 2400 Series-II CHN analyzer, Perkin Elmer, USA. FT-IR spectra were obtained on a Perkin Elmer spectrometer (Spectrum Two) with the solid samples using ATR method. The UV-vis spectral analysis was performed using an Agilent 8453 diode array spectrophotometer. The ESI-MS spectra were recorded on QTOF Waters' HRMS spectrometer (Model XEVO G2QToF). Fluorescence spectra were acquired using a Horiba Fluoromax-4C spectrofluorometer. The cyclic voltammetry instrument used was a personal computer (PC)-controlled PAR model 273A electrochemistry system. A glassy carbon as working electrode, a platinum wire as auxiliary electrode and saturated Ag/AgCl as reference electrode were employed in a standard three-electrode configuration. CD spectrum was obtained utilizing a quartz cuvette of 10 mm path length in a JASCO J-815 CD spectropolarimeter.

### 2.2. Synthesis

#### 2.2.1. Synthesis of

1-((2-piperidin-1-yl)ethylimino)methyl)naphthalene-2-ol (HL)

1-(2-Aminoethyl)piperidine (0.6 mmol, 85.19  $\mu$ L) was added to an ethanol solution of 2-hydroxy-1-naphthaldehyde (0.6 mmol,

0.103 g) drop by drop under stirring condition. The stirring was continued for 15 min and the resultant mixture was refluxed for 2 h. The color of the solution turned yellow, indicating the formation of Schiff base ligand. The mixture was then cooled and collected after filtration. Yield = 0.155 g, 92%. Anal. calc. (%) for  $C_{18}H_{22}N_2O$ : C, 76.58; H, 7.85; N, 9.92. Found: C, 76.77; H, 7.96; N, 9.76.  $^1H$  NMR (300 MHz DMSO<sub>6</sub>;  $\delta$  ppm, TMS): 13.83 (1H, s), 9.07 (1H, s), 8.07 (1H, d, J = 8.4 Hz), 7.71 (1H, d, J = 9.2 Hz), 7.62 (1H, d, J = 7.6 Hz), 7.42 (1H, t, J = 7.2 Hz), 7.19 (1H, t, J = 7.2 Hz), 6.72 (1H, d, J = 9.2 Hz), 3.71 (2H, t, J = 3.0 Hz), 2.76 (2H, t, J = 5.2 Hz), 2.51 (4H, t, J = 3.0 Hz), 1.56 (6H, m). ESI-MS ( $m/z$ ): 283.11 [(HL + H<sup>+</sup>)].

#### 2.2.2. Synthesis of Complex 1

A solution of nickel(II) chloride hexahydrate (0.6 mmol, 0.143 g) in 10 mL of ethanol was added to 5 mL ethanol solution of HL (1.2 mmol, 0.339 g) under constant stirring condition. The mixture was stirred for another 15 min. It turned into brownish green in color. The resulting solution was then refluxed for 1 h. It was finally cooled to room temperature and the mixture was filtered to remove any undissolved material(s) and/or precipitate. The filtrate was kept under ambient condition for slow evaporation of solvent. Green single crystals of complex 1 suitable for X-ray diffraction study were grown within few days. Yield 0.243 g, 65%. Anal. calc. (%) for  $C_{36}H_{46}N_4NiO_2Cl_2$ : C, 60.70; H, 6.51; N, 7.86. Found: C, 60.57; H, 6.64; N, 7.95. ESI-MS ( $m/z$ ): 339.02 [(NiL)<sup>+</sup>].

#### 2.3. X-ray data collection and structure determination

Data collection and other related parameters for complex 1 are given in Table 1. Single crystal data collections were done using an automated Bruker D8 VENTURE diffractometer with graphite monochromatized Mo K $\alpha$  radiation. The spots were considered using 10 s counting time. Unit cell parameters were determined from least-squares refinement of setting angles with  $\theta$  in the range  $2.67 \leq \theta \leq 27.091^\circ$ . Data were then processed using Bruker SAINT package [19]. Absorption corrections based on multi scans were considered to all intensity data using the SADABS software. The structure was solved by direct methods using SHELXT [20] and refined by full-matrix least-squares techniques on F<sup>2</sup> using the SHELXS-2014/7 program [21]. The absorption corrections were carried out by the multi-scan technique. All data were then corrected for Lorentz and polarization effects. Non-hydrogen atoms were refined anisotropically.

#### 2.4. DNA binding and cleavage studies

The stock solution of CT-DNA was made in 5 mM Tris-HCl/50 mM NaCl buffer at pH 7.2. It showed a ratio of UV absorbance at 260 nm and 280 nm ( $A_{260}/A_{280}$ ) of about 1.8–1.9 which indicated that the DNA was adequately free of protein [22]. Its

**Table 1**  
Crystal data of complex 1

Complex	1
Formula	C <sub>36</sub> H <sub>48</sub> Cl <sub>2</sub> N <sub>4</sub> NiO <sub>3</sub>
Formula weight	714.39
T (K)	298(2)
Crystal color	green
Crystal system	triclinic
Space group	<i>P</i> -1
<i>a</i> (Å)	11.4177(9)
<i>b</i> (Å)	13.2176(10)
<i>c</i> (Å)	13.3395(11)
$\alpha$ (°)	106.450(2)
$\beta$ (°)	106.839(2)
$\gamma$ (°)	103.604(2)
<i>V</i> (Å <sup>3</sup> )	1734.1(2)
<i>Z</i>	2
Crystal dimensions (mm)	0.4 × 0.2 × 0.1
<i>F</i> (0 0 0)	756.0
<i>D<sub>c</sub></i> (g cm <sup>-3</sup> )	1.368
$\lambda$ (Mo K $\alpha$ ) (Å)	0.71073
$\theta$ Range (°)	2.67–27.091
Reflection collected/unique/observed	58157, 7626, 5962
Absorption correction	multi-scan
<i>R<sub>int</sub></i>	0.0542
Final <i>R<sub>1</sub></i> index [ <i>I</i> > 2 $\sigma$ ( <i>I</i> )]	0.0737
Final <i>wR<sub>2</sub></i> index (all reflections)	0.1330
Goodness-of-fit	1.087

concentration was measured by using absorbance at 260 nm ( $\epsilon = 6600 \text{ M}^{-1}\text{cm}^{-1}$ ) whereas the plasmid DNA was used as it is in the wet lab for cleavage studies. Absorption titrations were performed in Tris-HCl/NaCl buffer at room temperature to determine the binding affinity of the metal complex towards CT-DNA. The effect of the presence of complex 1 to the EB-DNA complex was studied by recording fluorescence emission spectra with excitation at 510 nm and emission maximum at 602 nm. The DNA cleavage experiments were carried out by agarose gel electrophoresis following a published procedure [23].

## 2.5. HSA binding studies

HSA of  $1.0 \times 10^{-4} \text{ M}$  was made by dissolving the protein in Tris-HCl buffer solution (pH 7.2) [24]. Concentration of the protein was evaluated in a spectrophotometer considering molar extinction coefficient as  $35,219 \text{ M}^{-1}\text{cm}^{-1}$  at 280 nm.

## 2.6. MTT assay

The Lung carcinoma A549 and normal lung fibroblast WI-38 cells at a density ( $1 \times 10^4$ ) were seeded in 24 well tissue culture plate prior to treatment with complex 1 at concentrations of (0–200  $\mu\text{M}$ ) for 12 h. After incubation, the cells were washed using  $1 \times \text{PBS}$  twice and then they were incubated with MTT solution (450  $\mu\text{g}/\text{mL}$ ) for 3 to 4 h at 37 °C. The absorbance of the resulting formazan crystals were measured at 570 nm using a spectrophotometer and the values were compared with untreated cells [25].

## 2.7. Apoptotic nuclear morphology study by DAPI staining

To visualize nuclear changes, after exposure of complex 1 at LD<sub>50</sub> dose for 12 h and 24 h, cells were washed using  $1 \times \text{PBS}$  thrice and then they were stained with 4',6-diamidino-2-phenylindole (DAPI) in Vectashield (0.2 g mL<sup>-1</sup>, Vector Laboratories Inc.). Change of nuclear morphology, if any, was noticed under a fluorescence microscope (Leica) [26].

## 2.8. Roles of caspase-3 in complex-induced apoptosis in A549 cells

After treatment, the whole cell lysate was extracted with a lysis buffer containing 1% Triton X-100, 50 mM sodium fluoride (NaF), 50 mM sodium chloride (NaCl), 20 mM Tris (pH 7.4), 1 mM EGTA, 1 mM EDTA, 1 mM sodium vanadate (Na<sub>3</sub>VO<sub>4</sub>), 0.2 mM phenylmethanesulfonyl fluoride (PMSF), 0.5% NP-40 and protease inhibitors. Equal amounts of cell lysate (50  $\mu\text{g}$ ) were solubilized in loading buffer and then boiled for 5 min, and electrophoresized in 10 % polyacrylamide gel in Tris-glycine buffer (pH 8.3). After that, proteins were transferred to a polyvinylidene difluoride membrane. Nonspecific binding was restricted using 5% non-fat dry milk and 0.05% Tween-20 in 20 mM Tris-Cl, pH 7.6 (TBS-T). After incubation with the suitable primary antibodies, the membranes were washed with TBS-T and were then incubated again with the respective secondary antibodies [25].

## 3. Results and discussion

### 3.1. Synthesis and characterization

#### 3.1.1. Synthesis and characterization of HL

Synthesis of the ligand, 1-((2-piperidin-1-yl)ethylimino)methyl)naphthalene-2-ol (HL), has been carried out by reacting one eqv. of 2-hydroxy-1-naphthaldehyde with one eqv. of 1-(2-aminoethyl)piperidine in ethanol as depicted in Scheme 1. The ligand has been obtained in good yield and it has been characterized by ESI-mass spectrometric measurement, and FT-IR and <sup>1</sup>H NMR spectral analysis. ESI-mass spectrometric measurement of the ligand was performed with its methanolic solution (Fig. s1). ESI mass spectrum shows an *m/z* peak at 283.11 which may be attributed to the presence of [HL+ H]<sup>+</sup> species (calculated value: 283.18). It has been further characterized by <sup>1</sup>H NMR spectral analysis (Fig. s2). It exhibits a peak at 13.83 ppm indicating the presence of phenolic OH proton. Presence of imine proton has been indicated by the appearance of peak at 9.07 ppm. Emergence of this peak confirms the conversion of the aldehyde group into the corresponding azomethine moiety. Peaks for aromatic protons and aliphatic protons appear in their usual positions.

In IR spectrum of the ligand (Fig. s3) a broad absorption band has been obtained around 3225 cm<sup>-1</sup> which may be assigned to the O-H stretching arising from the presence of the hydroxyl group. The intense band has appeared at 1617 cm<sup>-1</sup> which may be attributed to the presence of the azomethine group (C=N moiety). These bands suggest the formation of the ligand.

#### 3.1.2. Synthesis and characterization of complex 1

Complex 1 has been synthesized by reacting with one eqv. of nickel(II) chloride hexahydrate and two eqv. of HL in ethanol without adding any external base. Complex 1 has been obtained in good yield and has been characterized by several standard methods.

ESI mass spectrum of complex 1 shows an *m/z* peak at 339.02 which may be assigned to the presence of [NiL]<sup>+</sup> fragment (calculated value: 339.10) (Fig. s4). Another *m/z* peak at 283.11 indicates the presence of [HL + H]<sup>+</sup> species (calculated value: 283.18) in the solution which may be fragmented from the complex.

In IR spectrum of the complex 1 (Fig. s5) a broad band around 3430 cm<sup>-1</sup> is observed that can be assigned to the O-H stretching arising from the presence of uncoordinated water molecule. The hydrocarbon part of the complex has been evidenced by the presence of unsymmetrical and symmetrical frequencies of  $\nu_{\text{C-H}}$  observed at the region of 2615–2958 cm<sup>-1</sup>. In the spectrum of complex 1, the intense band around 1658 cm<sup>-1</sup> is due to the stretching vibration of the azomethine group. The formation of Ni-N and Ni-O bonds in the complex is also shown by the appearance of the

bands at 481 and 541  $\text{cm}^{-1}$ , respectively. The band at 481  $\text{cm}^{-1}$  may be attributed to  $\nu_{\text{Ni-N}}$  stretching frequency. The band at 541  $\text{cm}^{-1}$  may be assigned to the  $\nu_{\text{Ni-O}}$  stretching frequency.

The electronic spectrum of complex **1** has been recorded in DMF at room temperature (Fig. s6). A broad band at around 600 nm (Inset, Fig. s6) has been observed for the complex which may be assigned to the  $d-d$  transition. This is weaker in intensity as it is Laporte forbidden. Moreover, the complex is almost centrosymmetric which allows very little mixing of  $d$  and  $p$  orbitals. The band at 305 nm may be assigned to  $n-\pi^*$  transitions of  $>\text{C}=\text{N}$  groups. Whereas higher intensity charge transfer transition is obtained at the wavelength 402 nm for this complex. This is attributed to  $\text{O}^-$  (of naphthalen-1-olate)  $\rightarrow$  Ni(II), N(amino)  $\rightarrow$  Ni(II) LMCT (transfer occurs from the MO with ligand-like character to the metal-like one) transitions.

Electrochemical studies of complex **1** have been carried out in DMF using TBAP as supporting electrolyte at room temperature under argon atmosphere. A typical cyclic voltammogram (CV) has been obtained by using a glassy carbon as working electrode and an Ag/AgCl reference electrode (Fig. s7). As shown in the figure, cyclic voltammogram of complex **1** in DMF exhibits one quasi-reversible couple and one irreversible couple at  $-1.05$  and  $-1.77$  V, respectively, versus Ag/AgCl, which can be assigned to the metal-centred  $\text{Ni}^{\text{II/I}}$  and  $\text{Ni}^{\text{II/0}}$  processes, respectively [27].

### 3.2. Crystal structure of complex 1

Complex **1** has been obtained from ethanol and it crystallizes in the  $P-1$  space group. An ORTEP diagram of the complex is shown in Fig. 1. Selected bond angles and selected bond lengths are given in Table s1. Complex **1** consists of two deprotonated ligands, one nickel atom, two chloride ions and one water molecule. Nickel atom is in a tetra-coordinated environment. Ni1 is coordinated to two oxygen atoms (O1 and O2) and two nitrogen atoms (N1 and N2). O1 and N1 are from one ligand while O2 and N2 are from another ligand. Both the *trans* angles of O2-Ni1-O1 and N1-Ni1-N2 are  $179.44^\circ$  and  $178.81^\circ$ , respectively and the O-Ni-N bond angles are very close to  $90^\circ$ . Houser et al. used the four-coordinate  $\tau_4$  index for the first time to find out the geometry around a metal center in its four coordination arrangement [28]. The value of  $\tau_4$

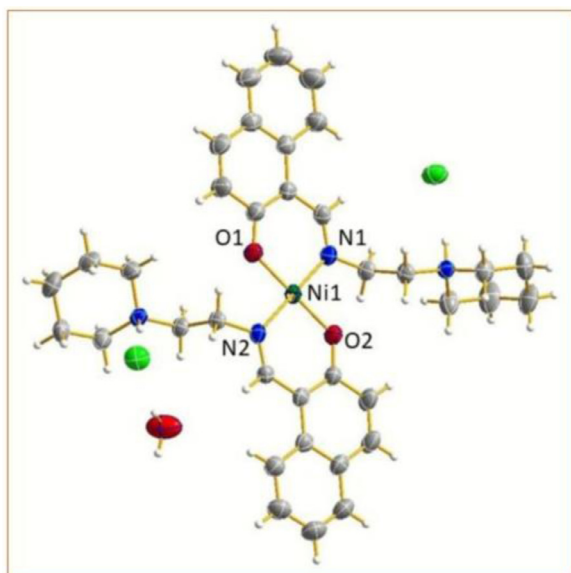


Fig. 1. A perspective view of complex **1** with displacement ellipsoids drawn at the 50% probability level.

index is determined using the following formula

$$\tau_4 = \frac{360^\circ - (\alpha + \beta)}{141^\circ}$$

where  $\alpha$  and  $\beta$  are the two largest angles in the complex. For a perfect tetrahedral geometry, its value is 1.00 while  $\tau_4$  index is 0.00 for a perfect square planar geometry. The value of  $\tau_4$  index comes out as 0.004 for complex **1** which shows very close square planar geometry around the nickel center. The Ni-O and Ni-N bond lengths are in good agreement with the literature values [29]. It is interesting to note that complex cation is formed with two uncoordinated chloride anions. The complex cation is obtained on protonation of two of piperidine N atoms which is quite common for this type complex with other metal ions [30].

### 3.3. DNA binding studies

#### 3.3.1. UV-visible spectral studies

For the development of effective metal based chemotherapeutic drugs, interaction of small molecules or metal complexes with DNA has been studied extensively for last few decades. It has been found that almost all the drugs are able to interact with DNA via a number of ways such as non-covalent interaction (e.g. groove binding), intercalation and non-specific electrostatic surface binding [24, 31]. Hence, the potential binding ability and the nature of binding of molecules with DNA are observed by using absorption spectroscopy.

The absorption spectra of complex **1** have been recorded in absence and in the presence of increasing amount of CT-DNA (at constant concentration of the complex) (Fig. 2). On addition of increasing amounts of CT-DNA to the complex, ratio [DNA]/[Complex **1**] is changed as 0.0, 1.8, 3.7, 5.5, 7.3, 9.1, 10.9. The absorption band of free complex at 402 nm undergoes a slight bathochromic shift on addition of DNA and the event indicates that the binding of the metal complex with DNA occurs in a non-covalent mode. The observed hypochromic shift indicated that the complex **1** is in groove binding mode with CT DNA [32]. However, the nickel complex may bind with the double-helical DNA in different ways which are dependent on the structure, charge and type of ligands. It is well known that DNA has a number of hydrogen bonding sites in its major and minor grooves [33]. It is possible that azomethine group of the Schiff-base ligand forms H-bonds with the base pairs of DNA helix which may lead to partial unwinding and destabilization of

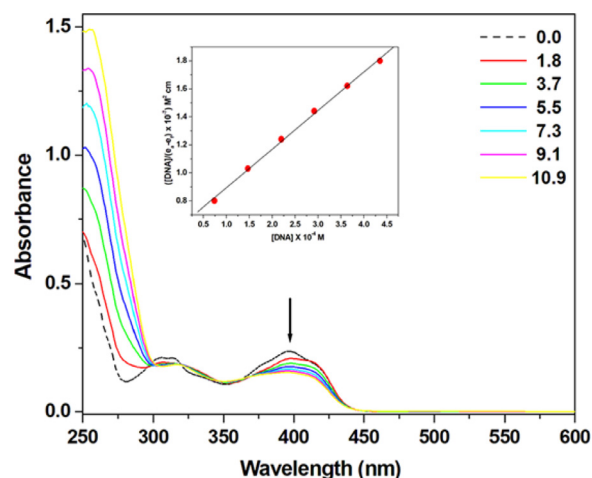


Fig. 2. Absorption spectra of complex **1** in absence (dashed line) and in the presence (solid line) of increasing concentration of CT-DNA. [Complex **1**] =  $4 \times 10^{-5}$  M. The downside arrow shows the absorbance changes upon increasing the DNA concentration. Inset: linear plot for the calculation of the intrinsic DNA binding constant ( $K_b$ ).

the DNA double helix structure. In addition to this, the interaction between square planar complex and DNA is stronger than that between octahedral complex and DNA as in the hexacoordinated complex there is no suitable vacant coordination site where the nitrogen atom of DNA base pair can interact with metal ion.

To determine the DNA binding ability of the complex, the intrinsic binding constant,  $K_b$ , has been determined using Wolfe-Shimer Equation [34],

$$[\text{DNA}]/(\varepsilon_a - \varepsilon_f) = [\text{DNA}]/(\varepsilon_b - \varepsilon_f) + 1/K_b(\varepsilon_a - \varepsilon_f)$$

where  $[\text{DNA}]$ ,  $\varepsilon_a$ ,  $\varepsilon_f$  and  $\varepsilon_b$  represent the concentration of DNA, the apparent extinction coefficient ( $A_{\text{obs}}/[\text{M}]$ ), the extinction coefficient for free metal complex (M), and the extinction coefficient for the metal complex (M) in the fully bound form, respectively.  $K_b$  is calculated from the ratio of slope to intercept obtained from the plot of  $[\text{DNA}]/(\varepsilon_a - \varepsilon_f)$  vs.  $[\text{DNA}]$ .  $K_b$  has been determined as  $3.6 \times 10^3 \text{ M}^{-1}$ . This value suggests that complex **1** binds with CT DNA possibly via electrostatic binding because for intercalative binding, it has been reported that the binding constants are of much higher value [8a,10a,b,35].

### 3.3.2. Fluorescence quenching studies

To investigate binding mode of complex **1** with calf thymus DNA, a competitive binding experiment has been performed using ethidium bromide (EB) as a probe. EB is a classical indicator of intercalation. It forms soluble complexes with nucleic acids and exhibit strong fluorescence in the presence of calf thymus DNA because of excellent intercalation of the planar phenanthridinium ring between neighbouring base pairs on the double helix of the DNA. If a molecule is able to replace or exclude the EB from EB-DNA complex or can rupture the secondary structure of CT-DNA, then the increased fluorescence is quenched severely.

The fluorescence of EB-DNA complex has been determined in absence and in the presence of complex **1** (Fig. 3). The mixture containing equimolar ( $1.53 \times 10^{-4} \text{ M}$ ) EB and

DNA has been titrated with varying concentration of complex **1** ( $[\text{complex } \mathbf{1}]/[\text{DNA}]$ ) ratio of 0.29 to 1.50). With the gradual addition of complex **1** to CT DNA pretreated with EB solution, the emission intensity at 592 nm quenches in remarkable extent with a red shift. This event clearly demonstrates that EB molecules are replaced from EB bound DNA and complex **1** binds with the same DNA with similar affinity. It is clearly evident from the figure that all of the EB molecules are not displaced from the EB-DNA com-

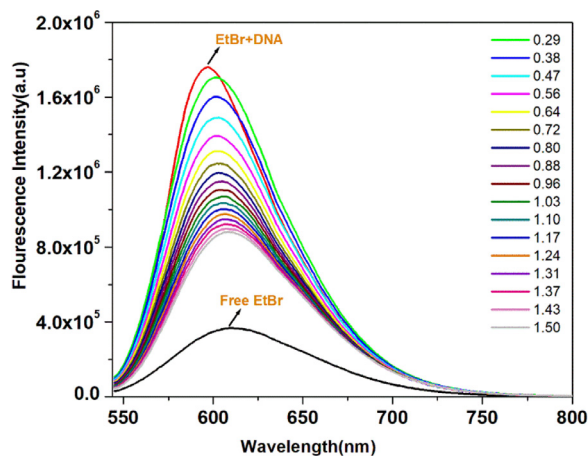


Fig. 3. Emission spectra of EB bound to CT-DNA in absence (red) and in the presence of complex **1**.  $[\text{Complex } \mathbf{1}]/[\text{DNA}] = 0, 0.29, 0.38, 0.47, 0.56, 0.64, 0.72, 0.80, 0.88, 0.96, 1.03, 1.10, 1.17, 1.24, 1.31, 1.37, 1.43, 1.50$ ; Inset: Stern-Volmer quenching curve.

plex, so partial intercalation in addition to the electrostatic interaction cannot be completely ruled out.

Furthermore, the quenching extents have been determined quantitatively by using the following Stern-Volmer equation [36]:

$$I_0/I = 1 + K_{\text{sq}}r$$

where  $I_0$  and  $I$  represent fluorescence intensity in absence and in the presence of complex **1**, respectively, and  $r$  signifies the ratio of concentration of complex **1** to concentration of DNA.  $K_{\text{sq}}$  is known as the linear Stern-Volmer quenching constant. The quenching plots demonstrate that the fluorescence quenching of EB-DNA complex in the presence of the nickel complex is in excellent agreement with the linear Stern-Volmer equation.  $K_{\text{sq}}$  value has been determined as the ratio of the slope to intercept and it has been found to be 0.763. The  $K_{\text{sq}}$  value so obtained for complex **1** reveals that some of the EB molecules have been displaced from their DNA binding sites, which is in accordance with the results obtained in absorption spectral experiments.

### 3.3.3. Circular Dichroism spectral studies

Circular Dichroism (CD) spectroscopy is a useful technique to diagnose any changes in the morphology of DNA while studying drug-DNA interactions. The CD spectrum of CT DNA displays a positive band at 274 nm arising from base stacking interactions and a negative band at 243 nm due to the right-handed helicity of B-DNA form, in the UV region. These two bands result from the excitation coupling interactions of the bases and they depend on the tilted orientation on DNA backbone. Thus, they are reasonably sensitive when small molecules interact with the DNA. Classical intercalative interaction enhances the intensities of both bands. On the other hand, when there is an electrostatic or groove binding interaction between the complex and DNA, small or no perturbation of the base stacking and helicity bands have been observed. It is to mention that hydrophobic base stacking in the oligomers and polymers produces close contacts and Coulombic interaction resulting strong CD bands which correspond to each base transition [37]. Therefore, in the presence of small molecules, which restrict interactions between DNA bases and make base stacking weak, should cause a lowering in the intensities of CD bands.

The interaction of complex **1** with DNA induces a change in the CD spectrum (Fig. 4). With increasing concentration of the Ni(II) complex, both the positive and negative bands show slight change in the intensity, which implies a non-intercalative groove binding interaction between DNA and complex **1** that stabilizes the right-

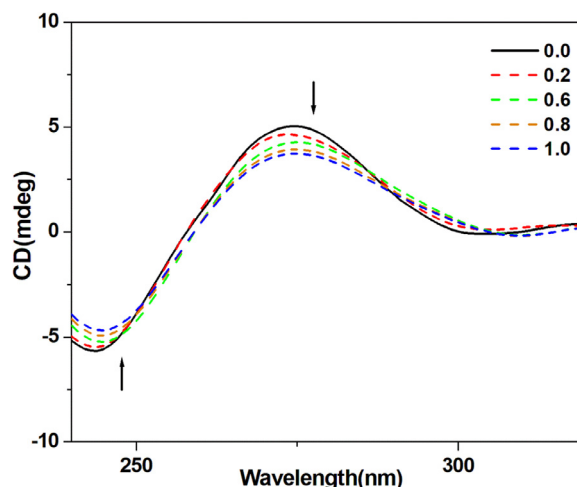
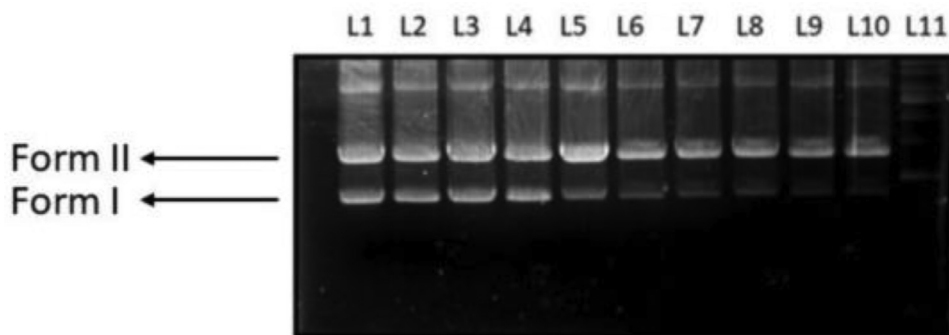


Fig. 4. CD spectra of DNA ( $1.2 \times 10^{-4} \text{ M}$ ) in absence (solid line) and in the presence (dashed line) of complex **1** in  $[\text{Complex } \mathbf{1}]/[\text{DNA}] = 0.0, 0.2, 0.6, 0.8$  and  $1.0$ .



**Fig. 5.** Agarose gel electrophoresis depicting cleavage of plasmid PUC19 DNA (500 ng) by complex **1** at different concentrations for an incubation time of 30 min at 37°C; Lane 1:DNA+ H<sub>2</sub>O; lane 2: DNA+ Complex **1**+ H<sub>2</sub>O; lane 3: DNA + Complex **1** + DMSO; lane 4: DNA + DMSO; lane 5: DNA + H<sub>2</sub>O<sub>2</sub>; lane 6: DNA +H<sub>2</sub>O<sub>2</sub> + complex **1** (20 μM); lane 7: DNA + H<sub>2</sub>O<sub>2</sub>+ complex **1** (40 μM); lane 8: DNA + H<sub>2</sub>O<sub>2</sub> + complex **1** (60 μM); lane 9: DNA + H<sub>2</sub>O<sub>2</sub> + complex **1** (80 μM); lane 10: DNA + H<sub>2</sub>O<sub>2</sub> + complex **1** (100 μM); lane 11: Ladder.

handed B-form of DNA. It is to note that the nickel complex is positively charged ion. So, there is high possibility that the complex **1** would exercise strong attraction with the negatively charged phosphate backbone of DNA. Thus, electrostatic binding is highly suggested.

### 3.3.4. DNA cleavage studies

Transition metal complexes are suitable for application as metallo-nucleases, because their redox potential can be tuned by the choice of proper metal ion and the ligand. Thus, the DNA cleavage ability of nickel(II) complex has been studied using supercoiled PUC19 plasmid DNA as a substrate in 50 mM Tris-HCl/NaCl buffer (pH=7.2). The original supercoiled form (i.e. Form I) of plasmid DNA exists in nicked form. When it is cleaved, an open circular relaxed form i.e. Form II is observed.

At first, it has been detected that the DNA cleavage activity of complex **1** is dependent on the concentration. Results of gel electrophoretic separations of plasmid PUC19 DNA (0.5 μg/μL) induced by increasing concentration of complex **1** from 20 to 100 μM gradually in 100 mM Tris-HCl/NaCl buffer (pH = 7.2) in the presence H<sub>2</sub>O<sub>2</sub> (200 μM) at 37°C for 30 min have been shown in Fig. 5. With increase in concentration of complex **1**, the cleavage becomes more pronounced. Here with increase in complex concentration, Form I gradually diminishes whereas Form II appears, suggesting the single strand DNA cleavage [38]. This result indicates that the nickel(II) complex can efficiently cleave plasmid DNA. The control tests have been done also as shown in Fig. 5. The role of H<sub>2</sub>O<sub>2</sub> is very important in this process because it has been observed from experimental results that in absence of H<sub>2</sub>O<sub>2</sub>, the DNA cleavage is not very successful. Here, H<sub>2</sub>O<sub>2</sub> acts as an exogenous activator which enables complex **1** to cleave the DNA.

### 3.3.5. DNA cleavage in the presence of reactive oxygen species

To determine the plausible mechanism for DNA cleavage activity of complex **1**, DNA cleavage experiment has been carried out in the presence of various reactive oxygen species (ROS) such as hydroxyl radical scavenger (ethanol), singlet oxygen scavenger, <sup>1</sup>O<sub>2</sub> (NaN<sub>3</sub>), hydrogen peroxide scavenger (KI) and chelating agent (EDTA) (Fig. s8). The hydroxy radical EtOH depicts no inhibitory effect on the cleavage pattern (Fig. s8, lane3) indicative of non-involvement of diffusible hydroxyl radicals in the cleavage process. Additionally, KI and NaN<sub>3</sub> (Fig. s8, lanes 5 and 6) scarcely quenches the DNA cleavage. However, the chelating agent EDTA completely inhibits DNA cleavage (lane 4), signifying the key role of Ni(II) complex in the DNA breakage. Thus, in the presence of H<sub>2</sub>O<sub>2</sub>, complex **1** cleaves plasmid DNA significantly as mentioned above, which emphasizes the crucial role of H<sub>2</sub>O<sub>2</sub> in DNA degradation via oxidative cleavage pathway [39].

### 3.3.6. DNA interaction in the presence of groove binders

To ascertain the possible interaction site of complex **1** with plasmid PUC19 DNA, the cleavage experiment has been performed with the addition a minor groove binder, DAPI [40] and a major groove binder, methyl green (MG) [41]. The results show that considerable restriction of the DNA cleavage activity of complex **1** has been observed in DAPI bound DNA (Fig. s9, lane 2, 3). This indicates the minor groove binding property of the complex. On the other hand, upon addition of MG to the reaction mixture results in some curbing in the DNA cleavage activity signifying the affinity of the complex **1** towards the major groove binding.

## 3.4. HSA binding studies

Understanding and characterizing the interaction of a small molecule as drug with blood plasma protein is of immense importance in research because serum albumin makes up of nearly 55% of total blood plasma protein and exhibits its pivotal role in the transportation of exogenous and endogenous molecules in human plasma. Therefore, different spectral techniques are employed to investigate the interaction of complex **1** with human serum albumin (HSA).

### 3.4.1. Absorption spectra studies

UV-Vis absorption spectroscopy has been used as a reliable tool to check any alteration in the secondary structure of HSA in the presence of complex **1** (Fig. 6). HSA shows a strong absorption peak at 208 nm which may be assigned to n → π\* transition for the peptide bond of α helix. It exhibits another band at 280 nm which is comparatively weak in nature and it may arise due to the presence of the phenyl ring in aromatic acid residues such as Trp, Tyr and Phe [42]. Upon addition of complex **1** with an increase in concentration (3.85-37.04 × 10<sup>-6</sup> M) to HSA of constant concentration (8.1 × 10<sup>-5</sup> M), a gradual increase in absorption intensity at 280 nm has been observed. This implies that the aromatic acid residues, which originally reside in a hydrophobic cavity of the protein, are exposed to an aqueous environment to a certain extent. All the observations suggest that complex **1** has interacted with the carrier protein via non-covalent interaction most probably via electrostatic interaction. This type of interaction may be influenced by H-bond formation which shows effect in the absorption spectra. The changes in spectra are mainly due to the effect of polar solvent e.g. water and an alteration of the function of micro-environment of the polypeptide chain of HSA protein.

To determine the binding ability of complex **1** with HSA quantitatively, the intrinsic binding constant, K, has been determined by

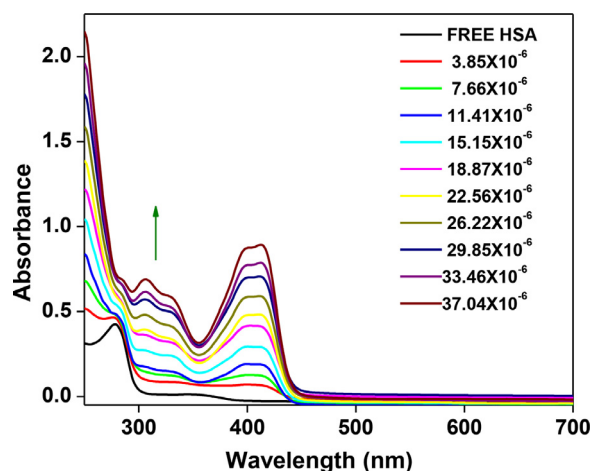


**Fig. 6.** UV-Vis absorption spectra of complex **1** in the presence of HSA obtained in 5 mM Tris-HCl buffer, pH 7.2, at room temperature: [HSA] =  $8.1 \times 10^{-5}$  M; [complex **1**] = 0, 3.85, 7.66, 11.41, 15.15, 18.87, 22.56, 26.22, 29.85, 33.46, 37.04  $\mu$ M, respectively. Arrow shows the intensity changes upon increasing concentration of complex **1**.

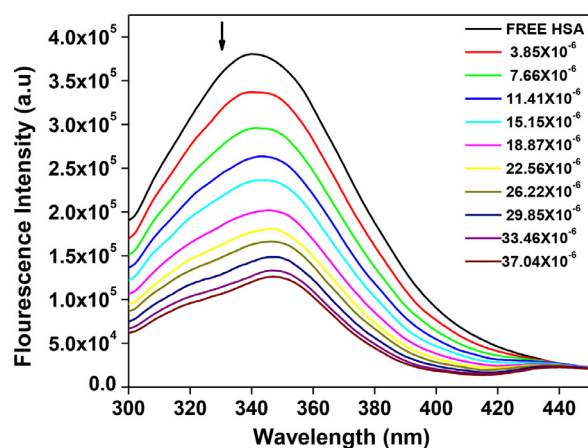
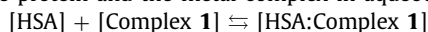


**Fig. 7.** The fluorescence quenching spectra of HSA by different concentrations of complex **1** with the excitation wavelength at 280 nm in 5 mM Tris-HCl buffer, pH 7.2, at room temperature: [HSA] =  $6.5 \times 10^{-5}$  M; the concentration of complex **1** = 0, 0.76, 1.51, 2.25, 2.98, 3.70, 4.41, 5.12,  $5.81 \times 10^{-5}$  M. Arrow shows the intensity changes upon increasing concentration of the quencher.

considering that there exists only one type of interaction between the protein and the metal complex in aqueous solution [42],



$K = [\text{HSA:Complex } \mathbf{1}] / [\text{HSA}] [\text{Complex } \mathbf{1}]$  where  $K$  is the binding constant and  $[\text{HSA:Complex } \mathbf{1}] = C_B$

Thus,  $K = C_B / [C_{\text{HSA}} - C_B] [C_{\text{Complex } \mathbf{1}} - C_B]$  where,  $C_{\text{HSA}}$  and  $C_{\text{Complex } \mathbf{1}}$  represent analytical concentrations of HSA and the complex, respectively, in the solution, respectively.

From the Beer-Lambert law, we can write

$$C_{\text{HSA}} = A_0 / \varepsilon_{\text{HSA}} \cdot l$$

$C_B = (A - A_0) / \varepsilon_B \cdot l$  where  $A_0$  and  $A$  represent the absorbance of HSA in absence and in the presence of complex **1**, respectively at 280 nm [7d].  $\varepsilon_{\text{HSA}}$  and  $\varepsilon_B$  are the molar extinction coefficients of the free protein and the bound complex, respectively, and  $l$  represents the light path of the cuvette as usual (1 cm).

By substituting  $\varepsilon_{\text{HSA}}$  and  $\varepsilon_B$  in Equations

$$A_0 / (A - A_0) = \varepsilon_{\text{HSA}} / \varepsilon_B + \varepsilon_{\text{HSA}} \cdot l / \varepsilon_B K C_{\text{Complex } \mathbf{1}} \cdot l$$

Thus, the double reciprocal plot of  $1/(A - A_0)$  vs.  $1/[\text{Complex } \mathbf{1}]$  is linear (Fig. s10) and the binding constant can be estimated from the ratio of the intercept and the slope.  $K_B$  has been calculated to be  $1.6 \times 10^4 \text{ M}^{-1}$ . The  $K_B$  value suggests that complex **1** binds moderately to HSA followed by conformational changes in its structure.

### 3.4.2. Fluorescence quenching studies

Fluorescence spectroscopy is another effective method used to monitor progress of the interaction of small molecules with the bio macromolecules. The fluorescence emission spectra of HSA have been measured in the range of 300–450 nm by exciting HSA at 280 nm in the presence of increasing concentration of the Ni(II) complex (Fig. 7). HSA displays fluorescence mainly due to the presence of tryptophan residue ( $\lambda_{\text{ex}}$ : 295 nm). Another residue phenylalanine has a low quantum yield. On the other hand, fluorescence of tyrosine residue is generally quenched if it is in ionized form or resides near to an  $-\text{NH}_2$  group, a  $-\text{COOH}$  group or a tryptophan because Tyr and Phe do not absorb in this region. HSA displays a strong fluorescence peak at 344 nm, while complex **1** does not show any fluorescence under the same experimental conditions. The fluorescence intensity of the HSA (fixed concentration,  $6.5 \times 10^{-5}$  M) decreases gradually with increasing concentration of the complex ( $3.85 \times 10^{-6}$  to  $37.04 \times 10^{-6}$  M) and it is accompanied by a hypsochromic or red shift (10 nm) from the initial HSA emission intensity indicating the enhancement in polarity

of the microenvironment about Trp residue [43]. These results indicate the binding ability of complex **1** to HSA. The complex induces conformational changes in HSA. The intramolecular force, that is for maintaining the secondary structure, may be changed and hydrophobicity is also decreased signifying that the tryptophan residues are more uncovered to the solvent medium.

Commonly, by the following Stern-Volmer equation, fluorescence quenching can be described [44]:

$F_0/F = 1 + K_q \tau_0 [Q] = 1 + K_{\text{SV}} [Q]$  where  $F_0$  and  $F$  represent the fluorescence intensity in absence and in the presence of quencher, respectively.  $K_q$  is the quenching rate constant of the biomolecules,  $K_{\text{SV}}$  is the Stern-Volmer quenching constant,  $\tau_0$  is the average life time of the molecule without quencher ( $\tau_0 = 10^{-8}$  s) and  $[Q]$  is the concentration of the quencher. The plot of  $F_0/F$  versus  $[Q]$  for the quenching of fluorescence of HSA in the presence of complex **1** is depicted in Fig. s11.  $K_{\text{SV}}$  and  $K_q$  values have been calculated to be  $5.95 \times 10^4 \text{ M}^{-1}$  and  $5.95 \times 10^{12} \text{ M}^{-1} \text{ s}^{-1}$ , respectively. It indicates that the quenching rate constant of the biomolecules is bigger than that their limiting diffusion constant ( $2.0 \times 10^{10} \text{ M}^{-1} \text{ s}^{-1}$ ) implying quenching occurs due to a particular interaction between the nickel complex and the protein molecule [45].

Now, the Scatchard equation has been used to evaluate the binding constant and number of binding sites [46]:

$$\log [F_0 - F / F] = \log K + n \log [Q]$$

where,  $F_0$  and  $F$  are the fluorescence intensity of HSA in absence and in the presence of a quencher, respectively  $K$  is the binding constant and  $n$  is the number of binding sites. From the plot of  $\log [(F_0 - F)/F]$  vs.  $\log [Q]$  both  $K$  and  $n$  can be determined from the intercept on Y-axis and the slope, respectively (Fig. s12). The binding constant and the number of binding sites have been calculated to be  $7.16 \times 10^5 \text{ M}^{-1}$  and 1.25, respectively, which are comparable to those observed for previously reported binding constant [10a-b]. The value of  $n$  is about 1 which suggests that the complex is bonded to HSA in 1:1 ratio.

### 3.4.3. Energy transfer mechanism and binding distance between complex 1 and HSA

Fluorescence energy transfer happens because of overlapping of the emission spectrum of HSA, which acts as the donor, with the absorption spectrum of complex **1**, which behaves as the acceptor (Fig. s13). The extent of energy transfer depends on several factors such as the success of the overlap between emission spectrum of the donor and absorption spectrum of the acceptor, orientation of

transition dipole and the distance between the donor and acceptor (Fig. s14). Quenching of fluorescence of Trp residue occurs in the presence of the Ni(II) complex via Forster resonance energy transfer (FRET) mechanism. Efficiency of energy transfer ( $E$ ) can be determined by the following equation [47]:

$$E = 1 - \frac{F}{F_0} = \frac{R_0^6}{R_0^6 + r^6}$$

where  $F_0$  and  $F$  represent the fluorescence intensity of HSA in absence and in the presence a quencher, respectively,  $r$  is distance between the acceptor and the donor, and  $R_0$  is the critical distance at 50% transfer efficiency.

$R_0$  can be determined with the help of the following equation [48]:

$$R_0^6 = 8.78 \times 10^{-25} K^2 n^{-4} \varphi J$$

where  $K^2$  represents spatial orientation factor between the emission dipole and absorption dipole,  $n$  is refractive index of the medium,  $\varphi$  is emission quantum yield of the donor, and  $J$  is the overlap integral of emission spectrum of donor and absorption spectrum of acceptor.  $J$  can be evaluated by the following equation [49]:

$$J = \frac{\int_0^\infty F(\lambda) \varepsilon(\lambda) \lambda^4 d\lambda}{\int_0^\infty F(\lambda) d\lambda}$$

where  $F(\lambda)$  is the proper fluorescence intensity of the donor at wavelength,  $\lambda$ , and  $\varepsilon(\lambda)$  represents molar absorption coefficient of the acceptor at wavelength,  $\lambda$ . Under the experimental conditions, the value of  $K^2$  is 2/3,  $n$  is 1.36,  $\varphi$  is 0.15 for a solution with haphazard orientation as in present case. The value of  $J$  has been determined to be  $7 \times 10^{-14}$  (from the graph),  $R_0$  has been calculated to be 3.48 nm,  $E$  as 0.47 and  $r$  as 3.55 nm. The donor (HSA) to acceptor (complex 1) distance ( $r$ ) is less than 7 nm which indicates that the energy transfer from tryptophan residue of HSA to the metal complex occurs with high possibility [50]. These results are in accordance with the static quenching interaction observed between HSA and complex 1 [45].

#### 3.4.4. IR spectral studies

IR spectrum of proteins has been generally used to investigate any alteration in conformation in the structure of proteins induced by a possible candidate as a drug. The IR spectra at the mid IR frequency bands of proteins usually exhibit a number of amide bands attributed to different stretching vibrations of the peptide moieties. Here the spectrum has been obtained by subtracting the absorption of Tris buffer from the spectrum of HSA solution (Fig. s15). The protein amide I band, which mainly appears due to C=O stretching and amide II band, which is due to C-N stretching coupled with N-H bending mode, bear a relationship with the secondary structure of proteins. However, the former one is more sensitive to the perturbation of protein secondary structure than rest of its part. As depicted in Fig. s15, upon interaction with complex 1, the peak position of amide I band is shifted from 1654 to 1674  $\text{cm}^{-1}$  and that of amide II band from 1557 to 1553  $\text{cm}^{-1}$ . These changes in the IR spectra indicate that complex 1 has been able to alter secondary structure of HSA while interacting.

#### 3.4.5. 3D fluorescence spectral studies

These conformational and micro-environmental changes of HSA induced by complex 1 have further been monitored by 3D fluorescence spectroscopy of HSA in the absence and in the presence of the complex 1. The 3D fluorescence spectra of HSA and complex 1-HSA system are shown in Fig. s16. Peak A represents a Rayleigh scattering peak ( $\lambda_{\text{ex}} = \lambda_{\text{em}}$ ) while Peak B ( $\lambda_{\text{ex}} = 280 \text{ nm}$ ,  $\lambda_{\text{em}} = 350 \text{ nm}$ ) primarily shows spectral behaviour of tryptophan residue. On the other hand, Peak C indicates the second-order scattering peak ( $\lambda_{\text{em}} \approx 2 \lambda_{\text{ex}}$ ) [48]. It has been observed from Fig.

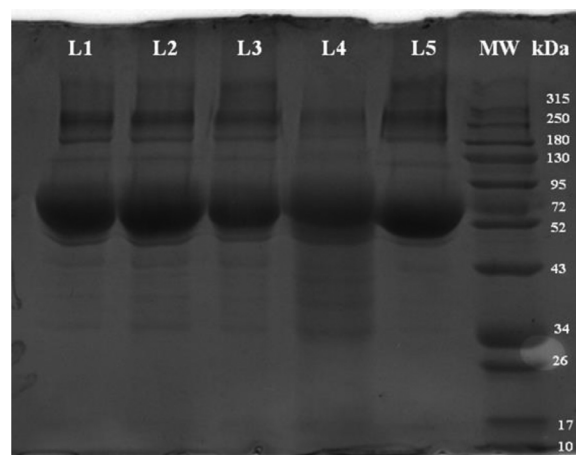


**Fig. 8.** SDS-PAGE electrophoresis in 0.8% polyacrylamide gel of HSA fragmentation, in the presence of complex 1, treated with  $\text{H}_2\text{O}_2$ , for 30 min at 37°C, in Tris buffer 100 mM, pH 7.2. Lane 1: 75  $\mu\text{M}$  HSA, Lane 2: 75  $\mu\text{M}$  HSA and 100 mM  $\text{H}_2\text{O}_2$ , Lane 3: 75  $\mu\text{M}$  HSA, 100 mM  $\text{H}_2\text{O}_2$  and 40  $\mu\text{M}$  complex, Lane 4: 75  $\mu\text{M}$  HSA, 100 mM  $\text{H}_2\text{O}_2$  and 80  $\mu\text{M}$  complex, Lane 5: 75  $\mu\text{M}$  HSA, 100 mM  $\text{H}_2\text{O}_2$  and 100  $\mu\text{M}$  complex.

s16 that both the fluorescence intensities of peaks A and B have been quenched appreciably and the emission maximum peaks alter. These facts indicate that the interaction of complex 1 with HSA induces some conformational and micro environmental changes in HSA. These results are in accordance with that obtained from UV-vis, fluorescence and CD spectral analysis.

#### 3.4.6. CD spectral studies on changes of the HSA conformation with complex 1

To study effect of complex 1 binding on the secondary structure of HSA, CD measurement has been carried out in the presence of the Ni(II) complex at different concentrations. The CD spectrum of the protein displays two negative bands at 208 and 219 nm which may be assigned to  $\pi \rightarrow \pi^*$  and  $n \rightarrow \pi^*$  transfers, respectively, for the peptide bond (Fig. s17). These are typical characteristic of  $\alpha$ -helix structure of the protein [51]. The CD signal of the protein molecule enhances with the increase in concentration of complex 1 as the helical secondary structure of HSA is destroyed to some extent in the presence of the complex. This suggests a considerable amount changes in the conformation of HSA [52]. However, spectral pattern of HSA before and after addition of complex 1 is similar that indicates the predominant presence of  $\alpha$ -helical structure in HSA.

#### 3.4.7. Oxidative damage of HSA by complex 1

Oxidative damage of HSA has been studied with different concentrations of the protein and complex 1 [53]. HSA exhibits remarkable degradation after incubation with complex 1, for 30 min, at 37°C in the presence of  $\text{H}_2\text{O}_2$ . It is indicated by a continuum of protein fragments at SDS-PAGE in 0.8% acrylamide gel (Fig. 8). Clear and thick protein band is observed at the expected molecular weight range (around 66 kDa). As shown in Fig. 8, it is observed that the control condition (Lane 1) does not show any apparent cleavage, while upon gradual addition of complex 1 (40-100  $\mu\text{M}$ ), HSA displays its proficient cleavage activity with appreciable smearing or fading of the band. Possibly nonspecific binding of the nickel complex with the protein results in the fading out of the band and leads to very small fragments [54].

### 3.5. Cytotoxicity evaluation

#### 3.5.1. MTT assay

MTT assay has been performed to examine the ability of complex 1 to hinder cell growth and induce cell death in both lung

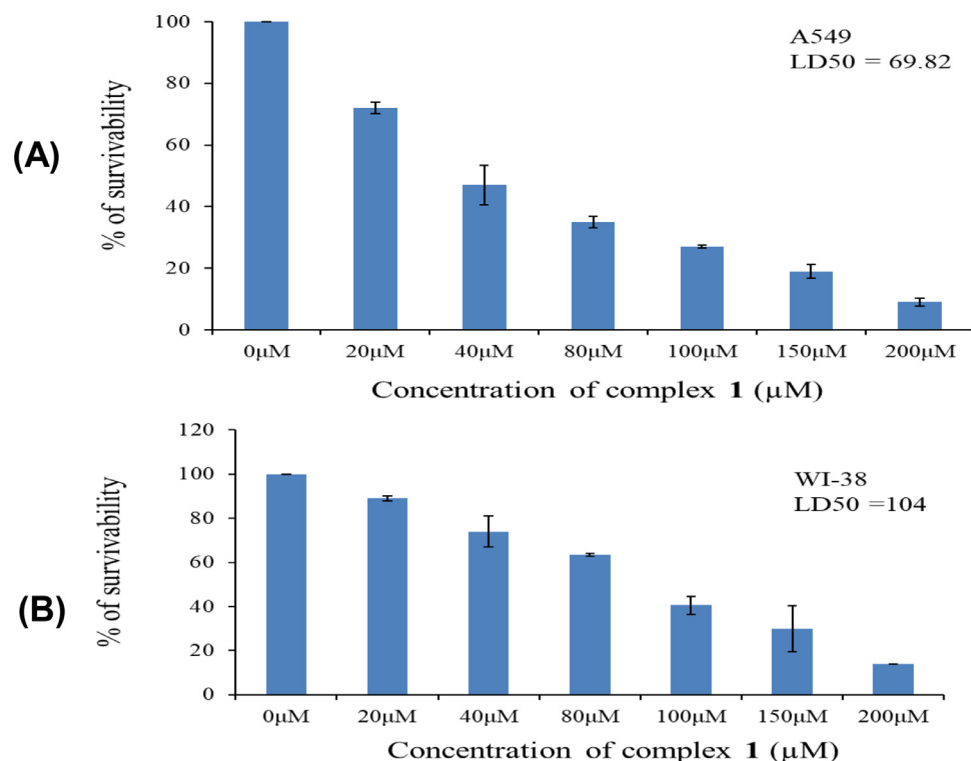


**Fig. 9.** Effect of complex **1** on viability of (A) lung carcinoma (A549) and (B) normal lung fibroblast (WI-38). Cells were treated with different concentration (0-200 μM) of complex **1** for 12 h. Cell viability was measured by MTT assay. Data represented as mean ± SE of three independent experiments made in three replicates.

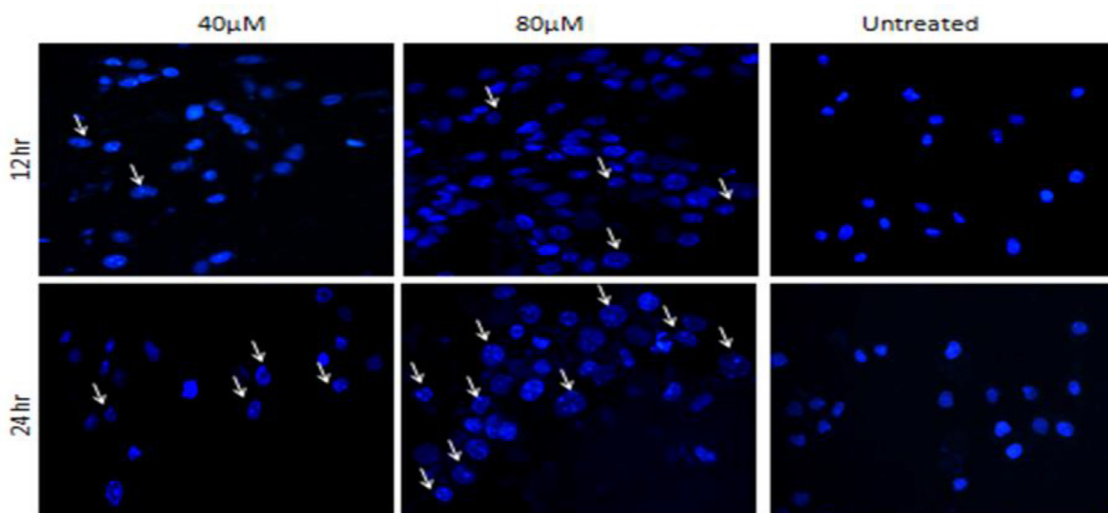


**Fig. 10.** Apoptotic nuclear morphology study by DAPI staining in A549 cell.

carcinoma and normal lung fibroblast cell line. The cytotoxic effect of complex **1** has been investigated after 12 h of treatment on A549 (lung carcinoma) and WI-38 (normal lung fibroblast) by using MTT assay. As shown in Fig. 9, cell survivability has significantly ( $p < 0.0002$ , 40-200 μM) decreased in a dose dependent manner in carcinoma cell line. In A549 cells proliferation has been significantly inhibited by complex **1** with LD<sub>50</sub> value of 69.82, whereas, in normal fibroblast WI-38 cells proliferation, the LD<sub>50</sub> value is 104. Since, complex **1** shows significant cytotoxicity towards A549 cells, and less toxicity to WI-38, suggesting potential anticancer drug for lung carcinoma.

### 3.6. Apoptosis evaluation

#### 3.6.1. Apoptotic nuclear morphology study by DAPI staining

Apoptotic morphology has been performed in cells treated with complex **1** at their respective LD<sub>50</sub> dose for 12 h and 24 h by DAPI staining. It reveals that the untreated cells exhibit no nucleus shrinking or polynuclear fragmentations. However, clear polynuclear fragmentation as well as nucleus shrinking has been noticed in cells treated with the metal complex (Fig. 10). It has been estimated that around 52% (40 μM) and 57% (70 μM) apoptotic cells have been observed in 24 h in complex **1** treated A549 cells.



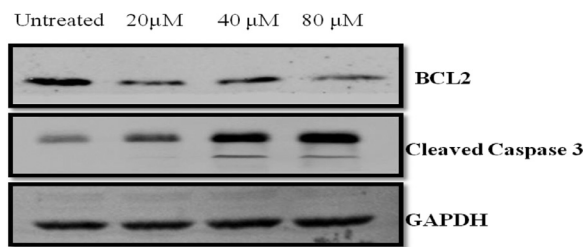


**Fig. 11.** Western blot of apoptotic protein Bcl2, cleaved Caspase 3 and loading control GAPDH. Lane 1: Untreated A549 cell, lane 2: 20  $\mu\text{M}$  of complex **1** treated A549 cell, lane 3: 40  $\mu\text{M}$  of complex **1** treated A549 cell, lane 4: 80  $\mu\text{M}$  of complex **1** treated A549 cell. This result suggests upregulation of apoptotic pathway upon treatment with complex **1** in lung carcinoma cell line.

### 3.6.2. Treatment of complex 1 in A549 promotes apoptosis

We have evaluated the expression of apoptotic marker cleaved caspase-3 and antiapoptotic protein Bcl-2 in the total cellular extract of 12 h complex **1** treated A549 cell line. It has been found that the expression of cleaved caspase-3 has been increased in a dose dependent manner while the expression of Bcl-2 decreases in the same set of experiments (Fig. 11). Thus, this fact indicates that complex **1** induces apoptosis by downregulating Bcl-2 and upregulation of caspase-3 activity, which leads to activation of caspase-3. Upregulation of caspase-3 leads to successful apoptosis and subsequent cell death [55].

## 4. Conclusions

We have synthesized and characterized a mononuclear Ni(II) complex (Complex **1**) with 1-((2-piperidin-1-yl)ethylimino)methyl)naphthalene-2-ol as the ligand. It interacts with DNA and binds mainly with minor groove. Several studies indicate that complex **1** is able to bind with human serum albumin efficiently. In this present study, we explore whether the nickel complex has any tumor suppressive function in lung cancer cell line (A549). To attain this aim, the lung carcinoma cells have been treated with different concentrations of nickel complex. The study shows that the mononuclear Ni(II) complex exhibits selective cytotoxicity towards A549 cell but it does not kill normal healthy cell (WI-38). Thus, it could be used as a potential anti-cancer drug. In this study we have shown that the complex can induce apoptosis in lung carcinoma cell by downregulating Bcl2 and upregulation of caspase-3 activity. We have also observed higher percentage of apoptotic bodies in A549 nucleus compared to normal fibroblast which is a major characteristic feature of apoptosis. Thus, this Ni(II) complex can bring about cell death and pave the way for further evaluation as a potential therapeutic agent. These findings suggest that this nickel complex might be a tumor suppressor and a potential target for lung carcinoma. In our previous study with Cu-complex [19], it has been observed that the complex was involved in intercalative binding with DNA whereas in the present study, complex **1** involves in minor groove binding. Both of the complexes can bind HSA with same efficiency. In the present study it has been established that the complex exhibits selective cytotoxicity towards cancer cell whereas it is not harmful for normal cell indicating its tumor suppressing ability.

## Declaration of Competing Interest

The authors declare that they have no known competing financial interests or personal relationships that could have appeared to influence the work reported in this paper.

## Acknowledgments

AB wishes to thank CSIR, New Delhi for providing her a fellowship.

## Supplementary materials

Supplementary material associated with this article can be found, in the online version, at doi:10.1016/j.molstruc.2021.131687.

## References

- [1] (a) K.E. Erkkila, D.T. Odom, J.K. Barton, Recognition and reaction of metallointercalators with DNA, *Chem. Rev.* 99 (1999) 2777–2796; (b) C. Santini, M. Pellei, V. Gandin, M. Porchia, F. Tisato, C. Marzano, Advances in copper complexes as anticancer agents, *Chem. Rev.* 114 (2014) 815–862.
- [2] (a) A. Erdem, M. Ozsoz, Electrochemical DNA biosensors based on DNA-drug interactions, *Electroanalysis* 14 (2002) 965–974; (b) H.J. Lozano, N. Busto, G. Espino, A. Carbayo, J.M. Leal, J.A. Platts, B. García, Interstrand DNA covalent binding of two dinuclear Ru(II) complexes. Influence of the extra ring of the bridging ligand on the DNA interaction and cytotoxic activity, *Dalton Trans* 46 (2017) 3611–3622; (c) S. Ambika, S. Arunachalam, R. Arunb, K. Premkumar, Synthesis, nucleic acid binding, anticancer and antimicrobial activities of polymer-copper(II) complexes containing intercalative phenanthroline ligand(DPQ), *RSC Adv* 3 (2013) 16456–16468.
- [3] (a) Barnett Rosenberg, Loretta Vancamp, James E. Trosko, Virginia H. Mansour, Platinum Compounds: a New Class of Potent Antitumour Agents, *Nature* 222 (1969) 385–386; (b) B. Rosenberg, L. Vancamp, T. Krigas, Inhibition of Cell Division in *Escherichia coli* by Electrolysis Products from a Platinum Electrode, *Nature* 205 (1965) 698–699; (c) B. Rosenberg, E. Renshaw, L. Vancamp, J. Hartwick, J. Drobnik, Platinum-Induced Filamentous Growth in *Escherichia coli*, *J. Bacteriol.* 93 (1967) 716–721; (d) L. Kelland, The resurgence of platinum-based cancer chemotherapy, *Nat. Rev. Cancer* 7 (2007) 573–584.
- [4] Y.F. Sun, H. Wu, G.Q. Zhao, Y. Shi, Binding of amifostine to human serum albumin: A biophysical study, *Luminescence* 30 (2015) 79–85.
- [5] P. Krishnamoorthy, P. Sathyadevi, R.R. Butorac, A.H. Cowley, N.S.P. Bhuvanesh, N. Dharmaraj, Copper(I) and nickel(II) complexes with 1:1 vs. 1:2 coordination of ferrocenyl hydrazone ligands: Do the geometry and composition of complexes affect DNA binding/cleavage, protein binding, antioxidant and cytotoxic activities? *Dalton Trans.* 41 (2012) 4423–4436.
- [6] (a) E. Denkhaus, K. Salnikow, Nickel essentiality, toxicity, and carcinogenicity, *Crit. Rev. Oncol. Hemat.* 42 (2002) 35–56; (b) J.G. Muller, L.A. Kayser, S.J. Paikoff, V. Duarte, N. Tang, R.J. Perez, S.E. Rokita, C.J. Burrows, Formation of DNA adducts using nickel (II) complexes of redox-active ligands: a comparison of salen and peptide complexes, *Coord. Chem. Rev.* 185–186 (1999) 761–774; (c) G. Barone, A. Terenzi, A. Lauria, A.M. Almerico, J.M. Leal, N. Busto, B. García, DNA-binding of nickel (II), copper (II) and zinc (II) complexes: Structure–affinity relationships, *Coord. Chem. Rev.* 257 (2013) 2848–2862.
- [7] (a) B. Fei, W. Li, W. Xu, J. Long, Q. Liu, W. Sun, C.E. Anson, A.K. Powell, Crystal Structure Synthesis, DNA Binding, Antibacterial, and Cytotoxic Activities of Two Chiral Copper(II) Complexes, *Eur. J. Inorg. Chem.* (2013) 5919–5927; (b) J. Patole, D. Shingnapurkar, S. Padhye, C. Ratledge, Schiff base conjugates of  $\alpha$ -aminosalicylic acid as antimycobacterial agents, *Bioorg. Med. Chem. Lett.* 16 (2006) 1514–1517; (c) Z.H. Chohan, Antibacterial copper (II) complexes of 1, 1'-symmetric ferrocene-derived Schiff-base ligands: studies of the effect of anions on their antibacterial properties, *Appl. Organomet. Chem.* 16 (2002) 17–20; (d) G. Ceyhan, M. Kose, M. Tumer, I. Demirtas, A. Yaglioglu, V. McKee, Structural characterization of some Schiff base compounds: Investigation of their electrochemical, photoluminescence, thermal and anticancer activity properties, *J. Lumin.* 143 (2013) 623–634.
- [8] (a) J.G. Deng, G. Su, P. Chen, Y. Du, Y. Gou, Y. Liu, Evaluation of DNA binding and DNA cleavage of nickel (II) complexes with tridentate  $\alpha$ -N-heterocyclic thiosemicarbazones ligands, *Inorg. Chim. Acta* 471 (2018) 194–202; (b) G. Kalariasi, Ruchi Jain, H. Puselman, S.P. Chandrika, K. Preethi, R. Prabhakaran, New binuclear Ni(II) metallates containing ONS chelators: synthesis, characterization, DNA binding, DNA cleavage, protein binding, antioxidant activity, antimicrobial and in vitro cytotoxicity, *New J. Chem.* 41 (2017) 2543–2560.
- [9] R.R. Kumar, M.K.M. Subarkhan, R. Ramesh, Synthesis and structure of nickel(II) thio-carboxamide complexes: effect of ligand substitutions on DNA/protein binding, antioxidant and cytotoxicity, *RSC Adv* 5 (2015) 46760–46773.
- [10] (a) Y. Li, Z. Yang, M. Zhou, Y. Li, Synthesis and crystal structure of new monometallic Ni(II) and Co(II) complexes with an asymmetrical aroylhydrazone: effects of the complexes on DNA/protein binding property, molecular docking, and in vitro anticancer activity, *RSC Adv* 7 (2017) 49404–49422; (b) Y. Li, Y. Li, Z. Yang, F. Meng, N. Wang, M. Zhou, Z. Xia, Q. Gong, Q. Gao, Distinct supramolecular assemblies of Fe(III) and Ni(II) complexes constructed from the o-vanillin salicylhydrazone ligand: syntheses, crystal structures, DNA/protein interaction, and antioxidant and cytotoxic activity, *New J. Chem.* 46 (2019) 8024–8043; (c) A.C. Ekenna, E.C. Ibezim, O.C. Okpareke, C.U. Ibeji, C.J.O. Anarado, I. Babahan, B. Coban, B. Abulhasanov, F. Cömert, O.T. Ujam, Novel 3-Hydroxy-2-naphthoic hydrazone and Ni(II), Co(II) and Cu(II) Complexes: Synthesis, Spectroscopic Characterization, Antimicrobial, DNA Cleavage and Computational Studies, *Appl. Organometal. Chem.* 33 (2019) e4913.

- [11] L. Zarei, Z. Asadi, M. Dusek, V. Eigner, Homodinuclear Ni (II) and Cu (II) Schiff base complexes derived from O-vanillin with a pyrazole bridge: Preparation, crystal structures, DNA and protein (BSA) binding, DNA cleavage, molecular docking and cytotoxicity study, *J. Photochem. Photobiol. A* 374 (2019) 145–160.
- [12] A.-N.M.A. Alaghaz, S.A.A. Aldulmani, Preparation, Structural characterization and DNA binding/cleavage affinity of new bioactive nano-sized metal (II/IV) complexes with oxazon-Schiff's base ligand, *Appl. Organometal. Chem.* 33 (2019) e5135.
- [13] R.L.B. Alanazi, M. Zaki, W.A. Bawazir, Synthesis and characterization of new metal complexes containing Triazino [5, 6-b] indole moiety: In vitro DNA and HSA binding studies, *J. Mol. Struct.* 1246 (2021) 131203.
- [14] C.-N. Ko, G. Li, C.-H. Leung, D.-L. Ma, Dual function luminescent transition metal complexes for cancer theranostics: The combination of diagnosis and therapy, *Coord. Chem. Rev.* 381 (2019) 79–103.
- [15] Y. Xia, C.-D. Fan, B.-X. Zhao, J. Zhao, D.-S. Shin, J.-Y. Miao, Synthesis and structure–activity relationships of novel 1-aryl-methyl-3-aryl-1H-pyrazole-5-carbohydrazide hydrazone derivatives as potential agents against A549 lung cancer cells, *Eur. J. Med. Chem.* 43 (2008) 2347–2353.
- [16] C.D. Fan, H. Su, J. Zhao, B.X. Zhao, S.L. Zhang, J.Y. Miao, A novel copper complex of salicylaldehyde pyrazole hydrazone induces apoptosis through up-regulating integrin  $\beta 4$  in H322 lung carcinoma cells, *Eur. J. Med. Chem.* 45 (2010) 1438–1446.
- [17] T.T.-H. Fong, C.-N. Lok, C.Y.-S. Chung, Y.-M.E. Fung, P.-K. Chow, P.-K. Wan, C.-M. Che, Cyclometalated Palladium (II) N-Heterocyclic Carbene Complexes: Anticancer Agents for Potent In Vitro Cytotoxicity and In Vivo Tumor Growth Suppression, *Angew. Chem. Int. Ed.* 55 (2016) 11935–11939.
- [18] A. Bhattacharjee, S. Das, B. Das, P. Roy, Intercalate DNA binding, protein binding, antibacterial activities and cytotoxicity studies of a mononuclear copper (II) complex, *Inorg. Chim. Acta* 514 (2021) 119961.
- [19] BrukerAPEX2, SAINT and SADABS, Bruker AXS Inc., Madison, Wisconsin, USA, 2008.
- [20] G.M. Sheldrick, SHELXT - Integrated space-group and crystal-structure determination, *Acta Cryst. A71* (2015) 3.
- [21] G.M. Sheldrick, Crystal structure refinement with SHELXL, *Acta Cryst. C71* (2015) 3–8.
- [22] B. Selvakumar, V. Rajendiran, P.U. Maheswari, H. Stoeckli-Evans, M. Palaniandavar, Structures, spectra, and DNA-binding properties of mixed ligand copper(II) complexes of iminodiacetic acid: The novel role of diimine co-ligands on DNA conformation and hydrolytic and oxidative double strand DNA cleavage, *J. Inorg. Biochem.* 100 (2006) 316–330.
- [23] Y. Gultneh, A.R. Khan, D. Blaise, S. Chaudhry, B. Ahvazi, B.B. Marvey, R.J. Butcher, Syntheses and structures of and catalysis of hydrolysis by Zn (II) complexes of chelating pyridyl donor ligands, *J. Inorg. Biochem.* 75 (1999) 7–18.
- [24] M. Zaki, M. Afzal, M. Ahmad, S. Tabassuma, Synthesis and crystal structure elucidation of new copper(II)-based chemotherapeutic agent coupled with 1,2-DACH and orthovanillin: Validated by in vitro DNA/HSA binding profile and pBR322 cleavage pathway, *J. Photochem. Photobiol. B* 161 (2016) 318–327.
- [25] D. Ghosh, V.A. Bohr, P. Karmakar, Acetylation of Werner protein at K1127 and K1117 is important for nuclear trafficking and DNA repair, *DNA Repair* 79 (2019) 22–31.
- [26] D. Laha, A. Pramanik, S. Chattopadhyay, S.K. Dash, S. Roy, P. Pramanik, P. Karmakar, Folic acid modified copper oxide nanoparticles for targeted delivery in in vitro and in vivo systems, *RSC Adv* 5 (2015) 68169–68178.
- [27] S. Anbu, M. Kandaswamy, B. Varghese, Structural, electrochemical, phosphate-hydrolysis, DNA binding and cleavage studies of new macrocyclic binuclear nickel (II) complexes, *Dalton Trans* 39 (2010) 3823–3832.
- [28] L. Yang, D.R. Powell, R.P. Houser, Structural variation in copper(I) complexes with pyridylmethylamide ligands: structural analysis with a new four-coordinate geometry index,  $\tau_4$ , *Dalton Trans* (2007) 955–964.
- [29] (a) A. Bhattacharjee, S. Dey, P. Roy, Synthesis, characterization and catalytic properties of dinuclear complexes of copper(II) and nickel(II): Oxidation of cyclohexane, toluene and cyclopentane, *Inorg. Chim. Acta* 490 (2019) 93–103; (b) S. Halder, J. Mondal, J. Ortega-Castro, A. Frontera, P. Roy, A Ni-based MOF for selective detection and removal of  $Hg^{2+}$  in aqueous medium: a facile strategy, *Dalton Trans* 46 (2017) 1943–1950; (c) J. Chakraborty, M. Nandi, H. Mayer-Figge, W.S. Sheldrick, L. Sorace, A. Bhaumik, P. Banerjee, Nickel Complexes with  $N_2O$  Donor Ligands: Syntheses, Structures, Catalysis and Magnetic Studies, *Eur. J. Inorg. Chem.* (2007) 5033–5044.
- [30] K. Ghosh, S. Dey, S. Halder, A. Bhattacharjee, C. Rizzoli, P. Roy, A turn-on fluorescent chemosensor for  $Zn^{2+}$  ion: X-ray structure and application in cell imaging study, *J. Mol. Struct.* 1118 (2016) 325–334.
- [31] A. Kurutos, I. Orehovec, A.T. Paic, I. Crnolatac, L. Horvat, N. Gadjev, I. Pitanida, T. Deligeorgiev, New series of non-toxic DNA intercalators, mitochondria targeting fluorescent dyes, *Dyes Pigment* 148 (2018) 452–459.
- [32] (a) J. Rajesh, A. Gubendran, G. Rajagopal, P. Athappan, Synthesis, spectra and DNA interactions of certain mononuclear transition metal(II) complexes of macrocyclic tetraaza diacetyl curcumin ligand, *J. Mol. Struct.* 1010 (2012) 169–178; (b) N. Revathi, M. Sankarganesh, J. Rajesh, J.D. Raja, Biologically Active Cu(II), Co(II), Ni(II) and Zn(II) Complexes of Pyrimidine Derivative Schiff Base: DNA Binding, Antioxidant, Antibacterial and In Vitro Anticancer Studies, *J. Fluoresc.* 27 (2017) 1801–1814.
- [33] S. Sujatha, S. Balasubramanian, B. Varghese, M. Jayaprakashvel, N. Mathivanan, Synthesis, characterization and DNA interaction of hexaaza macrotricyclic copper (II) complexes, *Inorg. Chim. Acta* 386 (2012) 109–115.
- [34] A. Wolfe, G.H. Shimer, T. Meehan, Polycyclic aromatic hydrocarbons physically intercalate into duplex regions of denatured DNA, *Biochemistry* 26 (1987) 6392–6396.
- [35] Q. Wei, J. Dong, P. Zhao, M. Li, F. Cheng, J. Kong, L. Li, DNA binding, BSA interaction and SOD activity of two new nickel (II) complexes with glutamine Schiff base ligands, *J. Photochem. Photobiol. B* 161 (2016) 355–367.
- [36] M.E.K. Wahba, N. El-Enany, F. Belal, Application of the Stern–Volmer equation for studying the spectrofluorimetric quenching reaction of eosin with clindamycin hydrochloride in its pure form and pharmaceutical preparations, *Anal. Methods* 7 (2015) 10445–10451.
- [37] J.A. Pachter, C.H. Huang, V.H. DuVernay Jr., A.W. Prestayko, S.T. Crooke, Viscometric and fluorometric studies of DNA interactions of several new anthracyclines, *Biochemistry* 21 (1982) 1541–1547.
- [38] S. Tabassum, A. Asim, F. Arjmand, M. Afzal, V. Bagchi, Synthesis and characterization of copper(II) and zinc(II)-based potential chemotherapeutic compounds: Their biological evaluation viz. DNA binding profile, cleavage and antimicrobial activity, *Eur. J. Med. Chem.* 58 (2012) 308–316.
- [39] P. Daroui, S.D. Desai, T.-K. Li, A.A. Liu, L.F. Liu, Hydrogen peroxide induces topoisomerase I-mediated DNA damage and cell death, *J. Biol. Chem.* 279 (2004) 14587–14594.
- [40] E. Trotta, N.D. Grosso, M. Erba, M. Paci, The ATT Strand of AAT $\odot$  ATT Trinucleotide Repeats Adopts Stable Hairpin Structures Induced by Minor Groove Binding Ligands, *Biochemistry* 39 (2000) 6799–6808.
- [41] P. Wittung, P. Nielsen, B. Norden, Direct observation of strand invasion by peptide nucleic acid (PNA) into double-stranded DNA, *J. Am. Chem. Soc.* 118 (1996) 7049–7054.
- [42] J.J. Stephanos, Drug-protein interactions: two-site binding of heterocyclic ligands to a monomeric hemoglobin, *J. Inorg. Biochem.* 62 (1996) 155–169.
- [43] Y. Lu, Q. Feng, F. Cui, W. Xing, G. Zhang, X. Yao, Interaction of 3'-azido-3'-deamino daunorubicin with human serum albumin: Investigation by fluorescence spectroscopy and molecular modeling methods, *Bioorg. Med. Chem. Lett.* 20 (2010) 6899–6904.
- [44] J.R. Lakowicz, G. Weber, Quenching of protein fluorescence by oxygen. Detection of structural fluctuations in proteins on the nanosecond time scale, *Biochemistry* 12 (1973) 4171–4179.
- [45] B. Valeur, J.C. Brochon, *New Trends in Fluorescence Spectroscopy*, 6th ed., Springer, Berlin, 1999.
- [46] S. Naveenraj, S. Anandan, Binding of serum albumins with bioactive substances–nanoparticles to drugs, *J. Photochem. Photobiol. C* 14 (2013) 53–71.
- [47] T. Forster, in *Modern Quantum Chemistry: O. Sinanoglu (Ed.), Modern Quantum Chemistry*, vol. 3, Academic, New York, 1996, pp. 93–137.
- [48] X.-B. Fu, G.-T. Weng, D.-D. Liu, X.-Y. Le, Synthesis, characterization, DNA binding and cleavage, HSA interaction and cytotoxicity of a new copper(II) complex derived from 2-(2'-pyridyl)benzothiazole and glycylglycine, *J. Photochem. Photobiol. A* 276 (2014) 83–95.
- [49] S. Tabassum, M. Zaki, M. Ahmad, M. Afzal, S. Srivastav, S. Srikrishna, F. Arjmand, Synthesis and crystal structure determination of copper(II)-complex: In vitro DNA and HSA binding, pBR322 plasmid cleavage, cell imaging and cytotoxic studies, *Eur. J. Med. Chem.* 83 (2014) 141–154.
- [50] C. Li, F. Cui, R. Mao, R. Huo, G. Qu, Synthesis of N-(2-chloro purin-6-yl) aza-18-crown-6 and its interaction with human serum albumin, *Org. Biomol. Chem.* 10 (2012) 869–875.
- [51] Y.Q. Wang, X.Y. Wang, J. Wang, Y.M. Zhao, W.J. He, Z.J. Guo, Noncovalent interactions between a trinuclear monofunctional platinum complex and human serum albumin, *Inorg. Chem.* 50 (2011) 12661–12668.
- [52] B. Ahmad, S. Parveen, R.H. Khan, Effect of albumin conformation on the binding of ciprofloxacin to human serum albumin: a novel approach directly assigning binding site, *Biomacromolecules* 7 (2006) 1350–1356.
- [53] S. Tabassum, W.M. Al-Asbahy, M. Afzal, F. Arjmand, R.H. Khan, Interaction and photo-induced cleavage studies of a copper based chemotherapeutic drug with human serum albumin: spectroscopic and molecular docking study, *Mol. Biosyst.* 8 (2012) 2424–2433.
- [54] T. Tanimoto, D. Takahashi, K. Toshima, Chemical methods for degradation of target proteins using designed light-activatable organic molecules, *Chem. Commun.* 48 (2012) 7659–7671.
- [55] (a) N. Rainey, L. Motte, B.B. Aggarwal, P.X. Petit, Curcumin hemeses mediates a cross talk between autophagy and cell death, *Cell Death Dis* 6 (2015) e2003; (b) U. Banik, S. Parasuraman, A.K. Adhikary, N.H. Othman, Curcumin: the spicy modulator of breast carcinogenesis, *J. Exp. Clin. Cancer Res.* 36 (2017) 98; (c) K. Pal, S. Roy, P.K. Parida, A. Dutta, S. Bardhan, S. Das, K. Jana, P. Karmakar, Folic acid conjugated curcumin loaded biopolymeric gum acacia microsphere for triple negative breast cancer therapy in invitro and in vivo model, *Mater. Sci. Engg. C* 95 (2019) 204–216.

# Dinuclear Copper(II) Complexes with N,O Donor Ligands: Partial Ligand Hydrolysis and Alcohol Oxidation Catalysis

Arpita Barma,<sup>[a]</sup> Aradhita Bhattacharjee,<sup>[a]</sup> and Partha Roy\*<sup>[a]</sup>

Two copper(II) complexes  $[\text{Cu}_2(\text{L}^1)_2]$  (**1**) and  $[\text{Cu}_2(\text{L}^2)_2]$  (**2**) where  $\text{H}_2\text{L}^1 = 2\text{-hydroxy-3-}((3\text{-hydroxy-2,2-dimethylpropylimino methyl})\text{-5-methylbenzaldehyde})$  and  $\text{H}_2\text{L}^2 = 2\text{-hydroxy-3-}(((1\text{-hydroxypropan-2-yl})\text{imino})\text{methyl})\text{-5-methylbenzaldehyde}$  have been synthesized and used as catalysts in alcohol oxidation. 2,6-Diformyl-4-methylphenol (DFP) based Schiff-base ligands, 3,3'-(2-hydroxy-5-methyl-1,3-phenylene)bis(methan-1-yl-1-ylidene)bis(azan-1-yl-1-ylidene)bis(2,2-dimethylpropan-1-ol) ( $\text{H}_3\text{L}'$ ) and 2,2'-((2-hydroxy-5-methyl-1,3-phenylene)bis(methanylylidene))bis(azanylylidene))bis(propan-1-ol) ( $\text{H}_3\text{L}''$ ), undergo partial hydrolysis to convert one of the azomethine groups to aldehyde group to give  $\text{H}_2\text{L}^1$  and  $\text{H}_2\text{L}^2$ , and then react

with copper(II) acetate to yield complex **1** and **2**, respectively. These complexes have been characterized by standard methods such as elemental analysis, room temperature magnetic studies, FT-IR, UV-vis, ESI-mass spectral analyses, cyclic voltammogram, etc. The structures of dinuclear complexes with modified ligands have been confirmed by single crystal X-ray diffraction analysis. Complex **1** and **2** have been used as catalysts for the oxidation of benzyl alcohol, 4-methyl benzyl alcohol, 4-methoxy benzyl alcohol, 4-nitro benzyl alcohol and 4-bromo benzyl alcohol to the corresponding aldehyde as the sole product. Efficiency of the catalyst depends on the chain length and substitution on the chain of the ligand.

## Introduction

Attention on metal Schiff-base complexes is high among the researchers for last few decades. Appropriate coordination environment can easily be incorporated into the Schiff-base ligands by the judicious choice of the starting amine and aldehyde/keto compounds. These ligands stabilize different oxidation states of the transition metal ions offering opportunity to use such complexes in the diverse field of applications such as catalysis, redox processes, etc.<sup>[1,2]</sup> Apart from this, transition metal complexes were applied in the field of magnetism, biological sciences, optoelectronics, sensing, etc.<sup>[3–6]</sup> The Schiff-base ligands derived from 2,6-diformyl-4-methylphenol (DFP) are useful in the preparation of dinuclear or multinuclear transition metal complexes because phenoxy oxygen atom of DFP unit acts as the binucleating bridging center.<sup>[7]</sup> Depending on transition metal ions, reaction conditions and bridging ligands, di-,<sup>[8]</sup> tri-,<sup>[9]</sup> tetra-,<sup>[7d–e,10]</sup> penta-,<sup>[10b]</sup> hexa-,<sup>[7e,11]</sup> hepta-,<sup>[8a]</sup> or higher nuclear transition metal complexes<sup>[12]</sup> were obtained with the Schiff-base ligands of DFP which found different applications.

Copper(II) complexes with Schiff-base ligands were used as the catalyst in different oxidation reactions<sup>[13]</sup> such as oxidation of alkane,<sup>[14]</sup> alkene,<sup>[15]</sup> sulfide,<sup>[16]</sup> catechol,<sup>[17]</sup> alcohol,<sup>[18]</sup> etc. Pompeiro *et al.* reported a landmark work on copper catalyzed oxidation of cyclohexane.<sup>[14a]</sup> After that a number of copper

complexes were employed as the catalyst for such oxidation reactions.<sup>[19]</sup> The products of cycloalkane oxidation are, primarily, cycloalkanol and cycloalkanone. Alkene has been converted to corresponding epoxide as the main product by copper complex as the catalyst using various oxidants such as hydrogen peroxide, *tert.*-butyl hydroperoxide, molecular oxygen, etc.<sup>[15]</sup> Epoxides are important building blocks for several fine organic materials. Apart from oxidation of these substrates, dimethyl ether has been synthesized from syngas using copper-based catalyst.<sup>[20]</sup> Click reaction yields different triazoles from azides. This reaction is catalyzed by copper(I) compounds in homogeneous as well as in heterogeneous media.<sup>[21]</sup> Copper compounds catalyze several C–C, C–X (where X is B, Si and F) bond-formation reactions where unactivated alkyl electrophiles have been used as the substrates.<sup>[22]</sup>

Oxidation of alcohol is important in organic chemistry as it offers transformation of alcohol to aldehyde group. Alcohol oxidation is generally achieved in the presence of stoichiometric amounts of metal containing toxic and/or hazardous oxidizing agents.<sup>[23]</sup> Work up procedure to achieve the target oxidized compounds requires huge labor. Thus, the use of appropriate catalyst for such transformation is an alternative option in terms of economy and environmental pollution. In this respect, it may be suitable to mention galactose oxidase (GO).<sup>[24]</sup> It is a fungal enzyme and catalyzes the oxidation of various primary alcohols to the corresponding aldehyde solely with the reduction of dioxygen to  $\text{H}_2\text{O}_2$ .<sup>[25]</sup> It has one copper atom with square pyramidal geometry at the active site.

Aerobic oxidation of alcohols has been achieved by different metals as the catalyst. Abdel-Rahman *et al.* reported some Cu(II)-Schiff base complexes as the catalyst for oxidation of alcohol under different reaction conditions.<sup>[26]</sup> Zhan and co-workers reported some mononuclear copper(II) complexes with ligands containing phenol derivatives and used them in the

[a] A. Barma, A. Bhattacharjee, Dr. P. Roy  
Department of Chemistry, Jadavpur University  
Jadavpur, Kolkata-700 032, India  
E-mail: partha.roy@jadavpuruniversity.in  
proy@chemistry.jdvu.ac.in  
<http://www.jaduniv.edu.in/>

Supporting information for this article is available on the WWW under <https://doi.org/10.1002/ejic.202100263>

aerobic oxidation of benzyl alcohol.<sup>[27]</sup> Sulfonated Schiff base copper(II) complexes were used as the catalyst for the oxidation of primary and secondary alcohols.<sup>[28]</sup> One mononuclear copper (II) complex with non-innocent aminophenol based ligand has been reported as biomimetic model for galactose oxidase enzyme.<sup>[29]</sup> We have also utilized some copper(II)-Schiff base complexes as the catalyst for the oxidation of different benzyl alcohols.<sup>[30]</sup> The oxidation of primary alcohols to the corresponding aldehydes in the presence of  $\text{Cu}^{\text{I}}\text{OTf}$  or  $\text{Cu}^{\text{I}}(\text{OTf})_2$  as metal sources, 2,2'-bipyridine as ligand, *N*-methylimidazole as base and 2,2,6,6-tetramethylpiperidine-1-oxyl (TEMPO) as the co-catalyst has been studied by different groups<sup>[31]</sup> to establish the mechanism of the oxidation reaction. Amongst the reported catalytic systems, TEMPO has been used as a co-catalyst in almost every system. However, there are some problems with the processes, for example, reaction conditions, recyclability of the catalyst, catalyst loading, chemo-/stereo-selectivity, etc. Thus, attempts for better catalysts to overcome such challenges are continuing.

We report here synthesis, characterization, and catalytic properties of two dinuclear complexes,  $[\text{Cu}_2(\text{L}^1)_2]$  (1) and  $[\text{Cu}_2(\text{L}^2)_2]$  (2) where  $\text{H}_2\text{L}^1 = 2\text{-hydroxy-3-}((3\text{-hydroxy-2,2-dimethylpropylimino)methyl)-5\text{-methylbenzaldehyde}$  and  $\text{H}_2\text{L}^2 = (E)\text{-2-hydroxy-3-}(((1\text{-hydroxypropan-2-yl)imino)methyl)-5\text{-methylbenzaldehyde}$  (Scheme 1). Complex 1 and 2 have been synthesized under mild conditions.  $\text{H}_2\text{L}^1$  is the product of partial hydrolysis of 3,3'-(2-hydroxy-5-methyl-1,3-phenylene)bis(methan-1-yl-1-ylidene)bis(azan-1-yl-1-ylidene)bis(2,2-dimethylpropan-1-ol) ( $\text{H}_3\text{L}'$ ) and  $\text{H}_2\text{L}^2$  is obtained by partial hydrolysis of 2,2'-(((2-hydroxy-5-methyl-1,3-phenylene)bis(methanylylidene)) bis(azanylylidene))bis(propan-1-ol) ( $\text{H}_3\text{L}''$ ). It is documented that Cu(II) can convert the ligand to its oxidized products on several occasions.<sup>[32]</sup> Cu(II) catalyzed partial hydrolysis of imine group of some Schiff-base ligands has been reported.<sup>[33]</sup> However, partial modification of DFP based ligands have been reported with metal ions generally other than Cu(II) ion.<sup>[7e,8,9,11b]</sup> In this report,

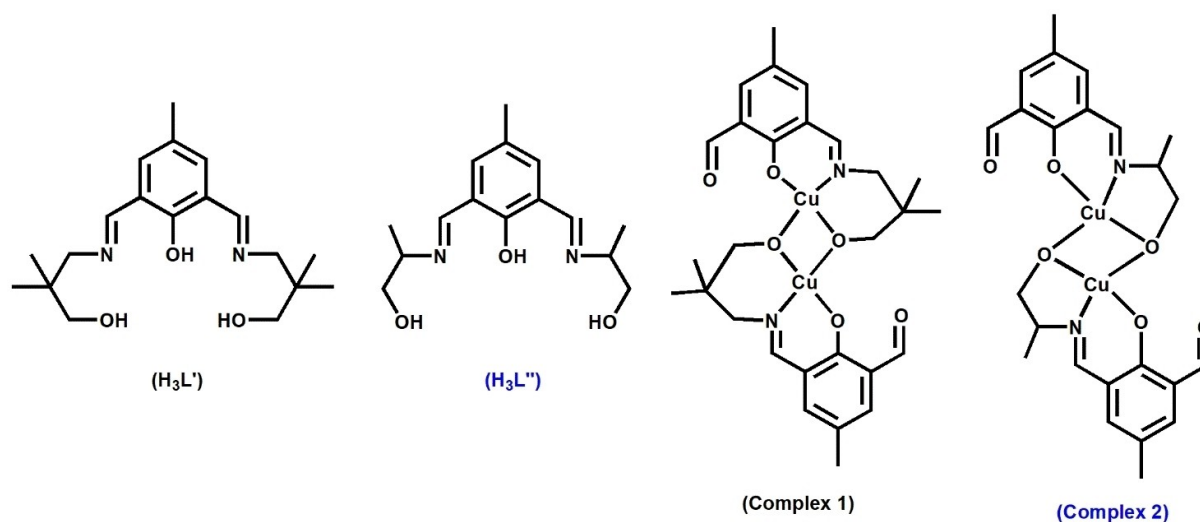
two dinuclear copper(II) complexes with partially hydrolyzed DFP based ligands have been used as the catalysts for the oxidation of some benzyl alcohols in the presence of *tert*-butyl hydroperoxide (TBHP) as the oxidant.

## Results and Discussion

### Synthesis of $\text{H}_3\text{L}'$ , $\text{H}_3\text{L}''$ , complex 1 and complex 2

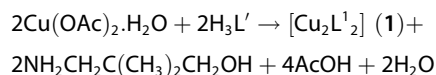
Complex 1 and 2 were synthesized following the route as depicted in Scheme S1. First ligands,  $\text{H}_3\text{L}'$  and  $\text{H}_3\text{L}''$  were synthesized by 1:2 condensation between DFP and the respective amine, characterized and thought to get multi-nuclear copper(II) complexes where phenolic oxygen atom could act as the bridge. Both  $\text{H}_3\text{L}'$  and  $\text{H}_3\text{L}''$  have been characterized by elemental analysis,  $^1\text{H}$  NMR and ESI mass spectral analysis. ESI-mass spectrometric measurements were performed with methanolic solutions of  $\text{H}_3\text{L}'$  and  $\text{H}_3\text{L}''$ . Mass spectrum of  $\text{H}_3\text{L}'$  shows the  $m/z$  peak at 335.18, which may be attributed to the presence of  $[\text{H}_3\text{L}' + \text{H}^+]$  species (Figure S1). For  $\text{H}_3\text{L}''$ , the  $m/z$  peak at 279.13 may be attributed to the presence of  $[\text{H}_3\text{L}'' + \text{H}^+]$  (Figure S2).

$^1\text{H}$  NMR spectra of  $\text{H}_3\text{L}'$  and  $\text{H}_3\text{L}''$  were recorded in  $\text{CDCl}_3$  (Figure S3 and Figure S4). Signals for phenolic proton of  $\text{H}_3\text{L}'$  and  $\text{H}_3\text{L}''$  appear at 10.39 and 10.47 ppm, respectively. Peaks at 8.56 and 8.42 ppm may be attributed to the imine protons of  $\text{H}_3\text{L}'$  and  $\text{H}_3\text{L}''$ , respectively. The aromatic protons of  $\text{H}_3\text{L}'$  appear at 7.51 ppm. Signal for aromatic protons of  $\text{H}_3\text{L}''$  emerges at 7.28 ppm. Peak of  $\text{H}_3\text{L}'$  at 4.93 ppm may appear due to the presence of alcoholic protons. Alcoholic protons of  $\text{H}_3\text{L}''$  give signal at 5.27 ppm. Methylene protons of  $\text{H}_3\text{L}'$  appear at 3.52 and 3.48 ppm whereas signals for the other compound appear at 3.71 and 3.10 ppm. Peaks at 2.30 and 1.00 ppm may be attributed to the various methyl protons of  $\text{H}_3\text{L}'$ . Signals for methyl protons of  $\text{H}_3\text{L}''$  appear at 2.80 and 1.23 ppm.

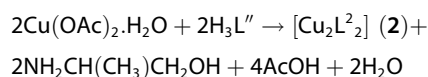


Scheme 1. Structures of ( $\text{H}_3\text{L}'$ ), ( $\text{H}_3\text{L}''$ ), complex 1 and 2.

However, during the synthesis of complex 1 and complex 2, the ligand modification has been noticed for both the cases. Partial hydrolysis of  $H_3L'$  and  $H_3L''$  leads to the generation of  $H_2L^1$  and  $H_2L^2$ , respectively, where one of the imine bonds of the ligand has been converted to aldehyde group. Schiff-base ligands derived from DFP tend to undergo partial hydrolysis. In previous studies, partial hydrolysis of azomethine bond occurred in the presence of  $Ni^{2+}$  ion<sup>[11]</sup> as well as  $Zn^{2+}$  ion.<sup>[9]</sup> Reaction between  $H_3L'$  and copper(II) acetate gives complex 1 without adding any external base to deprotonate the phenolic oxygen atom. Overall reaction may be written as:



Similar reaction occurs between  $H_3L''$  and copper(II) acetate to produce complex 2.



### Crystal structures of complex 1 and 2

Complex 1 crystallizes in the P-1 space group, whereas complex 2 crystallizes in the P 21/n space group. Perspective views of the molecules are shown in Figure 1. Selected bond angles and bond lengths are listed in Table S1. Both of the complexes consist of two deprotonated dianions of the partially hydrolyzed ligand,  $H_2L^1$  for complex 1 and  $H_2L^2$  for complex 2, and two copper atoms. Both the copper atoms are in a tetracoordinated environment. Each copper in 1 and 2 is coordinated with one phenolic oxygen atom (O2), two alcoholic oxygen atoms (O3, O3a) and one nitrogen atom (N1) from the ligands,  $H_2L^1$  and  $H_2L^2$ , respectively. The metal center in both the cases is in a distorted square planar geometry. O2, N1, O3 and O3a form the square plane and Cu1 is slightly out the mean plane by a distance of 0.034 Å. The smaller donor-metal-donor angle around Cu1 deviates from 90° for both the cases. The

$O3-Cu1-O3^a$  angle is 77.49° and 82.9° for complex 1 and 2, respectively while the  $O3-Cu1-N1$  angle is 96.14° and 84.2° for complex 1 and 2, respectively. The larger donor-metal-donor angle around Cu1 also shifts from ideal 180° for both the complexes. The  $O2-Cu1-O3$  angles are 161.78° for complex 1, 178.3° for complex 2 while  $O3^a-Cu1-N1$  angles are 166.97° for complex 1 and 161.0° for complex 2.

For five coordinate complex, trigonal bipyramidal or square pyramidal geometry is ascertained from the value of trigonal index parameter ( $\tau$  parameter).<sup>[34]</sup> However, for four-coordinate complexes, Houser *et al.* introduced four-coordinate  $\tau_4$  index to find the geometry around the metal center with the following formula<sup>[35]</sup>

$$\tau_4 = \frac{360^\circ - (\alpha + \beta)}{141^\circ}$$

where  $\alpha$  and  $\beta$  are the two largest angles in the four-coordinate species. When the value of  $\tau_4$  is 1.00, the geometry is perfect tetrahedral. For the perfect square planar geometry, it is 0.00. Other values indicate different seesaw geometry. The values of four-coordinate  $\tau_4$  index have been calculated to be 0.037 and 0.123 for complex 1 and 2, respectively. These indicate that there is almost perfect square planar geometry around metal center in complex 1. For complex 2,  $\tau_4$  index indicate the fluctuation of square planar geometry. The donor metal bond distances are in the range of 1.8821 and 1.9302 Å. The metal-metal bond distances are 2.989 Å for complex 1 and 2.902 Å for complex 2 which are significantly short.

### Room temperature magnetic moment determination

Room temperature magnetic susceptibility of complex 1 and 2 were determined with the powder samples using the Guoy Balance Method. The effective magnetic moment has been determined to be 1.96 and 2.26 BM per dimer for complex 1 and 2, respectively ( $X_M T$  values are 0.5 and 0.6 emu K mol<sup>-1</sup> per two copper atoms for complex 1 and 2, respectively). Both the complexes show lower magnetic moment value than the

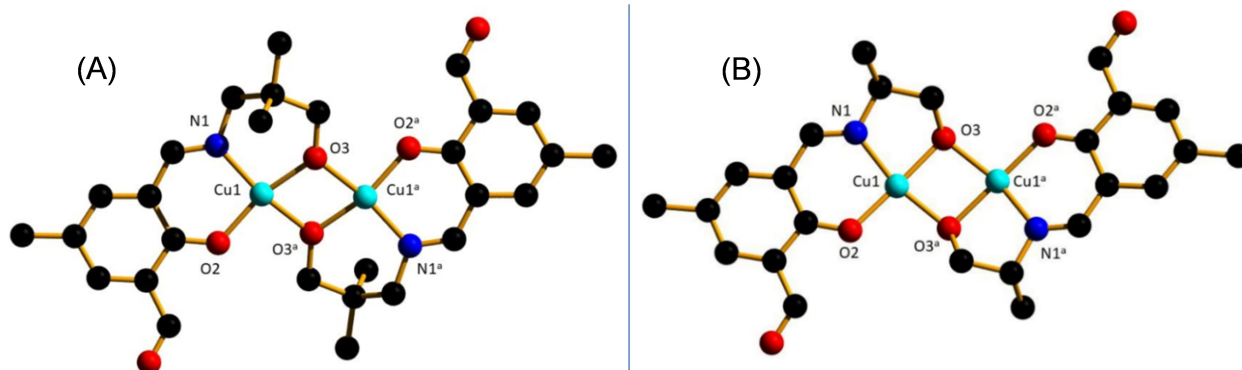


Figure 1. Perspective views of (A) complex 1 and (B) complex 2. Hydrogen atoms have been omitted for clarity. Symmetry code: (a) 1-x, 2-y, 1-z (for complex 1) and (a) 1-x, 1-y, 1-z (for complex 2).

calculated value, which is 2.83 BM for two copper atoms, indicating partial spin pairing by antiferromagnetic interaction in the complexes at room temperature.

### UV-vis spectral studies

The electronic spectra of complex **1** and **2** were recorded in dimethylformamide (DMF) at room temperature (Figure S5 and Figure S6). For an octahedral geometry, the expected  ${}^2T_{2g}$  to  ${}^2E_g$  transition takes place at around 800 nm. This band will undergo a significant blue shift when the octahedral geometry changes to a square pyramidal and square planar structure.<sup>[36]</sup> The absorption band observed in the range 542–694 nm corresponds to the  $d-d$  transitions (Inset of Figure S5 and Figure S6). On the basis of the crystal structures of complex **1** and **2**, the geometry around each copper(II) center is assumed to have a square-planar geometry. The observed  $d-d$  transitions around 600 nm also indicate the square planar Cu(II) centers. These are weaker in intensity as they are Laporte forbidden. Moreover, both the complexes are centro-symmetric which allows very little mixing of  $d$  and  $p$  orbitals. The medium intensity bands appear in the range 330–450 nm for complex **1** and 334–452 nm for **2**.<sup>[37]</sup> The strong bands at ~415 nm for both the complexes are due to the phenolate-to-copper(II) ligand-to-metal charge transfer (LMCT) (transfer occurs from the MO with ligand-like character to the metal-like one) and other band may be due to the intra-ligand charge transfer transitions.<sup>[37]</sup>

### FT-IR spectral studies

FT-IR spectra of complex **1** and **2** were obtained with powder samples by ATR technique. In the IR spectra of the complexes (Figure S7 and Figure S8), the presence of hydrocarbon part (methyl and methylene groups) of the complexes have been evidenced from the appearance of the unsymmetrical and

symmetrical frequencies at the region of 2800–3000  $\text{cm}^{-1}$ . The sharp band at around 1670  $\text{cm}^{-1}$  may be attributed to the presence of aldehyde group of  $\text{H}_2\text{L}^1$  and  $\text{H}_2\text{L}^2$  species. Another intense band at around 1625  $\text{cm}^{-1}$  is due to the presence of the stretching vibration of the azomethine group (C=N moiety). These observed bands explain the structural similarities between the complex **1** and complex **2**.

### Mass spectral studies

ESI-mass spectra of complex **1** and **2** were obtained in methanol (Figure S9 and Figure S10). As indicated by the spectra, both the complexes have been found to exist mainly as dinuclear copper(II) species in the solution. Mass spectrum of complex **1** shows an  $m/z$  peak at 621.19 which may be attributed to the  $[\text{Cu}_2(\text{L}^1)_2 + \text{H}^+]$  species (calculated value: 621.11). The complex undergoes fragmentation to show the presence of the partially hydrolyzed ligand,  $\text{H}_2\text{L}^1$ . Two other significant  $m/z$  peaks are observed at 272.17 and 250.18. These peaks may be assigned to the presence of  $[\text{H}_2\text{L}^1 + \text{Na}^+]$  and  $[\text{H}_2\text{L}^1 + \text{H}^+]$ , respectively (calculated values: 272.13 and 250.14). Mass spectrum of complex **2** shows an  $m/z$  peak at 565.09 which may be attributed to the existence of  $[\text{Cu}_2(\text{L}^2)_2 + \text{H}^+]$  species (calculated value: 565.05).

### Electrochemical studies

Electrochemical studies of complex **1** and **2** were carried out in DMF using TBAP as supporting electrolyte. Both dinuclear Cu(II) complexes exhibit two pairs of redox events which indicate the electronic communication present between the two metal ions of these two dinuclear Cu(II) complexes (Figure 2). These redox processes involved between two metal centers can be expressed as

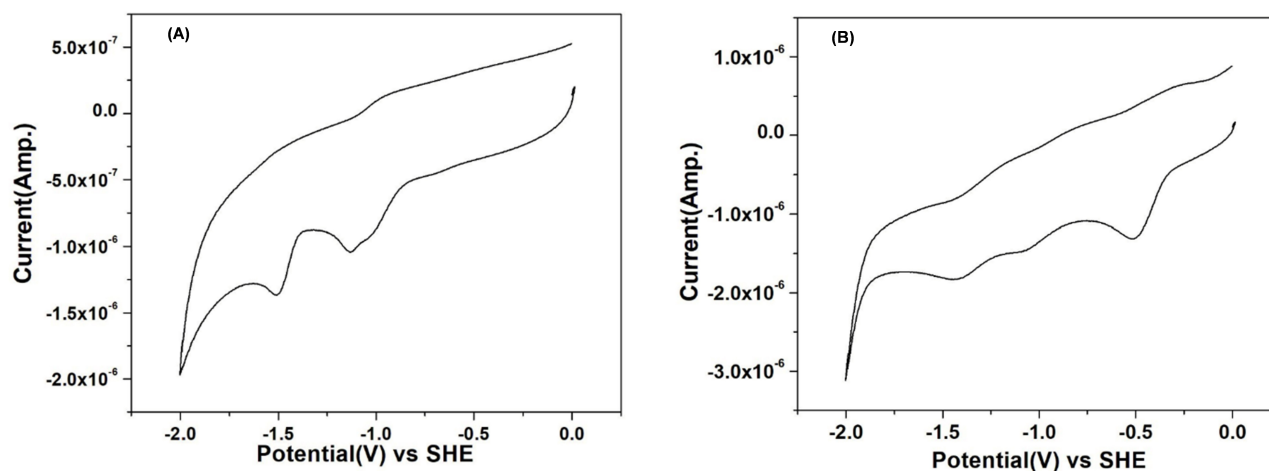
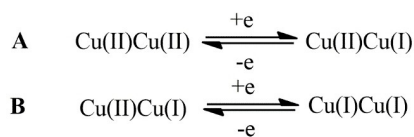


Figure 2. Cyclic voltammogram of (A) complex **1** and (B) complex **2** in DMF. Conditions: 0.1 M  $[\text{n-Bu}_4\text{N}]\text{ClO}_4$  as supporting electrolyte, glassy carbon as working electrode and Ag/AgCl as reference electrode (scan rate: 25 mV/s).



The first pair of oxidation-reduction peaks corresponding to oxidation-reduction couples, i.e. Cu(II)Cu(I)/Cu(I)Cu(I) **B**,  $E_{pa_1} = -1.48$  V for complex **1** and  $-1.20$  V for complex **2**,  $E_{pc_1} = -1.50$  V for complex **1** and  $-1.43$  V for complex **2**, the average formal potential [ $E_{1/2} = (E_{pa_1} + E_{pc_1})/2$ ] is  $-1.49$  V for complex **1** and  $-1.31$  V for complex **2**. The second pair of oxidation-reduction peaks corresponding to oxidation-reduction couples, i.e. Cu(II)Cu(II)/Cu(II)Cu(I) **A**,  $E_{pa_2} = -0.96$  V for complex **1** and  $-0.83$  V for complex **2**,  $E_{pc_2} = -1.08$  V for complex **1** and  $-1.06$  V for complex **2**, the average formal potential [ $E_{1/2} = (E_{pa_2} + E_{pc_2})/2$ ] is  $-1.02$  V for complex **1** and  $-0.95$  V for complex **2**. The peak observed at  $-0.5$  V for complex **2** may be assigned to the ligand reduction event.

The stability of the mixed-valence Cu(II)Cu(I) species can be expressed in terms of the comproportionation constant,  $K_{con}$ ,

$$K_{con} = \frac{[\text{Cu(II)Cu(I)}]^2}{[\text{Cu(II)Cu(II)}][\text{Cu(I)Cu(I)}]} = \exp \left[ \frac{nF(\Delta E_{1/2}^0)}{RT} \right]$$

where,  $\Delta E_{1/2}^0 = E_{1/2}^0(\text{A}) - E_{1/2}^0(\text{B})$

The larger the separation between the potentials of the couple, the greater the stability of the mixed-valence species with respect to comproportionation. The values of  $\Delta E_{1/2}^0$  for complex **1** and **2** are 0.23 and 0.18 V, respectively whereas values of  $K_{con}$  for complex **1** and **2** have been determined as  $9.5 \times 10^3$  and  $1.1 \times 10^3$ , respectively.

The values imply the stability of the mixed valence state Cu(II)Cu(I) are comparable with those of the literature.<sup>[38]</sup> It has been reported that  $\Delta E_{1/2}^0$  separation value of non-interacting metal centers, which are in similar chemical environments, is not larger than 50 mV.<sup>[39]</sup> Thus, the cyclic voltammograms indicate significant copper-copper coupling present in these two dinuclear complexes which has also been observed in several other dinuclear metal complexes.<sup>[40]</sup>

The cyclic voltammograms of complex **1** and complex **2** were also recorded at different potential scan rates to show that the current is diffusion controlled, whereas the current ratio of the first to second waves increases with an increase in the potential scan rate (Figure S11 and Figure S12).

## Alcohol oxidation studies

Complex **1** and **2** have been used as catalyst for the oxidation of benzyl alcohols with TBHP as the oxidant at 343 K. The complexes show galactose oxidase mimicking activity *i.e.* they act as the catalyst for the oxidation of benzyl alcohols. The substrates used here are benzyl alcohol, 4-methyl benzyl alcohol, 4-methoxy benzyl alcohol, 4-nitro benzyl alcohol and 4-bromo benzyl alcohol. The corresponding aldehyde has been obtained as the sole product. The results of the oxidation reactions are given in Table 1. The results indicate moderate ability of the catalysts towards the conversion of benzyl alcohol to the corresponding aldehyde. Yield of the transformation for each of the substrate is remarkably high in comparison to the corresponding blank experiments signifying the relevance of the presence of the copper complex. The optimized conditions have been found by varying different parameters for the catalytic reaction.

In order to investigate the role of the solvent, the oxidation of benzyl alcohol has been carried out in different solvents and the results of the reactions are given in Table S2. Reaction in water shows poor conversions (9%) probably because of the low solubility of the catalysts in this solvent, hence the yield is similar to that obtained during the blank experiments (Table 1, entry 3). When acetonitrile is used, the catalytic reaction produces the highest yield. Hence acetonitrile has been selected as solvent for all the oxidation reactions. Another possible explanation for the higher yield of the catalysis in CH<sub>3</sub>CN may be found in the inclination of the solvent to stabilize the intermediate Cu(I) species *via* coordination.

In order to check the role of the oxidant, the oxidation of benzyl alcohol has been performed in the presence of different oxidants. The results are shown in Table S3. It is clear from the table the TBHP is far better oxidant to convert the benzyl alcohol in comparison to the other oxidants.

The effect of temperature on the reaction yield has also been examined. At room temperature, the reaction proceeds slowly and produces small amount of the aldehyde. The maximum yield has been obtained at 343 K. So, the reaction has been carried out at this temperature. Higher temperature may destroy the copper complex showing lower yield of catalytic reaction.

Oxidation of benzyl alcohol has been carried out in the presence of various amounts of the catalyst to check whether amount of the catalyst has any significant effect on yield of the

**Table 1.** Oxidation<sup>[a]</sup> of primary alcohol with complexes **1** and **2**.

Substrate	Product	Yield <sup>[b]</sup> in [%], (TON <sup>[c]</sup> )		
		Complex <b>1</b>	Complex <b>2</b>	Blank <sup>[d]</sup>
Benzyl alcohol	Benzaldehyde	72 (14.0)	50 (10.0)	9
4-Methylbenzyl alcohol	4-Methyl benzaldehyde	73 (14.6)	51 (10.2)	10
4-Methoxybenzyl alcohol	4-Methoxy benzaldehyde	81 (16.2)	62 (12.4)	9
4-Nitrobenzyl alcohol	4-Nitro benzaldehyde	59 (11.8)	35 (7.0)	10
4-Bromobenzyl alcohol	4-Bromo benzaldehyde	61 (12.2)	38 (7.6)	7

[a] Oxidant: TBHP; temperature: 343 K; solvent: acetonitrile. [b] Yield calculated after 24 h. [c] TON: turnover number = number of moles of product/number of moles of catalyst. [d] Oxidation reaction without any complex under identical conditions.

catalytic reactions. The results, however, indicate that it does not affect the reaction yield considerably. Thus, for all the substrates, a 1:20 catalyst/substrate ratio has been maintained.

Substrate variation has been done by introducing an electron donating or an electron withdrawing group in the aromatic ring of benzyl alcohol. The effect of these groups has been observed on the yield of the reaction (Table 1). It has been found that the yield of oxidation is increased with incorporation of electron donating groups. The highest yield has been obtained with 4-methoxy benzyl alcohol and the yield of the reaction is 81% with complex 1 and 62% with 2. Another substrate with electron donating (4-methylbenzyl alcohol with yield of 73% with complex 1 and 51% with 2) shows marginally higher yield than the unsubstituted substrate with both the catalysts (benzyl alcohol with yield of 72% for complex 1 and 50% for 2). However, the presence of a bromo or nitro group in the aromatic ring decreases the yield of the corresponding alcohol formation. The yields with 4-bromobenzyl alcohol and 4-nitrobenzyl alcohol are 61% and 59%, respectively for complex 1, and 35% and 38%, respectively for complex 2.

Aliquots from the catalytic reaction mixture have been collected after 2 h and 4 h, and then every 4 h up to 24 h and analyzed in the GC to check the progress of the reaction. Plots of yield vs. time for complex 1 and 2 are shown in Figure 3 and Figure S13, respectively. It is evident that yield of the reaction increases with passage of time for all the substrates, the maximum being observed after 24 h of reaction. With the passage of time, the conversion of benzyl alcohols is also increased. It has been found that it reaches saturation after 24 h of the reaction.

Blank reactions with all the substrates have been performed under the same experimental conditions but without any complex. It is to be noted that in case of blank reaction, the reaction proceeds very slowly, and conversion is very poor (Table 1, entry 3). It takes longer time for the conversion of benzyl alcohol into the aldehyde. In other words, when we

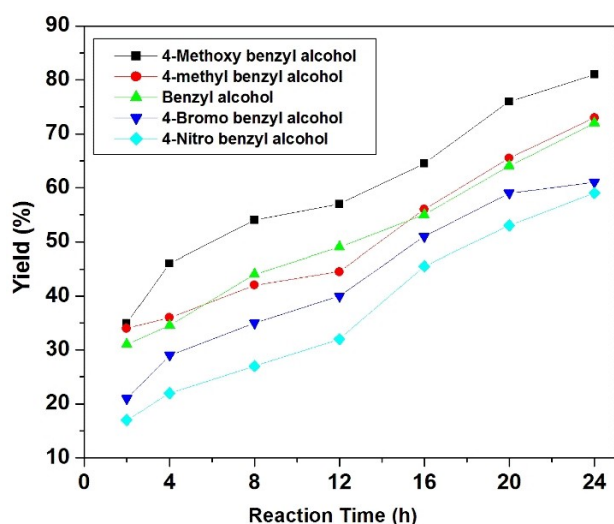
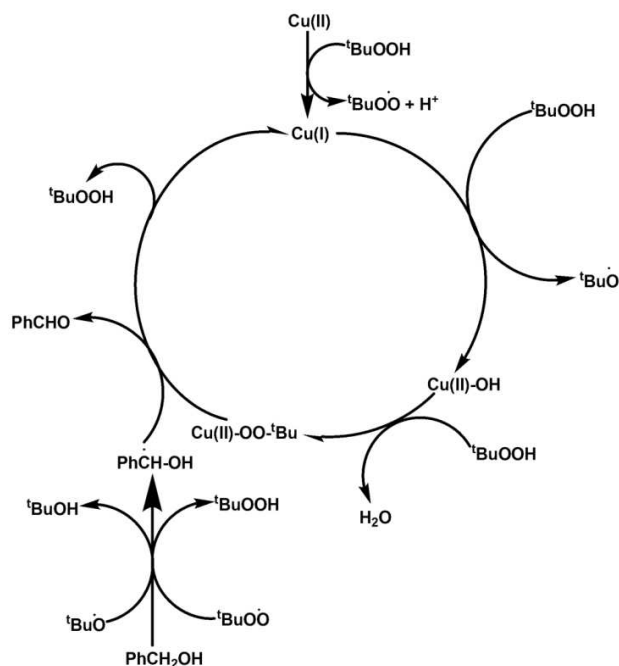


Figure 3. Plot of time vs. yield of aldehyde formation in the presence of complex 1 as the catalyst.

compare yield of a particular reaction in the same duration of time, e.g., 4 h, with and without catalyst, there is almost no conversion of alcohol to corresponding aldehyde in the initial time frame while the presence of copper complex as catalyst increases the yield of aldehyde manifold. These facts signify the importance of the copper(II) complex as catalysts.

We have tried to recover complex 1 and 2 after the catalytic reaction aiming to use it as catalyst for another reaction. However, attempts seem to be unsuccessful. The compound has been collected and dried after the catalytic reaction and characterized by IR spectroscopy attempting to find out the resemblance with the original catalyst. However, the spectrum of the material recovered is different from that of complexes. It indicates considerable decomposition of the complex and reuse of it as catalyst is inhibited.

A possible mechanistic pathway for the oxidation of the benzyl alcohols by the copper complex may be proposed based on the present work and results that were obtained from earlier studies (Scheme 2).<sup>[41]</sup> To explore the species responsible for the catalytic reaction, we have recorded the UV-vis spectra of complex 1 in absence and in the presence of TBHP in the range 250–800 nm in acetonitrile as this solvent has also been used in the catalytic reactions (Figure S14). Free complex 1 exhibits a sharp band at 410 nm which may be attributed to the phenolate-to-copper(II) ligand-to-metal charge transfer (LMCT). There are changes in the spectrum after addition of TBHP to the solution of the metal complex. Complex 1 shows a band at 379 nm which may be attributed to the shifting of charge transfer transition band position. It exhibits broad peak with a shoulder near 410–420 nm indicating the presence of peroxo-copper(II) species<sup>[2d]</sup> which may be generated during the catalytic process, and thus it may act as the active species



Scheme 2. Possible mechanism of benzyl alcohol oxidation.



responsible for the transformation of the substrate. The alcohol oxidation is believed to proceed mainly *via* a radical mechanism, which involves both carbon- and oxygen-centered radicals.<sup>[42]</sup> Reaction between the catalyst and TBHP may produce tBuO<sup>•</sup> radical and Cu(I) species. The Cu(I) may be converted to the corresponding Cu(II)–OOBu<sup>•</sup> species which has been detected by UV-vis measurement. A radical on benzyl alcohol may be generated by the action of TBHP on it. That radical and metal peroxo species produce the corresponding aldehyde.

It is clear from the electrochemical studies that the onset potential values for the reduction of Cu(II) to Cu(I) are –0.86 V and –0.91 V for complex 1 and 2 respectively, indicating that the reduction of metal center is easier for complex 1 than in 2. As discussed in the possible mechanism, formation of Cu(I) is necessary in the catalytic reaction. Thus, the system, where formation of Cu(I) is more feasible, should be more efficient in the oxidation reaction. Therefore, results obtained in electrochemical and catalytic studies corroborate perfectly establishing complex 1 is better catalyst than the complex 2.

Comparison of some copper compounds<sup>[30,43]</sup> acting as catalyst for the oxidation of benzyl alcohol has been made on few aspects of the catalytic reactions (Table S5). Most of the catalytic reactions have been carried out in organic solvent such as acetonitrile, dichloromethane, etc. The reactions have been carried out at room temperature as well as in elevated temperature. In the present study, temperature for oxidation has been set at 70 °C. Time of reaction varies from 1 h to 24 h. Yield of the reaction is in the range of 50 % to 100 %. Turn over number reported in these studies is in the range of 6.6 to 684. The discussion and results summarized in Table S5 indicate that complex 1 and 2 are moderate in their ability to produce the corresponding aldehyde solely from the benzyl alcohols.

## Conclusions

In summary, we have been able to synthesize and characterize two dinuclear copper(II) complexes, [Cu<sub>2</sub>(L<sup>1</sup>)<sub>2</sub>](1) and [Cu<sub>2</sub>(L<sup>2</sup>)<sub>2</sub>](2) where H<sub>2</sub>L<sup>1</sup> = 2-hydroxy-3-((3-hydroxy-2,2-dimethylpropylimino)methyl)-5-methylbenzaldehyde and H<sub>2</sub>L<sup>2</sup> = 2-hydroxy-3-(((1-hydroxypropan-2-yl)imino)methyl)-5-methylbenzaldehyde. 3,3'-(2-Hydroxy-5-methyl-1,3-phenylene)bis(methan-1-yl-1-ylidene)bis(azan-1-yl-1-ylidene)bis(2,2-dimethylpropan-1-ol) (H<sub>3</sub>L') and 2,2'-(((2-hydroxy-5-methyl-1,3-phenylene)bis(methanylylidene))bis(azanylylidene))bis(propan-1-ol) (H<sub>3</sub>L'') have been aimed to synthesize multinuclear complexes with Cu(II) but both the ligands undergo partial hydrolysis to yield H<sub>2</sub>L<sup>1</sup> and H<sub>2</sub>L<sup>2</sup>, respectively and then copper(II) species coordinate with the modified ligands to produce complex 1 and 2. Ligand used for complex 1 has longer side arm with branched alkyl groups. However, variation in chain length and presence of methyl group(s) here do not have any influence on partial hydrolysis of ligands during the synthesis of the complexes. DFP based ligands with azomethine linkage on both side arms undergo ligand modification in the presence of different metal ions during the synthesis of metal complexes many a times;

however, the ligand modification *i.e.* partial hydrolysis of azomethine linkage does not occur in the presence of copper(II) ion often. More examples may give the idea about the conditions under which the ligand modification occurs. Complex 1 and 2 were obtained after partial hydrolysis of DFP based ligand and used effectively as catalyst in oxidation of different benzyl alcohols. With different substituents on benzyl alcohol, yield of the formation of the corresponding aldehyde as the sole product varies. Efficiency of complex 2 as catalyst is lower in comparison to that of complex 1 although in both the complexes, copper atoms exist in similar coordination environment. Variation in chain length and the presence of methyl group have effect on the efficiency of the complexes as catalyst in such oxidation reactions.

## Experimental Section

### Materials and physical methods

3-Amino-2,2-dimethyl-1-propanol, DL-2-amino-1-propanol, copper (II) acetate monohydrate were purchased from Sigma Aldrich and were used without further purification. Other reagents were obtained from commercial sources and used as received. 2,6-diformyl-4-methylphenol was synthesized following a published procedure.<sup>[44]</sup> Elemental analyses (carbon, hydrogen and nitrogen) were performed using a Perkin-Elmer 2400 C elemental analyzer. FT-IR spectrum was obtained on a Perkin Elmer spectrometer (Spectrum Two) with the sample by using the attenuated total reflectance (ATR) technique. The UV-visible spectral measurement was done in Agilent 8453 diode array spectrophotometer. Electrochemical studies of the complexes were carried out in dimethylformamide (DMF) using tetrabutylammonium perchlorate (TBAP) as supporting electrolyte and all experiments were carried out at room temperature. A typical cyclic voltammogram (CV) was obtained by using a glassy carbon as working electrode, Pt as supporting electrode and saturated Ag/AgCl as reference electrode. Scan rate was set as 25 mV/s. Solutions of complex 1 and 2 were prepared freshly before use, and argon was passed through the solution for 15 min before recording CV to remove dissolved O<sub>2</sub>, if any. Analysis of reaction mixture of catalytic reactions was performed with a Shimadzu made next generation high speed gas chromatography system (model: GC-2025 AF) equipped with a fused silica capillary column and an FID detector. All experiments were carried out at room temperature in air unless reported otherwise.

**CAUTION:** Organic perchlorates are potentially explosive. Only small amount of the perchlorate salt should be handled with care.

### Synthesis of 3,3'-(2-hydroxy-5-methyl-1,3-phenylene)bis(methan-1-yl-1-ylidene)bis(azan-1-yl-1-ylidene)bis(2,2-dimethylpropan-1-ol) (H<sub>3</sub>L')

3-Amino-2,2-dimethyl-1-propanol (0.5 mmol, 0.052 g) was added to an acetonitrile solution (10 mL) of 2,6-diformyl-4-methylphenol (0.25 mmol, 0.041 g) under stirring condition. The mixture was stirred for 30 min. Then, the resulting solution was refluxed for 3 h. The color of the mixture turned yellow. The mixture was then cooled and filtered to remove any undissolved material. Yellow colored product of H<sub>3</sub>L' was obtained from the slow evaporation of the solvent.

Data for H<sub>3</sub>L': yield (0.073 g, 87%); C, H, N analysis: anal. calc. for C<sub>19</sub>H<sub>30</sub>N<sub>2</sub>O<sub>3</sub>: C, 68.23; H, 9.04; N, 8.38; found: C, 68.04; H, 8.95; N, 8.28%. <sup>1</sup>H NMR (400 MHz, CDCl<sub>3</sub>; δ ppm, TMS): 10.39 (1H, s), 8.56 (2H, s), 7.51 (2H, s), 4.93 (2H, s), 3.52 (4H, s), 3.49 (4H, s), 2.30 (3H, s), 1.00 (12H, s); ESI-MS<sup>+</sup> (*m/z*): 335.18 [(H<sub>3</sub>L' + H<sup>+</sup>)].

### Synthesis of 2,2'-(((2-hydroxy-5-methyl-1,3-phenylene)bis(methanylylidene))bis(azanylylidene))bis(propan-1-ol) (H<sub>3</sub>L'')

H<sub>3</sub>L'' was obtained following the same synthetic procedure which was used for the synthesis of H<sub>3</sub>L' except DL-2-amino-1-propanol (0.5 mmol, 0.038 g) was used in place of 3-amino-2,2-dimethyl-1-propanol (0.5 mmol, 0.052 g).

Data for H<sub>3</sub>L'': yield (0.139 g, 90%); C, H, N analysis: anal. calc. for C<sub>15</sub>H<sub>22</sub>N<sub>2</sub>O<sub>3</sub>: C, 64.73; H, 7.97; N, 10.06; found: C, 64.54; H, 7.88; N, 10.28%. <sup>1</sup>H NMR (400 MHz, CDCl<sub>3</sub>; δ ppm, TMS): 10.47 (1H, s), 8.42 (2H, s), 7.28 (2H, s), 5.27 (2H, s), 3.71 (4H, d, *J* = 2.4), 3.10 (4H, m), 2.30 (3H, s), 1.23 (6H, s); ESI-MS<sup>+</sup> (*m/z*): 279.13 [(H<sub>3</sub>L'' + H<sup>+</sup>)].

### Synthesis of [Cu<sub>2</sub>(L<sup>1</sup>)<sub>2</sub>] (1)

To an aqueous solution (5.0 mL) of copper(II) acetate monohydrate (0.5 mmol, 0.100 g), an acetonitrile solution (10.0 mL) of H<sub>3</sub>L' (0.5 mmol, 0.167 g) was added dropwise while stirring was continued. The mixture was stirred for another 1 h. The mixture was then filtered to remove suspended material and/or precipitate, if any. Green single crystals of complex 1 suitable for X-ray diffraction analysis were obtained on slow evaporation of the solvent within few days.

Data for 1: yield (0.202 g, 65%); C, H, N analysis: anal. calc. for C<sub>28</sub>H<sub>34</sub>Cu<sub>2</sub>N<sub>2</sub>O<sub>6</sub>: C, 54.10; H, 5.51; N, 4.51; found: C, 54.00; H, 5.57; N, 4.32%.

### Synthesis of [Cu<sub>2</sub>(L<sup>2</sup>)<sub>2</sub>] (2)

Complex 2 was synthesized following the same synthetic procedure which was used for the synthesis of complex 1 except H<sub>3</sub>L'' (0.5 mmol, 0.139 g) was used in place of H<sub>3</sub>L' (0.5 mmol, 0.167 g).

Data for 2: yield (0.164 g, 58%); C, H, N analysis: anal. calc. for C<sub>24</sub>H<sub>26</sub>Cu<sub>2</sub>N<sub>2</sub>O<sub>6</sub>: C, 50.97; H, 4.63; N, 4.95; found: C, 50.90; H, 4.57; N, 4.82%.

### X-ray data collection and structure determination

Details of the data collection and refinement parameters for complex 1 and 2 are summarized in Table S5. The single crystal X-ray diffraction experiments were performed on a Bruker APEX-II CCD diffractometer using graphite monochromated Mo K $\alpha$  radiation at 298 K. The data integration was carried out with SAINT program<sup>[45]</sup> and the absorption correction was done using SADABS. The structures of complexes 1 and 2 were solved by SHELXS 97<sup>[46]</sup> using the Patterson method with the successive Fourier and difference Fourier synthesis. Full matrix least-squares refinements were done on F<sup>2</sup> using SHELXL-97 with anisotropic displacement parameters for all of the non-hydrogen atoms.<sup>[47]</sup> All of the hydrogen atoms were fixed geometrically by HFIX command and placed in ideal positions. Calculations were performed using SHELXL 97, SHELXS 97, PLATON v1.15,<sup>[48]</sup> ORTEP-3v2<sup>[49]</sup> and WinGX system Ver-1.80.<sup>[50]</sup>

### Alcohol oxidation procedure

Oxidation of benzyl alcohol, 4-methyl benzyl alcohol, 4-methoxy benzyl alcohol, 4-nitro benzyl alcohol and 4-bromo benzyl alcohol was performed by using TBHP as the oxidant in the presence of complexes 1 and 2 as catalyst at 343 K. Typically, 0.5 mmol of the substrate (alcohol) in 8.0 mL of acetonitrile was taken in a two necked round-bottomed flask fitted with a condenser. 0.025 mmol of catalyst was added to it. The catalytic reaction was started as soon as 0.5 mmol of *tert*-butyl hydroperoxide was added to the mixture under stirring condition. The temperature of the reaction mixture was kept constant using a thermostat. Aliquots from the mixture were collected after 2 h and 4 h, and then every 4 h upto 24 h. The collected mixtures were analyzed by the gas chromatography. The substrate and product(s) were identified by the comparison with known standards.

Blank experiments for all of the substrates were carried out in absence of any catalyst under the same experimental conditions.

Deposition Numbers 2050745 (for 1) and 2050746 (for 2) contain the supplementary crystallographic data for this paper. These data are provided free of charge by the joint Cambridge Crystallographic Data Centre and Fachinformationszentrum Karlsruhe Access Structures service www.ccdc.cam.ac.uk/structures.

### Acknowledgements

A. Barma and A. Bhattacharjee wish to thank CSIR, New Delhi, for providing their fellowships.

### Conflict of Interest

The authors declare no conflict of interest.

**Keywords:** Alcohols · Copper · Ligand modification · Oxidation · Schiff bases

- [1] a) T. F. S. Silva, L. M. D. R. S. Martins, *Molecules* **2020**, *25*, 748; b) C. Wei, Y. He, X. Shi, Z. Song, *Coord. Chem. Rev.* **2019**, *385*, 1–19; c) R.-P. Ye, L. Lin, Q. Li, Z. Zhou, T. Wang, C. K. Russell, H. Adidharma, Z. Xu, Y.-G. Yao, M. Fan, *Catal. Sci. Technol.* **2018**, *8*, 3428–3449; d) C. Du, X. Gao, W. Chen, *Chin. J. Catal.* **2016**, *37*, 1049–1061.
- [2] a) M. Nasibipour, E. Safaei, G. Wrzeszcz, A. Wojtczak, *New J. Chem.* **2020**, *44*, 4426–4439; b) A. J. McNeece, K. Jesse, J. Xie, A. S. Filatov, J. S. Anderson, *J. Am. Chem. Soc.* **2020**, *142*, 10824–10832; c) X.-Y. Yu, Q.-Q. Zhao, J. Chen, J.-R. Chen, W.-J. Xiao, *Angew. Chem. Int. Ed.* **2018**, *57*, 15505–15509; *Angew. Chem.* **2018**, *130*, 15731–15735; d) J. Reim, R. Werner, W. Haase, B. Krebs, *Chem. Eur. J.* **1998**, *4*, 289–298.
- [3] a) A. Bhanja, R. Herchel, Z. Trávníček, D. Ray, *Inorg. Chem.* **2019**, *58*, 12184–12198; b) X. Liu, C. Manzur, N. Novoa, S. Celedón, D. Carrillo, J.-R. Hamon, *Coord. Chem. Rev.* **2018**, *357*, 144–172.
- [4] a) A. Bhattacharjee, S. Das, B. Das, P. Roy, *Inorg. Chim. Acta* **2021**, *514*, 119961; b) A. Arunadevi, N. Raman, *J. Coord. Chem.* **2020**, *73*, 2095–2116; c) R. Golbedaghi, A. M. Tabanez, S. Esmaeili, R. Fausto, *Appl. Organomet. Chem.* **2020**, *34*, e5884; d) M. A. Malik, O. A. Dar, P. Gull, M. Y. Wani, A. A. Hashmi, *MedChemComm* **2018**, *9*, 409–436.
- [5] a) G. He, X. Hua, N. Yang, L. Li, J. Xu, L. Yang, Q. Wang, L. Ji, *Bioorg. Chem.* **2019**, *91*, 103176; b) T. H. Sanatkar, A. Khorshidi, E. Sohoul, J. Janczak, *Inorg. Chim. Acta* **2020**, *506*, 119537; c) S. Das, Y. Sarkar, S. Mukherjee, J. Bandyopadhyay, S. Samanta, P. P. Parui, A. Ray, *Sens. Actuators B* **2015**, *209*, 545–554.
- [6] a) G. Li, D. Zhu, X. Wang, Z. Su, M. R. Bryce, *Chem. Soc. Rev.* **2020**, *49*, 765–838; b) A. Sakthivel, K. Jeyasubramanian, B. Thangagiri, J. Dhavée-

- thu Raja, *J. Mol. Struct.* **2020**, *1222*, 128885; c) Å. de Fátima, C. de Paula Pereira, C. R. S. D. G. Olímpio, B. G. de Freitas Oliveira, L. L. Franco, P. H. C. da Silva, *J. Adv. Res.* **2018**, *13*, 113–126.
- [7] a) P. Roy, *Coord. Chem. Rev.* **2021**, *427*, 213562; b) M. S. Jana, S. Dey, J. L. Priego, R. Jiménez-Aparicio, T. K. Mondal, P. Roy, *Polyhedron* **2013**, *59*, 101–106; c) P. Roy, M. Nandi, M. Manassero, M. Riccò, M. Mazzani, A. Bhaumik, P. Banerjee, *Dalton Trans.* **2009**, 9543–9554; d) T. S. Mahapatra, A. Bauzá, D. Dutta, S. Mishra, A. Frontera, D. Ray, *ChemistrySelect* **2016**, *1*, 64–75; e) M. Pait, A. Bauzá, A. Frontera, E. Colacio, D. Ray, *Inorg. Chem.* **2015**, *54*, 4709–4723.
- [8] a) A. K. Ghosh, A. Bauzá, V. Bertolasi, A. Frontera, D. Ray, *Polyhedron* **2013**, *53*, 32–39; b) M. Pait, A. Sarkar, E. Colacio, D. Ray, *Proc. Natl. Acad. Sci. India Sect. A* **2014**, *84*, 189–196.
- [9] A. Sarkar, A. K. Ghosh, V. Bertolasi, D. Ray, *Dalton Trans.* **2012**, *41*, 1889–1896.
- [10] a) P. Roy, M. Manassero, *Dalton Trans.* **2010**, *39*, 1539–1545; b) S. Halder, S. Dey, C. Rizzoli, P. Roy, *Polyhedron* **2014**, *78*, 85–93.
- [11] a) P. Roy, K. Dhara, M. Manassero, J. Ratha, P. Banerjee, *Inorg. Chem.* **2007**, *46*, 6405–6412; b) D. Mandal, V. Bertolasi, J. Ribas-Ariño, G. Aromí, D. Ray, *Inorg. Chem.* **2008**, *47*, 3465–3467.
- [12] K. Dhara, S. Karan, J. Ratha, P. Roy, G. Chandra, M. Manassero, B. Mallik, P. Banerjee, *Chem. Asian J.* **2007**, *2*, 1091–1100.
- [13] a) T. Punniyamurthy, L. Rout, *Coord. Chem. Rev.* **2008**, *252*, 134–154; b) K. C. Gupta, A. K. Sutar, *Coord. Chem. Rev.* **2008**, *252*, 1420–1450; c) K. C. Gupta, A. K. Sutar, C.-C. Lin, *Coord. Chem. Rev.* **2009**, *253*, 1926–1946.
- [14] a) A. M. Kirillov, M. N. Kopylovich, M. V. Kirillova, M. Haukka, M. F. C. G. da Silva, A. J. L. Pombeiro, *Angew. Chem.* **2005**, *117*, 4419–4423; *Angew. Chem. Int. Ed.* **2005**, *44*, 4345–4349; b) P. Roy, K. Dhara, M. Manassero, P. Banerjee, *Eur. J. Inorg. Chem.* **2008**, 4404–4412; c) G. B. Shul'pin, *J. Mol. Catal. A* **2002**, *189*, 39–66; d) G. B. Shul'pin, Y. N. Kozlov, L. S. Shul'pina, A. R. Kudinov, D. Mandell, *Inorg. Chem.* **2009**, *48*, 10480–10482; e) M. Nandi, P. Roy, *Indian J. Chem.* **2013**, *52 A*, 1263–1268; f) D. D. Mal, S. Khilari, D. Pradhan, *Green Chem.* **2018**, *20*, 2279–2289.
- [15] a) Z.-L. Li, G.-C. Fang, Q.-S. Gu, X.-Y. Liu, *Chem. Soc. Rev.* **2020**, *49*, 32–48; b) R. Sadasivan, A. Patel, *Inorg. Chim. Acta* **2020**, *510*, 119757.
- [16] T. Tamoradi, M. Ghadermazi, A. Ghorbani-Choghmarani, *Catal. Lett.* **2018**, *148*, 857–872.
- [17] a) K. Moschovitis, C. N. Banti, N. Kourkoumelis, E. E. Moushi, T. Lazarides, S. K. Hadjikakou, *Inorg. Chim. Acta* **2020**, *500*, 119209; b) N. Beyazit, D. Çakmak, C. Demetgül, *Tetrahedron* **2017**, *73*, 2774–2779.
- [18] a) S. Hazra, L. M. D. R. S. Martins, M. F. C. G. da Silva, A. J. L. Pombeiro, *RSC Adv.* **2015**, *5*, 90079–90088; b) A. Jehdaramarn, S. Pornsuwan, P. Chumsaeng, K. Phomphrai, P. Sangtrirunugul, *New J. Chem.* **2018**, *42*, 654–661.
- [19] a) A. M. Kirillov, M. V. Kirillova, A. J. L. Pombeiro, *Coord. Chem. Rev.* **2012**, *256*, 2741–2759; b) L. S. Shul'pina, M. M. Vinogradov, Y. N. Kozlov, Y. V. Nelyubina, N. S. Ikonnikov, G. B. Shul'pin, *Inorg. Chim. Acta* **2020**, *512*, 119889.
- [20] a) S. Asthana, C. Samanta, A. Bhaumik, B. Banerjee, R. K. Voolapalli, B. Saha, *J. Catal.* **2016**, *334*, 89–101; b) S. Tian, M. Tan, Q. Ma, X. Wu, C. Luan, Y. Fang, H. Li, G. Yang, N. Tsubaki, Y. Tan, *Ind. Eng. Chem. Res.* **2020**, *59*, 11087–11097.
- [21] a) M. Meldal, F. Diness, *Trends Chem.* **2020**, *2*, 569; b) L. Liang, D. Astruc, *Coord. Chem. Rev.* **2011**, *255*, 2933–2945; c) S. Roy, T. Chatterjee, M. Pramanik, A. Singha Roy, A. Bhaumik, S. M. Islam, *J. Mol. Catal. A* **2014**, *386*, 78–85.
- [22] L.-J. Cheng, N. P. Mankad, *Chem. Soc. Rev.* **2020**, *49*, 8036–8064.
- [23] J. March in *Advance Organic Chemistry; Reaction, Mechanisms and Structure*, 4th edn., John Wiley & Sons, New York, **1992**.
- [24] a) S. Itoh, M. Taki, S. Takayama, S. Nagatomo, T. Kitagawa, N. Sakurada, R. Arakawa, S. Fukuzumi, *Angew. Chem. Int. Ed.* **1999**, *38*, 2774–2776; *Angew. Chem.* **1999**, *111*, 2944–2946; b) H. Oshita, Y. Shimazaki, *Chem. Eur. J.* **2020**, *26*, 8324–8340.
- [25] J. P. Klinman, *Chem. Rev.* **1996**, *96*, 2541–2562.
- [26] L. H. Abdel-Rahman, A. M. Abu-Dief, M. S. S. Adam, S. K. Hamdan, *Catal. Lett.* **2016**, *146*, 1373–1396.
- [27] G. Zhan, W. Zhong, Z. Wei, Z. Liu, X. Liu, *Dalton Trans.* **2017**, *46*, 8286–8297.
- [28] S. Hazra, L. M. D. R. S. Martins, M. F. C. G. da Silva, A. J. L. Pombeiro, *Inorg. Chim. Acta* **2017**, *455*, 549–556.
- [29] E. Safaei, H. Bahrami, A. Pevec, B. Kozlevčar, Z. Jagličič, *J. Mol. Struct.* **2017**, *1133*, 526–533.
- [30] A. Bhattacharjee, S. Halder, K. Ghosh, C. Rizzoli, P. Roy, *New J. Chem.* **2017**, *41*, 5696–5706.
- [31] a) Z. Liu, Z. Shen, N. Zhang, W. Zhong, X. Liu, *Catal. Lett.* **2018**, *148*, 2709–2718; b) J. Rabeah, U. Bentrup, R. Stößler, A. Brückner, *Angew. Chem. Int. Ed.* **2015**, *54*, 11791–11794; *Angew. Chem.* **2015**, *127*, 11957–11960; c) B. L. Ryland, S. D. McCann, T. C. Brunold, S. S. Stahl, *J. Am. Chem. Soc.* **2014**, *136*, 12166–12173; d) J. M. Hoover, B. L. Ryland, S. S. Stahl, *J. Am. Chem. Soc.* **2013**, *135*, 2357–2367; e) J. M. Hoover, B. L. Ryland, S. S. Stahl, *ACS Catal.* **2013**, *3*, 2599–2605.
- [32] a) R. R. Koner, M. Ray, *Inorg. Chem.* **2008**, *47*, 9122–9124; b) O. Das, S. Paria, T. K. Paine, *Tetrahedron Lett.* **2008**, *49*, 5924–5927.
- [33] a) F. Conan, J.-M. Kerbaol, M. M. Kubicki, E. Vigier, Y. L. Mest, J. S. Pala, *Inorg. Chim. Acta* **2002**, *336*, 87–90; b) R. Gupta, R. Mukherjee, *Inorg. Chim. Acta* **1997**, *263*, 133–137; c) D. E. Fenton, G. P. Westwood, A. Bashall, M. McPartlin, I. J. Scowen, *J. Chem. Soc. Dalton Trans.* **1994**, 2213–2214.
- [34] A. W. Addison, T. N. Rao, J. Reedijk, J. van Rijn, G. C. Verschoor, *J. Chem. Soc. Dalton Trans.* **1984**, 1349–1356.
- [35] L. Yang, D. R. Powell, R. P. Houser, *Dalton Trans.* **2007**, 955–964.
- [36] a) L. Sacconi, M. Ciampolini, *J. Chem. Soc.* **1964**, 276–280; b) A. B. P. Lever, *Inorganic Electronic Spectroscopy*, Elsevier, New York, **1968**.
- [37] a) A. B. P. Lever, *Inorganic Electronic Spectroscopy*, Elsevier, Amsterdam, **1984**; pp. 553–572; b) C. T. Yang, B. Moubaraki, K. S. Murray, J. D. Ranford, J. J. Vittal, *Inorg. Chem.* **2001**, *40*, 5934–5941; c) W. Mazurek, B. J. Kennedy, K. S. Murray, M. J. O'Connor, J. R. Rodger, M. R. Snow, A. G. Wedd, P. R. Zwak, *Inorg. Chem.* **1985**, *24*, 3258–3264; d) R. C. Holz, J. M. Brink, F. T. Gobena, C. J. O'Connor, *Inorg. Chem.* **1994**, *33*, 6086–6092.
- [38] S. K. Mandal, L. K. Thompson, K. Nag, J. –P. Charland, E. G. Gabe, *Inorg. Chem.* **1987**, *26*, 1391–1395.
- [39] F. Ammar, J. M. Saveant, *J. Electroanal. Chem.* **1973**, *47*, 115–125.
- [40] a) R. N. Patel, *Inorg. Chim. Acta* **2010**, *363*, 3838–3846; b) H. Hadadzadeh, S. J. A. Fatemi, S. R. Hosseini, H. R. Khavasi, R. Pöttgen, *Polyhedron* **2008**, *27*, 249–254; c) S. K. Verma, V. K. Singh, J. R. Coord. Chem. **2015**, *68*, 1072–1087; d) R. N. Patel, D. K. Patel, K. K. Shukla, Y. Singh, *J. Coord. Chem.* **2013**, *66*, 4131–4143.
- [41] a) J. K. Kochi, *Tetrahedron* **1962**, *18*, 483–497; b) J. K. Kochi, *J. Am. Chem. Soc.* **1962**, *84*, 1572–1579; c) G. Rothenberg, L. Feldberg, H. Wiener, Y. Sasson, *J. Chem. Soc.-Perkin Trans.* **1998**, *2*, 2429–2434.
- [42] a) I. Timokhin, C. Pettinari, F. Marchetti, R. Pettinari, F. Condello, S. Galli, E. C. B. A. Alegria, L. M. D. R. S. Martins, A. J. L. Pombeiro, *Cryst. Growth Des.* **2015**, *15*, 2303–2317; b) A. Sabbatini, L. M. D. R. S. Martins, K. T. Mahmudov, M. N. Kopylovich, M. G. B. Drew, C. Pettinari, A. J. L. Pombeiro, *Catal. Commun.* **2014**, *48*, 69–72; c) M. N. Kopylovich, Y. Y. Karabach, M. F. C. G. da Silva, P. J. Figiel, J. Lasri, A. J. L. Pombeiro, *Chem. Eur. J.* **2012**, *18*, 899–914; d) R. R. Fernandes, J. Lasri, M. F. C. G. da Silva, J. A. L. Silva, J. J. R. F. da Silva, A. J. L. Pombeiro, *J. Mol. Catal. A* **2011**, *351*, 100–111.
- [43] a) C. Mukherjee, T. Weyhermüller, E. Bothe, P. Chaudhuri, *Inorg. Chem.* **2008**, *47*, 11620–11632; b) B. Xu, J.-P. Lumb, B. A. Arndtsen, *Angew. Chem. Int. Ed.* **2015**, *54*, 4208–4211; *Angew. Chem.* **2015**, *127*, 4282–4285; c) S. Velusamy, A. Srinivasan, T. Punniyamurthy, *Tetrahedron Lett.* **2006**, *47*, 923–926; d) Z. Alajji, E. Safaei, L. Chiang, R. M. Clarke, C. Mu, T. Storr, *Eur. J. Inorg. Chem.* **2014**, 6066–6074; e) E. Safaei, L. Hajikhanmirzaei, B. Karimi, A. Wojtczak, P. Cotic, Y. I. Lee, *Polyhedron* **2016**, *106*, 153–162; f) A. Soroceanu, M. Cazacu, S. Shova, C. Turta, J. Kozisek, M. Gall, M. Breza, P. Rapta, T. C. O. MacLeod, A. J. L. Pombeiro, J. Tesler, A. A. Dobrov, V. B. Arion, *Eur. J. Inorg. Chem.* **2013**, 1458–1474; g) K. C. Weerasiri, A. E. V. Gorden, *Eur. J. Org. Chem.* **2013**, 1546–1550.
- [44] R. R. Gagne, C. L. Spiro, T. J. Smith, C. A. Hamann, W. R. Thies, A. K. Schiemke, *J. Am. Chem. Soc.* **1981**, *103*, 4073–4081.
- [45] APEX-II, SAINT and SADABS, Bruker AXS Inc., Madison, WI, **2008**.
- [46] G. M. Sheldrick, *Acta Crystallogr. Sect. A* **2015**, *71*, 3–8.
- [47] G. M. Sheldrick, *Acta Crystallogr. Sect. C* **2015**, *71*, 3–8.
- [48] A. L. Spek, *Acta Crystallogr. Sect. D* **2009**, *65*, 148–155.
- [49] L. J. Farrugia, *J. Appl. Crystallogr.* **1997**, *30*, 565.
- [50] L. J. Farrugia, *J. Appl. Crystallogr.* **1999**, *32*, 837–838.

Manuscript received: April 1, 2021  
Revised manuscript received: April 24, 2021  
Accepted manuscript online: April 28, 2021

Cite this: *Mater. Adv.*, 2022,  
3, 7655

# Mononuclear nickel(II) complexes as electrocatalysts in hydrogen evolution reactions: effects of alkyl side chain lengths†

Arpita Barma,<sup>a</sup> Malay Chakraborty,<sup>a</sup> Swapan Kumar Bhattacharya,<sup>a</sup> Pritam Ghosh<sup>b</sup> and Partha Roy<sup>a</sup>

We report three mononuclear Ni(II) complexes, namely, [Ni(L<sup>1</sup>)<sub>2</sub>] (**1**), [Ni(L<sup>2</sup>)<sub>2</sub>] (**2**) and [Ni(L<sup>3</sup>)<sub>2</sub>] (**3**), where HL<sup>1</sup> = 1-((4-hydroxybutylimino)methyl)naphthalen-2-ol, HL<sup>2</sup> = 1-((5-hydroxypentylimino)methyl)naphthalen-2-ol and HL<sup>3</sup> = 1-((6-hydroxyhexylimino)methyl)naphthalen-2-ol, as electrocatalysts for hydrogen evolution reactions (HERs). Complexes **1**, **2** and **3** were characterized by various standard analytical methods. Single-crystal X-ray structure analysis reveals that nickel is in square planar geometry in all the complexes. These complexes act as efficient electrocatalysts in HERs using acetic acid (AA) and trifluoroacetic acid (TFA) as the proton source in DMF. Controlled-potential electrolysis experiments show that these complexes are capable of reducing protons of AA and TFA to produce H<sub>2</sub>. Control experiments show that the complexes are essential for improved production of hydrogen. Theoretical calculations were performed to support the mechanism of HER and to check the effect of chain lengths on the catalytic activity. The catalytic activity runs in the order of complex **1** > **2** > **3**.

Received 25th April 2022,  
Accepted 1st August 2022

DOI: 10.1039/d2ma00462c

rsc.li/materials-advances

## Introduction

The need for the development and improvement of secure, sustainable and eco-friendly energy resources is one of the most vital scientific and technical challenges in the present century due to the finite resources of fossil fuels. It is common to use fossil fuel that releases the greenhouse gas, carbon dioxide, into the environment resulting in global warming. In this respect, hydrogen may be considered as a potential candidate for use as an apt energy carrier. The reaction by which molecular hydrogen is produced by two protons *via* the two-electron reduction is known as the hydrogen evolution reaction (HER).<sup>1</sup>

To design an efficient and suitable catalyst for HERs few things such as low price of the metal, metal with labile oxidation states, and coordination sites are to be kept in mind. Platinum has been established as an efficient catalyst for the production of hydrogen.<sup>2</sup> However, it is available in limited quantity and highly expensive. Thus, its extensive use as the catalyst is restricted. Therefore, alternatives are being investigated

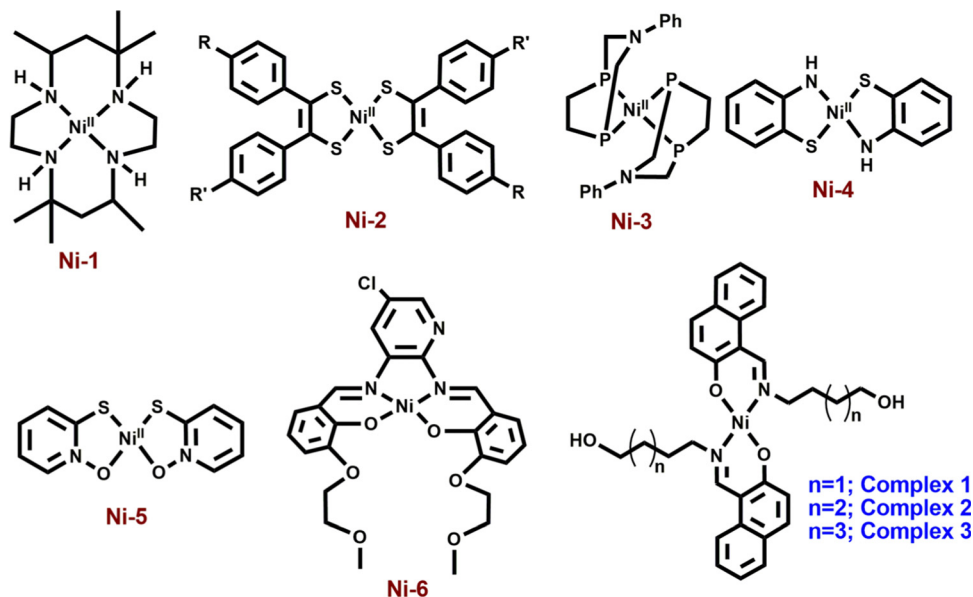
with much cheaper earth-abundant metals as the catalyst. There are reports of different transition metal complexes<sup>3</sup> with Fe,<sup>4</sup> Mn,<sup>5</sup> Cu,<sup>6</sup> Co<sup>7</sup> and Ni<sup>8</sup> as electrocatalysts for HERs. Various compounds of nickel and cobalt have also been used as the electrocatalysts for water splitting, hydrogen generation, and carbon dioxide reduction, showing their efficient role as electrocatalysts.<sup>9</sup> Due to their inherent better ability towards hydrogen evolution, complexes of cobalt and nickel gain intense interest of researchers as high-performance catalysts.<sup>10</sup> Moreover, Ni(II) systems are abundant in earth,<sup>11</sup> and have relevance to biology.<sup>12</sup> Typically, the hydrogen evolution reaction is operated *via* a metal-centered route, and involves a metal hydride. However, the electrocatalysts consisting of earth-abundant elements are rarely prevailing for HERs under pure aqueous conditions. In most of the cases, organic acids have been used as the substrate in organic media with metal complexes as electrocatalysts.

Nickel(II) complexes with a square planar geometry have been used as catalysts for HERs. Ligands with different donor atoms were designed to get various types of Ni(II) complexes. Generally, NiN<sub>4</sub>, NiS<sub>4</sub>, NiP<sub>4</sub>, NiN<sub>2</sub>S<sub>2</sub> and NiS<sub>2</sub>O<sub>2</sub> cores have been employed in such catalytic reactions (Scheme 1). Fisher and Eisenberg reported a nickel(II) complex involving a macrocycle with a NiN<sub>4</sub> core as the ligand, as an electrocatalyst for the reduction of carbon dioxide into carbon monoxide and hydrogen as major products.<sup>13</sup> After that, a number of complexes with N<sub>4</sub>-donor atoms have been reported in the literature for the same. Mitsopoulou *et al.* reported three Ni(II) diphenyl-1,2-

<sup>a</sup> Department of Chemistry, Jadavpur University, Kolkata 700 032, India.

E-mail: partha.roy@jadavpuruniversity.in, skbhattach7@yahoo.co.in

<sup>b</sup> Institut für Chemie, Humboldt-Universität zu Berlin, Brook-Taylor-Straße 2, 12489 Berlin, Germany. E-mail: ppritamghosh@gmail.com† Electronic supplementary information (ESI) available. CCDC 2062677 (**1**), 2062678 (**2**) and 2062679 (**3**). For ESI and crystallographic data in CIF or other electronic format see DOI: <https://doi.org/10.1039/d2ma00462c>



**Scheme 1** Different types of mononuclear nickel complexes with  $\text{NiN}_4$  (**Ni-1**),<sup>12</sup>  $\text{NiS}_4$  (**Ni-2**),<sup>13</sup>  $\text{NiP}_4$  (**Ni-3**),<sup>14</sup>  $\text{NiS}_2\text{N}_2$  (**Ni-4**),<sup>16</sup>  $\text{NiS}_2\text{O}_2$  (**Ni-5**)<sup>16</sup> and  $\text{NiN}_2\text{O}_2$  (**Ni-6**)<sup>17</sup> cores for hydrogen evolution reactions.

dithiolene complexes with different substituents on the benzene ring having a  $\text{NiS}_4$  core for this purpose and showed the effects of the substituents on the results.<sup>14</sup> Helm and coworkers used a mononuclear nickel(II) complex with two seven-membered cyclic diphosphine ligands having P donor atoms as an highly efficient electrocatalyst for the hydrogen generation.<sup>15</sup> Bergamini and Natali reported a nickel(II) bis(diphosphine) complex as a catalyst for the HER in homogeneous media as well as in heterogeneous media.<sup>16</sup> Eisenberg *et al.* reported a series of nickel complexes with two ligands of N,S or O,S donor sites having square planar coordination for hydrogen evolution with a high turnover number and high stability under conditions of hydrogen production.<sup>17</sup> In comparison to these square planar Ni(II) complexes, very limited number of articles describe the  $\text{NiN}_2\text{O}_2$  core as the electrocatalyst for hydrogen evolution. Soo *et al.* reported a  $\text{NiN}_2\text{O}_2$  core as an electrocatalyst for the HER. The presence of alkali metals in the second sphere ether appendages actually increased the hydrogen evolution.<sup>18</sup> The same group has recently reported another nickel complex with a  $\text{NiO}_2\text{N}_2$  core with different ligand backbones for hydrogen evolution with TONs up to 3880.<sup>19</sup>

Herein, we report the electro-catalytic behavior of three neutral, monomeric Ni(II) complexes,  $[\text{Ni}(\text{L}^1)_2]$  (**1**),  $[\text{Ni}(\text{L}^2)_2]$  (**2**) and  $[\text{Ni}(\text{L}^3)_2]$  (**3**), where  $\text{HL}^1 = 1-((4\text{-hydroxybutylimino)methyl})\text{-naphthalen-2-ol}$ ,  $\text{HL}^2 = 1-((5\text{-hydroxypentylimino)methyl})\text{-naphthalen-2-ol}$  and  $\text{HL}^3 = 1-((6\text{-hydroxyhexylimino)methyl})\text{-naphthalen-2-ol}$ , for HERs. Complexes **1**, **2** and **3** have been synthesized easily and characterized by several standard methods including single-crystal X-ray diffraction analysis. All of these complexes have been used as electrocatalysts for the reduction of proton in DMF with acetic acid (AA) and trifluoroacetic acid (TFA) as the proton source. Here, we aim to make variation in the ligand chain length of the complexes and to compare the electro-catalytic results obtained under identical conditions. Some

theoretical calculations have been performed with insights into the hydrogen evolution mechanism and the effect of chain lengths of ligands on the results.

## Experimental section

### Materials and physical methods

2-Hydroxy-1-naphthaldehyde, 4-amino-1-butanol, 5-amino-1-pentanol, 6-amino-1-hexanol and nickel(II) perchlorate hexahydrate were purchased from Sigma Aldrich and were used without further purification. Other reagents and solvents were obtained from different commercial sources and used without further purification. Elemental analyses of complexes **1**, **2** and **3** were performed using a Perkin Elmer 2400C elemental analyzer. <sup>1</sup>H NMR spectra of three Schiff-base ligands, complexes **1**, **2** and **3**, were recorded using a Bruker 400 MHz spectrometer. FT-IR spectra of complexes **1**, **2** and **3** were recorded using a Perkin Elmer spectrometer (Spectrum Two) with the samples by the ATR method. The UV-visible spectral measurements of complexes **1**, **2** and **3** were performed using an Agilent 8453 diode array spectrophotometer. Cyclic voltammograms were obtained using an electrochemical analyzer (CHI 600C, CH Instruments,) under air-free conditions using a conventional three-electrode cell in which a glassy carbon electrode was used as the working electrode, a saturated Ag/AgCl electrode as the reference electrode, and a platinum wire as the auxiliary electrode. The surface area of the glassy carbon working electrode is 0.07 cm<sup>2</sup>. The gas evolved during bulk electrolysis was detected using a GC instrument of model no. 7890B (G3440B), serial no. CN14333203, fitted with TCD. For this, 500  $\mu\text{L}$  gas was taken out in a gas tight syringe from the head space and was injected into the inlet of the GC.



### Synthesis of complexes 1, 2 and 3

**Synthesis of 1-((4-hydroxybutylimino)methyl)naphthalen-2-ol (HL<sup>1</sup>), 1-((5-hydroxypentylimino)methyl)naphthalen-2-ol (HL<sup>2</sup>) and 1-((6-hydroxyhexylimino)methyl)naphthalen-2-ol (HL<sup>3</sup>).** All of the ligands, namely, H<sub>2</sub>L<sup>1</sup>, H<sub>2</sub>L<sup>2</sup> and H<sub>2</sub>L<sup>3</sup>, were synthesized following a general synthetic procedure. Typically, 0.3 mmol of respective amino alcohol (0.027 g for 4-amino-1-butanol, 0.031 g for 5-amino-1-pentanol and 0.035 g for 6-amino-1-hexanol) was added dropwise into an acetonitrile solution of 2-hydroxy-1-naphthaldehyde (0.3 mmol, 0.0516 g) under stirring. Stirring was continued for further 30 min. The mixture was then refluxed for 4 h when the color of the reaction mixture became yellow. The mixture was then cooled to room temperature. It was filtered to remove solid materials, if any. Solid products were obtained after few days on slow evaporation of acetonitrile.

Data for HL<sup>1</sup>: yield = 0.068 g, 92%; anal. calc. (%) for C<sub>15</sub>H<sub>17</sub>NO<sub>2</sub>: C, 74.05; H, 7.04; N, 5.76. Found: C, 73.97; H, 6.96; N, 5.79; <sup>1</sup>H NMR (400 MHz, DMSO-d<sub>6</sub>, δ ppm, TMS) 14.13 (1H, s), 9.08 (1H, s), 8.07 (1H, d, *J* = 8.4 Hz), 7.71 (1H, d, *J* = 9.2 Hz), 7.62 (1H, d, *J* = 7.6 Hz), 7.42 (1H, m), 7.19 (1H, t, *J* = 7.2 Hz), 6.72 (1H, d, *J* = 9.2 Hz), 4.51 (1H, s), 3.66 (2H, t, *J* = 4.4 Hz), 3.45 (2H, t, *J* = 4.4 Hz), 1.72 (2H, m), 1.54 (2H, m); ESI-MS<sup>+</sup> (*m/z*): 244.23 [(HL<sup>1</sup> + H<sup>+</sup>)].

Data for HL<sup>2</sup>: yield = 0.070 g, 90%; anal. calc. (%) for C<sub>16</sub>H<sub>19</sub>NO<sub>2</sub>: C, 74.68; H, 7.44; N, 5.44. Found: C, 74.57; H, 7.36; N, 5.39; <sup>1</sup>H NMR (400 MHz, DMSO-d<sub>6</sub>, δ ppm, TMS) 14.13 (1H, s), 9.09 (1H, s), 8.06 (1H, d, *J* = 8.0 Hz), 7.71 (1H, d, *J* = 9.2 Hz), 7.62 (1H, d, *J* = 7.6 Hz), 7.42 (1H, t, *J* = 7.6 Hz), 7.18 (1H, t, *J* = 7.2 Hz), 6.72 (1H, d, *J* = 9.2 Hz), 4.33 (1H, s), 3.65 (2H, t, *J* = 6.8 Hz), 3.42 (2H, t, *J* = 6.0 Hz), 1.49 (2H, m), 1.29 (2H, m); ESI-MS<sup>+</sup> (*m/z*): 258.11 [(HL<sup>2</sup> + H<sup>+</sup>)].

Data for HL<sup>3</sup>: yield = 0.069 g, 85%; anal. calc. (%) for C<sub>17</sub>H<sub>21</sub>NO<sub>2</sub>: C, 75.25; H, 7.80; N, 5.16. Found: C, 75.17; H, 7.76; N, 5.29; <sup>1</sup>H NMR (400 MHz, DMSO-d<sub>6</sub>, δ ppm, TMS) 14.12 (1H, s), 9.08 (1H, s), 8.06 (1H, d, *J* = 8.4 Hz), 7.70 (1H, d, *J* = 9.2 Hz), 7.61 (1H, d, *J* = 8.0 Hz), 7.41 (1H, t, *J* = 7.2 Hz), 7.18 (1H, t, *J* = 7.6 Hz), 6.71 (1H, d, *J* = 9.2 Hz), 4.36 (1H, s), 3.63 (2H, t, *J* = 7.2 Hz), 3.39 (2H, t, *J* = 6.0 Hz), 1.67 (2H, m), 1.33 (2H, m); ESI-MS<sup>+</sup> (*m/z*): 272.13 [(HL<sup>3</sup> + H<sup>+</sup>)].

**Synthesis of [Ni(L<sup>1</sup>)] (1).** HL<sup>1</sup> (0.6 mmol, 0.146 g) in 5.0 mL of acetonitrile was added slowly into a solution of nickel(II) perchlorate hexahydrate (0.3 mmol, 0.1097 g) in acetonitrile (5.0 mL) under continuous stirring. The mixture was stirred till it turned greenish. Then, it was refluxed for one hour. The color of the solution changed to dark green. The mixture was then cooled to room temperature and filtered to remove solid materials, if any. The filtrate was kept in a beaker under ambient conditions for slow evaporation. Green crystals of complex 1 suitable for single-crystal X-ray diffraction were produced after few days.

Data for 1: yield, 0.094 g, 58%; anal. calc. for C<sub>30</sub>H<sub>31</sub>NiN<sub>2</sub>O<sub>4</sub>: C, 66.45; H, 5.76; N, 5.17; found: C, 66.33; H, 5.80; N, 5.06%. <sup>1</sup>H NMR (400 MHz, DMSO-d<sub>6</sub>, δ ppm, TMS) 9.11 (1H, s), 8.12 (1H, d, *J* = 8.4 Hz), 7.83 (1H, d, *J* = 8.8 Hz), 7.74 (1H, d, *J* = 8.0 Hz), 7.50 (1H, t, *J* = 7.6 Hz), 7.25 (1H, t, *J* = 7.2 Hz), 6.82 (1H, d, *J* = 8.8 Hz), 4.45 (1H, s), 4.17 (2H, t, *J* = 5.2 Hz), 3.50 (2H, t, *J* = 5.6 Hz), 1.97 (2H, m), 1.65 (2H, m).

**Synthesis of [Ni(L<sup>2</sup>)] (2) and [Ni(L<sup>3</sup>)] (3).** Complexes 2 and 3 were synthesized following the method used for the synthesis of complex 1. HL<sup>2</sup> (0.6 mmol, 0.154 g) and HL<sup>3</sup> (0.6 mmol, 0.163 g) were used for complexes 2 and 3, respectively, in place of HL<sup>1</sup>.

Data for 2: yield, 0.106 g, 62%; anal. calc. for C<sub>32</sub>H<sub>36</sub>NiN<sub>2</sub>O<sub>4</sub>: C, 67.27; H, 6.35; N, 4.90; found: C, 67.20; H, 6.26; N, 5.05%. <sup>1</sup>H NMR (400 MHz, DMSO-d<sub>6</sub>, δ ppm, TMS) 9.15 (1H, s), 8.12 (1H, d, *J* = 8.8 Hz), 7.85 (1H, d, *J* = 8.8 Hz), 7.74 (1H, d, *J* = 8.0 Hz), 7.48 (1H, t, *J* = 7.6 Hz), 7.27 (1H, t, *J* = 7.2 Hz), 6.80 (1H, d, *J* = 8.8 Hz), 4.35 (1H, s), 4.24 (2H, t, *J* = 5.2 Hz), 3.43 (2H, t, *J* = 5.2 Hz), 1.94 (2H, m), 1.52 (2H, m).

Data for 3: yield, 0.104 g, 58%; anal. calc. for C<sub>34</sub>H<sub>40</sub>NiN<sub>2</sub>O<sub>4</sub>: C, 68.13; H, 6.73; N, 4.67; found: C, 68.05; H, 6.80; N, 4.58%. <sup>1</sup>H NMR (400 MHz, DMSO-d<sub>6</sub>, δ ppm, TMS) 9.12 (1H, s), 8.11 (1H, d, *J* = 8.0 Hz), 7.89 (1H, d, *J* = 8.8 Hz), 7.74 (1H, d, *J* = 7.2 Hz), 7.50 (1H, t, *J* = 7.2 Hz), 7.25 (1H, t, *J* = 8.0 Hz), 6.79 (1H, d, *J* = 8.8 Hz), 4.32 (1H, s), 3.38 (2H, t, *J* = 5.2 Hz), 3.33 (2H, t, *J* = 6.4 Hz), 2.29 (2H, m), 1.48 (2H, m).

CAUTION: nickel(II) perchlorate hexahydrate can be explosive on heating. Therefore, the perchlorate salts should be handled with care.

### X-ray data collection and structure determination

Data collection and refinement parameters for complexes 1, 2 and 3 are summarized in Table 1. The X-ray diffraction experiments were performed using a BRUKER D8 QUEST CCD diffractometer for 1 and a Bruker APEX-II CCD diffractometer for 2 and 3 with graphite-monochromated Mo Kα radiation at 294(2) K. Data processing was done using the Bruker APEX2 and SAINT packages.<sup>20</sup> Absorption corrections, which are based on multi-scans using the SADABS software,<sup>20</sup> were applied to intensity data. The structures of complexes 1, 2 and 3 were solved by direct methods utilizing SHELXT<sup>21</sup> and refined with full-matrix least-squares on *F*<sup>2</sup> on all unique reflections employing SHELXL-2014/7.<sup>22</sup> All the non-hydrogen atoms of all of three complexes were refined anisotropically. The crystals selected for the single-crystal X-ray diffraction analysis of complexes 1 and 3 were refined as merohedral twins in both the complexes with a fractional contribution of minor components of 0.18(3) and 0.03(2), respectively. In complex 1, the quality of crystal was poor. The poor quality as well as the presence of twinning in 1 may account for the limited overall precision of its structure, high residual peaks and the relatively high values of *R* and *wR*<sub>2</sub> parameters.

CCDC 2062677, 2062678 and 2062679 contain the supplementary crystallographic data for complexes 1, 2 and 3, respectively.†

## Results and discussion

### Synthesis of ligands and their characterization by ESI mass and <sup>1</sup>H spectral analysis

1-((4-Hydroxybutylimino)methyl)naphthalen-2-ol (HL<sup>1</sup>), 1-((5-hydroxypentylimino)methyl)naphthalen-2-ol (HL<sup>2</sup>) and 1-((6-hydroxyhexylimino)methyl)naphthalen-2-ol (HL<sup>3</sup>) were synthesized by a Schiff-base condensation reaction between 2-hydroxy-1-naphthaldehyde and the respective amine in 1:1 proportion in



Table 1 Crystal data of complexes 1, 2 and 3

Complex	1	2	3
Formula	C <sub>30</sub> H <sub>31</sub> N <sub>2</sub> Ni <sub>1</sub> O <sub>4</sub>	C <sub>32</sub> H <sub>36</sub> N <sub>2</sub> Ni <sub>1</sub> O <sub>4</sub>	C <sub>34</sub> H <sub>40</sub> N <sub>2</sub> Ni <sub>1</sub> O <sub>4</sub>
Formula weight	542.26	571.32	599.39
<i>T</i> (K)	298(2)	298(2)	298(2)
Crystal color	Green	Green	Green
Crystal system	Monoclinic	Triclinic	Triclinic
Space group	<i>P</i> 2 <sub>1</sub> / <i>c</i>	<i>P</i> $\bar{1}$	<i>P</i> $\bar{1}$
<i>a</i> (Å)	10.7840(8)	4.9186(4)	5.1838(7)
<i>b</i> (Å)	4.9890(4)	16.7080(14)	16.905(2)
<i>c</i> (Å)	23.8099(18)	16.9064(14)	17.141(2)
$\alpha$ (°)	90	86.436(3)	84.192(5)
$\beta$ (°)	90.846(2)	84.966(2)	87.843(4)
$\gamma$ (°)	90	89.509(2)	89.703(4)
<i>V</i> (Å <sup>3</sup> )	1280.87(17)	1381.3(2)	1493.3(3)
<i>Z</i>	2	2	2
Crystal dimensions (mm)	0.40 × 0.26 × 0.13	0.41 × 0.23 × 0.12	0.46 × 0.29 × 0.16
<i>F</i> (0 0 0)	570.0	604.0	636.0
<i>D</i> <sub>c</sub> (g cm <sup>-3</sup> )	1.406	1.374	1.333
$\lambda$ (Mo K $\alpha$ ) (Å)	0.71073	0.71073	0.71073
$\theta$ range (°)	2.53–27.11	2.65–27.25	2.39–27.00
Reflection collected/unique/observed	29 207, 2837, 2507	70 198, 6202, 5565	78 729, 6626, 5259
Absorption correction	Multi-scan	Multi-scan	Multi-scan
<i>R</i> <sub>int</sub>	0.0306	0.0320	0.0350
Final <i>R</i> <sub>1</sub> index [ <i>I</i> > 2 $\sigma$ ( <i>I</i> )]	0.0352	0.0348	0.0498
Final <i>wR</i> <sub>2</sub> index (all reflections)	0.1324	0.1024	0.1397
Goodness-of-fit	1.166	1.022	0.925

acetonitrile with high yields (Scheme S1, ESI<sup>†</sup>). Complexes 1, 2 and 3 were obtained by the reactions between the ligands and nickel(II) perchlorate hexahydrate in 2 : 1 proportion without the addition of any external base.

ESI-mass spectrometric measurements of HL<sup>1</sup>, HL<sup>2</sup> and HL<sup>3</sup> were performed with their methanolic solutions (Fig. S1–S3, ESI<sup>†</sup>). Mass spectrum of HL<sup>1</sup> shows an *m/z* peak at 244.23, which may be attributed to the [HL<sup>1</sup> + H<sup>+</sup>] species (calculated value 244.31). The *m/z* peak at 258.11 may be assigned to the presence of [HL<sup>2</sup> + H<sup>+</sup>] species (calculated value 258.15). The mass spectrum of HL<sup>3</sup> shows an *m/z* peak at 272.13, which may be due to the presence of [HL<sup>3</sup> + H<sup>+</sup>] (calculated value 272.17). These ligands were further characterized by <sup>1</sup>H NMR spectral studies (Fig. S4–S6, ESI<sup>†</sup>). Spectra were obtained in DMSO-*d*<sub>6</sub>. NMR spectral studies support the formation of Schiff-base ligands. All of these compounds show a peak at around 14.1 ppm, which indicates the presence of a phenolic OH group. The peak at around 9.0 ppm in all the ligands may be due to the presence of an imine proton, indicating the formation

of Schiff-base compounds. Signals for aromatic protons for all of the ligands appear in the appropriate positions. Signals for methylene protons also appear in their usual positions. All of these analyses support formation of the Schiff-base ligands.

### Characterization of complexes 1, 2 and 3

**Crystal structures of complexes 1, 2 and 3.** Single crystals of complexes 1, 2 and 3 were obtained on slow evaporation of their acetonitrile solution. Complex 1 crystallizes in a monoclinic system and a *P*2<sub>1</sub>/*c* space group. However, both complexes 2 and 3 crystallize in a triclinic system and *P* $\bar{1}$  space group. The asymmetric unit consists of one nickel centre and a pair of ligands for all of the complexes (Fig. 1). All of 1, 2 and 3 are mononuclear complexes (Fig. S7–S9, ESI<sup>†</sup>). The selected bond lengths and bond angles are listed in Table S1 (ESI<sup>†</sup>). All of these complexes may be summarized as the NiO<sub>2</sub>N<sub>2</sub> core. For all of the complexes, the Ni atom is coordinated to N and O donor atoms from a ligand and another set of N and O donor

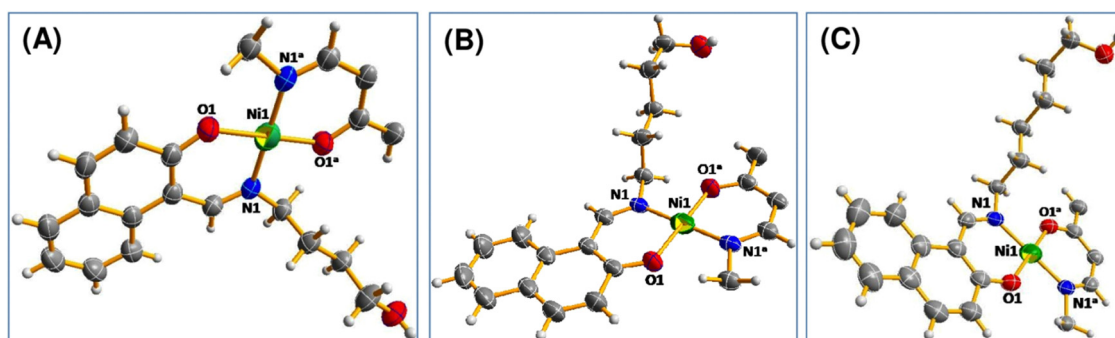


Fig. 1 Perspective view of (A) complex 1, (B) complex 2 and (C) complex 3 with displacement ellipsoids drawn at the 50% probability level.



atoms from a different ligand. Ni atom is in a square planar geometry. Apart from the hydroxyl alkyl chain, the rest of the molecule is planar. For complex **1**, angles O1–Ni1–O1<sup>a</sup> and N1–Ni1–N1<sup>a</sup> are 180°, whereas other donor–metal–donor angles range from 87.86 to 92.14°. While other donor–metal–donor angles vary from 87.82 to 92.18° for complex **2**, they vary from 88.44 to 91.56° for complex **3**.

For other two complexes, all of the large donor–metal–donor angles are 180°. For a four-coordinate complex, Houser and co-workers proposed the four-coordinate  $\tau_4$  index to ascertain the geometry around the metal center. The four-coordinate  $\tau_4$  index value was obtained using the following formula:<sup>23</sup>

$$\tau_4 = \frac{360^\circ - (\alpha + \beta)}{141^\circ}$$

where  $\alpha$  and  $\beta$  are the two largest donor–metal–donor angles in a tetra-coordinated complex. For a tetrahedral geometry, the value of  $\tau_4$  is 1.00, while for an ideal square planar arrangement, it is 0.00. As two largest donor–metal–donor angles are 180° for all of these three complexes, the values of four-coordinate  $\tau_4$  index come out as 0.00 for all the complexes. This fact indicates that there exists the perfect square planar geometry around the nickel atom in complexes **1**, **2** and **3**. The O–Ni bond distances are close to 1.82 Å and the O–Ni bond distances are about 1.91 Å. These values are in agreement with the published results.<sup>24</sup>

#### ESI-mass, FT-IR, UV-vis and <sup>1</sup>H NMR spectral characterization of the complexes

ESI-mass spectra of complexes **1**, **2** and **3** were obtained with their methanolic solutions (Fig. S10–S12, ESI†). All of them behave similarly. The mass spectrum of **1** exhibits an  $m/z$  peak at 565.0727, which may be attributed to the  $[\text{Ni}(\text{L}^1)_2 + \text{Na}^+]$  species (calculated value = 565.16). This indicates that the complex exists mainly as a mononuclear nickel(II) species in solution. For complex **2**, an  $m/z$  peak appears at 593.10, which may be assigned to  $[\text{Ni}(\text{L}^2)_2 + \text{Na}^+]$  (calculated value = 565.19). Similarly, the  $m/z$  peak at 621.14 of complex **3** appears due to the presence of  $[\text{Ni}(\text{L}^3)_2 + \text{Na}^+]$  species (calculated value = 621.22).<sup>25</sup>

FT-IR spectra of complexes **1**, **2** and **3** were recorded with a solid sample by the ATR technique (Fig. S13–S15, ESI†). In the IR spectra, broad bands appear at 3536 cm<sup>-1</sup>, 3316 cm<sup>-1</sup> and 3272 cm<sup>-1</sup> for complexes **1**, **2** and **3**, respectively. The peaks were assigned to O–H stretching for the presence of a hydroxyl group in the ligand part of the complexes. The presence of a methylene group in the complexes has been evidenced by the appearance of unsymmetrical and symmetrical frequencies of  $\nu_{\text{C-H}}$  in the range of 2800–3000 cm<sup>-1</sup>. In the IR spectra of complexes **1**, **2** and **3**, intense bands appeared at ~1657 cm<sup>-1</sup>, 1658 cm<sup>-1</sup> and 1642 cm<sup>-1</sup> respectively. These may be attributed to the presence of the C=N moiety in the complexes. The conclusive evidence for the formation of Ni–N and Ni–O bonds in the IR spectra of these complexes is also observed with characteristic bands. These bands support the fact that the metal ion has been effectively coordinated to the four

coordinating heteroatoms (NONO). These data are also supported by the literature (Table S2, ESI†).<sup>26</sup>

The UV-vis spectra of complexes **1**, **2** and **3** were recorded in the range of 200–800 nm in DMF at room temperature (Fig. S16–S18, ESI†). The electronic spectra of these complexes are grossly similar in nature. A broad band at around 600 nm was observed for each of the complexes, which may be attributed to the  $d-d$  transition. These are weak in intensity as they are Laporte forbidden.<sup>27</sup> The bands at 275 nm for complex **1**, 279 nm for complex **2** and 274 nm for complex **3** may be assigned to the  $\pi-\pi^*$  transitions of the phenolic chromophore. The bands between 300 and 500 nm may be assigned to the  $\pi-\pi^*$  transition of the azomethine chromophore and the benzene ring and the  $n-\pi^*$  transition of the azomethine chromophore.<sup>28</sup> The higher intensity charge-transfer transition has been observed at a wavelength near 420 nm for all three complexes. These are attributed to O<sup>-</sup> (of naphthalen-1-olate) → Ni(II), N(amino) → Ni(II) LMCT and intra-ligand charge transfer transitions.<sup>29</sup> All of these bands corroborate the structure of the complexes (Table S3, ESI†).

<sup>1</sup>H NMR spectra of complexes **1**, **2** and **3** were obtained in DMSO-d<sub>6</sub> (Fig. S19–S21, ESI†). The behavior of all the ligands in the presence of Ni<sup>2+</sup> is grossly similar. All of these complexes are square planar in geometry and the metal ion in the complex does not possess any unpaired electron. The peak for phenolic OH at ~14 ppm is absent in the NMR spectra of all the complexes. This indicates that the phenolic OH group is deprotonated during complex formation and then coordinated to the metal center. The signal for the imine proton at ~8 ppm in the ligands undergoes a shift to ~9 ppm for all the complexes, confirming complex formation *via* azomethine nitrogen atoms. Signals for aromatic protons shift towards higher  $\delta$  values. All other peaks appear in their usual positions. The fact indicates that all of the complexes remain the same in the DMSO solution.<sup>25</sup>

#### Electrochemistry

**Cyclic voltammetric studies.** As shown in Fig. 2(A)–(C), cyclic voltammograms of complexes **1**, **2** and **3** respectively were recorded in air-free DMF containing 0.1 M tetrabutylammonium bromide in the range of –2 V to +2 V *versus* Fc/Fc<sup>+</sup>. An important feature of these cyclic voltammograms is the nickel(II)–nickel(I) redox couple with cathodic peak potentials ( $E_{\text{pc}}$ ) of –1.48, –1.51, –1.52 V *versus* Fc/Fc<sup>+</sup> for complexes **1**, **2** and **3** respectively, while anodic peak potentials ( $E_{\text{pa}}$ ) of –0.77, –0.68 and –0.74 V *versus* Fc/Fc<sup>+</sup> for complexes **1**, **2** and **3** respectively.<sup>30</sup> Considering the reduction sweep, initially, an irreversible event is observed at –0.85, –0.76 and –0.73 V *versus* Fc/Fc<sup>+</sup> for complexes **1**, **2** and **3** respectively due to the electrochemically irreversible Ni(III)/Ni(II) reductive response,<sup>31</sup> while another quasi reversible redox event observed for each of the complexes at 0.5 V *versus* Fc/Fc<sup>+</sup> appears for the solvent DMF. The nature of the voltammograms of the complexes scanned over the presently important region of potential of reversible Ni(II/I) couple (–2 V *versus* Fc/Fc<sup>+</sup> to +0.6 V *versus* Fc/Fc<sup>+</sup>) is shown in the insets of Fig. 2. In Fig. 2(D), the cyclic voltammogram of ferrocene is presented in the DMF





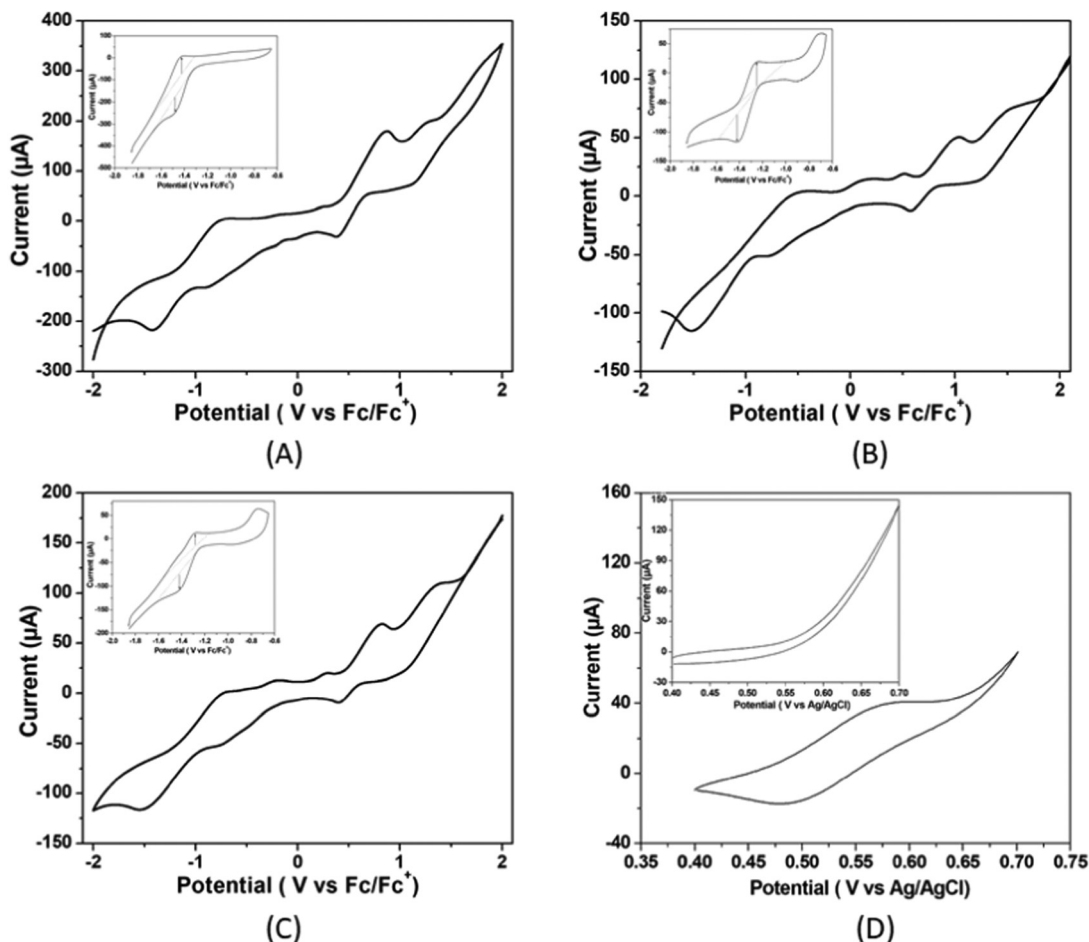


Fig. 2 Cyclic voltammograms of 5.36  $\mu\text{M}$  of (A) complex **1**, (B) complex **2** (C) complex **3** and (D) ferrocene (inset: cyclic voltammograms scanned over the presently important region of potential of reversible Ni(II/I) couple) in air free DMF solutions with 0.1 M of  $[n\text{-Bu}_4\text{N}]\text{Br}$  as the supporting electrolyte at a scan rate of 50  $\text{mV s}^{-1}$ . Here, ferrocene is the internal standard.

solution on the same working electrode. The  $E_{1/2}$  value obtained (0.535 V versus aqueous AgCl/Ag,  $\text{Cl}^-$  electrode or 0.559 V versus NHE) is very close to the value reported in the literature.<sup>32</sup>

The current responses of the redox events at  $-1.48$ ,  $-1.51$ , and  $-1.52$  V versus  $\text{Fc}/\text{Fc}^+$  for complexes **1**, **2** and **3** respectively at multiple scan rates from 0.02 to 0.15  $\text{V s}^{-1}$  were used to construct the Cottrell plot. The plots show linear dependence of the current response on the square root of the scan rate (Fig. S22, ESI†). This indicates that for the three complexes, the reduction is diffusion limited with a diffusion coefficient of  $1.07 \times 10^{-5}$  for complex **1**,  $0.77 \times 10^{-5}$  for complex **2** and  $0.72 \times 10^{-5}$  for complex **3** (please see ESI†). It has been observed that the catalytic-to-peak current ratio ( $i_{\text{cat}}/i_{\text{p}}$ ) increases for all the three complexes with the increase in acid concentration (Fig. S23, ESI†).

The electrochemical properties of three nickel(II) complexes with salen-type ligands were influenced by the presence of different substituents of the imine linkage.<sup>33</sup> Ren and co-workers showed that the electrochemical reduction ability of nickel(II) complexes with cyclam ligands from  $\text{H}^+$  to  $\text{H}_2$  is dependent on the substituents of the macrocyclic ligands.<sup>34</sup> Thus, it is expected that changes in the chain length of ligands in the Ni(II) complexes

in the present study could influence Ni(II)/Ni(I) potentials of the complexes.

**Electrocatalytic hydrogen evolution in DMF: CV studies.** The performance of these three mononuclear Ni(II) complexes as effective electrocatalysts for the HER was assessed under various conditions, in which the proton source ( $\text{CH}_3\text{COOH}$  or  $\text{CF}_3\text{COOH}$ ) has been systematically varied.

To determine the activity of complexes **1**, **2** and **3** as electrocatalysts, first, cyclic voltammograms of the complexes were recorded in the presence of acetic acid ( $\text{p}K_{\text{a}} = 13.5$ ) in DMF.<sup>35</sup> The addition of  $\text{CH}_3\text{COOH}$  aliquots at a concentration ranging from 0.00 to 24.00 mM to the solutions of complexes **1**, **2** and **3** in DMF triggers the systematic increase in catalytic current ( $i_{\text{cat}}$ ) at  $-1.48$ ,  $-1.51$ , and  $-1.52$  V respectively versus  $\text{Fc}/\text{Fc}^+$  (Fig. 3).

The onset potentials for the reduction of hydrogen ions in the presence of the three complexes studied are  $-1.13$  V,  $-1.15$  V and  $-1.20$  V versus  $\text{Fc}/\text{Fc}^+$ , respectively, indicating that the catalytic activity is in the order: complex **1** > complex **2** > complex **3**.

The electrocatalytic activity of these complexes was also accessed using trifluoroacetic acid ( $\text{p}K_{\text{a}} = 6.0$ ) in DMF as a proton source.<sup>36</sup> As shown in Fig. 4, there is an increase in the



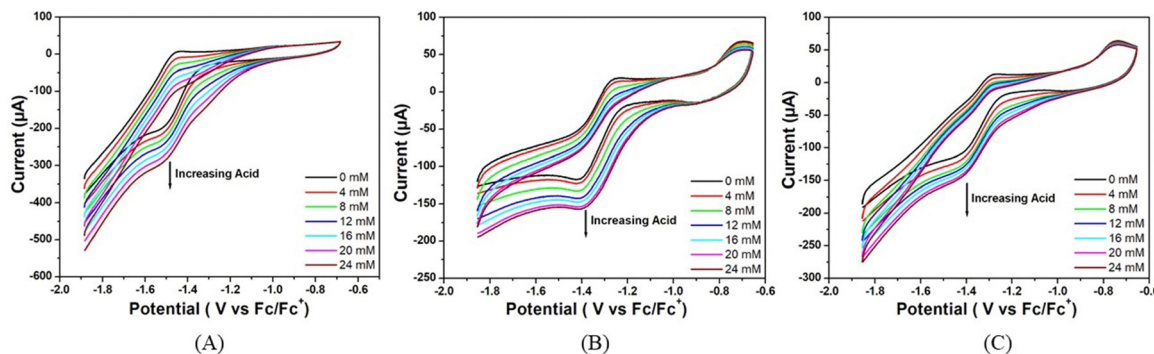


Fig. 3 Cyclic voltammograms of (A) complex **1**, (B) complex **2** and (C) complex **3** (5.36 μM) in the absence of acetic acid (black trace) and in the presence of different concentrations of acetic acid in air-free DMF. Conditions: 25 °C, 0.1 M  $[n\text{-Bu}_4\text{N}]\text{Br}$  as the supporting electrolyte, scan rate = 50  $\text{mV s}^{-1}$ , glassy carbon working electrode, Pt wire counter electrode and the potential are referenced against  $\text{Fc}/\text{Fc}^+$ .

catalytic current ( $i_{\text{cat}}$ ) at  $-1.48$ ,  $-1.51$ , and  $-1.52$  V versus  $\text{Fc}/\text{Fc}^+$  for complexes **1**, **2** and **3** respectively upon successive addition of  $\text{CF}_3\text{COOH}$  (0.00 to 24.00 mM). For all the three complexes, the peak current increases and the peak potential is shifted towards less negative potential (anodically) with the increase in acid concentration in the solution. This signifies that the greater diffusion of proton from bulk solution to the electrode surface makes the reduction process much easier at high concentrations of acid. Notably, for all the three complexes, the sequence of peak currents that also represents their catalytic activity at any particular acid concentration is the same as the order of post peak current values, which decrease sharply with the decrease in potential due to increased hydrogen evolution.

This rise in current in both the cases could be attributed to the generation of  $\text{H}_2$  from catalytic reduction of protons. The reduction potentials of these complexes slightly change towards more anodic values with the sequential enhancements in the concentration of the acid. The overpotential for hydrogen evolution was calculated following the methods reported by Fourmond *et al.*<sup>35</sup> from the theoretical half wave potential,  $E_{1/2}^T$ , based on the expression found in the supporting document and the experimental potential  $E_{\text{cat}/2}$  (eqn (1)):

$$\text{Over potential } (\eta) = |E_{1/2}^T - E_{\text{cat}/2}| \quad (1)$$

Based on eqn (1), this reduction occurs at overpotentials of  $-0.52$  V,  $-0.55$  V and  $-0.56$  V for complexes **1**, **2** and **3** respectively for the former case, where acetic acid is the proton source. The corresponding values are  $-0.22$  V,  $-0.23$  V and  $-0.24$  V for complexes **1**, **2** and **3** respectively for the latter case, where trifluoroacetic acid is the proton source.

In both the cases, the catalytic activity of the three homogeneous catalysts as obtained from the overpotential value is in the following order: complex **1** > complex **2** > complex **3**. Moreover, the large difference in overpotential for each complex for the two proton sources is expected for the increased diffusion of protons in the latter case.

A table is given in ESI<sup>†</sup> (Table S4), where few of recently reported Ni(II) complexes<sup>3b,c,37</sup> are listed with their overpotential values. In most of the cases, the medium of experiment was organic. The proton source varies as acetic acid, trifluoroacetic acid, perchloric acid or buffer solution. If we look into the values of overpotential, they are in the range of few millivolts. While comparing with the other reported overpotential values for the electrocatalytic hydrogen evolution catalysed by nickel complexes as enlisted in the table, it can be concluded that these three nickel(II) complexes are more effective in this field.

The stability of all three complexes have been checked by repeated cyclic voltammetry (CV) studies up to 65 cycles using

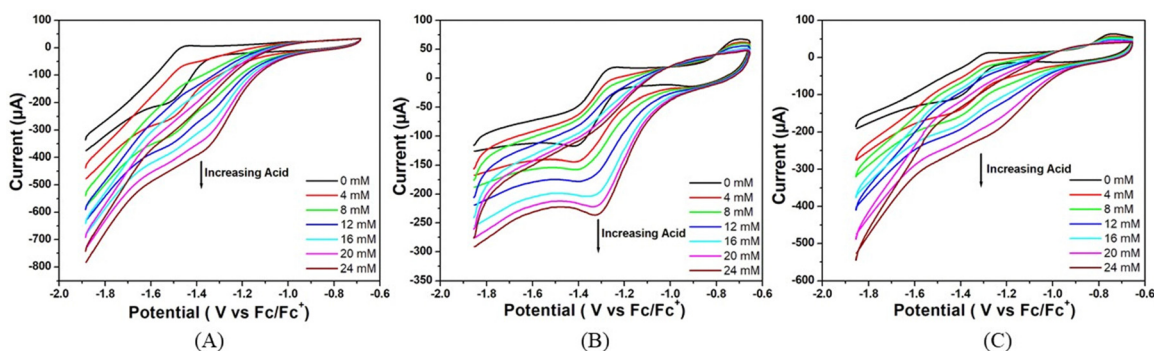


Fig. 4 Cyclic voltammograms of (A) complex **1**, (B) complex **2** and (C) complex **3** (5.36 μM) in the absence of trifluoroacetic acid (black trace) and in the presence of different concentrations of trifluoroacetic acid in air-free DMF. Conditions: 25 °C, 0.1 M  $[n\text{-Bu}_4\text{N}]\text{Br}$  as supporting electrolyte, scan rate = 50  $\text{mV s}^{-1}$ , glassy carbon working electrode, Pt wire counter electrode and the potential is referenced against  $\text{Fc}/\text{Fc}^+$ .



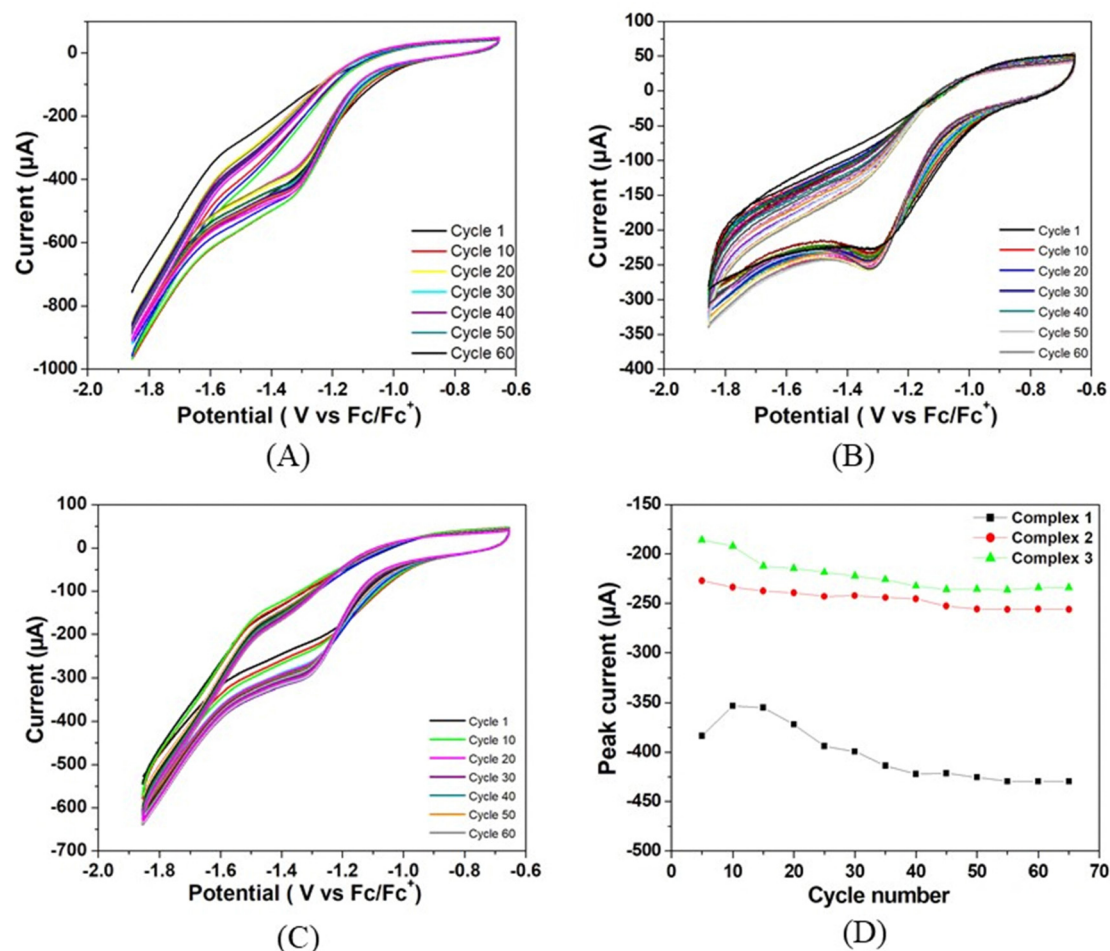


Fig. 5 Repeated cyclic voltammetry studies of (A) complex 1, (B) complex 2, and (C) complex 3. (D) Peak current vs. cycle number profiles for all the three complexes.

TFA as the proton source (Fig. 5). It has been observed that no new peaks are generated in the CV and also the colour of the solution remains the same during the study. In all cases, the reduction peak current increases continuously and reaches almost a steady value at the 55th cycle. The peak current with respect to the lowest amount is increased by 12% for complex 1, 14% for complex 2, and 28% for complex 3. The current of complex 1 is always greater than the remaining two complexes. The increase in current during repeated cyclic voltammetric operation might be due to the cleansing of the fine surface of the electrode and opening up of new channels by the initial  $H^+$  ion penetration at the metal centre and the associated  $H_2$  evolution. Thus, more active sites of the electrode surface are created for further reaction. Greater the size of the alkyl group, the greater is the initial prevention of  $H^+$  for approaching towards the metal centre for reduction. On application of the negative potential, the proton penetrates through the barrier and creates new channels for further reaction. Since the initial barrier varies in the order of complex 3 > complex 2 > complex 1, the increase in the peak current on cycling is in the reverse order.

**Electrocatalytic hydrogen evolution: CPE studies.** Further evidence for the electrocatalytic activity of these mononuclear

nickel(II) complexes for HERs was evaluated in DMF by conducting controlled-potential electrolysis (CPE) experiments over a period of 1 h, as in Fig. 6, 7 and Table 2. Fig. 6 shows the total charge of bulk electrolysis of 5.36  $\mu M$  of complex 1, 2 and 3 separately in DMF solutions in the presence of acetic acid (24 mM). At an applied potential of  $-1.5 V$  versus  $Fc/Fc^+$ , the maximum charge reached during 1 hour of electrolysis is 0.73 C for complex 1, 0.51 C for complex 2 and 0.44 C for complex 3, accompanied by gas bubbles appearing on the electrode (Fig. S24, ESI<sup>†</sup>).

However, when the CPE experiments were done with 5.36  $\mu M$  of complexes 1, 2 and 3 separately in DMF solutions in the presence of trifluoroacetic acid (24 mM), the same trend was obtained (Fig. 7). At an applied potential of  $-1.50 V$  versus  $Fc/Fc^+$ , the maximum charge reached 1.41 C for complex 1, 0.61 C for complex 2 and 0.49 C for complex 3 during 1 hour of electrolysis. CPE experiments under the same potential with a catalyst-free solution gave only a charge of 0.11 C, showing that complex 1 is again more effective than the remaining two complexes in hydrogen production under such conditions. This study suggests that all these three complexes are capable of catalysing the reduction of protons from acid to  $H_2$ . The



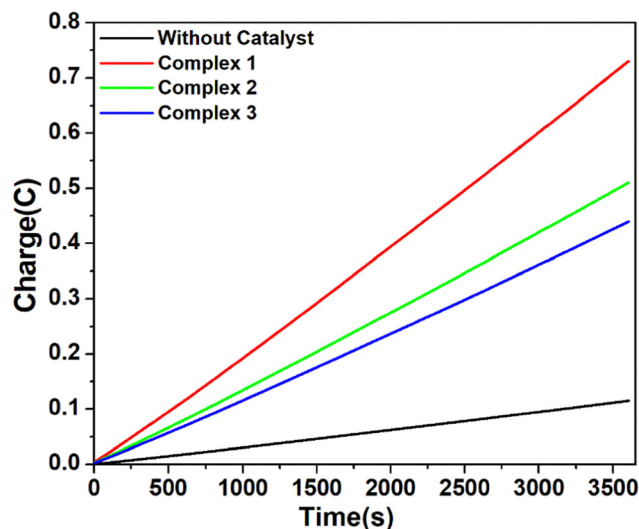


Fig. 6 Charge build up vs. time plots in the CPE (controlled potential electrolysis) experiment of complex **1** (red), complex **2** (green), and complex **3** (blue) and without catalyst (black) at potential  $-1.5$  V versus  $\text{Fc}/\text{Fc}^+$ . Conditions:  $5.36 \mu\text{M}$  complex in air-free DMF with  $0.1$  M  $[n\text{-Bu}_4\text{N}]\text{Br}$  as the supporting electrolyte and  $24$  mM  $\text{CH}_3\text{COOH}$  as the proton source.

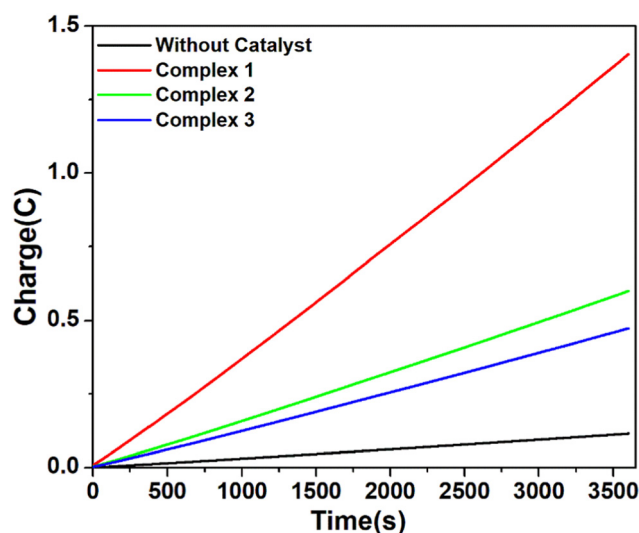


Fig. 7 Charge build up vs. time plots in the CPE (controlled potential electrolysis) experiment of complex **1** (red), complex **2** (green), and complex **3** (blue) and without catalyst (black) at potential  $-1.5$  V versus  $\text{Fc}/\text{Fc}^+$ . Conditions:  $5.36 \mu\text{M}$  complex in air-free DMF with  $0.1$  M  $[n\text{-Bu}_4\text{N}]\text{Br}$  as the supporting electrolyte and  $24$  mM  $\text{CF}_3\text{COOH}$  as the proton source.

evolution of  $\text{H}_2$  gas has been confirmed by the use of gas chromatography (Fig. S25, ESI $^\dagger$ ). The turn over number (TON) and faradaic efficiency were calculated for all the complexes (Tables S5 and S6, ESI $^\dagger$ ), and the result of CPE experiments is enlisted in Table 2.

The turnover frequency (TOF) for hydrogen evolution using all the three complexes **1**, **2** and **3** as electrocatalysts was estimated by the foot-of-the-wave analysis (FOWA).<sup>38</sup> The FOWA

Table 2 Results of CPE experiments with complexes **1**, **2** and **3**

Complex	Solvent	Proton source	$q$ (C)	$n$ ( $\times 10^{-6}$ )	TON	TOF ( $\text{s}^{-1}$ )	Faradaic efficiency (%)
1	DMF	Acetic acid	0.62	3.21	23.95	251.25	67.56
2			0.40	2.07	15.45	133.75	48.64
3			0.33	1.71	12.76	92.92	41.35
1	Trifluoroacetic acid	Trifluoroacetic acid	1.30	6.74	50.30	426.67	81.78
2			0.50	2.59	19.33	188.75	61.41
3			0.38	1.97	14.70	126.67	59.58

has been considered near the foot of the catalytic wave, where the catalytic wave does not get affected much by phenomena such as substrate consumption, diffusion and shape of CV dominated mainly by catalytic phenomenon.<sup>39</sup> The  $i_{\text{cat}}/i_{\text{p}}$  was plotted against  $1/(1 + \exp[(F/RT)(E - E_{1/2}]])$  for both the complexes, as given in Fig. S26 and S27 (ESI $^\dagger$ ), and the obtained TOF values are presented in Table S5 (ESI $^\dagger$ ).

**Determination of the reaction mechanism of HERs by the Tafel analysis.** The Tafel analysis is generally employed to understand the catalytic kinetics of hydrogen evolution reactions (Fig. 8). The Tafel slope is regarded as an inherent property of electrocatalyst and is evaluated by the rate limiting step for HERs. Its analysis is vital for enlightening the mechanism of the HER. According to the Tafel equation,

$$\eta = a + b \log i \quad (2)$$

where  $\eta$  = overpotential,  $a$  = constant,  $b$  = Tafel slope and  $i$  = measured current density.

A low  $\eta$  value corresponds to a large exchange current density ( $i_0$ , current density at  $\eta = 0$ ), whereas a low  $b$  value indicates better hydrogen evolution and hence a better catalytic activity.<sup>40</sup> In this case, the determined Tafel slopes for complex **1** are  $1.81$  V  $\text{dec}^{-1}$  and  $1.86$  V  $\text{dec}^{-1}$  for the acid sources trifluoroacetic acid and acetic acid, respectively indicating that trifluoroacetic acid will lead to a faster increase in reaction rate (fast proton discharge kinetics on the working electrode) with the increase in potential.

**Electrocatalytic hydrogen evolution: control experiments.** To confirm the role of these three nickel complexes in HERs and to ascertain the hydrogen evolution not due to the complex adsorbed on the surface or degradation products of the complex, different control experiments were conducted. First, blank CVs were recorded with  $\text{CH}_3\text{COOH}$  or  $\text{CF}_3\text{COOH}$  and without the addition of these complexes, showing a lower measurable current at potentials associated with hydrogen evolution (Fig. S28 and S29, ESI $^\dagger$ ). A series of CVs were obtained with complexes **1**, **2** and **3** in DMF with acid as the substrate to confirm the HER activity. Then, the glassy carbon working electrode was withdrawn from the solution and washed thoroughly with deionized water, but it was not polished. It is pertinent to mention that upon immersion of this electrode into a fresh set of acid solution and electrolyte, no catalytic current was observed on sweeping the potential in the cathodic region. This fact shows that the HER activity is neither due to the film of catalyst compound nor due to its degraded product,



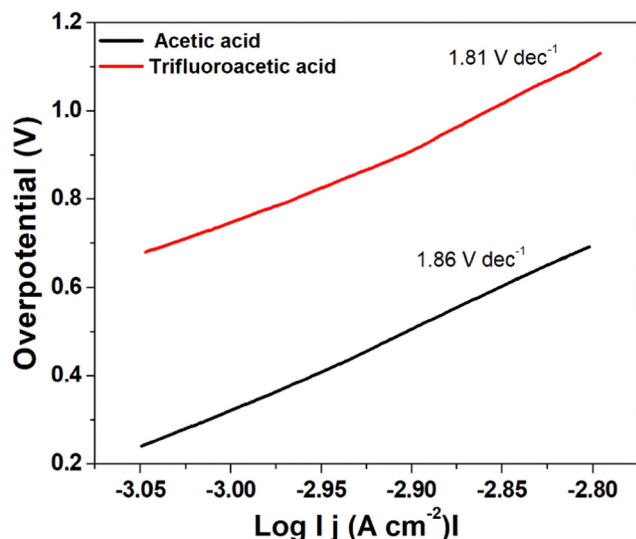


Fig. 8 Tafel plot for hydrogen evolution catalysed by complex **1** using trifluoroacetic acid (red line) and acetic acid (black line) as the acid source.

which could be strongly adsorbed onto the electrode surface. As shown in Fig. S30 (ESI<sup>†</sup>), the electrolysis did not show appearance of any new bands. These results indicate that complex **1** is stable during electrocatalysis for hydrogen production.

**Computational analysis of catalysts and intermediates by DFT-D4.** All the complexes were initially optimized by DFT-D4 analysis with def2-TZVP for metal center and def2-SVP for other atoms with the solvent model COSMO (water) and B3LYP.<sup>41</sup> The comparison of the bond length between the geometry optimized structure and X-ray analysis data has been tabulated in ESI<sup>†</sup> (Table S8). Theoretically calculated UV-vis spectra of complexes **1** and **2** are displayed in ESI<sup>†</sup> (Fig. S31).

Mechanistic pathways are reportedly known in the literature, based on different reports we propose the plausible mechanism, as depicted in Fig. S32a (ESI<sup>†</sup>). The pristine catalyst with the Ni(II) center reduced first to Ni(I), which then undergoes oxidative protonation to form a hydride complex {Ni(III)-H} (Tables S9–S20 for geometry optimized coordinates and summary of natural population analysis for complexes and intermediates, ESI<sup>†</sup>). As per the report of Cao *et al.*,<sup>42</sup> this Ni(III)-H hydride complex either reacts with a proton to produce H<sub>2</sub> and Ni(III) complex (heterolytic route), or is further reduced to Ni(II)-H. This Ni(II)-H can react with a proton to give Ni(II) and H<sub>2</sub>, or react with another Ni(II)-H to produce H<sub>2</sub> and 2 molecules of Ni(I) complex. Another way is that Ni(III)-H underwent bimolecular hydrolysis to produce H<sub>2</sub> and the original starting Ni(II) complex. It can be concluded that once the hydride complex is formed, it can liberate hydrogen, and by simultaneous reduction, it gets back to the initial catalyst to continue the cycle.<sup>42,43</sup> This suggests that the key intermediate is Ni(III)-H complexes in a mechanistic cycle of HER. In this work, we wanted to model those complexes and understand their geometries, which, on the one hand, helps to understand the present outcome and, on the other hand, can suggest better geometries for future development. Therefore, we took aid of DFT calculation that helps to understand an

interesting trend in dipole moment (Table S21, ESI<sup>†</sup>), where the highest value was obtained for complex **1**. Indeed, we hypothesize that one reason of showing better catalytic activity for complex **1** can be associated with a higher dipole moment that possibly helps in forming the hydride complex leading to catalysis.<sup>42–44</sup> To understand the geometry of the hydride intermediates, it was calculated at the level of B3LYP + COSMO(H<sub>2</sub>O) + def2TZVP(Ni) + def2-SVP(C,H,N,O) which reveals a distorted penta-coordination network for the Ni(III) centre in the complexes. Metal centres of catalysts (complexes **1**, **2** and **3**) comprise the HOMO density, whereas for hydride complexes the metal centres in LUMO comprise the density as obtained from the examined frontier molecular orbitals (Fig. S32b–d and ESI<sup>†</sup> for population analysis). Thus, from DFT calculations, we understood that shorter aliphatic substitution gives a higher dipole moment that could have an influence on higher catalytic activity. Another aspect that originates from the DFT calculation regarding future development is to keep an aromatic group at the end of the aliphatic chain for aromatic interaction with adjacent aromatic groups for complex **2**. As we observed for complex **2** and its hydride derivative, the aliphatic group is finally inclined towards the aromatic groups. However, for complexes **1** and **3**, such observation was not seen. This possibly suggests an optimum chain length for inclination, and here substitution with an aromatic group could give higher stability of the complex, eventually better catalytic activity.

## Conclusions

In summary, we have successfully synthesized three mononuclear nickel(II) complexes with similar N and O donor ligands and characterized them by various standard methods. These complexes have been found to be active electrocatalysts for hydrogen evolution reactions using acetic acid and trifluoroacetic acid as the substrates in DMF. The TOF values of these catalysts decrease with the increase in the chain length of the hydroxyalkyl group. The Ni(II) centre in these complexes is reduced to Ni(I) species and then converted into Ni(III)-hydride, which ultimately generates hydrogen and returns to the Ni(II) state. This possible mechanism has been supported by theoretical calculations. Thus, in this study, it has been demonstrated that the length of the alkyl side chain has significant effects on the catalytic ability in HERs and can be judiciously designed to get optimized efficiency.

## Author contributions

Arpita Barma: conceptualization, formal analysis, investigation, methodology; Malay Chakraborty: formal analysis, investigation; Swapan Kumar Bhattacharya: formal analysis, supervision, validation, writing – original draft; Pritam Ghosh: methodology, software, validation, writing – original draft; Partha Roy: conceptualization, resources, supervision, validation, writing – review & editing.



## Conflicts of interest

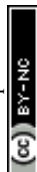
There are no conflicts to declare.

## Acknowledgements

AB wishes to thank CSIR, New Delhi for providing her a fellowship.

## References

- 1 J.-W. Wang, W.-J. Liu, D.-C. Zhong and T.-B. Lu, *Coord. Chem. Rev.*, 2019, **378**, 237–261.
- 2 (a) M. G. Pfeffer, T. Kowacs, M. Wächtler, J. Guthmüller, B. Dietzek, J. G. Vos and S. Rau, *Angew. Chem., Int. Ed.*, 2015, **54**, 6627–6631; (b) H. Ozawa, M.-A. Haga and K. Sakai, *J. Am. Chem. Soc.*, 2006, **128**, 4926–4927; (c) D. Liu, X. Li, S. Chen, H. Yan, C. Wang, C. Wu, Y. A. Haleem, S. Duan, J. Lu, B. Ge, P. M. Ajayan, Y. Luo, J. Jiang and L. Song, *Nat. Energy*, 2019, **4**, 512–518; (d) K. Zeng and D. K. Zhang, *Prog. Energy Combust. Sci.*, 2010, **36**, 307–326; (e) A. Lasia, Hydrogen evolution reaction, In *Handbook of Fuel Cells*, John Wiley & Sons, New York, 2010; (f) J. K. Nørskov, T. Bligaard, A. Logadottir, J. R. Kitchin, J. G. Chen, S. Pandelov and U. Stimming, *J. Electrochem. Soc.*, 2005, **152**, J23–J26; (g) J. Greeley, T. F. Jaramillo, J. Bonde, I. Chorkendorff and J. K. Nørskov, *Nat. Mater.*, 2006, **5**, 909–913.
- 3 (a) K. E. Dalle, J. Warnan, J. J. Leung, B. Reuillard, I. S. Karmel and E. Reisner, *Chem. Rev.*, 2019, **119**, 2752–2875; (b) L. Tong, L. Duan, A. Zhou and R. P. Thummel, *Coord. Chem. Rev.*, 2020, **402**, 213079.
- 4 T. Agarwal and S. Kaur-Ghumaan, *Coord. Chem. Rev.*, 2019, **39**, 88–219.
- 5 M. D. Sampson and C. P. Kubiak, *Inorg. Chem.*, 2015, **54**, 6674–6676.
- 6 (a) A. Z. Haddad, S. P. Cronin, M. S. Mashuta, R. M. Buchanan and C. A. Grapperhaus, *Inorg. Chem.*, 2017, **56**, 11254–11265; (b) P. Zhang, M. Wang, Y. Yang, T. Yao and L. Sun, *Angew. Chem., Int. Ed.*, 2014, **53**, 13803–13807.
- 7 (a) N. Queyriaux, D. Sun, J. Fize, J. Pécaut, M. J. Field, M. Chavarot-Kerlidou and V. Artero, *J. Am. Chem. Soc.*, 2020, **142**, 274–282; (b) T. Straistari, R. Hardré, J. Fize, S. Shova, M. Giorgi, M. Réglie, V. Artero and M. Orto, *Chem. Eur. J.*, 2018, **24**, 8779–8786; (c) N. Kaeffer, M. Chavarot-Kerlidou and V. Artero, *Acc. Chem. Res.*, 2015, **48**, 1286–1295.
- 8 (a) T. Fogeron, T. K. Todorova, J.-P. Porcher, M. Gomez-Mingot, L.-M. Chamoreau, C. Mellot-Draznieks, Y. Li and M. Fontecave, *Dalton Trans.*, 2019, **48**, 14653–14661; (b) Y.-P. Zhang, M. Zhang, X.-R. Chen, C. Lu, D. J. Young, Z.-G. Ren and J.-P. Lang, *Inorg. Chem.*, 2020, **59**, 1038–1045; (c) R. Shen, J. Xie, Q. Xiang, X. Chen, J. Jiang and X. Li, *Chin. J. Catal.*, 2019, **40**, 240–288; (d) D. Jana, H. K. Kolli, S. Sabnam and S. K. Das, *Chem. Commun.*, 2021, **57**, 9910–9913; (e) S. Sinha, G. N. Tran, H. Na and L. M. Mirica, *Chem. Commun.*, 2022, **58**, 1143–1146; (f) A. Cabrera-García, V. Blay, R. Blay-Roger, Á. G. Ravelo, J. González-Platas, M. C. Arévalo, J. Sanchiz and P. Martín-Zarza, *Chem. Eng. J.*, 2021, **420**, 130342.
- 9 (a) P. Bhanja, B. Mohanty, S. Chongdar, A. Bhaumik, B. K. Jena and S. Basu, *ACS Appl. Energy Mater.*, 2022, **5**, 3558–3567; (b) S. Bhattacharjee, S. Bera, R. Das, D. Chakraborty, A. Basu, P. Banerjee, S. Ghosh and A. Bhaumik, *ACS Appl. Mater. Interfaces*, 2022, **14**, 20907–20918; (c) H. Xu, H. Shang, C. Wang and Y. Du, *Coord. Chem. Rev.*, 2020, **418**, 213374; (d) J. Mohammed-Ibrahim and X. Sun, *J. Energy Chem.*, 2019, **34**, 111–160.
- 10 R. M. Bullock, A. M. Appel and M. L. Helm, *Chem. Commun.*, 2014, **50**, 3125–3143.
- 11 J. W. Morgan and E. Anders, *Proc. Natl. Acad. Sci. U. S. A.*, 1980, **77**, 6973–6977.
- 12 J. Fessler, J.-H. Jeoung and H. Dobbek, *Angew. Chem., Int. Ed.*, 2015, **54**, 8560–8564.
- 13 B. J. Fisher and R. Eisenberg, *J. Am. Chem. Soc.*, 1980, **102**, 7361–7363.
- 14 A. Zarkadoulas, M. J. Field, C. Papatriantafyllopoulou, J. Fize, V. Artero and C. A. Mitsopoulou, *Inorg. Chem.*, 2016, **55**, 432–444.
- 15 M. L. Helm, M. P. Stewart, R. M. Bullock, M. R. DuBois and D. L. DuBois, *Science*, 2011, **333**, 863–866.
- 16 G. Bergamini and M. Natali, *Dalton Trans.*, 2019, **48**, 14653–14661.
- 17 A. Das, Z. Han, W. W. Brennessel, P. L. Holland and R. Eisenberg, *ACS Catal.*, 2015, **5**, 1397–1406.
- 18 H. Shao, S. K. Muduli, P. D. Tran and H. S. Soo, *Chem. Commun.*, 2016, **52**, 2948–2951.
- 19 X. Li, Ho, H. Shao, Y. Y. Ng, R. Ganguly, Y. Lu and H. S. Soo, *Inorg. Chem.*, 2019, **58**, 1469–1480.
- 20 APEX-II, SAINT and SADABS, Bruker AXS Inc., Madison, WI, 2008.
- 21 G. M. Sheldrick, *Acta Crystallogr.*, 2015, **A71**, 3–8.
- 22 G. M. Sheldrick, *Acta Crystallogr.*, 2015, **C71**, 3–8.
- 23 L. Yang, D. R. Powell and R. P. Houser, *Dalton Trans.*, 2007, 955–964.
- 24 (a) S. Halder, J. Mondal, J. Ortega-Castro, A. Frontera and P. Roy, *Dalton Trans.*, 2017, **46**, 1943–1950; (b) A. Bhattacharjee, S. Dey and P. Roy, *Inorg. Chim. Acta*, 2019, **490**, 93–103.
- 25 D. L. Pavia, G. M. Lampman, G. S. Kriz and J. R. Vyvyan, *Introduction to spectroscopy*, Cengage Learning, Stamford, USA, 5th edn, 2015.
- 26 (a) M. F. Mehrjardi, H. Kargar, R. B.-Ardakani, M. Ashfaq, K. S. Munawar and M. N. Tahir, *J. Mol. Struct.*, 2022, **1251**, 132037; (b) G. R. Reddy, S. Balasubramanian and K. Chennakesavulu, *J. Mater. Chem. A*, 2014, **2**, 15598–15610; (c) A. D. Khalaji, M. Nikookar and D. Das, *J. Therm. Anal. Calorim.*, 2014, **115**, 409–417; (d) S. N. Shukla, P. Gaur, M. L. Raidas and B. Chaurasia, *J. Mol. Struct.*, 2020, **1202**, 127362; (e) H. Kargr, A. A. Ardakani, M. N. Tahir, M. Ashfaq and K. S. Munawar, *J. Mol. Struct.*, 2021, 129842.
- 27 (a) S. Chattopadhyay, M. S. Ray, S. Chaudhuri, G. Mukhopadhyay, G. Bocelli, A. Cantoni and A. Ghosh,



- Inorg. Chem. Acta*, 2006, **359**, 1367–1375; (b) M. S. Ray, S. Chaudhuri, L. Right, G. Bocelli, G. Mukhopadhyay and A. Ghosh, *Polyhedron*, 2003, **22**, 617–624.
- 28 (a) B. S. Garg and D. N. Kumar, *Spectrochim. Acta, Part A*, 2003, **59**, 229–234; (b) A. Anthonysamy and S. Balasubramanian, *Inorg. Chem. Commun.*, 2005, **8**, 908–911.
- 29 (a) M. Salehi, F. Rahimifar, M. Kubicki and A. Asadi, *Inorg. Chim. Acta*, 2016, **443**, 28–35; (b) A. Barma, D. Ghosh, P. Karmakar and P. Roy, *J. Mol. Struct.*, 2022, **1250**, 131687.
- 30 A. Ourari, Y. Ouennoughi, D. Aggoun, M. S. Mubarak, E. M. Pasciak and D. G. Peters, *Polyhedron*, 2014, **67**, 59–64.
- 31 L.-Q. Chai, H.-S. Zhang, J.-J. Huang and Y.-L. Zhang, *Spectrochim. Acta, Part A*, 2015, **137**, 661–669.
- 32 J. Datta, S. Bhattacharya and K. K. Kundu, *Aust. J. Chem.*, 1983, **36**, 1779–1784.
- 33 C. Chen, X. Li, F. Deng and J. Li, *RSC Adv.*, 2016, **6**, 79894–79899.
- 34 T. D. Cook, S. F. Tyler, C. M. McGuire, M. Zeller, P. E. Fanwick, D. H. Evans, D. G. Peters and T. Ren, *ACS Omega*, 2017, **2**, 3966–3976.
- 35 V. Fourmond, P.-A. Jacques, M. Fontecave and V. Artero, *Inorg. Chem.*, 2010, **49**, 10338–10347.
- 36 (a) V. Fourmond, S. Canaguier, B. Golly, M. J. Field, M. Fontecave and V. Artero, *Energy Environ. Sci.*, 2011, **4**, 2417–2427; (b) G. A. N. Felton, R. S. Glass, D. L. Lichtenberger and D. H. Evans, *Inorg. Chem.*, 2006, **45**, 9181–9184.
- 37 (a) J.-P. Cao, T. Fang, L.-Z. Fu, L.-L. Zhou and S. Zhan, *Int. J. Hydrogen Energy*, 2014, **39**, 10980–10986; (b) R. Jain, A. A. Mamun, R. M. Buchanan, P. M. Kozlowski and C. A. Grapperhaus, *Inorg. Chem.*, 2018, **57**, 13486–13493; (c) G. Bergamini and M. Natali, *Dalton Trans.*, 2019, **48**, 14653–14661; (d) Y.-P. Zhang, M. Zhang, X.-R. Chen, C. Lu, D. J. Young, Z.-G. Ren and J.-P. Lang, *Inorg. Chem.*, 2020, **59**, 1038–1045; (e) J.-M. Lei, S.-P. Luo and S.-Z. Zhan, *Int. J. Hydrogen Energy*, 2018, **43**, 19047–19056; (f) Q.-X. Peng, D. Xue, S.-Z. Zhan and C.-L. Ni, *Appl. Catal. B*, 2017, **219**, 353–361; (g) L. Chen, G. Chen, C.-F. Leung, S.-M. Yiu, C.-C. Ko, E. A. Mallart, M. Robert and T.-C. Lau, *ACS Catal.*, 2015, **5**, 356–364.
- 38 (a) C. Costentin, S. Drouet, M. Robert and J.-M. Saveant, *J. Am. Chem. Soc.*, 2012, **134**, 11235–11242; (b) C. Costentin, M. Robert and J.-M. Saveant, *Chem. Soc. Rev.*, 2013, **42**, 2423–2436; (c) C. Costentin and J.-M. Saveant, *ChemElectroChem*, 2014, **1**, 1226–1236; (d) R. J. DiRisio, J. E. Armstrong, M. A. Frank, W. R. Lake and W. R. McNamara, *Dalton Trans.*, 2017, **46**, 10418–10425.
- 39 N. Elgrishi, M. B. Chambers and M. Fontecave, *Chem. Sci.*, 2015, **6**, 2522–2531.
- 40 (a) V. S. Thoi, Y. Sun, J. R. Long and C. J. Chang, *Chem. Soc. Rev.*, 2013, **42**, 2388–2400; (b) M. Zeng and Y. Li, *J. Mater. Chem. A*, 2015, **3**, 14942–14962; (c) X. Zou and Y. Zhang, *Chem. Soc. Rev.*, 2015, **44**, 5148–5180.
- 41 (a) *TURBOMOLE, Version 7.3, a development*, University of Karlsruhe and Forschungszentrum Karlsruhe GmbH, 1989–2007; (b) E. Caldeweyher, C. Bannwarth and S. Grimme, *J. Chem. Phys.*, 2017, **147**, 034112.
- 42 Y. Han, H. Fang, H. Jing, H. Sun, H. Lei, W. Lai and R. Cao, *Angew. Chem., Int. Ed.*, 2016, **55**, 5457–5462.
- 43 K. Majee, J. Patel, S. Rai, B. Das, B. Panda and S. K. Padhi, *Phys. Chem. Chem. Phys.*, 2016, **18**, 21640–21650.
- 44 N. Villegas-Escobar, D. E. Ortega, D. Cortes-Arriagada, R. Duran, D. Yepes, S. Gutierrez-Oliva and A. Toro-Labbe, *J. Phys. Chem. C*, 2017, **121**, 12127–12135.

